

Combining Experiment and DFT to Study New Reactions

Ryan G. Epton

PhD

University of York

Chemistry

September 2022

Abstract

This thesis describes the use of density functional theory (DFT) to better understand chemical methods developed within the Unsworth and Lynam groups. Chapter 1 provides a summary of the theory underpinning computational chemistry and reviews the use of DFT to study gold(I)-catalysed reactions.

In Chapter 2, an established method for the rearrangement of spirocyclic indolenines into quinolines under acidic conditions with heating is described. The rearrangement was further explored using basic conditions, where it was found that mild conditions can be used. The mechanism was studied using DFT to compare both conditions, where it was proposed that keto-enol tautomerism under acidic conditions is rate-limiting.

In Chapter 3, the gold(I)-catalysed formation of 3-vinyl indole species was achieved using ynones. DFT was used to study the mechanisms of indole vinylation and *bis*indole formation, where it was found that ynones hinder the further addition of indole to the products. The speciation of the gold(I) complexes was studied using DFT and NMR spectroscopy, where a substituent dependence of the ynone was identified, and a gold(I)-pyrylium complex was characterised.

In Chapter 4, DFT calculations that can be used to predict the viability of successive ring expansion (SuRE) reactions are described. DFT methodologies were benchmarked which demonstrated that the B3LYP/6-31G* level of theory can be recommended as the optimum method for modelling SuRE reactions. This method was then used to aid in the development of further SuRE reactions.

In Chapter 5, a method for the acylation of lactams is described, *via* the intramolecular acyl migration of a nearby thioester moiety. DFT calculations aided in the development of the reaction, where it was predicted that the acyl-migrated intermediate would need to be trapped. The approach was validated with the use of ynones to trap the intermediate, and a successful SuRE reaction using this method, is described within.

Table of Contents

Abstract.....	ii
Table of Contents.....	iii
List of Tables	vii
List of Figures	x
Acknowledgements.....	xxvi
Author Declaration.....	xxvii
Abbreviations.....	xxviii
Chapter 1. Introduction	1
1.1 Computational Theory	1
1.1.1 Introduction	1
1.1.2 The Schrödinger Equation.....	1
1.1.3 The many-body Schrödinger Equation and the Hartree method	6
1.1.4 Electron spin and Hartree–Fock Theory.....	8
1.1.5 Density Functional Theory	11
1.1.6 Approximate Exchange–Correlation Functionals	13
1.1.7 Molecular Orbitals and Basis Sets.....	15
1.1.8 DFT Calculation Procedure.....	20
1.1.9 Frequency Calculations and Thermodynamic Corrections	24
1.1.10 Solvent Corrections.....	28
1.1.11 Dispersion Corrections.....	29
1.1.12 Summary	31
1.2 DFT studies of Au(I) catalysed reactions: anion effects and reaction selectivity.....	33
1.2.1 Introduction	33
1.2.2 Using DFT to explain the effects of the anion on the reaction mechanism.....	34
1.2.3 Using DFT to explore the regioselectivity and coordination in gold(I) catalysis	48
1.2.4 Summary	71
1.3 Project Aims and Thesis Structure	73
Chapter 2. Synthetic and Mechanistic Studies into the Rearrangement of Spirocyclic Indolenines into Quinolines	74
2.1 Introduction	74
2.1.1 Quinolines	74
2.1.2 Rearrangement of spirocyclic indolenines to quinolines.....	75
2.1.3 Project aims.....	77

2.2 Synthetic and Mechanistic Studies into the Rearrangement of Spirocyclic Indolenines into Quinolines.....	79
2.2.1 Starting Material Synthesis	79
2.2.2 Temperature Screening	83
2.2.3 Substrate Scope	85
2.2.4 DFT Calculations.....	88
2.2.5 Concluding Remarks.....	99
Chapter 3. Selectivity, Speciation, and Substrate Control in the Gold-Catalysed Coupling of Indoles and Alkynes	100
3.1 Introduction	100
3.1.1 3-vinylindoles	100
3.1.2 Gold-catalysed synthesis of 3-vinylindoles	101
3.1.3 Mechanism of <i>bis</i> aryl formation.....	104
3.1.4 Intramolecular indole-ynone coupling.....	108
3.1.5 Project aims.....	111
3.2 Coupling Reaction Development	113
3.2.1 Starting material synthesis.....	113
3.2.2 Reaction Optimisation	116
3.2.3 C-3 Vinylation substrate scope	120
3.2.4 C-2 Vinylation.....	127
3.3 Vinyl Indole Mechanistic Studies	132
3.3.1 Indole/Ynone coupling summary.....	132
3.3.2 Gold(I) coordination.....	132
3.3.3 Indole vinylation mechanism.....	139
3.3.4 <i>bis</i> -Indole formation	145
3.4 Ynone Gold(I) Speciation.....	148
3.4.1 Ketone versus alkyne gold(I) coordination	148
3.4.2 Ynone coordination.....	151
3.4.3 Ynone dimerisation	154
3.4.4 Pyrylium complex reactivity.....	161
3.5 Concluding Remarks.....	164
Chapter 4. Successive Ring Expansion (SuRE)	165
4.1 Introduction	165
4.1.1 Medium-sized rings and macrocycles.....	165
4.1.2 Synthesis of medium-sized rings and macrocycles.....	166

4.1.3 Ring Expansion Reactions	168
4.1.4 Use of DFT calculations to study Ring Expansion reactions.....	174
4.1.5 Successive Ring Expansions (SuRE)	179
4.1.6 SuRE DFT Calculations.....	183
4.2 Evaluating the viability of Successive Ring Expansions.....	186
4.2.1 Scope of the study	186
4.2.2 Lactam and α -amino acid expansion ring-size dependence.....	187
4.2.3 Further Scope.....	197
4.2.4 Thiolactone SuRE Viability.....	203
4.2.5 Dihydroxylation Ring Expansions	208
4.2.6 Concluding Remarks.....	211
Chapter 5. Acyl Transfer SuRE.....	213
5.1 Introduction and Previous Work.....	213
5.2 DFT Calculations.....	216
5.3 Starting Material Synthesis	219
5.4 Acyl-Transfer Studies	225
5.4.1 Studies using acid chloride trapping	225
5.4.2 Studies using Michael acceptors for trapping.....	229
5.4.3 Optimisation of acyl migration/ynone trapping reaction	233
5.4.4 Nucleophile-tethered acyl migration/ynone trapping.....	236
5.4.5 Future Work	241
5.4.6 Concluding Remarks.....	242
Chapter 6. Conclusions	245
Chapter 7. Experimental Data.....	251
7.1 General Methods	251
7.1.1 General Experimental Procedure.....	251
7.1.2 General Computational Information	252
7.1.3 Computational Procedure for the Quinoline Rearrangement Studies (Chapter 2) .	253
7.1.4 Computational Procedure for the Indole Vinylation and Gold(I) Speciation Studies (Chapter 3)	255
7.1.5 Computational Procedure for Evaluating the Viability of SuRE Reactions (Chapter 4)	256
7.1.6 Computational Procedure for the Acyl Transfer Studies (Chapter 5).....	258
7.2 Quinoline Rearrangement.....	259
7.2.1 General Procedures	259

7.2.2 Weinreb Amide Products	262
7.2.3 Indolyl-ynone Products	266
7.2.4 Spirocyclic Indolenine Products	271
7.2.5 Quinoline Products	279
7.3 Indole Vinylation	291
7.3.1 General Procedures	291
7.3.2 Alkyne Synthesis.....	292
7.3.3 N-alkylated Indole Synthesis.....	302
7.3.4 Vinylated-indole Products.....	305
7.3.5 Gold-pyrylium Complex	331
7.4 S-Acyl Transfer	334
7.4.1 General Procedures	334
7.4.1 Lactam Synthesis.....	335
7.4.2 Michael Acceptor Synthesis	345
7.4.3 Thiol Coupling	347
7.4.4 Michael Acceptor Screening	352
7.4.5 Acyl Transfer Products	355
References	367
Appendices.....	390
Paper 1 – Internal Nucleophilic Catalyst Mediated Cyclisation/Ring Expansion Cascades for the Synthesis of Medium-Sized Lactones and Lactams	390
Paper 2 – Synthetic and Mechanistic Studies into the Rearrangement of Spirocyclic Indolenines into Quinolines	396
Paper 3 – Visible-light-induced intramolecular charge transfer in the radical spirocyclisation of indole-tethered ynones.	405
Paper 4 – Evaluating the Viability of Successive Ring-Expansions Based on Amino Acid and Hydroxyacid Side-Chain Insertion	413
Paper 5 – Synthesis of macrocyclic and medium-sized ring thiolactones <i>via</i> the ring expansion of lactams	423
Paper 6 – Indole-ynones as Privileged Substrates for Radical Dearomatizing Spirocyclization Cascades	431
Paper 7 – Selectivity, Speciation, and Substrate Control in the Gold-Catalyzed Coupling of Indoles and Alkynes	438
Paper 8 – DFT Studies of Au(I) Catalysed Reactions: Anion Effects and Reaction Selectivity	449

List of Tables

Table 1. Scaling factors of common computational methods, where N is the size of the system. Note that whilst DFT scales to N^3 , the overall calculation time might be longer than the equivalent HF calculation.....	31
Table 2. NHCAuX catalysed Meyer–Schuster rearrangement of 1-phenyl-2-propyn-1-ol 1.5 to cinnamaldehyde 1.6 at 50 °C.	39
Table 3. Transition state energies for Markovnikov (ΔG_M^\ddagger) and anti-Markovnikov (ΔG_{aM}^\ddagger) addition of 1.14 catalysed by (L1)Au ⁺ , and geometrical parameters for the initial $\eta^2(\pi)$ -alkene gold(I) complexes. All data were computed at the M06/6-31G(d,p)&SDD(f) level of theory....	51
Table 4. DFT-calculated energies for the key transition states and intermediates of the gold-catalysed transposition reaction of ynones with different additives. Energies are Gibbs energies at the TPSS-D3/def2-TZVP//TPSS-D3/def2-SVP level of theory with COSMO solvent correction in CH ₂ Cl ₂	59
Table 5. Temperature scope of the rearrangement of spirocyclic indolenine 2.7a into quinoline 2.8a in acidic conditions.....	84
Table 6. Temperature scope of the rearrangement of spirocyclic indolenine 2.7a into quinoline 2.8a in basic conditions.....	85
Table 7. DFT-calculated energies of the basic pathway PES (referring to Figure 63), at various levels of theory. Energies are Gibbs energies at 298.15 K in kJ·mol ⁻¹ at various levels of theory, with PCM solvent correction in THF.	93
Table 8. Optimisation of the metal-catalysed intermolecular reaction of indole 3.16 with ynone 3.27	118
Table 9. Isodesmic reaction used to compare $\eta^1(O)$ and $\eta^2(\pi)$ coordinated isomers of substituted alkynes. Energies are Gibbs energies at 298.15 K at the D3(BJ)-PBE0/def2-TZVPP//BP86/SV(P) level of theory with COSMO solvation in CH ₂ Cl ₂	149
Table 10. DFT-calculated pathway for the dimerisation of different ynones and gold(I) cations. Energies are Gibbs energies at 298.15 K in kJ mol ⁻¹ at the D3(BJ)-PBE0/def2-TZVPP//BP86/SV(P) level of theory with COSMO solvent correction in CH ₂ Cl ₂	160

Table 11. DFT-calculated relative energies for the ring expansion of lactams using amino acids. Energies are Gibbs energies calculated at the M06-2X/6-31+G** level of theory. Where used, solvent corrections were applied using an SMD model in acetonitrile. R = <i>p</i> -NO ₂ -Bn.	176
Table 12. DFT-calculated energies for the isomers in the HIRE reaction. Energies are Gibbs energies at the B3LYP/6-31G* level of theory with solvent correction in water.	179
Table 13. DFT-calculated relative difference in Gibbs energy at 298.15 K at the B3LYP/6-31G* level of theory in a vacuum.....	184
Table 14. DFT-calculated relative difference for the α -amino acid lactam ring expansions series. All energies are Gibbs energy at 298.15 K at the B3LYP/6-31G* level of theory in a vacuum. Calculated by Dr Lawer.	188
Table 15. DFT-calculated relative difference for the α -amino acid lactam ring expansions (4.124–4.127) using either Spartan or Gaussian. All energies are Gibbs energy at 298.15 K at the B3LYP/6-31G* level of theory in a vacuum. Spartan calculations performed by Dr Lawer.	190
Table 16. DFT-calculated relative difference for the α -amino acid lactam ring expansions (4.124–4.127) with differing functionals. All energies are Gibbs energy at 298.15 K using the 6-31G* basis set in a vacuum.....	191
Table 17. DFT-calculated relative difference for the α -amino acid lactam ring expansions (4.124–4.127). All energies are Gibbs energy at 298.15 K using the 6-31G*. Where used, solvent corrections were applied using a PCM model with DCM as the solvent.	193
Table 18. DFT-calculated relative difference for the α -amino acid lactam ring expansions (4.124–4.127). All energies are Gibbs energy at 298.15 K using the 6-31G*. Where used, solvent corrections were applied using a PCM with DCM as the solvent. Dispersion corrections were applied using the D3(BJ) method.....	195
Table 19. DFT calculated relative energies for the SuRE reaction of cyclic β -ketoesters (Figure 153). Energies are Gibbs energies at 298.15 K at the given level of theory. Solvent corrections were applied for the M06-2X/6-31G* calculations using a PCM model in dichloromethane for 4.129–4.131 and chloroform for 4.132 and 4.133 . B3LYP calculations performed by Dr Lawer.	199
Table 20. DFT calculated relative energies for the SuRE reaction in Figure 154. Energies are Gibbs energies at 298.15 K at the given level of theory. Solvent corrections were applied for	

the M06-2X/6-31G* calculations using a PCM model in dichloromethane or chloroform as appropriate. B3LYP calculations performed by Dr Lawer.....	202
Table 21. DFT-calculated relative energy difference for the 4-atom thiolactone ring expansions (4.160–4.163). All energies are Gibbs energy at 298.15 K at the B3LYP/6-31G* level of theory in a vacuum.....	204
Table 22. DFT-calculated relative energy difference for the 3-atom thiolactone ring expansions (4.176 and 4.177). All energies are Gibbs energy at 298.15 K at the B3LYP/6-31G* level of theory in a vacuum.	207
Table 23. DFT-calculated relative energy difference for the 3- and 4-atom dihydroxylation CARE ring expansions (4.185–4.187). All energies are Gibbs energy at 298.15 K at the B3LYP/6-31G* level of theory in a vacuum.....	210
Table 24. DFT-calculated energies for $X \rightarrow N$ acyl migration. Energies are Gibbs energies at 298.15 K at the B3LYP/6-31G* level of theory in a vacuum.	217
Table 25. DFT-calculated energies for $X \rightarrow N$ -acyl migration under basic conditions. Energies are Gibbs energies at 298.15 K at the B3LYP/6-31+G* level of theory in a vacuum.....	218
Table 26. Reaction optimisation for the acyl transfer/ynone trapping reaction of thioester 5.41 . Reactions were performed on a 0.2 mmol scale, and after 18 hours, 100 μ L of a 0.2 M solution of trimethoxybenzene in DCM was added before the reaction was concentrated and a ^1H NMR spectrum recorded. Anhydrous THF, MeCN and DMF were used, and those reactions were performed under an argon atmosphere.....	235

List of Figures

Figure 1. Representation of the Rutherford model of an atom.....	2
Figure 2. Representation of the Bohr model of the atom.	2
Figure 3. Representation of polar spherical coordinates.....	5
Figure 4. Diagrammatic representation of the diatomic molecule with two electrons (<i>e.g.</i> H ₂). 6	
Figure 5. Representation of two 1s orbitals combining a) constructively and b) destructively. 16	
Figure 6. Representation of squared wavefunctions for bonding (left) and anti-bonding (right) orbitals.	16
Figure 7. A representation of the 1s STO and GTO orbitals. The image was produced using an Excel program provided by Magalhães. ⁴⁵	18
Figure 8. A representation of the 1s, using 3 GTO's (STO-3G). The image was produced using an Excel program provided by Magalhães. ⁴⁵	19
Figure 9. Representation of the DFT calculation procedure. Modified from a diagram produced by Cramer. ³	23
Figure 10. Representation of the harmonic oscillator model.....	24
Figure 11. Visual representation of the cavity built during the PCM and COSMO solvent models.	29
Figure 12. Typical scheme for alkyne activation by gold(I) cations.	33
Figure 13. 4-Me-styryl gold(I) complexes studied by Zuccaccia <i>et al.</i> ¹²⁸	35
Figure 14. Low temperature ¹⁹ F, ¹ H-HOESY spectra of 1.44PPh₃ (left) and 1.4NHC (right). Key ion-pairing contacts have been highlighted with assignments made by Zuccaccia <i>et al.</i> Reprinted with permission from American Chemical Society, Copyright 2009. ¹²⁸	36
Figure 15. Lowest energy arrangements of 1.4PPh₃ (left) and 1.4NHC (right) as calculated by DFT by Zuccaccia <i>et al.</i> , calculated at the BLYP/ZORA/TZ2P level of theory. Structures reproduced using coordinates located in the original paper's ESI. ¹²⁸	37
Figure 16. Side (left) and back (right) views of the DFT calculated structures of 1.4PPh₃ (top) and 1.4NHC (bottom), without counterion. Coulomb potential is mapped on an electronic isodensity surface ($\rho = 0.007 \text{ e}/\text{\AA}^3$. Coulomb potential in au). Reprinted with permission from American Chemical Society, Copyright 2009. ¹²⁸	37

Figure 17. Proposed intermediate structures calculated for the formation of $\eta^2(\pi)$ -alkyne complex 1.B from the uncoordinated species 1.5 and 1.7	40
Figure 18. σ -Bonded gold alkynyl complex 1.8 with the formation of acid 1.9 , calculated by DFT when trifluoroacetate was the counterion.....	40
Figure 19. Intermediates studied in the Meyer–Schuster rearrangement of 1.5 . X = OTs, OTf or BF ₄ . A simplified NHC was used in the calculations (R = Me).	41
Figure 20. DFT-calculated transition state structure for the Meyer–Schuster rearrangement, in which γ -valerolactone is modelled coordinating to the hydroxyl group. Structures reproduced using coordinates located in the original paper’s ESI.	42
Figure 21. a) Reaction studied by Ma <i>et al.</i> , ¹³⁵ the cyclisation of propargylic amide 1.10 , resulting in methylene-3-oxazoline 1.11 , first reported by Hashmi <i>et al.</i> and then used as a standard reaction when comparing different NHC ligands. ^{135–138} b) Mechanism proposed by Hashmi <i>et al.</i> for the formation of 1.11 . ^{136–138}	43
Figure 22. DFT-calculated structures at the SMD(CHCl ₃)-PBE0-D3BJ/def2-TZVP,6-311+G(d,p)//PBE0-D3BJ/ SDD,6-31G(d) level of theory. Energies are Gibbs energies in kcal mol ⁻¹ . [Au] = IPrAu ⁺ . a) Preferred configuration of gold(I)-coordination to 1.10 . b) Other calculated configurations of higher energy. [a] States resulting from loss of HNTf ₂ from 1.I	44
Figure 23. DFT-calculated energies for the transition states of 5- <i>exo-dig</i> (1.L) and 6- <i>endo-dig</i> (1.M) cyclisations of 1.H . Energies are Gibbs energies at the SMD(CHCl ₃)-PBE0-D3BJ/def2-TZVP,6-311+G(d,p)//PBE0-D3BJ/ SDD,6-31G(d) level of theory in kcal mol ⁻¹ with G as the reference point. [Au] = IPrAu ⁺ . PMP = <i>p</i> -methoxyphenyl.....	44
Figure 24. DFT-calculated structures at the SMD(CHCl ₃)-PBE0-D3BJ/def2-TZVP,6-311+G(d,p)//PBE0-D3BJ/ SDD,6-31G(d) level of theory. Energies are Gibbs energies in kcal mol ⁻¹ . [Au] = IPrAu ⁺ . a) Ion-separated-coordination of Au(I) to 1.10 . b) Transition states energies of 5- <i>exo-dig</i> (1.O) and 6- <i>endo-dig</i> (1.P) cyclisations of 1.N	45
Figure 25. DFT-calculated structures at the SMD(CHCl ₃)-PBE0-D3BJ/def2-TZVP,6-311+G(d,p)//PBE0-D3BJ/ SDD,6-31G(d) level of theory. Energies are Gibbs energies in kcal mol ⁻¹ . [Au] = IPrAu ⁺ . Energies of the intermediate gold(I)-oxazoline species, before and after the removal of triflimide.	45

Figure 26. DFT-calculated pathway for oxazoline-assisted proton-migration of 1.Q . Energies are Gibbs energies at the SMD(CHCl ₃)-PBE0-D3BJ/def2-TZVP,6-311+G(d,p)//PBE0-D3BJ/SDD,6-31G(d) level of theory in kcal mol ⁻¹ . [Au] = IPrAu ⁺	46
Figure 27. Catalytic cycle proposed by Ma <i>et al.</i> for propargylic amide cyclisation. The anion plays a role in the reaction process throughout.	47
Figure 28. Gold(I)-catalysed hydroamination of ACP derivatives 1.13 with 1-methylimidazolidin-2-one 1.14 as reported by Timmerman <i>et al.</i> ¹⁴¹	48
Figure 29. DFT-calculated transition state energies for Markovnikov and anti-Markovnikov addition into gold(I)-coordinated ACP 1.U . Energies are Gibbs energies in kcal mol ⁻¹ at 298 K, calculated at the M06/6-31G(d,p)&SDD(f) level of theory with SMD solvent correction in 1,4-dioxane.	49
Figure 30. Plot of the difference in transition state energy between Markovnikov and anti-Markovnikov addition ($\Delta\Delta G^\ddagger$) against the difference in distance of the gold centre from the terminal (d_1) and internal (d_2) carbons. Values refer to the entries in Table 3. Adapted with permission from American Chemical Society, Copyright 2019. ¹⁴²	52
Figure 31. Proposed 6- <i>exo</i> and 7- <i>endo</i> cyclisations of β -yne furan derivative 1.19	53
Figure 32. Synthesis of cyclohexafuran 1.20 as reported by Menon <i>et al.</i> in their total synthesis of furansesquiterpenes. ¹⁵² b) Optimised conditions for the 7- <i>endo</i> -dig cyclisation of β -yne furan 1.21	53
Figure 33. DFT-calculated energies for 6- <i>exo</i> and 7- <i>endo</i> cyclisation of β -yne furans. Energies are Gibbs energies at 298 K in kcal mol ⁻¹ at the B3LYP/SDD-6-31G(d) level of theory. Calculated NPA charges for the alkyne carbons of 1.X are given. L = PMe ₃	54
Figure 34. Additional reactions to explore the substrate scope following the DFT analysis.	55
Figure 35. Gold-catalysed transposition reaction of ynone 1.34	55
Figure 36. DFT-calculated energies for the gold-catalysed 1,3 transposition of ynone 1.34 . Energies are Gibbs energies at the TPSS-D3/def2-TZVP//TPSS-D3/def2-SVP level of theory in kcal mol ⁻¹ with COSMO solvent correction in CH ₂ Cl ₂	57
Figure 37. Aldehydes used in the further studies.	58
Figure 38. Transposition reaction using challenging substrate 1.42	60

Figure 39. Gold(I)-catalysed 1,2-haloalkynylation reactions of haloalkynes, alkynes and alkenes.	61
Figure 40. ¹³ C-labelling experiments of 1,2-haloalkynylation reactions. The red circled atoms denote ¹³ C-labelled atoms. [Au] ⁺ = [(JohnPhos)AuNCMe] ⁺	62
Figure 41. DFT-calculated energies for the initial nucleophilic attack in gold(I)-coordinated alkyne. Energies are Gibbs energies in kcal mol ⁻¹ at the B3LYP-D3BJ//6-311++G(d,p),def2TZVP//B3LYP-D3BJ/6-31G(d),def2-TZVP level of theory with SMD solvent correction in DCE. [Au] = (JohnPhos)Au ⁺	63
Figure 42. DFT-calculated energies of possible reaction routes from 1.AI . Energies are Gibbs energies in kcal mol ⁻¹ at the B3LYP-D3BJ//6-311++G(d,p),def2TZVP//B3LYP-D3BJ/6-31G(d),def2-TZVP level of theory with SMD solvent correction in DCE. [Au] = (JohnPhos)Au ⁺	65
Figure 43. DFT-calculated energies for the initial nucleophilic attack in gold(I)-coordinated alkyne with isobutene. Energies are Gibbs energies in kcal mol ⁻¹ at the B3LYP-D3BJ//6-311++G(d,p),def2TZVP//B3LYP-D3BJ/6-31G(d),def2-TZVP level of theory with SMD solvent correction in DCE. [Au] = (JohnPhos)Au ⁺	66
Figure 44. DFT-calculated energies of possible reaction routes from 1.AP . Energies are Gibbs energies in kcal mol ⁻¹ at the B3LYP-D3BJ//6-311++G(d,p),def2TZVP//B3LYP-D3BJ/6-31G(d),def2-TZVP level of theory with SMD solvent correction in DCE. [Au] = (JohnPhos)Au ⁺	67
Figure 45. DFT-calculated energies of possible reaction routes from 1.AK , with different reactants. Energies are Gibbs energies in kcal mol ⁻¹ at the B3LYP-D3BJ//6-311++G(d,p),def2TZVP//B3LYP-D3BJ/6-31G(d),def2-TZVP level of theory with SMD solvent correction in DCE. [Au] = (JohnPhos)Au ⁺	69
Figure 46. DFT-calculated energies of possible reaction routes from 1.AK , with different ligands. Energies are Gibbs energies in kcal mol ⁻¹ at the B3LYP-D3BJ//6-311++G(d,p),def2TZVP//B3LYP-D3BJ/6-31G(d),def2-TZVP level of theory with SMD solvent correction in DCE. [Au] = (JohnPhos)Au ⁺	70
Figure 47. Reactions comparing the ¹³ C-labelling of 1,2-haloalkynylation reactions using (JohnPhos)Au ⁺ and (Me ₃ P)Au ⁺ . Ar = C ₆ H ₄ -4-OMe.	71
Figure 48. Select examples of quinoline-containing molecules (2.1–2.5) which display biological activity, with the quinoline moiety highlighted.	74

Figure 49. Divergent synthesis of spirocyclic indolenines 2.7 , quinolines 2.8 and carbazoles 2.9 from indolyl-tethered ynones 2.9 , as reported by Liddon <i>et al.</i> ¹⁷³	75
Figure 50. Mechanism for the quinoline rearrangement proposed by Liddon <i>et al.</i> to form quinoline 2.8 from 2.7 . ¹⁷³ X = Cl or <i>i</i> PrO.....	76
Figure 51. Control experiments performed by Liddon <i>et al.</i> a) The reaction of cyclopentanol spirocyclic indolenine 2.13 with AlCl ₃ .6H ₂ O. b) The reaction of spirocyclic indolenine 2.7a with LHMDS.....	77
Figure 52. Temperature-switchable TFA mediated synthesis of 2.7a and 2.8a from indolyl-tethered ynone 2.6a , as reported by Fedoseev <i>et al.</i> ¹⁷⁴	77
Figure 53. Synthesis of Weinreb amides 2.16a–c using CDI amide coupling with indole-3-acetic acid derivatives 2.17 using the method reported by Liddon <i>et al.</i> ¹⁷³	79
Figure 54. Synthesis of benzyl-substituted Weinreb amide 2.16d , as reported by James <i>et al.</i> ¹⁷⁵	80
Figure 55. Synthesis of indolyl-tethered ynones 2.6a–f using acetylenes 2.18a–c , as reported by James <i>et al.</i> ¹⁷⁵	81
Figure 56. Synthesis of spirocycles 2.7a–h , as reported by James <i>et al.</i> ¹⁷⁵ ^a Reaction time of 1 hour. ^b Reaction time of 3.5 hours. ^c Reaction time of 2 hours. ^d Reaction time of 1.5 hours. ^e The indolyl-tethered ynones required for 2.7g and 2.7h were made by Dr Aimee Clarke and Dr Hon Eong Ho respectively.....	82
Figure 57. Palladium-catalysed synthesis of spirocycles 2.7i and 2.7j , as reported by Ho <i>et al.</i> ¹⁷⁶	83
Figure 58. Successful synthesis of quinolines 2.8a–k using LHMDS. ^a Reaction time of 30 minutes. ^b Reaction time of 1 hour. ^c Reaction time of 1.5 hours. ^d Quinoline 2.8h was made by Dr Aimee Clarke. ^e The spirocyclic indolenine required for 2.8k was synthesised during a previous study. ¹⁷³	86
Figure 59. Formation of quinoline 2.8i and oxidised quinoline 2.19 from the LHMDS-mediated reaction of 2.7i	87
Figure 60. a) Trimer species 2.20 formed from <i>n</i> -butyl substituted spirocyclic indolenine 2.7b . b) Unsuccessful quinoline formation from spirocyclic indolenine 2.7b	88

Figure 61. DFT-calculated energy for the formation of quinoline 2.7a from spirocyclic indolenine 2.8a . Energies are Gibbs free energies calculated at the D3(BJ)-PBE0/def2-TZVPP//BP86/SV(P) level of theory with PCM solvent correction in THF.....	89
Figure 62. TMEDA control reaction of the rearrangement of spirocyclic indolenine 2.7a using LHMDS. ^a Calculated by the ratio of 2.7a to 2.8a in the crude ¹ H NMR spectra.	89
Figure 63. DFT-calculated pathway for the base-promoted rearrangement of 2.7a to 2.8a . Energies are Gibbs free energies at 298.15 K in kJ mol ⁻¹ at the D3(BJ)-PBE0/def2-TZVPP//BP86/SV(P) level with PCM solvent correction in THF.	91
Figure 64. a) Reaction of spirocyclic indolenine 2.7f with LHMDS. b) Reaction of indolyl-tethered ynone 2.7l using the one-pot quinoline rearrangement procedure as reported by Liddon <i>et al.</i> , ¹⁷³ resulting in quinoline 2.8l	94
Figure 65. Control reactions of 2.7a with a) aluminium <i>iso</i> -propoxide and b) conc. HCl.....	95
Figure 66. DFT-calculated pathway for the acid-promoted rearrangement of 2.7a to 2.8a . Energies are Gibbs free energies at 298.15 K in kJ mol ⁻¹ at the D3(BJ)-PBE0/def2-TZVPP//BP86/SV(P) level with PCM solvent correction in chloroform.	96
Figure 67. Dication 2.P formed from the double-protonation of 2.7a	97
Figure 68. DFT-calculated energies for the 1,2-migration of enol 2.1 . Energies are Gibbs free energies at 298.15 K in kJ mol ⁻¹ at the D3(BJ)-PBE0/def2-TZVPP//BP86/SV(P) level with PCM solvent correction in chloroform.	98
Figure 69. Select examples of 3-vinylindole-containing molecules (3.1–3.5) which display biological activity, with the 3-vinylindole moiety highlighted.....	100
Figure 70. a) Gold(I) catalysed synthesis of <i>bis</i> indolemethanes 3.8 from indoles 3.6 and acetylenes 3.7 , as reported by Echavarren and co-workers. ¹⁹⁰ b) Proposed mechanism for the formation of <i>bis</i> indolemethanes 3.8 , <i>via</i> 3-vinylindole 3.11 , as reported by Echavarren and co-workers. ¹⁹⁰	102
Figure 71. Ratios of mono- and <i>bis</i> -addition products as determined by ¹ H NMR spectroscopy for a) pyrrole 3.12 and b) indole 3.16 as reported by Schießl <i>et al.</i> ¹⁹² ^a 51% conversion of 3.13 . ^b 100% conversion of 3.13 . ^c 70% conversion of 3.13	103
Figure 72. Gold(I) catalysed hydroarylation of a) C-2 or C-4 substituted indoles 3.19 and b) indole 3.16 as reported by McLean <i>et al.</i> ¹⁹³	104

Figure 73. Formation of 3-vinylindole 3.17 from C-2 Bpin-substituted indole 3.21 and phenylacetylene 3.13 in 2 steps using gold(I) catalysis with subsequent deborylation, as reported by McLean <i>et al.</i> ¹⁹³ ^a Reported as unstable to silica during column chromatography.	104
Figure 74. Gold(I) catalysed formation of <i>bispyrrole</i> 3.15 , as reported by Luo <i>et al.</i> ¹⁹¹	105
Figure 75. DFT-calculated energies for the gold(I) catalysed addition of pyrrole 3.12 to 2-vinylpyrrole 3.22 . Energies are Gibbs energies in kcal mol ⁻¹ at the D3-M06/def2-TZVP//M06/LANL2DZ-6-31G(d) level of theory with CPCM solvent correction in AcOH. Reported by Mehrabi <i>et al.</i> ¹⁹⁴	106
Figure 76. DFT-calculated energies for the acid catalysed addition of pyrrole 3.12 to 2-vinylpyrrole 3.22 . Energies are Gibbs energies in kcal mol ⁻¹ at the D3-M06/def2-TZVP//M06/LANL2DZ-6-31G(d) level of theory with CPCM solvent correction in AcOH. Reported by Mehrabi <i>et al.</i> ¹⁹⁴	107
Figure 77. Control experiments performed by Scheißl <i>et al.</i> for the addition of pyrrole 3.12 to 2-vinylpyrrole 3.14 using a) gold(I) catalysis and b) acid catalysis. ¹⁹²	107
Figure 78. Divergent synthesis of spirocyclic indolenines 2.7 and carbazoles 2.9 from indolyl-tethered ynones 2.6 , as reported by Liddon <i>et al.</i> ¹⁷³	108
Figure 79. Synthesis of carbazoles 3.25 from indolyl-tethered propargyl alcohols 3.24 using silver(I) catalysis, as reported by James <i>et al.</i> ²⁰⁰	109
Figure 80. DFT-calculated pathway for the silver(I) and gold(I) catalysed cyclisations of indolyl-tethered ynones 2.9 , as reported by Liddon <i>et al.</i> ²⁰¹ Energies are Gibbs energies at 298.15 K in kJ mol ⁻¹ at the D3-PBE0/def2-TZVPP//BP86/SV(P) level of theory with COSMO solvent correction in CH ₂ Cl ₂	110
Figure 81. Proposed formation of 3-vinylindole 3.28 using a transition metal catalysed indole-ynone coupling reaction.	111
Figure 82. Comparison of the silver triflate catalysed cyclisation of a) indolyl-tethered ynones 2.6 and b) indolyl-tethered propargyl alcohols 3.24 . ^{173,200}	112
Figure 83. Proposed formation of 3-vinylindole 3.28 using a transition metal catalysed indole-ynone coupling reaction.	112
Figure 84. Synthesis of ynones 3.33 and 3.34 , using the method reported by Schubert <i>et al.</i> ²⁰²	113

Figure 85. Friedel–Crafts acylation for the synthesis of 4-Br ynone 3.37 , as reported by Schubert <i>et al.</i> ²⁰²	113
Figure 86. a) Synthesis of amide substituted alkynes 3.39–3.41 , using the method reported by Dong and co-workers. ²⁰³ b) Synthesis of ester substituted alkynes 3.43 and 3.44 , using the method reported by Vilotijevic and co-workers. ²⁰⁴	114
Figure 87. The two step synthesis of alkyne 3.47 , using methods reported in the literature. ^{205,206}	115
Figure 88. Synthesis of <i>N</i> -alkylated indoles (3.49 , 3.51 and 3.52) using methods reported in literature. ^{207–209} ^a Indole 3.50 was made by Dr James Donald in prior work. ²¹⁰	116
Figure 89. Successful formation of vinyl indole 3.28 , from the gold(I)-catalysed coupling of indole 3.16 and ynone 3.27	119
Figure 90. Proposed mechanism for the gold(I)-catalysed coupling of indole 3.16 and ynone 3.27	120
Figure 91. Indole variation scope of the gold(I)-catalysed coupling with phenyl-substituted ynone 3.27 . ^a 2 hour reaction time. ^b 18 hour reaction time. ^c 21 hour reaction time at room temperature. ^d 24 hour reaction time. ^e 19 hour reaction time. ^f 3 hour reaction time.	122
Figure 92. Alkyne variation scope of the gold(I)-catalysed coupling with indole 3.16 . ^a 2 hour reaction time. ^b 24 hour reaction time.	124
Figure 93. Structure of (<i>E</i>)- 3.74 , with the key stereochemical assignment highlighted, as reported by Godoi <i>et al.</i> ²¹³	125
Figure 94. NOESY spectrum of 3.73 recorded at 500 MHz in CDCl ₃ , with the key assignment highlighted. Parameters - D1 = 2 s, D8 = 0.5 s.	126
Figure 95. NOESY spectrum of 3.77 recorded at 500 MHz in CDCl ₃ , with the key assignments highlighted. Parameters - D1 = 2 s, D8 = 0.5 s.	127
Figure 96. Proposed formation of C-2 vinylated product 3.78 from the gold(I)-catalysed coupling of skatole 3.48 and ynone 3.27	128
Figure 97. The formation of 9 <i>H</i> -pyrrolo[1,2- <i>a</i>]indole compound 3.79 observed during the gold(I)-catalysed coupling of skatole 3.48 and ynone 3.27	128

Figure 98. a) Formation of 9 <i>H</i> -pyrrolo[1,2- <i>a</i>]indole compounds 3.82 using Brønsted acid catalysis, as reported by Tian <i>et al.</i> ²¹⁴ b) Mechanism proposed by the authors for the formation of 3.88 .	129
Figure 99. Successful formation of vinyl indole 3.89 , from the gold(I)-catalysed coupling of 1,3-dimethyl indole 3.49 and ynone 3.27 .	130
Figure 100. C-3 substituted indole 3.90 and alkyne 3.91 variation scope of the gold(I)-catalysed coupling reaction. ^a 27 hour reaction time. ^b 24 hour reaction time. ^c 48 hour reaction time.	131
Figure 101. XRD data of 3.92 , solved by Dr Adrian Whitwood (see CCDC 2116351). Hydrogens atoms removed for clarity. ORTEPS at 50% probability level.	131
Figure 102. DFT-calculated energies of gold(I) coordination to the indole 3.16 and skatole 3.48 , against the ketone and alkyne of ynone 3.27 . Energies are Gibbs energies at 298.15 K at the D3(BJ)-PBE0/def2-TZVPP//BP86/SV(P) level of theory with COSMO solvent correction in toluene.	133
Figure 103. DFT-calculated energies comparing species with varied [Au(PPh ₃)] ⁺ and triflimide anion coordination. All energies are Gibbs energies at 298.15 K at the D3(BJ)-PBE0/def2-TZVPP//BP86/SV(P) level of theory with COSMO solvent correction in CH ₂ Cl ₂ (top value) and toluene (bottom value).	135
Figure 104. ³¹ P{ ¹ H} NMR spectra recorded at 162 MHz in CD ₂ Cl ₂ . A 1:1 gold:substrate ratio was used.	136
Figure 105. ³¹ P{ ¹ H} NMR spectra recorded at 162 MHz in CD ₂ Cl ₂ , titrated with indole 3.16 in various ratios of gold:substrate.	137
Figure 106. ³¹ P{ ¹ H} NMR spectra recorded at 162 MHz in CD ₂ Cl ₂ , titrated with skatole 3.48 in various ratios of gold:substrate.	138
Figure 107. ³¹ P{ ¹ H} NMR spectra recorded at 162 MHz in CD ₂ Cl ₂ , titrated with ynone 3.27 in various ratios of gold:substrate.	139
Figure 108. DFT-calculated changes in energy for the C-3 and C-2 products arising from the addition of indole 3.16 and skatole 3.48 into ynone 3.27 . Energies are Gibbs energies at 298.15 K at the D3(BJ)-PBE0/def2-TZVPP//BP86/SV(P) with COSMO solvent correction in toluene.	140
Figure 109. DFT-calculated pathways for the addition of indole 3.16 or skatole 3.48 to gold(I) coordinated alkyne complex 3.P27 . Energies are Gibbs energies in kJ mol ⁻¹ at 298.15 K at the	

D3(BJ)-PBE0/def2-TZVPP//BP86/SV(P) level of theory with COSMO solvent correction in toluene.....	142
Figure 110. a) DFT-calculated pathway for the addition of indole 3.16 to $\eta^1(\text{O})$ gold(I) ketone coordinated ynone complex 3.O₂₇ . Energies are Gibbs energies in kJ mol^{-1} at 298.15 K at the D3(BJ)-PBE0/def2-TZVPP//BP86/SV(P) level of theory with COSMO solvent correction in toluene. b) Attempted transition state 3.TS_{NAD} , for the addition of ynone 3.27 to indole-coordinated gold(I) complex 3.N₁₆	143
Figure 111. Comparison of the a) intermolecular and b) intramolecular indole addition to ynones.....	144
Figure 112. DFT-calculated energy for the formation of <i>bis</i> indole compounds 3.29 and 3.18 . Energies are Gibbs energies at 298.15 K at the D3(BJ)-PBE0/def2-TZVPP//BP86/SV(P) level of theory with COSMO solvent correction in toluene.	145
Figure 113. DFT-calculated pathways for the acid-catalysed addition of indole 3.16 to a) ynone derived vinyl indole 3.28 and b) acetylene derived vinyl indole 3.17 . Energies are Gibbs energies at 298.15 K at the D3(BJ)-PBE0/def2-TZVPP//BP86/SV(P) level of theory with COSMO solvent correction in toluene.....	147
Figure 114. $^{31}\text{P}\{^1\text{H}\}$ NMR spectra recorded at 242 MHz in CD_2Cl_2 , with a 2:1 substrate:gold ratio. Proposed $\eta^1(\text{O})$ and $\eta^2(\pi)$ gold(I) coordination modes of DMF and alkyne 3.47 respectively.	150
Figure 115. Potential pyrylium-type complexes 3.99 and 3.100 formed by dimerisation of 4-NMe ₂ substituted ester and amide compounds 3.44 and 3.41 respectively. Ar = C ₆ H ₄ -4-NMe ₂	151
Figure 116. a) Isodesmic reaction used to calculate affinity of alkynes for gold. Energies are Gibbs energies at 298.15 K at the D3(BJ)-PBE0/def2-TZVPP//BP86/SV(P) level with COSMO solvation in CH_2Cl_2 . b) Linear free energy relationship between the calculated change in free energy against Hammett parameter σ_p . Dashed line shows fit to a least mean squares linear regression ($R^2 = 0.92$).	152
Figure 117. $^{31}\text{P}\{^1\text{H}\}$ NMR spectra recorded at 162 MHz in CD_2Cl_2 , with various ynones (3.27 , 3.33 , 3.34 and 3.37) in a 10:1 ratio of substrate:gold.	153
Figure 118. $^{13}\text{C}\{^1\text{H}\}$ NMR spectra recorded at 100 MHz in CD_2Cl_2 , of the dimer complex formed from ynone 3.34 and gold triflimide. Note that toluene is present due to its inclusion in the crystal structure of gold triflimide.	154

Figure 119. a) Formation of pyrylium complex 3.102 . b) Plausible mechanism for the formation of 3.102 . Triflimide anion omitted for clarity. Ar = C ₆ H ₄ -4-NMe ₂	155
Figure 120. ¹³ C{ ¹ H} NMR spectra recorded at 100 MHz in CD ₂ Cl ₂ of pyrylium complex 3.101 . Selected assignments are highlighted.	156
Figure 121. a) Gold(I)-catalysed ynone transposition, reported by Gevorgyan <i>et al.</i> ²²⁰ b) A likely mechanism for the gold(I)-catalysed transposition of ynones, identified by Burés <i>et al.</i> ¹⁵³ [Au] = IPrAu ⁺	157
Figure 122. DFT-calculated pathway for the dimerisation of ynone 3.34 . Energies are Gibbs energies at 298.15 K in kJ mol ⁻¹ at the D3(BJ)-PBE0/def2-TZVPP//BP86/SV(P) level of theory with COSMO solvent correction in CH ₂ Cl ₂	158
Figure 123. Resonance structures of η ² (π) gold(I) ynone complex 3.P₃₄	159
Figure 124. Formation of benzopyrylium complex 3.111 , from <i>o</i> -alkynyl benzaldehydes 3.109	161
Figure 125. a) Attempted reaction with ethyl vinyl ether 3.112 , as reported by Hammond and co-workers. ²²² b) Proposed mechanism for the formation of 3.113 . c) Proposed formation for the formation of 3.114 . Ar = C ₆ H ₄ -4-NMe ₂	162
Figure 126. Attempted reaction of ynone 3.34 (<i>via</i> pyrylium complex 3.102) with phenyl acetylene 3.13 , as reported by Asao <i>et al.</i> ²²³ Ar = C ₆ H ₄ -4-NMe ₂	163
Figure 127. Attempted reduction of pyrylium complex 3.102 with HEH, as reported by Michelet and co-workers. ²²⁴ Ar = C ₆ H ₄ -4-NMe ₂	163
Figure 128. Select examples of medium-ring containing and macrocyclic molecules, with the macrocyclic core highlighted in blue.	166
Figure 129. a) General representation of the end-to-end cyclisation to form 6-membered ring 4.10 . b) Undesired dimerisation during the cyclisation of 11-membered linear starting material 4.11	167
Figure 130. Eschenmoser fragmentation reported by Reese <i>et al.</i> resulting in 10-membered cyclic alkyne 4.18 . ²⁵³	169
Figure 131. Sidechain ring expansion using a radical addition pathway as reported by Dowd <i>et al.</i> ²⁵⁶	170
Figure 132. Ring contraction of cyclodecanone 4.25 reported by Beckwith <i>et al.</i> ²⁵⁷	170

Figure 133. Iterative ring expansion <i>via</i> [2,3]-sigmatropic rearrangements of cyclic thioether reported by Schmid <i>et al.</i> ²⁶³	171
Figure 134. Representation of the transamidation equilibrium exploited by Hesse <i>et al.</i>	171
Figure 135. Transamidation "zip" reactions for ring expansion as reported by Hesse <i>et al.</i> ²⁶⁴	172
Figure 136. a) Unsuccessful 3-atom ring expansion of 7-membered lactam 4.46 reported by Hesse <i>et al.</i> ²⁶⁸ b) Successful "zip" reaction of barbiturate derivivate 4.48 , to yield 14-membered product 4.50 , reported by Hesse <i>et al.</i> ²⁷⁰	173
Figure 137. Ring size dependence in transesterification ring expansion reactions of lactones, as reported by Corey <i>et al.</i> ²⁷¹	174
Figure 138. Ring expansion of lactams 4.57 using β -amino acids as proposed by Yudin <i>et al.</i> ²⁷²	175
Figure 139. Attempted ring expansion reactions using <i>N</i> -Boc protected α - and β -amino acids, as reported by Yudin <i>et al.</i> ²⁷² R = <i>p</i> -NO ₂ -Bn.	175
Figure 140. Hydrolytic imidazoline ring expansion (HIRE) concept reported by Krasavin <i>et al.</i> ²⁷³	177
Figure 141. An example of a HIRE reaction as reported by Krasavin <i>et al.</i> ²⁷³	177
Figure 142. Sidechain insertion development of HIRE reactions reported by Krasavin <i>et al.</i> ..	178
Figure 143. HIRE ring expansions resulting in larger ring sizes as reported by Krasavin <i>et al.</i> ²⁷⁵ The times in brackets refer to the required time of base treatment.	178
Figure 144. Examples of successful SuRE reactions reported by Unsworth <i>et al.</i> ^{276,278,279}	180
Figure 145. Proposed mechanism for the SuRE reactions of lactams.	181
Figure 146. Ring-size dependence on the scope of SuRE reactions using α - and β -hydroxyacids.	182
Figure 147. SuRE reactions resulting in equilibrium mixtures. Ratios were determined by ¹ H NMR spectroscopy.	183
Figure 148. The three isomers considered in the DFT calculations.	183
Figure 149. SuRE reactions to be studied by DFT calculations.	186
Figure 150. Previous example of an α -amino acid SuRE reaction as reported by Stephens <i>et al.</i> ²⁷⁸	187

Figure 151. Structures used for evaluating the lactam ring-size dependence with sarcosine. $m = 1-4$	187
Figure 152. Synthetic experiments exploring the ring-size requirements of SuRE reactions using α -amino acids, as performed by various co-workers.....	189
Figure 153. Cyclic β -ketoester SuRE reactions that were studied using DFT. Yields for lactams 4.129_{RE} – 4.131_{RE} were taken from previous studies ²⁷⁶ The other reactions were performed by various co-workers.....	198
Figure 154. New SuRE reactions that were studied by DFT. Yields as reported by various co-workers. ²⁸⁷	200
Figure 155. Biologically active normal sized thiolactones.	203
Figure 156. Proposed thiolactone SuRE reactions.	203
Figure 157. Thiolactone SuRE reaction of 13-membered lactam 4.121 , optimised by Dr Palate.	205
Figure 158. Ring-size screen of thiolactone forming SuRE reactions performed by Dr Palate.	206
Figure 159. Side-products isolated or observed in thiolactone forming SuRE reactions performed by Dr Palate.	207
Figure 160. a) Attempted thiolactone SuRE reaction using Fm-protected imide 4.178 performed by Dr Palate. b) Proposed degradation pathway.	208
Figure 161. Conjugate addition/ring expansion (CARE) reaction reported by Palate <i>et al.</i> ²⁹⁹	208
Figure 162. Dihydroxylation of acryloyl imide 4.181 resulting in 4-atom ring expansion product 4.184β_{RE} as performed by Balazs Pogranyi.....	209
Figure 163. Dihydroxylation of acryloyl imide 4.188 resulting in 4-atom ring expansion product 4.186β_{RE} as performed by Balazs Pogranyi.....	211
Figure 164. Proposed acyl migration SuRE reactions.	213
Figure 165. a) Proposed scheme for the insertion of a linear fragment into peptide chains. b) Native chemical ligation reactions used in protein synthesis.....	214
Figure 166. Selected examples of attempted acyl transfer reactions, performed by Dr Lawer. ³⁰⁴	215
Figure 167. Isomers with which the energies were to be compared using DFT.....	216

Figure 168. Proposed strategy for <i>S</i> → <i>N</i> acyl transfer for imide formation.....	218
Figure 169. Synthesis of alcohol 5.18 from <i>L</i> -lysine methyl ester dihydrochloride 5.36 , using the methods reported by Angle <i>et al.</i> ³¹⁷	219
Figure 170. Mitsunobu reaction of alcohol 5.18 , adapted from a patent. ³¹⁸	220
Figure 171. Hydrolysis of thioacetate 5.41	220
Figure 172. Synthesis of 5-membered thioacetate 5.46 . Using methods reported in the literature. ^{318,320,321}	221
Figure 173. Synthesis of ethyl-substituted lactam 5.48 as reported by Chen <i>et al.</i> ³²²	221
Figure 174. Synthesis of exocyclic maleimide 5.50 , as reported by Yan <i>et al.</i> ³²⁴	222
Figure 175. Synthesis of terminal ynone 5.52 , as reported in literature. ^{326,327}	222
Figure 176. Methylation of <i>N</i> -Boc β-alanine 5.53 , as reported in the literature. ³²⁸	223
Figure 177. HATU coupling procedure of thiol 5.21 with <i>N</i> -benzyl <i>N</i> -Fmoc β-alanine 5.55 . ^a Determined by ¹ H NMR spectroscopy.	223
Figure 178. T3P coupling procedure of thiol 5.21 with <i>N</i> -benzyl <i>N</i> -Fmoc β-alanine 5.56	224
Figure 179. T3P coupling procedure of thiol 5.21 with <i>N</i> -Boc <i>N</i> -methyl β-alanine 5.54 and Bn-protected β-hydroxyacid 5.58	224
Figure 180. Proposed process for iterative acyl migration and SuRE ring expansion reactions.	225
Figure 181. Proposed acyl transfer reaction of thioester 5.41 , trapping with propionyl chloride 5.67	226
Figure 182. Cations observed in the crude mass spectrum in the attempted acyl transfer reaction of 5.41 using triethylamine. Structures given are examples only, and no characterisation was done.....	226
Figure 183. Mechanism highlighting a proposed enolisation and substitution pathway.....	227
Figure 184. Reaction of thioacetate 5.41 with propionyl chloride 5.67 and pyridine.....	227
Figure 185. HMBC data with selected assignments used to determine the structure of 5.74 . NMR data recorded on 400 MHz spectrometer, in CDCl ₃	228
Figure 186. Reaction of thioacetate 5.46 with propionyl chloride 5.67 and pyridine.....	228

Figure 187. Representation of the Michael acceptor study.	229
Figure 188. Trial reaction between isobutyl mercaptan 5.77 and <i>N</i> -ethyl maleimide 5.49	230
Figure 189. Unsuccessful reaction of ethyl-substituted lactam 5.48 and <i>N</i> -ethyl maleimide 5.49	230
Figure 190. Unsuccessful reaction of thiol 5.79 and 5.48 with phenyl-substituted exocyclic maleimide 5.50	231
Figure 191. Reactions of thiol 5.77 and lactam 5.48 with phenyl-substituted ynone 3.27 . a) Stereochemistry assigned by comparison of an analogous compound, reported by Nishio <i>et al.</i> ³³⁹	232
Figure 192. Reactions of thioester 5.41 with phenyl-substituted ynone 3.27 . a) Stereochemistry assigned by comparison of an analogous compound, reported by Nishio <i>et al.</i> ³³⁹	232
Figure 193. Proposed mechanisms for <i>bis</i> (acetate) 5.85 formation.	233
Figure 194. Unsuccessful reactions of thioester 5.41 with phenyl-substituted ynone 3.27 with no base added.....	233
Figure 195. Unsuccessful reactions of thioester 5.41 with phenyl-substituted ynone 3.27 with triethylamine or pyridine added.	234
Figure 196. Reactions of thioester 5.46 with phenyl-substituted ynone 3.27 . a) Stereochemistry assigned by comparison of an analogous compound, reported by Nishio <i>et al.</i> ³³⁹	236
Figure 197. Reactions of thioester 5.41 with terminal ynone 5.52 . a) Stereochemistry was assigned by analysis of the ³ <i>J</i> alkene coupling constant (15.0 Hz for the <i>E</i> -isomer, and 9.5 Hz for the <i>Z</i> -isomer).....	236
Figure 198. Unsuccessful acyl migration of thioester 5.56 with terminal ynone 5.52	237
Figure 199. Proposed mechanism of thioester cleavage, for the formation of 5.92 from 5.56	238
Figure 200. Base-mediated acyl migration of Boc-protected thioester 5.57 . ^a Stereochemistry assigned by comparison of an analogous compound, reported by Nishio <i>et al.</i> ³³⁹	238
Figure 201. Attempted ring expansion reaction of 5.98 . ^a Stereochemistry assigned by comparison of the ¹³ C and ¹ H NMR resonances for the enone moiety, with 5.98	239

Figure 202. HMBC data with selected assignments used to determine the structure of 5.99 . NMR data recorded on 600 MHz spectrometer, in CDCl ₃	240
Figure 203. Base-mediated acyl migration of benzyl-protected thioester 5.59	241
Figure 204. Attempted hydrogenation reactions of imide 5.100	241
Figure 205. Successful acyl transfer reactions of thioacetate compounds 5.41 and 5.46 , using phenyl-substituted ynone 3.27	243
Figure 206. Successful ring expansion process with an acyl-migration step, starting from thiol 5.21	244
Figure 207. Overview of the substrate scope performed for the LHMDS-mediated quinoline rearrangement of spirocyclic indolenines.	245
Figure 208. Comparison of the silver triflate catalysed cyclisation of a) indolyl-tethered ynones 2.6 and b) indolyl-tethered propargyl alcohols 3.24 . ^{173,200}	246
Figure 209. Summary of the substrate scopes performed for the gold(I)-catalysed vinylation of a) indoles 3.56 and b) C-3 substituted indoles 3.90	247
Figure 210. DFT-calculated energy for the formation of <i>bis</i> indole compounds 3.29 and 3.18 . Energies are Gibbs energies at 298.15 K at the D3(BJ)-PBE0/def2-TZVPP//BP86/SV(P) level of theory with COSMO solvent correction in toluene.	248
Figure 211. Formation of pyrylium complex 3.102 , from electron-rich ynone 3.34 . Ar = C ₆ H ₄ -4- NMe ₂	248
Figure 212. The three isomers considered in the DFT calculations.	249
Figure 213. Successful ring expansion process with an acyl-migration step, starting from thiol 5.21	250

Acknowledgements

I would first like to thank both my supervisors, Will Unsworth and Jason Lynam, who put their faith in me, and gave me the opportunity to complete my PhD here at York. I don't think I could ask for a better pair of supervisors, who have motivated and encouraged me throughout the last four years. I will never hear the words "sure" or "nice" the same way ever again. I can also safely say that whilst my chemistry has (hopefully) improved, I can't say the same about my pop culture references!

I also need to thank Heather Fish and Alex Heyam, for making me feel like a welcome member of the NMR team. Your support and kind words have helped me greatly throughout the years, and I have always enjoyed our chats, which made the helium fills feel that much shorter.

Additional thanks must go to all the technical staff within the Department of Chemistry, particularly with the challenges that COVID brought. My research has benefitted greatly from all your work.

To the members of the WPU and SLUG groups, both past and present, I have thoroughly enjoyed the time spent working alongside each of you. There's far too many of you to mention by name but thank you all for making it a joy to come in every day. A particular thanks does have to go to Aimee Clarke, for getting me on my feet at the start of my degree, and to Chris Goult for your assistance throughout.

To Rosalind Booth, Katie Huxley and Catherine Russell – who would've thought when we first met four years ago, that we would be such good friends at the other end. Board games, escape rooms, brunches, copious amounts of gin and your friendship have been a much-needed comfort throughout my time here.

To my parents, I can't express enough my gratitude for the encouragement, love and support that you have given me throughout my entire life that has allowed me to grow as a person, and without which, I would never have gotten where I am today.

Finally, to my long-suffering partner, Oliver Ribchester, a special thank you for your love and understanding throughout my PhD, I really couldn't have done this without you. Your ability to smile and nod through my chemistry ramblings must be commended, as well as your patience during many a late-night working. Now I don't know about you, but I think it's time for a holiday?

Author Declaration

I declare that this thesis is a presentation of original work, to the best of my knowledge, except where due reference has been made to other workers. The research presented in this Thesis was carried out at the University of York between October 2018 and September 2022.

This work has not previously been presented for an award at this, or any other, University. All sources are acknowledged as references.

This work has been reported in a number of recent publications, which can be found in the Appendices, ordered by publication date. Additional publications which I have co-authored, but not discussed in this thesis, are also included.

Ryan G. Epton

Abbreviations

ACE	angiotensin converting enzyme
ACP	alkylidenecyclopropanes
AD	asymmetric dihydroxylation
AIBN	2,2-azobis(2-methylpropionitrile)
Ac	acetyl
Alk	alkyl
Aq.	aqueous
Ar	aryl
app.	apparent
BJ	Becke–Johnson
Bn	benzyl
Boc	<i>tert</i> -butyloxycarbonyl
Bpin	pinacolborane
br	broad
Bu	butyl
CARE	conjugate addition/ring expansion
CCDC	Cambridge Crystallographic Data Centre
CCSD	coupled-cluster singles and doubles
CCSD(T)	coupled-cluster singles and doubles plus perturbative triples
CDI	1,1'-carbonyldiimidazole
COSMO	conductor-like screening model
COSY	correlated spectroscopy
CPCM	conductor-like polarizable continuum model
Catcat	<i>trans</i> -bromo(<i>N</i> -succinimidyl) <i>bis</i> (triphenylphosphine)palladium(II)
Conv.	conversion
CyJohnPhos	2-(dicyclohexylphosphino)biphenyl
DBU	1,8-diazabicyclo[5.4.0]undec-7-ene
DCE	1,2-dichloroethane
DCM	dichloromethane
DEPT	distortionless enhancement by polarization transfer
DFT	density functional theory
DIAD	diisopropyl azodicarboxylate

DIPEA	<i>N,N</i> -diisopropylethylamine
DMAP	4-(dimethylamino)pyridine
DME	1,2-dimethoxyethane
DMF	<i>N,N</i> -dimethylformamide
DMSO	dimethyl sulfoxide
DRC	dynamic reaction coordinate
DenV	Dengue virus
d	doublet
d.r.	diastereomeric ratio
ECP	electrostatic core potential
ESI	electrospray ionisation
Et	ethyl
eq	equivalent(s)
Fm	9-fluorenylmethyl
Fmoc	9-fluorenylmethoxycarbonyl
GGA	general gradient approximation
GCPII	glutamate carboxypeptidase II
GTO	gaussian-type orbital
HATU	1-[bis(dimethylamino)methylene]-1 <i>H</i> -1,2,3-triazolo[4,5- <i>b</i>]pyridinium 3-oxid hexafluorophosphate
HEH	Hantzsch ester hydride (diethyl 2,6-dimethyl-1,4-dihydropyridine-3,5-dicarboxylate)
HF	Hartree–Fock
HIRE	hydrolytic imidazoline ring expansion
HMBC	heteronuclear multiple bond correlation
HRMS	high-resolution mass spectroscopy
HSQC	heteronuclear single quantum coherence
h	hour(s)
IEF	integral equation formalism
IPr	1,3-bis(2,6-diisopropylphenyl)imidazol-2-ylidene
IRC	Intrinsic reaction coordinate
JohnPhos	2-(di- <i>tert</i> -butylphosphino)-1,1'-biphenyl
KAPA	potassium 3-aminopropylamide
KS	Kohn–Sham

LCAO	linear combination of atomic orbitals
LDA	local density approximation
	lithium diisopropylamide
LHMDS	lithium hexamethyldisilazane
LSDA	local spin density approximation
M	mol dm ⁻³
MM	molecular mechanics
MMFF	Merck molecular force field
MP2	Møller–Plesset perturbation theory of the second order
Me	methyl
Mes	mesityl
Ms	methanesulfonyl
m	multiplet
mins	minutes
mp	melting point
NCL	native chemical ligation
NHC	<i>N</i> -heterocyclic carbene
NIS	<i>N</i> -iodosuccinimide
NMR	nuclear magnetic resonance
NOESY	nuclear Overhauser effect spectroscopy
NPA	natural population analysis
non.	nonet
ORTEP	Oak Ridge thermal ellipsoid plot
PCM	polarisable continuum model
PES	potential energy surface
PG	protecting group
pent.	pentet
Ph	phenyl
Pr	propyl
q	quartet
RC	ring-closed
RE	ring expanded
RI	resolution of identity
RO	ring opened

RT	room temperature
R_f	retention factor
SCF	self-consistent field
SDD	Stuttgart/Dresden ECPs
SMD	solvation model based on density
STO	Slater-type orbital
SuRE	successive ring expansion
s	singlet
sat.	saturated
sex.	sextet
TBS	<i>tert</i> -butyldimethylsilyl
TDO	tryptophan-2,3-dioxygenase
TFA	trifluoroacetic acid
TFE	2,2,2-trifluoroethanol
THF	tetrahydrofuran
TLC	thin layer chromatography
TMEDA	tetramethylethylenediamine
TOF	turnover frequency
TS	transition state
Tf	trifluoromethylsulfonyl
Tol	toluene
TrixiePhos	<i>rac</i> -2-(di- <i>tert</i> -butylphosphino)-1,1'-binaphthyl
Ts	toluenesulfonyl
T3P	propylphosphonic anhydride
t	triplet
UATR	universal attenuated total reflectance
XRD	X-ray diffraction
ZPE	zero-point energy
ZORA	zeroth-order regular approximation to the Dirac equation
μ W	microwave

Chapter 1. Introduction

1.1 Computational Theory

1.1.1 Introduction

Density functional theory (DFT) is a computational method which was used extensively during the research described in this thesis as a method to calculate the energies and properties of molecules based on their electronic structure. The calculated relative energies of different molecules (assuming the same number and identity of atoms are present) can then be used to study chemical processes, and provide information regarding the thermodynamics of a reaction (*e.g.* the change in Gibbs free energy), or the transition state energies, which can then be compared to experimental data when available (*e.g.* transition state energies can be compared with experimental kinetic data). Other properties, such as NMR chemical shifts, may also be calculated, however these methods were not used in this thesis.

To explain certain aspects and considerations of DFT (*e.g.* functionals and basis sets) which have been used within this thesis, a brief overview of the necessary quantum mechanics is needed, starting with the Schrödinger equation and its application to the hydrogen atom, leading to more complex atomic and molecular systems. This is then followed by a discussion of Hartree–Fock theory and its application to DFT.

The original publications for the theories and developments within are cited as necessary, and other resources which were insightful are cited here.^{1–6}

1.1.2 The Schrödinger Equation

The proposed structure of atoms has undergone several iterations and refinements. In 1911, experiments were performed by Rutherford in which a beam of α -particles were directed at a gold foil.⁷ A small proportion of α -particles were deflected by the foil, rather than passing through, which suggested the presence of a dense, highly charged core, which later became referred to as the nucleus. It was proposed that the area surrounding the nucleus was surrounded by electrons, and it was suggested that this might take the form of a circular orbit (Figure 1), however, classical mechanics would suggest that due to the attraction of the electron to the nucleus, its orbit would decay.

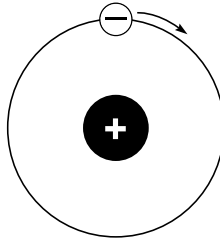


Figure 1. Representation of the Rutherford model of an atom.

Work by Bohr further refined the Rutherford model of the atom. It was assumed that the electrons exist in stable orbits around the nucleus which do not decay, and that the electron could be excited into an orbit further away from the nucleus by photons with the correct, specific energy. Bohr calculated that the angular momentum (L) of the allowed stable orbits were integers of the reduced Planck's constant (\hbar , Equation 1), and using this, Bohr was able to derive the Rydberg constant (R) and accurately predict the observed emission spectrum of the hydrogen atom (Equation 2, where n_1 and n_2 are both integers).⁸⁻¹⁰

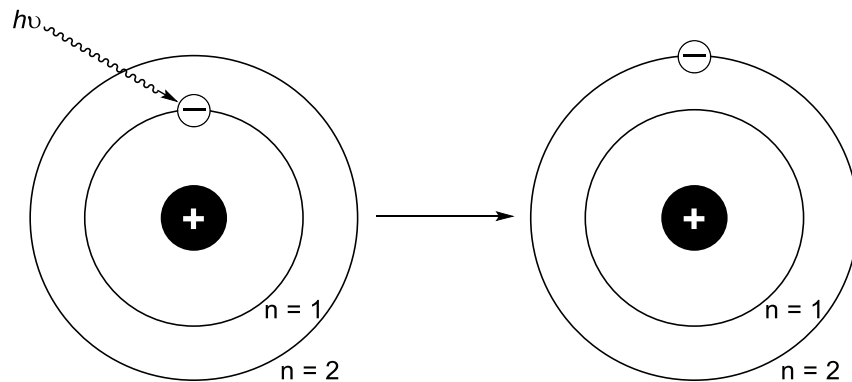


Figure 2. Representation of the Bohr model of the atom.

$$L = n\hbar \quad \text{Equation 1}$$

$$\Delta E = R \left(\frac{1}{n_1^2} - \frac{1}{n_2^2} \right) \quad \text{Equation 2}$$

In 1925, de Broglie hypothesised that matter could be treated as both a particle and a wave, and that the momentum (p) of the particle could be related to its wavelength (Equation 3, where h is the Planck constant and λ is the wavelength of the particle).¹¹ Experiments performed by Davisson, Germer and Thomson,¹²⁻¹⁴ demonstrated that electrons were able to be diffracted by a crystal of nickel metal, which confirmed that electrons can be treated as waves. The quantised

energy of the electron orbits from the Bohr model, and the wave-particle nature of the electrons led to the further development of quantum theory.

$$p = \frac{h}{\lambda} \quad \text{Equation 3}$$

The wave form of electrons in a theoretically circular orbit around a nucleus must be treated as a standing wave, since these types of waves terminate at the boundary of the available space they occupy. Therefore, an electron can be considered to have a discrete set of wavelengths (*e.g.* $n\lambda$, where n is an integer) that can exist in a circular orbit of length, r (Equation 4).⁹

$$n\lambda = 2\pi r \quad \text{Equation 4}$$

The angular wavenumber (k , the number of complete waves per unit 2π) can then be related to the wavelength of the electron (Equation 5), and substitution of Equation 5 into Equation 3 then relates the angular wavenumber with the momentum of the particle (Equation 6).

$$k = \frac{2\pi}{\lambda} \quad \text{Equation 5}$$

$$p = \hbar k \quad \text{Equation 6}$$

Schrödinger used a modified wave equation to develop an equation for describing the energy of an atom.¹⁵ Here, some definitions are required. In one-dimensional space, the general function of a wavefunction ψ , can be expressed as in Equation 7. It can therefore be seen that the second derivative of this wavefunction returns the original function, multiplied by a constant (Equation 8). Here, the second derivative is considered the operator, which acts upon the given eigenfunction (ψ), with the constant ($-k^2$) being referred to as the eigenvalue.

$$\psi = e^{ikx} \quad \text{Equation 7}$$

$$\frac{d^2\psi}{dx^2} = -k^2\psi \quad \text{Equation 8}$$

The kinetic energy of a particle (T) can be expressed in terms of its momentum (Equation 9), which can therefore be related to the angular wavenumber *via* substitution of the de Broglie relationship shown in Equation 6 (Equation 10).

$$T = \frac{1}{2}mv^2 = \frac{p^2}{2m} \quad \text{Equation 9}$$

$$T = \frac{(\hbar k)^2}{2m} \quad \text{Equation 10}$$

Further substitution of Equation 8 and Equation 10, results in Equation 11. Here, the left side of equation is the operator, and acts upon a wavefunction to return the kinetic energy (T) as the eigenvalue. Equation 11 can be further expanded to describe the energy of a hydrogenic system (*e.g.* a system containing one nucleus and one electron), with the inclusion of a potential energy term, V (Equation 12, Z is the nuclear charge and ϵ_0 is the permittivity of a vacuum), to describe the electronic attraction between the nucleus and the electron. Combining both the kinetic energy (T) and potential energy (V) terms (Equation 13) now gives a representation of the total energy and is often written in the form shown in Equation 14, where \hat{H} is referred to as the Hamiltonian operator.

$$-\frac{\hbar^2}{2m} \frac{d^2\psi}{dx^2} = T\psi \quad \text{Equation 11}$$

$$V = -\frac{Z^2}{4\pi\epsilon_0 r} \quad \text{Equation 12}$$

$$\left(-\frac{\hbar^2}{2m} \frac{d^2\psi}{dx^2} - \frac{Z^2}{4\pi\epsilon_0 r} \right) \psi = E\psi \quad \text{Equation 13}$$

$$\hat{H}\psi = E\psi \quad \text{Equation 14}$$

The Schrödinger equation (Equation 13) provides a suitable description for so called hydrogenic systems (*e.g.* in which there is only one nucleus and one electron considered, as in H, He⁺ and Li²⁺), with analytical solutions available. However, for more complex atomic and molecular systems, the Schrödinger can no longer be solved exactly, but approximations are used to provide reasonable estimates, which will be discussed further in Section 1.1.3.

Until now, the wavefunction (ψ) has only been considered in one-dimension, however it is possible to expand this into three-dimensions by using the Laplacian operator, ∇^2 (Equation 15). Whilst it is possible to express this in terms of Cartesian coordinates, for atomic systems it is more relevant to express the Laplacian as spherical coordinates (Equation 16), in which r is the radius of sphere, and Λ^2 is a shorthand for representing two spherical angles, θ and ϕ (Equation 17). The coordinate system is represented in Figure 3.

$$\left(-\frac{\hbar^2}{2m}\nabla^2 - \frac{Z^2}{4\pi\epsilon_0 r}\right)\psi = E\psi \quad \text{Equation 15}$$

$$\nabla^2 = \frac{1}{r^2} \left[\frac{d}{dr} \left(r^2 \frac{d}{dr} \right) + \Lambda^2 \right] \quad \text{Equation 16}$$

$$\Lambda^2 = \frac{1}{\sin\theta} \frac{d}{d\theta} \left(\sin\theta \frac{d}{d\theta} \right) + \frac{1}{\sin^2\theta} \frac{d^2}{d\phi^2} \quad \text{Equation 17}$$

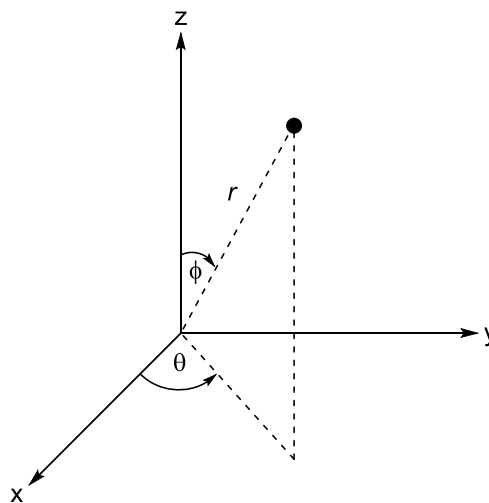


Figure 3. Representation of polar spherical coordinates.

It is important to note that it is possible to derive information on the probability of locating a particle in a particular position within the wavefunction, by taking the square of the wavefunction.¹⁶ It therefore follows that the integral of the square of the wavefunction, in all space (dV), must equal 1 (Equation 18), and therefore a normalisation constant (commonly denoted as N) can be calculated and applied to the wavefunction to ensure this condition is met. Whilst the normalisation condition will not always be referred to, it should be considered that all wavefunctions mentioned here within are normalised.

$$\int_{-\infty}^{+\infty} \psi^* \psi dV = 1$$

Equation 18

1.1.3 The many-body Schrödinger Equation and the Hartree method

Atoms and molecules containing more than one electron and/or nucleus are referred to as many-body systems. Figure 4 shows a representation of a molecule containing two nuclei (denoted as A and B), and two electrons (denoted as i and j). Now, rather than only the kinetic energy contribution from the single electron in the hydrogenic system (Equation 15), the kinetic energy of both nuclei (T_N) and all the electrons (T_e) must be considered. Furthermore, the potential energy must now include each electrons attraction to all nuclei (V_{Ne}), and the repulsion between the electrons (V_{ee}) and between the nuclei (V_{NN}). The Hamiltonian of these many body systems can therefore be generalised as shown in Equation 19, with a simplified representation shown in Equation 20.

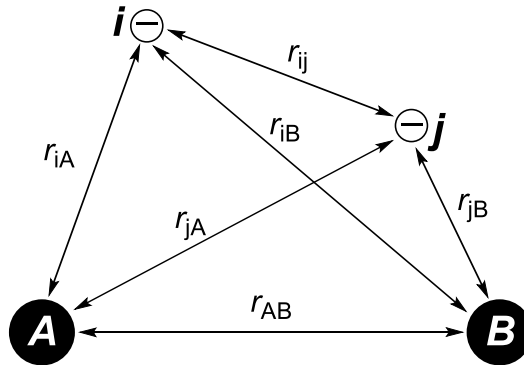


Figure 4. Diagrammatic representation of the diatomic molecule with two electrons (e.g. H_2).

$$\hat{H} = -\frac{\hbar^2}{2} \sum_A \frac{1}{m_A} \nabla_A^2 - \frac{\hbar^2}{2m_e} \sum_i \nabla_i^2 + \sum_A \sum_{A>B} \frac{Z_A Z_B e^2}{r_{AB}} - \sum_A \sum_i \frac{Z_A e^2}{r_{iA}} + \sum_i \sum_{i>j} \frac{e^2}{r_{ij}}$$

Equation 19

$$\hat{H} = -T_N - T_e + V_{NN} - V_{Ne} + V_{ee}$$

Equation 20

The Born–Oppenheimer approximation simplifies the many-body Schrödinger equation.¹⁷ Due to the large difference in mass of the electrons and nuclei, it can be assumed that given the same

momentum, the electrons will move much faster than the nuclei. This allows the Hamiltonian to be separated into nuclear and electronic contributions, with the electronic Hamiltonian given in Equation 21.

$$\hat{H}_{elec} = -\frac{\hbar^2}{2m_e} \sum_i \nabla_i^2 - \sum_A \sum_i \frac{Z_A e^2}{r_{iA}} + \sum_i \sum_{i>j} \frac{e^2}{r_{ij}} \quad \text{Equation 21}$$

Whilst the Hamiltonian has been simplified greatly, the electron-electron repulsion term (V_{ee}) remains problematic, since the coordinates of each electron must be solved simultaneously. As the system under consideration becomes larger, this quickly becomes too complex to compute, and even for systems containing only two electrons, there is no analytical solution.

Hartree developed a method to approximate the electronic wavefunction of a many-body system.¹⁸⁻²¹ Consider the wavefunction of a system which consists of two electrons (Ψ_{ij}), Hartree showed that the wavefunction can be treated as a product of the wavefunction for each individual electron, ϕ_i and ϕ_j (Equation 22), which is referred to as the independent electron approximation.

$$\Psi_{ij} = \phi_i \phi_j \quad \text{Equation 22}$$

The energy of the wavefunction of each individual electron can now be represented by Equation 23. The potential energy term (V_i , Equation 24) contains both the nuclear-electron attraction (V_{Ne} , shown in Equation 25), and also includes the electron-electron repulsion (V_{ee} , shown in Equation 26) by considering the other electrons as a mean-field (*e.g.* the average potential acting upon electron i).

$$\left(-\frac{\hbar^2}{2m_e} \nabla^2 - V_i \right) \phi_i = E_i \phi_i \quad \text{Equation 23}$$

$$V_i = \sum_A \frac{Z_A e^2}{r_{iA}} + e^2 \sum_{i \neq j} \int \frac{\sum_j |\phi_j^2(r_j)|}{|r_i - r_j|} dr_i \quad \text{Equation 24}$$

$$V_{Ne} = \sum_A \frac{Z_A e^2}{r_{iA}} \quad \text{Equation 25}$$

$$V_{ee} = e^2 \sum_{i \neq j} \int \frac{\sum_j |\phi_j^2(r_j)|}{|r_i - r_j|} dr_i \quad \text{Equation 26}$$

Whilst the electron-electron repulsion term (V_{ee}) in Equation 24, makes solving the one-electron wavefunction possible, there are some associated problems. Firstly, to calculate the potential energy of the one-electron wavefunction, the other one-electron wavefunctions (*e.g.* ϕ_j) are required. To solve this cyclic problem, Hartree developed a method known as the self-consistent field (SCF) theory, in which the one-electron wavefunctions for each electron are initially guessed. The guessed wavefunctions are then used to solve the Schrödinger equation, and in turn, generate an improved set of wavefunctions. This process iterates until the energy no longer changes within the convergence criteria. At this point, it is said that the wavefunction is self-consistent and converged.

An additional problem with the Hartree method arises due to neglecting the spin of the electrons,^{22,23} which therefore doesn't accurately represent that electrons with the same spin would repel each other more than electrons with the opposite spin. This is referred to as the 'exchange interaction'.

1.1.4 Electron spin and Hartree–Fock Theory

The spin of an electron is an intrinsic property which results in it having angular momentum. The spin of an electron is quantised, and the spin magnetic quantum number (m_s) can only take the values $+\frac{1}{2}$ or $-\frac{1}{2}$. The spin of an electron can also be referred to as "spin up" or "spin down", or given the symbols α and β .

The Pauli exclusion principle states that no two electrons of an atom can have the same four quantum numbers to describe it,²⁴ that is, the principal (n), the angular (l), the magnetic (m_l) and spin magnetic (m_s) quantum numbers must be different. The consequence of this is any spatial orbital (*e.g.* a 1s orbital), can only be occupied by two electrons with opposite spin.

Consider the helium atom, which in its ground state contains two electrons in the 1s orbital, the electron configuration for the two electrons can be written as in Equation 27 or Equation 28 – we don't know which electron is which due to the Heisenberg uncertainty principle and therefore both options must be considered.²⁵

$$\alpha(1)\beta(2) \quad \text{Equation 27}$$

$$\beta(1)\alpha(2) \quad \text{Equation 28}$$

Another aspect of the Pauli exclusion principles states that for electrons (a fermion), the total wavefunction must be antisymmetric; if any particles are exchanged, the wavefunction changes sign. Consider Equation 27 and Equation 28, assuming that the spatial wavefunction of both electrons in the 1s orbital are the same, these equations could be equated, and the antisymmetric condition isn't satisfied. This can be overcome using Equation 29 (where $\frac{1}{\sqrt{2}}$ is the normalisation constant), now when the electrons are exchanged, the sign of the wavefunction changes.

$$\frac{1}{\sqrt{2}}[\alpha(1)\beta(2) - \alpha(2)\beta(1)] \quad \text{Equation 29}$$

The two electron wavefunction for the helium atom can therefore be represented as given in Equation 30, where each electron has both a spatial wavefunction (ψ) and a spin function (α or β). This notation can also be represented in a matrix (Equation 31), in which a key property of matrices forces the sign of the wavefunction to be swapped when the rows are exchanged.²⁶

$$\Psi_{He}(1,2) = \psi(1)\psi(2) \frac{1}{\sqrt{2}}[\alpha(1)\beta(2) - \alpha(2)\beta(1)] \quad \text{Equation 30}$$

$$\Psi_{He}(1,2) = \frac{1}{\sqrt{2}} \begin{vmatrix} \psi(1)\alpha(1) & \psi(1)\beta(1) \\ \psi(2)\alpha(2) & \psi(2)\beta(2) \end{vmatrix} \quad \text{Equation 31}$$

The Hartree method was modified by Fock in 1930 to take into consideration electron spin,²³ with Hartree later further refining the method.²⁷ The wavefunction is now represented as a general matrix, known as the Slater determinant (Equation 32, where N is the number of electrons), in which one-electron orbitals are a product of a spatial orbital component (χ) and a spin function (x).

$$\psi = \frac{1}{\sqrt{N!}} \begin{vmatrix} \chi_1(\vec{x}_1) & \chi_2(\vec{x}_1) & \cdots & \chi_N(\vec{x}_1) \\ \chi_1(\vec{x}_2) & \chi_2(\vec{x}_2) & \cdots & \chi_N(\vec{x}_2) \\ \vdots & \vdots & \ddots & \vdots \\ \chi_1(\vec{x}_N) & \chi_2(\vec{x}_N) & \cdots & \chi_N(\vec{x}_N) \end{vmatrix} \quad \text{Equation 32}$$

Now, rather than the Hamiltonian acting upon the wavefunction (in the form of the Slater determinant, Equation 32) to calculate the energy, the Fock operator (F) is used (Equation 33), which is composed of the electron kinetic energy and the nuclear-electron attraction potential (combined in the term \hat{h}), and a Hartree–Fock potential term (V_{HF} , Equation 34).

$$\hat{F}_i \psi_i = E_i \psi_i \quad \text{Equation 33}$$

$$\hat{F}_i = \hat{h}_i + V_{HF} \quad \text{Equation 34}$$

The Hartree–Fock potential is itself the sum of the coulombic (J) and exchange (K) terms (Equation 35). The coulombic term, J (Equation 36), is responsible for calculating the electron-electron repulsion as in the Hartree method, however the exchange term, K (Equation 37), accounts for the antisymmetric requirement of the wavefunction, when electrons χ_i and χ_j are exchanged. This has the effect of ensuring that electrons which have the same spin repel each other more than those with the opposite spin. The Hartree–Fock equations are then solved using the same SCF method as previously described for the Hartree method.

$$V_{HF} = \sum_J^{N/2} (2\hat{J}_J - \hat{K}_J) \quad \text{Equation 35}$$

$$\hat{J}_J = e^2 \sum_{i \neq j} \int \frac{|\chi_i(x_i)|^2 |\chi_j(x_j)|^2}{|r_i - r_j|} dr_i dr_j \quad \text{Equation 36}$$

$$\hat{K}_J = e^2 \sum_{i \neq j} \int \frac{\chi_i(x_i) \chi_j(x_j) \chi_i(x_j) \chi_j(x_i)}{|r_i - r_j|} dr_i dr_j \quad \text{Equation 37}$$

An additional key principle when solving these equations, is the variational principle. When solving the Schrödinger equation, if the true wavefunction (ψ_{exact}) is known, then the lowest calculated energy is referred to as the ground-state energy (E_0). It can be shown that the average

energy of a trial wavefunction (ψ_{trial}), referred to as the expectation energy ($\langle E \rangle$, Equation 35) is always higher than or equal to that of the true ground-state energy (Equation 36).

$$\langle E \rangle = \frac{\int \psi_{\text{trial}}^* \hat{H}_{\text{trial}} \psi_{\text{trial}} d^3r}{\int \psi_{\text{trial}}^* \psi_{\text{trial}} d^3r} \quad \text{Equation 38}$$

$$E_0 \leq \langle E \rangle \quad \text{Equation 39}$$

Therefore, whilst Hartree–Fock theory was the first method which was able to provide a solution for the many-body Schrödinger equation, there were still problems associated with the method. Namely, since the electrons are treated in the mean-field approximation as an averaged potential, spontaneous electron interactions are not accounted for. Due to the approximations to the wavefunction, and the variational principle described above, the calculated Hartree–Fock energy (E_{HF}) is always higher than the true energy of the system (E_{exact}). This difference is known as the correlation energy (E_c , Equation 40) and computational methods such as Møller–Plesset theory (not used or presented in this thesis) and DFT theory have been developed to reduce this.

$$E_c = E_{\text{exact}} - E_{\text{HF}} \quad \text{Equation 40}$$

1.1.5 Density Functional Theory

The central idea behind density functional theory, is that the energy of a system can be obtained purely by using the electron density. In 1927, Thomas proposed the theory that the electronic state of a uniform electron gas can be a valid solution of the Schrödinger equation based on electron density.²⁸ An equation for the kinetic energy functional was proposed by both Thomas and Fermi, which later became known as the Thomas–Fermi method,²⁹ however this model was very limited in its application.

In 1964, the Hohenberg–Kohn theorems were published to expand and account for deficiencies of the Thomas–Fermi method.³⁰ Two theories were proved that were essential for the development of DFT. First, it was shown that the external potential ($v_{\text{ext}}[r]$) of a system is a unique functional (a function of a function) of the electron density ($\rho[r]$), and hence the Hamiltonian of the system can be related to the electron density itself. Therefore, the energy of a system can be expressed as a sum of the electron kinetic energy term (T) and both electron–electron (V_{ee}) and nuclear–electron (V_{Ne}) potential energy terms (Equation 41).

$$E_0[\rho] = T[\rho] + V_{ee}[\rho] + V_{Ne}[\rho] \quad \text{Equation 41}$$

The external potential of an isolated N -electron system is fixed by the positions and charges of the nuclei, and therefore the energy can be represented as in Equation 42, where F^{HK} is an unknown functional which combines the electron kinetic (T) and electron-electron interaction (V_{ee}) terms.

$$E_0[\rho] = F^{HK}[\rho] + \int \rho[r]v[r]dr \quad \text{Equation 42}$$

The second of the Hohenberg–Kohn theorems demonstrates that the variational principle is able to be used in conjunction with the electron density, as with the Hartree–Fock method, and it follows that for any trial electron density, the calculated energy will be higher than or equal to the real energy.

Further work by Kohn and Sham sought to provide insight into the nature of the unknown functional (F^{HK}).³¹ They assumed that the system contains non-interacting electrons in an averaged potential of all the other electrons, and that the electron density of this system is the same as if the electrons did interact. The electrons were then treated in a similar method to Hartree–Fock theory, with the wavefunction represented as single electron spin orbitals (ψ) and electrons (r), with a Slater determinant (Equation 43) used to ensure the antisymmetric principle for the electron spin is maintained.

$$\Psi = \frac{1}{\sqrt{N!}} \begin{vmatrix} \psi_1(\vec{r}_1) & \psi_2(\vec{r}_1) & \cdots & \psi_N(\vec{r}_1) \\ \psi_1(\vec{r}_2) & \psi_2(\vec{r}_2) & \cdots & \psi_N(\vec{r}_2) \\ \vdots & \vdots & \ddots & \vdots \\ \psi_1(\vec{r}_N) & \psi_2(\vec{r}_N) & \cdots & \psi_N(\vec{r}_N) \end{vmatrix} \quad \text{Equation 43}$$

The authors then further assumed that F^{HK} can be separated (Equation 44), where T_s is the sum of the kinetic energy from all the single electron kinetic energies, J is the coulombic electron-electron repulsion term (these two terms were initially combined into F^{HK}), and E_{XC} is a self-defined term, which contains any remaining undefined energies (referred to as the exchange and correlation energy).

$$F^{HK}[\rho] = T_s[\rho] + J[\rho] + E_{XC}[\rho] \quad \text{Equation 44}$$

The kinetic energy, T_s , can be represented as Equation 45, however this itself is a result of the approximation of non-interacting electrons and the single electron spin orbitals. Therefore, it can be shown that the difference between the true kinetic energy (T , Equation 41) and T_s , can be represented as T_c (Equation 46).

$$T_s[\rho] = -\frac{1}{2} \sum_i^N \langle \psi_i | \nabla^2 | \psi_i \rangle \quad \text{Equation 45}$$

$$T_c[\rho] = T[\rho] - T_s[\rho] \quad \text{Equation 46}$$

Furthermore, the coulombic electron-electron interaction term, J , is similar to that in Hartree–Fock theory (Equation 47), which utilises the mean-field approximation. Therefore, the electron-electron potential energy can again be shown to differ from the true value (E_{ee} , Equation 41), which is represented as E_{ncl} (Equation 48).

$$J[\rho] = \frac{1}{2} \iint \frac{\rho[r_i]\rho[r_j]}{r_{ij}} dr_i dr_j \quad \text{Equation 47}$$

$$E_{ncl}[\rho] = E_{ee}[\rho] - J[\rho] \quad \text{Equation 48}$$

The exchange and correlation energy functional (E_{xc}) can therefore be shown to be the sum of the deviations from the true value for both the kinetic energy, and electron-electron repulsion (Equation 49). This functional remains unknown and the different functionals used within DFT calculations are used to provide approximations for E_{xc} .

$$E_{xc}[\rho] = T_c[\rho] + E_{ncl}[\rho] \quad \text{Equation 49}$$

1.1.6 Approximate Exchange-Correlation Functionals

The accuracy of DFT calculations depends on how successfully the exchange-correlation functional function is approximated. There are three main methods that are used to model this energy, with varied success.

The first is known as the Local Density Approximation (LDA). LDA functionals model the electron density using the assumption that the electron density exists as a uniform electron gas (as in the

Thomas–Fermi theory), and the LDA form of the exchange–correlation energy can be written as in Equation 50.

$$E_{XC}^{LDA}[\rho] = \int \rho[r] \epsilon_{XC}(\rho[r]) dr \quad \text{Equation 50}$$

The term, ϵ_{XC} , refers to the exchange–correlation energy per particle in a uniform electron density, and can be further broken down into exchange (ϵ_X) and correlation (ϵ_C) components (Equation 51), and approximations have been made for these terms. The LDA approach can also be modified to take spin into consideration, using the Local Spin Density Approximation (LSDA, Equation 52). Due to the LDA model assuming that the electron density is uniform throughout a system, these functionals mostly perform well only when considering systems such as metal bonding.

$$\epsilon_{XC}(\rho[r]) = \epsilon_X(\rho[r]) + \epsilon_C(\rho[r]) \quad \text{Equation 51}$$

$$E_{XC}^{LSDA}[\rho_\alpha, \rho_\beta] = \int \rho[r] \epsilon_{XC}(\rho_\alpha[r], \rho_\beta[r]) dr \quad \text{Equation 52}$$

For molecular systems, the electron density will change throughout the system, therefore it is more appropriate to consider how the electron density changes ($\nabla\rho$), which is referred to as the General Gradient Approximation (GGA). The exchange–correlation energy functional for the GGA approach takes the form Equation 53, with the gradient approximation typically applied to LDA functionals. The BP86 functional used throughout this thesis is a GGA functional,^{32,33} which has shown to be successful at generating accurate geometries, particularly for transition metal complexes.

$$E_{XC}^{GGA}[\rho_\alpha, \rho_\beta] = \int \rho[r] \epsilon_{XC}(\rho_\alpha[r], \rho_\beta[r], \nabla\rho_\alpha, \nabla\rho_\beta) dr \quad \text{Equation 53}$$

Hybrid functionals are a further class of functionals which incorporates a certain proportion of the Hartree–Fock exchange (E^{HF}) into the exchange–correlation energy. For example, the PBE0 hybrid functional,^{34–36} which has been used throughout this thesis, can be represented as shown in Equation 54, in which the exchange energy from the PBE GGA functional (E_X^{PBE}) and Hartree–Fock exchange energies (E_X^{HF}) are used in a 3:1 ratio, in conjunction with the PBE correlation energy (E_C^{PBE}). Other hybrid functionals used within this thesis are the B3LYP functional,^{37–40} the

Minnesota M06 and M06-2X functionals,⁴¹ and the ω B97XD functional.⁴² The authors of the Minnesota functionals refer to these as meta-hybrid GGA functionals, however they do contain Hartree–Fock exchange.

$$E_{XC}^{PBEO} = \frac{3}{4}E_X^{PBE} + \frac{1}{4}E_X^{HF} + E_C^{PBE} \quad \text{Equation 54}$$

1.1.7 Molecular Orbitals and Basis Sets

Throughout the previous discussion regarding Hartree–Fock theory and DFT, the concept of orbitals has been used. However, in molecules the molecular orbitals can span multiple atoms, and both bonding and anti-bonding orbitals must be considered.

The molecular orbitals are therefore approximated using the Linear Combination of Atomic Orbitals (LCAO) approach. This is represented in Equation 55, where in this example, the total wavefunction is considered as the constructive or destructive overlap of the atomic orbitals from differing nuclei, with the coefficient, c , determining the contribution of each atomic orbital.

$$\psi = c_A\psi_A \pm c_B\psi_B \quad \text{Equation 55}$$

Consider the overlap of two 1s orbitals, with atoms A and B, having an internuclear distance of R . If the orbitals are in the same phase (Figure 5a, left), constructive overlap occurs (Figure 5a, right). Likewise, if the orbitals phase is different (Figure 5b, left), destructive overlap occurs (Figure 5b, right).

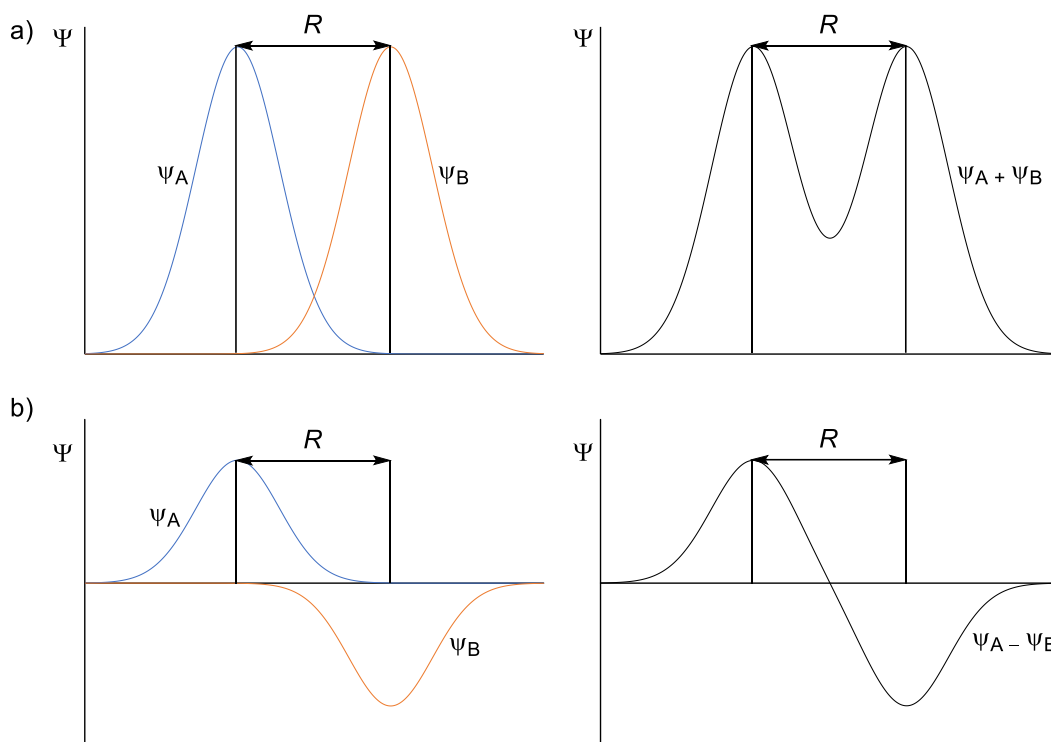


Figure 5. Representation of two 1s orbitals combining a) constructively and b) destructively.

As previously mentioned in Section 1.1.2, the probability of finding an electron is given by the square of the wavefunction. If we therefore consider the same orbital arrangements as in Figure 5, the electron probability can be shown as in Figure 6. These figures demonstrate bonding (σ) and anti-bonding (σ^*) orbitals respectively, where either electron density or a node can be seen between the two nuclei.

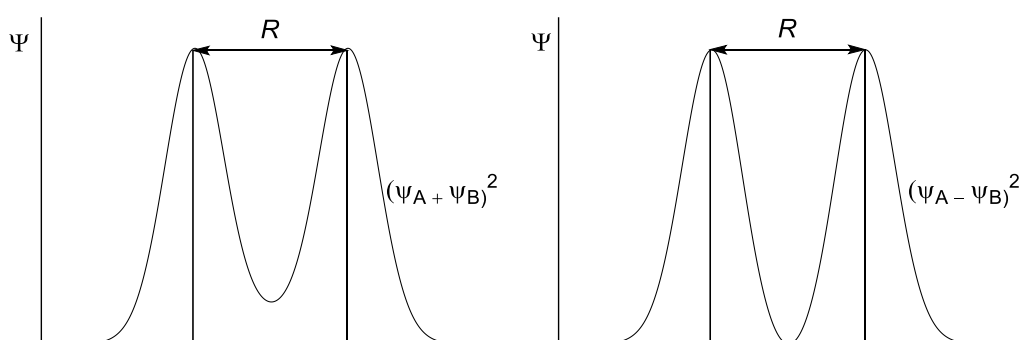


Figure 6. Representation of squared wavefunctions for bonding (left) and anti-bonding (right) orbitals.

In the examples shown in Figure 6, the molecular orbitals only consist of one orbital per atom. In real systems, it can be considered that the molecular orbitals consist of the sum of many atomic orbital wavefunctions (ψ_f , Equation 56). These atomic orbitals are referred to as a basis set.

$$\Psi = \sum c\psi_f \quad \text{Equation 56}$$

Slater proposed that the atomic orbitals take the form shown in Equation 57,⁴³ where N is the normalisation constant, n is the principal quantum number, r is the distance from the nucleus and ζ is the effective nuclear charge (which controls how quickly the electron density decays from the nucleus). The final term, Y_{lm} , is the spherical harmonic for the angular contribution and determines the shape of the orbital. These orbitals are referred to as Slater-type orbitals (STOs).

$$\psi_f^{STO} = Nr^{n-1}e^{-\zeta r}Y_{lm}(\theta, \phi) \quad \text{Equation 57}$$

A more computationally efficient method for generating the orbitals, is the use of Gaussian-type orbitals (GTOs).⁴⁴ The form of the GTO is similar to that of the STO (Equation 58), however, now the radial distribution depends on r^2 rather than r .

$$\psi_f^{GTO} = Nr^{n-1}e^{-\zeta r^2}Y_{lm}(\theta, \phi) \quad \text{Equation 58}$$

Whilst GTOs are more computationally efficient, STO's perform better in their modelling of the orbital shape. Consider Figure 7, which shows a representation of the STO (in black) and GTO (in red) for the 1s orbital of the hydrogen atom. The shape of the STO and the GTO differ largely at the nucleus.

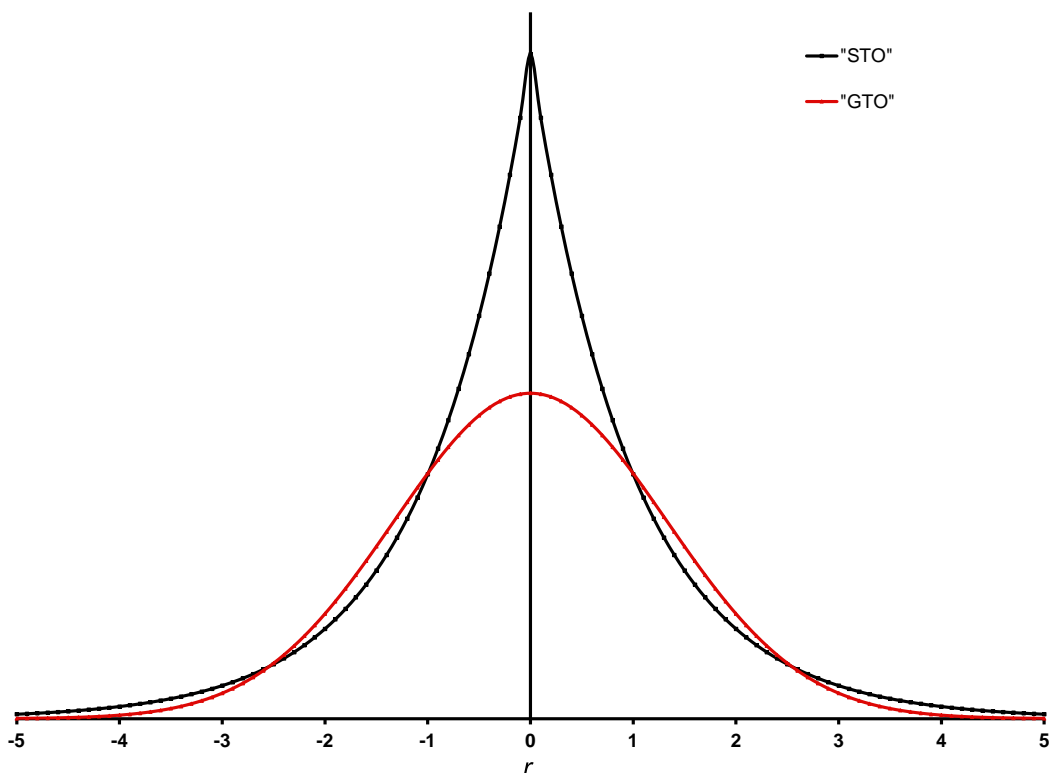


Figure 7. A representation of the 1s STO and GTO orbitals. The image was produced using an Excel program provided by Magalhães.⁴⁵

To overcome the deficiencies of the GTOs, the idea of a contracted basis set was formed (Equation 59). For example, in Figure 8, the red line shows the result of the addition of 3 different GTOs (the orange, blue and green lines), which is termed as STO-3G. Each GTO has varied orbital coefficients (c) and exponents (the $e^{-\zeta r^2}$ term), that were mathematically fit to provide the best approximation of the STO. Whilst the STO-3G basis set still doesn't model the shape of the orbital at the nucleus correctly, it is better than a single GTO (Figure 7), and it more accurately follows the shape of the STO as the orbital moves further from the nucleus.

$$\Psi^{STO-3G} = c_1\psi_1^{GTO} + c_2\psi_2^{GTO} + c_3\psi_3^{GTO} \quad \text{Equation 59}$$

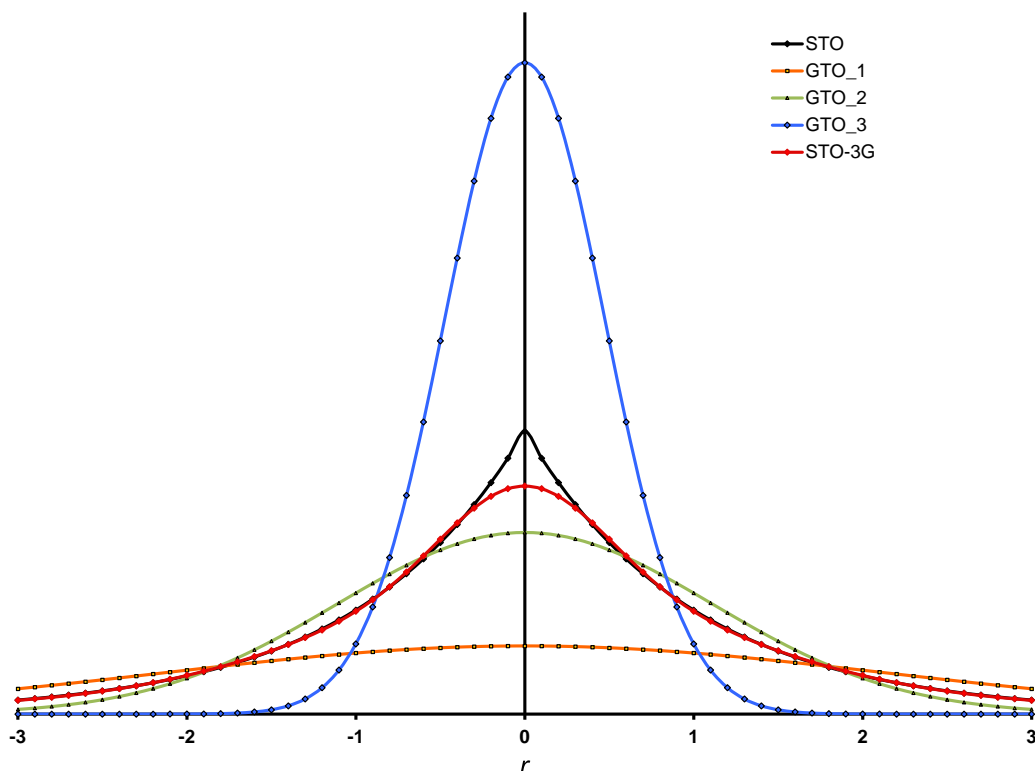


Figure 8. A representation of the 1s, using 3 GTO's (STO-3G). The image was produced using an Excel program provided by Magalhães.⁴⁵

The STO-3G basis set is now rarely used, with larger, more complicated basis sets now readily available. Basis sets are typically referred to by the ζ -type, which describes the number of sets of contracted orbitals that are used. The more functions that are available, the larger the basis set is said to be, with more variational freedom in the basis set variables.

The 6-31G*,⁴⁶⁻⁵⁰ and 6-31+G*,⁴⁶⁻⁵² Pople basis sets have been used within this thesis. These are both split-valence double- ζ basis sets, with the core orbitals described by 6 functions, and the valence orbitals each described by a contracted set which contains 3 functions, and an additional, uncontracted function. The 6-311+G* basis set has also been used,^{52,53} which is a triple- ζ basis set similar to those previously described, however the valence electrons contain an additional uncontracted function. In the Pople basis sets, a single "*" refers to an additional polarisation function on the heavy atoms (*e.g.* not hydrogen), which gives the atom an additional orbital not considered occupied at the ground-state (*e.g.* a d-orbital for carbon atoms) which allows the electron density to be modelled in an unsymmetrical fashion round the nucleus. The single "+" denotes an additional diffuse function on the heavy atoms. These are larger orbitals

which allows for electron density to be located further away from the nucleus, which can be important when modelling anions.

The Ahlrichs def-SV(P),^{54–56} and def2-TZVPP,^{56–58} basis sets have also been used in the following studies in this thesis. These are both split-valence basis sets of double- and triple- ζ quality respectively. Here, the (P) of the def-SV(P) basis set denotes that heavy atoms contain polarisation functions (similar to the “*” of the Pople basis sets). The def2-TZVPP is a large basis set which contains 2 sets of polarisation functions, which gives hydrogen atoms both p- and d-orbitals, and heavy atoms, such as carbon, d- and f- orbitals, which results in a high degree of freedom within the basis set.

Finally, an electrostatic core potential (ECP) has been used to describe the core electrons of the gold atom used in Chapter 3.⁵⁶ ECP’s are commonly used to describe the core electrons of large atoms such as transition metals by treating these electrons as a pseudopotential which then acts upon the valence electrons. This takes into consideration nuclear shielding and relativistic effects, whilst reducing the overall cost of modelling the transition metal element.

1.1.8 DFT Calculation Procedure

DFT calculations are formulated similarly to Hartree–Fock calculations. The one electron Kohn–Sham (KS) operator (\hat{f}^{KS}) operates on the single-electron orbitals (ψ) contained within the Slater determinant (Equation 43, repeated here as Equation 60) to return the energies (ϵ) of the orbitals (Equation 61).

$$\Psi = \frac{1}{\sqrt{N!}} \begin{vmatrix} \psi_1(\vec{r}_1) & \psi_2(\vec{r}_1) & \cdots & \psi_N(\vec{r}_1) \\ \psi_1(\vec{r}_2) & \psi_2(\vec{r}_2) & \cdots & \psi_N(\vec{r}_2) \\ \vdots & \vdots & \ddots & \vdots \\ \psi_1(\vec{r}_N) & \psi_2(\vec{r}_N) & \cdots & \psi_N(\vec{r}_N) \end{vmatrix} \quad \text{Equation 60}$$

$$\hat{f}_i^{KS} \psi_i = \epsilon_i \psi_i \quad \text{Equation 61}$$

The KS operator is separated into kinetic energy, electron-nuclear attraction potential, electron-electron repulsion potential, and the exchange-correlation potential (V_{xc}) operator terms (Equation 62). Here, the exchange-correlation operator (Equation 63) is the first derivative of the exchange-correlation energy (E_{xc}), which is defined by the choice of functional.

$$\left(-\frac{1}{2m} \nabla^2 - \sum_A \frac{Z_A}{r_{1A}} + \sum_j \frac{|\psi_j(\vec{r}_2)|}{r_{12}} d\vec{r}_2 + V_{XC}(\vec{r}_1) \right) \psi_i = \epsilon_i \psi_i \quad \text{Equation 62}$$

$$V_{XC}(\vec{r}) = \frac{\partial E_{XC}[\rho(r)]}{\delta \rho(r)} \quad \text{Equation 63}$$

The single-electron molecular orbitals (ψ) in the Slater determinant are described using the LCAO approach as discussed in Section 1.1.7 and can therefore be represented as in Equation 64, in which a number (L) of basis set functions (ϕ), with the respective coefficient (c), describes the molecular orbital.

$$\psi = \sum_{\mu=1}^L c_{i\mu} \phi_i \quad \text{Equation 64}$$

Equation 64 can be substituted into Equation 61, in place of the single electron wavefunction (Equation 65). The equation can then be multiplied by another wavefunction (ϕ_j) and integrated over all space (Equation 66) to set up a matrix equation (Equation 67), where F^{KS} is the Kohn-Sham matrix and S is the overlap matrix. Additionally, now the coefficients (C) and the energies (ϵ) are also represented in matrices.

$$\hat{f}_i^{KS}(\vec{r}) \sum_{\mu=1}^L c_{i\mu} \phi_i(\vec{r}) = \epsilon_i \sum_{\mu=1}^L c_{i\mu} \phi_i(\vec{r}) \quad \text{Equation 65}$$

$$\sum_{\mu=1}^L c_{i\mu} \int \phi_j(\vec{r}) \hat{f}_i^{KS}(\vec{r}) \phi_i(\vec{r}) d\vec{r} = \epsilon_i \sum_{\mu=1}^L c_{i\mu} \int \phi_j(\vec{r}) \phi_i(\vec{r}) d\vec{r} \quad \text{Equation 66}$$

$$F^{KS} C = S C \epsilon \quad \text{Equation 67}$$

The electron-electron coulombic repulsion term, J (Equation 47, repeated here in Equation 68), requires the electron density. The electron density can now be represented as an expanded set of all basis functions and their respective coefficients (Equation 69). The coefficients, c , can be represented together in density matrix, P , and the coulombic repulsion term, J , can now be given in terms of substituent basis functions (Equation 70).

$$J[\rho] = \frac{1}{2} \iint \frac{\rho[r_i]\rho[r_j]}{r_{ij}} dr_i dr_j \quad \text{Equation 68}$$

$$\rho(r) = \sum_i^N \sum_\mu^L \sum_\nu^L c_{\mu i} \phi_i(r) c_{\nu j} \phi_j(r) \quad \text{Equation 69}$$

$$J[\rho] = \sum_\lambda^L \sum_\sigma^L \mathbf{P}_{\lambda\sigma} \iint \frac{\phi_\mu(\vec{r}_1)\phi_\nu(\vec{r}_1)\phi_\mu(\vec{r}_2)\phi_\nu(\vec{r}_2)}{r_{12}} d\vec{r}_1 d\vec{r}_2 \quad \text{Equation 70}$$

To calculate the potential energy J , L^4 integrals (where L is the number of basis set functions, Equation 64) are required to be calculated. However, the resolution of identity approximation (RI-J), can be used, which states that the electron density can be approximately equal ($\tilde{\rho}(\vec{r})$) to a separate set of basis functions (Equation 71). The coulombic potential can therefore be represented as Equation 72, with the calculation now requiring the solutions to L^2K integrals, a large reduction in the number of integrals computed, without a significant decrease in the accuracy of the calculation. This approximation, as implemented in TURBOMOLE, was used throughout Chapter 3.⁵⁹

$$\rho(\vec{r}) \approx \tilde{\rho}(\vec{r}) = \sum_\kappa^K c_\kappa \omega_\kappa \quad \text{Equation 71}$$

$$J[\rho] = \sum_\kappa^K \iint \frac{\phi_\mu(\vec{r}_1)\phi_\nu(\vec{r}_1)\omega_\kappa(\vec{r}_2)}{r_{12}} d\vec{r}_1 d\vec{r}_2 \quad \text{Equation 72}$$

The overall procedure can be summarised in a simplified scheme (Figure 9).

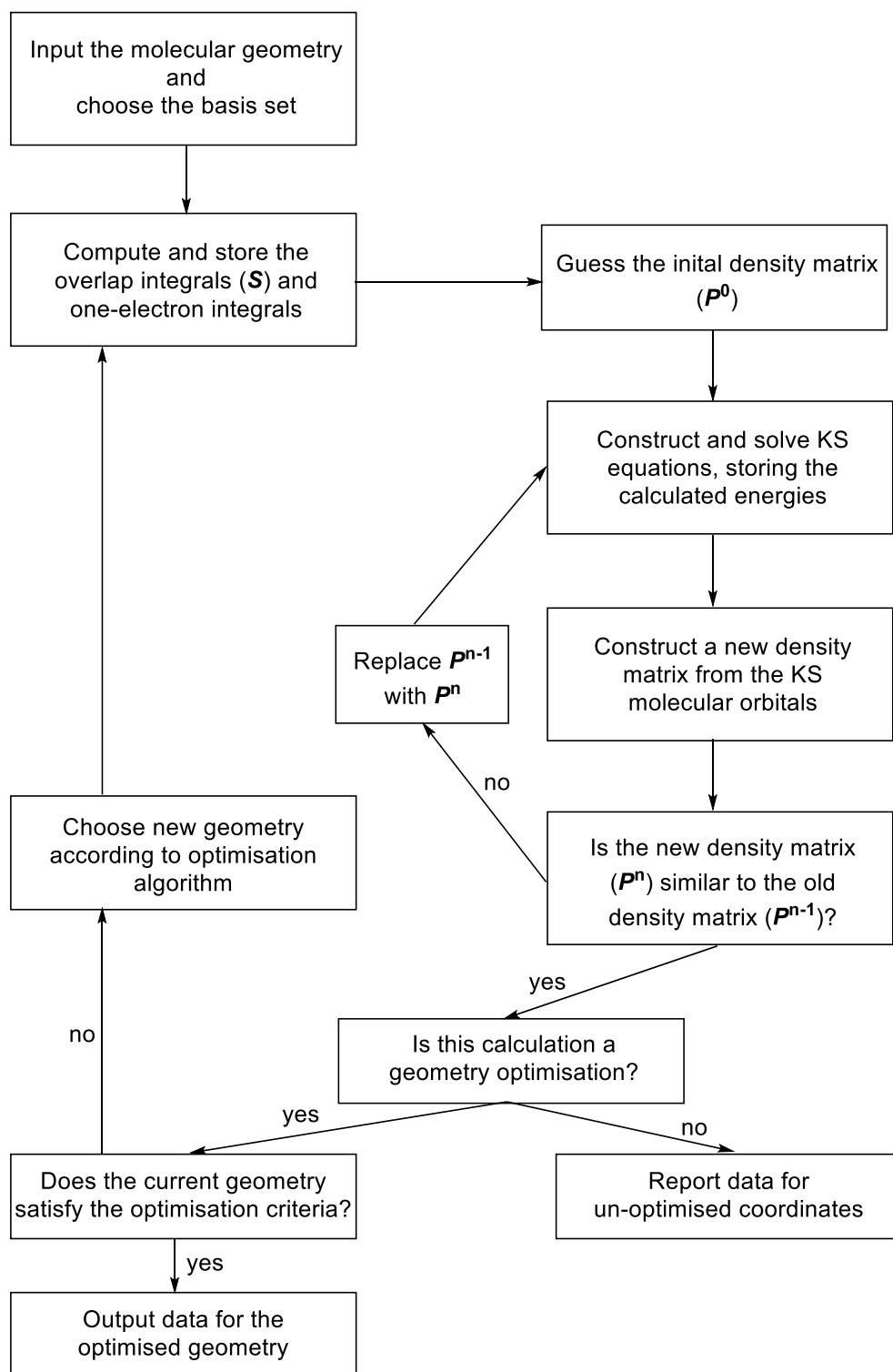


Figure 9. Representation of the DFT calculation procedure. Modified from a diagram produced by Cramer.³

1.1.9 Frequency Calculations and Thermodynamic Corrections

The procedure for the DFT calculations described in Section 1.1.8 results in the electronic energy of the molecule, however this doesn't take into consideration important enthalpic and entropic effects. To calculate these, frequency calculations are required, which also generates a vibrational spectrum. The vibrational spectrum is also useful and has primarily been used within this thesis to ensure that the calculated geometry of a molecule is a true minimum, or a transition state, by ensuring that there are either 0 or 1 imaginary (negative) frequencies respectively, the reasons for this are discussed shortly.

The frequency calculations use the assumption that molecules can be treated with the classical harmonic oscillator model (Figure 10), which assumes that the bond between two atoms acts as a spring, with a force constant, k . The potential energy of the bond therefore increases when the internuclear distance, R , is both extended or compressed from the equilibrium geometry, R_e . The vibrational energy levels are then evenly distributed throughout this curve.

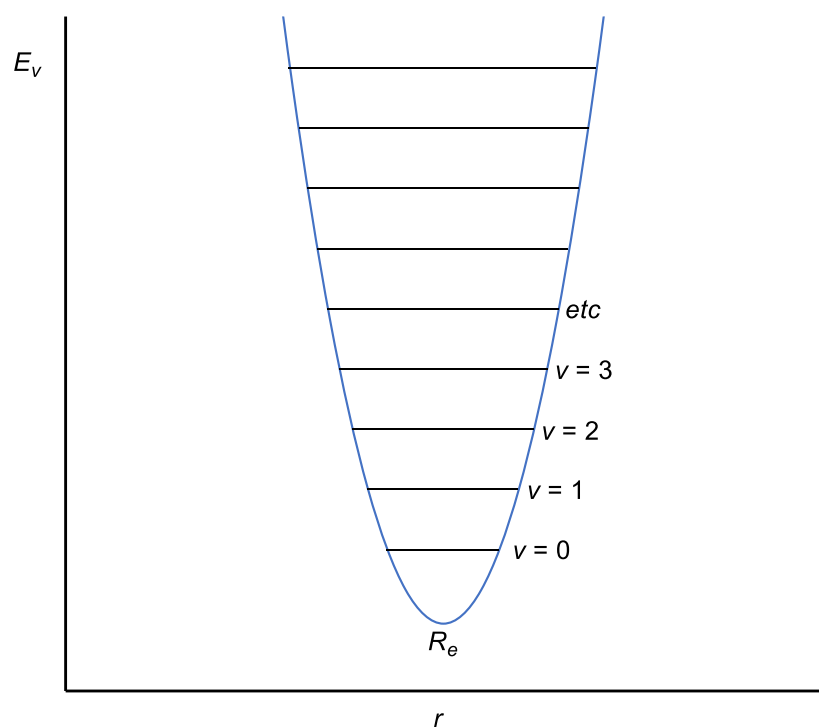


Figure 10. Representation of the harmonic oscillator model.

The energy of a vibrational level is given by Equation 73, where v is the vibrational quantum number, and ν (Equation 74) is related to the reduced mass of the atoms (μ) and the force constant (k). To satisfy the Heisenberg uncertainty principle,²⁵ the molecule must always be in vibration (otherwise both the location and velocity of the atoms is known), and the lowest

energy vibration is given when $v = 0$. The difference in energy between this state, and the energy at R_e is known as the zero-point energy (ZPE).

$$E_v = \left(v + \frac{1}{2} \right) h\nu \quad \text{Equation 73}$$

$$\nu = \frac{1}{2\pi} \sqrt{\frac{k}{\mu}} \quad \text{Equation 74}$$

Both the Gaussian and TURBOMOLE software packages calculate the vibrational spectra by forming a square matrix of size $3N$ (where N is the number of atoms in the molecule) referred to as the Hessian matrix. The Hessian matrix is an analogue of the second derivative for functions in multiple dimensions (*e.g* the potential energy surface (PES) of a molecule) and it describes the curvature of the function. The elements of the Hessian matrix contain the second derivative of the energy, with respect to each Cartesian coordinate, which is then transformed to mass-weighted coordinates.^{59,60} The diagonal of the mass-weighted Hessian matrix defines the mutually orthogonal directions on the PES (the eigenvectors), and also gives the eigenvalues (λ) which describes the curvature in the direction of the eigenvector. If all the eigenvalues are positive, the geometry is said to be a true minimum, and is a requirement for intermediates on the PES. At a transition state, one eigenvalue is negative, which corresponds to the energy increasing in the direction of its corresponding eigenvector. The eigenvalues (λ) are then used to give the vibrational frequency (ν , in cm^{-1}) as shown in Equation 75 (where c is the speed of light and is used to convert frequency units to wavenumbers), using the harmonic oscillator model.⁶¹

$$\nu_i = \frac{\sqrt{\lambda_i}}{2\pi c} \quad \text{Equation 75}$$

With the vibrational frequencies (ν_i) calculated, it is now possible to calculate the ZPE (E_0 , Equation 76) and the thermodynamic quantities using statistical thermodynamics. It is assumed that the molecules of the system are non-interacting and therefore are treated as an ideal gas. Then, the partition function, q_{tot} (Equation 77), is given as the sum of the translational (q_t), rotational (q_r), vibrational (q_v) and electronic (q_e) partition functions.⁶⁰

$$E_0 = \sum_i \frac{1}{2} \nu_i \quad \text{Equation 76}$$

$$q_{tot} = q_t + q_r + q_v + q_e \quad \text{Equation 77}$$

The translational partition function (q_t) is given in Equation 78, where m is the mass of the molecule, k_B is the Boltzmann constant, T is the temperature, P is the pressure and h is Planck's constant. The rotational partition function (q_r) for a nonlinear, polyatomic molecule is shown in Equation 79, where σ_r is the symmetry number for rotation and θ_r is the rotational temperature (defined in Equation 80, where I is the moment of inertia).

$$q_t = \left(\frac{2\pi m k_B T}{h^2} \right)^{\frac{3}{2}} \frac{k_B T}{P} \quad \text{Equation 78}$$

$$q_r = \frac{\sqrt{\pi}}{\sigma_r} \left(\frac{T^{\frac{3}{2}}}{\sqrt{\theta_{r,x} \theta_{r,y} \theta_{r,z}}} \right) \quad \text{Equation 79}$$

$$\theta_r = \frac{h^2}{8\pi^2 I k_B} \quad \text{Equation 80}$$

To calculate the vibrational partition function (q_v), the contribution to the energy from each vibrational mode, K , must be considered (Equation 81). Here, θ_v is the vibrational temperature of each mode and is calculated as shown in Equation 82 for each vibrational mode, K . It should be noted that the contributions from imaginary frequencies (*e.g.* in transition states) are neglected in these calculations. To calculate the electronic partition function (q_e), Gaussian assumes that all electronically excited states are thermally inaccessible, and therefore the partition function is given as Equation 83, where ω_0 is the degeneracy of the ground state.

$$q_v = \prod_K \left(\frac{e^{-\frac{\theta_{v,K}}{2T}}}{1 - e^{-\frac{\theta_{v,K}}{T}}} \right) \quad \text{Equation 81}$$

$$\theta_{v,K} = \frac{h\nu_K}{k_B} \quad \text{Equation 82}$$

$$q_e = \omega_0 \quad \text{Equation 83}$$

The Gaussian software then uses Equation 84 and Equation 85 as the general forms for the entropy (S) and internal energy (E) respectively for each type of motion,⁶⁰ where R is the ideal gas constant, V is the volume, N is the number of molecules and q_x refers to the relevant partition function. The total entropic and internal energies can then be used to calculate the thermodynamic corrections.

$$S_x = R(\ln(q_x) + T \left(\frac{\partial \ln(q_x)}{\partial T} \right)_V) \quad \text{Equation 84}$$

$$E_x = Nk_B T^2 \left(\frac{\partial \ln(q_x)}{\partial T} \right)_V \quad \text{Equation 85}$$

The Gaussian software package reports the thermodynamic corrections as follows, with the corresponding formulae (Equation 86–Equation 90). The energies reported in Chapters 2, 4 and 5 are all Gibbs energies, calculated by the addition of the Thermal correction to Gibbs Free Energy (Equation 89), to the calculated electronic energy, with the thermodynamic corrections calculated at $T = 298.15$ K. The contributions to the entropy S_{corr} (Equation 90), are calculated from the derivatisation of the partition function for each mode of motion, with Equation 84.

$$\text{Zero-point correction} = E_0 = \sum_i \frac{1}{2} \nu_i \quad \text{Equation 86}$$

$$\text{Thermal correction to Energy} = E_{tot} = E_t + E_r + E_v + E_e \quad \text{Equation 87}$$

$$\text{Thermal correction to Enthalpy} = H_{corr} = E_{tot} + k_B T \quad \text{Equation 88}$$

$$\text{Thermal correction to Gibbs Free Energy} = G_{corr} = H_{corr} - TS_{corr} \quad \text{Equation 89}$$

$$S_{corr} = S_t + S_r + S_v + S_e \quad \text{Equation 90}$$

The TURBOMOLE software calculates the energies using a similar methodology,⁵⁹ with different nomenclature. Here, the chemical potential (Chem. pot., Equation 91) is calculated using partition functions. The Gibbs energy is then calculated with the addition of the chemical

potential to the electronic energy. The energies reported in Chapter 3 are all Gibbs energies, calculated at $T = 298.15$ K.

$$\text{Chem. pot.} = ZPE - RT \cdot \ln(q_t q_r q_v q_e) \quad \text{Equation 91}$$

1.1.10 Solvent Corrections

Until now, the calculations presented assumed that the molecules are in the gas phase, however, in systems such as charged species, it is often more appropriate to consider the energy of the system with a solvent correction applied.

There are two main methods to model the solvent interaction. The first method is known as explicit solvation, which directly includes solvent molecules in the calculations.⁶² These methods cannot usually be used to model bulk solution in quantum mechanical methods, since the number of electrons (and therefore, the number of basis set functions) is too large. Instead, explicit solvation is commonly used with less-computationally expensive models, such as molecular mechanics (MM). For DFT calculations, implicit solvation is usually included, which treats the solvent as a continuous medium.⁶³

Where used, the solvent models in this thesis were applied using the polarisable continuum model (PCM),⁶⁴ in Chapters 2,4 and 5 for the Gaussian calculations, or the conductor-like screening model (COSMO) used within TURBOMOLE,^{65,66} for Chapter 3. Both methods build a cavity surrounding the molecules being studied (Figure 11). Spheres corresponding to the van der Waals radii (defined by the software) of the atoms are constructed around the molecules, defining the solvent excluded surface. Additional spheres, the radii of which is determined by the solvent (referred to as a solvent probe), are then built around the solvent excluded surface, the centre points of these defines the solvent accessible surface.

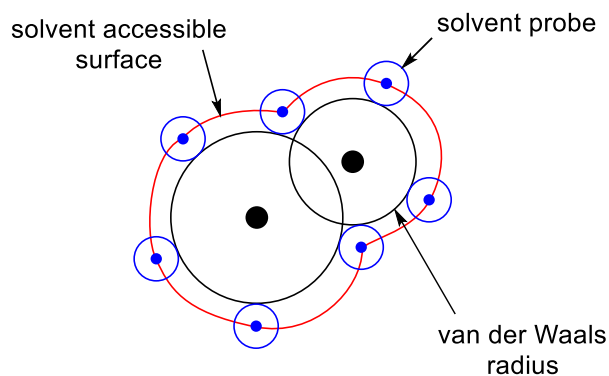


Figure 11. Visual representation of the cavity built during the PCM and COSMO solvent models.

Outside the cavity, the solvent is considered as its dielectric constant, with the solvent correction calculated depending on the molecular interaction with the solvent accessible surface, which is where the COSMO and PCM models differ in their approach.

1.1.11 Dispersion Corrections

London dispersion interactions are a type of stabilising van der Waals force, which occurs over long distances,⁶⁷ with the energy calculated as in Equation 92 (for non-identical atoms or molecules), where I is the first ionisation energy, α is the polarizability, and r is the internuclear distance.

$$V = -\frac{3}{2} \frac{I_1 I_2}{I_1 + I_2} \frac{\alpha_1 \alpha_2}{r^6} \quad \text{Equation 92}$$

Due to the dependence on r^{-6} for the energy of the interaction, these long-range interactions are often considered weak. However, since London interactions are additive, the overall contribution to the energy of large molecules can be considered significant,⁶⁸ and examples have been found where increasing steric bulk have increased the stability of a molecule, both computationally and experimentally.^{69,70}

Since DFT theory calculates the energy of a system based on the local electron density, or its gradient, DFT calculations fail to adequately account for the long-range London interactions. Establishing methods to account for this energy has therefore been the subject of study for the improvement of DFT accuracy.

Two methods for accounting for London dispersion have been used within this thesis. The first method, used the Minnesota functionals, M06 and M06-2X.⁴¹ These functionals were specifically highly parametrised to account for non-covalent interactions, by using a training set of data, with which various coefficients could then be optimised to produce the best fit to the available data. The M06 and M06-2X functionals do perform well in benchmarking, with the M06 functional described as a general functional, whereas the M06-2X is more specific to organic molecules.

The second method used in this thesis, is the inclusion of Grimme's D3 correction,⁷¹ with Becke–Johnson damping (D3(BJ)).^{72–75} In 2010, Grimme and co-workers published the D3 dispersion method (also referred to as DFT-D3), which takes the general form shown in Equation 93, where C^{AB} denotes the average n th order dispersion correction, for each atom pair, R_{AB} is the internuclear distance, s is a functional dependant scaling factor, and f_{damp} is a damping function. The damping function is used to define the cut-off for the dispersion corrections to ensure that close-range interactions aren't overestimated. Overall, the D3 method has advantages over using the Minnesota functionals, since the energy is calculated using formulae derived from the electron density, rather than from fitting to test data.

$$E_{disp}^{DFT-D} = -\frac{1}{2} \sum_{A \neq B} \sum_{n=6,8,10,\dots} s_n \frac{C_n^{AB}}{R_{AB}^n} f_{damp}(R_{AB}) \quad \text{Equation 93}$$

Becke and Johnson published an alternative method for calculating the dispersion, with a different approach to better model the effects of spatially close atoms (Equation 94). The Becke–Johnson (BJ) damping model was then included in a revised DFT-D3 method (Equation 95), and referred to as D3(BJ), where α_1 and α_2 are parameters established experimentally. Overall, the D3(BJ) method was shown to more accurately model the short-range behaviour for dispersion,⁷⁵ and is now often considered a standard addition in DFT calculations.

$$E_{disp} = -\frac{1}{2} \sum_{A \neq B} \frac{C_n^{AB}}{R_{AB}^n + const.} \quad \text{Equation 94}$$

$$E_{disp}^{D3(BJ)} = -\frac{1}{2} \sum_{A \neq B} s_6 \frac{C_6^{AB}}{R_{AB}^6 + [f(R_{AB}^0)]^6} + s_8 \frac{C_8^{AB}}{R_{AB}^8 + [f(R_{AB}^0)]^8} \quad \text{Equation 95}$$

$$f(R_{AB}^0) = \alpha_1 R_{AB}^0 + \alpha_2 \quad \text{Equation 96}$$

$$R_{AB}^0 = \sqrt{\frac{C_8^{AB}}{C_6^{AB}}} \quad \text{Equation 97}$$

1.1.12 Summary

This section has summarised the background theory of computational chemistry, with a focus on DFT calculations, which are used throughout the work described in this thesis, since they provide a good balance between accuracy,^{76–79} whilst also scaling favourably, such that calculations for systems containing more than 100 atoms are possible within a reasonable time frame (Table 1).³ In performing DFT calculations the choice of functional and basis set is an important consideration, which can have an impact on the calculated energies. This is particularly important when changing from LDA to GGA and hybrid functionals, where the method of calculating the exchange-correlation energy is significantly different.

Table 1. Scaling factors of common computational methods, where N is the size of the system. Note that whilst DFT scales to N^3 , the overall calculation time might be longer than the equivalent HF calculation.

Method	Scaling Factor
Hartree–Fock (HF)	N^4
DFT	N^3
MP2	N^5
CCSD	N^6
CCSD(T)	N^8

Other considerations must be made to consider how accurately the DFT model compares to the reaction conditions. Solvent corrections can have a significant effect, particularly when modelling charged species, although intramolecular reactions don't necessarily need the solvent effects to be considered.

It is advised when first performing DFT calculations, to benchmark the computational method used. This can be done by comparison with reported literature which uses similar compounds, or by comparing the results of DFT calculations using different methods, with relevant experimental data. Calculated transition state energies at different methods could be compared with kinetic data, or by comparing the regio- or stereochemical outcomes.

With these considerations in mind, DFT can be a powerful tool to explore different aspects of chemistry and provide insight to experimental data.

1.2 DFT studies of Au(I) catalysed reactions: anion effects and reaction selectivity

1.2.1 Introduction

Whilst DFT calculations have been used throughout the work described in this thesis, one of the most significant applications is within Chapter 3, in which the gold(I) coordination chemistry of alkynes substituted with electron-withdrawing groups was studied in detail. It was therefore considered appropriate to review the application of DFT with gold(I) catalysis, to highlight factors that were important to consider, such as solvation effects and a suitable choice of basis set and functional. The work presented in this section is the subject of a published review article.⁸⁰

Interest in gold catalysis has increased exponentially over the last 20 years.⁸¹ Primarily, the catalytic applications of gold(I) are based on its ability to act as a π -acid. Au(I) complexes are able to coordinate to and activate unsaturated C–C bonds, particularly alkynes,^{82,83} although similar reactivity has also been observed with alkenes^{84,85} and allenes.^{86,87} The typical mechanism proposed for gold(I)-catalysed reactions involves the coordination of the gold(I) complex to the unsaturated C–C bond, forming an $\eta^2(\pi)$ complex, which activates the π -system to undergo attack by a nucleophile (**1.1** \rightarrow **1.2**). Protodemetalation then occurs (**1.2** \rightarrow **1.3**), regenerating the Au(I) catalyst and allowing further reactions to take place (Figure 12).^{88–90}

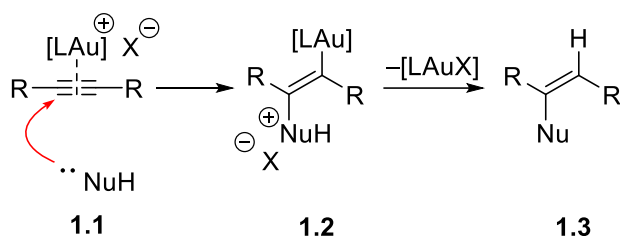


Figure 12. Typical scheme for alkyne activation by gold(I) cations.

The nature of the gold catalyst used, and its coordination environment, can have a significant effect on reaction outcomes. This may be by simply increasing the reaction yield, but in many cases, it can also alter the reaction selectivity and change the ratio of products that are formed. The ligand used can also influence the reaction outcomes, with phosphine or *N*-heterocyclic carbene (NHC) ligands being the most common, and the counterion used is also often altered during reaction optimisation.^{91,92}

Computational chemistry utilising density-functional theory (DFT) is frequently used in studies of catalytic reactions.^{93–95} DFT offers a good balance of calculation time versus accuracy and is,

therefore, often the method of choice to explore the mechanism of transition metal catalysed reactions.

Papers benchmarking the success of DFT calculations to study gold(I) complexes have been published, which provide recommendations on the level of theory best employed for studying reactions using gold(I) catalysis.^{96–100} The double-hybrid B2PLYP functional performed well across multiple studies, with BP86,^{97,99} PBE0,⁹⁸ wB97X⁹⁸ and M06^{96,97} functionals also shown to be successful at modelling the energies and geometries of gold(I) complexes. Ahlrichs' def2 basis sets generally performed well, with a triple- ζ type basis set with polarisation recommended.⁹⁹ Electrostatic core potentials (ECPs) such as LANL2DZ or SDD are commonly used on the gold atom to account for relativistic effects.

In this section, recent examples of the use of DFT to explore reaction processes are provided, focused on the effects of including the anions used in the reaction, and studying how DFT can be used to explore the selectivity of gold(I)-catalysed reactions. A wide range of literature was available, and it was not possible to review them all, however other papers which were instructive are highlighted.^{101–108}

Throughout this section, numbers are used to indicate compounds (*e.g.* **1.1**), whereas DFT calculated states are denoted by letters (*e.g.* **1.A**), with transition states labelled specifically as 'TS' (*e.g.* **1.TS_{CD}**, which refers to the transition state connecting state **1.C** and **1.D**).

1.2.2 Using DFT to explain the effects of the anion on the reaction mechanism

In reactions utilising gold(I) catalysts, typically a ligated gold(I) chloride (LAuCl) precatalyst is used, which is then activated by a metal salt containing a weakly coordinating anion. This results in salt metathesis, enabling the formation of an active Lewis acidic cationic gold(I) species (LAu⁺) in solution which is catalytically active.^{109–111} Other activation methods, such as protonolysis of an alkylgold and hydroxide species,^{112–114} or *via* sonication and centrifugation,¹¹⁵ have been used to avoid any competing "silver effects".^{115,116}

Many studies utilising DFT methods have successfully captured the experimental reaction outcomes by focussing solely on the cationic gold-based component of the catalyst system without consideration of the counteranion.^{117–124} However, recent papers have detailed

instances where optimising the counterion has been important for the course of the reaction.^{91,92,125–127}

In 2009, Zuccaccia *et al.* studied ion pairing in cationic olefin-gold(I) complexes.¹²⁸ Two 4-Me-styryl gold(I) complexes were synthesised with either a triphenylphosphine (**1.4PPh₃**) or NHC ligand (**1.4NHC**, NHC = 1,3-bis(di-*iso*-propylphenyl)-imidazol-2-ylidene) (Figure 13). Both complexes had a tetrafluoroborate anion which enabled the use of ¹⁹F,¹H-HOESY NMR experiments to study the preferred orientation of the anion with respect to the gold complex under low temperature conditions.

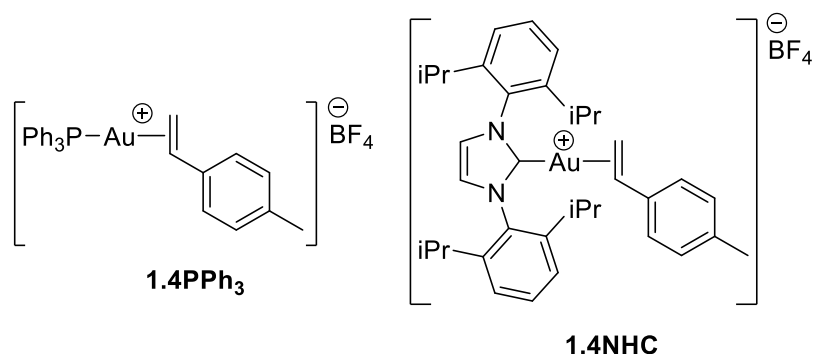


Figure 13. 4-Me-styryl gold(I) complexes studied by Zuccaccia *et al.*¹²⁸

These NMR studies showed that the choice of ligand influenced the ion-pairing (Figure 14), with strong contacts observed between the olefinic protons and the tetrafluoroborate anion in complex **1.4PPh₃**. In contrast, for complex **1.4NHC**, contacts were observed primarily with the imidazole protons furthest away from the styrene.

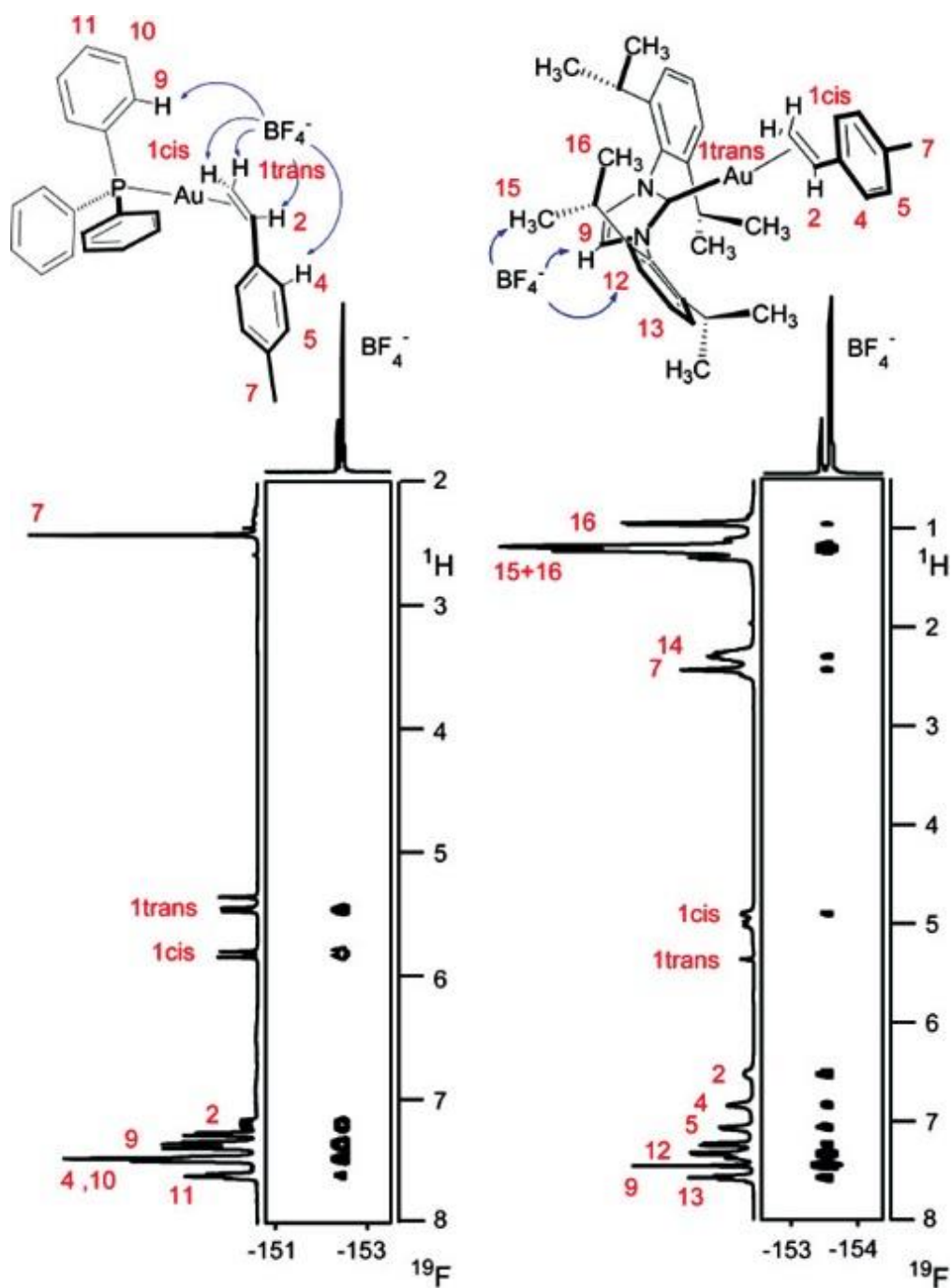


Figure 14. Low temperature $^{19}\text{F},^1\text{H}$ -HOESY spectra of **1.44PPh₃** (left) and **1.4NHC** (right). Key ion-pairing contacts have been highlighted with assignments made by Zuccaccia *et al.* Reprinted with permission from American Chemical Society, Copyright 2009.¹²⁸

The observed NMR data were further supported by DFT calculations. Geometry optimisations (at the BLYP/ZORA/TZ2P level of theory) of varying configurations were performed, and these confirmed that the lowest energy arrangement of the complexes agreed with the NMR experiments (Figure 15).

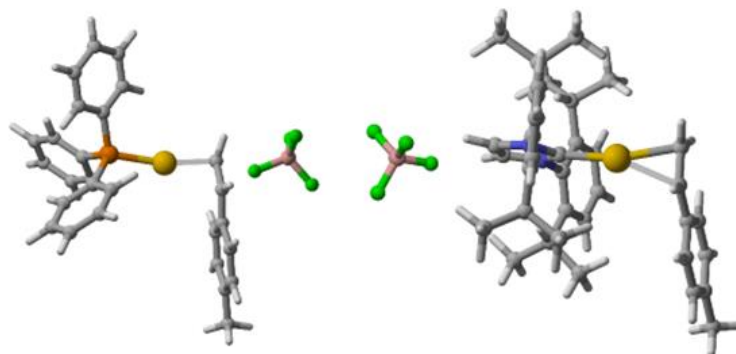


Figure 15. Lowest energy arrangements of **1.4PPh₃** (left) and **1.4NHC** (right) as calculated by DFT by Zuccaccia *et al.*, calculated at the BLYP/ZORA/TZ2P level of theory. Structures reproduced using coordinates located in the original paper's ESI.¹²⁸

This effect was rationalised by analysing the charge distribution and the Coulomb potential of both the styrene cationic complexes (Figure 16). The olefinic protons of the coordinated styrene and, in the case of complex **1.4NHC**, the imidazolium protons at the back of the complex were shown to have the greatest positive charge within the complex (denoted as a blue colour on the isodensity surface), and therefore are the most attractive points for counterion coordination.

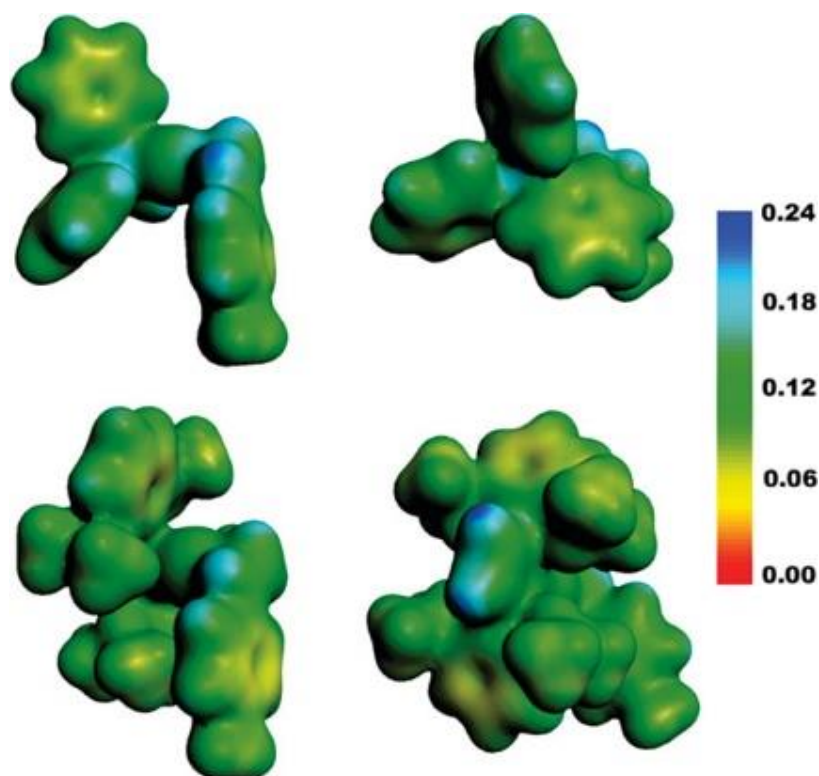


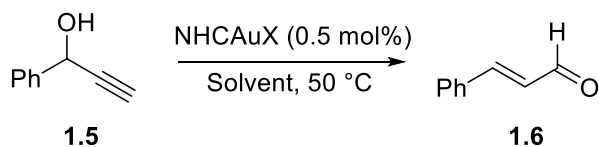
Figure 16. Side (left) and back (right) views of the DFT calculated structures of **1.4PPh₃** (top) and **1.4NHC** (bottom), without counterion. Coulomb potential is mapped on an electronic isodensity surface ($\rho = 0.007 \text{ e}/\text{\AA}^3$. Coulomb potential in au). Reprinted with permission from American Chemical Society, Copyright 2009.¹²⁸

Further studies examined the effects of changing both the ligand and the unsaturated hydrocarbon coordinated to the gold(I) cation, which highlighted that the anion coordination depends greatly on the ligands in the cationic unit, with coordination most likely observed around the most acidic protons, rather than the gold centre.^{129–131}

This body of work has demonstrated that the location of the anion with respect to the catalytically active cation can be predicted and is often near the most positively charged sites within the complex, providing a starting point for other researchers to consider when including the counterion in their DFT calculations.

In 2021, an extensive report by Sorbelli *et al.* on the gold(I)-catalysed Meyer–Schuster rearrangement of 1-phenyl-2-propyn-1-ol **1.5** was published, particularly focused upon the effects of both the solvent and the counteranion on the turnover frequency (TOF) of the reaction.¹³² Experimentally, clear trends were found in the turnover frequency (TOF) of the reaction, with the efficiency of the reaction decreasing with increasing polarity of the solvent, and the specific counterion used ($\text{TfO}^- > \text{TsO}^- > \text{BF}_4^- > \text{TFA}^-$). Selected optimisation results are shown in Table 2.

Table 2. NHCAuX catalysed Meyer–Schuster rearrangement of 1-phenyl-2-propyn-1-ol **1.5** to cinnamaldehyde **1.6** at 50 °C.



Entry	Solvent	Catalytic System ^[a]	Conv. ^[b] / %	TOF ^[c] / h ⁻¹
1	<i>p</i> -Cymene	NHCAuOTf	91	394
2	<i>p</i> -Cymene	NHCAuCl/ AgOTs ^[d]	11	44
3	<i>p</i> -Cymene	NHCAuCl/ AgTFA ^[d]	0.4	2
4	<i>p</i> -Cymene	NHCAuCl/ AgBF ₄ ^[d]	7	28
5	<i>p</i> -Cymene	NHCAuCl/ AgOTf ^[d]	30	115
6	γ -Valerolactone	NHCAuOTf	23	105

[a] NHCAuOTf (0.0025mmol), **1.5** (0.5 mmol), solvent (200 μ L). [b] Determined by the average value of three measurements after 30 minutes by ¹H NMR. [c] TOF = (mol_{product}/mol_{catalyst})/*t* calculated after 30 minutes. [d] 1.1 eq of silver salt used. NHC = 1,3-bis(di-*iso*-propylphenyl)-imidazol-2-ylidene

The authors used DFT studies to rationalise these data. Formation of $\eta^2(\pi)$ -alkyne complex **1.B** from the uncoordinated species (**1.5** and **1.7**) was considered. Intermediates involved during de-coordination of the counterion demonstrated that the anion interacts with both the gold atom and the hydrogen of the terminal alkyne (Figure 17).

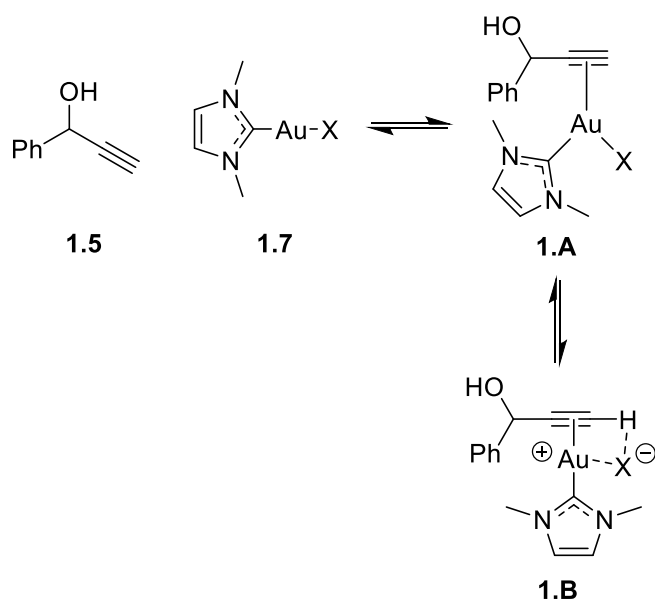


Figure 17. Proposed intermediate structures calculated for the formation of $\eta^2(\pi)$ -alkyne complex **1.B** from the uncoordinated species **1.5** and **1.7**.

Whereas both the tosylate and triflate anions ($X^- = \text{TsO}^-$ and TfO^- , Figure 17) were predicted to be able to form complex **1.B**, a low-lying transition state ($+4.2 \text{ kcal mol}^{-1}$ from **1.5** and **1.7** at the BP86/ZORA//B2PLYP/CPCM level of theory) was found when trifluoroacetate was calculated as the anion ($X = \text{TFA}$, Figure 17), in which the alkyne was deprotonated, resulting in σ -bonded gold alkynyl complex **1.8** (Figure 18). It was postulated that this was the reason behind the poorest efficiency observed in the experiments using AgTFA as the co-catalyst.

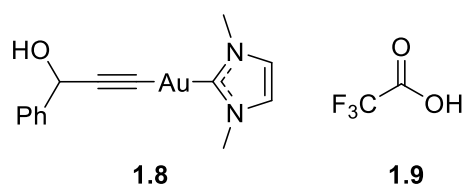


Figure 18. σ -Bonded gold alkynyl complex **1.8** with the formation of acid **1.9**, calculated by DFT when trifluoroacetate was the counterion.

The proposed mechanism for the Meyer–Schuster rearrangement, and the intermediates studied, are shown in Figure 19. To explain the difference in reactivity when using the other anions (namely OTf^- , OTs^- and BF_4^-), the energies of the proposed transition states and intermediates involved in the catalytic cycle were calculated (BP86/ZORA/D3//B2PLYP/CPCM), with the anion proposed to coordinate to the alcohol of the starting material *via* hydrogen bonding. The authors found that the first transition state (**1.TS_{cd}**), corresponding to attack of the alcohol into the gold-coordinated alkyne, was the highest energy, and the relative energies for

the three counterions were consistent with the experimental data, in which the triflate was fastest (+32.6 kcal mol⁻¹ relative to **C**), followed by the tosylate (+34.3 kcal mol⁻¹) and then the tetrafluoroborate (+36.9 kcal mol⁻¹). The authors proposed that the main factors in the energy of transition state (**1.TS_{cb}**) were the hydrogen bonding ability of the anion, and how well the anion coordinates to the gold atom.

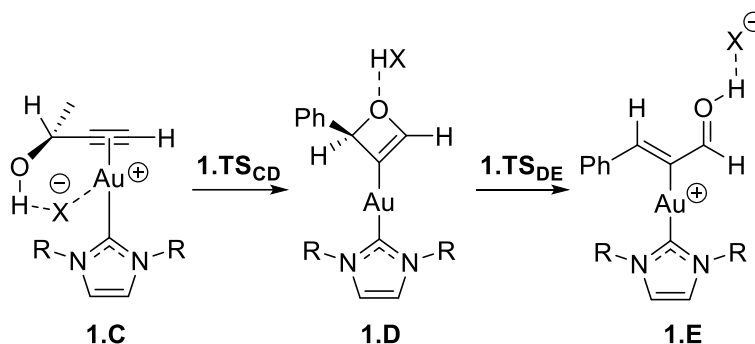


Figure 19. Intermediates studied in the Meyer–Schuster rearrangement of **1.5**. X = OTs, OTf or BF₄. A simplified NHC was used in the calculations (R = Me).

Finally, the effect of solvent polarity was considered. In low polarity media it is understood that an ion pair is formed due to the solvent's inability to strongly coordinate the cation and anion. In more polar solvents, solvation of the cation and anion is efficient, separating the ions.^{133,134} This effect was studied by explicitly modelling a molecule of γ -valerolactone to coordinate to the alcohol. Whilst a structure for the equivalent oxetene intermediate (**1.D**, Figure 19) couldn't be found, the transition state for a one-step process was calculated (**1.F**, Figure 20) which showed a higher energy than the triflate-assisted process (+33.4 vs +31.6 kcal mol⁻¹ in the gas phase at the BP86/ZORA/D3//B2PLYP level of theory), which is consistent with the experimental observations.

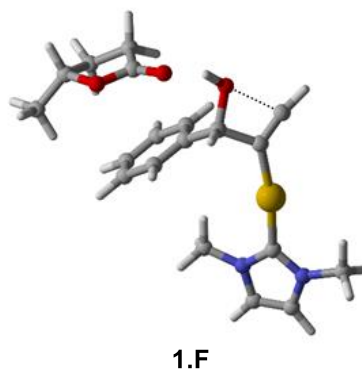


Figure 20. DFT-calculated transition state structure for the Meyer–Schuster rearrangement, in which γ -valerolactone is modelled coordinating to the hydroxyl group. Structures reproduced using coordinates located in the original paper’s ESI.

Overall, the study demonstrates how DFT enables the rationalisation of the reaction rates with different anions, in both the formation of the active catalytic species, and then also in the key intramolecular cyclisation step of the catalytic cycle. Insight from computational chemistry was also able to rationalise the solvent effects, in that higher polarity solvents restrict the ability for the anion to participate, with higher energy transition states observed.

In 2021, Ma *et al.* described the impact of different ring-sized NHC ligands on the gold(I)-catalysed cyclisation of propargylic amide **1.10** to give methylene-3-oxazoline **1.11** (Figure 21a).¹³⁵ As part of this work, DFT was used to study the mechanism of the reaction, to address the role of the counterion in the reaction. It was proposed that the reaction occurs *via* nucleophilic attack of the amide carbonyl, aided by the lone pair of the adjacent nitrogen (Figure 21b).^{136–138}

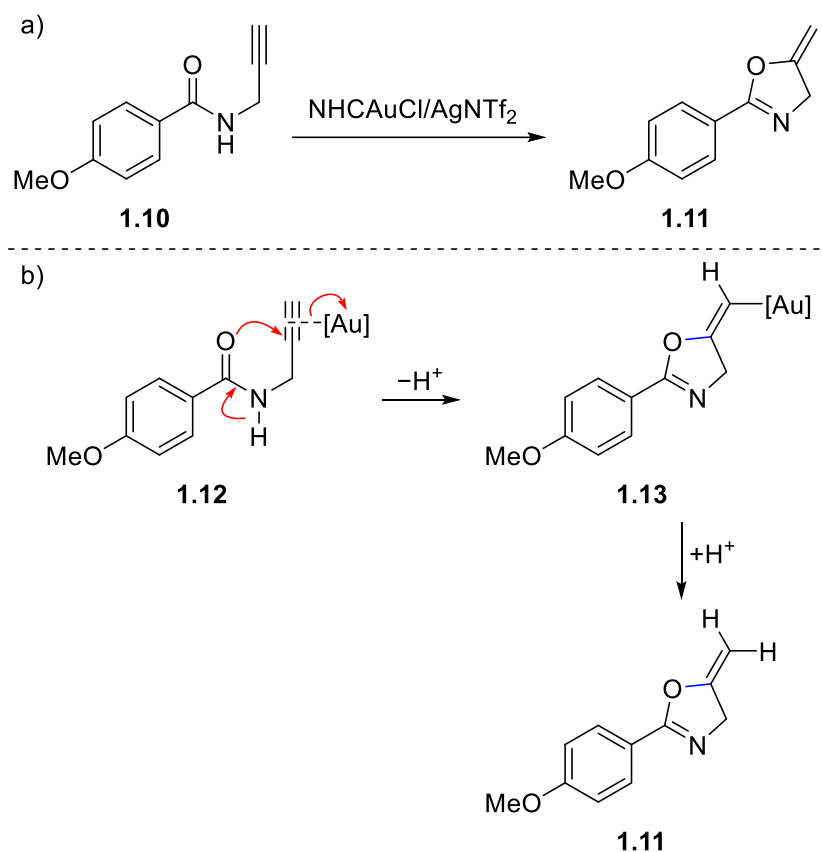


Figure 21. a) Reaction studied by Ma *et al.*,¹³⁵ the cyclisation of propargylic amide **1.10**, resulting in methylene-3-oxazoline **1.11**, first reported by Hashmi *et al.* and then used as a standard reaction when comparing different NHC ligands.^{135–138} b) Mechanism proposed by Hashmi *et al.* for the formation of **1.11**.^{136–138}

The authors first considered different coordination binding modes, both with and without the anion. The $\eta^2(\pi)$ alkyne gold(I) complex with hydrogen bonding of the triflimide anion (**1.H**, Figure 22a) was found to be the lowest energy bound complex at +9.6 kcal mol⁻¹ energy higher than the separate species, at the SMD(CHCl₃)-PBE0-D3BJ/def2-TZVP,6-311+G(d,p)//PBE0-D3BJ/SDD,6-31G(d) level of theory. Other coordination modes were studied, including *O*-coordinated gold species, both with (**1.I**, Figure 22b) and without deprotonation of the amide nitrogen (**1.J** and **1.K**, Figure 22b), however these complexes were much higher in energy.

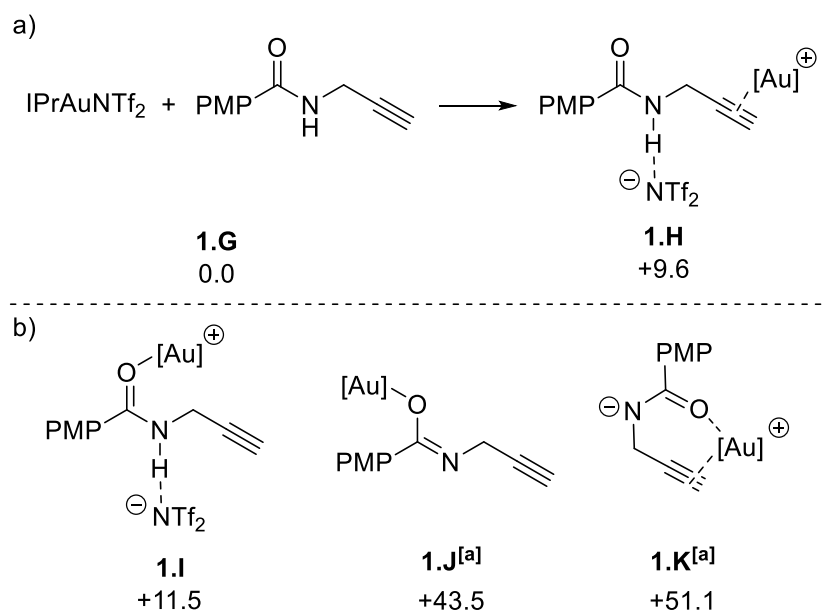


Figure 22. DFT-calculated structures at the SMD(CHCl₃)-PBE0-D3BJ/def2-TZVP,6-311+G(d,p)//PBE0-D3BJ/SDD,6-31G(d) level of theory. Energies are Gibbs energies in kcal mol⁻¹. [Au] = IPrAu⁺. a) Preferred configuration of gold(I)-coordination to **1.10**. b) Other calculated configurations of higher energy. [a] States resulting from loss of HNTf₂ from **1.I**.

Considering again the gold(I) alkyne complex with hydrogen bonding anion (**1.H**), transition states for the possible cyclisations were found (Figure 23). 5-*exo-dig* cyclisation (**1.L**) was calculated to be energetically preferred over 6-*endo-dig* cyclisation (**1.M**) by 4.6 kcal mol⁻¹ (+16.1 vs +20.7 kcal mol⁻¹), which was consistent with the experimentally observed outcome.

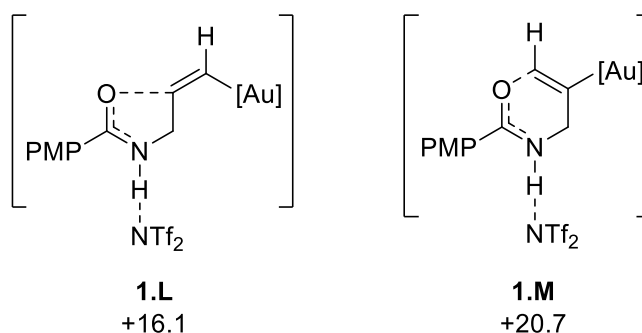


Figure 23. DFT-calculated energies for the transition states of 5-*exo-dig* (**1.L**) and 6-*endo-dig* (**1.M**) cyclisations of **1.H**. Energies are Gibbs energies at the SMD(CHCl₃)-PBE0-D3BJ/def2-TZVP,6-311+G(d,p)//PBE0-D3BJ/SDD,6-31G(d) level of theory in kcal mol⁻¹ with **G** as the reference point. [Au] = IPrAu⁺. PMP = *p*-methoxyphenyl.

When gold(I)-coordination was considered without the anion, the energy of the intermediate was greatly increased at +16.7 kcal mol⁻¹ (**1.N**, Figure 24). Transition states for the cyclisation of **1.N**, however, were higher in energy than the equivalent triflimide-coordinated transition states, at +25.5 and +27.2 kcal mol⁻¹ for the 5-*exo*- (**1.O**) and 6-*endo-dig* (**1.P**) cyclisations

predicted this to be higher in energy. Generation of the protonated product **1.T** and vinyl-gold species **1.S** by participation of the basic nitrogen in the oxazole ring in the product was therefore also considered (Figure 26). Transition state **1.TS_{Qs}** (+10.4 kcal mol⁻¹) was found at a much lower energy than the triflimide-promoted pathway. The transition state of protodemetalation was then calculated as **1.TS_{S1.11}** (+13.7 kcal mol⁻¹) resulting in two units of the product **1.11**. Overall, this process was calculated to be lower in energy than the equivalent triflimide anion-assisted process, with the rate-limiting step predicted to be the initial cyclisation (**1.L**) at 16.1 kcal mol⁻¹ in energy.

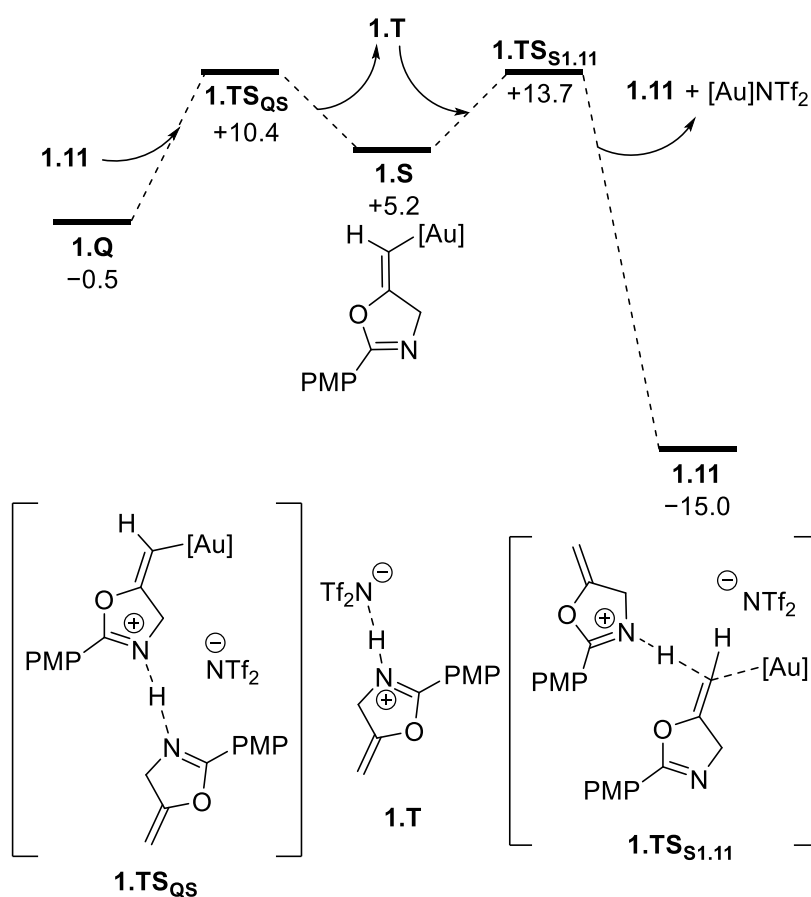


Figure 26. DFT-calculated pathway for oxazoline-assisted proton-migration of **1.Q**. Energies are Gibbs energies at the SMD(CHCl₃)-PBE0-D3BJ/def2-TZVP,6-311+G(d,p)//PBE0-D3BJ/SDD,6-31G(d) level of theory in kcal mol⁻¹. [Au] = IPrAu⁺.

The DFT data enabled a catalytic cycle to be proposed (Figure 27). First, an initiation cycle, in which cyclisation occurs via a 5-*exo-dig* cyclisation (**1.L**) promoted by the initial coordination of the gold(I) NHC complex to propargylic amide **1.10**, with hydrogen bonding of the triflimide anion to the amide nitrogen (**1.H**). A triflimide-assisted proton-migration then occurs resulting in the product (**1.11**). After initiation, an iterative cycle is predicted to take place, where the

oxazole product (**1.11**) deprotonates intermediate **1.Q**: this was calculated to be a lower energy pathway than deprotonation by NTf_2^- .

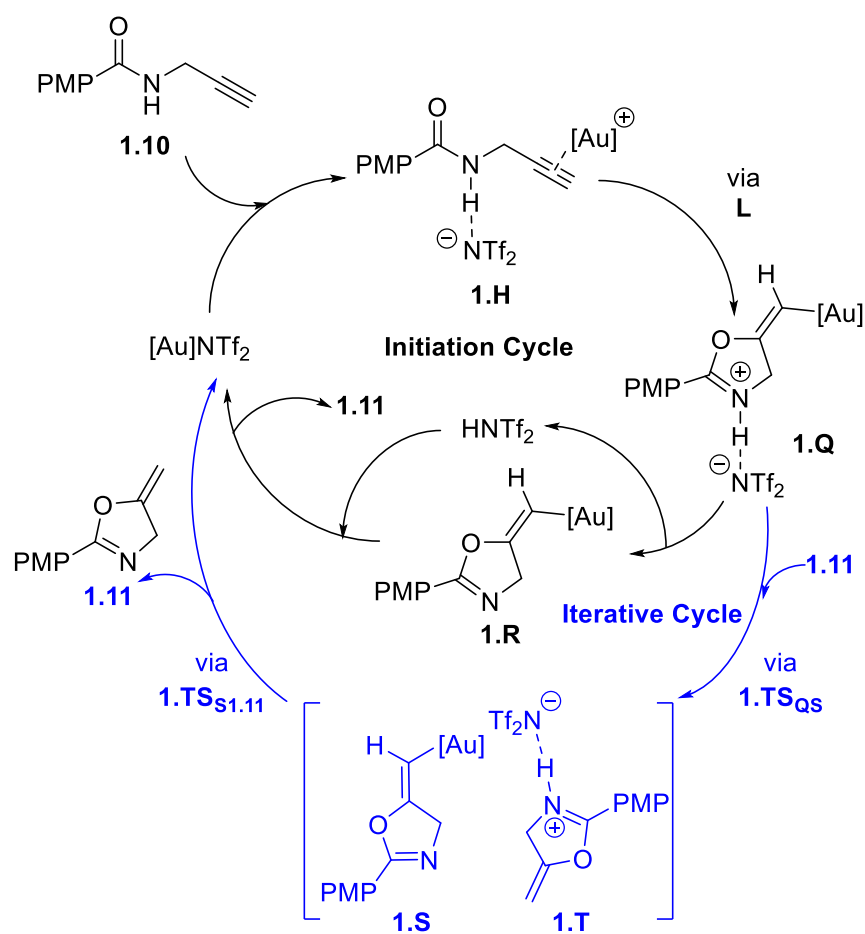


Figure 27. Catalytic cycle proposed by Ma *et al.* for propargylic amide cyclisation. The anion plays a role in the reaction process throughout.

The authors demonstrated that coordination of the anion can be important when discussing reaction mechanisms, potentially changing the viability of a predicted mechanism. In this reaction the product itself is predicted to take part in the catalysis. Product participation in this manner could have a pronounced effect on the observed kinetics, and without considering the anion effects, the rationale for this could be missed.

The handful of papers discussed here only shows a small subset of the studies within the field of gold(I) chemistry where anion effects have been studied by computational chemistry. These recent examples highlighted the importance of considering the anion when beginning to study a process theoretically. Ligand, substrate, anion, and solvent all should be considered, with the studies herein demonstrating that ion pairing is more notable in less polar solvents, with

coordination then present often in areas of greater positive charge density, and through hydrogen bonding of substrates.

1.2.3 Using DFT to explore the regioselectivity and coordination in gold(I) catalysis

DFT has been used extensively to provide evidence and understanding to observed experimental results, with a view that by understanding reaction mechanism, then improvements or further development can then take place. This has been useful in gold chemistry, in the study of reaction regioselectivity, due to either carbon atom of the gold-coordinated unsaturated C–C bond being potential options for nucleophilic attack.

Amongst the simplest gold-catalysed reactions of alkenes and alkynes, are their hydration and hydroamination reactions, which typically progress *via* Markovnikov addition. However, methodologies are being published which accomplish the less-common anti-Markovnikov addition.

Timmerman *et al.* reported a gold(I)-catalysed hydroamination reaction of alkylidenecyclopropanes **1.13** (ACP) derivatives which resulted in the anti-Markovnikov addition of imidazolidone **1.14** (Figure 28), with the diastereoselectivity of the reaction arising from the gold(I) catalyst coordinating preferentially to the least hindered face of the ACP derivative.¹⁴¹ Further work by Couce-Rios *et al.* used DFT to explore the origins of the observed regioselectivity.¹⁴²

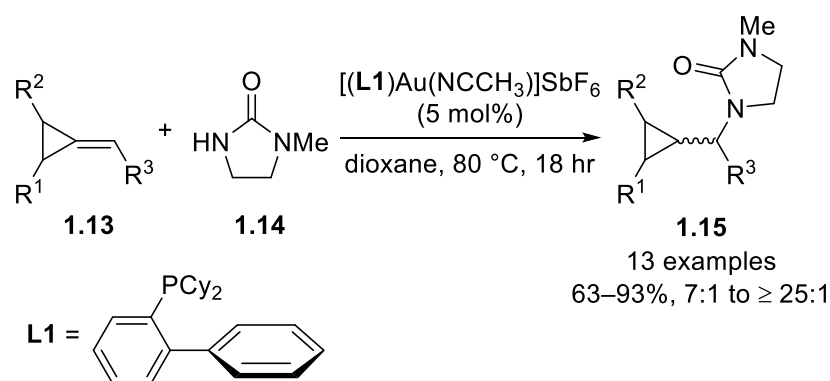


Figure 28. Gold(I)-catalysed hydroamination of ACP derivatives **1.13** with 1-methyl-imidazolidin-2-one **1.14** as reported by Timmerman *et al.*¹⁴¹

First, DFT was used to calculate the energies of the intermediates and transition states for the proposed mechanism, using the $\eta^2(\pi)$ gold(I)-coordinated benzyl-substituted ACP derivative (**1.U**) as the reference compound. Energies (calculated at the M06/6-31G(d,p)&SDD(f) level of theory) of +21.7 and +21.0 kcal mol⁻¹, were calculated for the transition states of Markovnikov (**1.TS_{UW}**) and anti-Markovnikov (**1.TS_{UV}**) addition respectively (Figure 29).

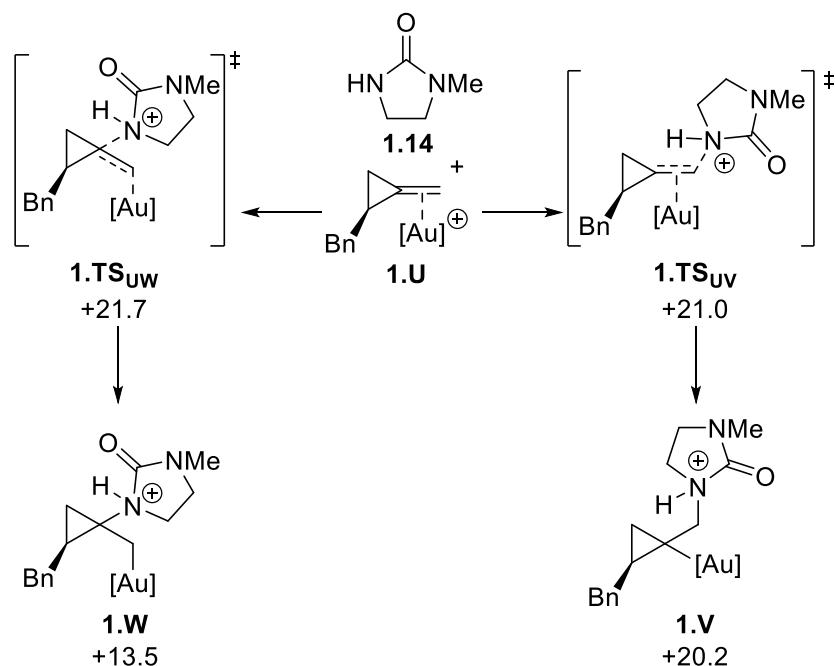


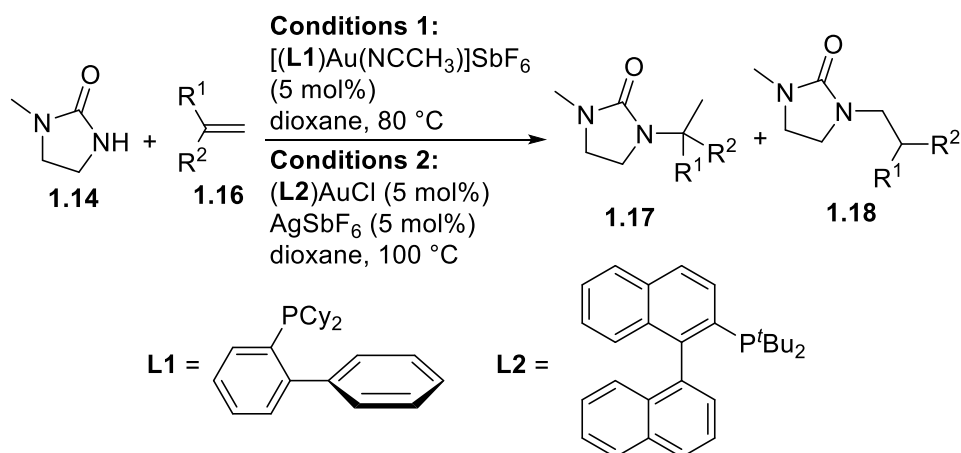
Figure 29. DFT-calculated transition state energies for Markovnikov and anti-Markovnikov addition into gold(I)-coordinated ACP **1.U**. Energies are Gibbs energies in kcal mol⁻¹ at 298 K, calculated at the M06/6-31G(d,p)&SDD(f) level of theory with SMD solvent correction in 1,4-dioxane.

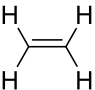
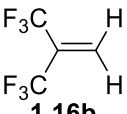
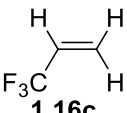
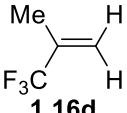
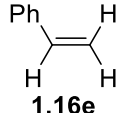
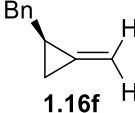
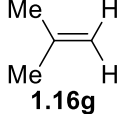
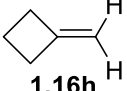
When considering the relative energy difference between pathways, it is important to note that due to the logarithmic relationship between the calculated energy and both the equilibrium and rate constants, a small difference in energy can contribute to a significant difference in the predicted outcome.¹⁴³ In this instance, whilst the calculated energies of the transition states are similar, and a mixture of products might be predicted, the formation of **1.15** was seen predominantly *via* lower energy transition state **1.TS_{UV}**, highlighting the need to consider both the experiments and calculations together.

The energies for the possible protodemetalation pathways were also calculated, which suggested that the initial nucleophilic addition was the rate-determining step. The height of the energy barriers is consistent with the elevated temperature required for these reactions to occur.

Next, alkenes bearing various substituents were considered to compare the geometries of the $\eta^2(\pi)$ -alkene gold(I) complex and the transition state energies for Markovnikov and anti-Markovnikov addition (Table 3). These data were then compared to the experimental results where available. It should be noted that all the calculations use CyJohnPhos (**L1**) as the ligand, however the experimental results of ethylene, styrene and isobutene were only available for TrixiePhos (**L2**).¹⁴⁴ Most of the experimental results match the predicted outcomes.^{141,144} Alkenes **1.16a**, **1.16e**, **1.16g** and **1.16h** proceeded with Markovnikov addition, and alkene **1.16f** is the previously discussed benzyl-substituted ACP derivative, which occurred with anti-Markovnikov addition. Styrene (**1.16e**) was the only example which the experimental outcome doesn't match the predicted outcome.

Table 3. Transition state energies for Markovnikov (ΔG_M^\ddagger) and anti-Markovnikov (ΔG_{aM}^\ddagger) addition of **1.14** catalysed by **(L1)Au⁺**, and geometrical parameters for the initial $\eta^2(\pi)$ -alkene gold(I) complexes. All data were computed at the M06/6-31G(d,p)&SDD(f) level of theory.



Substrate	$\Delta G_M^\ddagger /$ kcal mol ⁻¹	$\Delta G_{aM}^\ddagger /$ kcal mol ⁻¹	$\Delta\Delta G^\ddagger /$ kcal mol ⁻¹	$d_1 - d_2$ [a] / Å	1.17: 1.18 Ratio
 1.16a	+15.4	-	-	-0.002	100:0 ^[c]
 1.16b	+23.2	+8.1	+15.1	0.007	-
 1.16c	+19.0	+10.6	+8.4	-0.002	-
 1.16d	+23.5	+16.1	+7.4	-0.105	-
 1.16e	+21.4	+19.4	+2.0	-0.154	100:0 ^[c]
 1.16f	+21.7	+21.0	+0.7	-0.119	0:100 ^[b]
 1.16g	+20.4	+27.4	-7.0	-0.257	100:0 ^[c]
 1.16h	+20.0	+27.3	-7.3	-0.256	100:0 ^[d]

[a] $d_1 = \text{Au}-\text{C}_{\text{terminal}}$ distance; $d_2 = \text{Au}-\text{C}_{\text{internal}}$ distance. [b] Conditions 1 were used. [c] Conditions 2 were used. [d] Conditions 1 were used at 100 °C

A trend was observed in which the energy difference between the Markovnikov and anti-Markovnikov addition could be related to the degree that the gold(I) catalyst has slipped across the alkene (Figure 30). Additional work by the group showed that strain from the disfavoured addition was significantly higher than the favoured addition, which further highlighted the importance of the initial geometry of the gold-coordinated alkene.

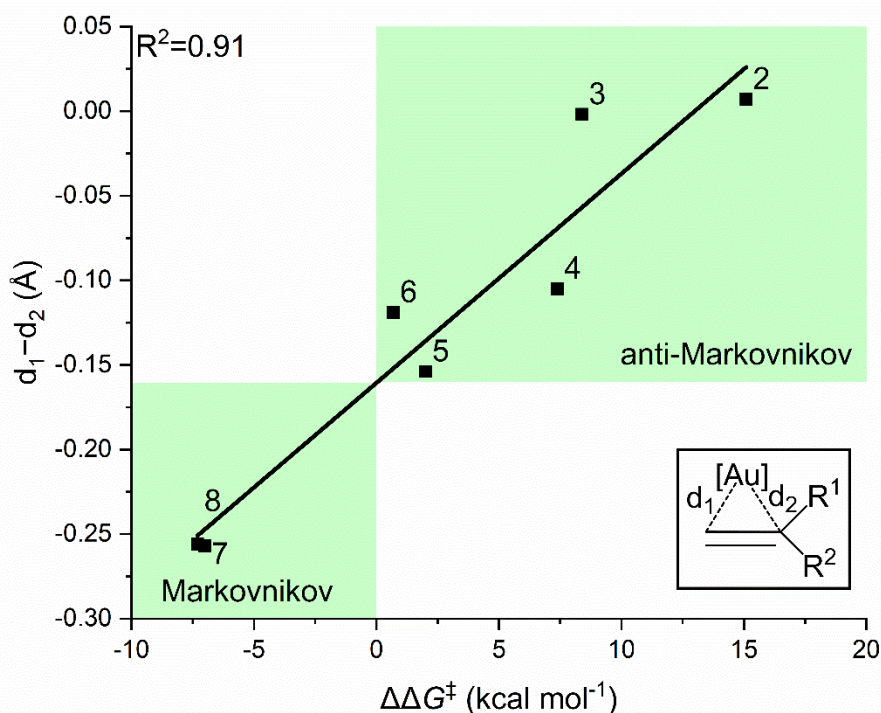


Figure 30. Plot of the difference in transition state energy between Markovnikov and anti-Markovnikov addition ($\Delta\Delta G^\ddagger$) against the difference in distance of the gold centre from the terminal (d_1) and internal (d_2) carbons. Values refer to the entries in Table 3. Adapted with permission from American Chemical Society, Copyright 2019.¹⁴²

A similar substituent-directed effect was studied in the gold(I)-catalysed cyclisation of β -yne furans, reported by Dong *et al*, as a method to make cyclohexafuran and cycloheptafuran derivatives.¹⁴⁵ The cycloheptafuran skeleton is found in natural products,^{146–148} but their synthesis is challenging using conventional methods.

With β -yne furans (*e.g.* **1.19**), nucleophilic attack can take place into the $\eta^2(\pi)$ -alkyne gold(I)-coordinated complex (Figure 31), either through a 6-*exo* cyclisation (**1.19** \rightarrow **1.22**) resulting in cyclohexafuran species **1.23**, or alternatively, attack can occur on the other carbon *via* a 7-*endo* cyclisation (**1.19** \rightarrow **1.20**), giving cycloheptafuran derivatives **1.21**.

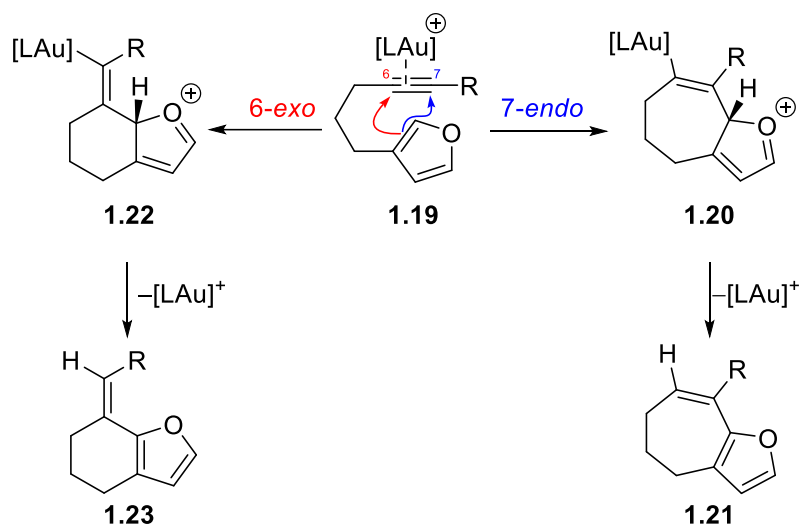


Figure 31. Proposed 6-*exo* and 7-*endo* cyclisations of β -yne furan derivative **1.19**.

Typically, cyclohexafuran analogues are formed when reacting β -yne furans with transition metal catalysts (Figure 32a).^{149–152} However, it was proposed by Dong *et al.* that tuning the electronic properties of the alkyne may allow for better control of the regioselectivity. Using internal alkyne **1.26**, it was possible to optimise for the formation of the desired cycloheptafuran product **1.27** using gold(I) catalysis (Figure 32b).

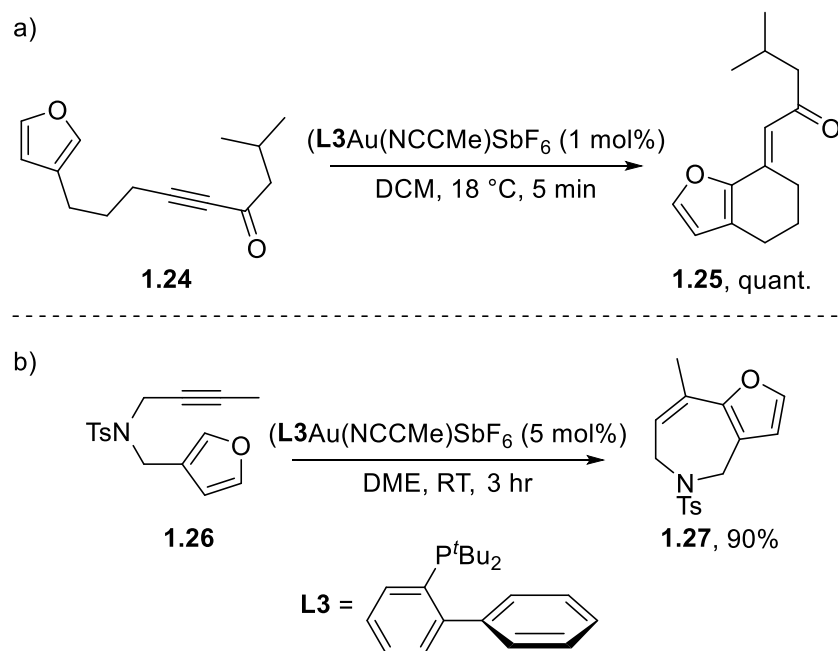


Figure 32. Synthesis of cyclohexafuran **1.20** as reported by Menon *et al.* in their total synthesis of furansesquiterpenes.¹⁵² b) Optimised conditions for the 7-*endo*-dig cyclisation of β -yne furan **1.21**.

To explore the mechanism using DFT (at the B3LYP/SDD-6-31G(d) level of theory), transition states for the 7-*endo* (**1.TS_{XV}**) and 6-*exo* (**1.TS_{XZ}**) pathways were calculated (Figure 33), from

$\eta^2(\pi)$ -alkyne gold(I) complex **1.X**, for different substituents. This was successful at matching the experimental outcomes, with the terminal alkyne favouring the 6-*exo* transition state by 2.3 kcal mol⁻¹, and the methyl- and phenyl-substituted pathways favouring the 7-*endo* transition state by 3.1 and 4.8 kcal mol⁻¹ respectively.

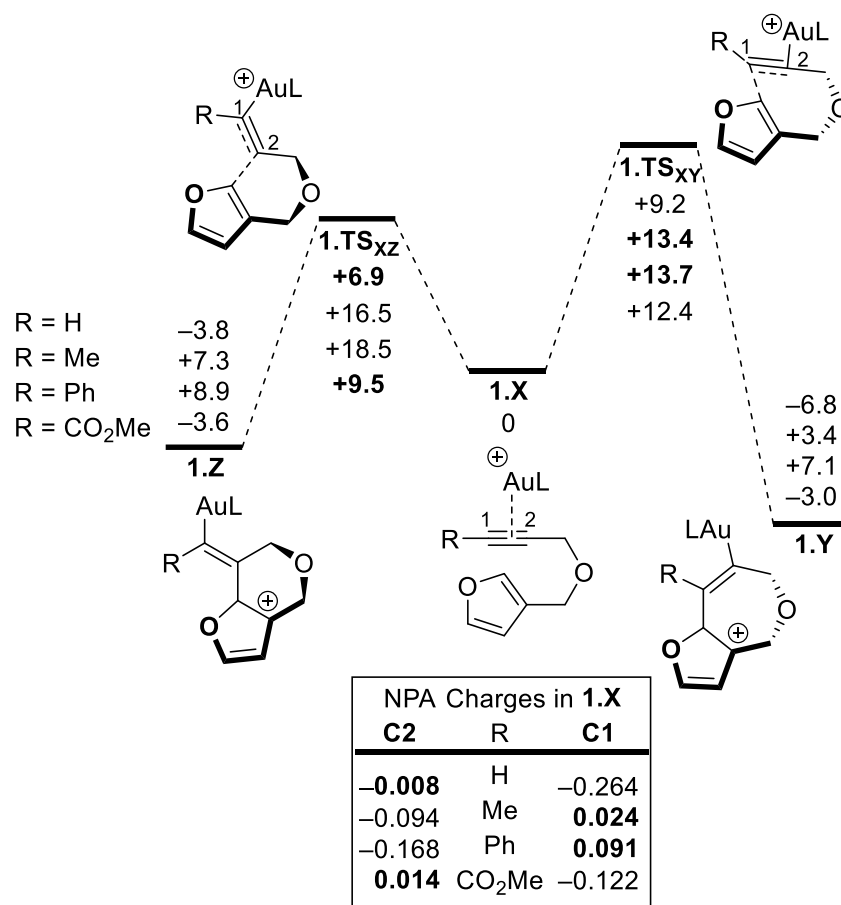


Figure 33. DFT-calculated energies for 6-*exo* and 7-*endo* cyclisation of β -yne furans. Energies are Gibbs energies at 298 K in kcal mol⁻¹ at the B3LYP/SDD-6-31G(d) level of theory. Calculated NPA charges for the alkyne carbons of **1.X** are given. L = PMe₃.

To determine the reasons between the difference in reaction outcome, natural population analysis (NPA) was used to compare the charges of the alkyne carbon atoms. This demonstrated that the different alkyne substituents affected the charge density of the alkyne, with nucleophilic attack then occurring onto the most 'positively' charged carbon of the alkyne. This then highlighted further ways the scope of the reaction could be expanded (Figure 34).

Firstly, introduction of a ketone on the tether to make an internal ynone moiety **1.28** still resulted in formation of the cycloheptafuran product **1.29**, which was proposed to be due to the synergistic effects of the substituents. Secondly, the calculations highlighted that substituting

the alkyne with an ester functionality (**1.30**) would promote formation of the 6-*exo* products, which was observed experimentally (**1.31**). Finally, by extending the tether (**1.32**), 7-*exo* cyclisation could be achieved with terminal alkynes (**1.33**). This highlights well the power of DFT to inform new directions for synthesis.

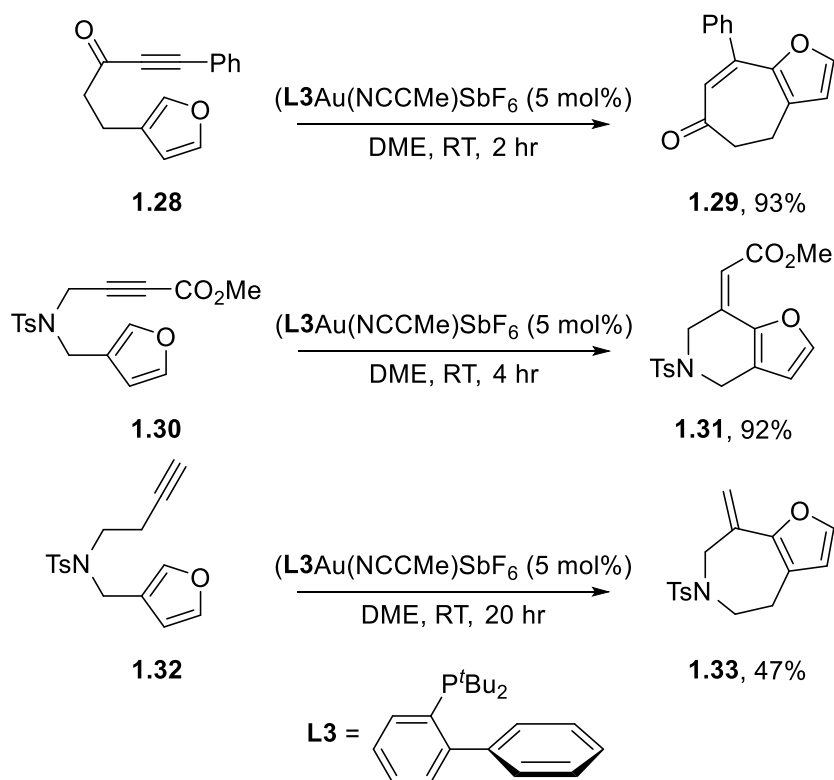


Figure 34. Additional reactions to explore the substrate scope following the DFT analysis.

In 2018, Aikonen and co-workers studied the gold-catalysed 1,3-*O*-transposition of ynones (Figure 35).¹⁵³ Initial kinetic studies highlighted that there was an order in **1.34** of 1.5 and a small order of 0.15 for **1.35**, thus two ynone molecules are required in the rate-determining step.

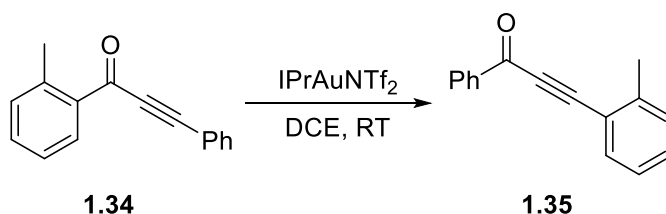


Figure 35. Gold-catalysed transposition reaction of ynone **1.34**.

An intermolecular mechanism was therefore proposed, with the energies calculated using DFT (at the TPSS-D3/def2-TZVP//TPSS-D3/def2-SVP level of theory, Figure 36), in which *O*-attack of the carbonyl of one ynone, into the $\eta^2(\pi)$ -coordinated alkyne of another ynone occurs with a

calculated energy of +13.5 kcal mol⁻¹ (**1.TS_{ABAC}**), followed by a low energy transition state of +7.3 kcal mol⁻¹ for intramolecular cyclisation (**1.TS_{ACAD}**) to form cyclic acetal complex **1.AD**. This process then happens in reverse, with the overall reaction yielding an unchanged ynone, and one in which the position of the carbonyl has changed.

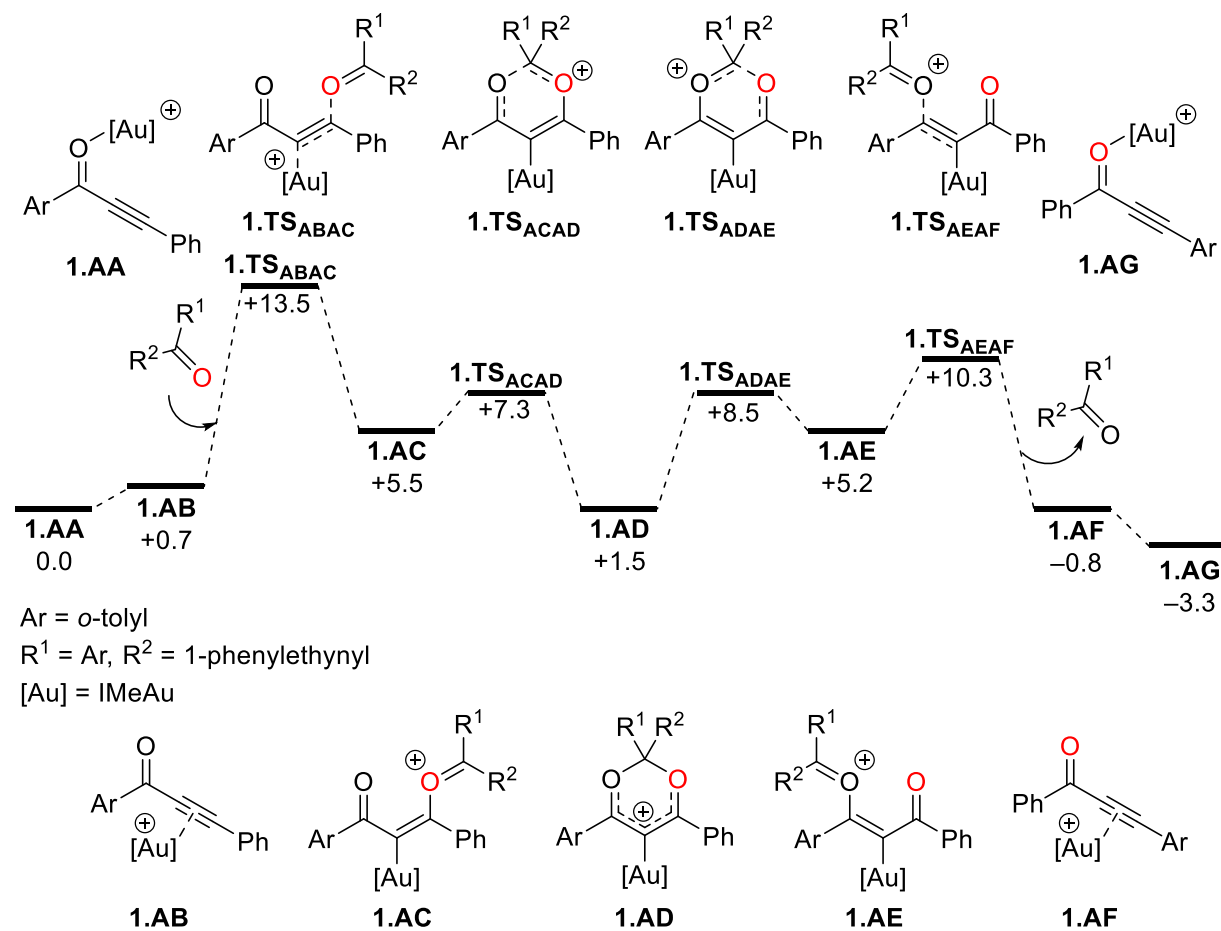


Figure 36. DFT-calculated energies for the gold-catalysed 1,3 transposition of ynone **1.34**. Energies are Gibbs energies at the TPSS-D3/def2-TZVP//TPSS-D3/def2-SVP level of theory in kcal mol⁻¹ with COSMO solvent correction in CH₂Cl₂.

It was noted that the carbonyl of the uncoordinated ynone acts as a nucleophile, so studies were performed to see if using an electron-rich aldehyde can increase the rate of reaction. A range of substituted aldehydes (Figure 37) were tested experimentally, and it was shown that the aldehyde did have a marked effect on the reaction rate, with benzaldehydes bearing electron-donating functionalities in conjugation with the aldehyde showing the greatest increase in reaction rate.

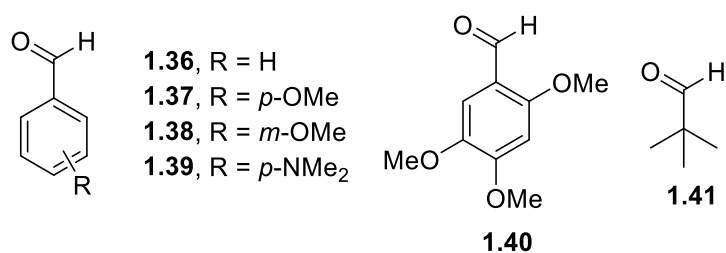
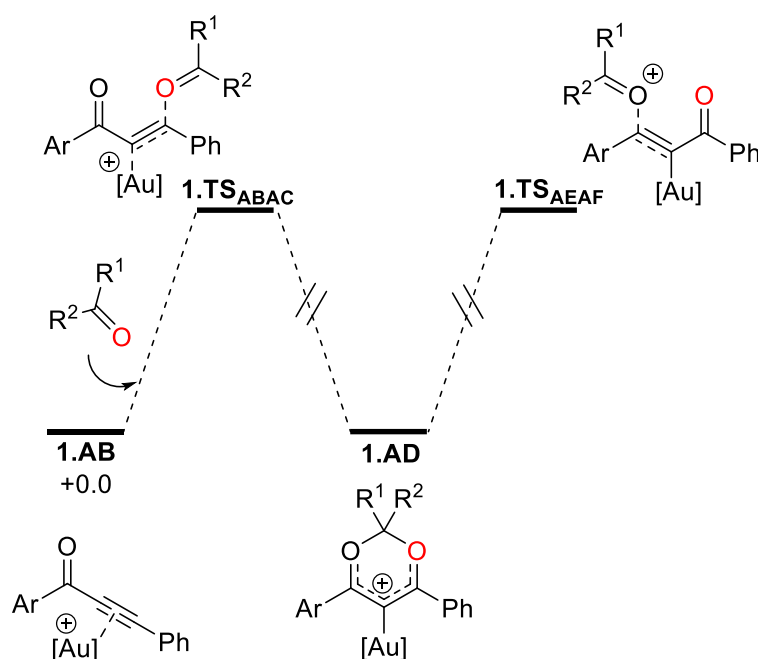


Figure 37. Aldehydes used in the further studies.

The DFT-calculated energies of the highest transition state barriers (**1.TS_{ABAC}** and **1.TS_{AEAF}**) were compared to the $\eta^2(\pi)$ -coordinated alkyne **1.AB** and the cyclic acetal complex **1.AD**, for the different additives (Table 4). This showed a difference in the transition state energies that correlated with the experimental rate differences, with aldehyde **1.40** showing the largest energy decrease for transition state **1.TS_{ABAC}**.

Table 4. DFT-calculated energies for the key transition states and intermediates of the gold-catalysed transposition reaction of ynones with different additives. Energies are Gibbs energies at the TPSS-D3/def2-TZVP//TPSS-D3/def2-SVP level of theory with COSMO solvent correction in CH₂Cl₂.



Entry	Additive	ΔG	ΔG	ΔG
		(1.TS_{ABAC} - 1.AB)	(1.AD - 1.AB)	(1.TS_{AEAF} - 1.AD)
		/ kcal mol ⁻¹	/ kcal mol ⁻¹	/ kcal mol ⁻¹
1	1.34	+13.5	+1.5	+8.9
2	1.35	+14.4	+2.1	+8.5
3	1.36	+14.9	-4.7	+18.7
4	1.37	+12.8	-2.3	+13.4
5	1.38	+14.1	-4.4	+17.1
6	1.39	+11.3	-1.3	+9.0
7	1.40	+10.5	-2.4	+11.3
8	1.41	+15.3	-9.9	+22.0

Furthermore, the energy of the transition state for loss of aldehyde (**1.TS_{AEAF}**), was calculated to be higher when pivaldehyde **1.41** was used (+22 kcal mol⁻¹) suggesting a greater kinetic stability for the cyclic acetal intermediate. When the transposition reaction was done with **1.41** at 15 °C, characterisation of the cyclic acetal intermediate was possible by recording ¹H and 2D NMR spectra at 15 °C and 0 °C respectively.

Additionally, using this improved methodology allowed for a challenging transposition reaction with terminal alkyne **1.42** (Figure 38). A marked improvement in the NMR yield of **1.43** was observed, from 11% to 69%, with fewer side products.

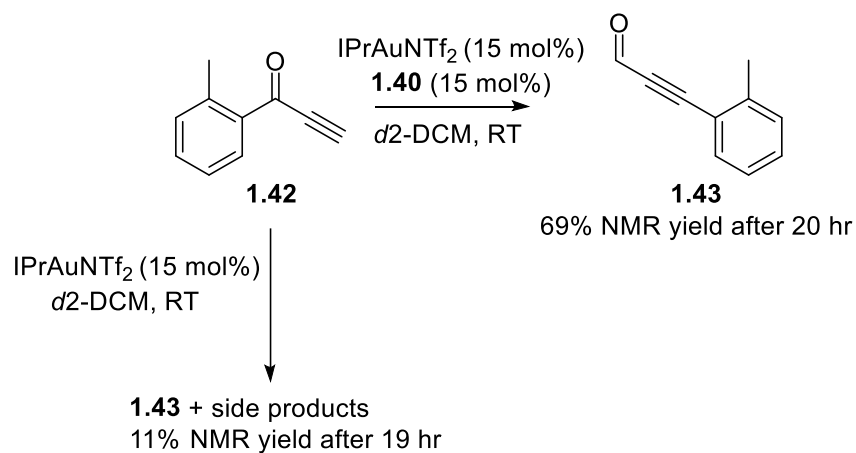


Figure 38. Transposition reaction using challenging substrate **1.42**.

Recent work published by Kreuzahler and Haberhauer,¹⁵⁴ explored the mechanism of the gold(I)-catalysed 1,2-haloalkynylation reactions of haloalkynes,¹⁵⁵ alkynes¹⁵⁶ and alkenes^{157,158} (Figure 39) using DFT and ¹³C-labelling, to compare previously proposed mechanisms.

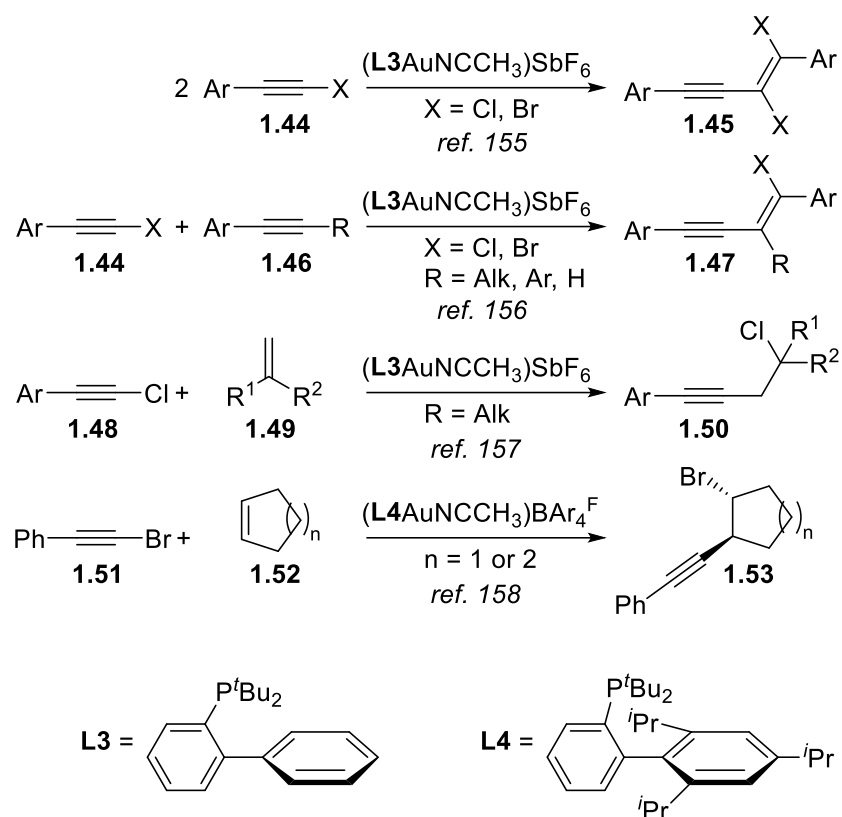


Figure 39. Gold(I)-catalysed 1,2-haloalkynylation reactions of haloalkynes, alkynes and alkenes.

^{13}C -labelling experiments (Figure 40) determined that in the 1,2-haloalkynylation of internal alkyne **1.55**, the ^{13}C -labelled atom was heavily biased to be closest to the aryl group in both alkyne products **1.56** (with chlorophenylacetylene **1.54**) and **1.58** (with bromophenylacetylene **1.57**). Further work which studied the dimerisation reactions of **1.54** and **1.57** showed a much less biased distribution of ^{13}C -labelled atoms, and the 1,2-haloalkynylation reaction with alkene **1.61** showed a single product (**1.62**). It was proposed that the selectivity was determined during the initial step and the observed distribution was related to the relative transition state energies.

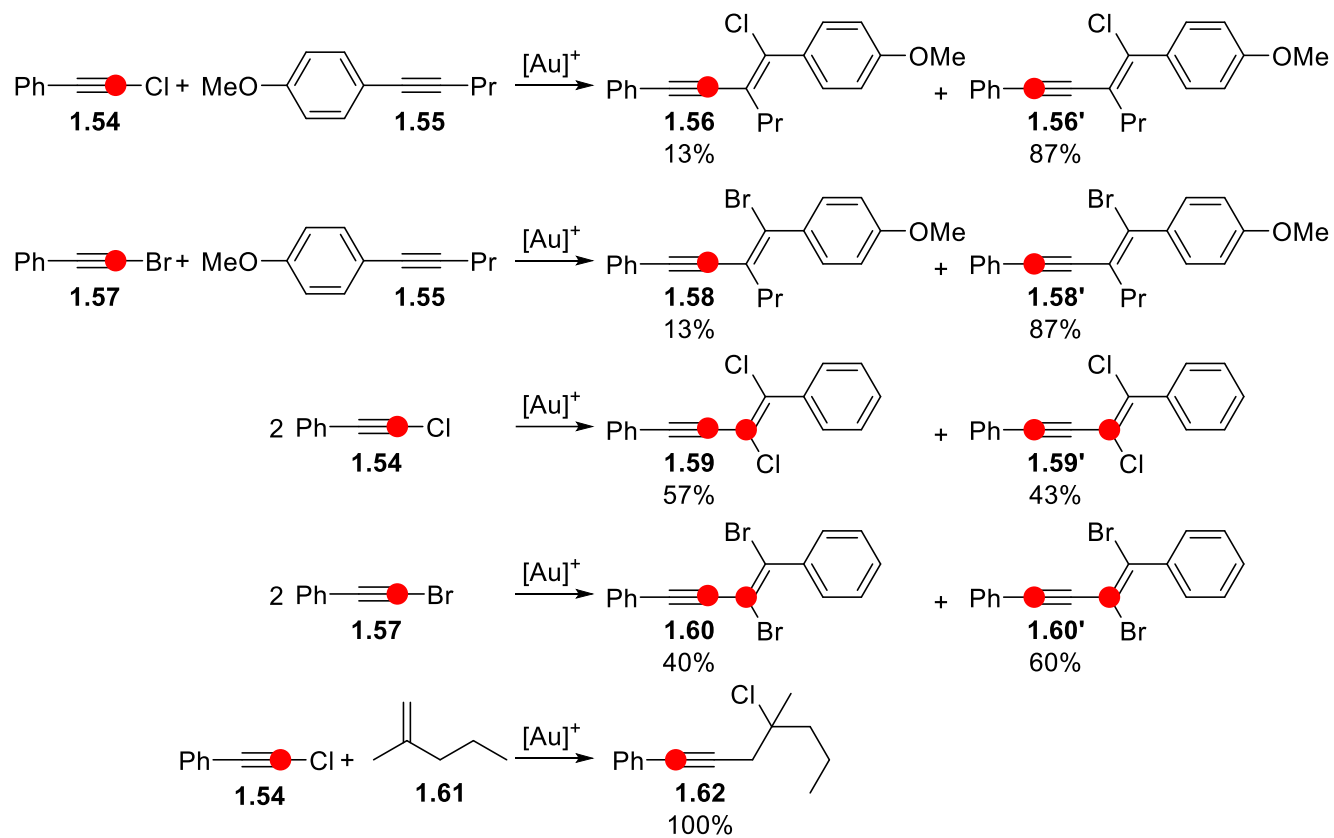


Figure 40. ^{13}C -labelling experiments of 1,2-haloalkynylation reactions. The red circled atoms denote ^{13}C -labelled atoms. $[\text{Au}]^+ = [(\text{JohnPhos})\text{AuNCMe}]^+$.

Initially, the energies of the transition states from both sites of possible nucleophilic attack of an alkyne into the $\eta^2(\pi)$ -alkyne gold(I) complex were calculated (Figure 41). A range of alkynes were considered, and in each case, route B was significantly lower in energy than route A (7.0–7.4 kcal mol⁻¹), corresponding to preferential attack adjacent to the aryl group of the gold(I)-coordinated alkyne (**1.TS_{AHAI}**). Due to the large difference in energies between the two transition states, only a single product isomer of **1.56**, **1.58**, **1.59** and **1.60** would be expected, if the initial nucleophilic step was key as initially proposed, therefore, the reactivity of carbocation **1.AI** and **1.AJ** was considered. Only carbocation **1.AI**, from the lowest energy pathway will be discussed.

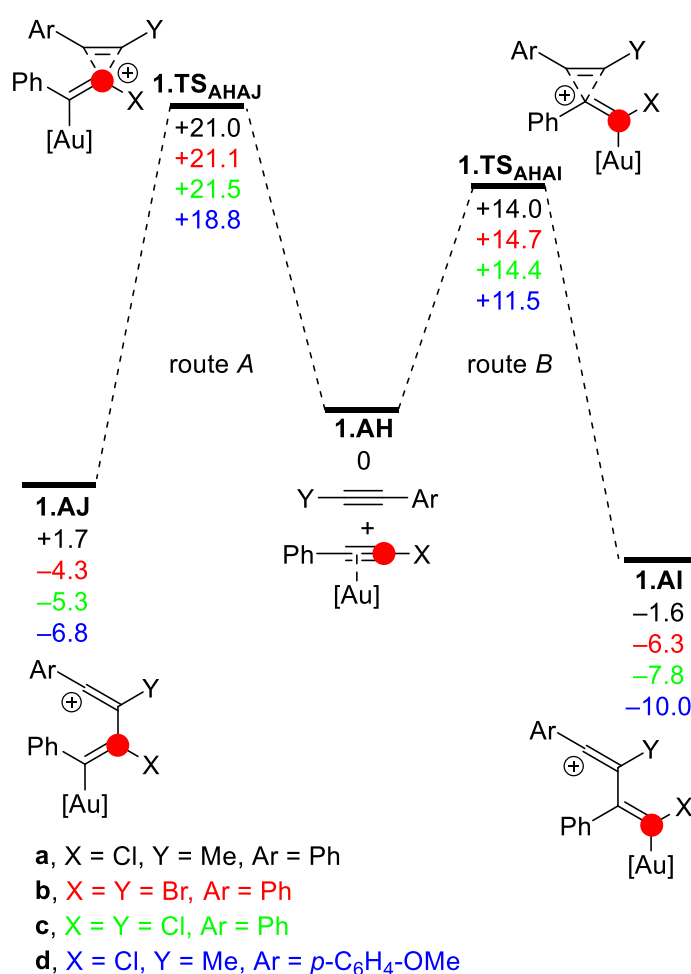


Figure 41. DFT-calculated energies for the initial nucleophilic attack in gold(I)-coordinated alkyne. Energies are Gibbs energies in kcal mol⁻¹ at the B3LYP-D3BJ//6-311++G(d,p),def2TZVP//B3LYP-D3BJ/6-31G(d),def2-TZVP level of theory with SMD solvent correction in DCE. [Au] = (JohnPhos)Au⁺.

Considering vinyl cation **1.AI** (Figure 42), a transition state for the formation of bicyclic indene complex **1.AN** was found, however this pathway was predicted to be 8.3 kcal mol⁻¹ in energy higher than the formation of chloronium complex **1.AK**. This complex can then form enyne **1.AL'** *via* direct phenyl migration **TS_{AKAL'}**, or alternatively, *via* unusual cyclopropenylmethyl cation

1.AM (discussed further in the paper), which facilitates an alkyl-migration *via* transition state **1.TS_{AMAL}** to also yield enyne **1.AL**, with the ¹³C-labelled carbon in a different position. These two pathways are predicted to differ only by an energy of 1.0 kcal mol⁻¹ and therefore both pathways could be expected to be followed. It should be highlighted here that no direct experimental outcome can be compared as 1-phenyl-1-propyne was used as a model substrate.

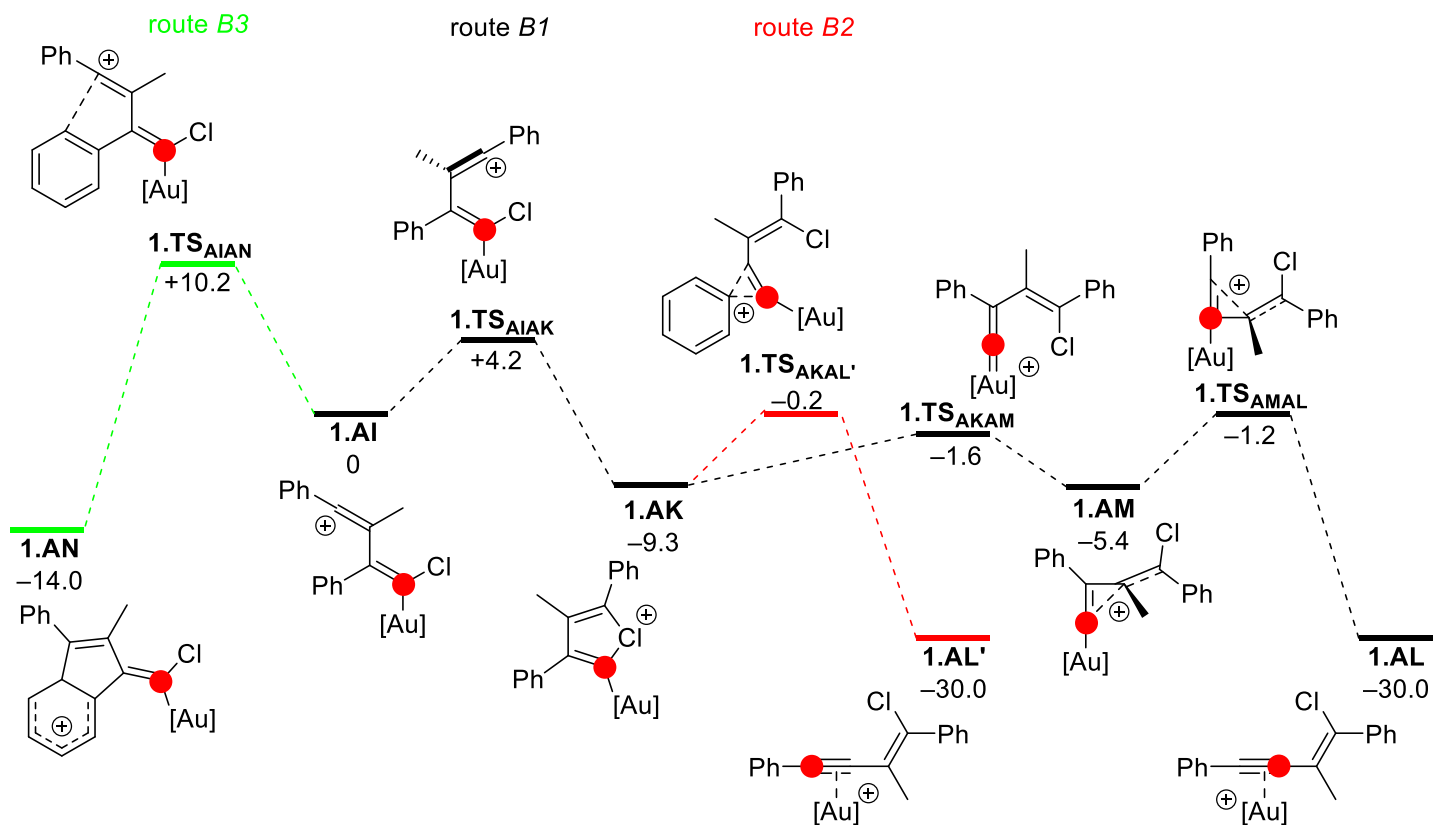


Figure 42. DFT-calculated energies of possible reaction routes from **1.AI**. Energies are Gibbs energies in kcal mol⁻¹ at the B3LYP-D3BJ//6-311++G(d,p),def2TZVP//B3LYP-D3BJ/6-31G(d),def2-TZVP level of theory with SMD solvent correction in DCE. [Au] = (JohnPhos)Au⁺

A similar series of calculations were performed for the addition of isobutene into chlorophenylacetylene **1.54**. Again, both possible transition states were considered for the initial nucleophilic attack in to the $\eta^2(\pi)$ -alkyne gold(I)-coordinated complex (Figure 43), with addition into the alkyne directly next to the aryl group predicted to be favoured by 6.3 kcal mol⁻¹ via transition state **1.TS_{AOAP}**. The authors considered the reactivity of carbocation **1.AP** and **1.AQ**, however, only carbocation **1.AP**, from the lowest energy pathway will be discussed here.

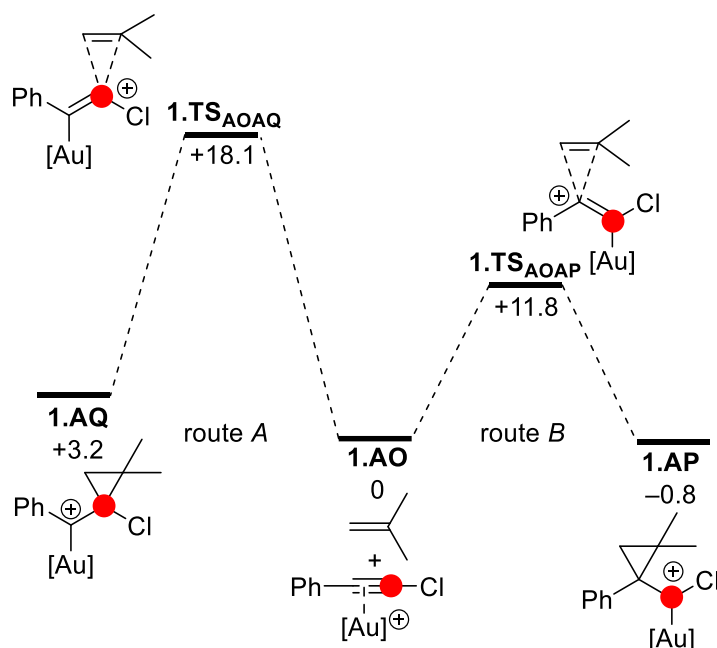


Figure 43. DFT-calculated energies for the initial nucleophilic attack in gold(I)-coordinated alkyne with isobutene. Energies are Gibbs energies in kcal mol⁻¹ at the B3LYP-D3BJ//6-311++G(d,p),def2TZVP//B3LYP-D3BJ/6-31G(d),def2-TZVP level of theory with SMD solvent correction in DCE. [Au] = (JohnPhos)Au⁺.

The fate of carbocation **1.AP** was considered (Figure 44). A transition state for a cyclisation was found (**1.TS_{APBU}**) but this was calculated to be 18.1 kcal mol⁻¹ higher in energy than the transition state for chlorine migration (**1.TS_{APAR}**). The resulting chloronium cation (**1.AR**) can then further migrate to gold(I)-vinylidene complex **1.AS** via low-lying transition state **1.TS_{ARAS}** (−0.3 kcal mol⁻¹) from carbocation **1.AR**. From vinylidene complex **1.AS**, either an aryl (**1.TS_{ARAS'}**) or alkyl (**1.TS_{ARAS}**) migration can take place, but the transition state energy for aryl migration is lower by 7.1 kcal mol⁻¹, so it was proposed that this was the only accessible pathway. This results in alkyne product **1.AS'** which matches the experimentally observed position of the ¹³C-labelled atom.

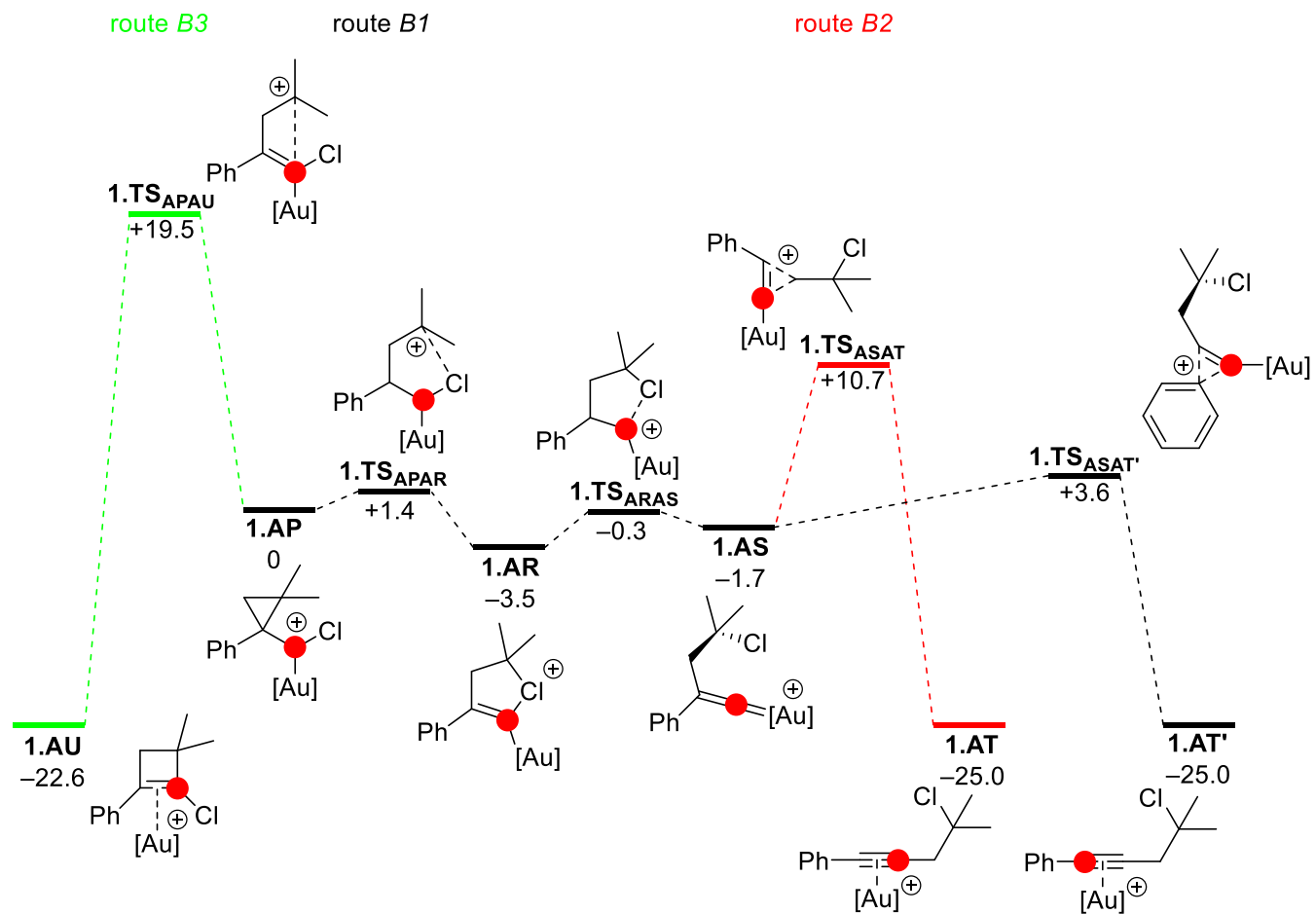


Figure 44. DFT-calculated energies of possible reaction routes from **1.AP**. Energies are Gibbs energies in kcal mol⁻¹ at the B3LYP-D3BJ//6-311++G(d,p),def2TZVP//B3LYP-D3BJ/6-31G(d),def2-TZVP level of theory with SMD solvent correction in DCE. [Au] = (JohnPhos)Au⁺.

With key transition states that control the position of ^{13}C -labelled atom of the haloalkynylation reaction postulated, substituent effects were then considered (Figure 45). The transition states **1.TS_{AKAL}d** and **1.TS_{AMAL}d** were found to only have a $0.6 \text{ kcal mol}^{-1}$ difference in energy when the *p*-methoxy-substituted alkyne (**d** in Figure 45) was investigated. This alkyne was selected as an analogue of **1.55** to directly compare the experimental outcome (Figure 40) more accurately. The gold(I)-catalysed dimerisation of chlorophenylacetylene **1.54** was considered, and a $1.9 \text{ kcal mol}^{-1}$ energy difference between routes B2 and B1, in favour of route B1, was found, which matches the experimentally observed outcome for the ^{13}C -labelled position, with a slight excess (57%) of β -aryl labelled product **1.59** formed. When the dimerisation of bromophenylacetylene **1.57** was considered, route B1 was again predicted to be lower in energy by $2.4 \text{ kcal mol}^{-1}$. Whilst it might be expected that experimentally the ratio of β -aryl labelled product **1.60** should increase, instead a 60% yield of α -aryl labelled product **1.60'** was achieved, further highlighting that care must be taken when working with calculated relative energy differences which are small, with experimental benchmarking required.

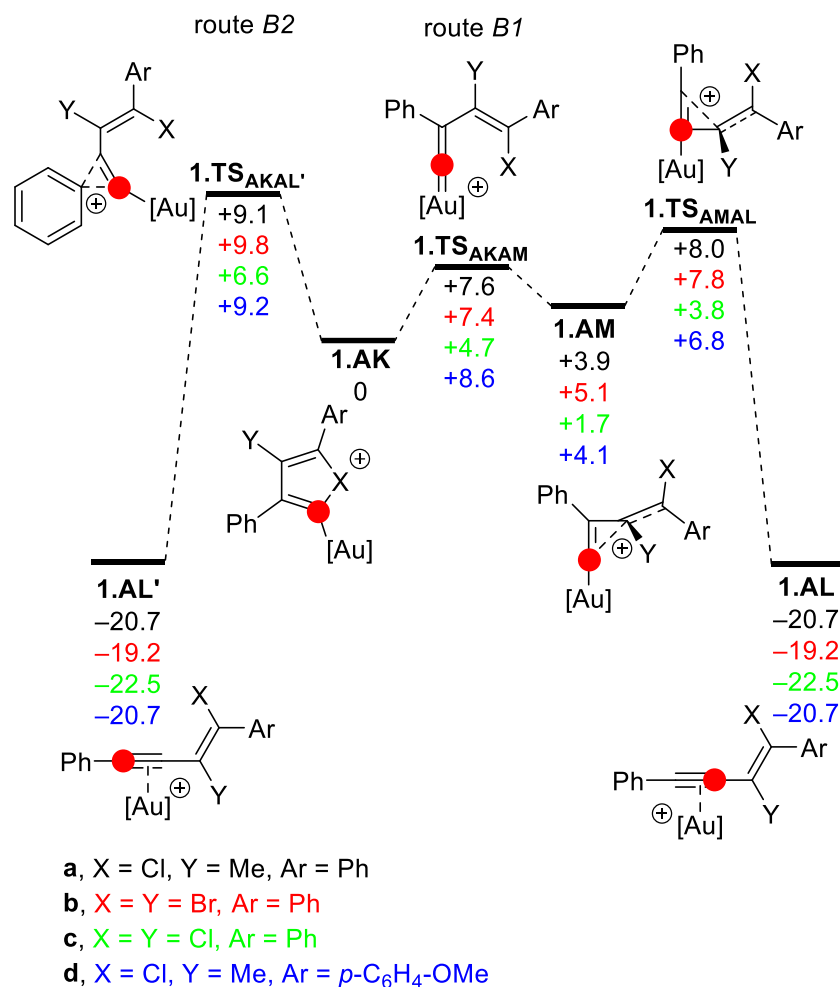


Figure 45. DFT-calculated energies of possible reaction routes from **1.AK**, with different reactants. Energies are Gibbs energies in kcal mol⁻¹ at the B3LYP-D3BJ//6-311++G(d,p),def2TZVP//B3LYP-D3BJ/6-31G(d),def2-TZVP level of theory with SMD solvent correction in DCE. [Au] = (JohnPhos)Au⁺.

A more significant selectivity effect was observed when comparing the effect of different ligands on the haloalkynylation reaction (Figure 46). Using trimethylphosphine instead of JohnPhos as the gold ligand in the calculations showed a significant change in the predicted selectivity. For the reaction of chlorophenylacetylene **1.54** and 1-methoxy-4-(prop-1-yn-1-yl)benzene (**d** and **g**), the transition state energy for route B1 using trimethylphosphine (**1.TS_{AKAMg}**) was increased to be above that of route B2 (**1.TS_{AKAL'g}**) by 1.4 kcal mol⁻¹. Experimentally (Figure 47), an increased yield of the α -aryl labelled product **1.56'** was observed, more closely matching the DFT-predicted outcome.

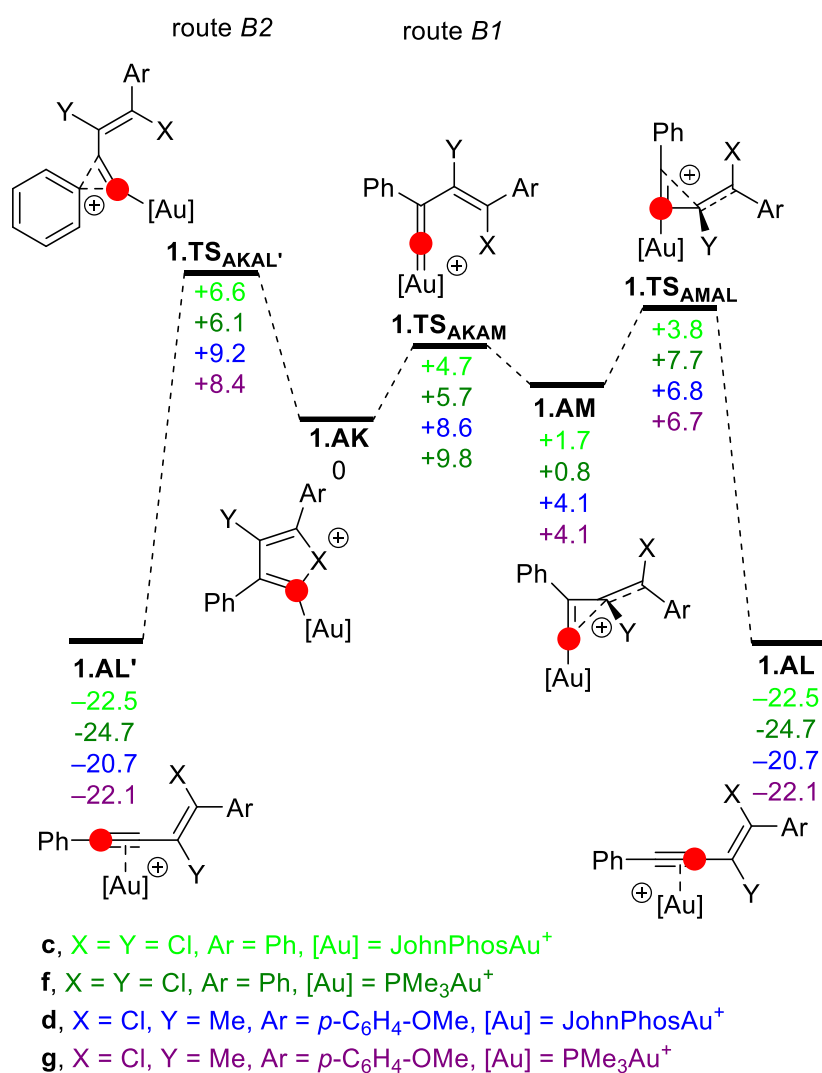


Figure 46. DFT-calculated energies of possible reaction routes from **1.AK**, with different ligands. Energies are Gibbs energies in kcal mol⁻¹ at the B3LYP-D3BJ//6-311++G(d,p),def2TZVP//B3LYP-D3BJ/6-31G(d),def2-TZVP level of theory with SMD solvent correction in DCE. [Au] = (JohnPhos)Au⁺.

Furthermore, a similar effect was observed with the dimerisation of chlorophenylacetylene **1.54**. Instead of an energy difference of 1.9 kcal mol⁻¹ in favour of route B1 (**1.TS_{AKAMC}**) with JohnPhos, the selectivity was reversed and route B2 (**1.TS_{AKAL'f}**) was favoured by an energy difference of 1.6 kcal mol⁻¹. Experimentally (Figure 47), rather than a 57:43 ratio of products, a 7:93 ratio was observed, with a higher amount of ¹³C-labelling being next to the alkene (**1.59'**), matching the DFT-predicted outcome.

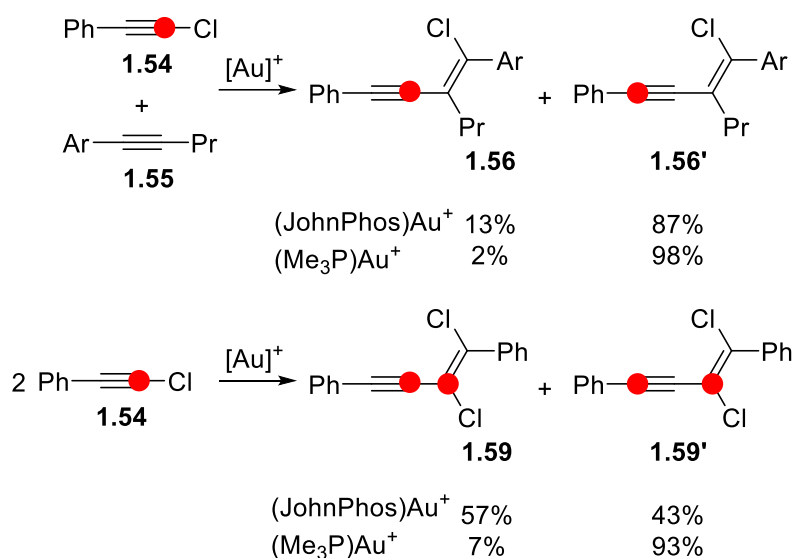


Figure 47. Reactions comparing the ^{13}C -labelling of 1,2-haloalkynylation reactions using $(\text{JohnPhos})\text{Au}^+$ and $(\text{Me}_3\text{P})\text{Au}^+$. Ar = C_6H_4 -4-OMe.

1.2.4 Summary

Computational chemistry can be an extremely useful tool to better understand reactions when used correctly, with the examples detailed herein demonstrating some such uses in gold(I) catalysis. However, as well as considering the level of theory used, care must also be taken that what is being modelled is an accurate description of the experimental conditions. This includes factors such as using a reasonable conformation of the molecules, factoring solvation into the calculations and whether to include the anion in the reaction.

The question of whether to include the anion from the gold(I) precatalyst in the calculation appears to be best answered on a case-by-case basis. In non-polar solvents, ion separation is not as pronounced, so a consideration of anion effects is particularly important – typically locating this in areas where a positive charge is localised or in positions that hydrogen-bonding can occur. If the reaction modelled directly involves groups where hydrogen-bonding is possible, alcohols or amines for example, then the anion could potentially have a pronounced effect on the observed energies calculated. In these cases, then it is proposed that the anion should be modelled explicitly, especially if the DFT model does not agree with experiment. In the case of close-contact ion-pairs, then additional evidence may need to be gathered to determine the topology of the ensemble.

Using DFT to explore the selectivity of gold(I)-catalysed reactions is a natural fit due to the often-unsymmetrical nature of the unsaturated C–C bonds which gold chemistry is famed for activating. The regioselectivity can often be accurately predicted by DFT, which can then lead to the development of new substrates or different ligands to see if the selectivity can be improved or altered. Therefore, care must be taken to ensure that over-analysis of small-energy differences does not contradict the experimental outcomes.

Benchmarking the DFT results with comparison to the experiment is key to ensure that the model used is an accurate description. Utilising methods such as NMR spectroscopy and *in situ* IR to monitor reactions in progress could provide the evidence which helps verify the model used. Additionally, exploring the kinetic profile of the reaction and comparing with the calculated transition-state energies is also important.

1.3 Project Aims and Thesis Structure

The overall aim of the work presented in this thesis, was to use DFT calculations to better understand chemistry developed within the Unsworth group and Lynam groups, and to then use the insight gained from the calculations to improve the work or inspire new methods.

In Chapter 2, work exploring an acid- and base-mediated quinoline rearrangement from spirocyclic indolenines is presented. The rearrangement was already established when acidic conditions were used (see Section 2.1 for further details), however the reaction under basic conditions presented an opportunity for further study. Additionally, the temperatures required to afford the rearrangement varied greatly depending on the conditions used, and DFT was used to study this in greater detail.

In Chapter 3, an intermolecular gold(I)-catalysed coupling reaction between an indole and alkyne was developed. This represents further progression from the silver(I)- or gold(I)-catalysed intramolecular spirocyclisation reactions which were developed within the Taylor and Unsworth groups and presented an opportunity to overcome the challenges of 3-vinyl indole formation (see Section 3.1 for further details). During this work, the intermolecular reaction was found to be less efficient than the intramolecular analogue, and this was studied further using DFT and NMR techniques, providing insight into the speciation and coordination chemistry of gold(I) catalysts.

Chapters 4 and 5 focus primarily on the Successive Ring Expansion (SuRE) chemistry developed previously within the Unsworth group (see Section 4.1.5 for further details). Chapter 4 provides a thorough benchmarking of DFT methods, with comparison to data from ring expansion reactions performed by members of the Unsworth group, to establish an accurate method to aid in the development of further SuRE reactions.

Chapter 5 focuses on work to further the scope of the SuRE reactions, using an acyl-transfer reaction to acylate the nitrogen atom of a lactam, rather than a direct *N*-acylation which is used currently (see Section 5.1.1 for further details). DFT calculations were used to determine a method to achieve the acyl-transfer reaction, with experiments then performed to validate the approach.

Chapter 2. Synthetic and Mechanistic Studies into the Rearrangement of Spirocyclic Indolenines into Quinolines

2.1 Introduction

2.1.1 Quinolines

The quinoline moiety is a bicyclic, heteroaromatic framework consisting of two 6-membered rings, one of which contains a basic nitrogen atom. They have shown to have a diverse range of biological activities, demonstrating antimalarial,¹⁵⁹ anti-bacterial,¹⁶⁰ anti-fungal,¹⁶¹ anti-viral,¹⁶² and anti-cancer¹⁶³ properties to name a few.^{164,165} Selected examples (**2.1–2.5**) are shown in Figure 48, with the quinoline moiety highlighted in blue.

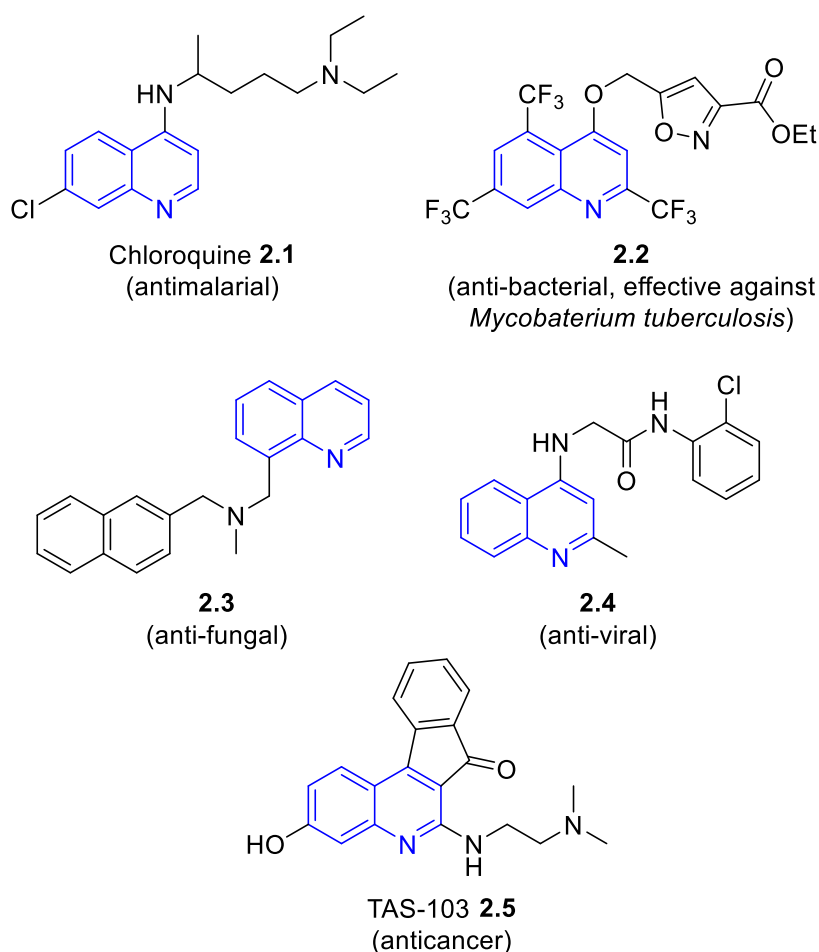


Figure 48. Select examples of quinoline-containing molecules (**2.1–2.5**) which display biological activity, with the quinoline moiety highlighted.

Many named reactions have been reported for the synthesis of quinolines.¹⁶⁶ Commonly simple anilines are used, such as in the Skraup,¹⁶⁷ Doebner-von Miller,¹⁶⁸ and Conrad-Limpach reactions.¹⁶⁹ However, other syntheses are available which use specifically substituted anilines, or closely related compounds, such as the Friedländer,^{170,171} and Pftizinger reactions.¹⁷²

2.1.2 Rearrangement of spirocyclic indolenines to quinolines

In 2016, Liddon *et al.* reported the synthetic utility of indolyl-tethered ynones **2.6** in divergent catalysis, with a range of structurally diverse compounds available from a common starting material (Figure 49),¹⁷³ including carbazoles (**2.9**), spirocyclic indolenines (**2.8**) and tricyclic-fused quinolines (**2.8**).

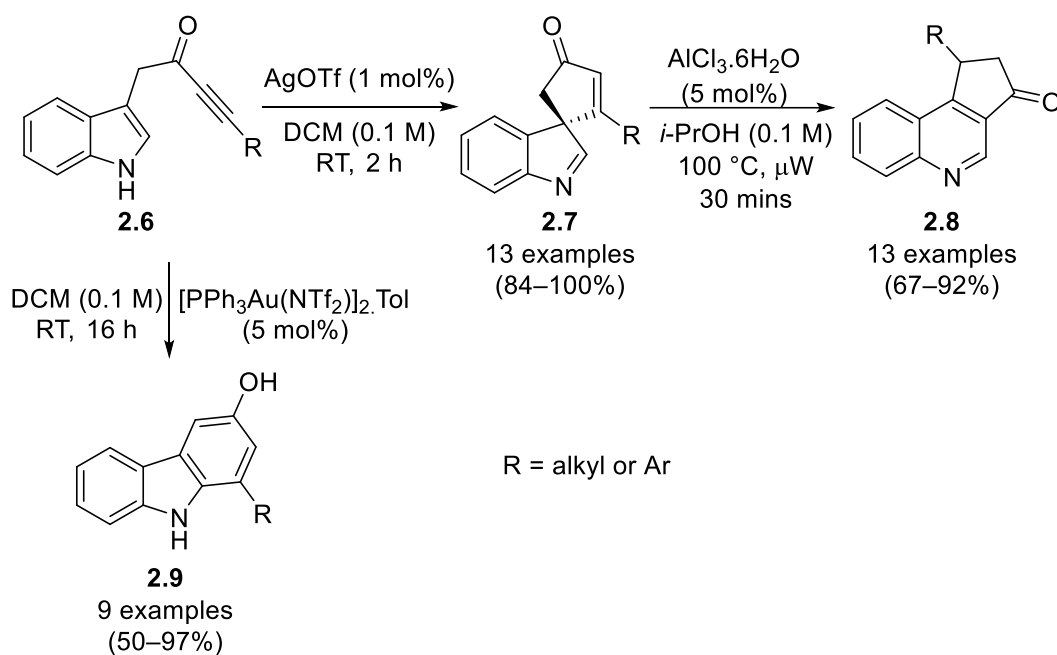


Figure 49. Divergent synthesis of spirocyclic indolenines **2.7**, quinolines **2.8** and carbazoles **2.9** from indolyl-tethered ynones **2.6**, as reported by Liddon *et al.*¹⁷³

The formation of quinoline compounds (**2.8**) from spirocyclic indolenine species (**2.7**) constitutes an unusual one-atom ring expansion. It was proposed that $\text{AlCl}_3 \cdot 6\text{H}_2\text{O}$ acts as a Lewis acid catalyst, and upon coordination to the imine and carbonyl of **2.7**, tautomerisation occurs (**2.7** \rightarrow **2.10**). The resultant enol species **2.10** then cyclises to form **2.11**, which contains a cyclopropyl ring. The fragmentation and ring expansion of **2.11**, followed by aromatisation, results in the quinoline product **2.8** (Figure 50).

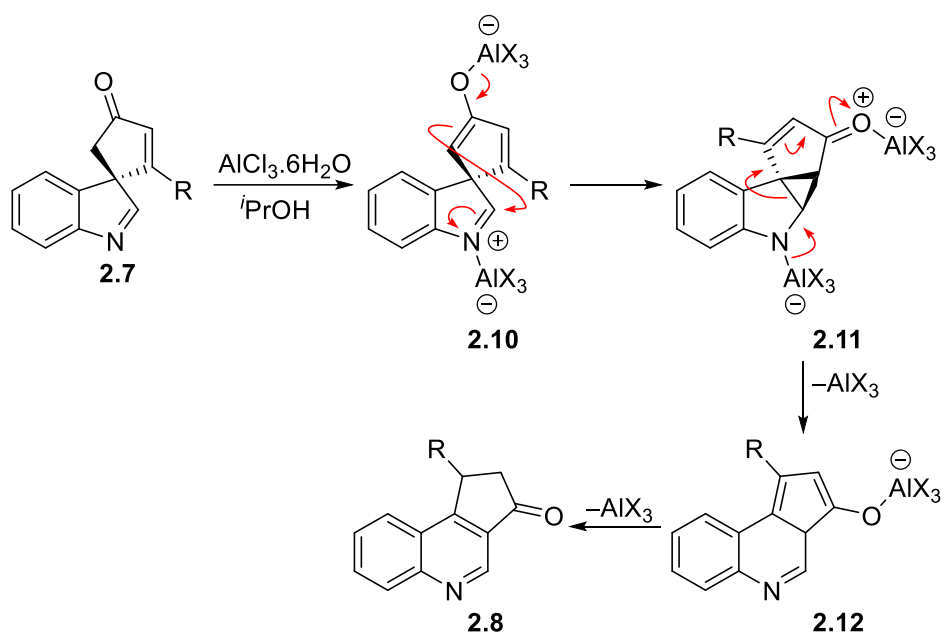


Figure 50. Mechanism for the quinoline rearrangement proposed by Liddon *et al.* to form quinoline **2.8** from **2.7**.¹⁷³ X = Cl or $i\text{PrO}$.

A series of control experiments were used to provide evidence for the proposed mechanism. Cyclopentanol-containing spirocyclic indolenine **2.13** was heated with $\text{AlCl}_3 \cdot 6\text{H}_2\text{O}$ (the standard quinoline rearrangement conditions), however, no quinoline product **2.14** was isolated (Figure 51a). Instead carbazole **2.15** was formed from an acid-catalysed 1,2-migration of the alkenyl group. Furthermore, the addition of LHMDS to spirocyclic indolenine **2.7a** to promote enolate formation, resulted in the desired quinoline **2.8a** (Figure 51b). These experiments reinforced the idea that enol or enolate formation is a key part of the rearrangement.

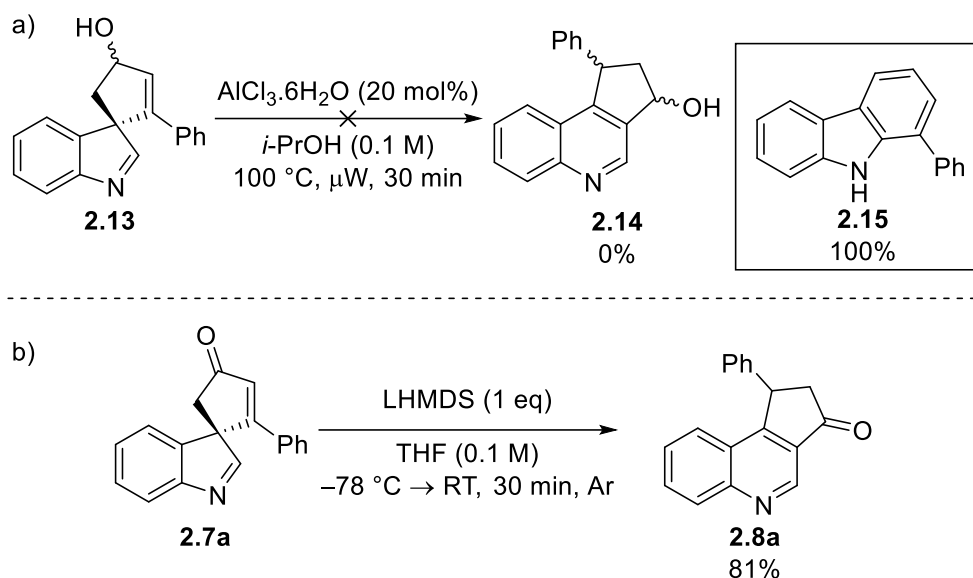


Figure 51. Control experiments performed by Liddon *et al.* a) The reaction of cyclopentanol spirocyclic indolenine **2.13** with $\text{AlCl}_3 \cdot 6\text{H}_2\text{O}$. b) The reaction of spirocyclic indolenine **2.7a** with LHMDS.

Fedoseev *et al.* expanded on the reported work by Liddon *et al.*, publishing metal-free variants of the spirocyclisation and quinoline rearrangement reactions of the indolyl-tethered indoles (**2.6**).¹⁷⁴ The authors were able to achieve a temperature-switchable synthesis of spirocycle **2.7** or quinoline **2.8** using Brønsted acids (Figure 52). A range of acids and temperatures were screened using indolyl-tethered ynone **2.6a** as a model substrate. The optimal conditions are shown in Figure 52, with spirocyclic indolenine **2.7a** formed at room temperature, and quinoline **2.8a** formed when high temperatures were used.

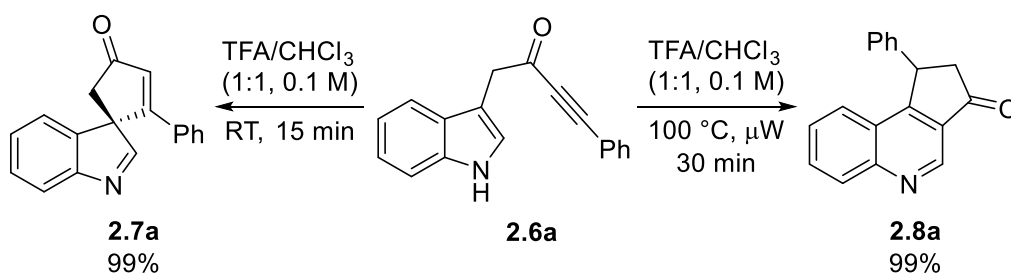


Figure 52. Temperature-switchable TFA mediated synthesis of **2.7a** and **2.8a** from indolyl-tethered ynone **2.6a**, as reported by Fedoseev *et al.*¹⁷⁴

2.1.3 Project aims

Whilst a mechanism was proposed for the $\text{AlCl}_3 \cdot 6\text{H}_2\text{O}$ -mediated quinoline rearrangement, there is no indication as to why a high temperature is required to afford the transformation, when the

LHMDS control reaction occurs readily at room temperature. Indeed, the TFA-mediated reaction reported by Fedoseev *et al.* forms spirocyclic indolenines **2.7** selectively at room temperature.¹⁷⁴

Therefore, the aims of this project were to use DFT calculations to explore the reasons why the quinoline rearrangement reaction occurs readily at room temperature with LHMDS, yet under acidic conditions, heating is needed. Furthermore, the scope of the LHMDS-mediated rearrangement was relatively unexplored. Therefore, the scope of the quinoline rearrangement under basic conditions was tested, to provide a milder and complementary approach to synthesise the quinoline products.

Throughout this section, numbers are used to indicate compounds (*e.g.* **2.1**), whereas DFT calculated states are denoted by letters (*e.g.* **2.A**), with transition states labelled specifically as 'TS' (*e.g.* **2.TS_{cd}**, which refers to the transition state connecting state **2.C** and **2.D**).

2.2 Synthetic and Mechanistic Studies into the Rearrangement of Spirocyclic Indolenines into Quinolines

2.2.1 Starting Material Synthesis

Throughout the project, a number of spirocyclic indolenines were required to be synthesised to be used as substrates for the quinoline rearrangement. This section discusses the synthesis of these molecules, and is broken up into Weinreb amide synthesis, indolyl-tethered ynone synthesis and spirocyclic indolenine synthesis.

Weinreb amide synthesis

Following the general procedure used within the Unsworth group,¹⁷³ Weinreb amides **2.16a–c** were made in high yields *via* an amide coupling reaction using commercially available indole-3-acetic acid derivatives (**2.17a–c**, Figure 53).

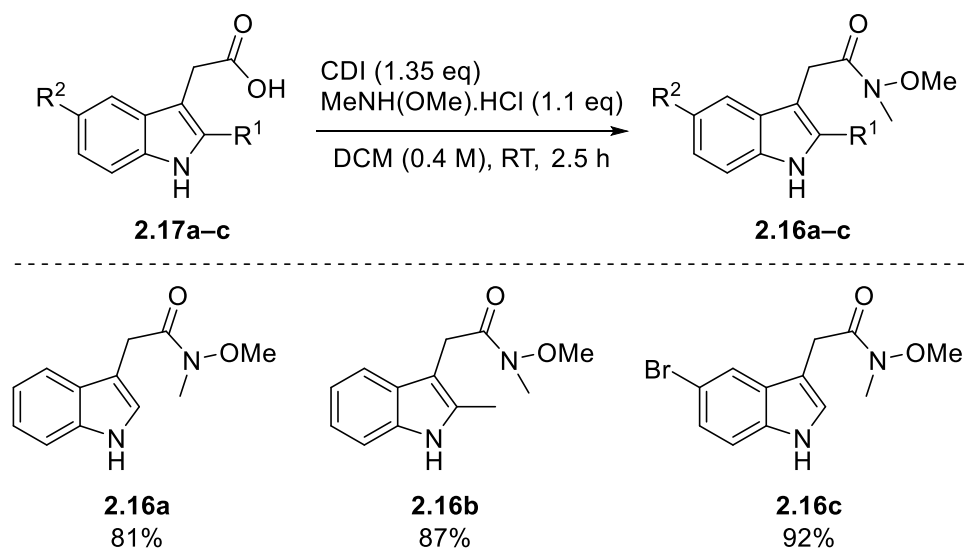


Figure 53. Synthesis of Weinreb amides **2.16a–c** using CDI amide coupling with indole-3-acetic acid derivatives **2.17** using the method reported by Liddon *et al.*¹⁷³

The synthesis of α -benzyl substituted amide **2.16d** was more challenging. Indole-3-acetic acid (**2.17a**) was treated with an excess of LDA to form a trianionic enolate species, which was reacted with benzyl chloride to introduce the benzyl group. After 16 hours, the reaction was worked-up, and the crude mixture was subjected to amide coupling using T3P and *N,O*-dimethylhydroxylamine hydrochloride, to afford the desired Weinreb amide (**2.16d**). A low yield of 21% was achieved over the two steps, which was similar to the 31% yield previously reported.¹⁷⁵

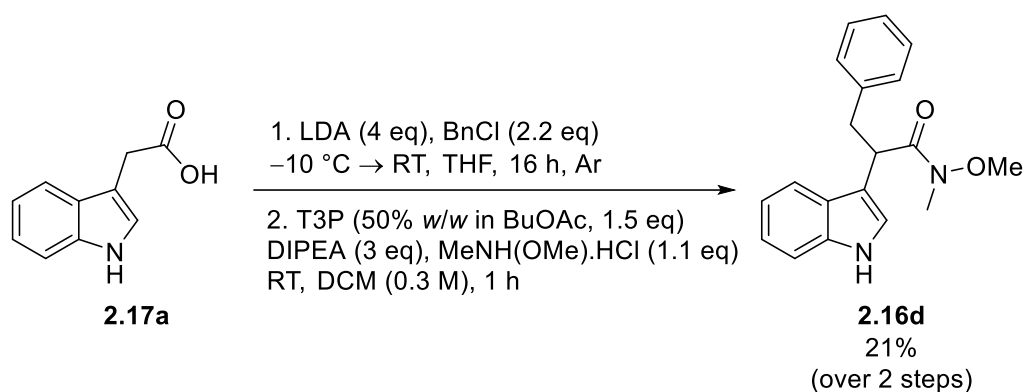


Figure 54. Synthesis of benzyl-substituted Weinreb amide **2.16d**, as reported by James et al.¹⁷⁵

Indolyl-tethered ynone synthesis

Next, the Weinreb amides (**2.16a–d**) were converted into indolyl-tethered ynones (**2.6a–f**), following a literature procedure (Figure 54).¹⁷⁵ Here, *n*-BuLi was used to deprotonate terminal acetylenes (**2.18a–c**) to form an excess of a lithiated acetylide species *in situ*, which was then transferred to a cooled solution of the previously synthesised Weinreb amides (**2.16a–d**). The resulting indolyl-tethered ynones (**2.6a–f**) were isolated in moderate to good yields.

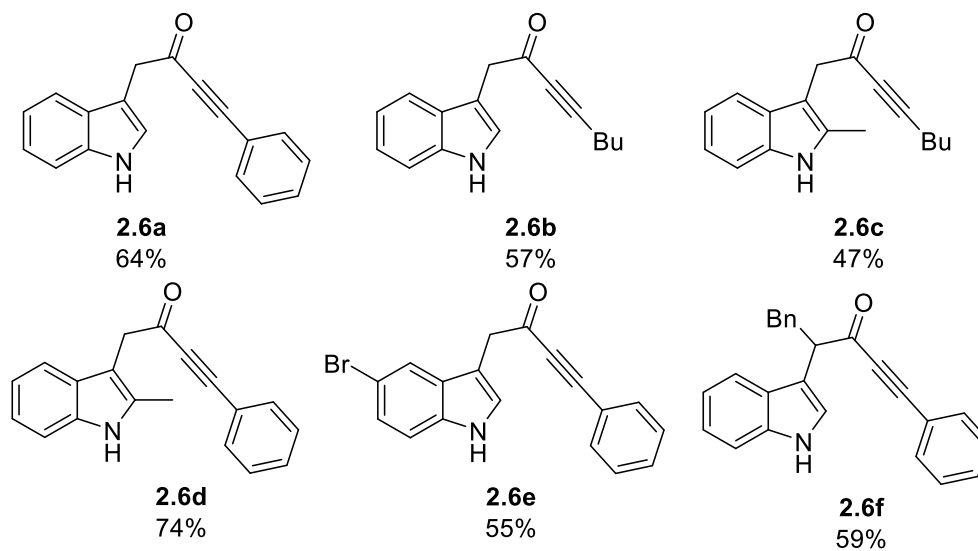
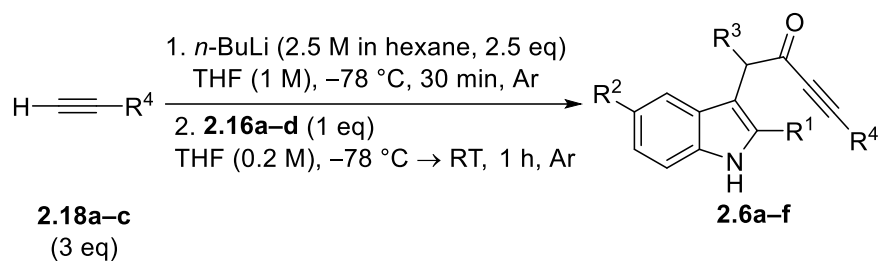


Figure 55. Synthesis of indolyl-tethered ynones **2.6a-f** using acetylenes **2.18a-c**, as reported by James *et al.*¹⁷⁵

Spirocyclic indolenine synthesis

Spirocyclisation of the indolyl-tethered ynones (**2.6a-f**) was then performed using silver triflate as a catalyst to activate the alkyne to nucleophilic attack from the indole moiety (Figure 56).¹⁷⁵ After purification, high yields of spirocyclic indolenines (**2.7a-h**) were isolated.

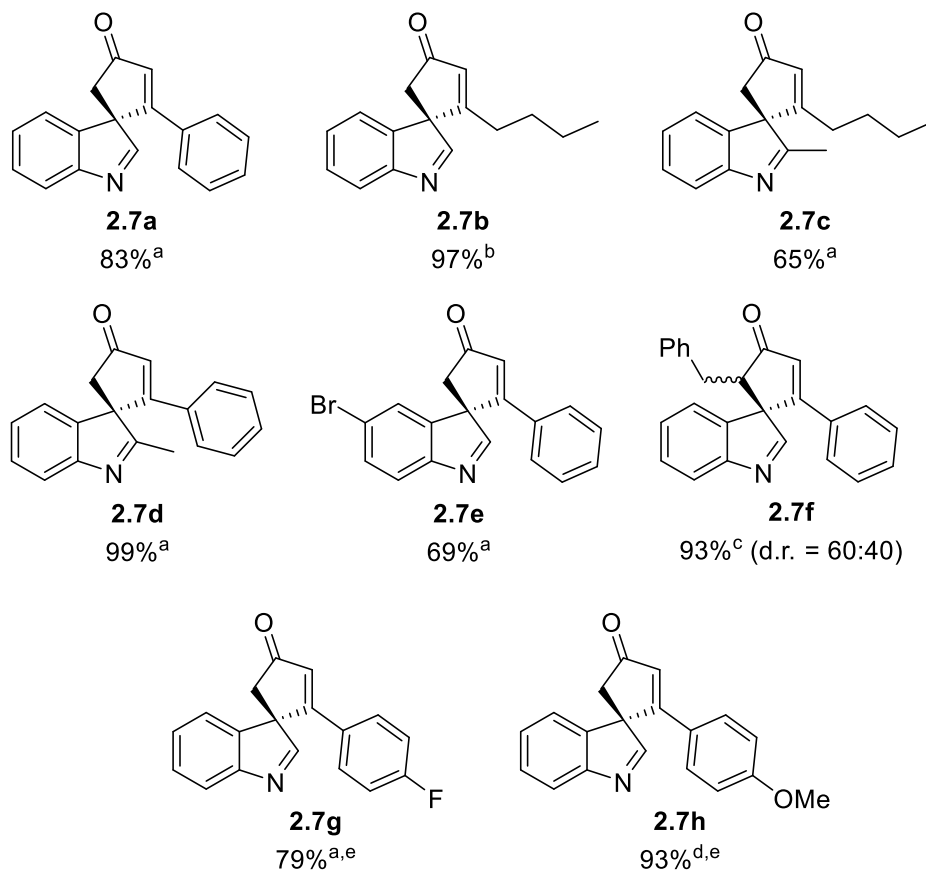
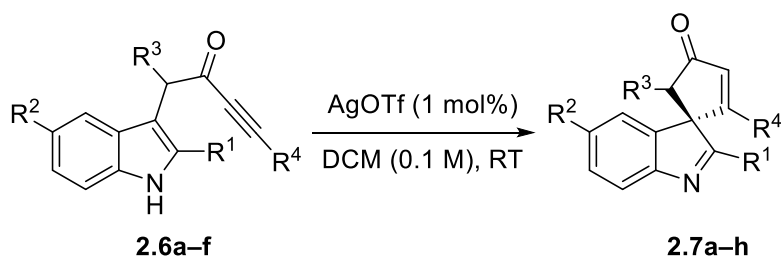


Figure 56. Synthesis of spirocycles **2.7a–h**, as reported by James *et al.*¹⁷⁵ ^a Reaction time of 1 hour. ^b Reaction time of 3.5 hours. ^c Reaction time of 2 hours. ^d Reaction time of 1.5 hours. ^e The indolyl-tethered ynone required for **2.7g** and **2.7h** were made by Dr Aimee Clarke and Dr Hon Eong Ho respectively.

Tetrasubstituted-alkene spirocycles were also synthesised, using a one-pot spirocyclisation and palladium cross-coupling procedure, reported by Ho *et al.*¹⁷⁶ Spirocyclic indolenines **2.7i** and **2.7j** were able to be successfully synthesised in modest to good yields respectively.

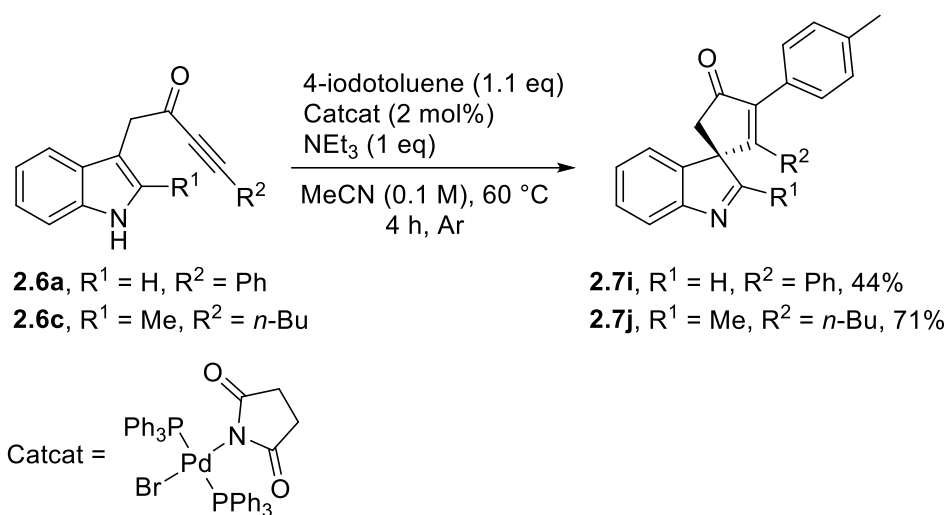


Figure 57. Palladium-catalysed synthesis of spirocycles **2.7i** and **2.7j**, as reported by Ho *et al.*¹⁷⁶

2.2.2 Temperature Screening

The conditions reported for the quinoline rearrangement as reported by Liddon *et al.* (using AlCl₃·6H₂O) and Fedoseev *et al.* (using TFA), both utilised microwave heating at high temperatures of 100 °C.^{173,174} Before starting the DFT studies it was decided to explore if the reactions needed such harsh conditions, due to the implications this would have on the viability of the DFT-calculated energies for the predicted transition states.

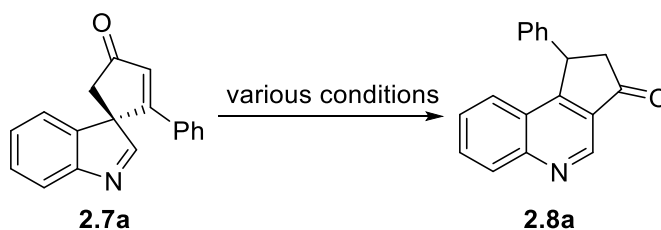
Phenyl-substituted spirocyclic indolenine **2.7a** was chosen as the model compound since high yields have been achieved using both acidic conditions to be studied. The acidic rearrangement reactions were performed under the standard reaction conditions, using conventional heating. The reactions were left for 24 hours before an aliquot was taken from the mixture, and a crude ¹H NMR spectrum was recorded to assess if the reaction was complete.

The reactions using AlCl₃·6H₂O (Entries 1–4, Table 5) demonstrated that whilst heating is required, 100% conversion can still be achieved at 80 °C. Partial conversion of 38% was seen at 50 °C, however upon lowering the reaction temperature to 40 °C, no conversion was seen, with only unreacted **2.7a** observed in the crude ¹H NMR spectra.

The reactions utilising TFA were similar in that the reactions tolerated lower temperatures than the optimal conditions reported by Fedoseev *et al.* at 100 °C (Entries 5–8, Table 5).¹⁷⁴ Full conversion was seen as low as 40 °C, albeit with unidentified side products becoming more prominent. Additionally, at room temperature 54% conversion was still achieved. It is possible

that the much larger amount of acid present in the TFA conditions (than the $\text{AlCl}_3 \cdot 6\text{H}_2\text{O}$ reactions) facilitated the increase in conversion.

Table 5. Temperature scope of the rearrangement of spirocyclic indolenine **2.7a** into quinoline **2.8a** in acidic conditions.



Entry	Temp / °C	Time / h	Conditions	Conversion ^[a]
1	40			0%
2	50	24	$\text{AlCl}_3 \cdot 6\text{H}_2\text{O}$ (5 mol%)	38%
3	80		<i>i</i> -PrOH (0.1 M)	100%
4	100			100%
5	RT			54%
6	40	24	1:1 TFA/ CHCl_3	100% ^[b]
7	50		(0.1 M, 60 eq of TFA)	100%
8	60			100%

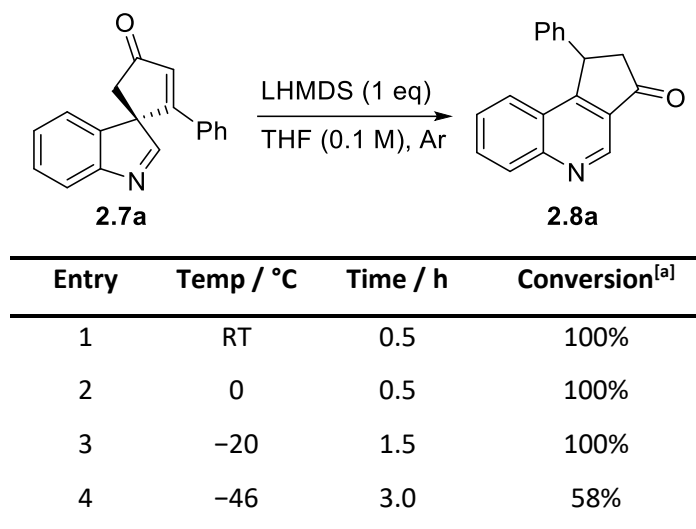
^[a] Calculated by the ratio of **2.7a** to **2.8a** in the crude ^1H NMR spectra. ^[b] All starting material was consumed, however unidentified products were also formed.

Whilst LHMDS was used to afford the quinoline rearrangement in the initial screening reported by Liddon *et al.*,¹⁷³ the scope of the reaction hadn't been explored. Therefore, the temperature required for the rearrangement of **2.7a** into quinoline **2.8a** using LHMDS was also evaluated. A solution of **2.7a** in THF was cooled to -78 °C for the addition of LHMDS. After 5 minutes the reaction was then transferred to an ice bath of the required temperature. After the chosen reaction time, a work-up was performed and a crude ^1H NMR spectra was recorded to determine the reaction conversion.

The results showed that the LHMDS-mediated quinoline rearrangement can be performed at much lower temperatures than under the acidic conditions (Table 6), with 58% conversion still seen at -46 °C in 3 hours. This demonstrated that the quinoline rearrangement of spirocyclic

indolenines can be performed under milder and complementary conditions, to potentially support a different range of functional groups to that of the acidic conditions.

Table 6. Temperature scope of the rearrangement of spirocyclic indolenine **2.7a** into quinoline **2.8a** in basic conditions.



^[a] Calculated by the ratio of **2.7a** to **2.8a** in the crude ¹H NMR spectra.

2.2.3 Substrate Scope

The scope of the LHMDS-mediated quinoline rearrangement was tested using the previously synthesised spirocyclic indolenine species **2.7a–j**, to compare its utility against the reported acidic-mediated reactions (Figure 58).^{173,174} In a minor change from the conditions previously used, a slight excess of LHMDS was used.

Generally, the LHMDS-mediated quinoline rearrangement was tolerant to a range of substitution patterns on the indolenine, with both substitution in the C-2 position, and electron-withdrawing groups tolerated. The quinoline rearrangement was successful with both alkyl and aromatic functionalities present on the cyclopentenone alkene. The TBS-protected alcohol present in quinoline **2.8k** also withstood the reaction, highlighting the synthetic utility of this additional approach, as TFA has been reported for the selective deprotection of primary TBS-protected alcohols.^{177,178}

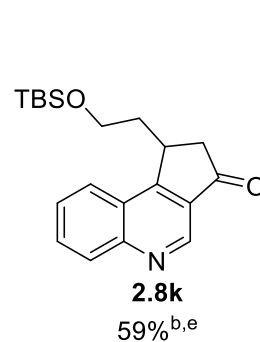
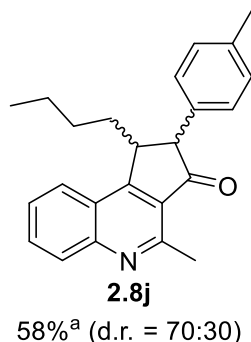
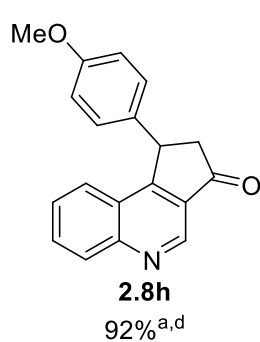
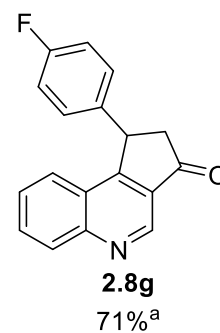
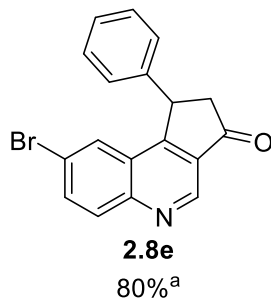
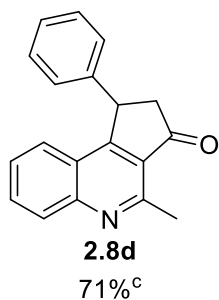
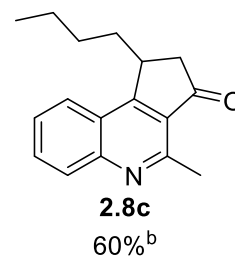
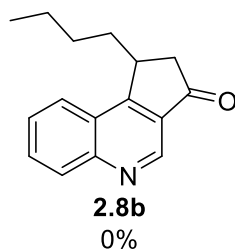
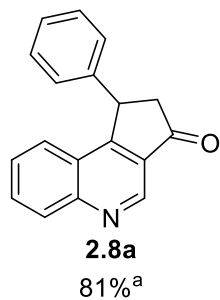
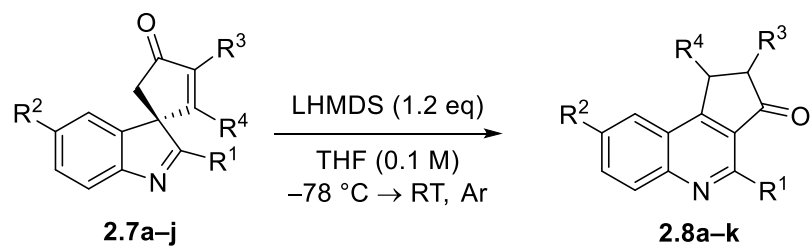


Figure 58. Successful synthesis of quinolines **2.8a–k** using LHMDS. ^a Reaction time of 30 minutes. ^b Reaction time of 1 hour. ^c Reaction time of 1.5 hours. ^d Quinoline **2.8h** was made by Dr Aimee Clarke. ^e The spirocyclic indolenine required for **2.8k** was synthesised during a previous study. ¹⁷³

Tolyl-substituted quinoline **2.8j** was formed as diastereoisomers in a 70:30 ratio. Comparison of the J values for **2.8j** with data reported previously for 2,3-disubstituted indanone species,¹⁷⁹ suggested that the major product is the *trans*-isomer, due to a small 3J coupling constant of 1.5 Hz; whilst the minor isomer has a larger 3J coupling constant of 7.0 Hz. When structurally related spirocyclic indolenine **2.7i** was used in the LHMDS-mediated reaction (Figure 59), the desired quinoline product **2.8i** was formed as a single diastereoisomer, which was assigned as the *trans*

configuration due to its small 3J coupling of 3.5 Hz.¹⁷⁹ Additionally, a low yield of oxidised quinoline **2.19** was also formed. It was proposed that the additional conjugation present in the product (**2.19**) made **2.8i** more susceptible to oxidation under the reaction conditions.

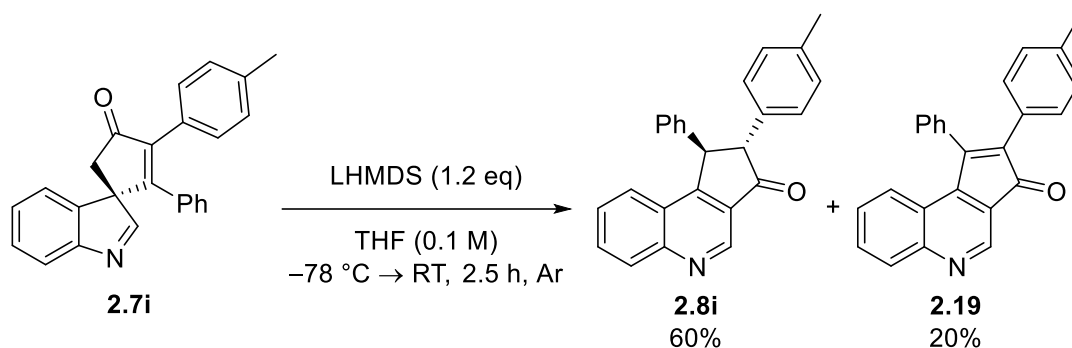


Figure 59. Formation of quinoline **2.8i** and oxidised quinoline **2.19** from the LHMDS-mediated reaction of **2.7i**.

The only substrate tested that failed to deliver the quinoline upon reaction with LHMDS was spirocyclic indolenine **2.7b**. Some spirocyclic indolenines are well documented to trimerise in solution, and this was the case for this system (**2.20**, Figure 60a). It was demonstrated by Jackson *et al.* that the addition of an acid such as TFA can break the trimer compound *in situ*.¹⁸⁰ However, upon addition of LHMDS to a solution of **2.7b**, an intractable mixture was formed, with no formation of the desired quinoline **2.8b** detected (Figure 60b). Therefore it is proposed that spirocyclic indolenines which display an equilibrium with a trimer species require the use of acidic conditions, with successful syntheses of this type previously reported.^{173,174}

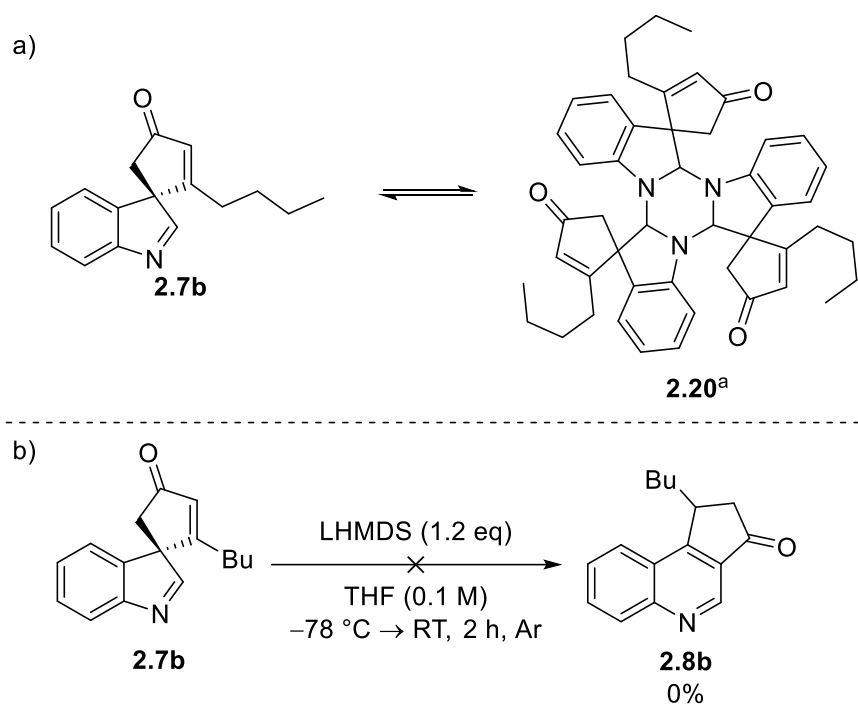


Figure 60. a) Trimer species **2.20** formed from *n*-butyl substituted spirocyclic indolenine **2.7b**. b) Unsuccessful quinoline formation from spirocyclic indolenine **2.7b**.

Overall, the scope of the LHMDS-mediated rearrangement is complementary to that of the acid-mediated rearrangement. Broadly, similar functionalities are tolerated, although the reactions using LHMDS are successful at lower temperatures, which should provide scope for compounds which are heat or acid sensitive.

2.2.4 DFT Calculations

The rearrangement of spirocyclic indolenines to quinolines was modelled using DFT methods. The procedure was as follows. Geometries were optimised at the BP86/SV(P) level of theory. Frequency calculations demonstrated that states were either minima on the potential energy surface (no imaginary frequencies) or transition states (one imaginary frequency). The frequency calculations were also used to provide the thermodynamic corrections. The electronic energies of the structures were then re-evaluated at the D3(BJ)-PBE0/def2-TZVPP level. Solvent effects were modelled using a PCM model in THF or chloroform for the basic and acidic conditions respectively.

The overall free energy change for the rearrangement were considered, using spirocyclic indolenine **2.7a** as the model compound (Figure 63). The reaction was calculated to be exergonic

by -89 kJ mol^{-1} , likely due to rearomatisation with the formation of the quinoline core. The mechanism of the rearrangement was then considered under both the base- and acid-mediated pathways.

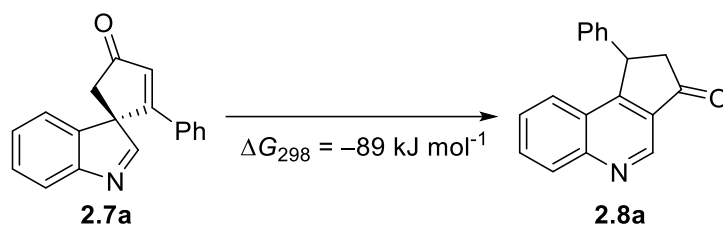


Figure 61. DFT-calculated energy for the formation of quinoline **2.7a** from spirocyclic indolenine **2.8a**. Energies are Gibbs free energies calculated at the D3(BJ)-PBE0/def2-TZVPP//BP86/SV(P) level of theory with PCM solvent correction in THF.

Base-mediated pathway

The pathway of the LHMDS-mediated reaction was considered first. It was proposed that a lithium enolate species would form by deprotonation of the most acidic protons, α to the carbonyl. To determine if the lithium ions are important to the reaction mechanism, a control reaction was performed in which 2 equivalents of TMEDA were added to chelate to and sequester the lithium ions. No change in the conversion of **2.7a** was seen by ^1H NMR spectroscopy, and therefore the lithium ion was believed not to be playing a significant role in the reaction and therefore omitted during the subsequent DFT calculations.

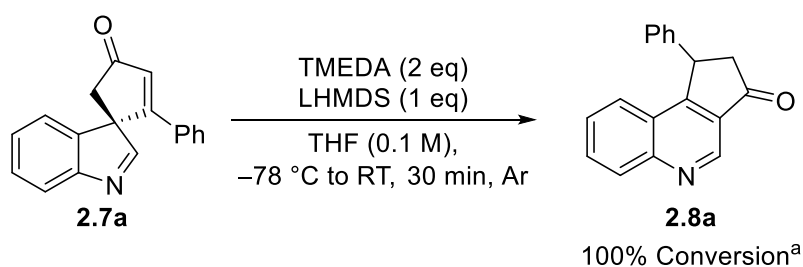


Figure 62. TMEDA control reaction of the rearrangement of spirocyclic indolenine **2.7a** using LHMDS. ^a Calculated by the ratio of **2.7a** to **2.8a** in the crude ^1H NMR spectra.

The pathway for ring-opening was then modelled assuming that deprotonation of **2.7a** had occurred to form enolate **2.A**, which was then used as the reference point for the calculations (Figure 63). A low-lying transition state (**2.TS_{AB}**) was found at $+19 \text{ kJ mol}^{-1}$ to result in tetracyclic amide anion **2.B**. Fragmentation of the cyclopropyl group then occurs *via* **2.TS_{BC}** at $+16 \text{ kJ mol}^{-1}$ to result in enolate **2.C**. From **2.C**, a series of 1,5-hydride migration steps would result in anions **2.D**, **2.E**, **2.F** and **2.G**. Migration through **2.TS_{CD}** was calculated to be most accessible at $+33 \text{ kJ}$

mol⁻¹ (as opposed to **2.TS_{CG}** at +77 kJ mol⁻¹) which corresponds to hydride migration in the “anticlockwise” direction as drawn. After a second migration from **2.D** through **2.TS_{DE}** (+16 kJ mol⁻¹), enolate **2.E** was identified as the resting state of the reaction, at -119 kJ mol⁻¹. Protonation of **2.E** during an acid work-up would result in the desired quinoline product **2.8a**.

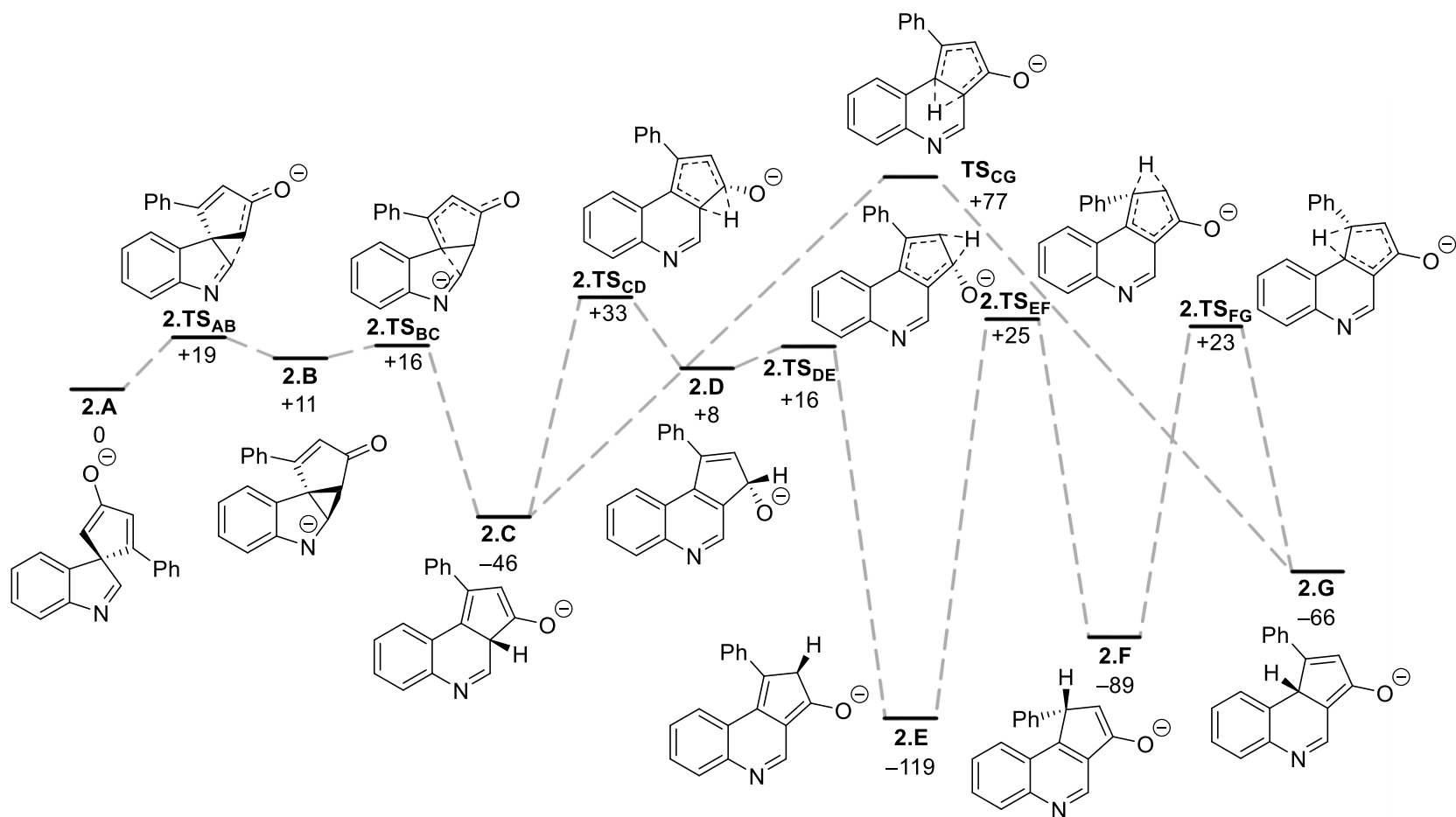


Figure 63. DFT-calculated pathway for the base-promoted rearrangement of **2.7a** to **2.8a**. Energies are Gibbs free energies at 298.15 K in kJ mol^{-1} at the D3(BJ)-PBE0/def2-TZVPP//BP86/SV(P) level with PCM solvent correction in THF.

The effect of using different DFT methods were determined for the base-mediated pathway. First, the effects of the ω B97XD and M06-2X functionals were tested by performing a single-point calculation on the BP86/SV(P) geometries. Additionally, the energies taken from only the BP86/SV(P) calculations were compared. Finally, when using the Pople basis sets, it is preferable to include diffuse functions when modelling anions, therefore the energies were evaluated at the D3(BJ)-PBE0/6-311+G**//BP86/6-31+G* level of theory.

The collated energies at the different levels of theory used are shown in Table 7. The energies at the D3(BJ)-PBE0/def2-TZVPP//BP86/SV(P) level of theory, and those calculated from the D3(BJ)-PBE0/6-311+G**//BP86/6-31+G* level of theory, are very similar, which therefore demonstrates that using the Ahlrichs def2-TZVPP basis set is suitable for modelling the anions without requiring diffuse functions. When different functionals were used, the energies of the intermediate species were largely unaffected. The BP86 functional was found to lower the transition state energies, whereas both the ω B97XD and M06-2X functionals increased the energies. Overall, the shape of the potential energy surface remains the same as when the PBE0 functional was used, with no significant change in the conclusion.

Table 7. DFT-calculated energies of the basic pathway PES (referring to Figure 63), at various levels of theory. Energies are Gibbs energies at 298.15 K in $\text{kJ}\cdot\text{mol}^{-1}$ at various levels of theory, with PCM solvent correction in THF.

Level of theory	2.A	2.TS _{AB}	2.B	2.TS _{BC}	2.C	2.TS _{CD}	2.TS _{CG}	2.D	2.TS _{DE}	2.E	2.TS _{EF}	2.F	2.TS _{FG}	2.G
ω B97XD/def2-TZVPP//BP86/SV(P)	0	+34	+29	+39	-35	+56	+103	+14	+33	-108	+48	-95	+40	-61
M06-2X/def2-TZVPP//BP86/SV(P)	0	+32	+24	+35	-38	+49	+96	+12	+29	-112	+42	-95	+36	-62
D3(BJ)-PBE0/def2-TZVPP//BP86/SV(P)	0	+19	+11	+16	-46	+33	+77	+8	+16	-119	+25	-89	+23	-66
BP86/SV(P)	0	+13	+2	+5	-60	+25	+65	+11	+10	-138	+12	-96	+11	-76
D3(BJ)-PBE0/6-311+G**//BP86/6-31+G*	0	+20	+13	+18	-44	+39	+83	+1	+20	-117	+31	-88	+24	-66

As an aside, the reaction of α -benzyl substituted spirocyclic indolenine **2.7f**, resulted in the formation of quinoline compound **2.21**, rather than the expected product **2.8f** (Figure 64a). It was proposed that **2.21** was formed from the migration of the benzyl group in an ‘anticlockwise’ fashion after ring expansion, analogous to the hydride migration through **2.TS_{CD}** as calculated in the DFT calculations (Figure 63). It should be noted that Liddon *et al.* reported the isolation of quinoline **2.8l** as a single diastereoisomer from indolyl-ynone **2.7l** (Figure 64b).¹⁷³ It is proposed that the higher temperature used in the acidic reactions is required for continued migration.

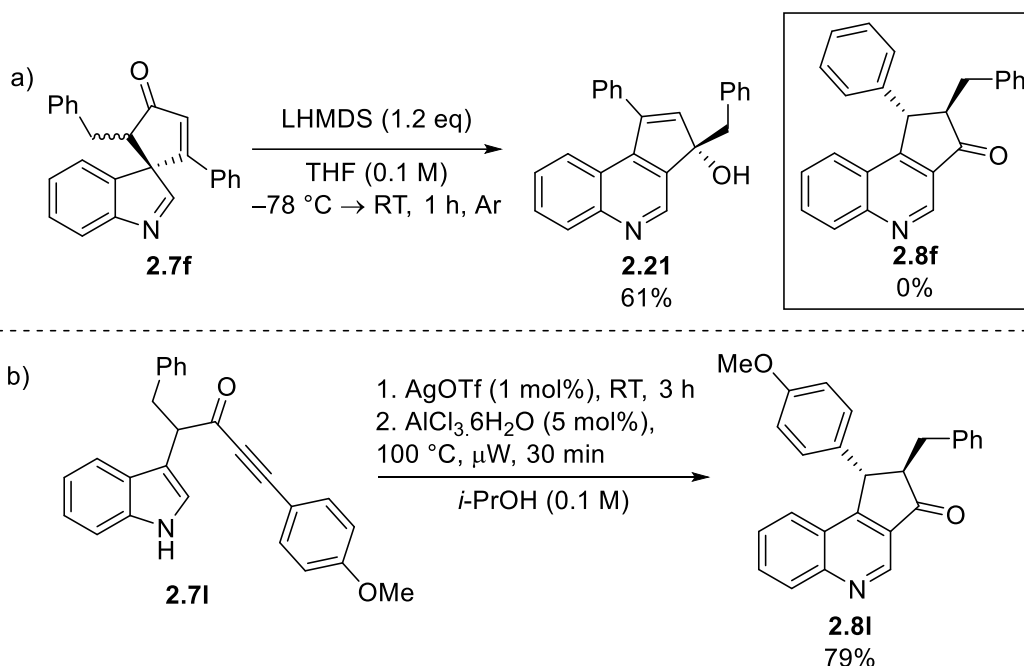


Figure 64. a) Reaction of spirocyclic indolenine **2.7f** with LHMDS. b) Reaction of indolyl-tethered ynone **2.7l** using the one-pot quinoline rearrangement procedure as reported by Liddon *et al.*,¹⁷³ resulting in quinoline **2.8l**.

Acid-mediated pathway

The acid-mediated pathway was also considered. However before starting the DFT calculations for the acid-mediated pathway, the catalytically active species had to be determined. It was proposed that in the quinoline rearrangement reactions using $\text{AlCl}_3 \cdot 6\text{H}_2\text{O}$, ligand exchange could occur between the chloride anions and the *iso*-propanol solvent, which would form aluminium *iso*-propoxide ($\text{Al}(\text{O}^i\text{Pr})_3$) and HCl.

Control reactions were performed in which either a catalytic amount of aluminium *iso*-propoxide was used as a Lewis acid (Figure 65a), or 15 mol% of HCl was used (Figure 65b). Only 7% conversion of spirocyclic indolenine **2.7a** was achieved when aluminium *iso*-propoxide was

used, whereas full conversion of **2.7a** was achieved using catalytic HCl. Therefore, it was proposed that the conditions reported by Liddon *et al.* were Brønsted acid catalysed, and hence only this pathway was considered in the DFT calculations.

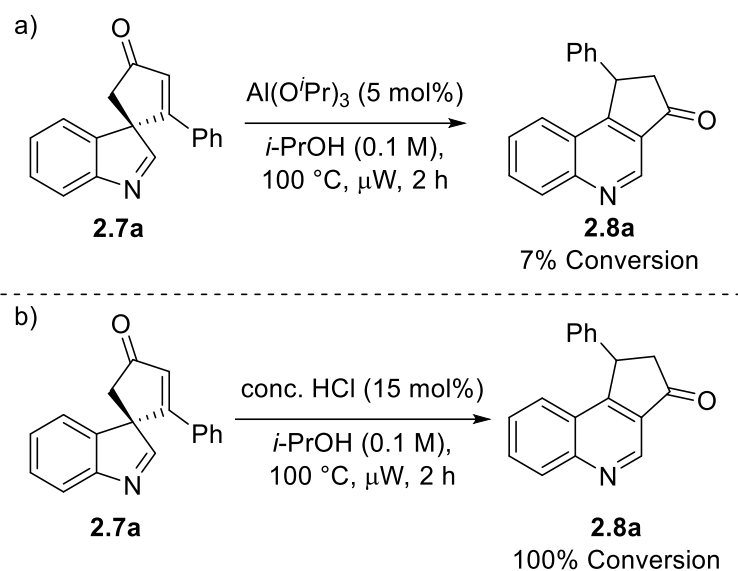


Figure 65. Control reactions of **2.7a** with a) aluminium *iso*-propoxide and b) conc. HCl.

It was considered that the indolenine nitrogen would be the most basic site and protonated first, therefore cation **2.H** was considered as the starting point and reference state for the acid-mediated quinoline rearrangement (Figure 66). Protonation on the carbonyl oxygen was also considered (**2.H'**) however this had an energy of +37 kJ mol⁻¹ corroborating the idea that protonation on the nitrogen is preferred.

A transition state to form the cyclopropyl ring from **2.H** was not located, however when the enol tautomer **2.I** (+40 kJ mol⁻¹) was considered (Figure 66), a low-lying transition state for ring-closing (**2.TS_{IJ}**) was found at +46 kJ mol⁻¹, to form cation **2.J** at +38 kJ mol⁻¹. Fragmentation of cation **2.J** through **2.TS_{JK}** (+60 kJ mol⁻¹) can then occur to give intermediate **2.K** (+26 kJ mol⁻¹). By analogy with the base-mediated pathway, a series of 1,5-hydride shifts can occur to give intermediates **2.L**, **2.M**, **2.N** and **2.O**. All the resulting cations are at a lower energy than **H**, with a small bias towards cation **2.M** (-64 kJ mol⁻¹). Tautomerisation and deprotonation can then occur, to yield the observed product **2.8a**.

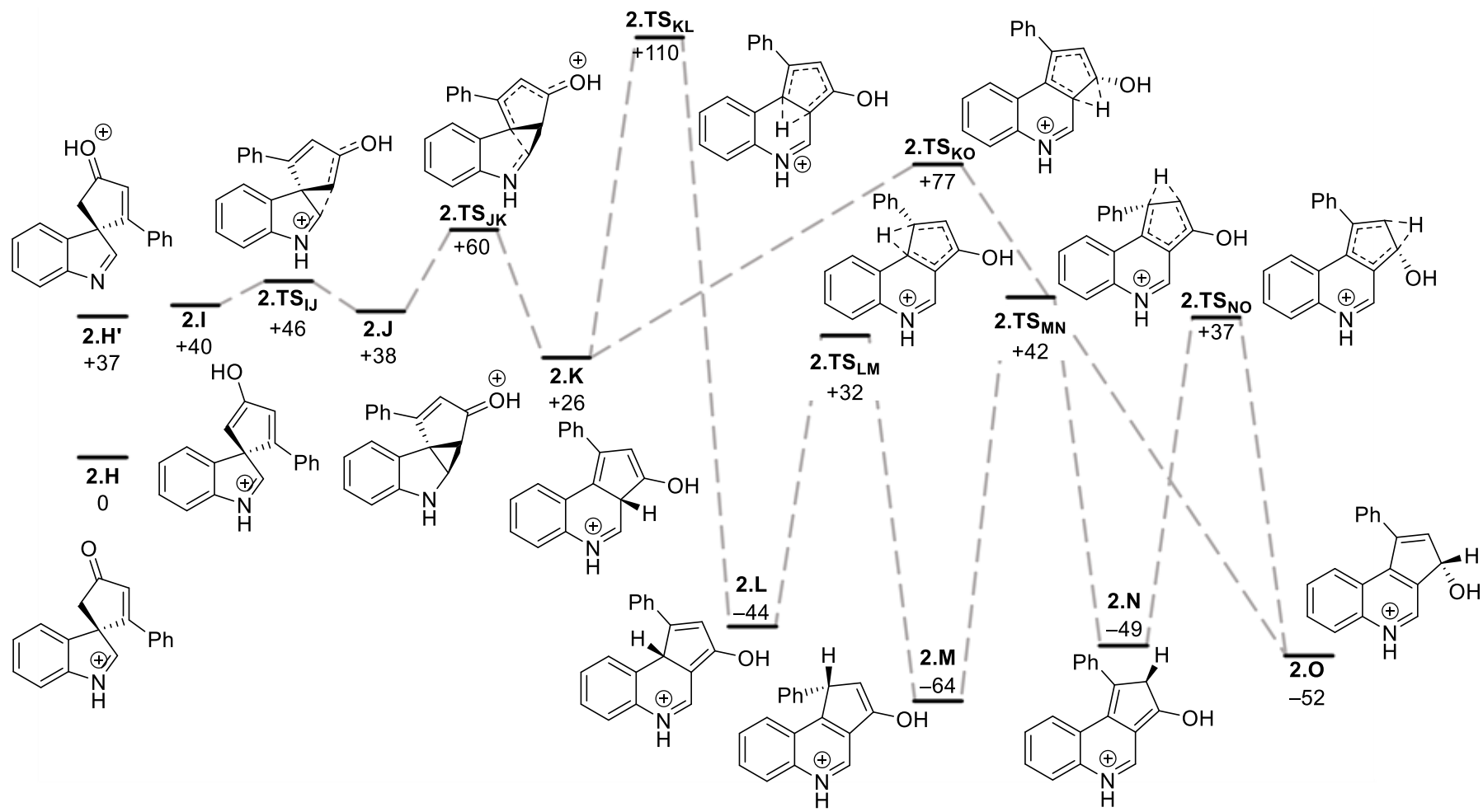


Figure 66. DFT-calculated pathway for the acid-promoted rearrangement of **2.7a** to **2.8a**. Energies are Gibbs free energies at 298.15 K in kJ mol⁻¹ at the D3(BJ)-PBE0/def2-TZVPP//BP86/SV(P) level with PCM solvent correction in chloroform.

Due to the strongly acidic conditions employed in the reactions using TFA, double protonation of **2.7a** could be envisioned to give state **2.P** (Figure 67), however, attempts to find a transition state were unsuccessful, a relaxed scan of the cyclopropanation C–C bond forming step (equivalent to **2.TS_{II}**) was performed, and the electronic energy greatly increased (+284 kJ mol⁻¹) until a sudden rearrangement of the carbon framework occurred during the geometry optimisation. Likewise, attempts starting from the neutral species **2.7a** were also unsuccessful, with a relaxed scan of the cyclopropanation C–C bond forming step (equivalent to **2.TS_{II}**) showing a greatly increased electronic energy (+240 kJ mol⁻¹ at the BP86/SV(P) level of theory), with no energy maximum observed. These data demonstrates that a reactive intermediate must be formed initially.

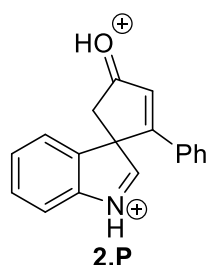


Figure 67. Dication **2.P** formed from the double-protonation of **2.7a**.

Under acidic conditions, a possible side reaction that might be seen with spirocyclic indolenine species is a rearrangement *via* a 1,2-migration pathway to form carbazole species, which are not observed during the quinoline rearrangement reactions.¹⁸¹ A transition state (**2.TS_{KR}**) was found for the C-3 to C-2 alkenyl migration from enol **2.I**. Transition state **2.TS_{KR}** had a DFT-calculated energy of +82 kJ mol⁻¹ which is much higher than the initial ring-closing step of the quinoline rearrangement (**2.TS_{II}**, +46 kJ mol⁻¹), which is in line with the lack of carbazole products formed in the synthetic reactions.

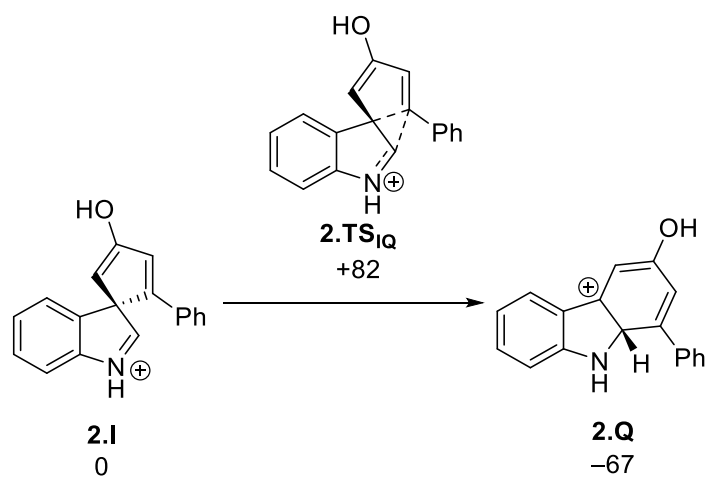


Figure 68. DFT-calculated energies for the 1,2-migration of enol **2.I**. Energies are Gibbs free energies at 298.15 K in kJ mol⁻¹ at the D3(BJ)-PBE0/def2-TZVPP//BP86/SV(P) level with PCM solvent correction in chloroform.

Pathway comparisons

The energetic spans of both the base- and acid-mediated pathways are $+79 \text{ kJ mol}^{-1}$ (between **2.C** and **2.TS_{CD}**) and $+91 \text{ kJ mol}^{-1}$ (between **2.N** and **2.TS_{MN}**) respectively. An energetic span of $+79 \text{ kJ mol}^{-1}$ is consistent with conversion at the low temperatures (58% at $-46 \text{ }^\circ\text{C}$) observed with the LHMDS-mediated reactions (Table 6). However, the quinoline rearrangements performed under acidic conditions would be predicted to occur readily at room temperatures, which is only seen when a large excess of acid is used in the TFA-mediated reactions (Table 5). However, the nature of the keto-enol tautomerisation (between **2.H** and **2.I**) wasn't modelled as it was presumed to be complex and likely bimolecular. Therefore, it is suggested that in the acid cases, keto-enol tautomerisation is rate-limiting, and the reason that much harsher conditions are required when performing the quinoline rearrangement under acidic conditions.

2.2.5 Concluding Remarks

DFT calculations were used to explore the basic and acidic mediated pathways for the rearrangement spirocyclic indolenines **2.7** to quinolines **2.8**, to determine the reasons for the large difference in temperature required. Both pathways were calculated to have energetic spans that would enable the reaction to occur at room temperature. It is therefore proposed that the unmodelled keto-enol tautomerisation under acidic conditions is the primary factor in the reactions requiring harsher conditions.

In addition, a substrate scope has been performed with the LHMDS-mediated rearrangement, which was previously used as a control reaction in previous work. The reaction demonstrates tolerance for functional groups and substitution patterns and would likely be useful as a complementary procedure where the spirocyclic indolenine might not tolerate acidic conditions or harsh heating.

The work described within this section is the subject of a publication.¹⁸²

Chapter 3. Selectivity, Speciation, and Substrate Control in the Gold-Catalysed Coupling of Indoles and Alkynes

3.1 Introduction

3.1.1 3-vinylindoles

The indole moiety is a bicyclic, heteroaromatic structure which can be considered to consist of both a benzene and pyrrole ring. Indoles are therefore electron-rich, with their chemistry dominated by C-3 substitution reactions (the C-3 position is labelled in **3.1**, Figure 69).¹⁸³ 3-vinyl substituted indoles have displayed a range of biological activities,^{184,185} such as acting as anticancer agents,^{186,187} or as enzyme inhibitors.^{188,189} Selected examples (**3.1–3.5**) are shown in Figure 69, with the 3-vinylindole moiety highlighted in blue.

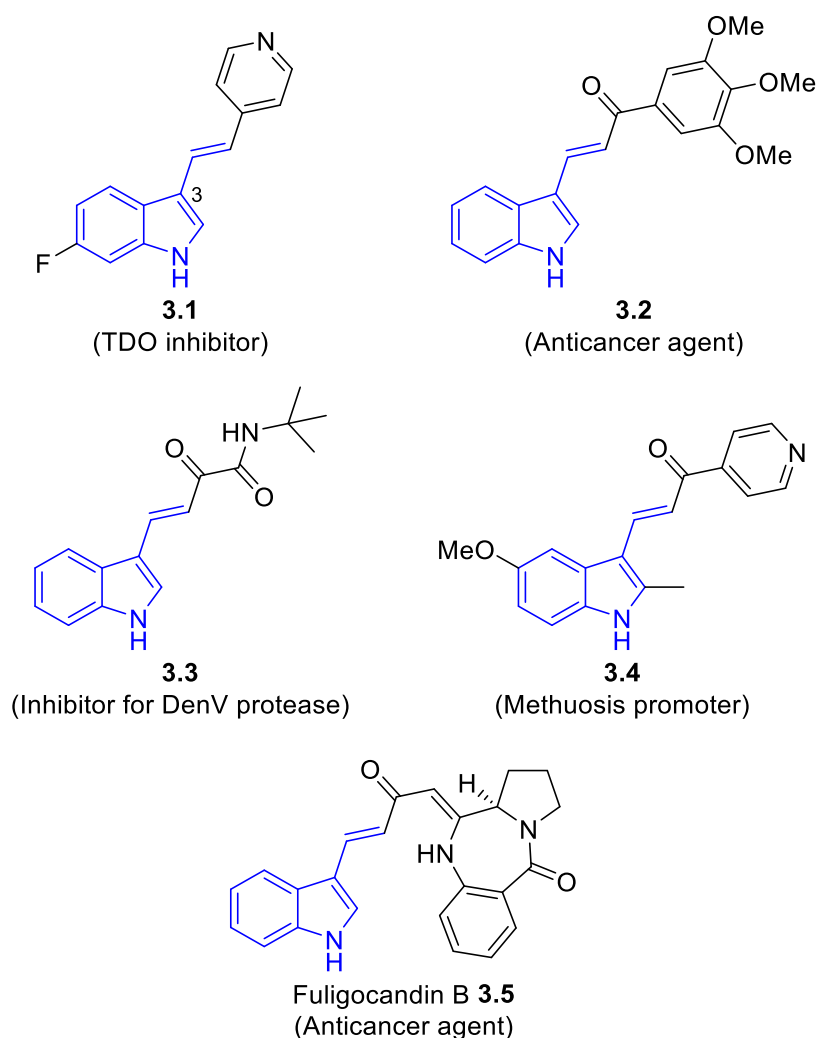


Figure 69. Select examples of 3-vinylindole-containing molecules (**3.1–3.5**) which display biological activity, with the 3-vinylindole moiety highlighted.

3.1.2 Gold-catalysed synthesis of 3-vinylindoles

The gold-catalysed synthesis of 3-vinylindoles from indoles and alkynes is challenging. In 2007, Echavarren and co-workers reported the synthesis of *bisindolemethane* products **3.8** from the gold(I) catalysed reaction between indoles **3.6** and terminal acetylenes **3.7** (Figure 70a).¹⁹⁰ The authors proposed that the formation of the *bisindolemethane* products **3.8** are formed *via* 3-vinylindole intermediates **3.11** (Figure 70b), which are made from the gold(I)-catalysed attack of indoles **3.6** into the $\eta^2(\pi)$ -coordinated alkyne (**3.9** \rightarrow **3.10**), followed by protodemetalation and proton transfer (**3.10** \rightarrow **3.11**). The addition of a second equivalent of indole **3.8** was then suggested to be catalysed by either the gold(I) catalyst, or Brønsted acid (from protons released during the catalysis). Analogous *bisaryl* products have also been isolated using other heteroaromatic compounds including pyrroles and furans.^{190,191} The formation of *bisindole* species was an important consideration throughout the work undertaken in this chapter.

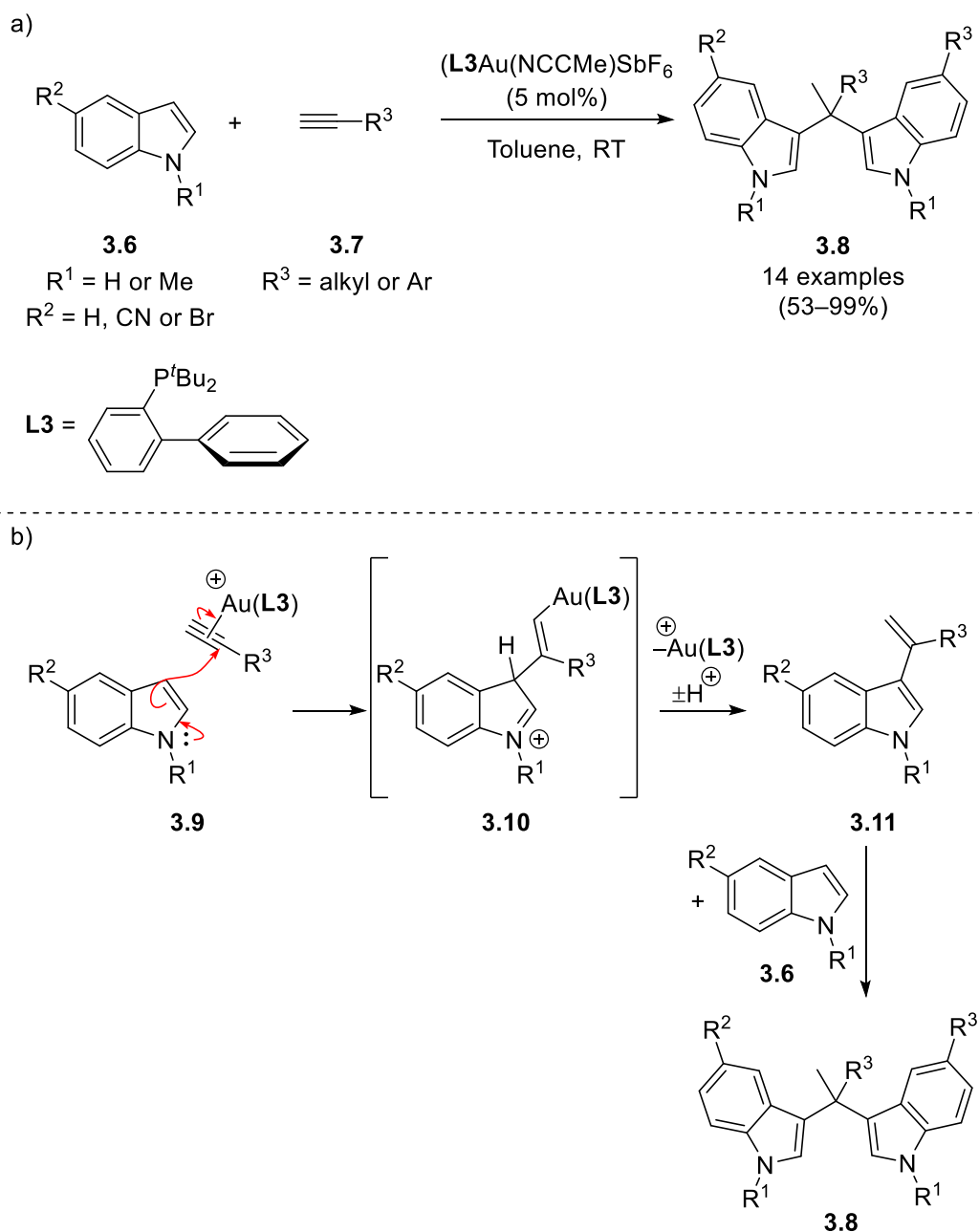


Figure 70. a) Gold(I) catalysed synthesis of *bisindolemethanes* **3.8** from indoles **3.6** and acetylenes **3.7**, as reported by Echavarren and co-workers.¹⁹⁰ b) Proposed mechanism for the formation of *bisindolemethanes* **3.8**, via 3-vinylindole **3.11**, as reported by Echavarren and co-workers.¹⁹⁰

Multiple research groups have attempted to develop methods to successfully isolate the 3-vinylindole intermediate. In 2017, Schießl *et al.* studied the hydroarylation of alkynes using electron-rich heteroaromatics.¹⁹² The authors reported an unusual effect, in which using a large excess of pyrrole **3.12** (5 equivalents) not only resulted in an increased conversion of phenylacetylene **3.13**, but also a higher amount of the monosubstituted product **3.14** (Figure

71a). However, this effect did not extend to indole **3.16**, with higher amounts of bisindolemethane **3.18** still observed in the ^1H NMR spectra (Figure 71b).

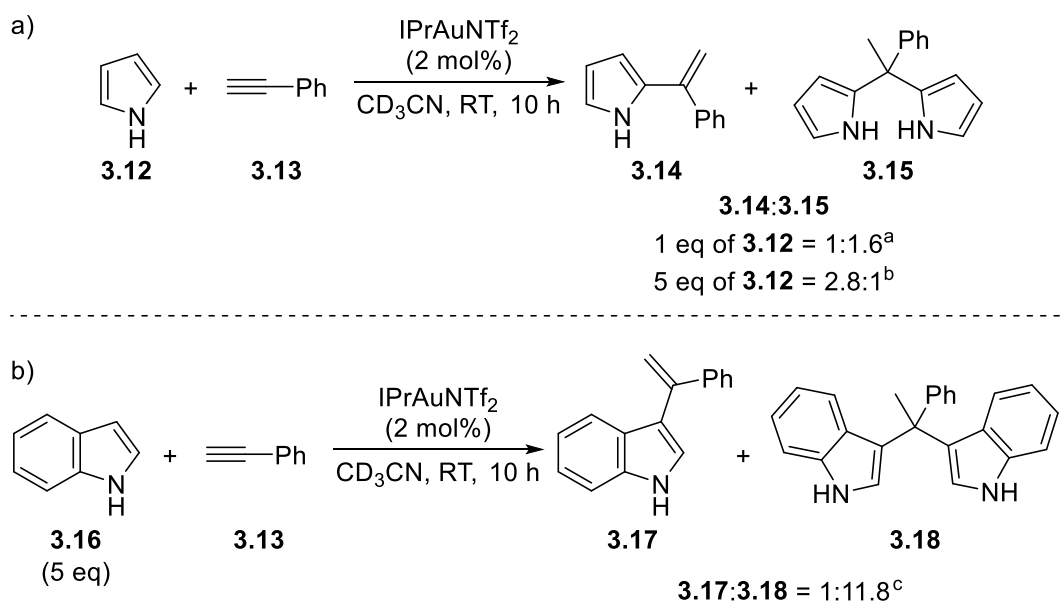


Figure 71. Ratios of mono- and *bis*-addition products as determined by ^1H NMR spectroscopy for a) pyrrole **3.12** and b) indole **3.16** as reported by Schiebl *et al.*¹⁹² ^a 51% conversion of **3.13**. ^b 100% conversion of **3.13**. ^c 70% conversion of **3.13**.

In 2020, McLean *et al.* reported the gold(I) catalysed synthesis of mono-substituted 3-vinylindole species **3.20** using an excess of phenylacetylene **3.13** (Figure 72a).¹⁹³ This method was limited to indoles substituted in either the C-2 or C-4 positions (**3.19**) and unsubstituted indole **3.16** still yielded the di-substituted product **3.18** (Figure 72b).

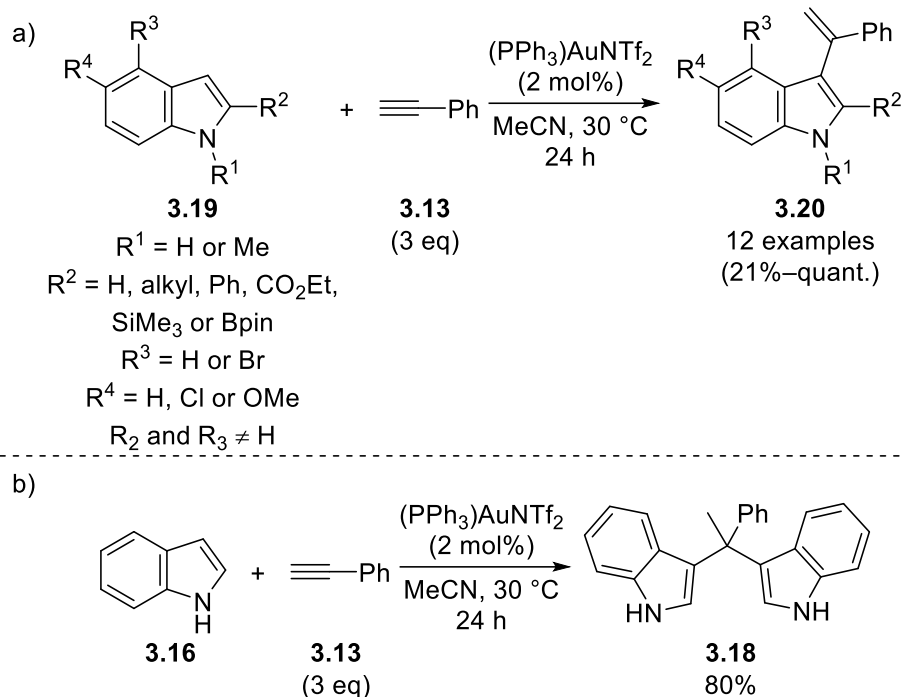


Figure 72. Gold(I) catalysed hydroarylation of a) C-2 or C-4 substituted indoles **3.19** and b) indole **3.16** as reported by McLean *et al.*¹⁹³

The authors were able to overcome this limitation using C-2 Bpin-substituted indole **3.21** with subsequent protodeborylation (Figure 73), however the direct formation of 3-vinylindoles (*e.g.* **3.17**) from unsubstituted indoles remained a challenge.

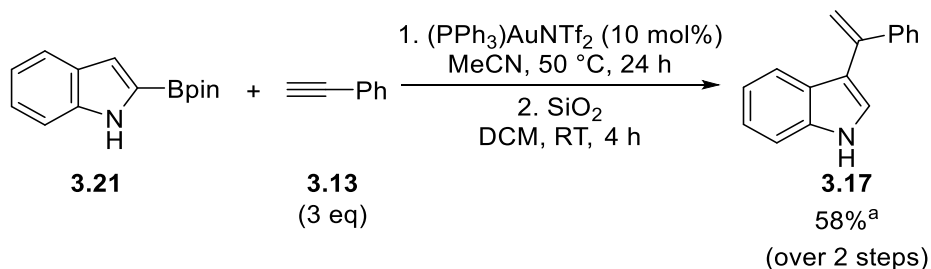


Figure 73. Formation of 3-vinylindole **3.17** from C-2 Bpin-substituted indole **3.21** and phenylacetylene **3.13** in 2 steps using gold(I) catalysis with subsequent deborylation, as reported by McLean *et al.*^{193 a} Reported as unstable to silica during column chromatography.

3.1.3 Mechanism of bisaryl formation

The mechanism for the formation of the *bisaryl* compounds (such as the *bisindolemethanes*) has been explored both computationally and experimentally. Mehrabi *et al.* used DFT to investigate the gold(I) catalysed formation of *bispyrrole* **3.15** with acetic acid as the solvent (Figure 74),¹⁹¹ a method which has also been used for the synthesis of *bisindolemethane* **3.18**.

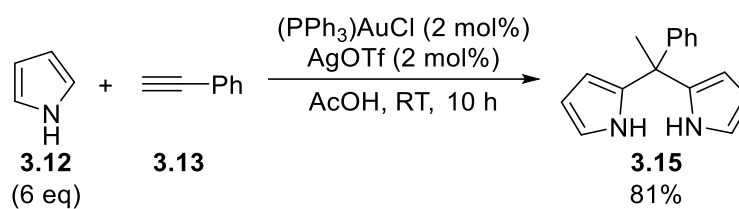


Figure 74. Gold(I) catalysed formation of *bispyrrole* **3.15**, as reported by Luo *et al.*¹⁹¹

Using propyne as a model acetylene, Mehrabi *et al.* reported the DFT-calculated energies for the gold(I) catalysed formation of 2-vinylpyrrole **3.22**, however more insightful were their studies into the generation of *bispyrrole* (**3.23**, Figure 75). First, the pathway was calculated for the gold-catalysed addition, starting from $\eta^2(\pi)$ -coordinated alkene **3.A**. The transition state for pyrrole **3.12** addition (**3.TS_{AB}**) was calculated at an energy of +29.1 kcal mol⁻¹ (at the D3-M06/def2-TZVP// M06/LANL2DZ-6-31G(d) level of theory), to give complex **3.B** at a high energy of +26.7 kcal mol⁻¹. Transition states for later deprotonation (**3.TS_{BC}**) and protiodemetallation (**3.TS_{CA}**) steps, mediated by acetic acid, were found to be inaccessible at energies of +45.5 and +51.6 kcal mol⁻¹ respectively.

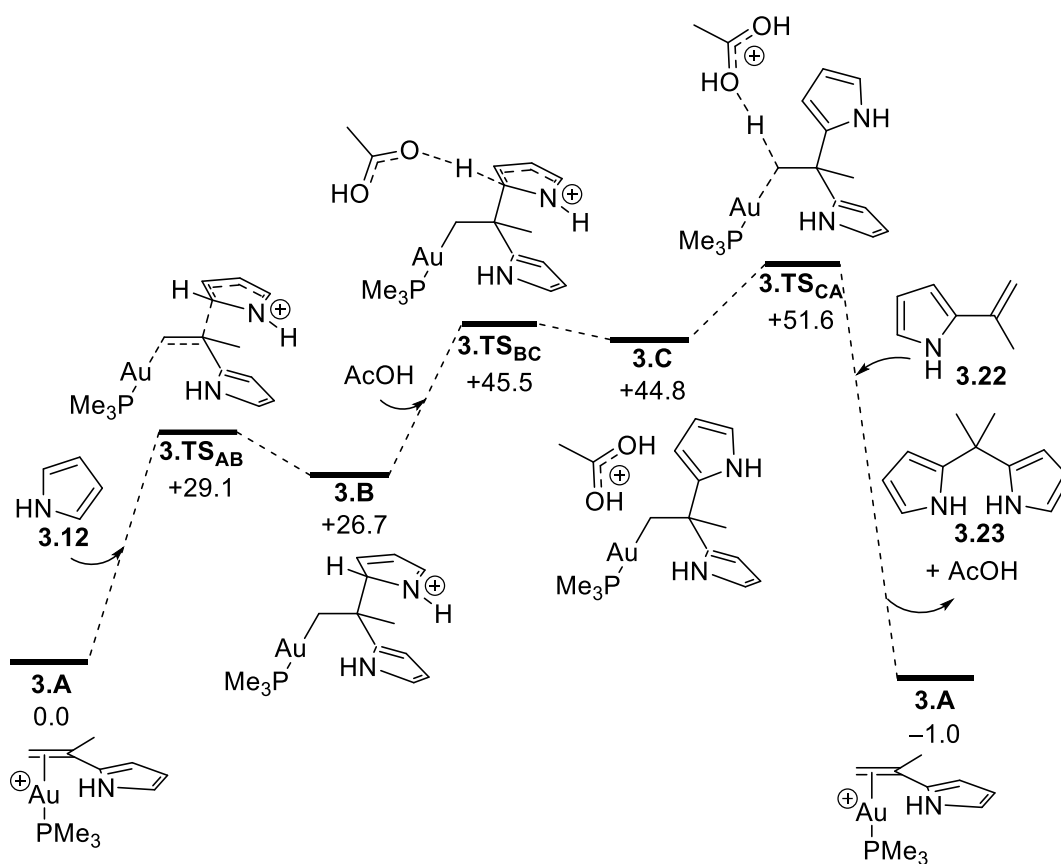


Figure 75. DFT-calculated energies for the gold(I) catalysed addition of pyrrole **3.12** to 2-vinylpyrrole **3.22**. Energies are Gibbs energies in kcal mol⁻¹ at the D3-M06/def2-TZVP// M06/LANL2DZ-6-31G(d) level of theory with CPCM solvent correction in AcOH. Reported by Mehrabi *et al.*¹⁹⁴

The energies were then calculated for the addition of pyrrole **3.12** to 2-vinylpyrrole **3.22**, promoted by Brønsted acid formed from the interaction of the gold(I) catalyst with the acetic acid solvent (Figure 76). The energetic span was calculated at +24.6 kcal mol⁻¹ with **3.TS_{EF}** as the highest energy state, which corresponded to pyrrole **3.12** addition to carbocation **3.F**. The data therefore suggests that the acid-promoted pathway is more likely to be in operation.

Whilst the computational study performed by Mehrabi *et al.* specifically focussed on the effects of acetic acid,¹⁹⁴ the formation of the *bisaryl* products has been efficient when no apparent acid was added (Figure 71),^{190,192,193} likely due to trace amounts of acid formed *in situ* during the reaction.¹⁹⁵

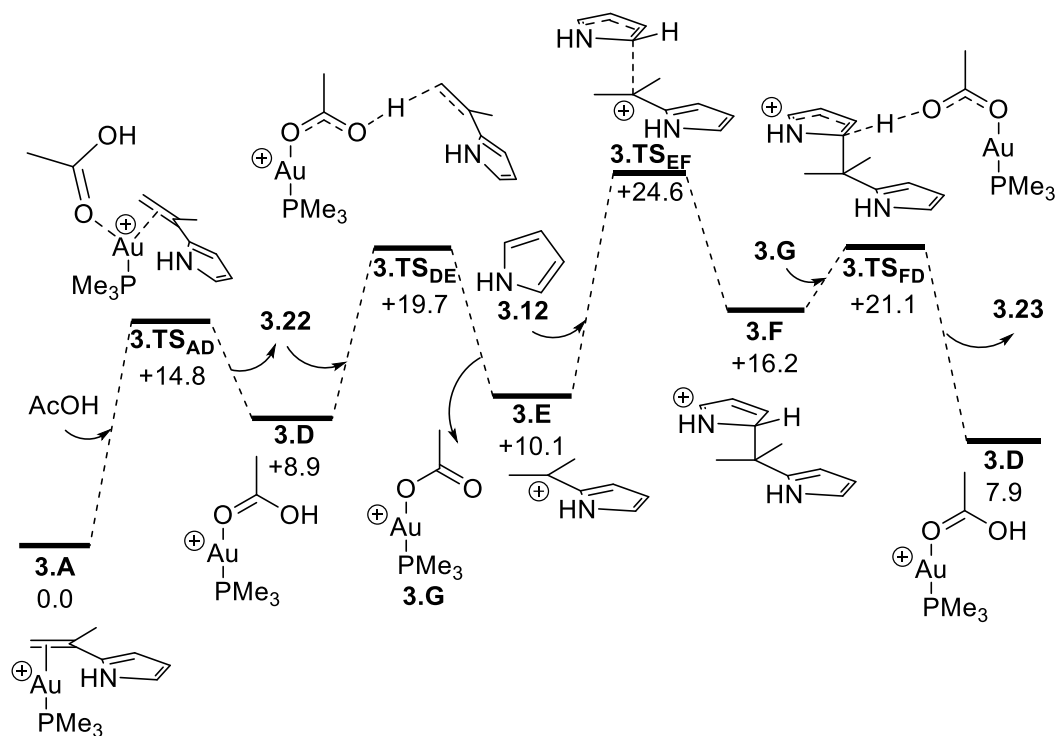


Figure 76. DFT-calculated energies for the acid catalysed addition of pyrrole **3.12** to 2-vinylpyrrole **3.22**. Energies are Gibbs energies in kcal mol⁻¹ at the D3-M06/def2-TZVP// M06/LANL2DZ-6-31G(d) level of theory with CPCM solvent correction in AcOH. Reported by Mehrabi *et al.*¹⁹⁴

A similar conclusion was found experimentally by Schießl *et al.*¹⁹² Control experiments performed by the treatment of isolated 2-vinylpyrrole **3.14** both with a gold(I) catalyst (Figure 77a) and bistriflimidic acid (Figure 77b) demonstrated that only the Brønsted acid-catalysed reaction formed the *bispyrrole* product (**3.15**).

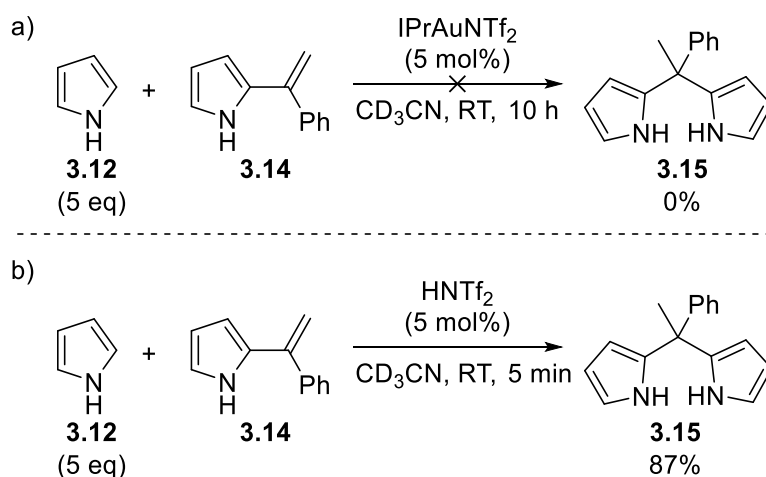


Figure 77. Control experiments performed by Schießl *et al.* for the addition of pyrrole **3.12** to 2-vinylpyrrole **3.14** using a) gold(I) catalysis and b) acid catalysis.¹⁹²

These studies have demonstrated that whilst the formation of the vinylaryl species (*e.g.* **3.17**) is likely gold(I) catalysed, Brønsted acid is required to promote the second addition.

3.1.4 Intramolecular indole-ynone coupling

The Taylor and Unsworth groups previously reported the divergent reactions of indolyl-tethered ynones **2.6**, using silver(I) and gold(I) catalysis to afford spirocyclic indolenines **2.7** and carbazoles **2.9** respectively (Figure 78).^{173,196} These divergent reactions allow for the rapid synthesis of a series of structurally diverse scaffolds from a single precursor, which could aid in exploring different chemical space for drug discovery.^{197,198} Interest in spirocyclic compounds (*e.g.* **2.7**) in particular has increased, due to the three-dimensional nature exhibited by the compounds.¹⁹⁹

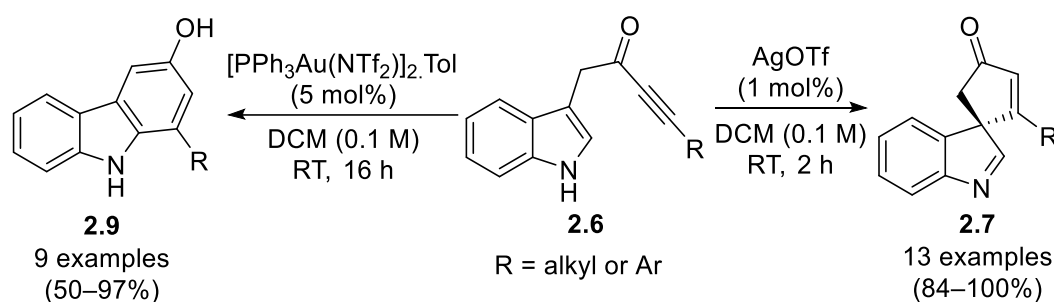


Figure 78. Divergent synthesis of spirocyclic indolenines **2.7** and carbazoles **2.9** from indolyl-tethered ynones **2.6**, as reported by Liddon *et al.*¹⁷³

Further studies to expand the scope of the cyclisation reactions were conducted using indolyl-tethered propargyl alcohols **3.24** (Figure 79).²⁰⁰ In contrast to the indolyl-tethered ynone (**2.6**) examples, the use of silver triflate (AgOTf) was found to afford carbazole products **3.25**, instead of spirocyclic indolenines **3.26**. It was suggested that this method proceed *via* an intermediate spirocycle, but trace Brønsted acid then promoted 1,2-alkenyl migration of the spirocyclic intermediates to form carbazoles.¹⁹⁵

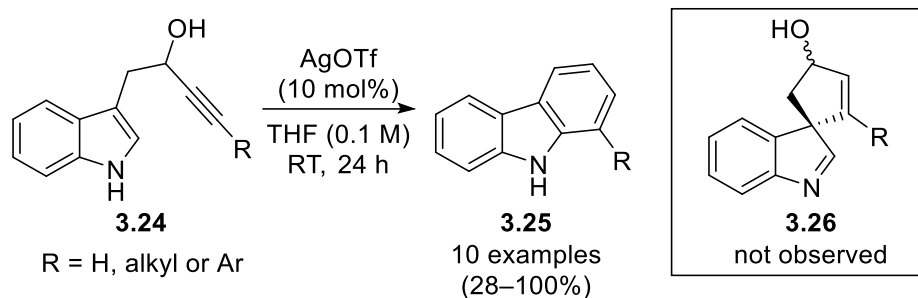


Figure 79. Synthesis of carbazoles **3.25** from indolyl-tethered propargyl alcohols **3.24** using silver(I) catalysis, as reported by James *et al.*²⁰⁰

A mechanistic study was performed using DFT calculations to investigate the reasons for the divergent cyclisation reactions of the indolyl-tethered ynones (**2.6**, Figure 80).²⁰¹ It was found that spirocyclisation through C-3 attack would be the kinetically favoured pathway for both silver and gold catalysis (*via* **3.TS_{JK}**), with C-2 attack (*via* **3.TS_{JL}**) calculated to be higher in energy. It was therefore proposed that carbazole **2.9** formation is the thermodynamic product, and that spirocyclisation is reversible. The protodemetalation rate of the metal catalyst in vinyl complex **3.K**, was proposed to be a major factor in the selectivity difference, with protonation of the gold–carbon bond occurring slower than the equivalent silver–carbon bond. No transition state was found for the 1,2-alkenyl migration of **3.K** (which would give carbazole **2.9**).

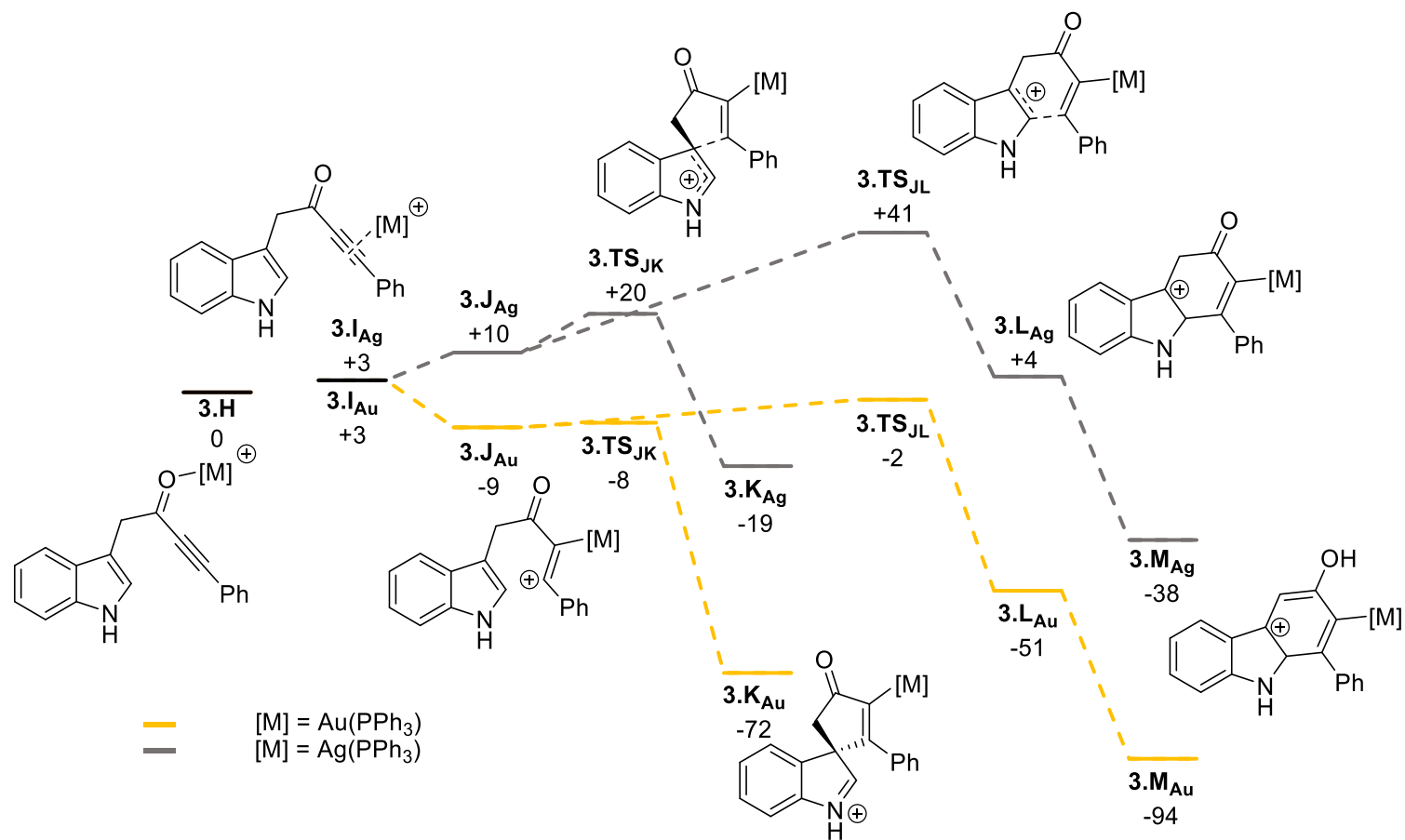


Figure 80. DFT-calculated pathway for the silver(I) and gold(I) catalysed cyclisations of indolyl-tethered ynones **2.9**, as reported by Lidden *et al.*²⁰¹ Energies are Gibbs energies at 298.15 K in kJ mol⁻¹ at the D3-PBE0/def2-TZVPP//BP86/SV(P) level of theory with COSMO solvent correction in CH₂Cl₂.

The energies of the transition states for the C–C bond forming steps were calculated to be very low, with $\eta^1(\text{O})$ coordinated complex **3.H** as the reference state for these calculated energies (for both silver and gold catalysis). C-3 attack, *via* **3.TS_{JK}**, was calculated at +20 kJ mol⁻¹ for silver catalysis, and –8 kJ mol⁻¹ with gold catalysis. Transition states were also found for C-2 attack, *via* **3.TS_{IL}**, calculated to be slightly higher in energy at +41 kJ mol⁻¹ and –2 kJ mol⁻¹ for silver and gold catalysis respectively. Due to the ease at which the intramolecular C–C bond formation occurs; it was envisioned that an intermolecular coupling between indole **3.16** and ynone **3.27** could be developed following a similar mechanistic pathway (Figure 81), to afford the challenging 3-vinylindole scaffold (**3.28**, highlighted in blue). The work in this chapter describes the realisation of this strategy.

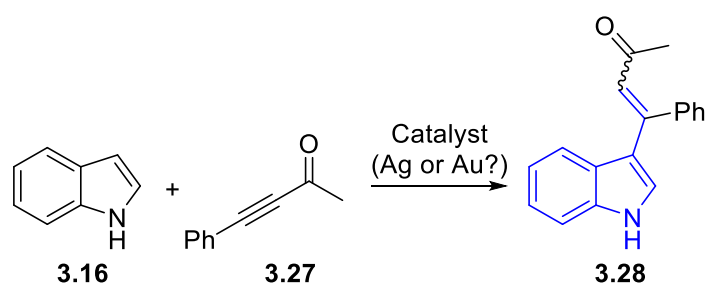


Figure 81. Proposed formation of 3-vinylindole **3.28** using a transition metal catalysed indole-ynone coupling reaction.

3.1.5 Project aims

The previously discussed intramolecular cyclisation reactions of indolyl-tethered ynones **2.6** (Figure 78) demonstrated that the electron-withdrawing group on the alkyne aided its spirocyclisation under mild conditions, corroborated by DFT calculations (Figure 80).^{173,201} Furthermore, a comparison of the silver triflate-catalysed reactions of the indolyl-tethered ynones (**2.6**) and propargyl alcohols (**3.24**) suggests that the ynones (**2.6**) are less prone to undergo 1,2-migration, and so are more resistant to the effects of trace Brønsted acid (Figure 82).^{173,200}

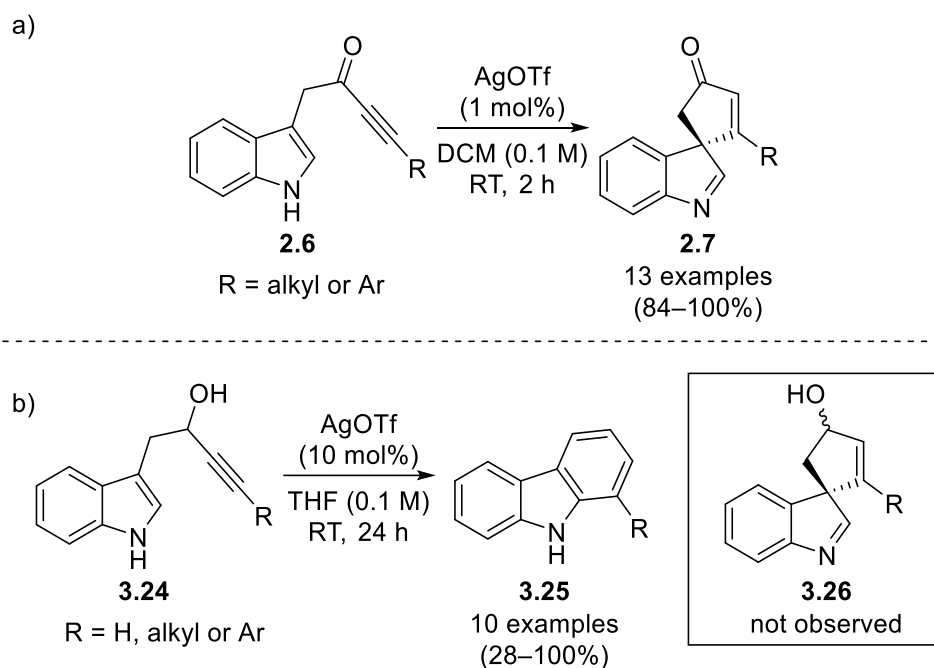


Figure 82. Comparison of the silver triflate catalysed cyclisation of a) indolyl-tethered ynones **2.6** and b) indolyl-tethered propargyl alcohols **3.24**.^{173,200}

It was therefore proposed that the use of an ynone partner (*e.g.* **3.27**) in the transition metal catalysed coupling reaction of indole **3.16** could hinder *bis*indole (**3.29**) formation and enable the selective formation of vinyl indoles **3.28**. The work presented in this chapter is focused on the development of the intermolecular coupling reaction (Figure 83), with further exploration of the reaction outcome using computational chemistry.

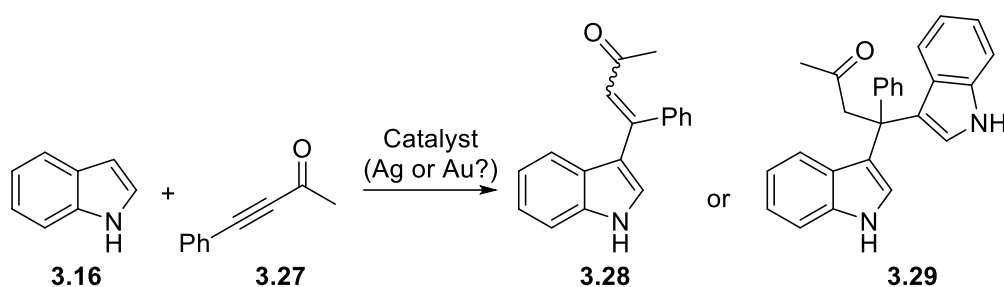


Figure 83. Proposed formation of 3-vinylindole **3.28** using a transition metal catalysed indole-ynone coupling reaction.

Throughout this section, numbers are used to indicate compounds (*e.g.* **3.1**), whereas DFT calculated states are denoted by letters (*e.g.* **3.A**), with transition states labelled specifically as 'TS' (*e.g.* **3.TS_{cd}**, which refers to the transition state connecting state **3.C** and **3.D**).

3.2 Coupling Reaction Development

3.2.1 Starting material synthesis

Throughout the project, a number of substituted alkynes and *N*-alkylated indoles were required to be synthesised for use as potential substrates. This section discusses the synthesis of these molecules and is organised firstly by alkyne synthesis and then *N*-alkylated indole synthesis.

Alkyne synthesis

The formation of ketone-substituted alkynes **3.33** and **3.34** was performed using the method reported by Schubert *et al.* (Figure 84).²⁰² Here, *n*-BuLi was used to deprotonate the terminal acetylene (**3.30** and **3.31**), before freshly distilled *N*-methoxy, *N*-methylacetamide **3.32** was added. The resultant ynones **3.33** and **3.34** were isolated in high yields.

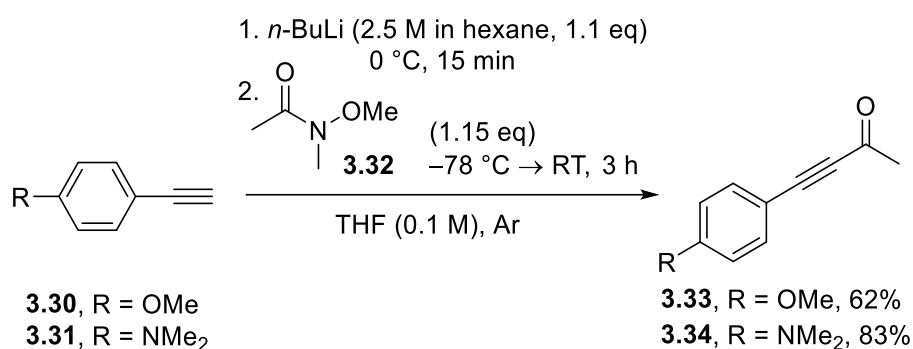


Figure 84. Synthesis of ynones **3.33** and **3.34**, using the method reported by Schubert *et al.*²⁰²

The authors also reported the synthesis of 4-Br-substituted ynone **3.37** (Figure 85) using a Friedel–Crafts acylation between TMS-protected alkyne **3.35** and acetyl chloride **3.36**, to avoid problems arising from lithium-halogen exchange of the acetylene.²⁰² The authors reported procedure was followed to yield the desired product **3.37** in an 86% yield, the same as reported by Schubert *et al.*

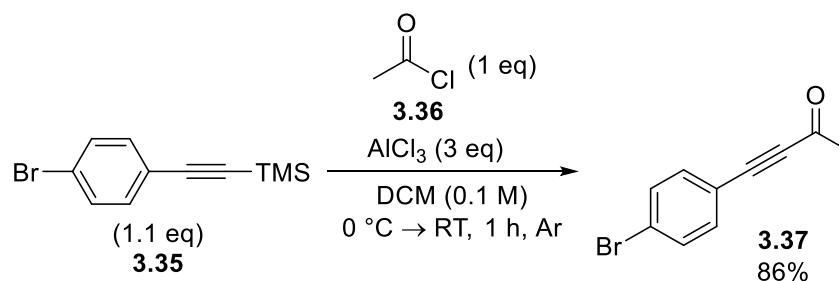


Figure 85. Friedel–Crafts acylation for the synthesis of 4-Br ynone **3.37**, as reported by Schubert *et al.*²⁰²

Lithium acetylide formation and nucleophilic substitution was also used for the synthesis of the amide-substituted alkynes (**3.39–3.41**, Figure 86a),²⁰³ and ester-substituted alkynes (**3.43** and **3.44**, Figure 86b),²⁰⁴ which used dimethylcarbamoyl chloride **3.38** and methyl chloroformate **3.42** respectively as the electrophiles.

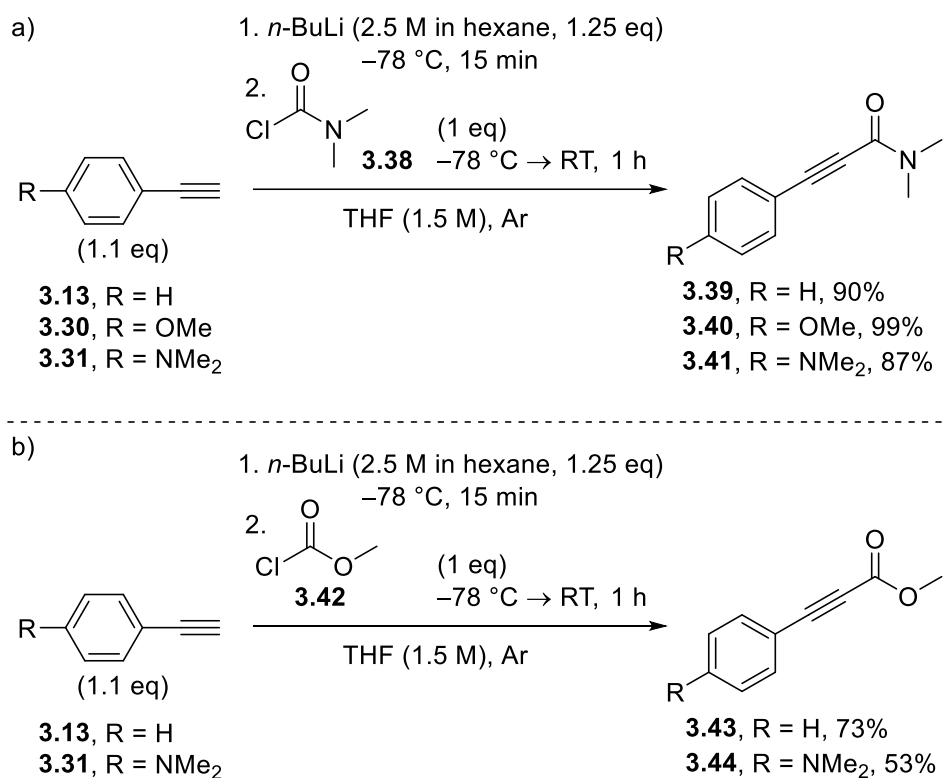


Figure 86. a) Synthesis of amide substituted alkynes **3.39–3.41**, using the method reported by Dong and co-workers.²⁰³ b) Synthesis of ester substituted alkynes **3.43** and **3.44**, using the method reported by Vilotijevic and co-workers.²⁰⁴

Finally, *bisaryl* internal alkyne **3.47** was synthesised in a high overall yield over two steps. The selective *para*-iodination of *N,N*-dimethylaniline **3.45** was achieved using a gold(I) catalyst and *N*-iodosuccinimide (NIS), following a method reported by Frontier and co-workers.²⁰⁵ The product (**3.46**) was then coupled to phenylacetylene **3.13**, using Sonogashira cross-coupling conditions previously reported by Tasseroul *et al.*²⁰⁶

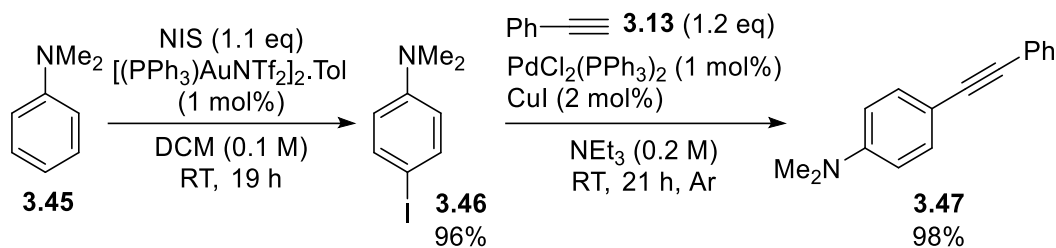


Figure 87. The two step synthesis of alkyne **3.47**, using methods reported in the literature.^{205,206}

***N*-alkylated indole synthesis**

The *N*-alkylation of C-3 substituted indoles was achieved following literature procedures,^{207–209} using sodium hydride and an alkyl halide (Figure 88). The formation of *N*-Me alkylated indole products **3.49** and **3.51** were successful, with good yields achieved. However, *N*-benzyl-substituted indole **3.52** was isolated in an unexpectedly low yield. The purification of **3.52** was problematic, with an unidentified impurity also formed, which co-eluted under all column conditions tried. A small amount of product was able to be cleanly isolated through recrystallisation for further use. It is likely that the yield of **3.52** could be improved, possibly by distilling the benzyl bromide prior to use, or changing the solvent from DMF to THF.

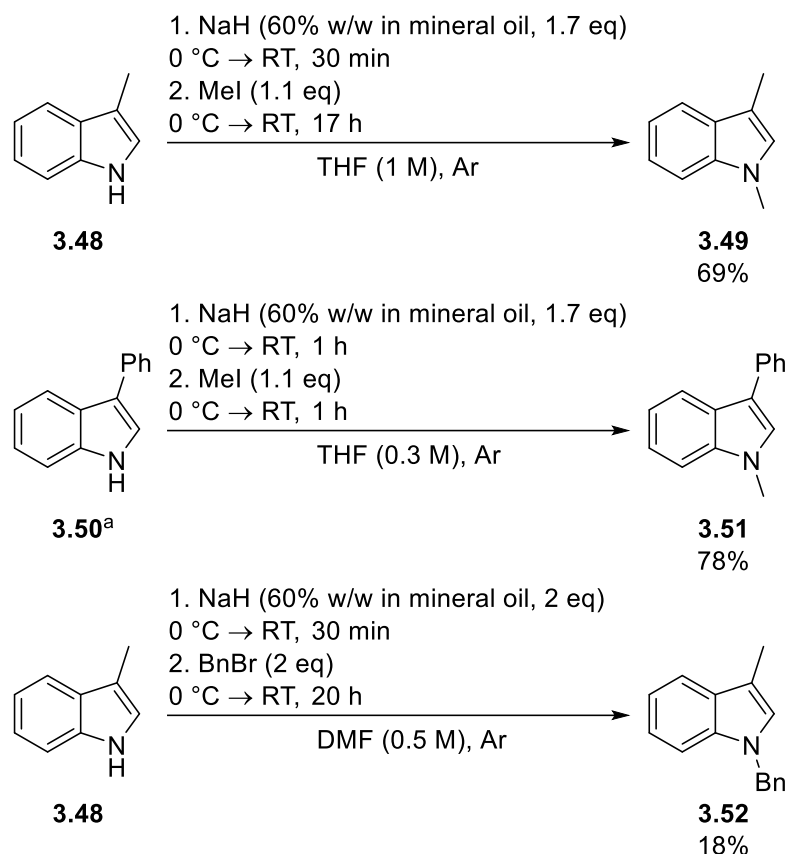


Figure 88. Synthesis of *N*-alkylated indoles (**3.49**, **3.51** and **3.52**) using methods reported in literature.^{207–209} ^a Indole **3.50** was made by Dr James Donald in prior work.²¹⁰

3.2.2 Reaction Optimisation

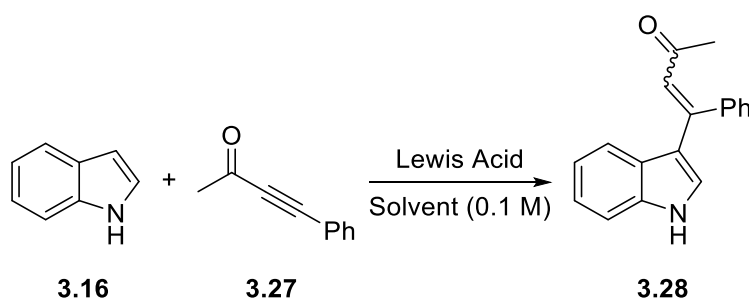
Indole **3.16** and phenyl-substituted ynone **3.27** were used as test substrates in an attempt to prepare vinylindoles through a metal-catalysed coupling reaction (Table 8). After the desired reaction time, the solvent was removed and a crude ¹H NMR spectrum was recorded. It was considered that the appearance of singlet resonances in the 6–7 ppm region of the ¹H spectra corresponding to the alkene proton in **3.28** could be used to determine if the reaction was successful.^{211,212}

Silver triflate (AgOTf), copper triflate (Cu(OTf)₂), tin(II) chloride (SnCl₂·2H₂O) and gold triflimide ([Au(NTf₂)(PPh₃)₂]₂·Tol) were chosen as potential Lewis acids due to their success in catalysing the analogous intramolecular cyclisation reactions (Figure 78).^{173,175} The silver, copper and tin salts (Entries 1–6, Table 8) were unsuccessful at catalysing any reaction, even at elevated temperatures, with only unreacted indole **3.16** and ynone **3.27** present in the ¹H NMR spectra of the crude reaction mixtures. However, new products were observed when using gold

triflimide, with 90% conversion to the product **3.28** observed at room temperature after 24 hours (Entry 7, Table 8). Compound **3.28** was identified by ^1H and ^{13}C NMR spectroscopy as well as mass spectrometry.

The effects of using different solvents were tested (Entries 8–11, Table 8), and both toluene and dichloromethane performed similarly, therefore toluene was chosen as the solvent of choice for further optimisation due to a higher range of temperatures tolerated if required. When the temperature was increased (Entries 12–14, Table 8), the overall conversion of **3.16** didn't change significantly, with 82–91% conversions still achieved, however, the time taken to achieve this was reduced, with no further reaction seen after two hours at 40 °C. Finally, in order to achieve full consumption of indole **3.16**, the number of equivalents of ynone **3.27** was increased (Entries 15–16, Table 8), which resulted in full conversion when a slight excess of ynone **3.27** was used (Entry 16, Table 8).

Table 8. Optimisation of the metal-catalysed intermolecular reaction of indole **3.16** with ynone **3.27**.



Entry	Catalyst	Solvent	Temp / °C	Time / h	3.27 Equiv.	Conversion ^[a] (E/Z) / %
1	AgOTf ^[b]	Toluene	RT	24	1	0
2	AgOTf ^[b]	Toluene	40	24	1	0
3	Cu(OTf) ₂ ^[b]	Toluene	RT	24	1	0
4	Cu(OTf) ₂ ^[b]	Toluene	40	24	1	0
5	SnCl ₂ ·2H ₂ O ^[b]	Toluene	RT	24	1	0
6	SnCl ₂ ·2H ₂ O ^[b]	Toluene	40	24	1	0
7	[Au(NTf ₂)(PPh ₃) ₂] ₂ ·Tol ^[c]	Toluene	RT	24	1	90 (73:27)
8	[Au(NTf ₂)(PPh ₃) ₂] ₂ ·Tol ^[c]	Toluene	RT	4	1	55 (72:28)
9	[Au(NTf ₂)(PPh ₃) ₂] ₂ ·Tol ^[c]	DCM	RT	4	1	57 (73:27)
10	[Au(NTf ₂)(PPh ₃) ₂] ₂ ·Tol ^[c]	MeCN	RT	4	1	45 (72:28)
11	[Au(NTf ₂)(PPh ₃) ₂] ₂ ·Tol ^[c]	EtOH	RT	4	1	17 (73:27)
12	[Au(NTf ₂)(PPh ₃) ₂] ₂ ·Tol ^[c]	Toluene	40	4	1	82 (73:27)
13	[Au(NTf ₂)(PPh ₃) ₂] ₂ ·Tol ^[c]	Toluene	40	24	1	88 (72:28)
14	[Au(NTf ₂)(PPh ₃) ₂] ₂ ·Tol ^[c]	Toluene	40	2	1	91 (73:27)
15	[Au(NTf ₂)(PPh ₃) ₂] ₂ ·Tol ^[c]	Toluene	40	2	1.2	94 (72:28)
16	[Au(NTf₂)(PPh₃)₂]₂·Tol ^[c]	Toluene	40	2	1.5	100 (71:29)
17	[Au(NTf ₂)(PPh ₃) ₂] ₂ ·Tol ^[c]	Toluene	40	2	2	100 (71:29)

^[a] Conversion determined by ratio of remaining indole **3.16** to both isomers of **3.28** by ¹H NMR spectroscopy. ^[b] 10 mol%. ^[c] 5 mol%.

Using the optimised conditions (Entry 16, Table 8), a 69% isolated yield of **3.28** was achieved, as a mixture of *E*- and *Z*-stereoisomers (Figure 89). The major isomer was assigned as the *E*-isomer (for further discussion on the assignment of stereochemistry see Section 3.2.3, Figure 94), and previous studies on a related compound demonstrated that alkene isomerisation occurred in solution to give the thermodynamic product distribution, likely aided by conjugation of the

electron-rich indole through to the carbonyl.²¹³ Notably, no *bis*indole **3.29** products were observed in the crude ¹H NMR spectra, or isolated during chromatography.

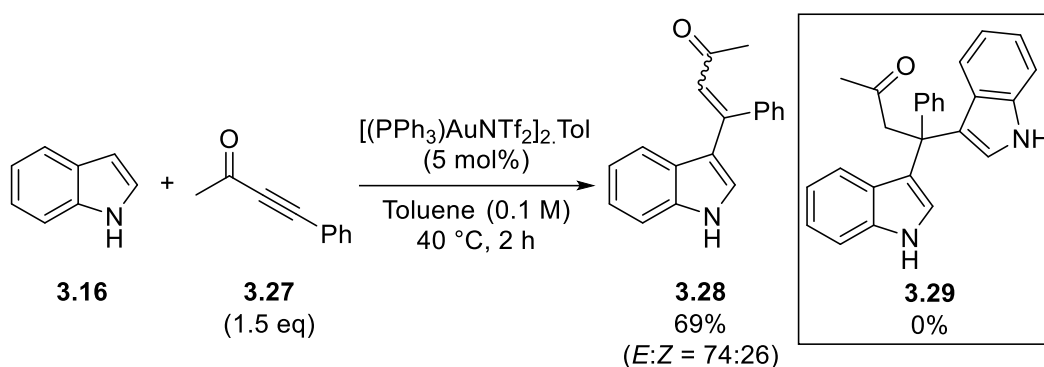


Figure 89. Successful formation of vinyl indole **3.28**, from the gold(I)-catalysed coupling of indole **3.16** and ynone **3.27**.

A plausible mechanism was proposed in which the gold(I) catalyst coordinates to the alkyne of ynone **3.27**, to give either $\eta^2(\pi)$ -coordinate alkyne **3.53** or slipped gold(I)-vinyl cation **3.53'** (Figure 90). Nucleophilic attack from the C-3 position of indole then occurs, likely on the face opposite the bulky gold catalyst, to give intermediate **3.55** (**3.54** \rightarrow **3.55**). Protodemetalation and isomerisation then occurs (**3.55** \rightarrow **3.28**) to yield the desired product **3.28**.

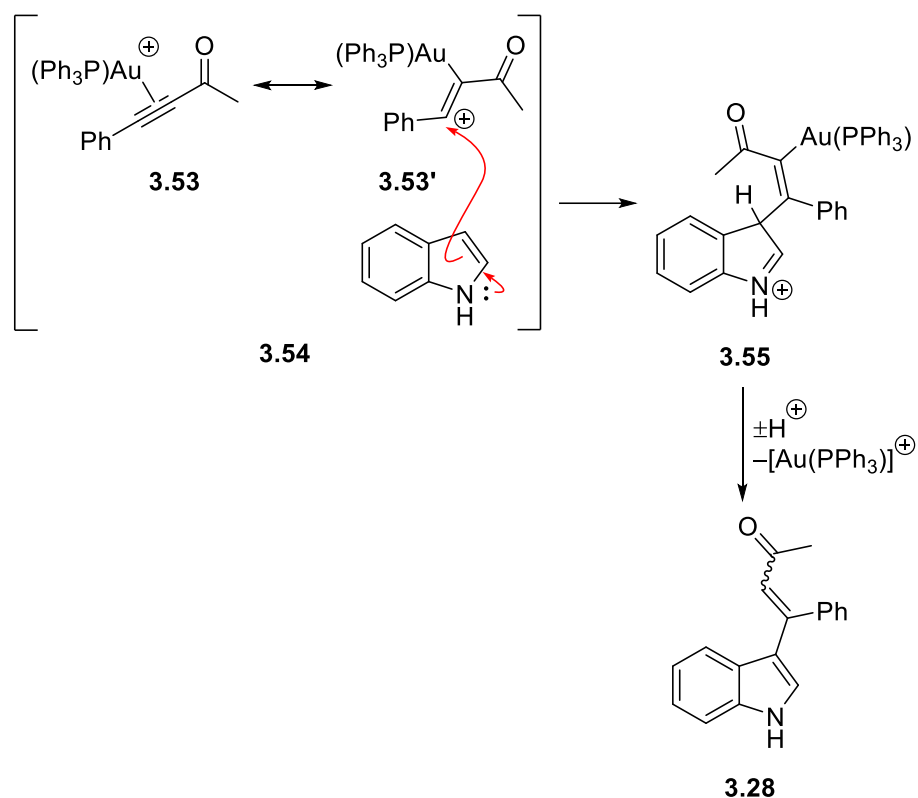


Figure 90. Proposed mechanism for the gold(I)-catalysed coupling of indole **3.16** and ynone **3.27**.

3.2.3 C-3 Vinylation substrate scope

With the conditions optimised for the coupling of indole **3.16** and phenyl-substituted ynone **3.27**, the scope of the reaction was tested. The identity of the indole partner (**3.56**) was changed first (Figure 91).

Overall, the indole-ynone coupling reaction tolerated a variety of substituents located in different positions on the indole moiety, however the reaction time did have to be varied, with TLC analysis used to determine the consumption of the indole partner. Substituents in the C-2 and C-4 position of indole had a significant effect on the *E/Z* stereochemistry ratio of the products (*e.g.* **3.63**–**3.66**), likely due to steric clashes of the substituent with the aromatic group of the ynone.

Electron-withdrawing groups, such as halogens (*e.g.* **3.58** and **3.59**) or nitro groups (*e.g.* **3.62** and **3.64**) slowed the reaction progress, which was proposed to be due to the reduced nucleophilicity of the indole. Starting material was remaining after 24 hours at 40 °C with the nitro-containing indoles (*e.g.* **3.62** and **3.64**), the reactions were repeated heated to 100 °C, and

higher yields of the products **3.62** and **3.64** were achieved, albeit only a minor increase from 39% to 46% for **3.64**.

Strongly electron-donating groups (*e.g.* **3.60** and **3.61**) on the indole hindered the coupling reaction. Low yields were achieved despite full consumption of the indole starting material by TLC analysis. Attempts were made to find any side-products, however no other compounds were able to be isolated during purification. The formation of product **3.61** was attempted at room temperature; however, similar yields of 31% and 30% for **3.60** and **3.61** respectively were achieved.

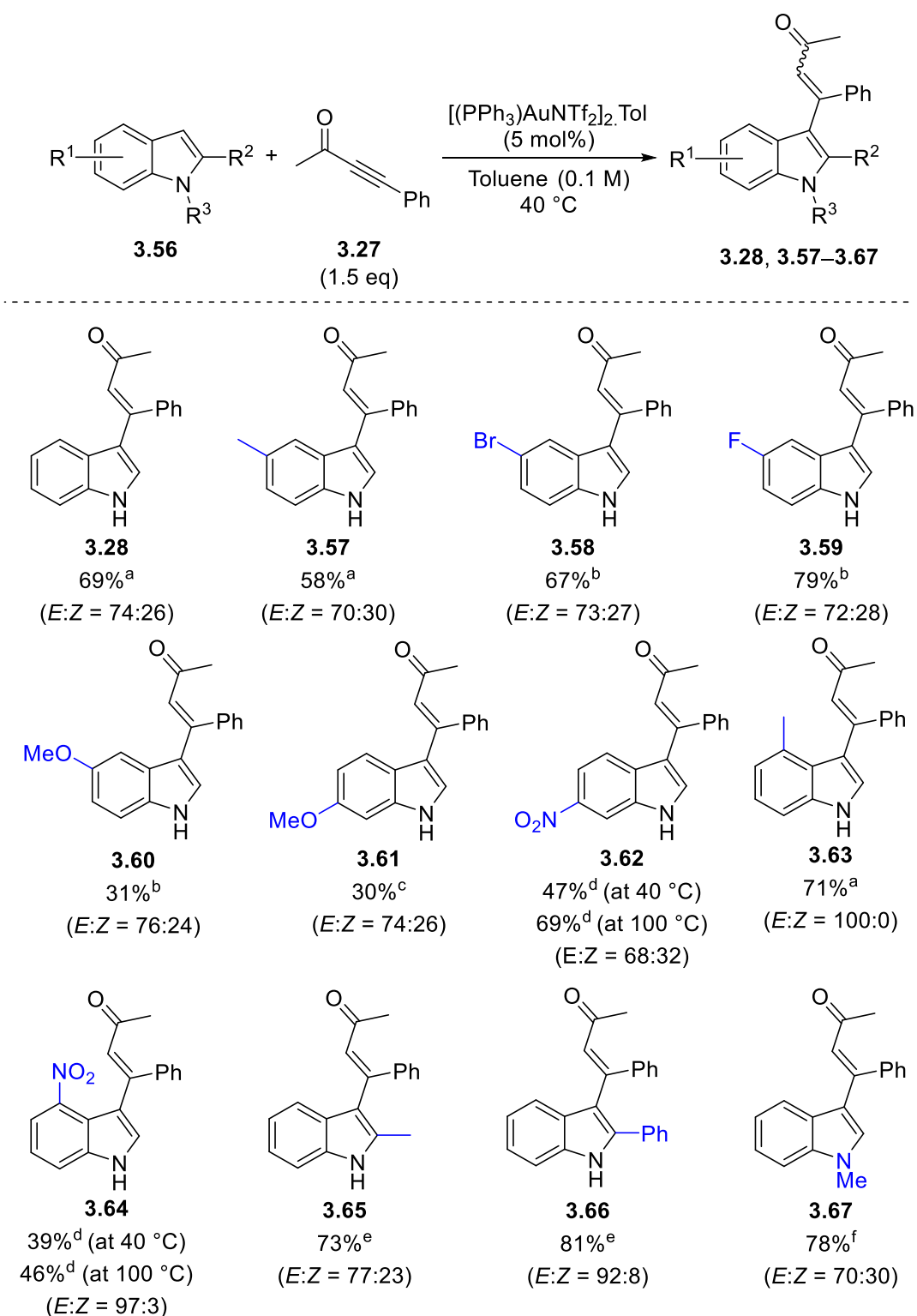


Figure 91. Indole variation scope of the gold(I)-catalysed coupling with phenyl-substituted ynone **3.27**. ^a 2 hour reaction time. ^b 18 hour reaction time. ^c 21 hour reaction time at room temperature. ^d 24 hour reaction time. ^e 19 hour reaction time. ^f 3 hour reaction time.

Next, the identity of the alkyne coupling partner was altered (Figure 92). Variation of the ynone ketone substituent (*e.g.* phenyl ketone instead of methyl ketone, **3.69**) and both electron-

withdrawing (**3.71**) and donating (**3.72** and **3.73**) groups on the aromatic group were tolerated in the coupling reaction. Other carbonyl functional groups were also able to be used, with alkynes bearing ester (**3.74** and **3.75**) and amide (**3.76** and **3.77**) functional groups also successful. An aromatic substituent on the alkyne was necessary, with the coupling reaction unsuccessful when oct-3-yn-2-one was used (**3.70**).

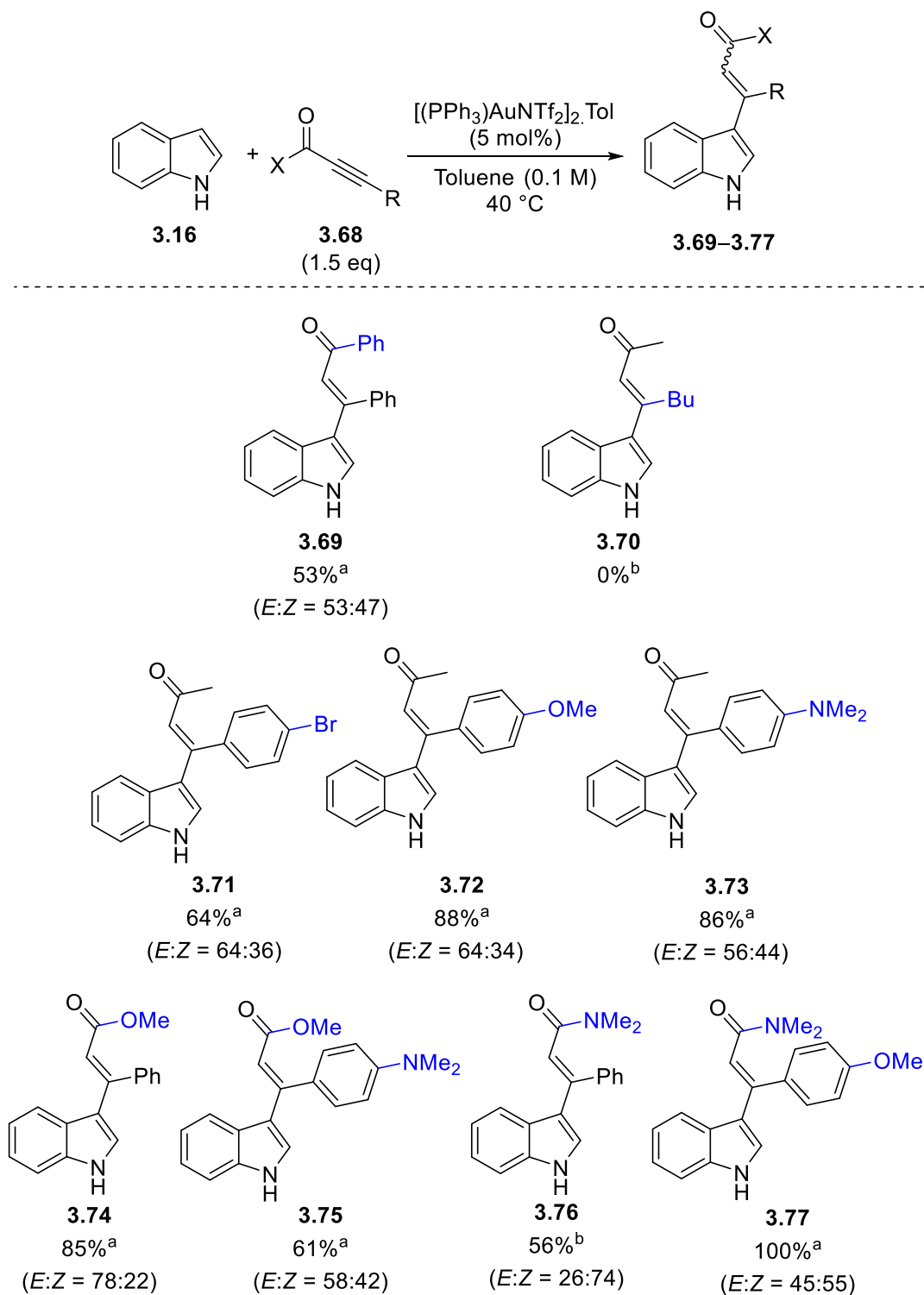


Figure 92. Alkyne variation scope of the gold(I)-catalysed coupling with indole **3.16**. ^a 2 hour reaction time. ^b 24 hour reaction time.

A 2D-NOESY experiment was used to assign the *E*- and *Z*-stereoisomers observed in the formation of the vinyl indoles. Godoi *et al.* previously reported a method to assign the stereochemistry of **3.74**,²¹³ in which the key interaction between the C-4 proton on indole, and

the vinyl proton was assigned to the *E*-isomer (Figure 93). This interaction was therefore used to assign the stereochemistry of **3.73** (Figure 94) and **3.77** (Figure 95).

In each case the resonance of the *E*-isomer vinyl proton was further downfield than the equivalent proton in the *Z*-isomer, which was used to assign the stereochemistry of all the C-3 vinyl indole substrates by analogy.

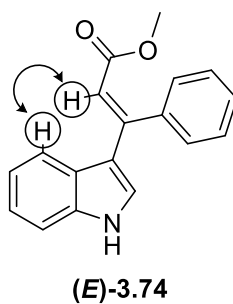


Figure 93. Structure of **(E)-3.74**, with the key stereochemical assignment highlighted, as reported by Godoi *et al.*²¹³

NOESY of 4-(4-(dimethylamino)phenyl)-4-(1*H*-indol-3-yl)but-3-en-2-one (**3.73**)

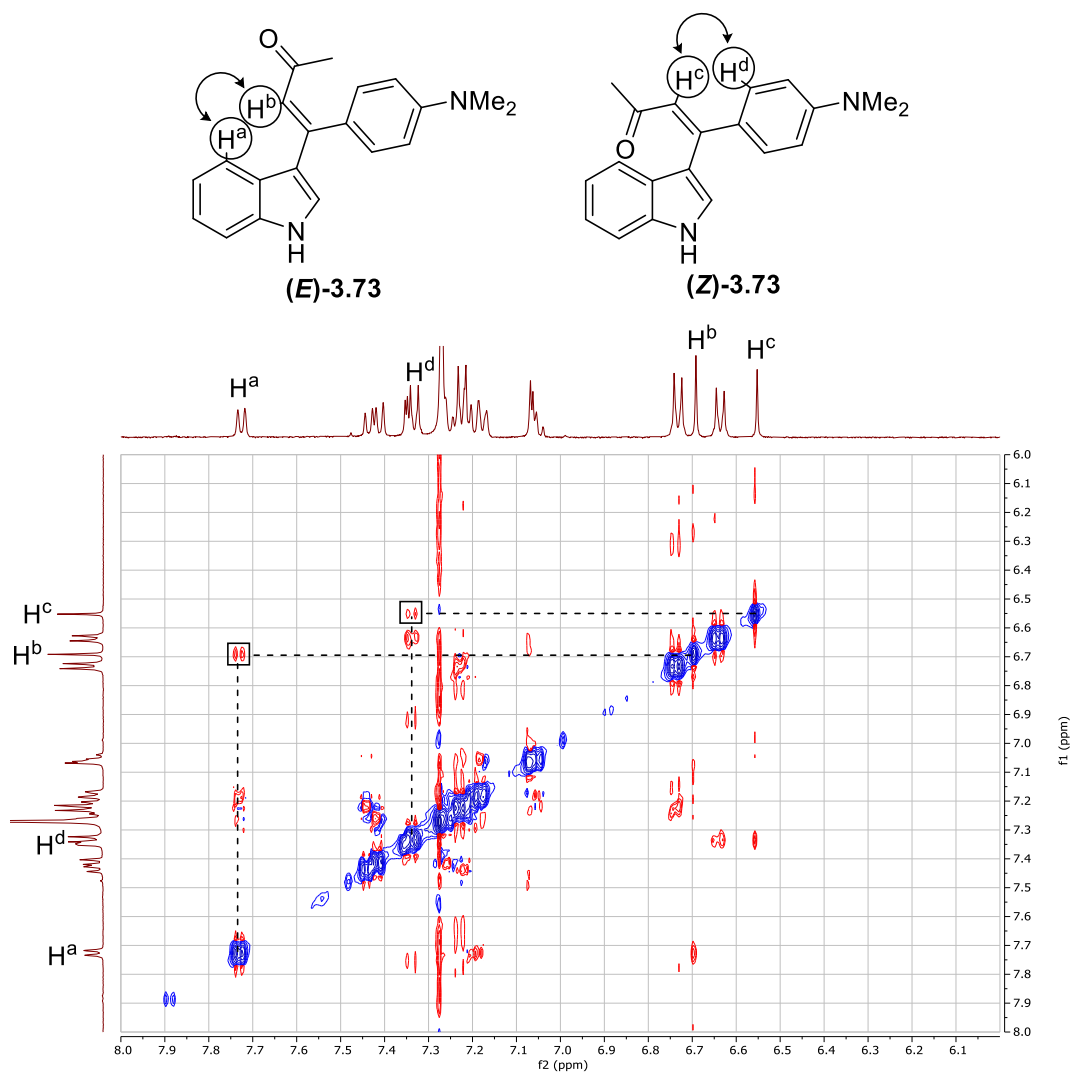


Figure 94. NOESY spectrum of **3.73** recorded at 500 MHz in $CDCl_3$, with the key assignment highlighted. Parameters - D1 = 2 s, D8 = 0.5 s.

NOESY of 3-(1*H*-indol-3-yl)-3-(4-methoxyphenyl)-*N,N*-dimethylacrylamide (**3.77**)

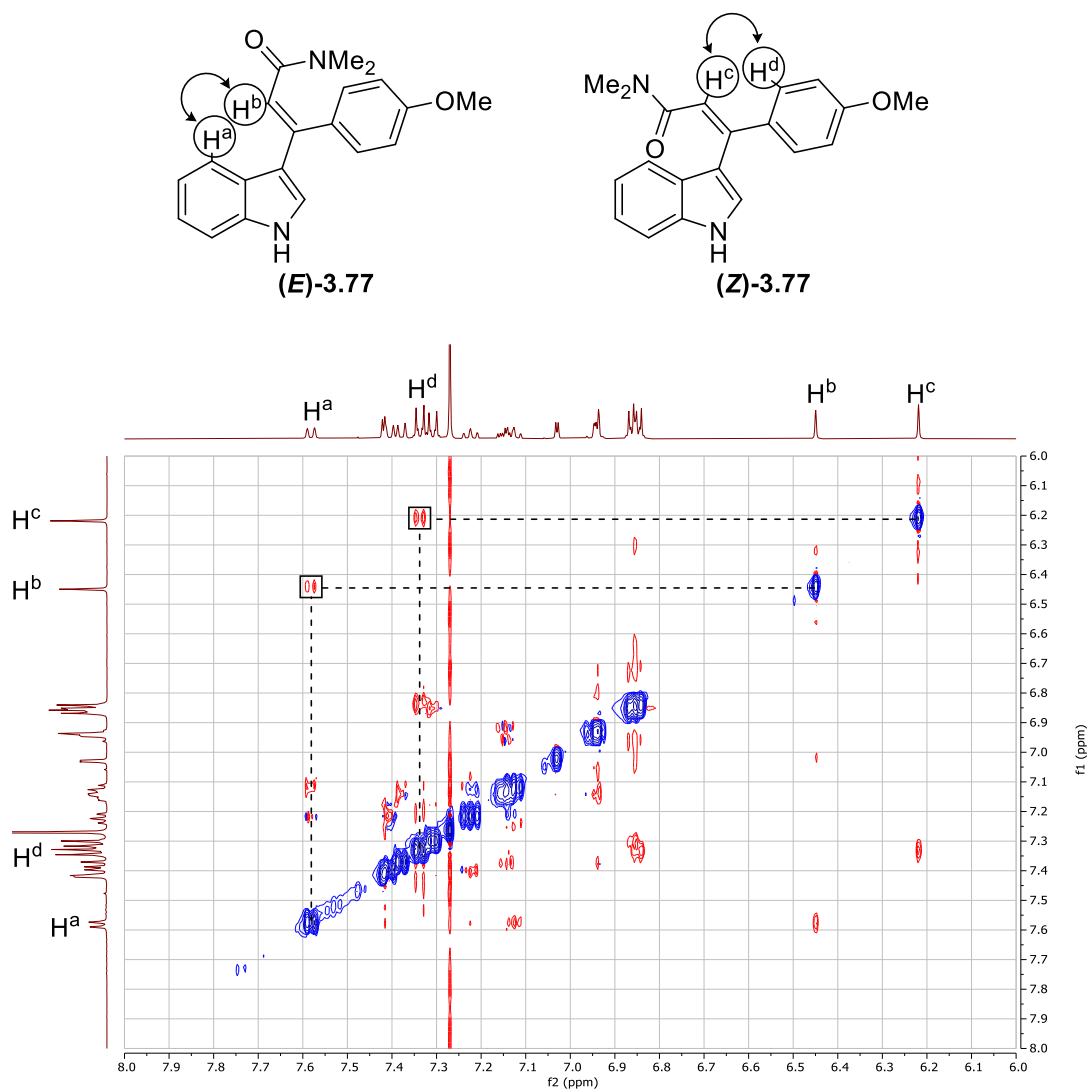


Figure 95. NOESY spectrum of **3.77** recorded at 500 MHz in $CDCl_3$, with the key assignments highlighted. Parameters - D1 = 2 s, D8 = 0.5 s.

3.2.4 C-2 Vinylation

It was proposed that the gold(I)-catalysed indole/ynone coupling reaction using indoles already substituted in the C-3 position (e.g. skatole **3.48**) would result in C-2 vinyolated products (e.g. **3.78**, Figure 96), in which a 1,2-migration of the vinyl group can occur to restore aromaticity.

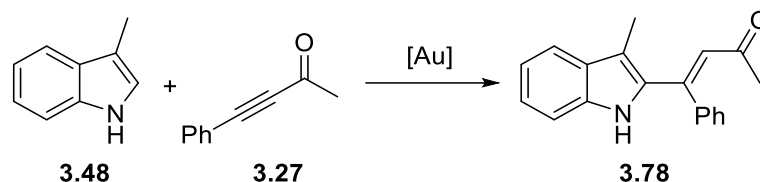


Figure 96. Proposed formation of C-2 vinylated product **3.78** from the gold(I)-catalysed coupling of skatole **3.48** and ynone **3.27**.

The coupling reaction was tested under the standard conditions, using skatole **3.48** as the heteroaromatic substrate (Figure 97). After 24 hours, a significant amount of skatole **3.48** remained according to the TLC analysis. However, a new product was formed which was isolated and identified as substituted *9H*-pyrrolo[1,2-*a*]indole compound **3.79**, first reported by Tian and co-workers in 2019.²¹⁴

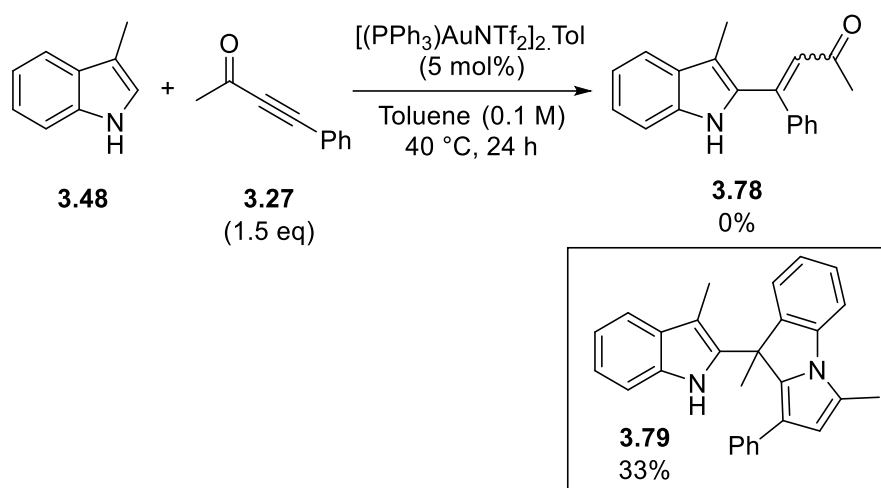


Figure 97. The formation of *9H*-pyrrolo[1,2-*a*]indole compound **3.79** observed during the gold(I)-catalysed coupling of skatole **3.48** and ynone **3.27**.

Tian and co-workers targeted these *9H*-pyrrolo[1,2-*a*]indole compounds **3.82** using Brønsted acid catalysis with C-3 substituted indoles **3.80** and ynones **3.81** (Figure 98a).²¹⁴ The authors proposed a mechanism (Figure 98b) in which acid-catalysed nucleophilic attack of skatole **3.48** into the alkyne of ynone **3.81** occurs (**3.83** → **3.84**), followed by 1,2-migration of the vinyl substituent (**3.84** → **3.85**). Then, a second equivalent of skatole **3.48** is added *via* a Michael addition, followed by a second 1,2-migration of the indoline fragment (**3.85** → **3.86**). 5-*exo-dig* cyclisation of the indoline nitrogen into the carbonyl can then take place (**3.86** → **3.87**), which after dehydration (**3.87** → **3.88**) yields the final compound (**3.88**).

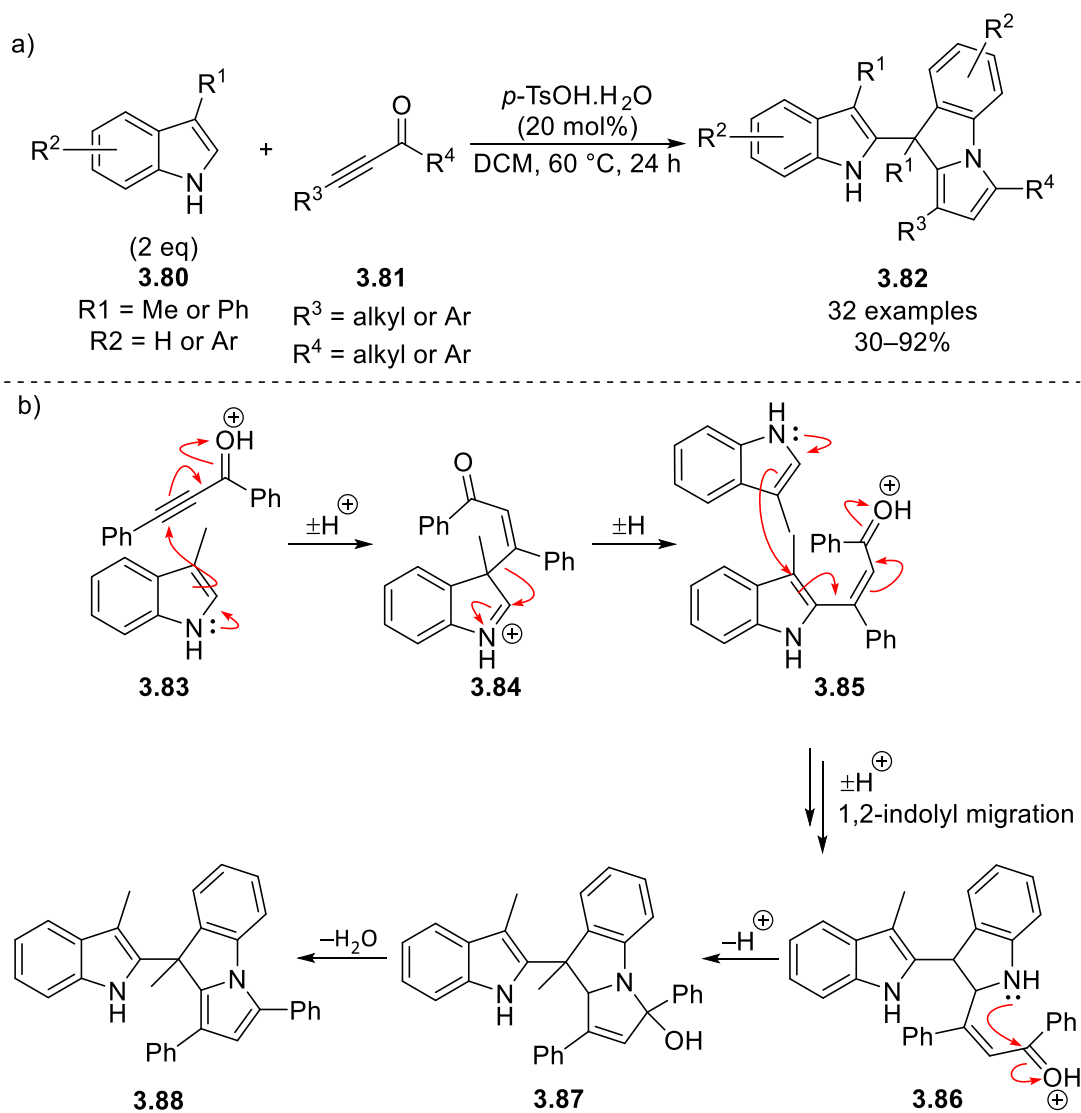


Figure 98. a) Formation of 9*H*-pyrrolo[1,2-*a*]indole compounds **3.82** using Brønsted acid catalysis, as reported by Tian *et al.*²¹⁴ b) Mechanism proposed by the authors for the formation of **3.88**.

Based on Tian's mechanism, it was proposed that substitution on the indole nitrogen might inhibit the addition of a second equivalent of skatole **3.48** and prevent over-reaction. The indole/ynone coupling reaction was attempted first using 1,3-dimethyl indole **3.49** under the standard conditions, with TLC analysis used to monitor the reaction progress. The coupling reaction took considerably longer than the equivalent reactions using indole **3.16**, requiring 27 hours for full consumption of the 1,3-dimethyl indole **3.49** starting material (Figure 99). However, the C-2 vinyl indole product **3.78** was isolated in a good yield, with the *Z*-stereoisomer identified as the major isomer (for further details see later, Figure 101).

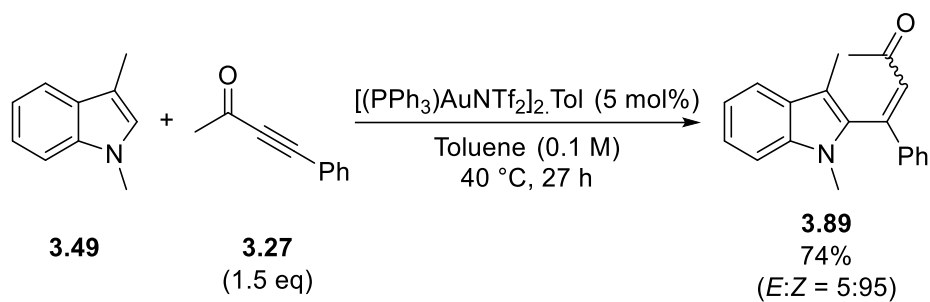


Figure 99. Successful formation of vinyl indole **3.89**, from the gold(I)-catalysed coupling of 1,3-dimethyl indole **3.49** and ynone **3.27**.

The scope of the reaction was then investigated for the *N*- and C-3 disubstituted indoles **3.90**, using phenyl-substituted alkynes **3.91** (Figure 100). A bulkier substituent in the C-3 position was tolerated (*e.g.* 3-Ph **3.92**), however the isolated yield was reduced. A reaction using *N*-benzyl-substituted indole was also successful (**3.93**), with the benzyl group being a commonly used protecting group. Finally, the use of amide- and ester-substituted alkynes were also tolerated for the synthesis of **3.94** and **3.95** respectively.

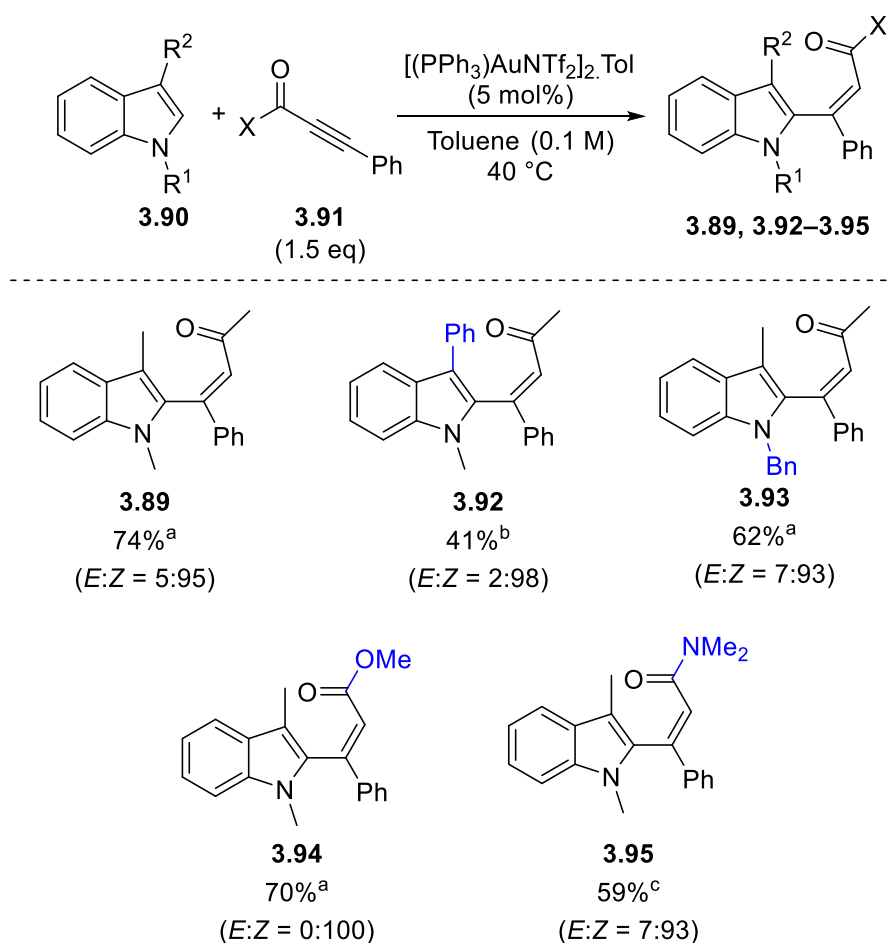


Figure 100. C-3 substituted indole **3.90** and alkyne **3.91** variation scope of the gold(I)-catalysed coupling reaction. ^a 27 hour reaction time. ^b 24 hour reaction time. ^c 48 hour reaction time.

To assign the *E*- and *Z*-stereochemistry, X-ray diffraction (XRD) was used with a crystal grown of **3.92** which unambiguously showed the *Z*-stereoisomer (Figure 101). A ¹H NMR spectrum of the bulk grown crystals was recorded, which showed resonances consistent with the major isomer, it was therefore assumed that the XRD data did not result from crystallisation of the minor isomer.

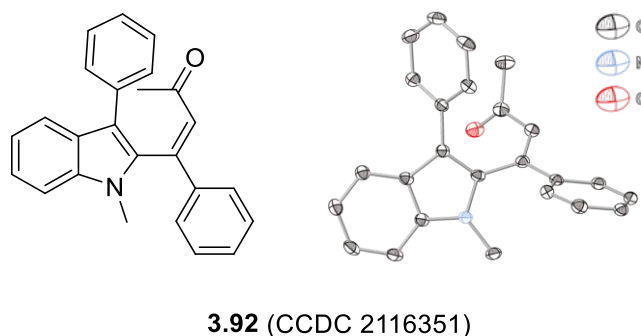


Figure 101. XRD data of **3.92**, solved by Dr Adrian Whitwood (see CCDC 2116351). Hydrogens atoms removed for clarity. ORTEPS at 50% probability level.

3.3 Vinyl Indole Mechanistic Studies

3.3.1 Indole/Ynone coupling summary

As described in Section 3.2, the synthesis of C-2 and C-3 substituted vinyl indoles was successful when using gold(I) catalysis and internal alkynes substituted with electron-withdrawing groups, namely ketones, esters and amides. The formation of the *bisindole* compounds (e.g. **3.29**) was suppressed hence one of the main aims of this project had been achieved.

However, the coupling reactions are synthetically more challenging when compared to the intramolecular spirocyclic indolenine and carbazole forming reactions (Section 3.1.4, Figure 78). Longer reaction times with higher heating are required, despite the DFT calculations already discussed in Section 3.1.4 showing almost barrierless carbon-carbon bond formation in the indolyl-tethered ynone (**2.6**) examples (Figure 80). Furthermore, the intermolecular coupling reaction time is required to be much longer for the C-3 substituted indoles for full completion.

It was decided to use DFT methods to address the following questions:

1. Why are the intermolecular coupling reactions more difficult than the tethered intramolecular counterparts?
2. Why are the coupling reactions using C-3 substituted indoles much slower than indoles that are unsubstituted in the C-3 position?
3. Why specifically does the use of electron-deficient alkynes stop the addition of a second indole equivalent?

3.3.2 Gold(I) coordination

Before the mechanism of the gold(I) catalysed indole/ynone coupling reaction was explored, the preferred coordination mode of the gold(I) cation was determined. DFT calculations were performed at the D3(BJ)-PBE0/def2-TZVPP//BP86/SV(P) level of theory (the same method as described for the tethered intramolecular reactions, Figure 80)²⁰¹ with COSMO solvent correction in toluene. An ECP was used to describe the core electrons of the gold atom which also accounted for relativistic effects.^{55,58}

The energies of three potential sites of coordination (the indole, and the ketone or the alkyne of ynone **3.27**) were compared using both indole **3.16** and skatole **3.48** (Figure 102). The

calculations demonstrated that there was a strong thermodynamic preference for gold(I) coordination to the indole substrate for indole (**3.N₁₆**) and skatole (**3.N₄₈**). Coordination of the gold(I) cation to the ketone (**3.O₂₇**) and alkyne (**3.P₂₇**) were disfavoured by 12 and 18 kJ mol⁻¹ respectively, when compared to gold(I) coordinated indole **3.N₁₆**, and 8 and 14 kJ mol⁻¹ relative to gold(I) coordinated skatole **3.N₄₈**.

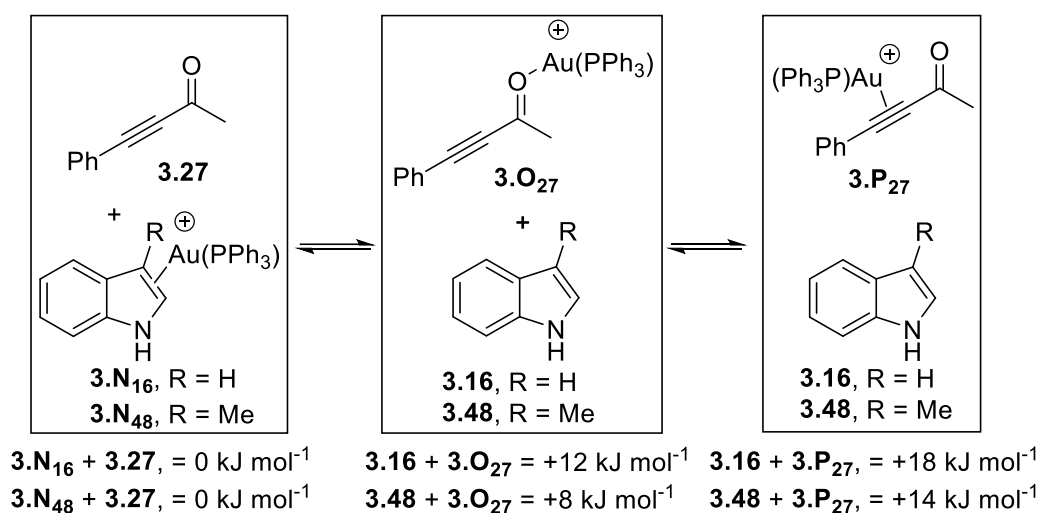


Figure 102. DFT-calculated energies of gold(I) coordination to the indole **3.16** and skatole **3.48**, against the ketone and alkyne of ynone **3.27**. Energies are Gibbs energies at 298.15 K at the D3(BJ)-PBE0/def2-TZVPP//BP86/SV(P) level of theory with COSMO solvent correction in toluene.

The DFT data described in Figure 102 neglects the triflimide anion, which as described in Chapter 1, can play a role in more accurately describing the energies of a system. Therefore, the gold(I) coordination calculations were repeated to compare the energies of the binding modes with inclusion of the triflimide anion.

The work of Bandini and co-workers (see Section 1.2.2 for further details) demonstrated that the preferred anion coordination site is typically located on more acidic protons on the complex, and away from the triphenylphosphine ligand.^{128–131} Therefore it was considered that in the indole/ynone systems, that the triflimide might prefer to locate either with hydrogen bonding to the indole N–H, to the more acidic protons α to the carbonyl of the ynone, or near the alkyne (when gold(I) is coordinated).

The relative change in free energy upon coordination of the gold catalyst to indole **3.16** and ynone **3.27** was recalculated with the triflimide anion included in the structures (Figure 103). Solvent corrections were applied in both CH₂Cl₂ (top value) and toluene (bottom value).

Numbers in the top left corner of each box will be referred to as the “state” number, and all states are considered to be in equilibrium.

State **1**, in which the gold(I) cation was coordinated to indole **3.16**, with the triflimide anion hydrogen bonded to the indole N–H (**3.Q**), was calculated as the lowest energy and taken as the reference point. When states including gold(I)-coordinated ynone complexes with the triflimide anion coordinated to the ynone were considered (**3.T**, **3.U** and **3.V**, states **4**, **5** and **7**), the energies were highly endergonic (+37 and +39 kJ mol⁻¹ in CH₂Cl₂), independent of the specific coordination mode. Higher energies were calculated for states in which the gold(I) cation and triflimide anion were separated (states **2**, **3** and **6**) – particularly so when the solvent correction was applied with toluene, likely caused by the polarity differences between CH₂Cl₂ and toluene.

These data support the findings from Figure 102 that indole coordination to the gold is more thermodynamically favourable than coordination to ynone **3.27**, in either the $\eta^1(\text{O})$ or $\eta^2(\pi)$ binding modes.

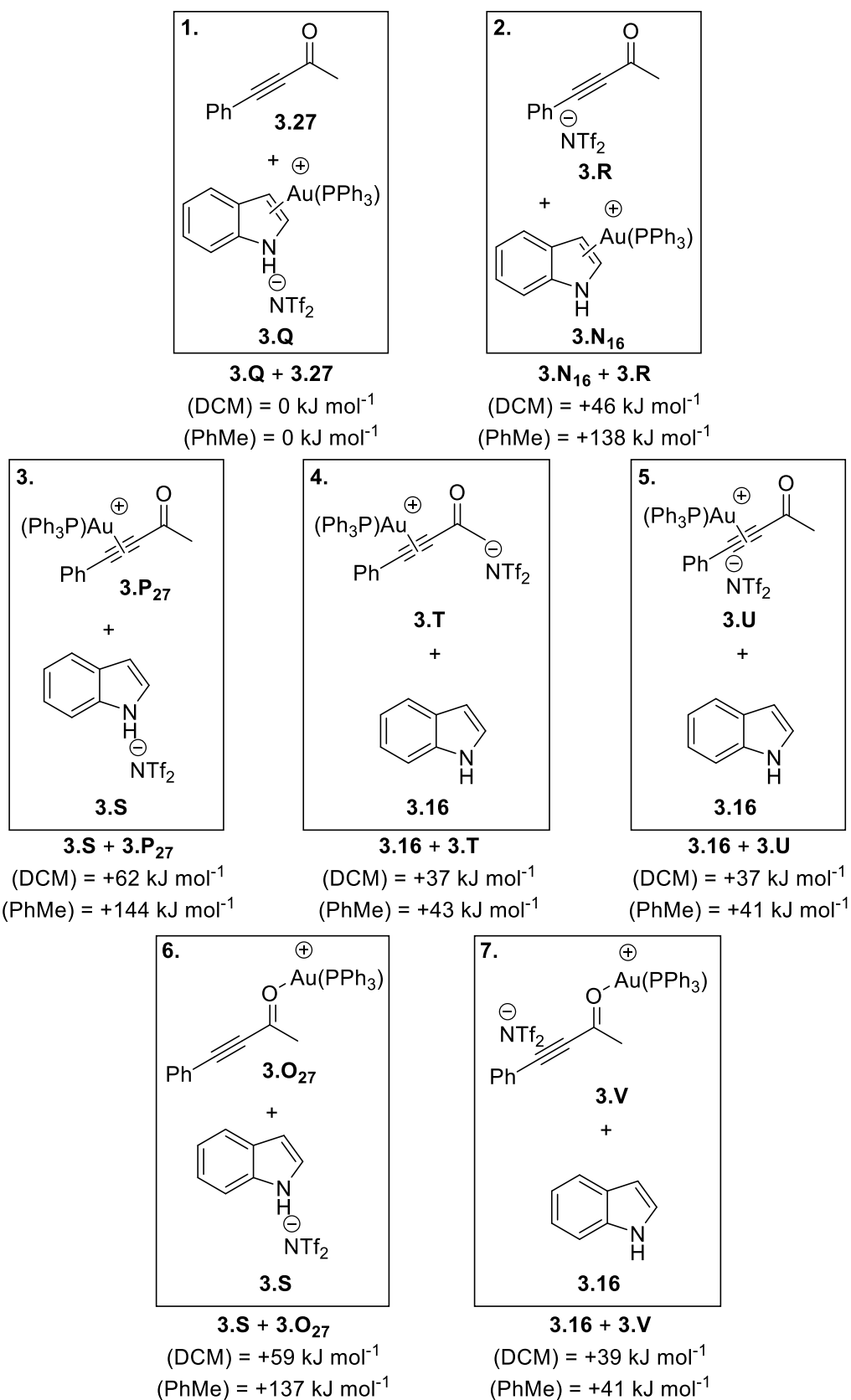


Figure 103. DFT-calculated energies comparing species with varied [Au(PPh₃)]⁺ and triflimide anion coordination. All energies are Gibbs energies at 298.15 K at the D3(BJ)-PBE0/def2-TZVPP//BP86/SV(P) level of theory with COSMO solvent correction in CH₂Cl₂ (top value) and toluene (bottom value).

Experimental evidence to support the DFT calculations was obtained by recording $^{31}\text{P}\{^1\text{H}\}$ NMR spectra with a 1:1 ratio of $(\text{PPh}_3)\text{AuNTf}_2$ and either indole **3.16**, skatole **3.48** or ynone **3.27**, to observe the gold(I) cation interactions (Figure 104). Gold(I) coordination was observed when indole **3.16** was the substrate, with a broad resonance observed at $\delta_{\text{P}} \approx 32$ ppm (Figure 104, Spectrum c), whereas no appreciable coordination was observed with ynone **3.27** (Figure 104, Spectrum a), with a resonance consistent with uncoordinated $(\text{PPh}_3)\text{Au}^+$ present (Figure 104, Spectrum d). A very minor chemical shift difference was observed when skatole **3.48** was added (Figure 104, Spectrum b). The resonance present at $\delta_{\text{P}} 45.5$ ppm was identified as $(\text{PPh}_3)_2\text{Au}^+$, which was compared with an authentic sample.

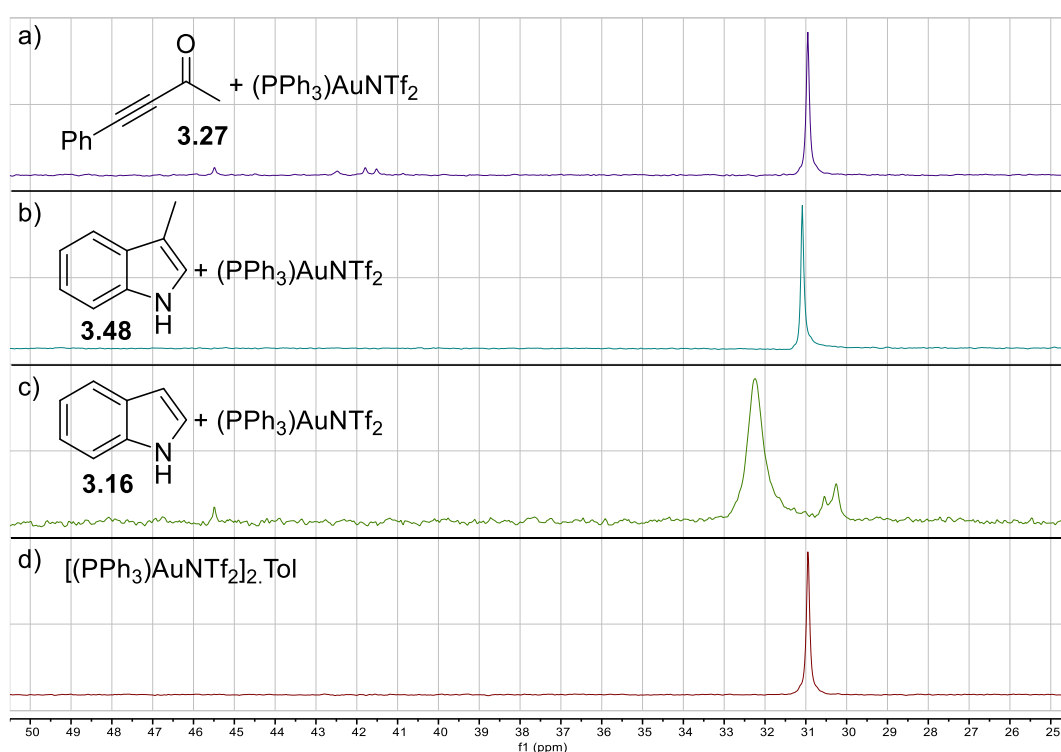


Figure 104. $^{31}\text{P}\{^1\text{H}\}$ NMR spectra recorded at 162 MHz in CD_2Cl_2 . A 1:1 gold:substrate ratio was used.

Further amounts of substrate was added to each of the three samples, and in each case the appearance of the $^{31}\text{P}\{^1\text{H}\}$ NMR spectra changed, therefore demonstrating that gold(I) coordination is concentration dependent. With increasing amounts of indole **3.16** (Figure 105), the resonance shifted further downfield, and became broadened. With skatole **3.48**, the resonance also shifted further downfield (Figure 106) and became clearer that there was indeed an interaction with the gold(I) cation. Finally, with ynone **3.27**, the resonance observed with $[(\text{PPh}_3)\text{AuNTf}_2]_2.\text{Tol}$ alone was still present in the $^{31}\text{P}\{^1\text{H}\}$ NMR spectra, however, a series of resonances appeared at $\delta_{\text{P}} 40\text{--}44$ ppm which suggested that unselective coordination and/or

reactions were occurring (Figure 107). The gold(I) coordination of the ynone species was explored further and is discussed in section 3.4.

The DFT and $^{31}\text{P}\{^1\text{H}\}$ NMR data showed that at like-for-like ratios, there is uncoordinated gold(I) catalyst with ynone **3.27**, however with indole **3.16**, there is no uncoordinated gold(I) catalyst remaining. Therefore, it is proposed that indole **3.16** coordinates to the gold(I) catalyst relatively more strongly. It was proposed that the electron rich indole moiety was a better ligand than the ynone due to the electron-withdrawing group in conjugation to the alkyne, which is significant as typically $\eta^2(\pi)$ coordination of a gold(I) cation to an alkyne functionality is considered the first step in gold(I)-catalysed reactions of alkynes.^{88–90}

Indole (**3.16**) Titration $^{31}\text{P}\{^1\text{H}\}$ NMR Spectra

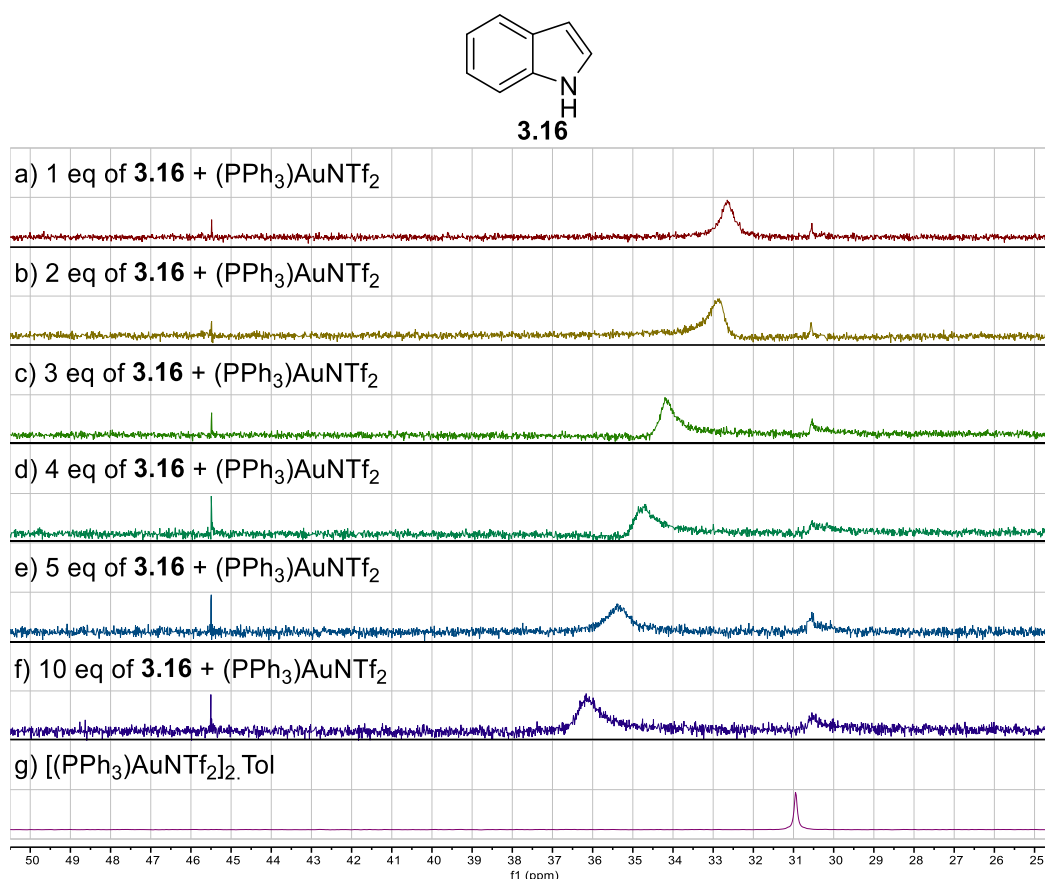


Figure 105. $^{31}\text{P}\{^1\text{H}\}$ NMR spectra recorded at 162 MHz in CD_2Cl_2 , titrated with indole **3.16** in various ratios of gold:substrate.

Skatole (3.48) Titration $^{31}\text{P}\{^1\text{H}\}$ NMR Spectra

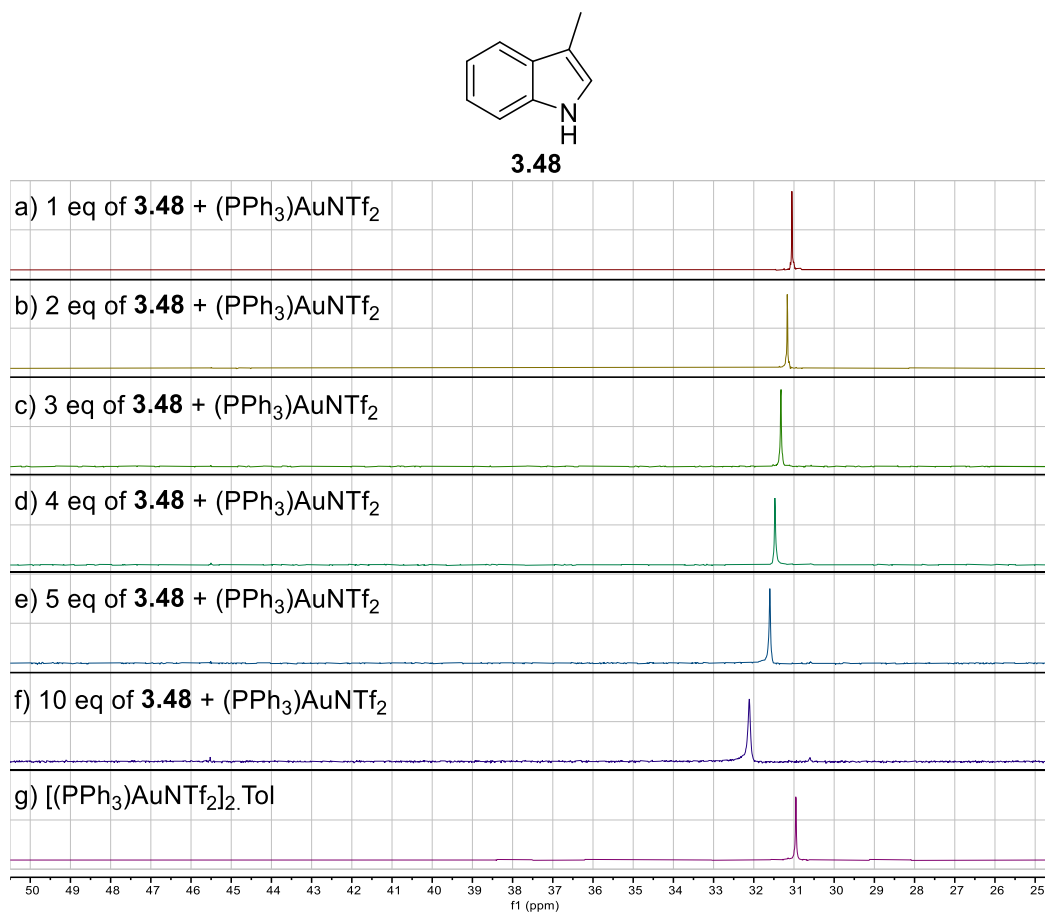


Figure 106. $^{31}\text{P}\{^1\text{H}\}$ NMR spectra recorded at 162 MHz in CD_2Cl_2 , titrated with skatole **3.48** in various ratios of gold:substrate.

Ynone (**3.27**) Titration $^{31}\text{P}\{^1\text{H}\}$ NMR Spectra

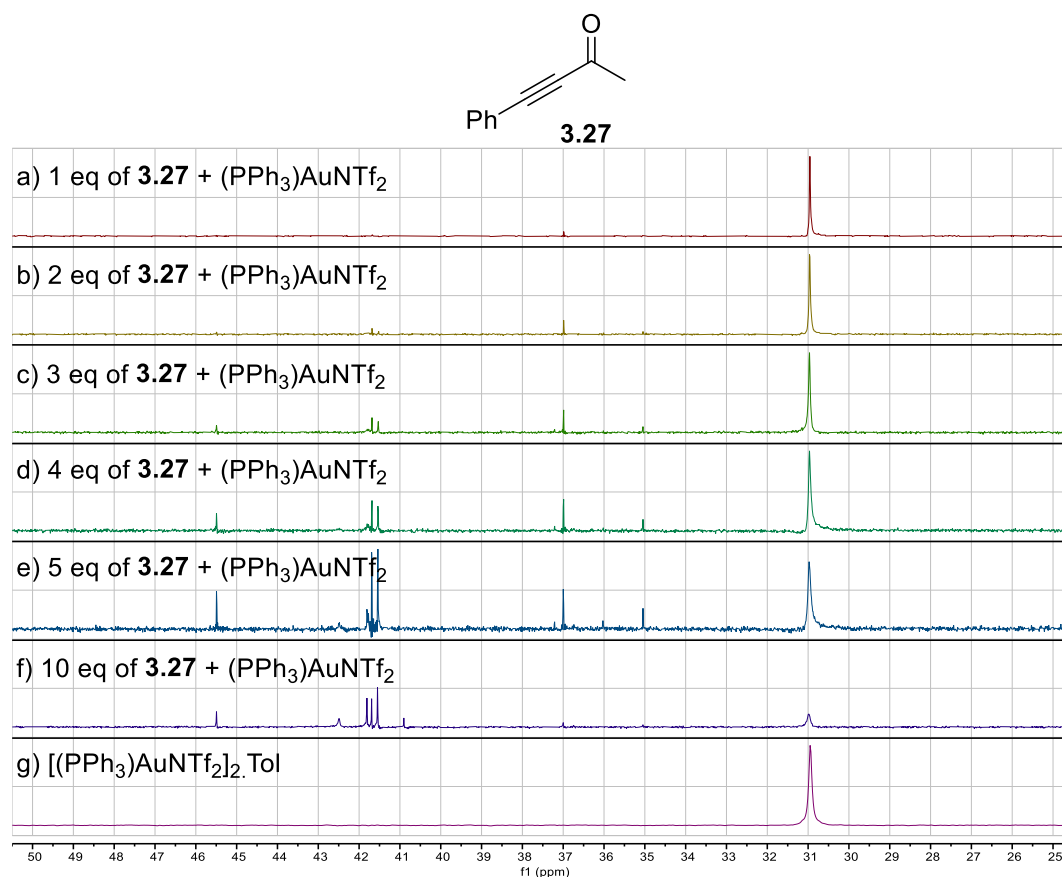


Figure 107. $^{31}\text{P}\{^1\text{H}\}$ NMR spectra recorded at 162 MHz in CD_2Cl_2 , titrated with ynone **3.27** in various ratios of gold:substrate.

3.3.3 Indole vinylation mechanism

DFT calculations were used to explore the possible reaction pathways of the gold(I) catalysed coupling reaction between indole **3.16** or skatole **3.48**, and ynone **3.27**. Initially, the thermodynamic preference for C-3 and C-2 selectivity with both the indole species was explored (Figure 108).

The calculated energies for the C-2 and C-3 vinyl indole products of indole **3.16** (**3.96** and **3.28**) were effectively the same at -110 and -111 kJ mol^{-1} respectively, demonstrating no thermodynamic preference for substitution at a specific site. When skatole **3.48** was considered, the C-3 vinyl indolenine product **3.97** (-6 kJ mol^{-1}) was considerably higher in energy than the C-2 vinyolated product **3.89** (-117 kJ mol^{-1}) likely due to a loss of aromaticity in the C-3 indolenine

products (**3.97**). Only the C-2 substituted products (**3.89**) were isolated which is consistent with the DFT-predicted outcome.

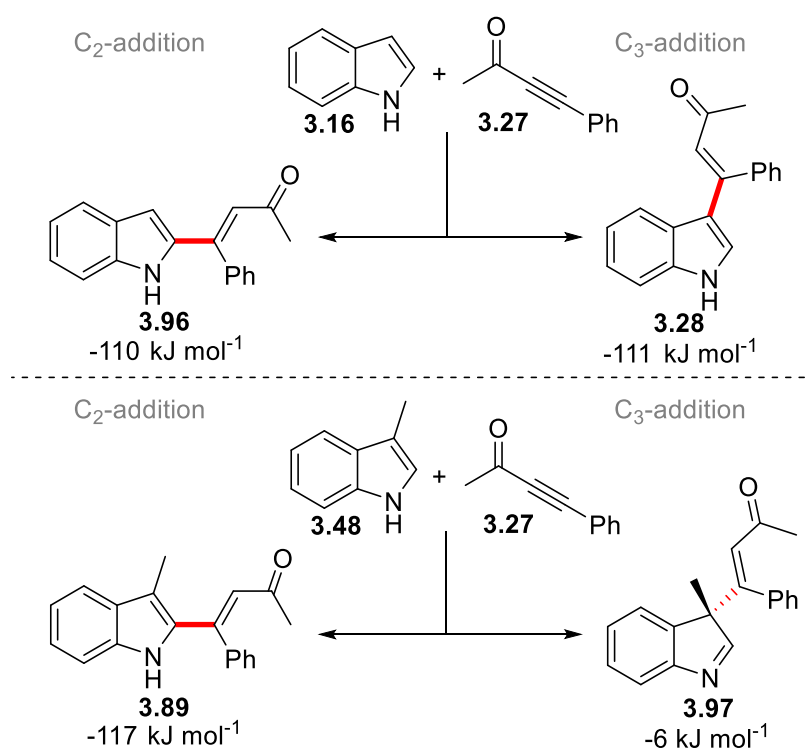


Figure 108. DFT-calculated changes in energy for the C-3 and C-2 products arising from the addition of indole **3.16** and skatole **3.48** into ynone **3.27**. Energies are Gibbs energies at 298.15 K at the D3(BJ)-PBE0/def2-TZVPP//BP86/SV(P) with COSMO solvent correction in toluene.

With the thermodynamic preference established, the energies of the transition states and intermediates for the C-2 and C-3 addition pathways were explored, for both indole **3.16** and skatole **3.48** with the $\eta^2(\pi)$ gold(I) coordinated alkyne complex **3.P₂₇** (Figure 109). The reference state for the energies was set as the gold(I) coordinated indole complex (**3.N₁₆** or **3.N₄₈** respectively) with uncoordinated ynone (Figure 102).

For indole **3.16** (Figure 109), the calculated energy for the direct C-3 addition vinylation pathway (**3.TS_{PW-H}**) was lower than that for direct C-2 addition (**3.TS_{PAA-H}**), with energies calculated at +59 and +67 kJ mol⁻¹ respectively. A structure for iminium complex **3.W_H**, was unable to be optimised, likely due to a low barrier for hydrogen abstraction by the carbonyl, leading to complex **3.X_H**, at a lower energy of -78 kJ mol⁻¹. Whilst there is no thermodynamic preference for either C-2 or C-3 addition (Figure 108), there is however a kinetic preference for C-3 addition. This is unsurprising as the C-3 position of indoles is expected to be the most nucleophilic

position,¹⁸³ which is also consistent with the observed outcomes of the gold(I) catalysed coupling reactions using indole **3.16**.

When skatole **3.48** was considered, the calculated transition state energy for direct C-2 substitution (+60 kJ mol⁻¹, **3.TS_{PAA-Me}**) was lower than the transition state for C-3 addition (+81 kJ mol⁻¹, **3.TS_{PW-Me}**). As before, a structure for the intermediate (**3.AA_{Me}**) resulting from C-2 addition (**3.TS_{PAA-Me}**) was unable to be found, due to hydrogen migration occurring during the geometry optimisation, which resulted in complex **3.Z_{Me}**, at an energy of -74 kJ mol⁻¹. The pathway for the disfavoured C-3 addition was explored and transition states were found for both the 1,2-vinyl migration (**3.TS_{WV-Me}**) and 1,2-methyl migration (**3.TS_{WAB-Me}**) of indolenine complex **3.W_{Me}**. Vinyl migration to give C-2 vinyl complex **3.Z_{Me}** was found to be significantly lower in energy, with a transition state energy calculated at +54 kJ mol⁻¹ in comparison to methyl migration at +102 kJ mol⁻¹. Therefore, whilst direct C-2 addition is favoured, both the C-2 and C-3 addition pathways would result in the C-2 vinyl indole products, which were observed experimentally using *N*-methyl skatole analogue **3.49**.

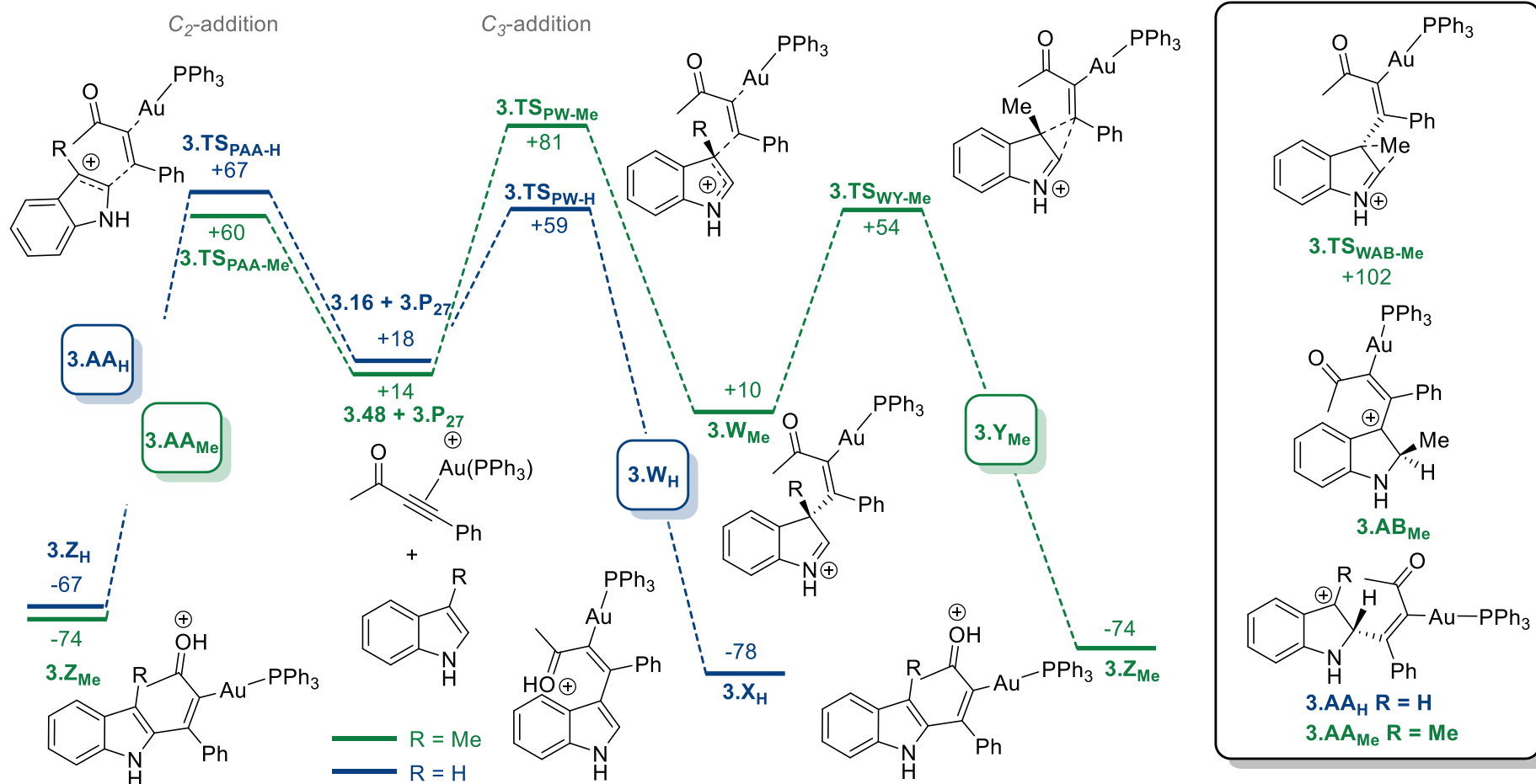


Figure 109. DFT-calculated pathways for the addition of indole **3.16** or skatole **3.48** to gold(I) coordinated alkyne complex **3.P₂₇**. Energies are Gibbs energies in kJ mol⁻¹ at 298.15 K at the D3(BJ)-PBE0/def2-TZVPP//BP86/SV(P) level of theory with COSMO solvent correction in toluene.

As discussed in Section 3.3.2, other gold(I) coordination modes are thermodynamically preferred to $\eta^2(\pi)$ -alkyne binding (**3.P₂₇**). A transition state (**3.TS_{OAC}**) for nucleophilic attack of indole **3.16** into $\eta^1(\text{O})$ gold(I) ketone coordinated complex **3.O₂₇** was located (Figure 110a) which was considerably higher in energy than the pathways found starting from the $\eta^2(\pi)$ gold(I)-coordinated alkyne complexes. A transition state starting from gold(I)-coordinated indole complex **3.N₁₆**, for the umpolung nucleophilic attack from ynone **3.27**, was not able to be found (**3.TS_{NAD}**, Figure 110b), various constrained structures were optimised and only imaginary frequencies corresponding to rotations of the indole and ynone structures were found. These DFT-calculations suggest that pathways starting from $\eta^2(\pi)$ -alkyne coordinated ynone **3.P₂₇** (Figure 109), are most likely to be in operation.

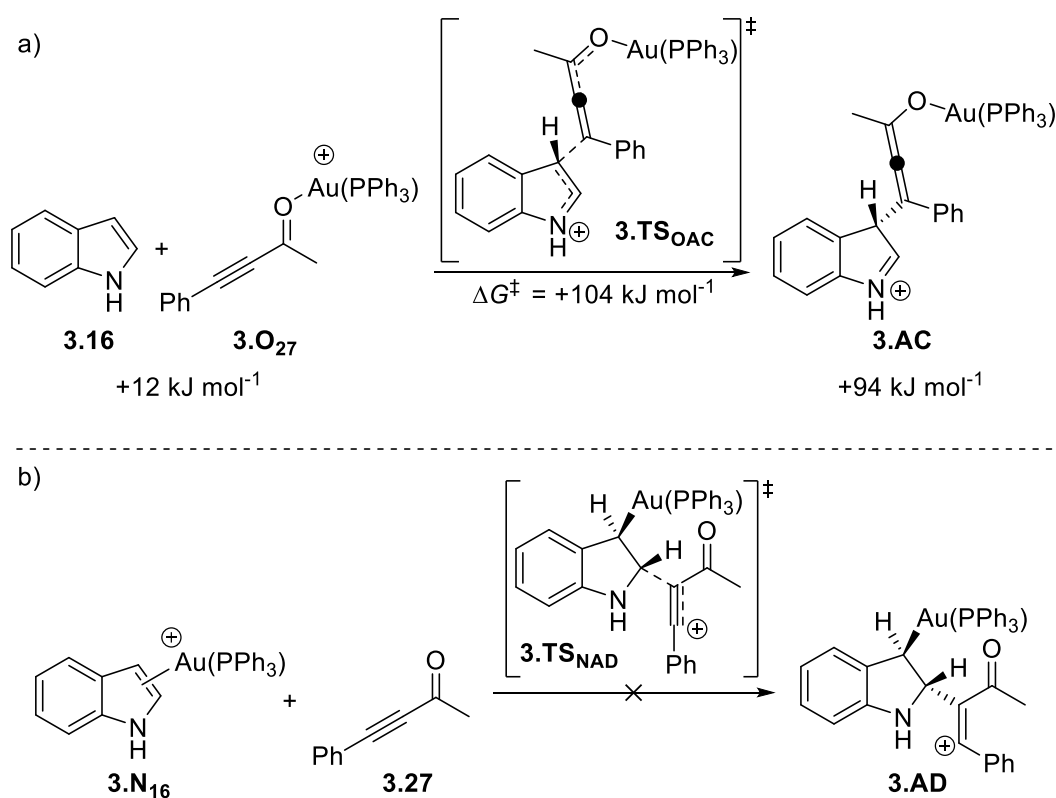


Figure 110. a) DFT-calculated pathway for the addition of indole **3.16** to $\eta^1(\text{O})$ gold(I) ketone coordinated ynone complex **3.O₂₇**. Energies are Gibbs energies in kJ mol⁻¹ at 298.15 K at the D3(BJ)-PBE0/def2-TZVPP//BP86/SV(P) level of theory with COSMO solvent correction in toluene. b) Attempted transition state **3.TS_{NAD}**, for the addition of ynone **3.27** to indole-coordinated gold(I) complex **3.N₁₆**.

The DFT calculations suggested that gold(I) coordination to the indole moiety is more thermodynamically favoured than coordination to the ynone (by 14 kJ mol⁻¹) and it is proposed that indole coordination (*e.g.* **3.N₁₆**) may cause the difference in reaction rates when comparing

the intramolecular cyclisations of tethered indoyl ynones **2.6**, and the intermolecular coupling reaction of indole **3.16**.

In the intermolecular reactions (Figure 111a), coordination of the gold(I) catalyst to the indole moiety (**3.N₁₆**) will inhibit access to the product forming pathways, which requires $\eta^2(\pi)$ coordination of the gold(I) catalyst to the alkyne (**3.P₂₇**). In the intramolecular reactions (Figure 111b), it is likely that coordination of the metal catalyst to the indole moiety (**3.98**) is thermodynamically preferred, however, due to the ynone being tethered to the indole, it might be easier for the metal catalyst to coordinate to the alkyne (**3.I**) *via* π -slippage events,^{215,216} after which cyclisation can occur readily through low energy transition states due to the preorganised nature of the indoyl-tethered ynones **2.6**.

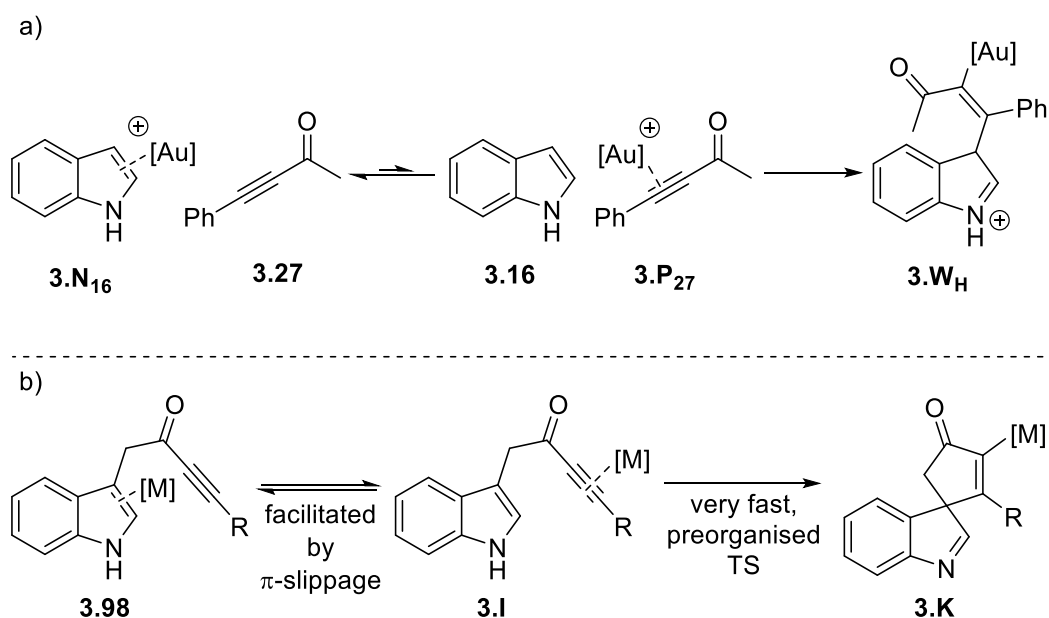


Figure 111. Comparison of the a) intermolecular and b) intramolecular indole addition to ynones.

The energy barriers for the coupling of indole **3.16** and skatole **3.48** with ynone **3.27**, were calculated to be similar, at energies of +59 and +60 kJ mol⁻¹ respectively (Figure 109). However, experimentally the reactions of skatole **3.48** (as seen with the formation of pyrrollo compound **3.79**, Figure 97) and *N*-methyl skatole **3.49**, requires significantly longer reaction times than indole **3.16**. It is tentatively proposed that the kinetics of gold(I) coordination to the indole moiety might factor into the coupling rate difference. The broadness of the ³¹P{¹H} NMR resonance with indole **3.16** (Figure 105), compared to the that of skatole **3.48** (Figure 106) suggests that gold(I)-coordination with indole **3.16** has a different rate of exchange at room temperature.

3.3.4 *bis*-Indole formation

As discussed in Section 3.1.2, *bis*indolemethanes **3.18** are a common product in the gold(I) catalysed addition of alkynes to indoles (Figure 70).^{190,193} Experimental and computational studies have shown that the second addition to the vinyl indole intermediate is likely catalysed by trace amounts of acid present in solution.^{192,194,195} In this work, the inhibition of a second equivalent of indole **3.16** has been achieved by using alkynes with electron-withdrawing groups, the nature of this observation was explored further using DFT methods.

Firstly, the thermodynamic viability of indole addition to both ynone-derived vinyl indole **3.28** and acetylene-derived vinyl indole **3.17** was assessed (Figure 112). The calculations showed that there is no significant energetic gain to form *bis*indole **3.29** from **3.28**, with a calculated Gibbs energy of only -3 kJ mol^{-1} . In contrast, the formation of *bis*indolemethane **3.18** from **3.17** was calculated to be more exergonic, with an energy difference of -25 kJ mol^{-1} .

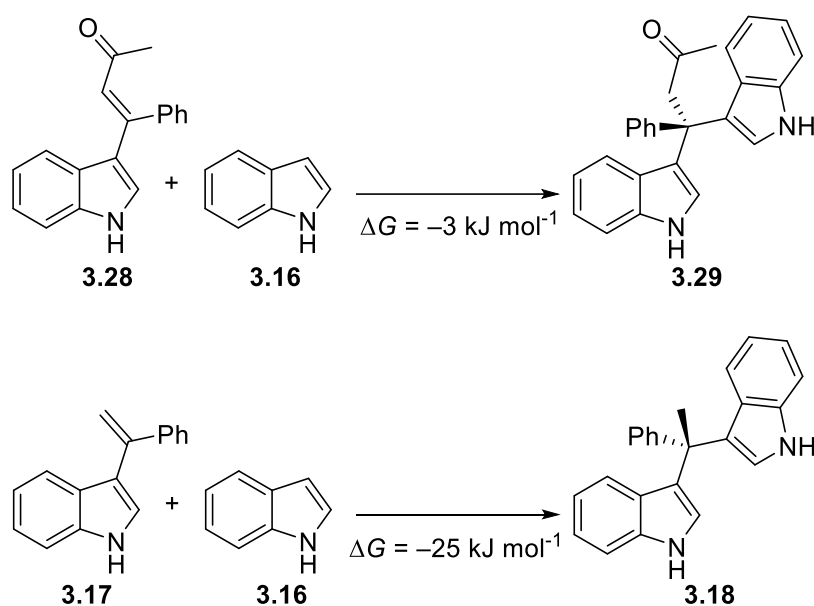


Figure 112. DFT-calculated energy for the formation of *bis*indole compounds **3.29** and **3.18**. Energies are Gibbs energies at 298.15 K at the D3(BJ)-PBE0/def2-TZVP//BP86/SV(P) level of theory with COSMO solvent correction in toluene.

The kinetic barriers to *bis*indole formation were also calculated. Two possible tautomers of the protonated enone functionality of **3.28** were considered (Figure 113a), with protonation at either the ketone (**3.AE**), or at the carbon in the α position to the ketone (**3.AF**). The calculated energies showed a significant preference for protonation at the carbonyl (**3.AE**) which was favoured by 20 kJ mol^{-1} , and hence chosen as the energy reference state. A transition state for the nucleophilic attack of indole **3.16** into **3.AE** was found (**3.TS_{AEAG}**), which was calculated to be

high in energy at +114 kJ mol⁻¹, to give *bisindole* intermediate **3.AG**, at an energy of +101 kJ mol⁻¹. When addition was considered from the disfavoured carbocation (**3.AF**), the calculated transition state (**3.TS_{AFAH}**) was lower in energy, at +87 kJ mol⁻¹, which would result in intermediate **3.AH**, at an energy of +68 kJ mol⁻¹.

Protonation of vinyl indole **3.17** was only considered on the terminal alkene carbon, to result in carbocation **3.AI** (Figure 113b). A transition state for nucleophilic attack by indole was found (**3.TS_{AIAl}**) at an energy of +67 kJ mol⁻¹.

The exact process for the indole addition into ynone-derived vinyl indole **3.28** will depend on the rate of proton transfer between cations **3.AE** and **3.AF**, however, due to the energy difference between the tautomers, it could be considered that there might be a low concentration of **3.AF** in solution if proton migration is fast. When the transition state energies of addition into **3.AE**, **3.AF** and **3.AI** are compared, it is clear that **3.TS_{AEAG}** and **3.TS_{AFAH}** are higher energy processes and hence the pathway through **3.TS_{AIAl}** has the lowest energetic span. Furthermore, with no significant thermodynamic driving force for the formation of **3.29**, the formation of *bisindole* **3.29** is overall significantly disfavoured than compared to the formation of *bisindolemethane* **3.18**.

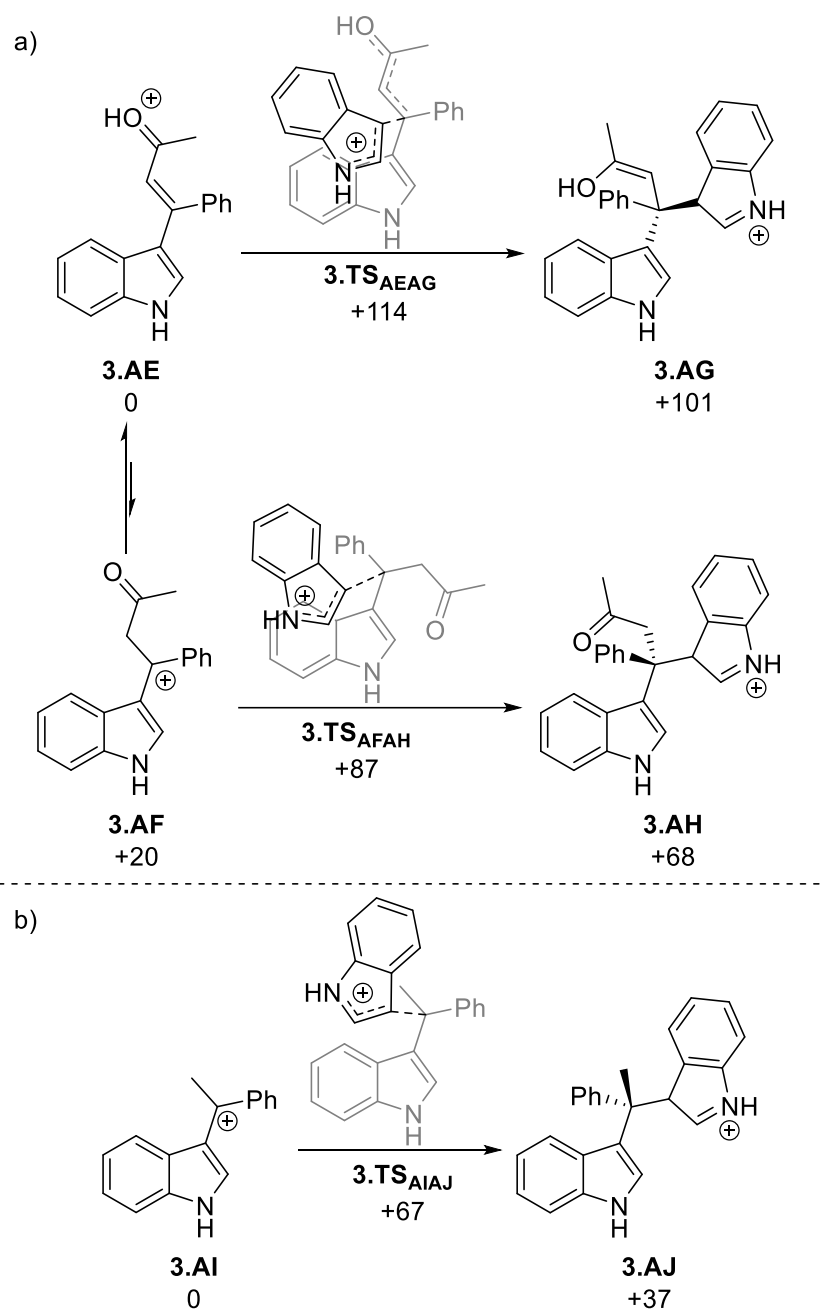


Figure 113. DFT-calculated pathways for the acid-catalysed addition of indole **3.16** to a) ynone derived vinyl indole **3.28** and b) acetylene derived vinyl indole **3.17**. Energies are Gibbs energies at 298.15 K at the D3(BJ)-PBE0/def2-TZVPP//BP86/SV(P) level of theory with COSMO solvent correction in toluene.

3.4 Ynone Gold(I) Speciation

3.4.1 Ketone versus alkyne gold(I) coordination

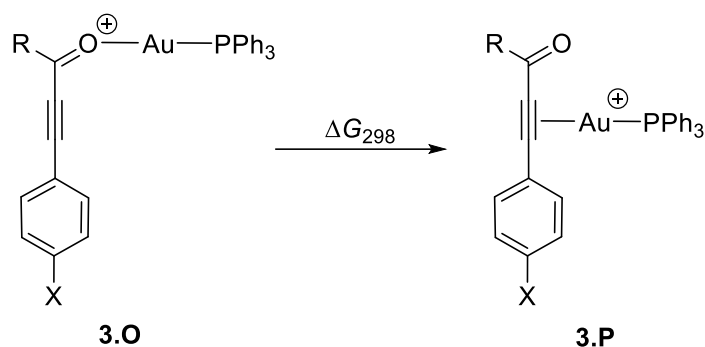
When the relative energies of gold(I) coordination with indole **3.16** and ynone **3.27** were compared (Figure 102), it was found that indole **3.16** was a better ligand than ynone **3.27**, and that $\eta^1(\text{O})$ ketone coordination (**3.O₂₇**) was preferred to $\eta^2(\pi)$ alkyne coordination (**3.P₂₇**). It was decided to further explore the factors that influence the speciation of the gold(I) catalyst.

It was considered that there are two main factors that might influence the gold(I) coordination, the nature of the carbonyl compound (*e.g.* ketone, ester or amide) and/or the electronic effects of the aryl substituent. It was proposed that the amide-substituted alkynes (*e.g.* **3.39** and **3.41**) might favour coordination to the carbonyl, due to the increased electron density from conjugation of the amide nitrogen. Likewise, it was thought that the inclusion of a strongly electron-donating group on the aryl substituent (*e.g.* **3.34**) might increase the electron density of the alkyne through conjugation.

DFT calculations were used to compare the energies of the $\eta^1(\text{O})$ and $\eta^2(\pi)$ alkyne gold(I) coordinated complexes (**3.O** and **3.P** respectively), for a range of substituted alkynes (Table 9). Comparing the DFT-calculated relative energies of the phenyl-substituted alkynes (**3.27**, **3.39** and **3.43**) showed that using an amide functionality (*e.g.* **3.39**) does indeed increase the preference for $\eta^1(\text{O})$ gold(I) coordination (**3.O**), and that the inverse effect is seen when the ester-substituted alkyne (**3.43**) is used, with the alkyne (**3.P**) now the thermodynamically preferred coordination site.

When the strongly electron-donating dimethylamino group ($\text{X} = \text{NMe}_2$) was substituted in conjugation to the alkyne (**3.34**, **3.41** and **3.44**), the relative energy difference of the complexes demonstrated an increased preference for alkyne coordination, with the largest influence seen with the amide- (**3.41**) and ester- (**3.44**) substituted alkynes.

Table 9. Isodesmic reaction used to compare $\eta^1(\text{O})$ and $\eta^2(\pi)$ coordinated isomers of substituted alkynes. Energies are Gibbs energies at 298.15 K at the D3(BJ)-PBE0/def2-TZVPP//BP86/SV(P) level of theory with COSMO solvation in CH_2Cl_2 .



Alkyne	R	X	$\Delta G_{298} / \text{kJ mol}^{-1}$
3.27	Me	H	+6
3.34	Me	NMe ₂	-1
3.39	NMe ₂	H	+17
3.41	NMe ₂	NMe ₂	+1
3.43	OMe	H	-7
3.44	OMe	NMe ₂	-23

$^{31}\text{P}\{^1\text{H}\}$ NMR spectra were recorded with a 2:1 substrate:gold ratio, to explore the gold(I) coordination using the ketone (**3.27** and **3.34**), amide (**3.39** and **3.41**) and ester (**3.43** and **3.44**) compounds. The NMR spectra of the amide- and ester-substituted alkynes were most instructive in exploring the gold(I) speciation and will be discussed here (Figure 114), whereas the ketone compounds will be discussed further in section 3.4.2. The $^{31}\text{P}\{^1\text{H}\}$ NMR spectra of the substrates with gold triflimide were compared with the DFT data (Table 9) and to the spectra of samples prepared with either DMF or alkyne **3.47** and the gold(I) catalyst, which were proposed as control compounds for the $\eta^1(\text{O})$ and $\eta^2(\pi)$ binding modes respectively (**3.O_{DMF}** and **3.P₄₇**).

The $^{31}\text{P}\{^1\text{H}\}$ NMR spectra of the amide-containing alkynes (**3.39** and **3.41**, Spectra a and b) were considered first. A resonance upfield of the uncoordinated gold(I) catalyst was seen in both spectra at $\delta_{\text{p}} = 29\text{--}30$ ppm, which by comparison with the resonances seen in the control NMR spectra of DMF (Spectrum f), can be assigned as the $\eta^1(\text{O})$ coordination mode (**3.O**). An additional singlet resonance was present at $\delta_{\text{p}} = 35.7$ ppm for the 4-NMe₂-substituted amide (**3.41**, Spectrum b). This is consistent with a resonance in the control sample prepared with alkyne **3.47** (Spectrum g) and suggests that these resonances are from the $\eta^2(\pi)$ alkyne

coordinated complex (**3.P**). These data were consistent with the DFT calculations (Table 9), which predicted that phenyl-substituted amide **3.39** would only demonstrate $\eta^1(\text{O})$ coordination (**3.O**), yet with 4-NMe₂ substituted amide **3.41**, both $\eta^1(\text{O})$ and $\eta^2(\pi)$ coordination (**3.O** and **3.P**) might be observed.

For the ester-substituted alkynes (**3.43** and **3.44**), no coordination of the phenyl-substituted ester was observed in the $^{31}\text{P}\{^1\text{H}\}$ NMR spectra (**3.43**, Spectrum c), with a resonance consistent with the uncoordinated catalyst visible (Spectrum e). However, the NMR spectra of 4-NMe₂ substituted ester (**3.44**) showed a singlet at $\delta_{\text{P}} = 35.8$ ppm, which was consistent with $\eta^2(\pi)$ alkyne coordination (**3.P**) as discussed previously. This matched the DFT calculations where it was predicted that alkyne coordination would be the preferred coordination mode.

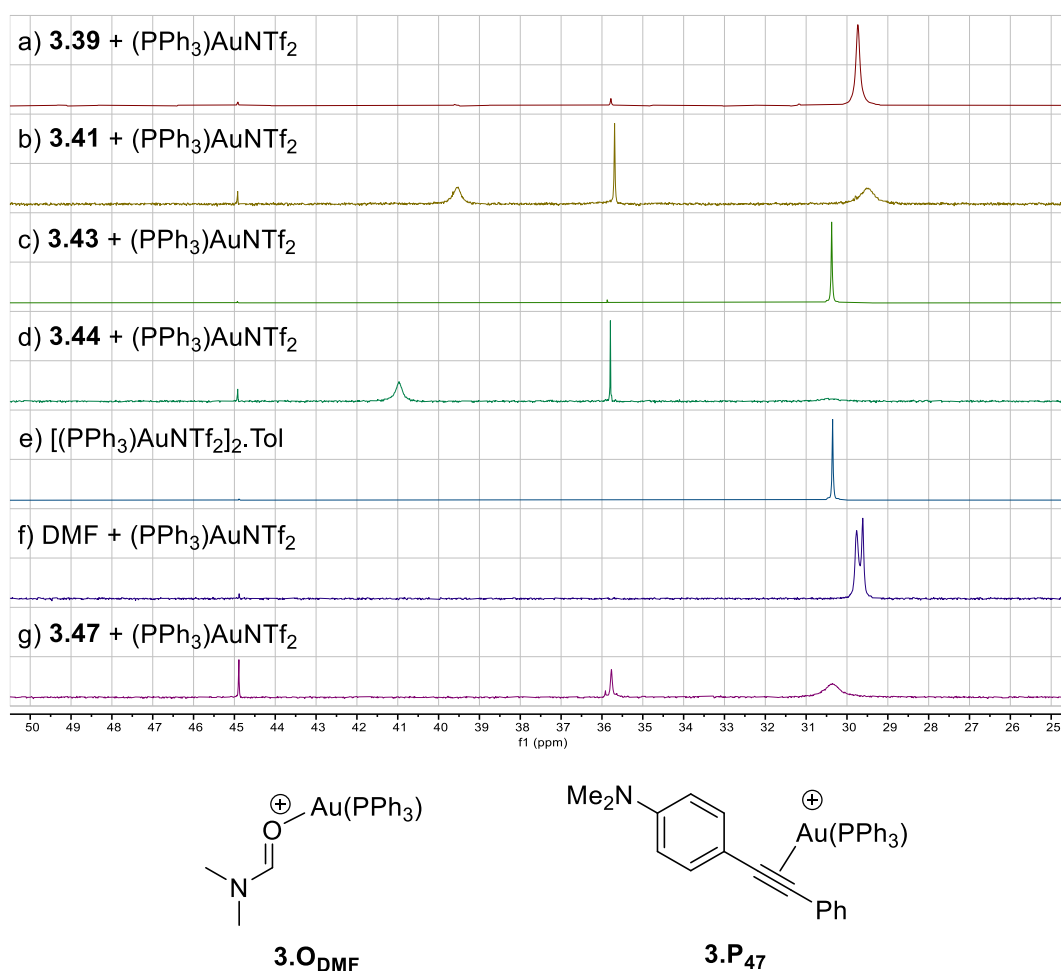


Figure 114. $^{31}\text{P}\{^1\text{H}\}$ NMR spectra recorded at 242 MHz in CD_2Cl_2 , with a 2:1 substrate:gold ratio. Proposed $\eta^1(\text{O})$ and $\eta^2(\pi)$ gold(I) coordination modes of DMF and alkyne **3.47** respectively.

An additional resonance was present in the $^{31}\text{P}\{^1\text{H}\}$ NMR spectra for the experiments using the 4-NMe₂-substituted alkynes (**3.41** and **3.44**, Spectra b and d) at $\delta_{\text{P}} = 39\text{--}41$ ppm. Further work

(see Section 3.4.3.) enabled these species to be proposed as gold(I) pyrylium complexes **3.99** and **3.100**, formed from the dimerisation of the 4-NMe₂ ester **3.44** and amide **3.41** respectively (Figure 115). However, no further evidence was obtained to unambiguously identify the compounds.

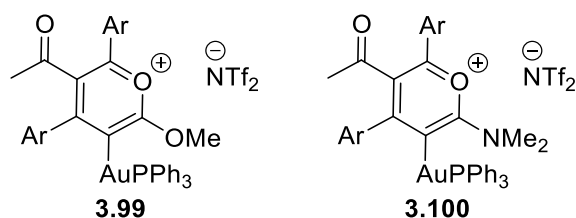


Figure 115. Potential pyrylium-type complexes **3.99** and **3.100** formed by dimerisation of 4-NMe₂ substituted ester and amide compounds **3.44** and **3.41** respectively. Ar = C₆H₄-4-NMe₂.

3.4.2 Ynone coordination

The ³¹P{¹H} NMR spectra recorded of ynone **3.27** with gold triflimide highlighted that the gold(I) cation has a low affinity for the ynone. A high proportion of uncoordinated gold(I) catalyst was present even when a large excess of ynone **3.27** was used (Figure 107). It was considered that substituents in the 4-position of the aryl group would change the electronic properties and could influence the gold(I) affinity.

An isodesmic reaction was proposed, in which the binding affinity of η²(π) coordination (**3.P**) for different ynone compounds could be compared relative to phenyl-substituted ynone **3.27** (Figure 116). A Hammett plot was produced, which demonstrated a linear relationship between the DFT-calculated energy change upon gold(I) coordination and the Hammett parameter (σ_p). The positive slope indicated that substituents which have an electron-donating effect, increased the gold(I) affinity for the alkyne.

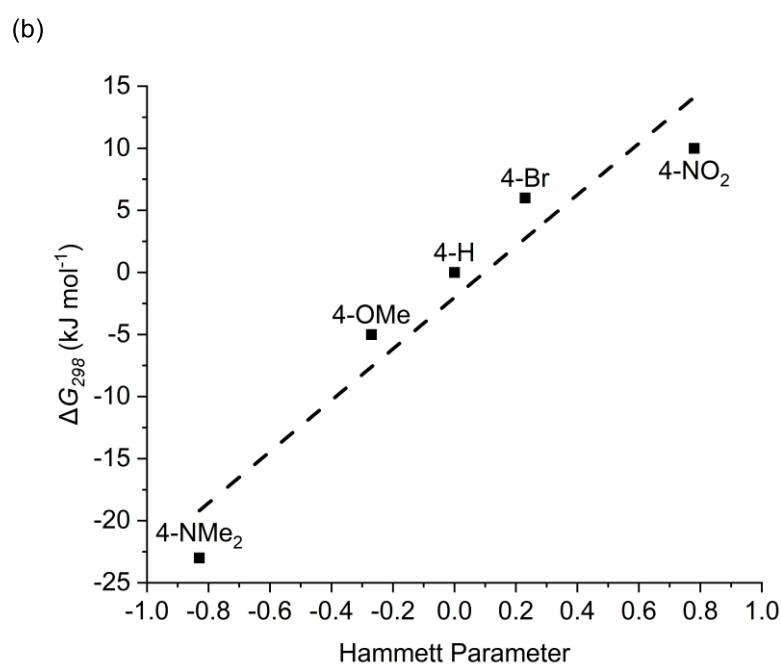
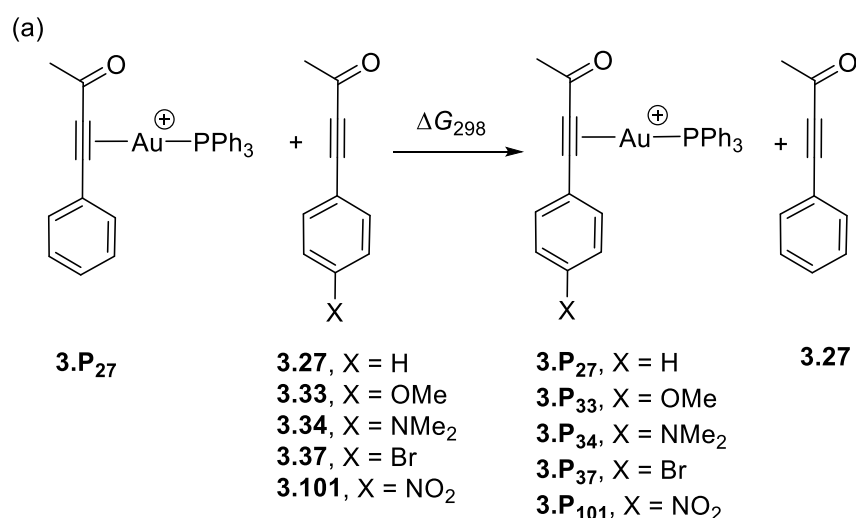


Figure 116. a) Isodesmic reaction used to calculate affinity of alkynes for gold. Energies are Gibbs energies at 298.15 K at the D3(BJ)-PBE0/def2-TZVPP//BP86/SV(P) level with COSMO solvation in CH₂Cl₂. b) Linear free energy relationship between the calculated change in free energy against Hammett parameter σ_p . Dashed line shows fit to a least mean squares linear regression ($R^2 = 0.92$).

To provide experimental evidence for the difference in ynone coordination, $^{31}\text{P}\{^1\text{H}\}$ NMR spectra were recorded of the various yrones (**3.27**, **3.33**, **3.34** and **3.37**) and gold triflimide in a 10:1 substrate:gold ratio (Figure 117). The $^{31}\text{P}\{^1\text{H}\}$ NMR spectra of 4-Br ynone **3.37** (Spectrum a), gave almost no indication of gold(I) coordination, with the most intense resonance present consistent with the gold(I) catalyst (Spectrum e). The DFT calculations predicted that 4-OMe and 4-NMe₂ yrones (**3.33** and **3.34**) had a higher gold(I) affinity than ynone **3.27**. The $^{31}\text{P}\{^1\text{H}\}$ NMR spectra

provided evidence of this, with the spectra of either ynone (Spectra c and d) showing no resonances consistent with the uncoordinated catalyst.

A minor resonance was observed in all spectra at $\delta_P \approx 37$ ppm, which by analogy with the spectra of the amide- and ester-substituted alkynes previously discussed (Figure 114), was assigned as the $\eta^2(\pi)$ alkyne coordinated complex (**3.P**). In the spectra of phenyl and 4-OMe substituted ynones (**3.27** and **3.33**, Spectra b and c) a series of resonances at $\delta_P = 41\text{--}43$ ppm were observed, suggesting the unselective formation of a series of unidentified complexes.

The $^{31}\text{P}\{^1\text{H}\}$ NMR spectra of 4-NMe₂ ynone **3.34** (Spectrum d) showed a resonance at $\delta_P = 41.9$ ppm, which suggests the selective formation of a single complex. A mass spectrum was recorded of the NMR sample with **3.34**, and a peak in the positive mode spectrum was observed at an m/z of 833.2579, which is consistent for a formulation of $[(\text{PPh}_3)\text{Au}(\mathbf{3.34})_2]^+$ demonstrating that two molecules of **3.34** were incorporated with the gold(I) cation, the precise identity of which was studied further (Section 3.4.3).

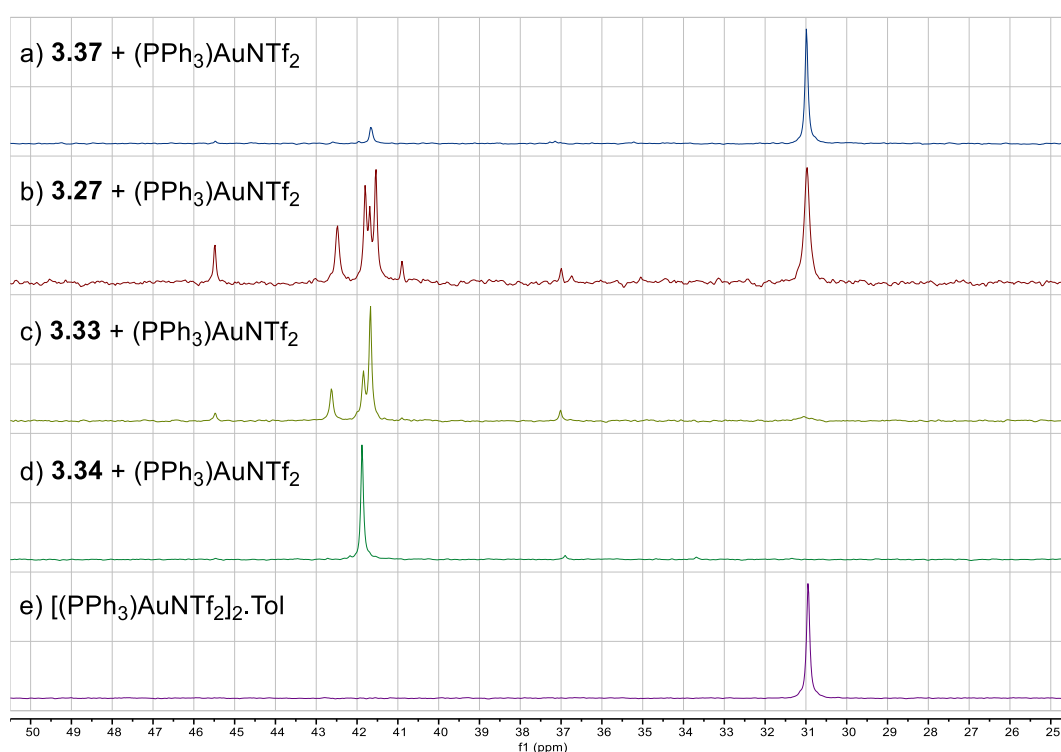


Figure 117. $^{31}\text{P}\{^1\text{H}\}$ NMR spectra recorded at 162 MHz in CD_2Cl_2 , with various ynones (**3.27**, **3.33**, **3.34** and **3.37**) in a 10:1 ratio of substrate:gold.

3.4.3 Ynone dimerisation

To identify the gold(I) complex formed from the dimerisation of 4-NMe₂ ynone **3.34**, described in Section 3.4.2, attempts were made to isolate the complex *via* crystallisation; however, this was unsuccessful. Different solvents and counteranions were used, however all attempts resulted in the decomposition of the complex, and the formation of either gold nanoparticles or a gold mirror on the surface of the glassware.

Instead, the complex was prepared in a stoichiometric fashion on a scale suitable for ¹³C and 2D NMR analysis, by dissolving ynone **3.34** and gold triflimide (in a 2:1 ratio) in CD₂Cl₂ in a sample vial and transferring the solution directly into an NMR tube. The ¹³C{¹H} NMR spectra showed no alkyne resonances which confirmed that both equivalents of ynone **3.34** had been structurally modified (Figure 118). Also notable was the presence of only one resonance consistent with a ketone functionality at $\delta_c = 202.3$ ppm. Finally, two different resonances were observed for the dimethylamino groups ($\delta_c = 40.1$ and 40.2 ppm) which showed that the two ynone equivalents were unsymmetrically modified.

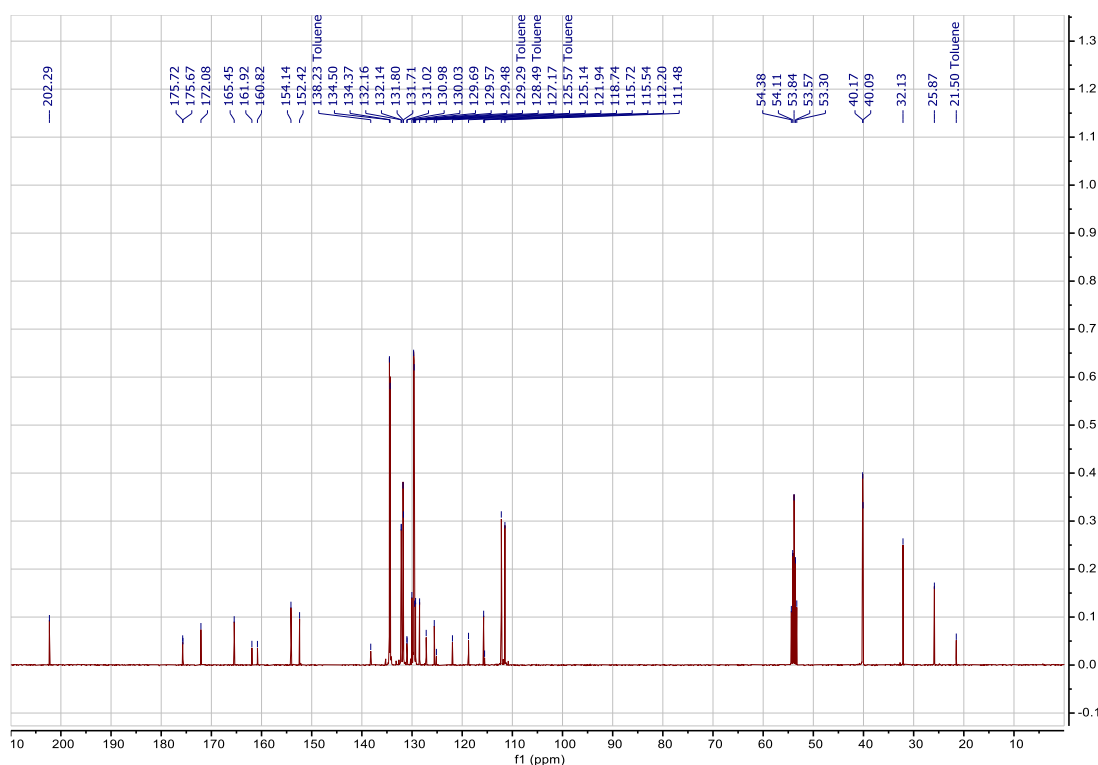


Figure 118. ¹³C{¹H} NMR spectra recorded at 100 MHz in CD₂Cl₂, of the dimer complex formed from ynone **3.34** and gold triflimide. Note that toluene is present due to its inclusion in the crystal structure of gold triflimide.

On the basis of these data, it was proposed that the dimer species was a gold(I) pyrylium complex **3.102** (Figure 119a). A plausible mechanism was suggested (Figure 119b) in which nucleophilic attack from the alkyne of ynone **3.34** into the $\eta^2(\pi)$ gold(I) ynone complex **3.103** (**3.103** \rightarrow **3.104**) results in carbocation intermediate **3.104**. The carbonyl of intermediate **3.104** cyclises *via* a 6-membered transition state (**3.104** \rightarrow **3.102**) to give the suspected pyrylium complex (**3.102**). The proposed structure of pyrylium complex **3.102** was consistent with the $^{13}\text{C}\{^1\text{H}\}$ NMR data discussed (Figure 118), with no alkyne carbons remaining, and one ketone remaining unaltered.

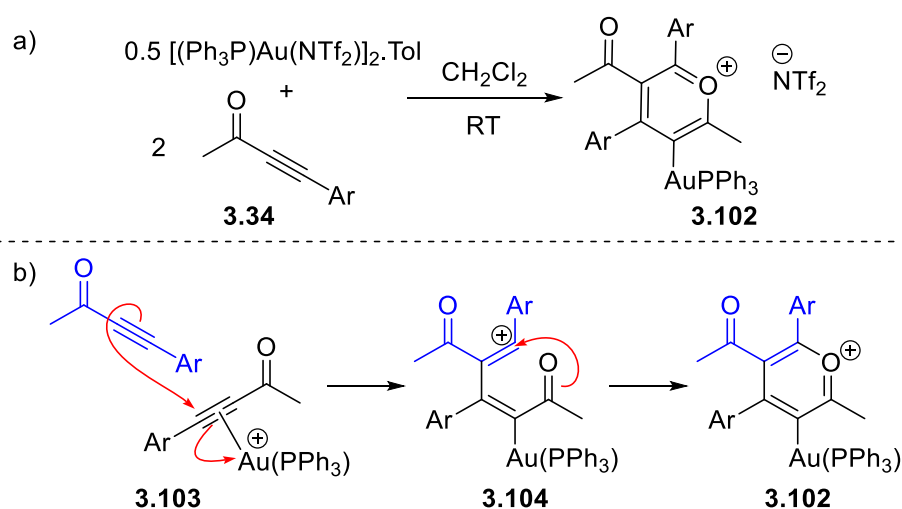


Figure 119. a) Formation of pyrylium complex **3.102**. b) Plausible mechanism for the formation of **3.102**. Triflimide anion omitted for clarity. Ar = C_6H_4 -4-NMe₂.

To confirm the structural proposal for **3.102**, the $^{13}\text{C}\{^1\text{H}\}$ NMR data was fully assigned using HMBC and HSQC spectra. Key structural assignments are shown in Figure 120. The chemical shifts of the resonances at $\delta_c = 165.6$, 172.1 and 175.7 ppm (d , $^3J_{\text{CP}} = 5.5$ Hz) matched the literature data of known organic pyrylium salts for the C-2, C-4 and C-6 positions.^{217,218} The resonance at $\delta_c = 161.4$ ppm (d , $^2J_{\text{CP}} = 111.0$ Hz) exhibits a large carbon-phosphorus coupling constant, which is indicative of the presence of a gold–carbon bond. The data are also consistent with the corresponding metal-bound carbon atom of $[(\text{PPh}_3)\text{Au}(\text{C}_6\text{H}_2\text{-2,4,6-Me}_3)]$ (δ_c 169.8, $^2J_{\text{PC}} = 111.2$ Hz), as reported by Croix *et al.*²¹⁹

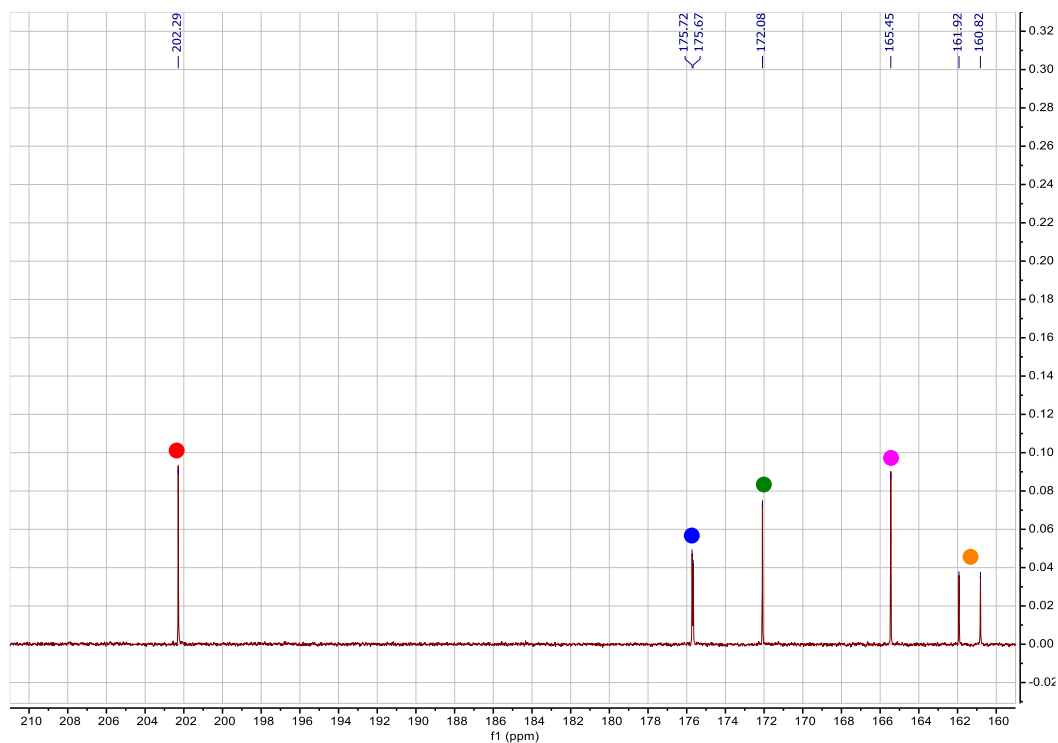
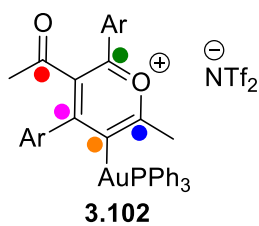


Figure 120. $^{13}\text{C}\{^1\text{H}\}$ NMR spectra recorded at 100 MHz in CD_2Cl_2 of pyrylium complex **3.101**. Selected assignments are highlighted.

An alternative mechanism for the gold(I)-catalysed dimerisation of ynones has been previously reported by Burés and co-workers, as an intermediate in the gold(I)-catalysed transposition of ynones (Figure 121a, for further details see Section 1.2.3).^{153,220} Using the data from both kinetic and computational studies, the authors proposed that the mechanism proceeded *via* a cyclic acetal intermediate **3.107** (Figure 121b), which was formed from the nucleophilic attack of a carbonyl of one ynone, into the alkyne of a $\eta^2(\pi)$ alkyne-coordinated ynone (**3.105**), followed by intramolecular cyclisation (**3.106** \rightarrow **3.107**). It was therefore decided to use DFT calculations to explore the factors that control acetal formation (*e.g.* **3.107**) or pyrylium formation (*e.g.* **3.102**).

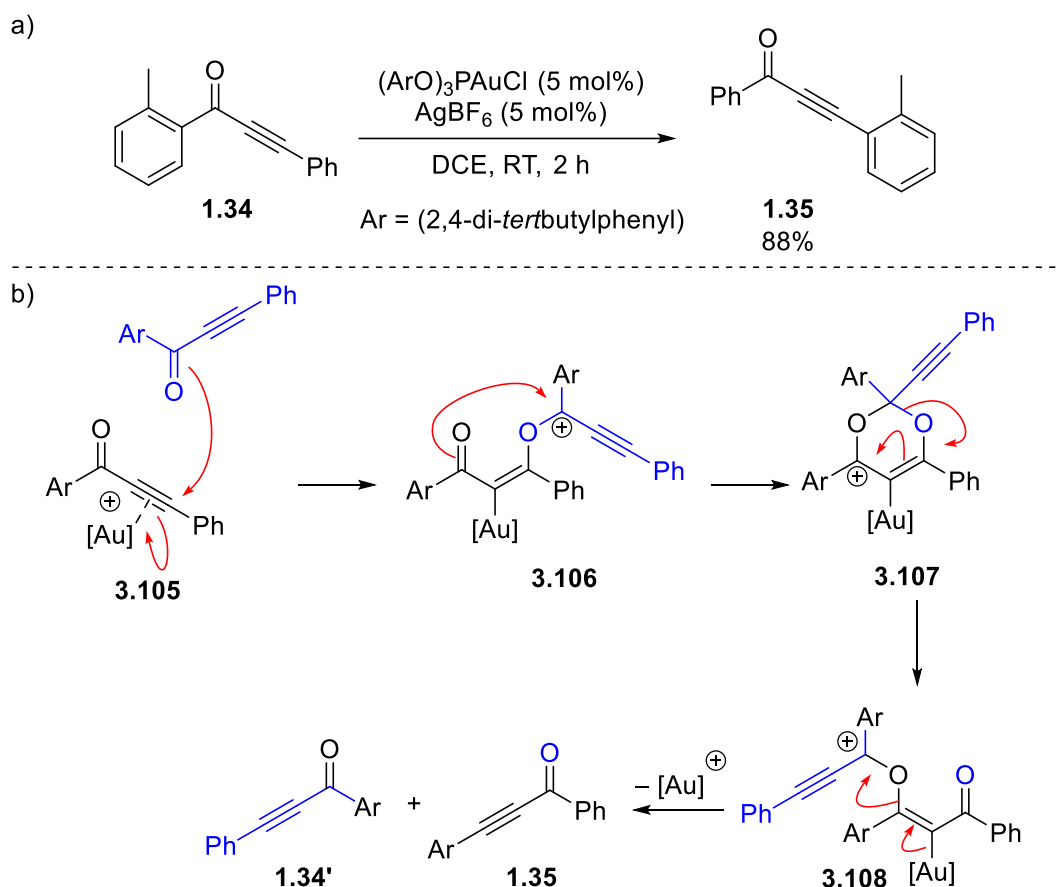


Figure 121. a) Gold(I)-catalysed ynone transposition, reported by Gevorgyan *et al.*²²⁰ b) A likely mechanism for the gold(I)-catalysed transposition of ynone, identified by Burés *et al.*¹⁵³ [Au] = IPrAu⁺

The energies of four potential pathways were calculated (Figure 122), with both *O*-attack and *C*-attack considered into carbons 1 and 2 (as labelled) of $\eta^2(\pi)$ gold(I) ynone complex **3.P₃₄**. State **3.AK**, the combined energies of **3.34** and **3.P₃₄**, was chosen as the reference state for the calculated energies. A pathway was found for the formation of pyrylium complex **3.102**, following the mechanism proposed in Figure 119b. *C*-attack into the C-1 position of $\eta^2(\pi)$ gold(I) ynone complex **3.P₃₄** through transition state **3.TS_{AK-102}** was calculated at an energy of +71 kJ mol⁻¹. The resultant intermediate **3.104** wasn't able to be found. Geometry optimisation of **3.104** resulted in the formation of complex **3.102**, likely due to the presence of a low-lying transition state for cyclisation. The formation of pyrylium complex **3.102** was found to be highly exergonic at an energy of -201 kJ mol⁻¹.

Alternatively, a transition state for *O*-attack into the C-1 position of $\eta^2(\pi)$ gold(I) ynone complex **3.P₃₄** was found (**3.TS_{AKAL}**) at an energy of +69 kJ mol⁻¹, to give cation **3.AL** at +27 kJ mol⁻¹. The energies of **3.TS_{AK-102}** and **3.TS_{AKAL}** are effectively the same in energy, and it could therefore be expected that both pathways are in operation. However, if it is considered that all states are in

equilibrium, pyrylium formation (**3.102**) is likely irreversible due the thermodynamic stability of the complex.

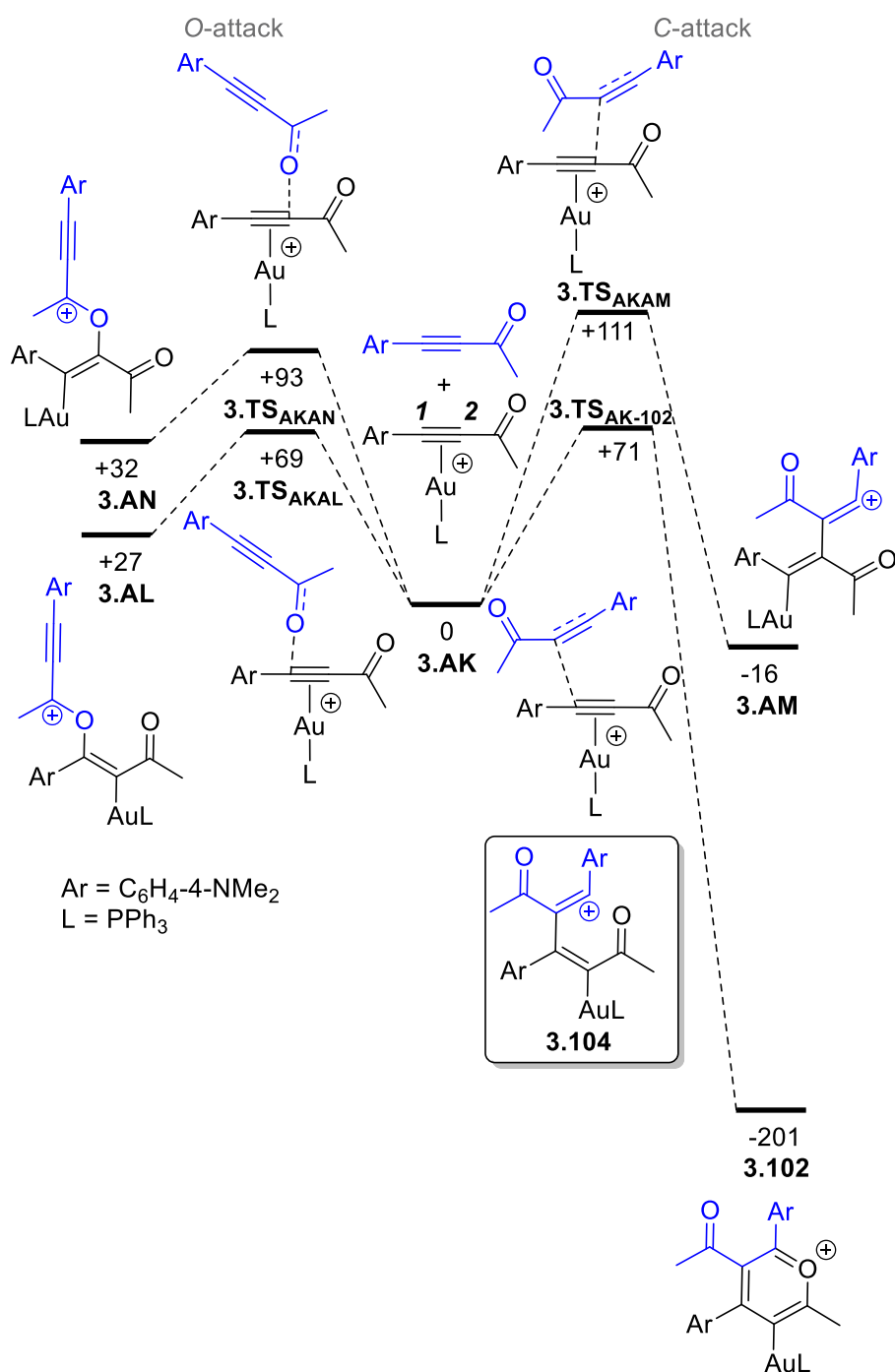


Figure 122. DFT-calculated pathway for the dimerisation of ynone **3.34**. Energies are Gibbs energies at 298.15 K in kJ mol⁻¹ at the D3(BJ)-PBE0/def2-TZVPP//BP86/SV(P) level of theory with COSMO solvent correction in CH₂Cl₂.

Transition states were also found for *C*-attack (**3.TS_{AKAM}**) and *O*-attack (**3.TS_{AKAN}**) into the C-2 position of η²(π)-gold(I) ynone complex **3.P₃₄**, calculated at +111 and +93 kJ mol⁻¹ respectively.

These transition states are much higher energy than addition into the C-1 position (**3.TS_{AK-102}** and **3.TS_{AKAL}**) and are therefore considered to be inaccessible. It is likely that the energies of C-2 attack are higher due to the reduced electrophilicity of the C-2 position (as compared to C-1). $\eta^2(\pi)$ -gold(I) coordination to unsymmetrical alkynes results in “slippage” of the gold(I) cation, which causes an uneven electron distribution across the alkyne.^{142,145} Slippage occurs to give the carbocation which is the most stable. In the instance of ynone **3.34**, the formation of a carbocation in the C-1 position of $\eta^2(\pi)$ gold(I) ynone complex **3.P₃₄'** would satisfy the electronic preference of the ketone and be stabilised by the aryl group (Figure 123), and hence be more activated towards nucleophilic attack.

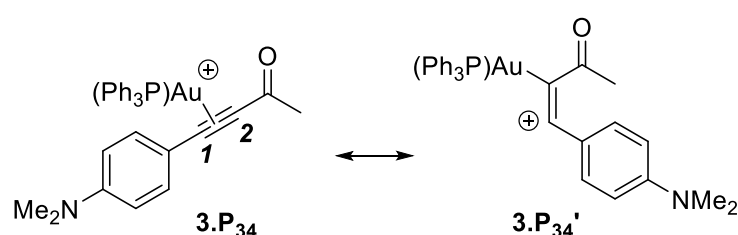
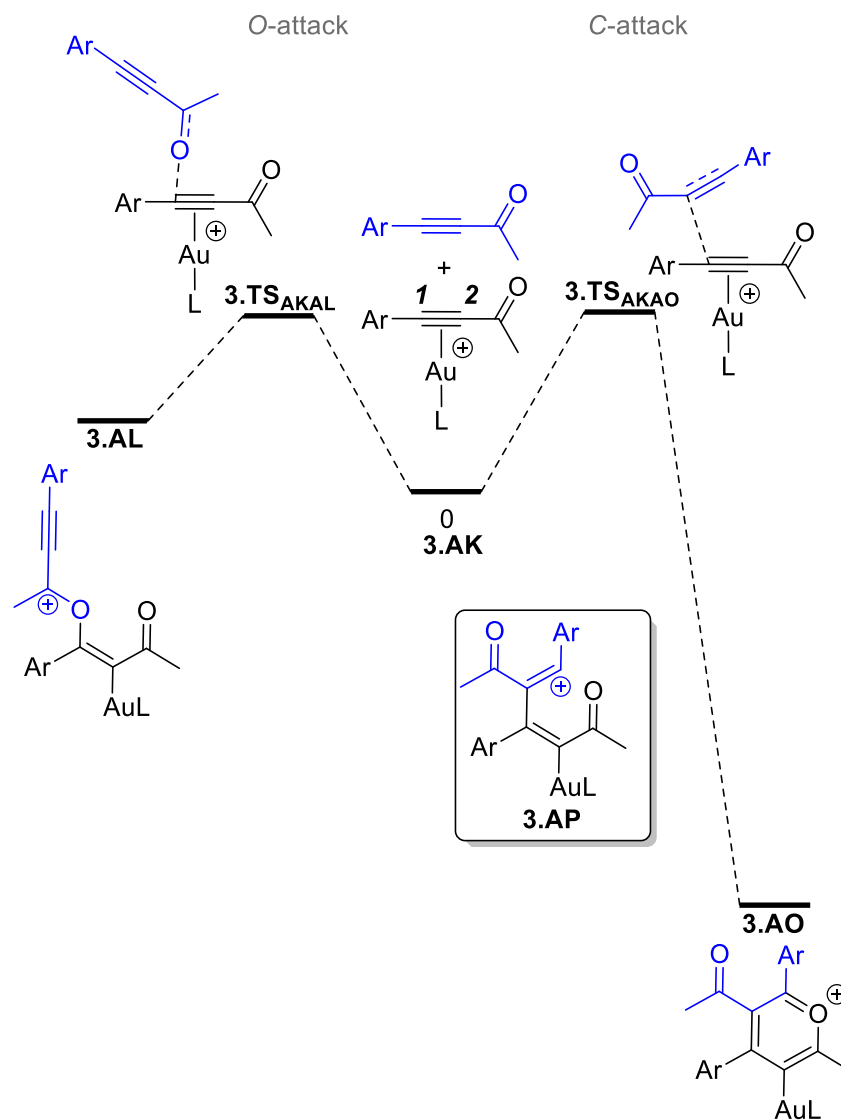


Figure 123. Resonance structures of $\eta^2(\pi)$ gold(I) ynone complex **3.P₃₄**.

When the $^{31}\text{P}\{^1\text{H}\}$ NMR spectra were recorded of the different yrones (Figure 117), unselective complex formation was observed in the spectra of phenyl- and 4-OMe substituted yrones **3.27** and **3.33** (Spectra b and c). The dimerisation DFT calculations were therefore repeated using these two yrones (**3.27** and **3.33**) to establish the cause of this (Table 10). In both cases, the transition state of *O*-attack (**3.TS_{AKAL}**) was lower in energy than *C*-attack (**3.TS_{AKAO}**). Therefore, it is more likely that the corresponding intermediate **3.AL** would be formed preferentially. It is proposed that a multitude of different unidentified reactions from **3.AL** could take place, to account for the many species observed in the $^{31}\text{P}\{^1\text{H}\}$ spectra.

Finally, the formation of a pyrylium complex from 4-NMe₂ ynone **3.34** was considered, using different gold(I) catalysts (Table 10). The identity of the gold(I) ligand, either PMe₃, IPr or JohnPhos, wasn't calculated to have a significant effect on pyrylium formation.

Table 10. DFT-calculated pathway for the dimerisation of different ynones and gold(I) cations. Energies are Gibbs energies at 298.15 K in kJ mol⁻¹ at the D3(BJ)-PBE0/def2-TZVPP//BP86/SV(P) level of theory with COSMO solvent correction in CH₂Cl₂.



Ar	L	3.TS _{AKAO}	3.TS _{AKAL}	3.AL	3.AO
C ₆ H ₄ -4-NMe ₂ (3.43)	PPh ₃	+71	+69	+27	-201
C ₆ H ₅ (3.27)	PPh ₃	+75	+63	+23	-224
C ₆ H ₄ -4-OMe (3.33)	PPh ₃	+69	+61	+20	-220
C ₆ H ₄ -4-NMe ₂ (3.43)	PMe ₃	+61	+70	+33	-197
C ₆ H ₄ -4-NMe ₂ (3.43)	IPr	+77	+77	+33	-198
C ₆ H ₄ -4-NMe ₂ (3.43)	JohnPhos	+70	+75	+37	-199

3.4.4 Pirylium complex reactivity

With the formation of pyrylium complex **3.102** established using NMR and DFT methods, attempts were made to study the reactivity of the complex. Benzopyrylium complexes **3.111** (Figure 124) are proposed as intermediates in the gold(I) chemistry of *o*-alkynyl benzaldehyde species (**3.109**),²²¹ formed *via* the intramolecular cyclisation of the carbonyl into $\eta^2(\pi)$ alkyne coordinated complex (**3.110**), and was therefore used as the basis to explore the chemistry of pyrylium **3.102**.

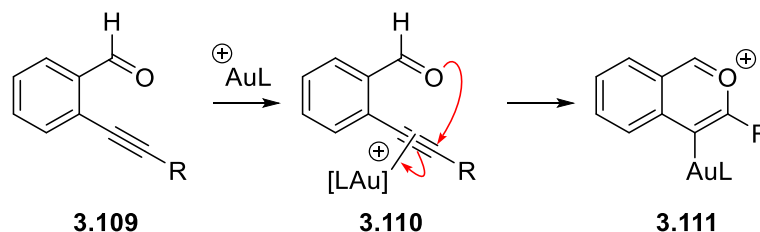


Figure 124. Formation of benzopyrylium complex **3.111**, from *o*-alkynyl benzaldehydes **3.109**.

Hammond and co-workers reported the gold(I) catalysed annulation of vinyl ethers with *o*-alkynyl benzaldehydes (**3.109**)²²² When ynone **3.34** was treated under the same conditions with vinyl enol ether **3.112**, no reaction was seen after 1 hour at room temperature (Figure 125). The reaction was heated to 50 °C overnight, however, again no reaction was observed, with the crude ¹H NMR spectrum only showing resonances corresponding to the unreacted ynone **3.34**. The mechanism for the formation of **3.113** and **3.114** (two potential products), based on the proposal of Hammond and co-workers, are shown (Figure 125b and c).

Both mechanisms (Figure 125b and c) start with a Diels–Alder reaction between pyrylium complex **3.102** with ethyl vinyl ether **3.112** (**3.115** → *rac*-**3.116** and **3.120** → *rac*-**3.121**). Pyrylium complex **3.102** contains two highly electron-rich aryl groups, which increases the electron density of the usually electron-deficient pyrylium core. It is this effect that likely reduces the ability of complex **3.102** to react with electron-rich dienophiles.

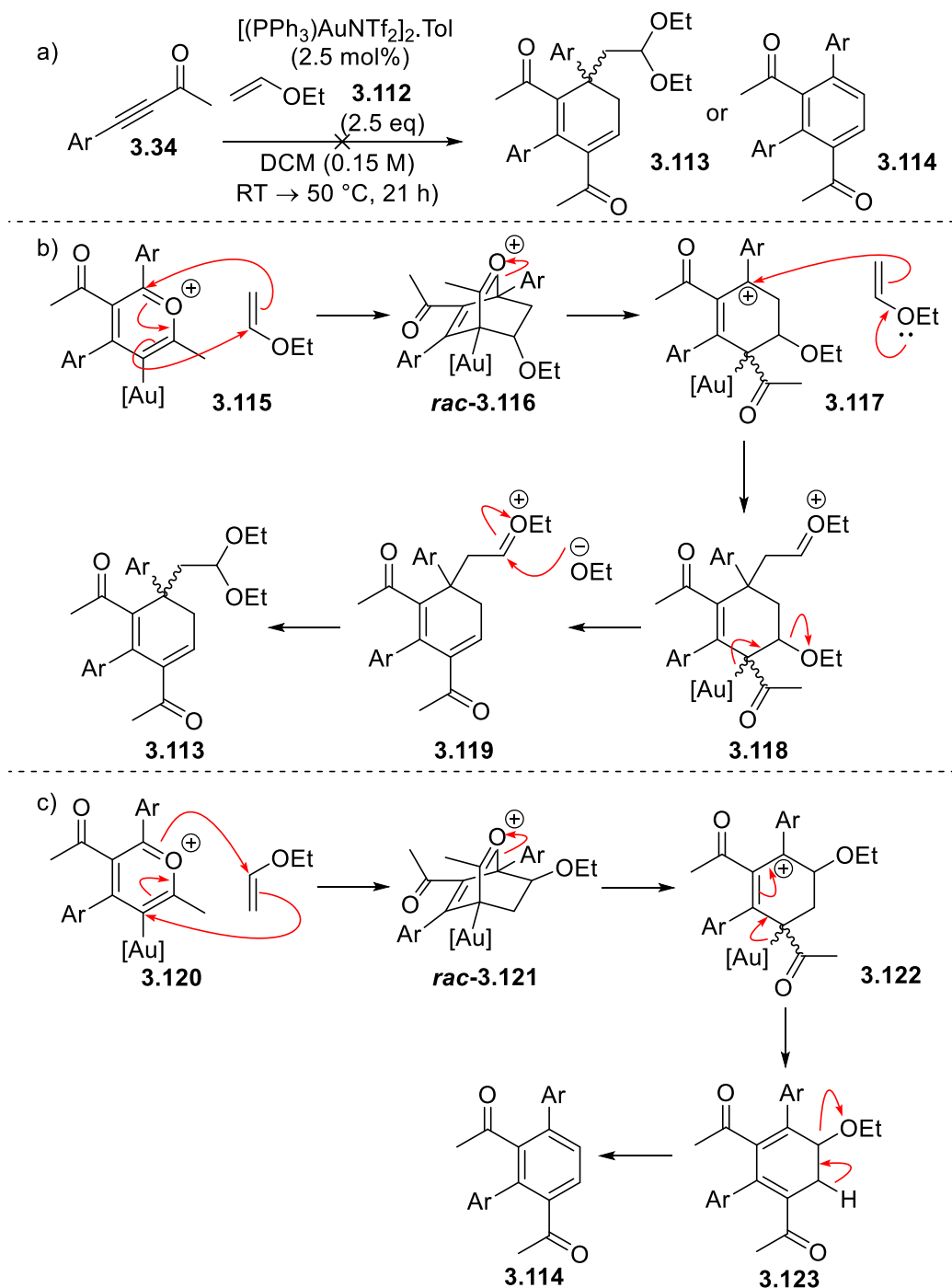


Figure 125. a) Attempted reaction with ethyl vinyl ether **3.112**, as reported by Hammond and co-workers.²²² b) Proposed mechanism for the formation of **3.113**. c) Proposed formation for the formation of **3.114**. Ar = C₆H₄-4-NMe₂.

It was considered that a less electron-rich dienophile might be able to react with pyrylium complex **3.102**. A procedure was published by Asao *et al.* for the reaction of *o*-alkynyl benzaldehyde **3.109** with terminal and internal alkynes, using catalytic gold(III) chloride.²²³ The authors conditions were replicated with ynone **3.34** and phenylacetylene **3.13** (Figure 126).

Again, the crude ^1H NMR spectra showed only unreacted starting material. The ESI mass spectrum recorded of the sample did show a minor peak for a mass consistent with the desired product, however, the spectrum was dominated by the unreacted ynone **3.34**.

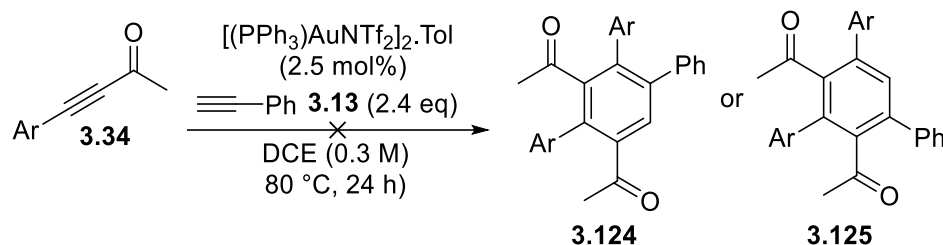


Figure 126. Attempted reaction of ynone **3.34** (via pyrylium complex **3.102**) with phenyl acetylene **3.13**, as reported by Asao *et al.*²²³ Ar = C₆H₄-4-NMe₂.

Michelet and co-workers developed a method for the reduction of the benzopyrylium complexes (**3.109**) intermediates using Hantzsch ester hydride (HEH).²²⁴ The conditions were used to reduce pyrylium complex **3.102** to either **3.126** or **3.127** (Figure 127).

The crude ESI mass spectrum did show a minor peak consistent with the mass of the desired products (**3.126** or **3.127**), however, a mass for *trans*-alkene **3.128** was also observed, from the direct reduction of ynone **3.34**. During purification, no desired product (**3.126** or **3.127**) was able to be isolated, however a 32% yield of **3.128** was found as a mixture with coeluted oxidised HEH **3.129**. The yield of 32% was calculated from the ratio of **3.128**:**3.129** in the ^1H NMR spectra.

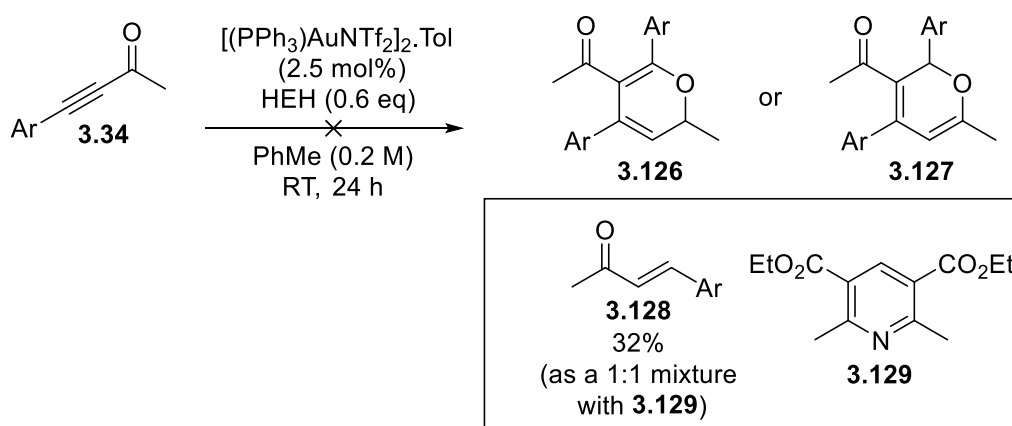


Figure 127. Attempted reduction of pyrylium complex **3.102** with HEH, as reported by Michelet and co-workers.²²⁴ Ar = C₆H₄-4-NMe₂.

The HEH reduction reaction highlighted that the desired products might form from the initial amounts of pyrylium complex **3.102** available at the start of the reaction. However, after protodemetalation, the gold(I) catalyst coordinates to another molecule of ynone **3.34**, and the

$\eta^2(\pi)$ gold complex **3.P₃₄** can react preferentially with available nucleophiles. It was therefore decided to stop exploring the potential reactivity of pyrylium complex **3.102**.

3.5 Concluding Remarks

An intermolecular gold(I)-catalysed coupling reaction between indoles and carbonyl substituted alkynes has been described, to give vinylindole species. Whereas trace Brønsted acid will typically promote *bis*-addition of another equivalent of indole, the carbonyl group of the alkyne coupling partner (*e.g.* ynone **3.27**) restricts further addition. DFT calculations demonstrated that there is both a thermodynamic and kinetic penalty to the second addition when using the carbonyl substituted alkynes (in comparison to simple acetylenes), due to the intermediate carbocations being destabilised.

The preference for gold(I) coordination between the indole substrates (**3.16** and **3.48**) and ynone **3.27** was explored using both DFT calculations and $^{31}\text{P}\{^1\text{H}\}$ NMR spectroscopy. The electron-rich indole moiety was found to be a better ligand for gold(I). This was proposed as the major reason that the intermolecular reactions are more challenging than the intramolecular counterparts (Figure 78), due to the need for the $\eta^2(\pi)$ alkyne complex for catalysis.

Further exploration of the gold(I) coordination to different carbonyl-substituted alkynes revealed that the electronic properties of both the aryl and carbonyl groups has a significant effect on gold(I) coordination. The $^{31}\text{P}\{^1\text{H}\}$ NMR spectrum recorded using 4-NMe₂-substituted ynone **3.34** revealed the formation of a new complex. This was identified as a novel gold(I)-pyrylium salt (**3.102**), from the dimerisation of 4-NMe₂ ynone **3.34**. DFT calculations were used to study the formation of **3.102**, which was likely formed by nucleophilic attack of the electron-rich alkyne of **3.34** into the $\eta^2(\pi)$ alkyne gold(I) complex **3.P₃₄**.

The reactivity of complex **3.102** was explored, however it found that only trace product formation was observed (using ESI mass spectrometry of the crude reaction mixtures) under the conditions used. It was proposed that the electron-rich nature of the aryl substituents of **3.102** lowers the reactivity of the complex.

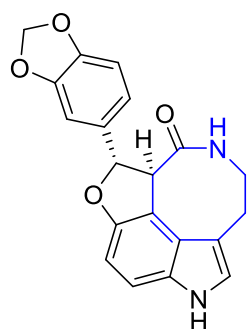
The work described within this section is the subject of a publication.²²⁵

Chapter 4. Successive Ring Expansion (SuRE)

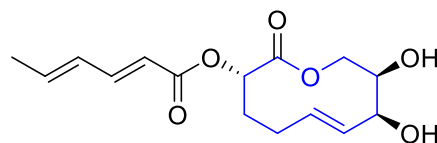
4.1 Introduction

4.1.1 Medium-sized rings and macrocycles

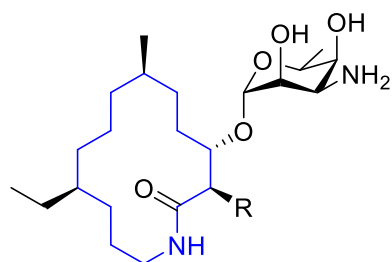
Medium-sized rings and macrocycles are cyclic molecules which are defined as containing 8–11 atoms, or greater than 12 atoms respectively. There has been great interest in medium-ring containing and macrocyclic molecules due to their many applications, for example in medicinal chemistry,^{226–233} chemical synthesis,^{234–236} or as chiral shift reagents.²³⁷ Selected examples (**4.1–4.8**) are shown in Figure 128, with the medium-sized ring/macrocyclic core highlighted.



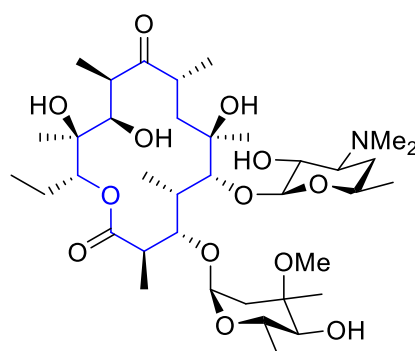
Decursivine **4.1**
(antimalarial)



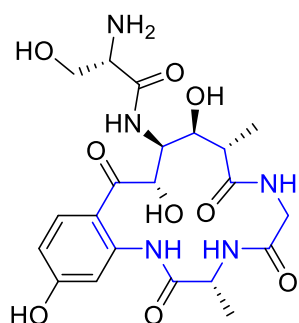
Pinolidoxin **4.2**
(pytotoxin)



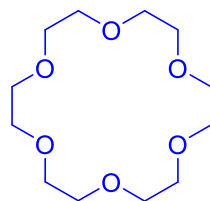
Fluvirucine A₁, **4.3** R = Me
A₂, **4.4** R = CH(OH)CH₃
(antibiotic)



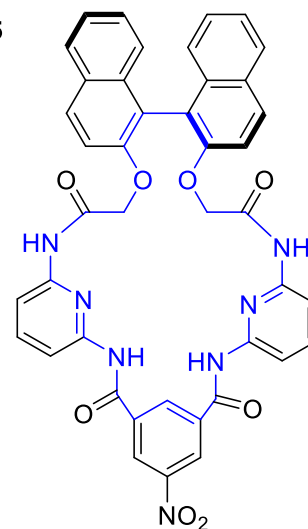
Erythromycin **4.5**
(antibiotic)



Solomonamide A **4.6**
(anti-inflammatory activity)



[18]-Crown-6 **4.7**
(Potassium ion chelater)



4.8
(chiral shift reagent)

Figure 128. Select examples of medium-ring containing and macrocyclic molecules, with the macrocyclic core highlighted in blue.

4.1.2 Synthesis of medium-sized rings and macrocycles

Due to the wide utility of medium-sized rings and macrocycles, efficient methods for their synthesis are desirable. However, there are significant synthetic challenges associated with their

synthesis. End-to-end cyclisations, for example *via* a simple S_N2 process or nucleophilic addition into carbonyl compounds, are generally very efficient when making 5- and 6-membered rings (Figure 129a). However, reactions using longer linear molecules tend to suffer problems with competing intermolecular dimerisation (**4.11** \rightarrow **4.13**) and higher order polymerisation reactions, rather than the desired intramolecular cyclisation reaction (**4.11** \rightarrow **4.12**, Figure 129b).^{238,239}

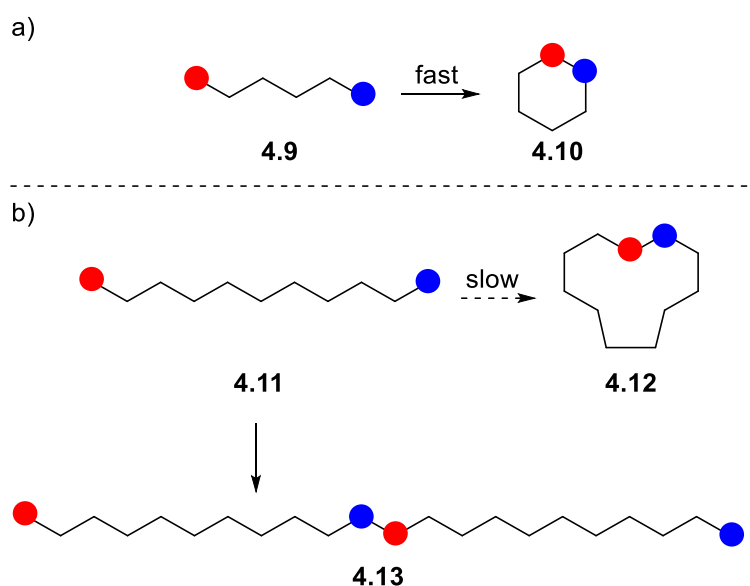


Figure 129. a) General representation of the end-to-end cyclisation to form 6-membered ring **4.10**. b) Undesired dimerisation during the cyclisation of 11-membered linear starting material **4.11**.

The challenges associated with the synthesis of medium-sized rings and macrocycles *via* end-to-end cyclisation can be attributed to different effects. Ring strain can be described as the combination of angle strain (deviation from the optimal geometry) or transannular strain (caused by clashing interactions of atoms within close proximity).^{240,241} Medium-sized rings are considerably more strained than smaller, normal sized rings as the molecules are distorted from the ideal geometry to minimise the transannular interactions present. The higher strain energy present increases the transition state energy of cyclisation and therefore oligomerisation can become more favourable. Ring strain is largely relieved when the ring size is 12 or larger,^{240,241} however end-to-end macrocyclisation is also challenging as the probability of intramolecular collisions are reduced due to the long chain length, and cyclisation of long chains is usually associated with a relatively large decrease in entropy, compared with analogous shorter chain cyclisation reactions.²³⁸

Methods have been reported which can improve the yields of large-ring forming reactions.²⁴² These typically involve using very dilute conditions, with concentrations in the millimolar range often reported.^{243–248} This approach can lead to improvements in the yields of cyclisation reactions, but the high dilution conditions can be a significant barrier to scaling up the reactions due to the large volumes of solvent required. This might also be a safety concern, and there are economic costs and impact to the environment also to consider with the use of large quantities of solvent. Other methods that have been successful in the cyclisation of linear substrates have been using resin-supported molecules (so called ‘pseudo’ high dilution),^{249,250} and using substrates which are templated or conformationally biased to favour the cyclisation reaction.^{251,252}

4.1.3 Ring Expansion Reactions

A method that can overcome some of the synthetic challenges summarised above relies on increasing the size of rings that are already present, a method often referred to as ring expansion. These reactions can be used for the synthesis of both medium-sized rings and macrocycles. One such method is based on the fragmentation of bicyclic molecules, and such reactions are commonly driven by the loss of a good leaving group (Groβ- or Eschenmoser-type fragmentations).

For example, Reese *et al.* described the ring expansion of fused bicyclic ketone **4.14** (Figure 130).²⁵³ After epoxidation of the alkene, further treatment of epoxide **4.15** with mesitylene-2-sulfonohydrazide under acidic conditions resulted in an *in situ* Eschenmoser fragmentation reaction,^{254,255} liberating nitrogen gas and breaking the internal C–C bond, resulting in the formation of 10-membered cycloalkynone **4.18** in a 69% yield. This method was suitable for the synthesis of a 9-membered derivative, however the smaller 8-membered cycloalkynone was unable to be made using this method.

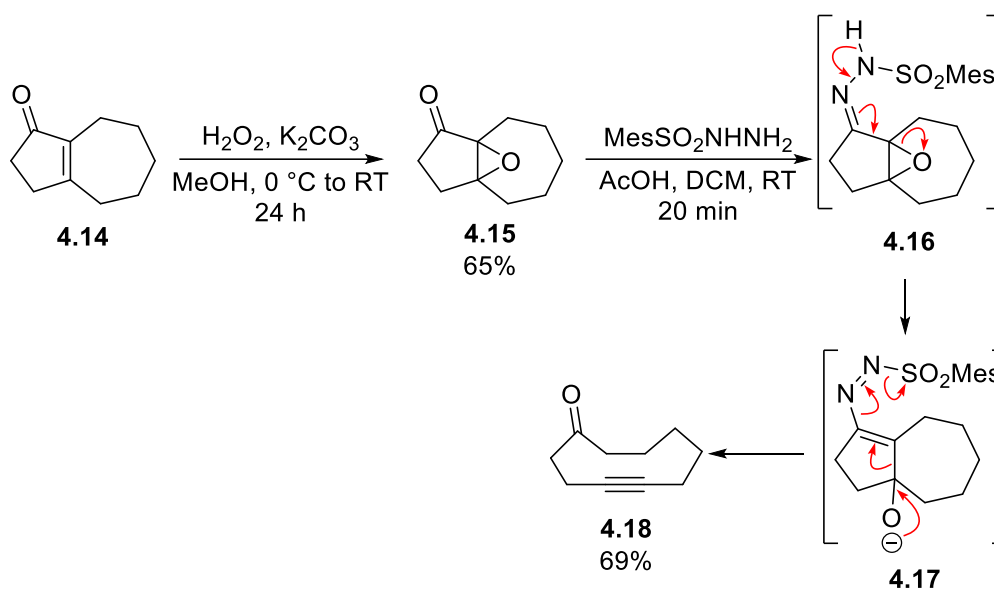


Figure 130. Eschenmoser fragmentation reported by Reese *et al.* resulting in 10-membered cyclic alkyne **4.18**.²⁵³

Another common method for ring expansion with a broad range of different examples, is known as sidechain insertion, with two-electron and radical variations both well established.

For example, an efficient radical method was reported by Dowd *et al.* for the expansion of cyclic β -ketoesters **4.19** (Figure 131).²⁵⁶ Their chemistry uses tributyltin hydride to abstract a halogen on an alkyl chain, situated for a 5-*exo-trig* cyclisation into a ketone (**4.22**). Bicyclic radical **4.23** can fragment, followed by ring expanded radical **4.24** abstracting a hydrogen from either starting material **4.19** or tributyltin hydride, resulting in desired product **4.20** and further propagation.

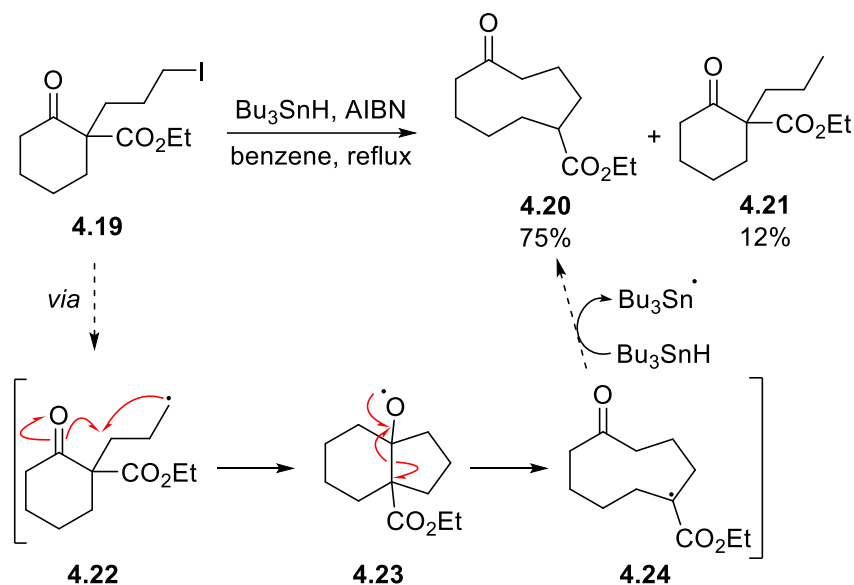


Figure 131. Sidechain ring expansion using a radical addition pathway as reported by Dowd *et al.*²⁵⁶

In previous work by Beckwith *et al.*, it was shown that when a radical was generated on related cyclodecanone substrate **4.25**, a ring contraction was observed (Figure 132).²⁵⁷ Therefore, the evidence indicates that Dowd's ring expansion reaction was driven by the thermodynamic stability of the tertiary radical next to an ester group (in **4.24**), in comparison to the primary radical in **4.22**.

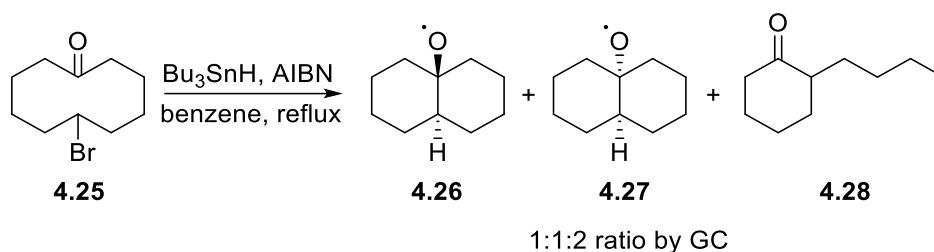


Figure 132. Ring contraction of cyclodecanone **4.25** reported by Beckwith *et al.*²⁵⁷

Another method to grow a cyclic molecule by sidechain insertion, is to use pericyclic reactions. Sigmatropic rearrangements are most frequently reported,²⁵⁸ however strategies utilising Diels–Alder reactions have been used as well.^{259–262}

An example of a [2,3]-sigmatropic ring expansion utilised a sulphur ylide in an iterative 3-atom ring expansion process reported by Schmid *et al.*²⁶³ Alkylation of cyclic thioether **4.29** with allyl bromide resulted in sulphonium bromide **4.30** which can be readily deprotonated to form the reactive ylide intermediate (**4.31**, Figure 133). Cyclisation of **4.31** *via* a [2,3]-sigmatropic rearrangement results in ring expanded products **4.33** and **4.34**. The allyl group alpha to the

sulphur atom is regenerated, which allowed for an iterative process that was repeated to successfully synthesise 17-membered macrocycles **4.38** and **4.38** in a 31% combined yield.

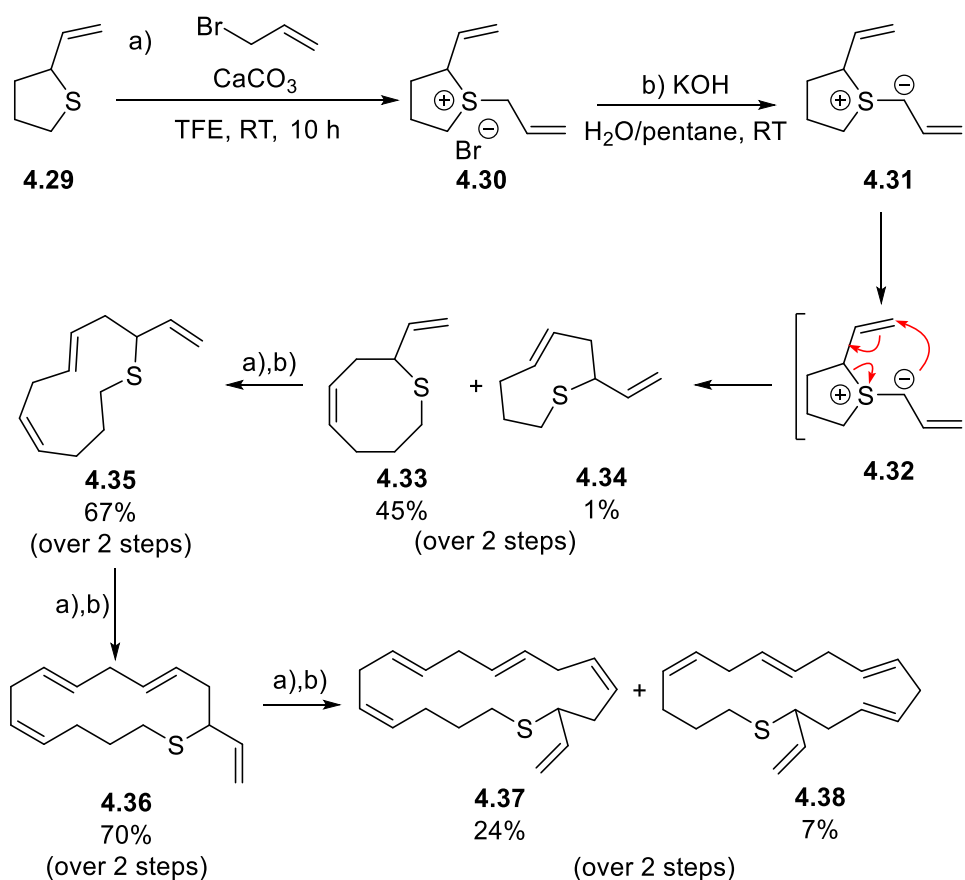


Figure 133. Iterative ring expansion *via* [2,3]-sigmatropic rearrangements of cyclic thioether reported by Schmid *et al.*²⁶³

Hesse and co-workers developed a series of methods for sidechain insertion ring expansion, based on intramolecular transamidation reactions (Figure 134).^{264–268}

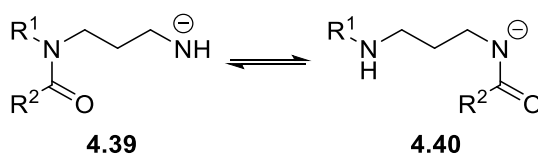


Figure 134. Representation of the transamidation equilibrium exploited by Hesse *et al.*

By alkylating lactams with aliphatic chains with a terminal primary amine, ring expansion was seen upon treatment with base. If the sidechain contained secondary amines in a suitable position (5-, 6- or 7- membered transition states are tolerated),²⁶⁸ it was possible to increase the ring-size further in one step.

This ring expansion method was referred to as a “zip” reaction in reference to how the linear chain closes. This series of reactions allowed for the synthesis of 21-membered lactam **4.45** in a high yield starting from 13-membered lactam **4.41** (Figure 135). The group even reported the synthesis of a 53-membered lactam from lactam **4.41** with a longer sidechain, although the reported characterisation data for the structure was limited.²⁶⁹

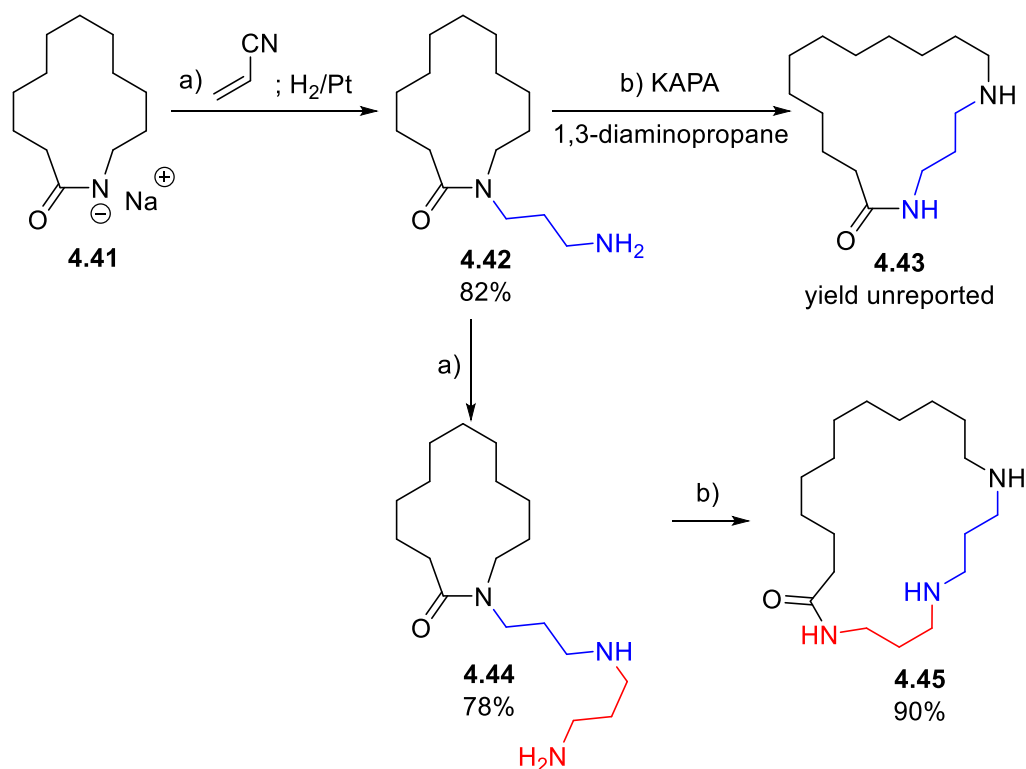


Figure 135. Transamidation “zip” reactions for ring expansion as reported by Hesse et al.²⁶⁴

An area where this method was particularly useful was in the formation of a macrocycle starting from a normal sized ring. A previous attempt within the Hesse group at expanding 7-membered lactam **4.46** into 11-membered product **4.47** with a single expansion proved unsuccessful (Figure 136a).²⁶⁸ It was proposed that the additional transannular strain within an 11-membered ring hindered the equilibrium of the transamidation, which then strongly favoured the ring opened isomer. However, by using a spermidine sidechain, it was possible to do a double ring expansion, increasing 6-membered barbiturate derivative **4.48** into 14-membered product **4.50**, via 10-membered intermediate **4.49** (Figure 136b).²⁷⁰

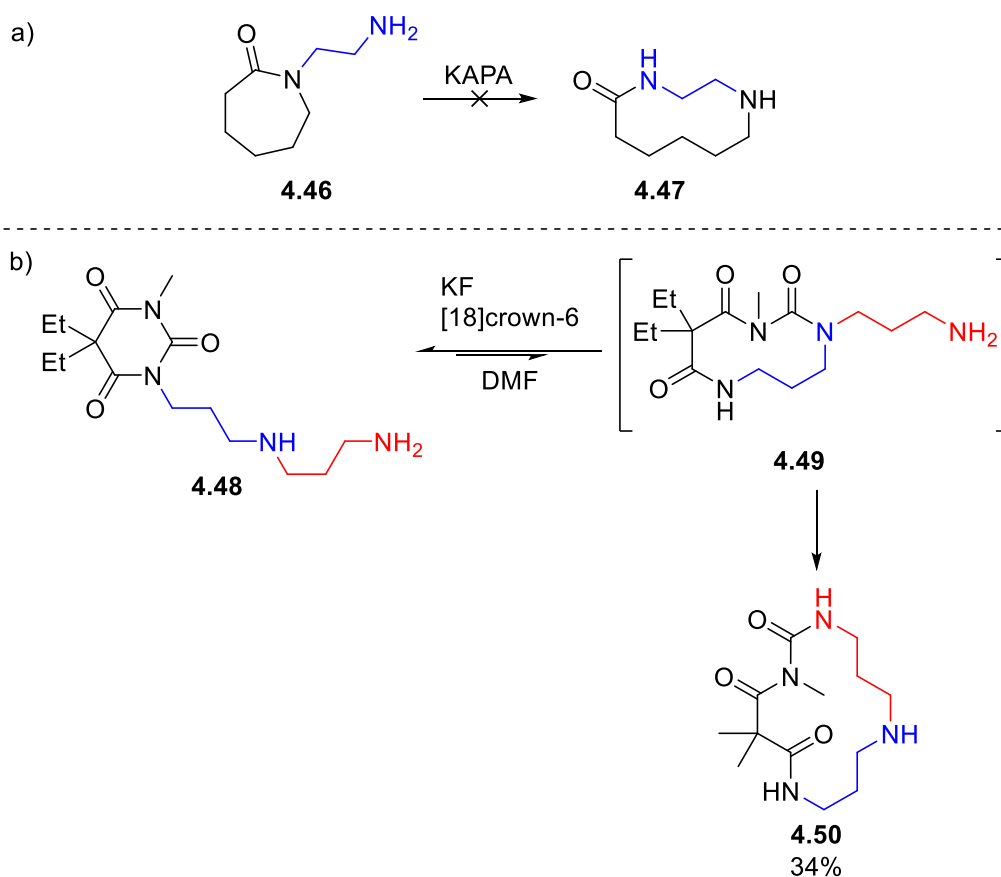


Figure 136. a) Unsuccessful 3-atom ring expansion of 7-membered lactam **4.46** reported by Hesse *et al.*²⁶⁸ b) Successful “zip” reaction of barbiturate derivative **4.48**, to yield 14-membered product **4.50**, reported by Hesse *et al.*²⁷⁰

Following a similar approach, Corey *et al.* developed a transesterification approach to ring expansion.²⁷¹ Lactones of varied ring sizes were synthesised with a (hydroxy)propyl side chain (**4.51–4.53**), which were then exposed to acidic or basic conditions. This proved to be insightful as a strong ring-size dependence was found, a theme which has been discussed throughout this section. It was shown that with a catalytic amount of *p*-toluenesulfonic acid, transesterification and ring expansion was only seen with an 8-membered ring or larger (**4.52** and **4.53**) which was proposed to be due to the release of ring strain upon ring expansion.

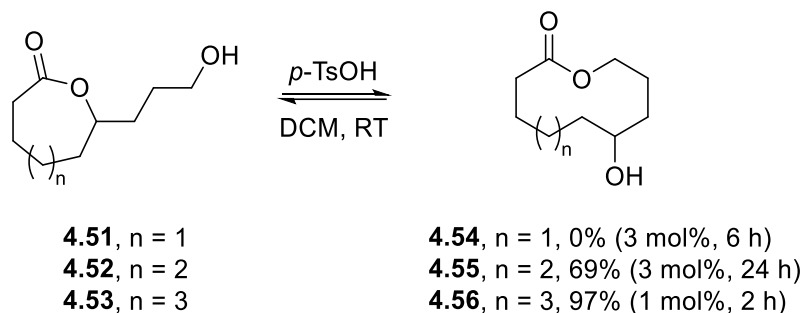


Figure 137. Ring size dependence in transesterification ring expansion reactions of lactones, as reported by Corey *et al.*²⁷¹

4.1.4 Use of DFT calculations to study Ring Expansion reactions

A common theme seen throughout ring expansion literature is the dependence on ring-size for the success of the reactions. To overcome the ring strain in the medium-sized ring products, another method to stabilise the product formed upon ring expansion is typically used, such as those discussed by the groups of Reese (Figure 130)²⁵³ and Dowd (Figure 131).²⁵⁶ Additionally, work into sidechain insertion using transamidation and transesterification reaction reported by Hesse (Figure 136),^{264–270} and Corey (Figure 137)²⁷¹ demonstrated that these reactions are likely in an equilibrium. Using DFT to calculate the relative energies of the species involved in ring expansion can therefore provide useful insight into the outcomes of these reactions.

Yudin and co-workers explored this during their synthesis of medium sized cyclic peptides (of the type **4.58**).²⁷² It was proposed that the insertion of a β -amino acid sidechain would allow for the ring expansion of normal sized lactams **4.57** *via* the breakdown of fused bicyclic intermediate **4.59** (commonly referred to as a cyclol).

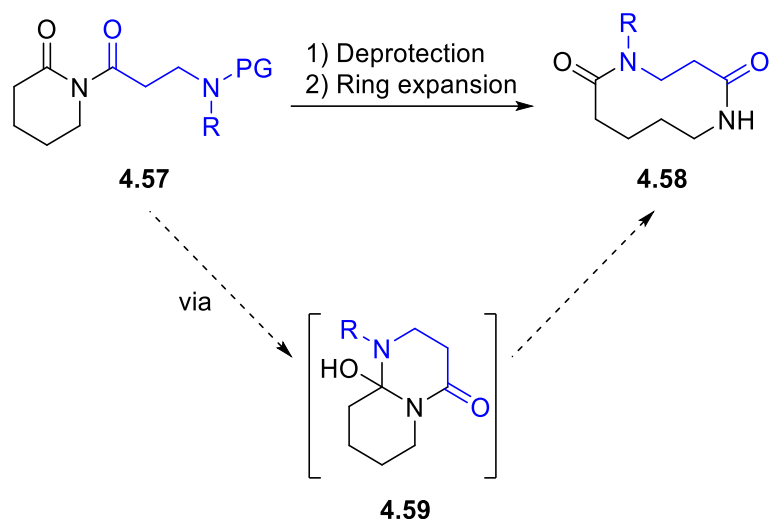


Figure 138. Ring expansion of lactams **4.57** using β -amino acids as proposed by Yudin *et al.*²⁷²

This method was successful, and a series of 4-atom ring expansions were able to be performed using an *N*-Boc protected β -amino acid strategy (**4.60** \rightarrow **4.61**, Figure 139). However, upon attempting the reaction for the 3-atom ring expansion of 6-membered lactam **4.62**, rather than the 9-membered ring product, oxidised cyclol **4.63** was isolated instead.

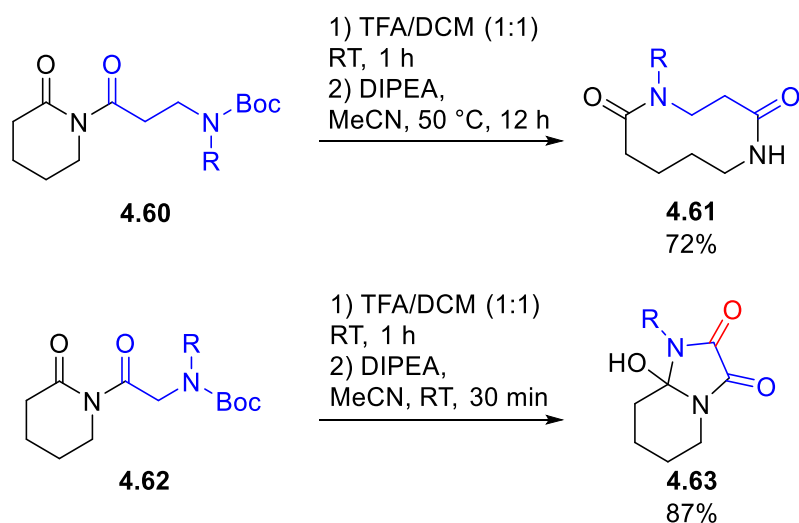


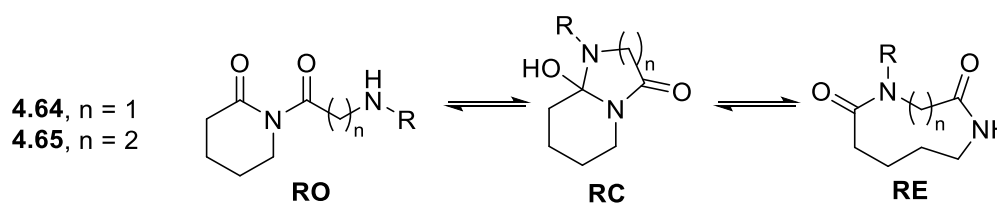
Figure 139. Attempted ring expansion reactions using *N*-Boc protected α - and β -amino acids, as reported by Yudin *et al.*²⁷² R = *p*-NO₂-Bn.

Considering that the ring-opened imide, cyclol and ring expanded isomers were in equilibrium, a DFT method was developed to explore the relative Gibbs energies of these isomers. A conformational analysis was performed on each of the isomers using the MMFF forcefield. Single-point calculations were then done on all conformers at the M06-2X/6-31G* level of theory, and all structures within 7 kcal mol⁻¹ of the lowest energy conformers were then fully

optimised at the M06-2X/6-31+G** level, with subsequent frequency calculations confirming that the structures were minima on the potential energy surface. These DFT calculations were performed for ring expansions using both the α - and β -amino acids.

The DFT calculated relative energies showed good correlation with the experimental results (Table 11), with ring expansion predicted to be successful for ring expansion to 10-membered product **4.65**_{RE}, and cyclol intermediate **4.64**_{RC} favoured with the α -amino acid, rather than 9-membered product **4.64**_{RE}. Solvent corrections using an SMD model with acetonitrile were considered however these made no significant difference to the predicted reaction outcome.

Table 11. DFT-calculated relative energies for the ring expansion of lactams using amino acids. Energies are Gibbs energies calculated at the M06-2X/6-31+G** level of theory. Where used, solvent corrections were applied using an SMD model in acetonitrile. R = *p*-NO₂-Bn.



Compound	Solvent Correction?	$\Delta G_{\text{rel RO}}$ / kcal mol ⁻¹	$\Delta G_{\text{rel RC}}$ / kcal mol ⁻¹	$\Delta G_{\text{rel RE}}$ / kcal mol ⁻¹
4.64	N	0.0	-3.4	-1.1
	Y	0.0	-4.1	-2.4
4.65	N	0.0	+9.7	-2.8
	Y	0.0	+6.0	-6.2

In 2017, the group of Krasavin reported a method for fragmentation ring expansions which were referred to as hydrolytic imidazoline ring expansion (HIRE) reactions.²⁷³ It was proposed that *N*-alkylation of a fused cyclic imidazoline (**4.66**), followed by the addition of a hydroxide (by the treatment of **4.67** under basic conditions) would result in a cyclol species (**4.69**), which would then fragment and result in a ring expanded product (**4.70**).

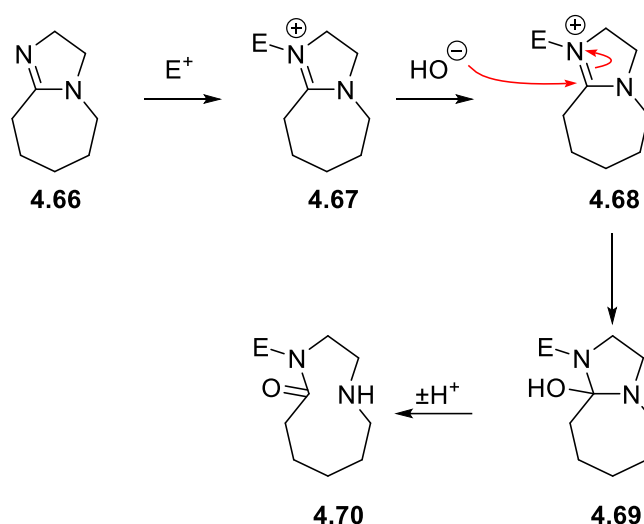


Figure 140. Hydrolytic imidazoline ring expansion (HIRE) concept reported by Krasavin *et al.*²⁷³

The group were able to validate this approach, with the sequential optimisation of both the *N*-alkylation and ring expansion reactions. It was then possible to employ these steps in a one pot protocol to allow for a 73% yield of ring expanded product **4.72** (Figure 141). This approach was general with a further 16 examples shown, and a following study expanding the scope to sulphur containing heterocycles.²⁷⁴

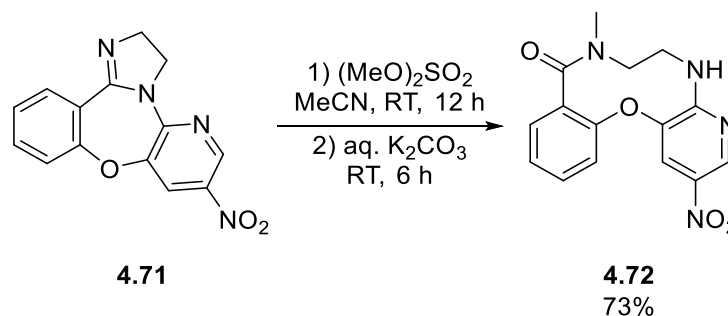


Figure 141. An example of a HIRE reaction as reported by Krasavin *et al.*²⁷³

A limitation of this method was that the ring-size could only be increased by 3-atoms. In 2019, the authors published a sidechain insertion method which could produce products with the same substitution pattern.²⁷⁵ It was proposed that a base-promoted intramolecular cyclisation could take place when starting from an *N*-alkylated lactam (e.g. **4.73**), to yield the ring expanded products. This concept was verified in the synthesis of ring expanded lactam **4.74** (an analogue of **4.72**) in a 68% yield, following an *N*-Boc deprotection of **4.73** (Figure 142).

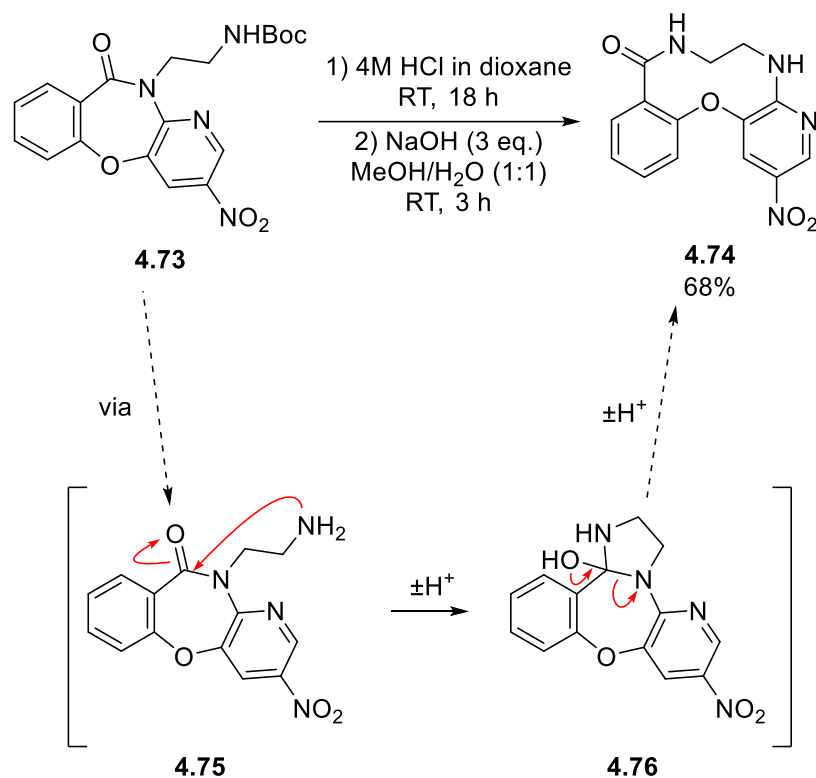


Figure 142. Sidechain insertion development of HIRE reactions reported by Krasavin *et al.*

The development of these sidechain insertion HIRE reactions allowed for the synthesis of structurally similar homologues with larger ring-sizes (**4.79** and **4.80**), as 4- and 5-atom ring expansions were possible by increasing the length of the linear sidechain in the starting materials (**4.77** and **4.78**). However, it was not possible to expand the ring by 6-atoms, likely due to the formation of a strained 8-membered ring intermediate.

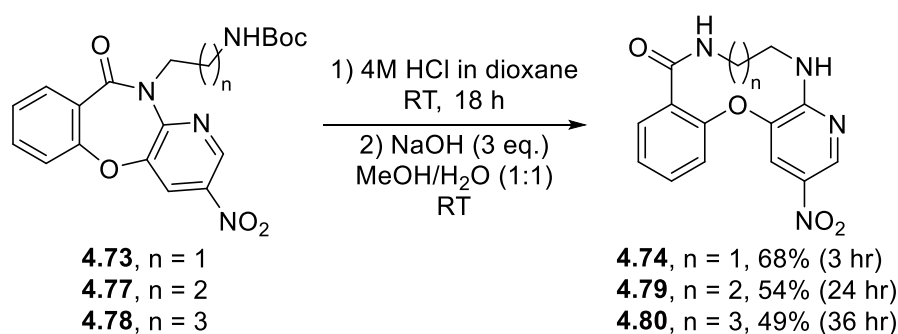
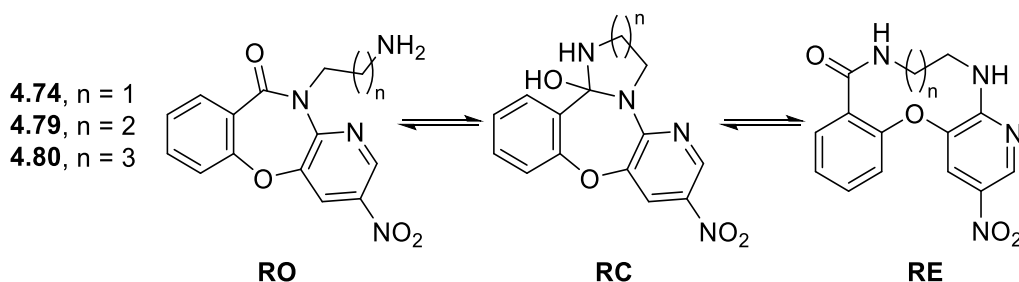


Figure 143. HIRE ring expansions resulting in larger ring sizes as reported by Krasavin *et al.*²⁷⁵ The times in brackets refer to the required time of base treatment.

Whilst the reactions were successful it was noted that an increased reaction time was required for the larger ring sizes. It was proposed that cyclisation of the sidechain becomes entropically less favoured as its length increased. DFT studies were used to explore this (at the B3LYP/6-31G*

level of theory) using a similar method to Yudin and co-workers as previously discussed.²⁷² It was found that the relative energy of the cyclol intermediate (**RC**) increased with the length of the sidechain, which likely increases the transition state energy for the cyclisation (Table 12). However, the energy of the ring expanded product decreased, likely due to a greater decrease in the ring-strain upon expansion.

Table 12. DFT-calculated energies for the isomers in the HIRE reaction. Energies are Gibbs energies at the B3LYP/6-31G* level of theory with solvent correction in water.



Compound	$\Delta G_{\text{rel}} \text{ RO} /$ kcal mol ⁻¹	$\Delta G_{\text{rel}} \text{ RC} /$ kcal mol ⁻¹	$\Delta G_{\text{rel}} \text{ RE} /$ kcal mol ⁻¹
4.74	0.0	+20.4	-3.6
4.79	0.0	+21.0	-5.0
4.80	0.0	+24.0	-6.7

4.1.5 Successive Ring Expansions (SuRE)

Successive ring expansion (SuRE) reactions have been developed within the Unsworth group as an alternative way to increase the ring size of cyclic β -keto esters (reported in 2015) or lactams (reported in 2017) *via* the insertion of a linear sidechain.^{276–279}

The synthetic process is summarised in Figure 144. First, the α -carbon of the β -keto ester (*e.g.* **4.81**) or the nitrogen of the lactam (*e.g.* **4.85** and **4.89**) is acylated by an acyl chloride formed *in situ*. Next, the protecting group of the nucleophile tethered onto the newly inserted chain is removed. Typically, oxygen nucleophiles are benzyl-protected and therefore cleaved *via* hydrogenation, whereas amines are protected using a 9-fluorenylmethoxycarbonyl (Fmoc) group, which is removed under basic conditions. Cyclisation and ring expansion then occurs under basic conditions. Crucially, the key functionality of the starting material is regenerated

following ring expansion, and another ring expansion can therefore be performed using the same method, which allows for an iterative process to produce functionalised macrocycles.

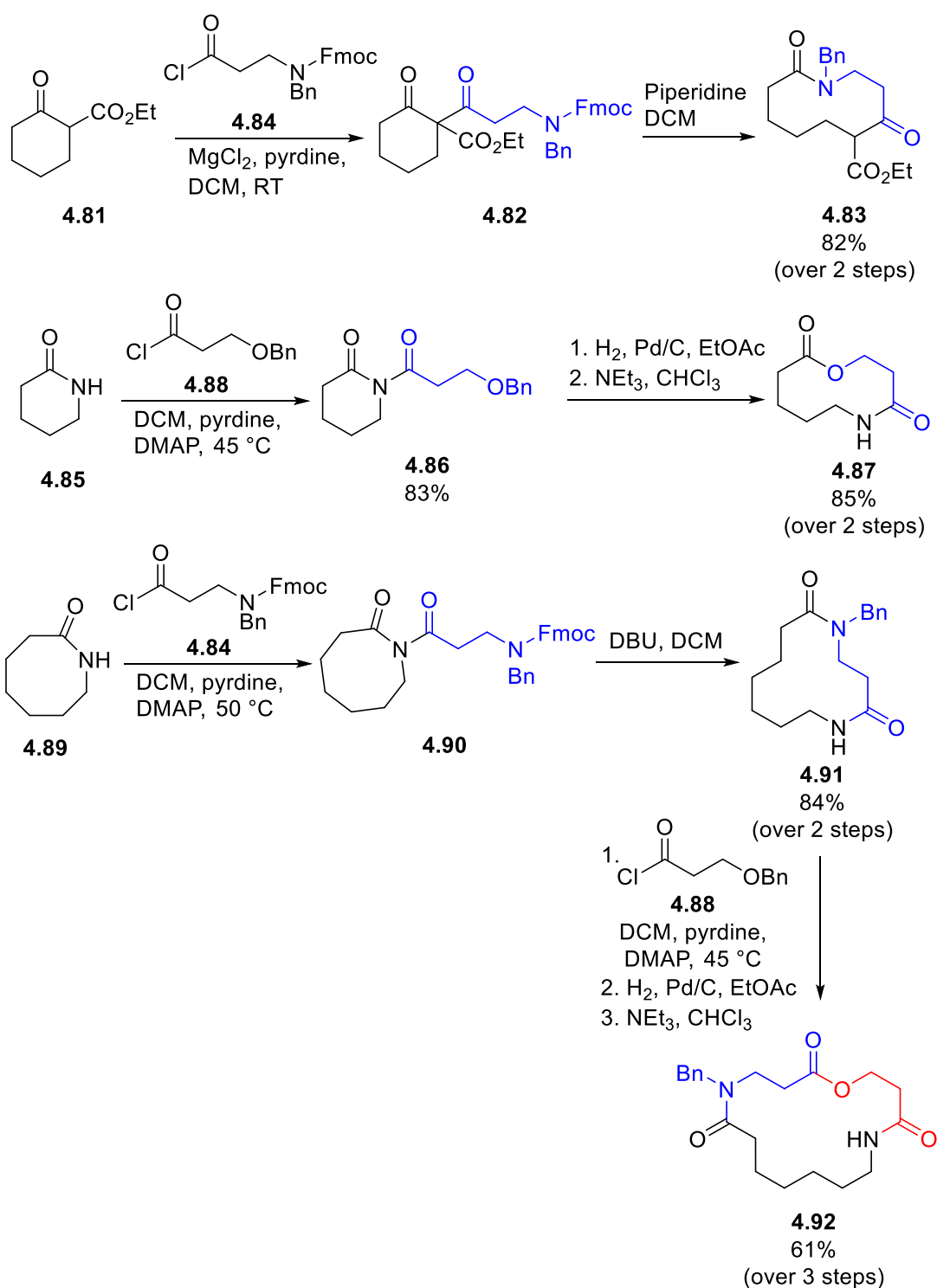


Figure 144. Examples of successful SuRE reactions reported by Unsworth *et al.*^{276,278,279}

The proposed mechanism for the ring expansion is similar to methods reported by Yudin and Krasavin,^{272,275} in which an intramolecular cyclisation of the nucleophile (secondary amine or

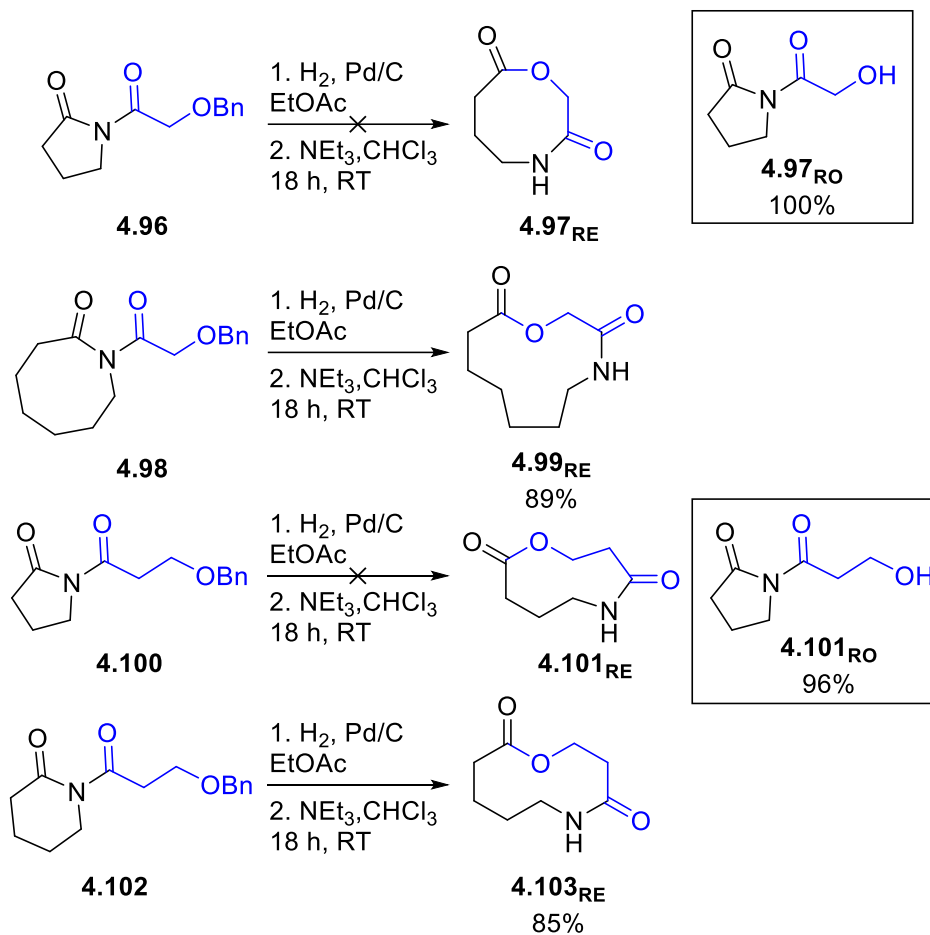


Figure 146. Ring-size dependence on the scope of SuRE reactions using α - and β -hydroxyacids.

A further two examples were reported with α -hydroxyacids **4.104** and **4.108** which after benzyl deprotection, the isolated products existed as a mixture of ring opened, ring expanded and bicyclic cyclol intermediates in CDCl_3 solution (Figure 147). It was therefore proposed that these intermediates are in equilibrium during the SuRE reactions, with the observed synthetic outcomes thermodynamically controlled.

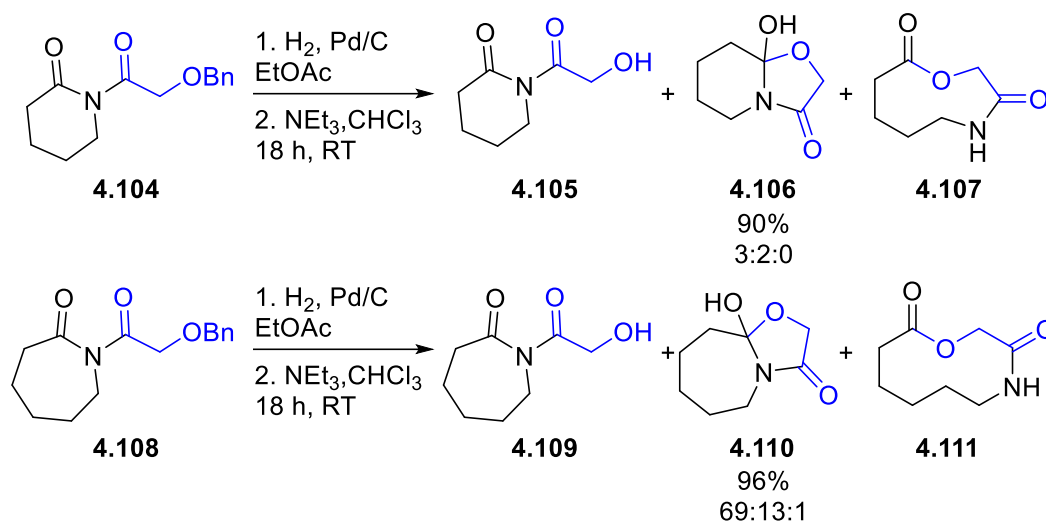


Figure 147. SuRE reactions resulting in equilibrium mixtures. Ratios were determined by ^1H NMR spectroscopy.

4.1.6 SuRE DFT Calculations

The experimental evidence suggested that the outcome of SuRE reactions is under thermodynamic control. Therefore, based on the previously discussed work by Yudin and co-workers on structurally similar substrates,²⁷² it was proposed that by using computational chemistry to calculate the relative Gibbs energy difference between the three isomers (**4.112**–**4.114**) in solution (Figure 148), the viability of a SuRE reaction could be predicted.

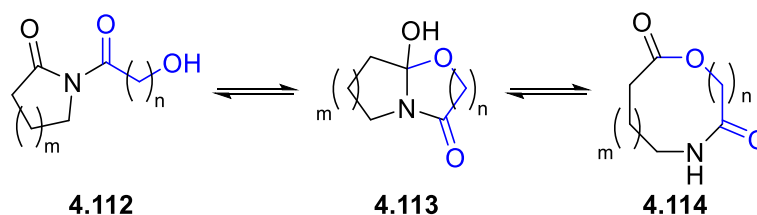


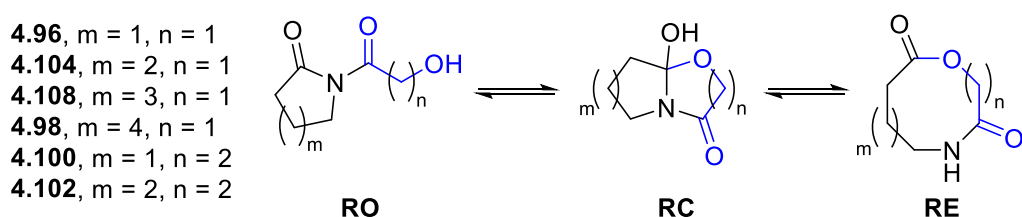
Figure 148. The three isomers considered in the DFT calculations.

Molecular mechanics was used to perform a conformational analysis using the MMFF forcefield. The electronic energy of each conformation was then calculated at the B3LYP/6-31G* level of theory. Finally, the conformation with the lowest DFT-calculated electronic energy was then submitted for a full geometry optimisation, followed by a frequency calculation to obtain the thermal energy corrections. This process was repeated for each structure to be compared.

The relative energies were calculated for the lactone-forming SuRE reactions discussed previously (Figure 146 and Figure 147), to compare whether the DFT calculations could indeed correctly predict the outcome of the reaction.

The data in Table 13 shows the results of the study, which demonstrated that the DFT calculations successfully predicted the outcome of the reactions if the calculated energy difference between the isomers is significant (*e.g.* compounds **4.96**, **4.98**, **4.100**). Where the relative energy difference is smaller, the prediction was less reliable. For example, compound **4.104** might be predicted to form only the ring-opened isomer, however instead a 3:2 mixture of ring-opened and ring closed isomers were observed. Additionally, for compound **4.108**, an equilibrium mixture of ring-opened and ring expanded isomers might be expected, however the ring-opened isomer was the major isomer observed, with only a small proportion of the ring expanded isomer seen.

Table 13. DFT-calculated relative difference in Gibbs energy at 298.15 K at the B3LYP/6-31G* level of theory in a vacuum.



Compound	m	n	$\Delta G_{\text{rel}} \text{ RO} /$ kcal mol ⁻¹	$\Delta G_{\text{rel}} \text{ RC} /$ kcal mol ⁻¹	$\Delta G_{\text{rel}} \text{ RE} /$ kcal mol ⁻¹	Experimental RO:RC:RE Ratio
4.96	1	1	0.0	+13.4	+10.3	1:0:0
4.104	2	1	0.0	+2.9	+5.2	3:2:0
4.108	3	1	0.0	+4.0	+0.7	69:13:1
4.98	4	1	0.0	+2.6	-6.3	0:0:1
4.100	1	2	0.0	+11.7	+4.1	1:0:0
4.102	2	2	0.0	+5.7	-2.4	0:0:1

A more comprehensive study was then started, which focused on the validation of the DFT methodology used with respect to the SuRE reactions that had previously been published, whilst also increasing the reaction scope. However, during this work it was noted that whilst the

published method (B3LYP/6-31G*) was successful, there were some potentially significant considerations that had been omitted.

Firstly, the effect of changing the functional and basis set wasn't considered. B3LYP is a commonly used functional, however, it has a reputation for being a 'default' option and doesn't always benchmark favourably.^{280–283} Larger basis sets (than 6-31G*) are available with which more accurate energies could theoretically be obtained,²⁸⁴ however this comes at a cost of increased computational expense without necessarily improving the model of the reactions. Additionally, it was noted that these calculations are performed in the gas phase so the effect of solvation stabilisation with the three calculated isomers could be considered. Finally, the effects of dispersion (long-range interactions, see Section 1.1.11) would normally be considered to represent the system more accurately. Therefore, it was decided to perform a more thorough methodology screen to ensure the most representative model was used.

The work presented in this chapter will focus on the author's contributions to validate or improve the DFT method used, building upon the work previously done by Dr Aggie Lawer in the Unsworth group. A discussion of how this computational method has been used to rationalise the experimental data from other members of the Unsworth group, which has furthered the scope of SuRE reactions, will be provided.

4.2 Evaluating the viability of Successive Ring Expansions

4.2.1 Scope of the study

As discussed previously, the only SuRE system which had been modelled using the B3LYP/6-31G* method, were the α - and β -hydroxyacid ring expansions starting from lactams (Table 13, page 184), in which a clear dependency on the ring-size of the starting lactam was observed. To screen this method more thoroughly, additional calculations to model the thermodynamics of SuRE reactions were performed. The reactions to be considered were the ring expansions using lactams with α -amino acid linear fragments (**4.115–4.117**), and the cyclic β -ketoesters variant using both β -amino acid and β -hydroxyacid starting materials (**4.118–4.120**) to evaluate their dependence on the starting ring-size (Figure 149).

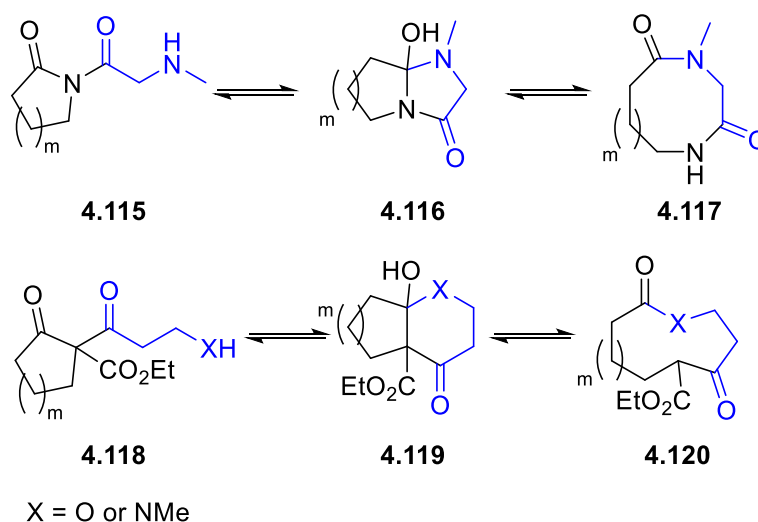


Figure 149. SuRE reactions to be studied by DFT calculations.

Additionally, the scope of the lactams used experimentally in the SuRE reactions was improved, to result in more functionalised ring expanded products. Therefore, further DFT calculations were done with these new examples to determine if it is possible to predict the outcome in specific examples. The computational data of the ring-size screen, and the new lactam substrates, would then be compared using different levels of theory to determine the best computational model to use.

4.2.2 Lactam and α -amino acid expansion ring-size dependence

The scope of SuRE ring expansions using α -amino acids was previously limited to one example in which a 13-membered lactam was acylated and successfully ring expanded using Fmoc-protected sarcosine.²⁷⁸

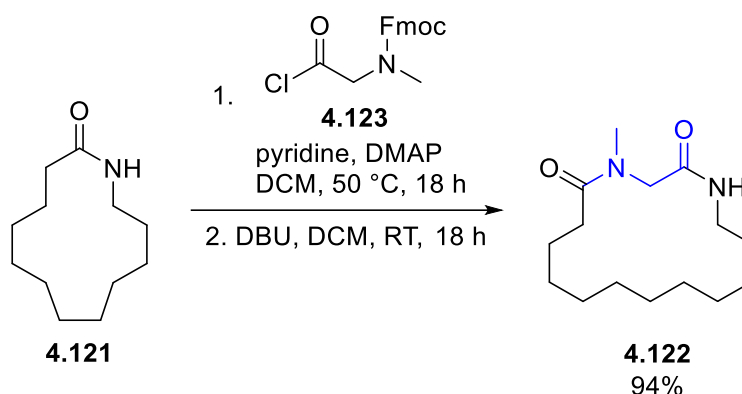


Figure 150. Previous example of an α -amino acid SuRE reaction as reported by Stephens *et al.*²⁷⁸

Based on the previous studies, it was suspected that there might be a ring size below which the ring expansions were no longer successful (referred to as the 'switch-on point'), so DFT calculations were used to examine the relative energy difference between the ring-opened imide, cyclol and ring expanded isomers of various starting lactam sizes (Figure 151, $n = 1-4$).

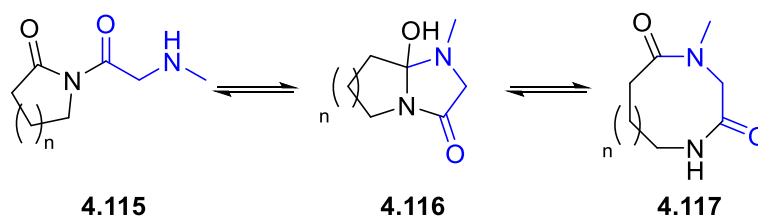


Figure 151. Structures used for evaluating the lactam ring-size dependence with sarcosine. $m = 1-4$.

As previously described (see Section 4.1.6), a conformational analysis was performed followed by single-point calculations at the B3LYP/6-31G* level of theory in the gas phase. The geometry of the lowest energy conformation was then optimised using DFT with a frequency calculation to both demonstrate that the structure was a true minimum, and to generate the thermodynamic corrections. The relative energy difference for the different starting ring-sizes were then compared (Table 14).

Table 14. DFT-calculated relative difference for the α -amino acid lactam ring expansions series. All energies are Gibbs energy at 298.15 K at the B3LYP/6-31G* level of theory in a vacuum. Calculated by Dr Lawer.

4.124, n = 1
4.125, n = 2
4.126, n = 3
4.127, n = 4

Compound	$\Delta G_{\text{rel RO}} /$ kcal mol ⁻¹	$\Delta G_{\text{rel RC}} /$ kcal mol ⁻¹	$\Delta G_{\text{rel RE}} /$ kcal mol ⁻¹
4.124	0.0	+16.5	+1.9
4.125	0.0	+3.9	+2.1
4.126	0.0	+6.4	+0.7
4.127	0.0	+6.8	-7.3

As before with the α -hydroxyacid series, the data showed a significant calculated energy difference when an 8-membered lactam was used as the starting material (Table 14, **4.127**), with the ring expanded product favoured. The ring opened isomer was calculated to be lower in energy for the smaller rings (**4.124–4.126**), albeit it might be expected to see both ring opened and ring expanded isomers in an equilibrium mixture when starting with 7-membered lactam (**4.126**), similar to the result of the analogous α -hydroxyacid example (Table 13, compound **4.108**).

Synthetic experiments were then attempted for the above calculated ring sizes (Figure 152), and only the 8-membered lactam starting material showed success in the ring expansion reaction, with a yield achieved of 82%. The smaller ring sizes were all unsuccessful, as predicted by the calculations, with no products isolated following the ring expansion. Notably, when starting from the 7-membered lactam, an equilibrium mixture of products was not observed.

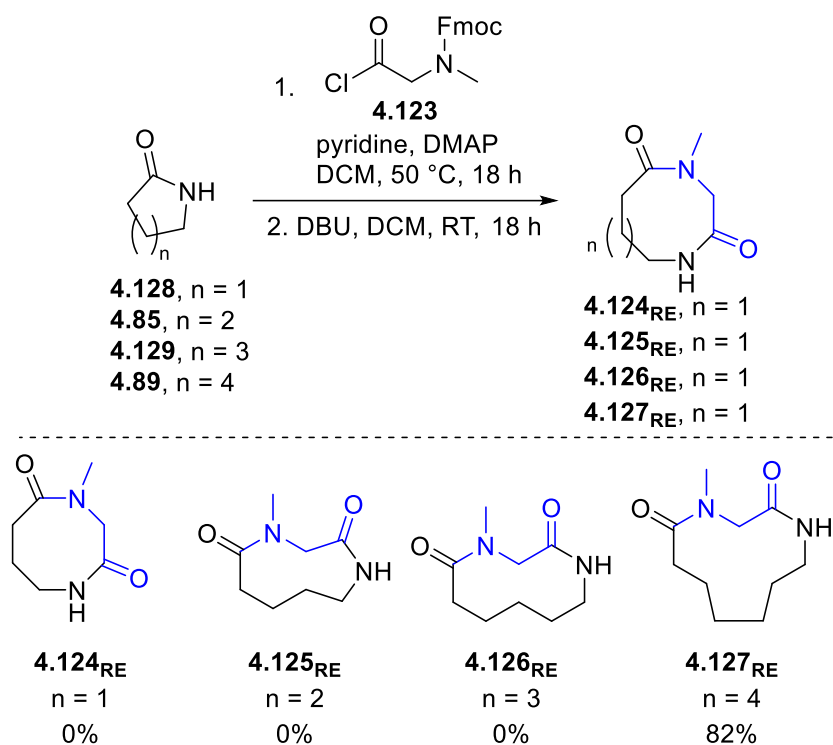


Figure 152. Synthetic experiments exploring the ring-size requirements of SuRE reactions using α -amino acids, as performed by various co-workers.

As before (see Section 4.1.6), the DFT results match the outcome of the experimental results, with the only successful reaction being the ring expansion of 8-membered lactam **4.89** to **4.127_{RE}**. It was decided that this series of molecules were ideal for benchmarking the DFT methodology due to the similarity of the substrates (*e.g.* a homologous series in which the ring size is increased).

Dr Lawer used the Spartan software package in the previous SuRE calculations.²⁸⁵ However, the Gaussian software package was used for the benchmarking studies (and for all future work in this area) due its availability on the University of York's high performance computing clusters.²⁸⁶ Therefore, initially, a comparison was made between the B3LYP/6-31G* energies as calculated between Spartan and Gaussian. The geometries from the Spartan geometry optimisations were used as the starting point for a geometry optimisation and frequency calculation in Gaussian at the B3LYP/6-31G* level of theory in a vacuum. The geometries of the resulting optimised structures were then compared to the starting input to ensure that there was no significant change in the conformation.

The relative energies between the two software packages were comparable (Table 15), with the only significant difference seen in the calculation of the 6-membered lactam series (**4.125**). The

start and end geometries of **4.125** were compared, however there was no significant difference in the geometry. The 6-membered lactam structures (**4.125**) were still used in the comparisons, however minimal consideration to this data set was made when conclusions were drawn.

Table 15. DFT-calculated relative difference for the α -amino acid lactam ring expansions (**4.124–4.127**) using either Spartan or Gaussian. All energies are Gibbs energy at 298.15 K at the B3LYP/6-31G* level of theory in a vacuum. Spartan calculations performed by Dr Lawer.

4.124, n = 1
4.125, n = 2
4.126, n = 3
4.127, n = 4

Compound	Software Used	ΔG_{rel} RO / kcal mol ⁻¹	ΔG_{rel} RC / kcal mol ⁻¹	ΔG_{rel} RE / kcal mol ⁻¹
4.124	Spartan	0.0	+16.5	+1.9
	Gaussian	0.0	+15.8	+2.2
4.125	Spartan	0.0	+3.9	+2.1
	Gaussian	0.0	+1.3	-0.3
4.126	Spartan	0.0	+6.4	+0.7
	Gaussian	0.0	+6.1	0.3
4.127	Spartan	0.0	+6.8	-7.3
	Gaussian	0.0	+6.2	-8.2

Further method screening was undertaken using Gaussian as these data indicated that the results were directly comparable with Dr Lawer's data from Spartan. First, the effects of using different functionals for the calculations were considered. GGA functional BP86,^{32,33} the hybrid functionals B3LYP,³⁷⁻⁴⁰ and PBE0,³⁴⁻³⁶ and the meta-hybrid Minnesota functional M06-2X,⁴¹ were compared using the same 6-31G* basis set, with no solvent correction applied.

The data showed that the BP86 and PBE0 calculations, whilst similar to the B3LYP results, did predict the energy of the ring expanded isomer to be relatively more stable in all cases (Table 16). This was particularly significant when the 7-membered lactam **4.126** was considered, where the BP86 and PBE0 functionals predicted that the ring expansion would be favourable.

The most significant difference in the relative energies was found when the M06-2X functional was employed. A much greater stabilisation for the ring-closed and ring expanded isomers was seen across all ring-sizes, predicting both that an equilibrium might be seen with 5-membered lactam **4.124**, and that ring expansion was favoured with 7-membered lactam **4.126**, neither of which was observed experimentally. It was noted that the M06-2X functional is parametrised to include medium-range interactions (akin to a separate dispersion correction), and it was proposed that this was the reason for the large difference.

Table 16. DFT-calculated relative difference for the α -amino acid lactam ring expansions (**4.124–4.127**) with differing functionals. All energies are Gibbs energy at 298.15 K using the 6-31G* basis set in a vacuum.

4.124, n = 1
4.125, n = 2
4.126, n = 3
4.127, n = 4

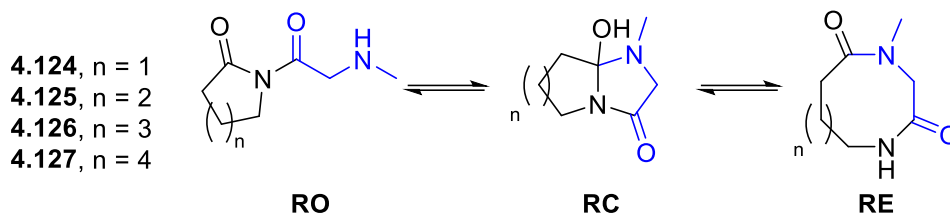
Compound	Functional	$\Delta G_{\text{rel RO}} /$ kcal mol ⁻¹	$\Delta G_{\text{rel RC}} /$ kcal mol ⁻¹	$\Delta G_{\text{rel RE}} /$ kcal mol ⁻¹
4.124	B3LYP ^[a]	0.0	+16.5	+1.9
	BP86	0.0	+14.9	+1.6
	PBE0	0.0	+14.1	+1.2
	M06-2X	0.0	+9.8	0.3
4.125	B3LYP ^[a]	0.0	+3.9	+2.1
	BP86	0.0	+0.5	-1.1
	PBE0	0.0	-0.6	-1.6
	M06-2X	0.0	-5.6	-3.7
4.126	B3LYP ^[a]	0.0	+6.4	+0.7
	BP86	0.0	+5.5	-0.4
	PBE0	0.0	+4.4	-1.3
	M06-2X	0.0	-0.5	-2.8
4.127	B3LYP ^[a]	0.0	+6.8	-7.3
	BP86	0.0	+5.5	-8.3
	PBE0	0.0	+4.5	-8.8
	M06-2X	0.0	-0.8	-9.9

^[a] Energies were taken from the Spartan calculations performed by Dr Lawer.

The effects of applying a solvent correction on the relative energies were next considered. B3LYP/6-31G* and M06-2X/6-31G* calculations were performed with an added solvent correction using a PCM model with DCM as the solvent to match the experimental conditions, these were directly compared with the equivalent calculation in the gas phase. A calculation at the BP86/SV(P) level of theory was also performed. The data are collated in Table 7.

Overall, the addition of a solvent correction did not significantly alter the predicted outcome of the ring expansion experiment when used with the B3LYP/6-31G* level of theory, although a slight reduction in the relative energy difference of the ring-closed and ring expanded isomers was observed. A larger preference for the ring expanded isomer was observed at both the BP86/SV(P) level of theory, and the M06-2X functional again.

Table 17. DFT-calculated relative difference for the α -amino acid lactam ring expansions (**4.124–4.127**). All energies are Gibbs energy at 298.15 K using the 6-31G*. Where used, solvent corrections were applied using a PCM model with DCM as the solvent.



Compound	Functional	RO		RC		RE
		Basis Set	Solvent Correction?	ΔG_{rel} RO / kcal mol ⁻¹	ΔG_{rel} RC / kcal mol ⁻¹	ΔG_{rel} RE / kcal mol ⁻¹
4.124	B3LYP ^[a]	6-31G*	N	0.0	+16.5	+1.9
	B3LYP	6-31G*	Y	0.0	+14.9	+0.2
	M06-2X	6-31G*	N	0.0	+9.8	0.3
	M06-2X	6-31G*	Y	0.0	+8.7	-1.6
	BP86	SV(P)	Y	0.0	+11.5	-2.1
4.125	B3LYP ^[a]	6-31G*	N	0.0	+3.9	+2.1
	B3LYP	6-31G*	Y	0.0	+2.2	-1.1
	M06-2X	6-31G*	N	0.0	-5.6	-3.7
	M06-2X	6-31G*	Y	0.0	-4.5	-4.1
	BP86	SV(P)	Y	0.0	-1.2	-3.0
4.126	B3LYP ^[a]	6-31G*	N	0.0	+6.4	+0.7
	B3LYP	6-31G*	Y	0.0	+6.2	-0.3
	M06-2X	6-31G*	N	0.0	-0.5	-2.8
	M06-2X	6-31G*	Y	0.0	-0.5	-3.4
	BP86	SV(P)	Y	0.0	+2.7	-1.8
4.127	B3LYP ^[a]	6-31G*	N	0.0	+6.8	-7.3
	B3LYP	6-31G*	Y	0.0	+6.2	-9.9
	M06-2X	6-31G*	N	0.0	-0.8	-9.9
	M06-2X	6-31G*	Y	0.0	-0.9	-11.4
	BP86	SV(P)	Y	0.0	+2.5	-11.1

^[a] Energies were taken from the Spartan calculations performed by Dr Lawer.

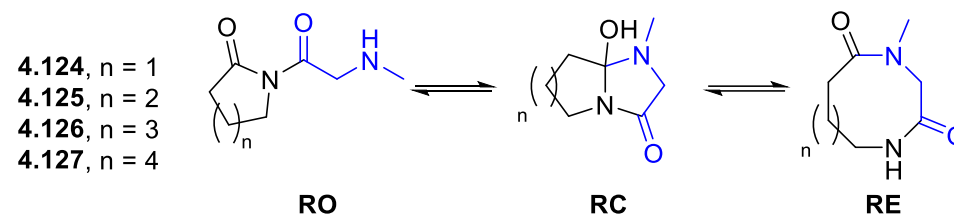
The final consideration applied was the use of dispersion corrections. As discussed previously (see Section 1.1.11), DFT functionals typically neglect the effects of London dispersion.²⁸⁰ This can be remedied by the inclusion of dispersion corrections, and Grimme's D3 variant with

Becke–Johnson damping (referred to as D3(BJ)) was used here.⁷⁵ Additionally, the Minnesota functionals (*e.g.* M06 and M06-2X) are parametrised to take medium-range interactions into consideration.⁴¹

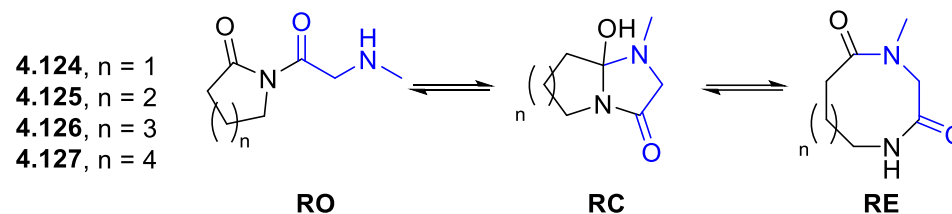
It had been noted during this study that the M06-2X functional was markedly worse in predicting the reaction outcome of the SuRE reaction (Table 16), so a range of methods for considering the effects of dispersion were applied. The D3(BJ) correction was added to the B3LYP functional, as well as taking the BP86/SV(P) geometries and performing a single-point calculation at the D3(BJ)-PBE0/def2-TZVPP level of theory. Additionally, the M06 functional was applied to compare the results with M06-2X.

The inclusion of dispersion corrections had the largest effect on the predicted outcome of the reaction (Table 18), whether this was included as an empirical correction, or with the Minnesota functionals. All ring sizes show a significant decrease in the relative energy difference of both the ring-closed and ring expanded isomers, which in the case of the 5- and 7-membered lactams (**4.124** and **4.126**), were now predicted to be successful, in disagreement with the experimental outcomes. This effect was also seen with 8-membered lactam **4.127**, however in this instance the predicted reaction outcome doesn't change, as the ring expanded product was already predicted to be significantly lower in energy.

Table 18. DFT-calculated relative difference for the α -amino acid lactam ring expansions (**4.124–4.127**). All energies are Gibbs energy at 298.15 K using the 6-31G*. Where used, solvent corrections were applied using a PCM with DCM as the solvent. Dispersion corrections were applied using the D3(BJ) method.



Compound	Functional	Basis Set	Solvent	Empirical	$\Delta G_{\text{rel}} \text{ RO} / \text{kcal mol}^{-1}$	$\Delta G_{\text{rel}} \text{ RC} / \text{kcal mol}^{-1}$	$\Delta G_{\text{rel}} \text{ RE} / \text{kcal mol}^{-1}$
			Correction?	Dispersion			
4.124	B3LYP ^[a]	6-31G*	N	N	0.0	+16.5	+1.9
	B3LYP	6-31G*	N	Y	0.0	+13.7	-0.2
	M06	6-31G*	Y	N	0.0	+10.8	-2.1
	M06-2X	6-31G*	Y	N	0.0	+8.7	-1.6
	PBE0 ^[b]	def2-TZVPP	Y	Y	0.0	+9.2	-3.3
4.125	B3LYP ^[a]	6-31G*	N	N	0.0	+3.9	+2.1
	B3LYP	6-31G*	N	Y	0.0	-1.5	-3.5
	M06	6-31G*	Y	N	0.0	-3.0	-3.8
	M06-2X	6-31G*	Y	N	0.0	-4.5	-4.1
	PBE0 ^[b]	def2-TZVPP	Y	Y	0.0	-3.0	-5.3



Compound	Functional	Basis Set	Solvent	Empirical		$\Delta G_{\text{rel}} \text{ RO} / \text{kcal mol}^{-1}$	$\Delta G_{\text{rel}} \text{ RC} / \text{kcal mol}^{-1}$	$\Delta G_{\text{rel}} \text{ RE} / \text{kcal mol}^{-1}$
				Correction?	Dispersion			
				Correction?				
4.126	B3LYP ^[a]	6-31G*	N	N		0.0	+6.4	+0.7
	B3LYP	6-31G*	N	Y		0.0	+3.8	-3.5
	M06	6-31G*	Y	N		0.0	+1.1	-3.8
	M06-2X	6-31G*	Y	N		0.0	-0.5	-3.4
	PBE0 ^[b]	def2-TZVPP	Y	Y		0.0	+0.7	-5.0
4.127	B3LYP ^[a]	6-31G*	N	N		0.0	+6.8	-7.3
	B3LYP	6-31G*	N	Y		0.0	+3.6	-9.8
	M06	6-31G*	Y	N		0.0	+0.6	-12.2
	M06-2X	6-31G*	Y	N		0.0	-0.9	-11.4
	PBE0 ^[b]	def2-TZVPP	Y	Y		0.0	+0.6	-13.4

^[a] Energies were taken from the Spartan calculations performed by Dr Lawer. ^[b] Geometry taken from BP86/SV(P) calculation.

To explain the difference in relative energies when the dispersion correction was applied, the geometry of the three isomers were considered. Due to the ring-opened isomer being stabilised less, it was proposed that the linear sidechain in the ring-opened isomer contains fewer long-range interactions due to the distance from the lactam. However, in the ring-closed and ring expanded isomers, this side chain is now incorporated into the ring, hence the atoms are closer, and an increased amount of stabilising long-range interactions are calculated.

It is suspected that in the real system, intermolecular interactions of the sidechain with the solvent stabilise the ring-opened isomers in reactions where the ring expansion is unsuccessful. These interactions are not modelled in the DFT calculations performed here due to the computational cost of explicit solvation (see Section 1.1.10 for discussion of solvation models in DFT methods). Therefore, it is proposed that the additional dispersion interactions in the ring expanded isomers, and the neglected solvent/solute interactions in the ring-opened isomers, provides a bias which leads to the calculations predicting a greater thermodynamic driving force to ring expansion.

4.2.3 Further Scope

Following the conclusion of the above study, the performance of the B3LYP/6-31G* and M06-2X/6-31G* methods on a wider range of substrates was tested. Solvent corrections were applied in the M06-2X calculations, so that the effects of both solvation and dispersion on the relative energies are considered.

Whilst the previous DFT studies on the SuRE reactions discussed focused on the ring size dependency of lactam starting materials, it is also possible to use cyclic β -ketoesters as starting materials in SuRE.^{276,277} Figure 153 shows the experimental results for the ring expansions utilising β -ketoesters to form medium-sized and macrocyclic lactams (**4.129_{RE}**–**4.131_{RE}**) and lactones (**4.132_{RE}** and **4.133_{RE}**). Whilst the lactams had been previously reported,²⁷⁶ the lactones were new for this study.

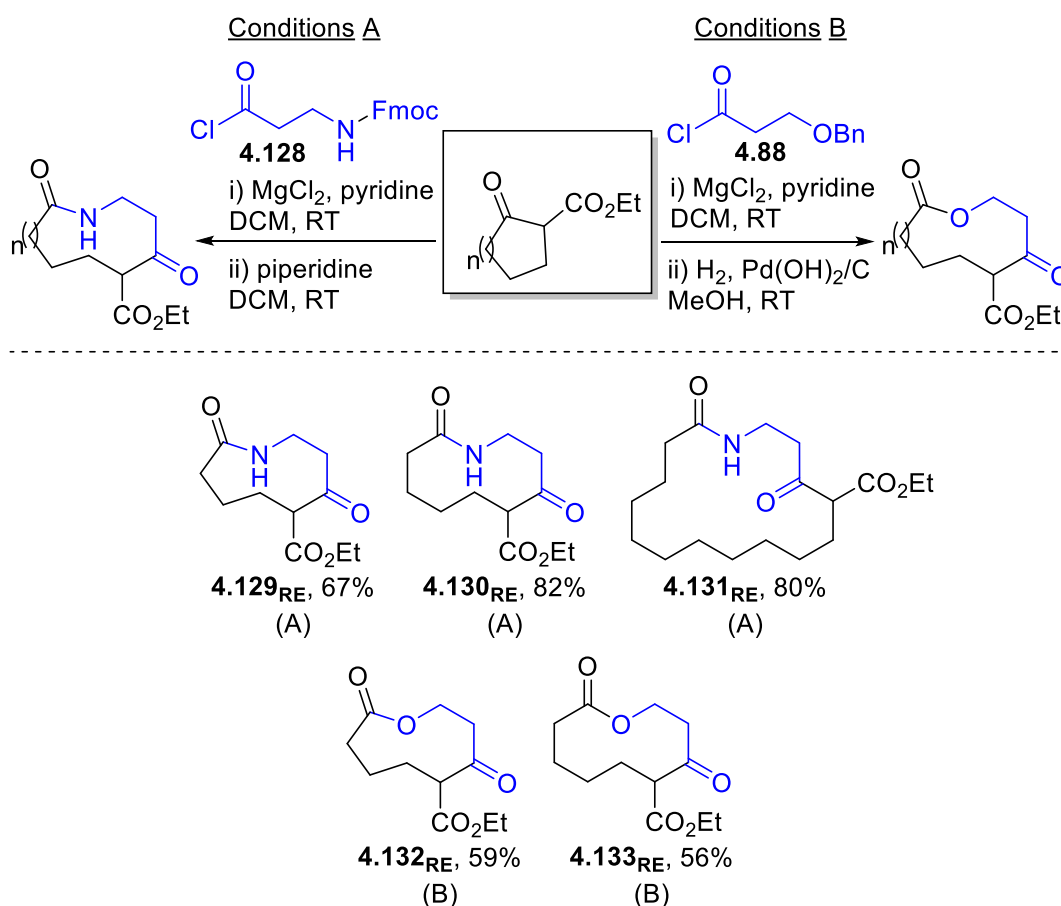


Figure 153. Cyclic β -ketoester SuRE reactions that were studied using DFT. Yields for lactams **4.129_{RE}**–**4.131_{RE}** were taken from previous studies²⁷⁶ The other reactions were performed by various co-workers.

Overall, both methods correctly predicted the outcome of the SuRE reactions, with ring expansion favoured greatly in each case (Table 19). As previously, the M06-2X functional lowered the relative energy of both the ring closed and ring expanded isomers. However, whilst the relative energy of the ring expanded isomer decreased between 0.5–2.5 kcal mol⁻¹, a much larger effect for the ring closed isomer was seen, with the difference in relative energy increasing as the size of the ring increased.

Table 19. DFT calculated relative energies for the SuRE reaction of cyclic β -ketoesters (Figure 153). Energies are Gibbs energies at 298.15 K at the given level of theory. Solvent corrections were applied for the M06-2X/6-31G* calculations using a PCM model in dichloromethane for **4.129–4.131** and chloroform for **4.132** and **4.133**. B3LYP calculations performed by Dr Lawer.

Compound	Method	RO / kcal mol ⁻¹	RC / kcal mol ⁻¹	RE/ kcal mol ⁻¹
4.129	B3LYP/6-31G*	0.0	+2.6	-10.0
	M06-2X/6-31G*	0.0	-2.3	-12.5
4.130	B3LYP/6-31G*	0.0	+1.6	-8.1
	M06-2X/6-31G*	0.0	-6.8	-10.5
4.131	B3LYP/6-31G*	0.0	+8.8	-36.6
	M06-2X/6-31G*	0.0	-3.3	-38.0
4.132	B3LYP/6-31G*	0.0	+2.5	-9.3
	M06-2X/6-31G*	0.0	-3.6	-11.7
4.133	B3LYP/6-31G*	0.0	-0.5	-10.8
	M06-2X/6-31G*	0.0	-6.6	-10.3

Furthermore, rather than focusing on just the ring size of the lactam, the effect of different modifications on the carbon chain was also considered. The SuRE reactions which were studied by DFT are shown in Figure 154.

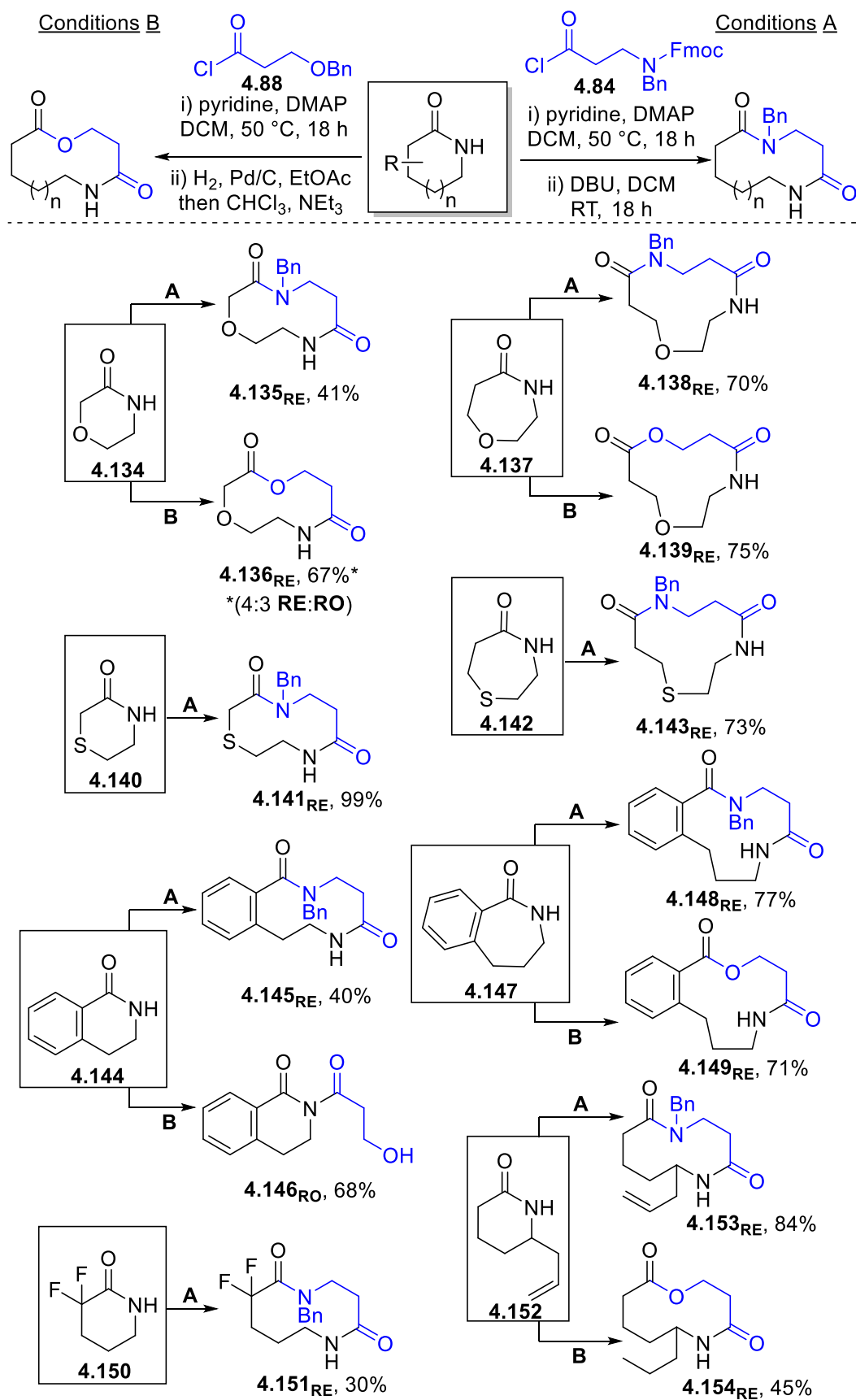


Figure 154. New SuRE reactions that were studied by DFT. Yields as reported by various co-workers.²⁸⁷

In most cases (9 out of 13), both computational methods predicted the same outcome of the reactions (Table 20). Notably, these were situations in which the B3LYP calculation already predicted a significant driving force for ring expansion. Examples where the M06-2X calculations were less successful in predicting the outcome included compound **4.136**, where ring expansion was strongly predicted to occur, but a mixture of isomers were observed experimentally. Also, for compound **4.146**, where no ring expansion was observed experimentally, an equilibrium mixture might be expected.

There were some results with which the B3LYP method was less successful in predicting the outcome. Compound **4.135** predicted that a mixture might be seen but only the ring expanded isomer was isolated. Compound **4.136** again proved difficult to model, a convincing energy difference of $-2.9 \text{ kcal mol}^{-1}$ in favour of ring expansion was seen however a mixture was observed. Finally ring expansion was observed with compound **4.145** however the B3LYP method predicted that the ring opened isomer would be favoured.

Table 20. DFT calculated relative energies for the SuRE reaction in Figure 154. Energies are Gibbs energies at 298.15 K at the given level of theory. Solvent corrections were applied for the M06-2X/6-31G* calculations using a PCM model in dichloromethane or chloroform as appropriate. B3LYP calculations performed by Dr Lawer.

Compound	Method	RO / kcal mol ⁻¹	RC / kcal mol ⁻¹	RE / kcal mol ⁻¹	Yield RE (%)
4.135	B3LYP/6-31G*	0.0	+9.7	0.0	41
	M06-2X/6-31G*	0.0	+0.2	-6.9	
4.136	B3LYP/6-31G*	0.0	+6.3	-2.9	67 ^a
	M06-2X/6-31G*	0.0	-0.5	-5.0	
4.138	B3LYP/6-31G*	0.0	+12.4	-5.5	70
	M06-2X/6-31G*	0.0	+2.1	-11.7	
4.139	B3LYP/6-31G*	0.0	+9.2	-10.4	75
	M06-2X/6-31G*	0.0	+2.6	-11.2	
4.141	B3LYP/6-31G*	0.0	+11.7	-6.7	99
	M06-2X/6-31G*	0.0	+1.1	-12.0	
4.143	B3LYP/6-31G*	0.0	+9.4	-10.9	73
	M06-2X/6-31G*	0.0	+0.6	-14.5	
4.145	B3LYP/6-31G*	0.0	+15.9	+2.5	40
	M06-2X/6-31G*	0.0	+7.2	-2.8	
4.146	B3LYP/6-31G*	0.0	+13.9	+3.3	0
	M06-2X/6-31G*	0.0	+6.3	-0.5	
4.148	B3LYP/6-31G*	0.0	+18.3	-5.9	77
	M06-2X/6-31G*	0.0	+9.7	-9.4	
4.149	B3LYP/6-31G*	0.0	+13.8	-3.9	71
	M06-2X/6-31G*	0.0	+6.8	-6.0	
4.151	B3LYP/6-31G*	0.0	+7.3	-3.9	30
	M06-2X/6-31G*	0.0	-3.5	-9.2	
4.153	B3LYP/6-31G*	0.0	+16.1	-3.5	84
	M06-2X/6-31G*	0.0	+4.7	-9.8	
4.154	B3LYP/6-31G*	0.0	+9.7	-4.8	45
	M06-2X/6-31G*	0.0	+2.6	-6.6	

[a] Isolated as a mixture (4:3 **4.136**_{RE}:**4.136**_{RO}).

4.2.4 Thiolactone SuRE Viability

Whilst SuRE reactions using amino acids and hydroxyacids in the formation of lactam and lactones respectively have been thoroughly studied,^{276–279} the formation of thiolactones using thiol-terminated sidechains remained unexplored. This was considered to be an interesting synthetic opportunity, given that some normal-sized thiolactones are biologically active (**4.155–4.157**, Figure 155).^{288–290}

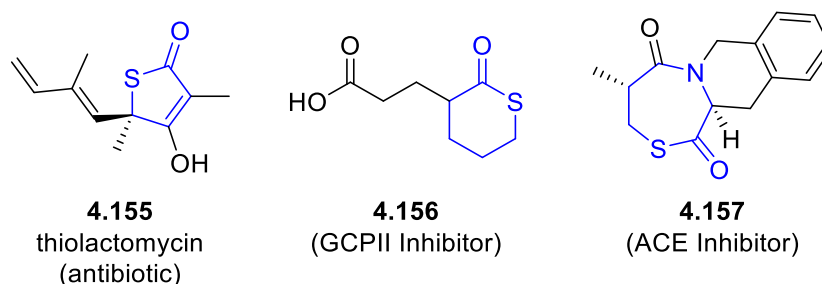


Figure 155. Biologically active normal sized thiolactones.

It had been proposed previously that the formation of stable, conjugated amide and esters functionalities offset the increase in ring strain observed upon ring expansion in the more establish *N*- and *O*-SuRE reactions. However, thioesters are generally considered to be less thermodynamically stable than amides and esters,^{291–293} and therefore SuRE reactions using thiols were expected to be a more challenging prospect.

To aid in the development of this chemistry, it was proposed that DFT calculations would be useful to address whether thiolactone formation was thermodynamically viable. The work presented in this section highlights the computational chemistry used during the development of thiolactone-forming SuRE reactions, and how this aided another Unsworth group member, Dr Kleopas Palate, during the development of a synthetic procedure (Figure 156).

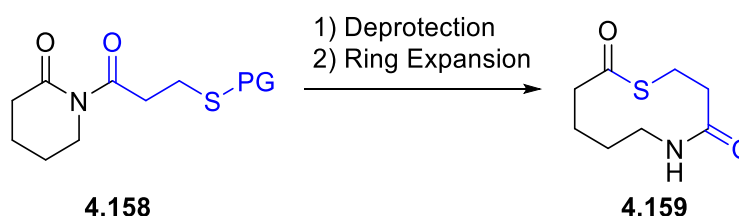


Figure 156. Proposed thiolactone SuRE reactions.

As discussed previously, SuRE reactions to increase the ring-size by 4 atoms for the formation of lactams and lactones are typically easier than the 3 atom counterparts.^{278,279,294} Therefore the equivalent thiolactone variant of these were studied first.

During the conformational search it was noted that whilst nitrogen and alkoxy oxygen atoms have been parametrised within the MMFF forcefield specifically for their inclusion in amide and ester functionalities respectively, parameters for the sulphur atom within thioesters are not included.²⁹⁵ Therefore, the functional group was treated as a thioether and a generic carbonyl. To account for this, the geometry of each conformation was optimised to ensure the most accurate comparison of the relative energies. Otherwise, the rest of the methodology used was the same as has been discussed and verified previously (see Sections 4.2.2 and 4.2.3),²⁹⁴ with all DFT calculations using the B3LYP/6-31G* level of theory in a vacuum.

The DFT calculations suggested that formation of the thiolactones using SuRE was indeed less thermodynamically favoured than the equivalent lactam and lactone formation (Table 21). Successful ring expansion was only predicted when starting from medium sized lactams (**4.162_{RO}** and **4.163_{RO}**), with 8-membered rings considered to be the 'switch on' point.

Table 21. DFT-calculated relative energy difference for the 4-atom thiolactone ring expansions (**4.160**–**4.163**). All energies are Gibbs energy at 298.15 K at the B3LYP/6-31G* level of theory in a vacuum.

4.160, n = 1

4.161, n = 2

4.162, n = 3

4.163, n = 4

Compound	$\Delta G_{\text{rel}} \text{ RO} /$ kcal mol ⁻¹	$\Delta G_{\text{rel}} \text{ RC} /$ kcal mol ⁻¹	$\Delta G_{\text{rel}} \text{ RE} /$ kcal mol ⁻¹
4.160	0.0	+15.4	+7.5
4.161	0.0	+17.1	+3.8
4.162	0.0	+20.0	-3.0
4.163	0.0	+17.5	-7.1

Encouraged that SuRE reactions using thiols might be possible, Dr Palate optimised the reaction, starting from commercially available 13-membered lactam **4.121**. Whilst the relative energies of the isomers formed in this ring expansion were not calculated, lactam **4.121** was past the

'switch on' point (e.g. the DFT calculations in Table 21 suggests that lactams containing more than 8 atoms will ring expand) and hence likely to be thermodynamically viable. It was found that an Fm-protecting group strategy was the most successful and a 54% yield of the 17-membered macrocyclic thiolactone was isolated (Figure 157).

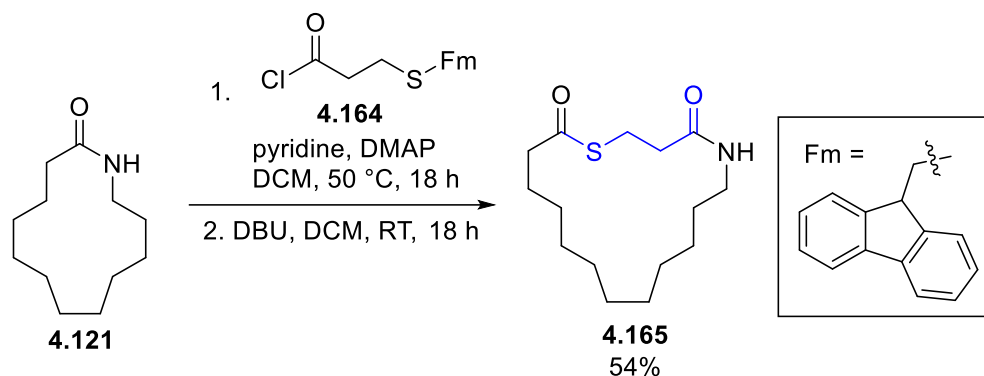


Figure 157. Thiolactone SuRE reaction of 13-membered lactam **4.121**, optimised by Dr Palate.

A ring-size substrate scope was then performed and the DFT data (Table 21) were consistent with the experimental outcomes. The thiolactone SuRE reactions were unsuccessful when starting with 6- or 7-membered lactams, **4.160** and **4.161**. However, expanded products were isolated for starting ring sizes between 8 and 13, in 15–54% yields (Figure 158, **4.162** and **4.163**).

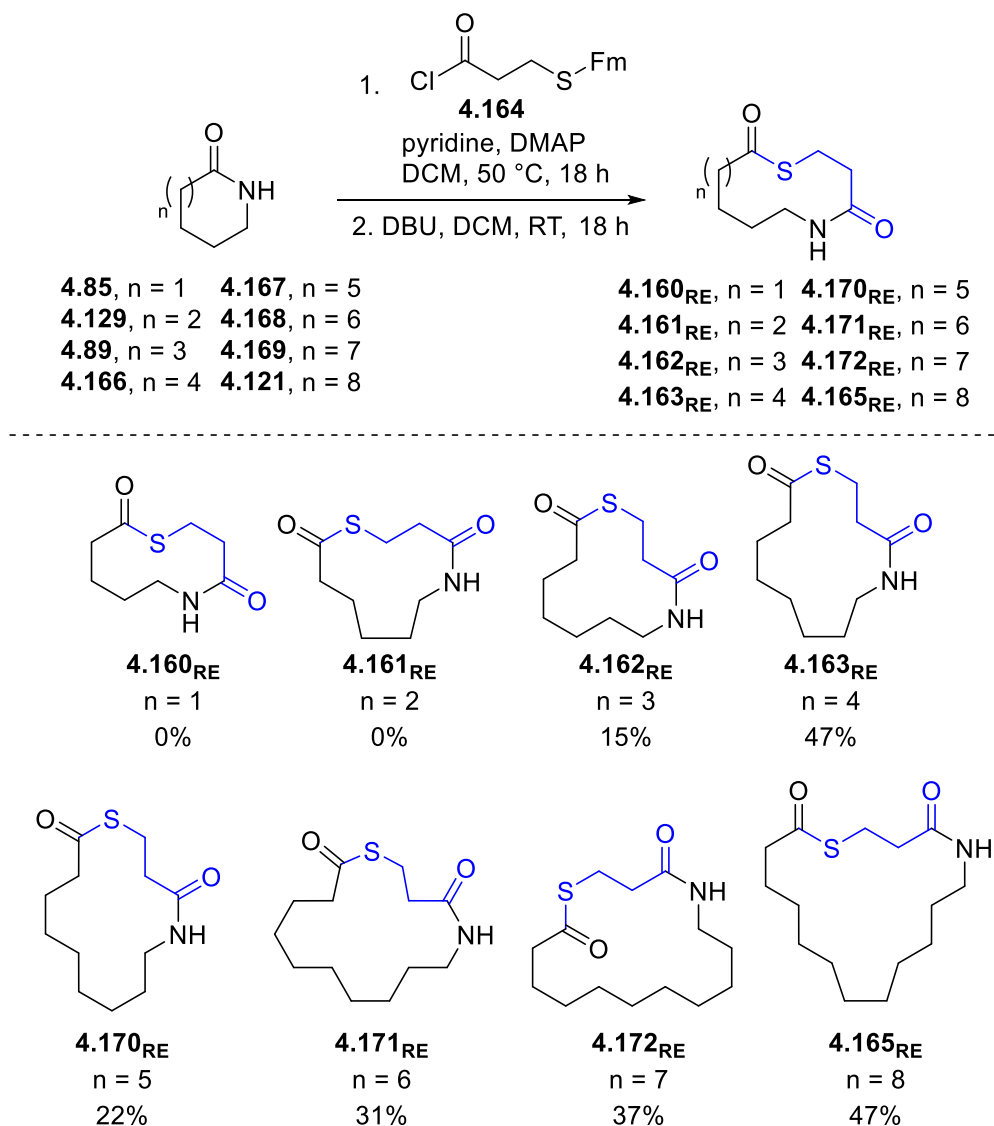


Figure 158. Ring-size screen of thiolactone forming SuRE reactions performed by Dr Palate.

Whilst the DFT calculations predicted that thiolactone SuRE reactions may be thermodynamically viable, it is important to note that they neglect the reaction kinetics for the sequential steps in the SuRE process, or indeed any competing side reactions. Therefore, they cannot reliably be used as an indicator of the reaction yield, just its viability. For instance, whilst the formation of **4.162_{RE}** was calculated to be thermodynamically viable (by 3.0 kcal mol⁻¹), only a 15% yield was achieved. A thioether side product (**4.173**) was isolated as the major product in a 43% yield, likely formed *via* a competing E_{1CB} and conjugate addition pathway (Figure 159). Similar products (**4.174** and **4.175**) were also observed by mass spectrometry and NMR spectroscopy for the unsuccessful ring expansions of **4.160_{RO}** and **4.161_{RO}**.

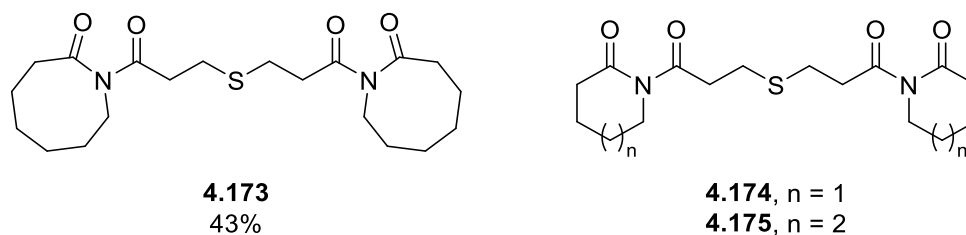


Figure 159. Side-products isolated or observed in thiolactone forming SuRE reactions performed by Dr Palate.

The development of a 3-atom ring expansion protocol was then considered, with the DFT calculations demonstrating again that for ring expansion to be successful, a large starting lactam was likely needed, to result in the formation of a macrocyclic product (Table 22).

Table 22. DFT-calculated relative energy difference for the 3-atom thiolactone ring expansions (**4.176** and **4.177**). All energies are Gibbs energy at 298.15 K at the B3LYP/6-31G* level of theory in a vacuum.

Compound	$\Delta G_{\text{rel RO}} /$ kcal mol ⁻¹	$\Delta G_{\text{rel RC}} /$ kcal mol ⁻¹	$\Delta G_{\text{rel RE}} /$ kcal mol ⁻¹
4.176	0.0	+7.9	+4.3
4.177	0.0	+6.9	-11.1

Acetylation of 13-membered lactam **4.121** using a variety of protected thioglycolic acids was challenging, and only by using the Fm-protecting group was imide **4.178** able to be isolated in good yield. However, despite the DFT calculations suggesting that ring expansion might be possible, no 16-membered ring expanded product (**4.177_{RE}**) was isolated after multiple attempts, with an intractable mixture formed (Figure 160a). It was proposed that under basic conditions degradation of the imide occurred, potentially *via* an intramolecular cyclisation (Figure 160b).^{296–298} Due to the observed problems during the attempted ring expansions, development of a synthetic route was discontinued.

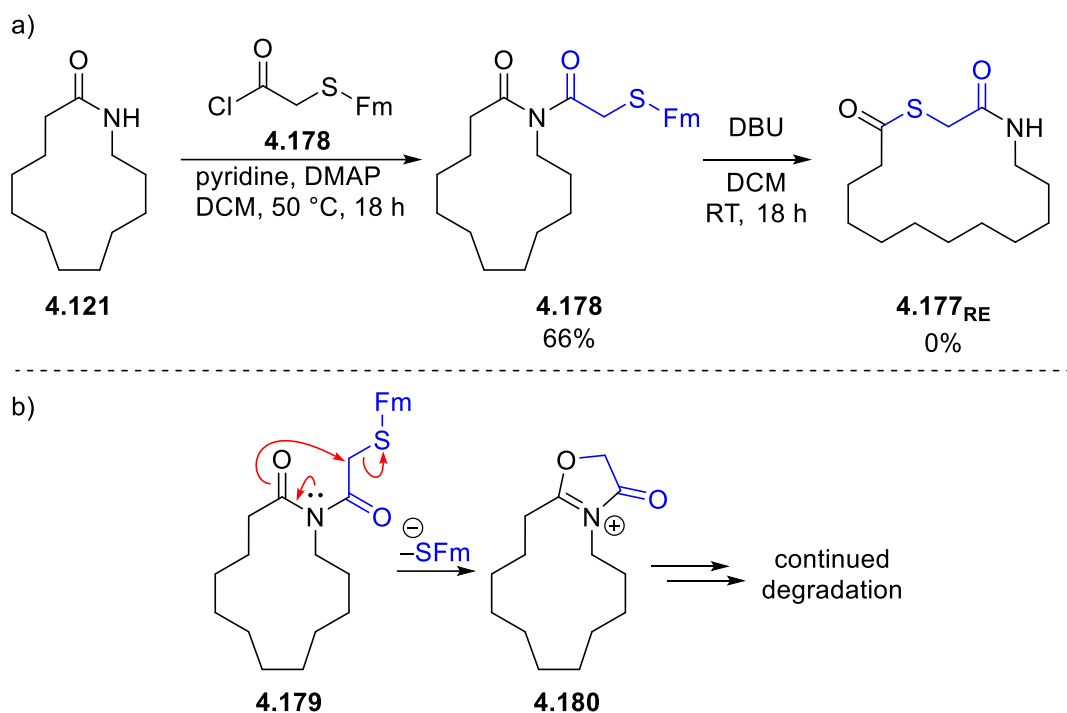


Figure 160. a) Attempted thiolactone SuRE reaction using Fm-protected imide **4.178** performed by Dr Palate. b) Proposed degradation pathway.

4.2.5 Dihydroxylation Ring Expansions

Further work by Dr Palate was in the development of a new variant of SuRE reactions. A procedure was developed in which the conjugate addition of an amine (**4.182**) into an acryloyl imide (**4.181**) allowed for formation of the ring expanded product (**4.183**, Figure 161). This method allows for the use of a common imide to result in a range of products by using different amines. These reactions were termed 'Conjugate Addition/Ring Expansion' reactions, or CARE.²⁹⁹

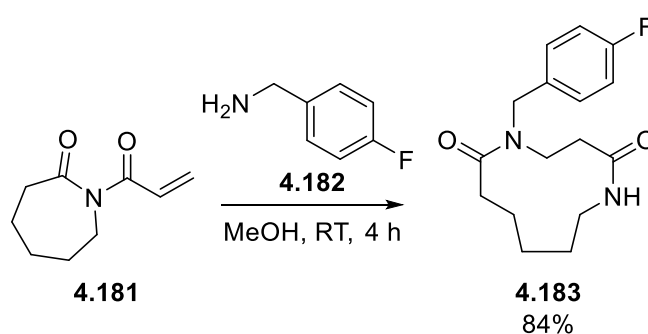


Figure 161. Conjugate addition/ring expansion (CARE) reaction reported by Palate *et al.*²⁹⁹

A natural expansion to this methodology was its use in the formation of lactones. Multiple methods at achieving this was attempted, the most successful of which was Sharpless dihydroxylation. Using this approach, 11-membered ring expanded lactone (**4.184 β -RE**) was isolated in 46% yield (Figure 162).

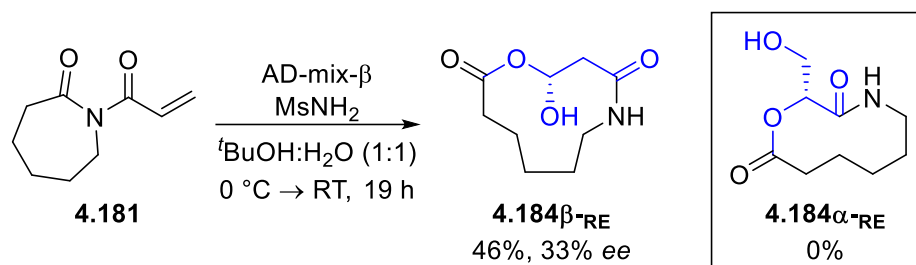


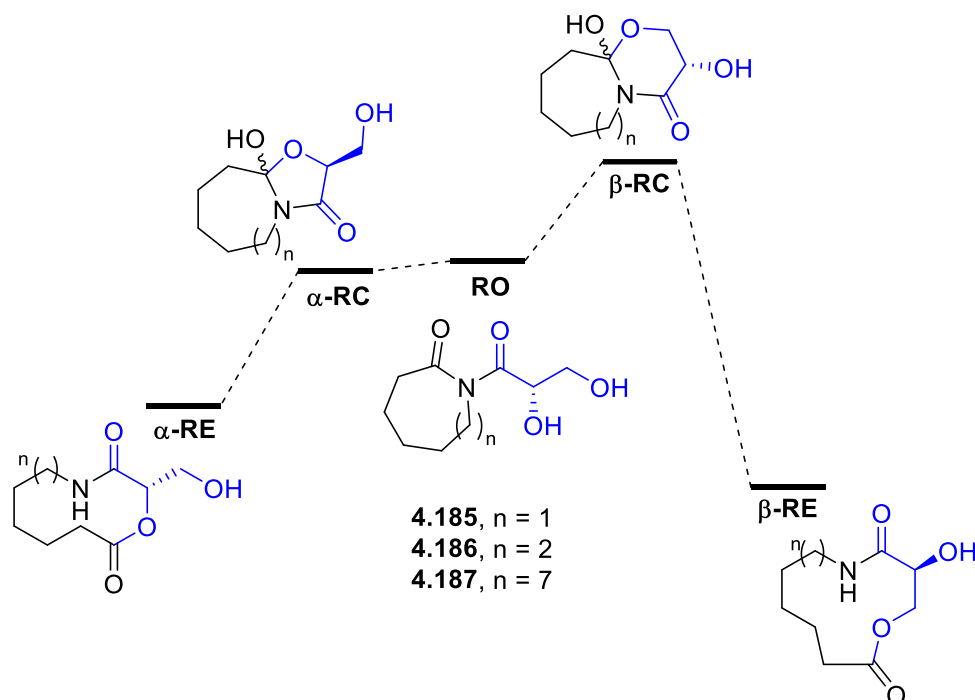
Figure 162. Dihydroxylation of acryloyl imide **4.181** resulting in 4-atom ring expansion product **4.184 β -RE** as performed by Balazs Pogranyi.

Whilst the 4-atom ring expansion took place during the dihydroxylation/ring expansion of 7-membered lactam **4.181**, another possible pathway was the analogous 3-atom ring expansion (*i.e.* via the other OH group) to form the equivalent 10-membered lactone product (**4.184 α -RE**). However, on the basis of the previously discussed experimental data with the α - and β -hydroxyacid ring expansions (Figure 146 and Figure 147), it was postulated that 4-atom ring expansion might be more thermodynamically favoured, and hence the only product observed.

DFT calculations were performed using the established method (conformational analysis followed by geometry optimisations at the B3LYP/6-31G* on the lowest energy conformation).²⁹⁴ The aim of these calculations were to determine both if there is a significant difference in the relative energy difference between the 3- and 4-atom ring expansion products, and how increasing the starting ring-size might effect this equilibrium. The 3-atom expansion intermediate and products are labelled as “ α -” and likewise the 4-atom isomers are labelled as “ β -”. Both possible diastereoisomers of the ring closed isomers (α -RC and β -RC) were considered, with only the lowest energy isomer shown.

The DFT-calculated energies demonstrated that in all cases the 4-atom ring expansion is significantly thermodynamically preferred, even in the case of the macrocyclic imide starting material (**4.187**). Compounds with 16- and 17-membered rings might be expected to have similar ring strain,²⁴⁰ so the DFT calculations provided encouraging evidence that the reactions might continue to be selective, even at very large ring sizes.

Table 23. DFT-calculated relative energy difference for the 3- and 4-atom dihydroxylation CARE ring expansions (**4.185–4.187**). All energies are Gibbs energy at 298.15 K at the B3LYP/6-31G* level of theory in a vacuum.



Compound	$\Delta G_{\text{rel RO}} /$ kcal mol ⁻¹	$\Delta G_{\text{rel } \alpha\text{-RC}} /$ kcal mol ⁻¹	$\Delta G_{\text{rel } \beta\text{-RC}} /$ kcal mol ⁻¹	$\Delta G_{\text{rel } \alpha\text{-RE}} /$ kcal mol ⁻¹	$\Delta G_{\text{rel } \beta\text{-RE}} /$ kcal mol ⁻¹
4.185	0.0	-0.5	5.7	-3.4	-9.4
4.186	0.0	-0.8	6.8	-10.0	-16.6
4.187	0.0	-0.3	6.3	-17.9	-21.0

Synthesis of 12-membered lactone (**4.186_{β-RE}**) from the 8-membered starting acryloyl imide (**4.188**) was successful with no evidence of the 11-membered product (**4.186_{α-RE}**) detected (Figure 163), which again was calculated by DFT to be the thermodynamic product. This is despite SuRE ring expansion reactions using α-hydroxyacids being successful with 8-membered lactams (Figure 146).

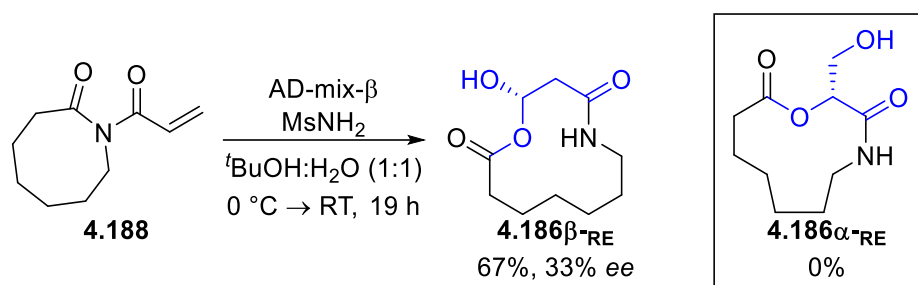


Figure 163. Dihydroxylation of acryloyl imide **4.188** resulting in 4-atom ring expansion product **4.186 β -RE** as performed by Balazs Pogranyi.

4.2.6 Concluding Remarks

An evaluation of different DFT methods was undertaken in relation to their success at predicting the outcome of successive ring expansion reactions. By comparing the experimental outcomes to the relative energies of the ring opened and ring expanded isomers, conclusions can be made.

The inclusion of dispersion corrections to the calculations, whether that be an empirical correction or the use of a Minnesota functional, can have a large effect on the ability to successfully predict the outcome of the SuRE reaction. It is therefore suggested, on the basis of the empirical fit to experimental data, that the B3LYP/6-31G* method is the most suitable to predict whether ring expansion can occur. It is also proposed that calculations where the difference in energy between the ring opened and ring expanded isomers is less than 3 kcal mol⁻¹, are less reliable in predicting the outcome.

With substrates where the ring expanded isomer is much lower in energy than the other isomers, the M06-2X/6-31G* method is equally successful (compared to the B3LYP/6-31G* method), and has indeed been used to good effect with studies such as those performed in the ring expansion reactions reported by Yudin.²⁷²

An instructive final remark is to highlight the fact that this method is now used routinely in the Unsworth group to assess the viability of new ring expansion reactions before committing to any synthetic effort, *e.g.* as was the case for the discussed thiolactone SuRE reactions. The combination of relatively short computation times and good predictive ability of the method make it a very useful tool to help synthetic focused group members make decisions on which reaction classes to prioritise, and to design better reactions.

The work described within this section is the subject of two publications,^{294,300} with a further manuscript draft currently in progress (dihydroxylation CARE). All synthetic and computational experiments performed by various co-authors were highlighted where necessary.

Chapter 5. Acyl Transfer SuRE

5.1 Introduction and Previous Work

In all the SuRE methodologies discussed in Chapter 4, *N*-acylation of the lactam is achieved *via* the use of acid chlorides, which are formed *in situ* by heating a carboxylic acid at reflux with oxalyl chloride. Whilst this has been successful, and good yields can be achieved, acid-sensitive molecules are unsuitable for these reactions. Attempts within the Unsworth group have been made at using carboxylic acid coupling reagents, but these have all been unsuccessful, with these alternative, less electrophilic acylating agents being too unreactive to react with the lactam nitrogen.³⁰¹

An alternative approach was therefore conceived, whereby the acylating agent could be added indirectly *via* a tethered side chain group (*i.e.* the 'YH' moiety in representative substrate **5.1**). The hope was that this could make *N*-acylation easier and negate the requirement to use acid chlorides. Thus, it was proposed that through acylation of lactams with alcohol or thiol sidechains (Y = O or S) using standard coupling procedures (**5.1** → **5.3**), the acyl group could migrate to the neighbouring amide (**5.4**), potentially through an increase in temperature or by using basic conditions. Once the imide (**5.5**) is formed ring expansion could then occur in the same way it does in regular SuRE reactions (Figure 164, see Section 4.1.5 for further details).

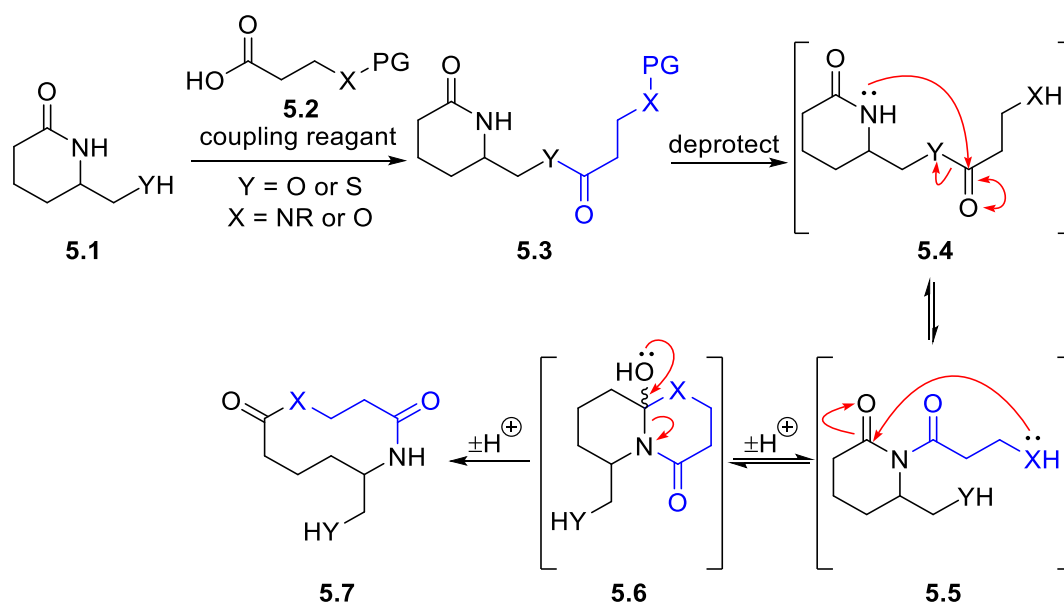


Figure 164. Proposed acyl migration SuRE reactions.

More ambitiously, it was postulated that if successful, this strategy may be used for the selective functionalisation of peptides (*e.g.* **5.8**, Figure 165a), and enable the selective insertion of a linear

fragment (*e.g.* another amino acid) into a peptide backbone by using the thiol group of cysteine moieties to direct peptide *N*-acylation (5.9 → 5.10). This route bears some similarity to native chemical ligation (NCL) reactions, which are well known for the synthesis of proteins (Figure 165b).^{302,303}

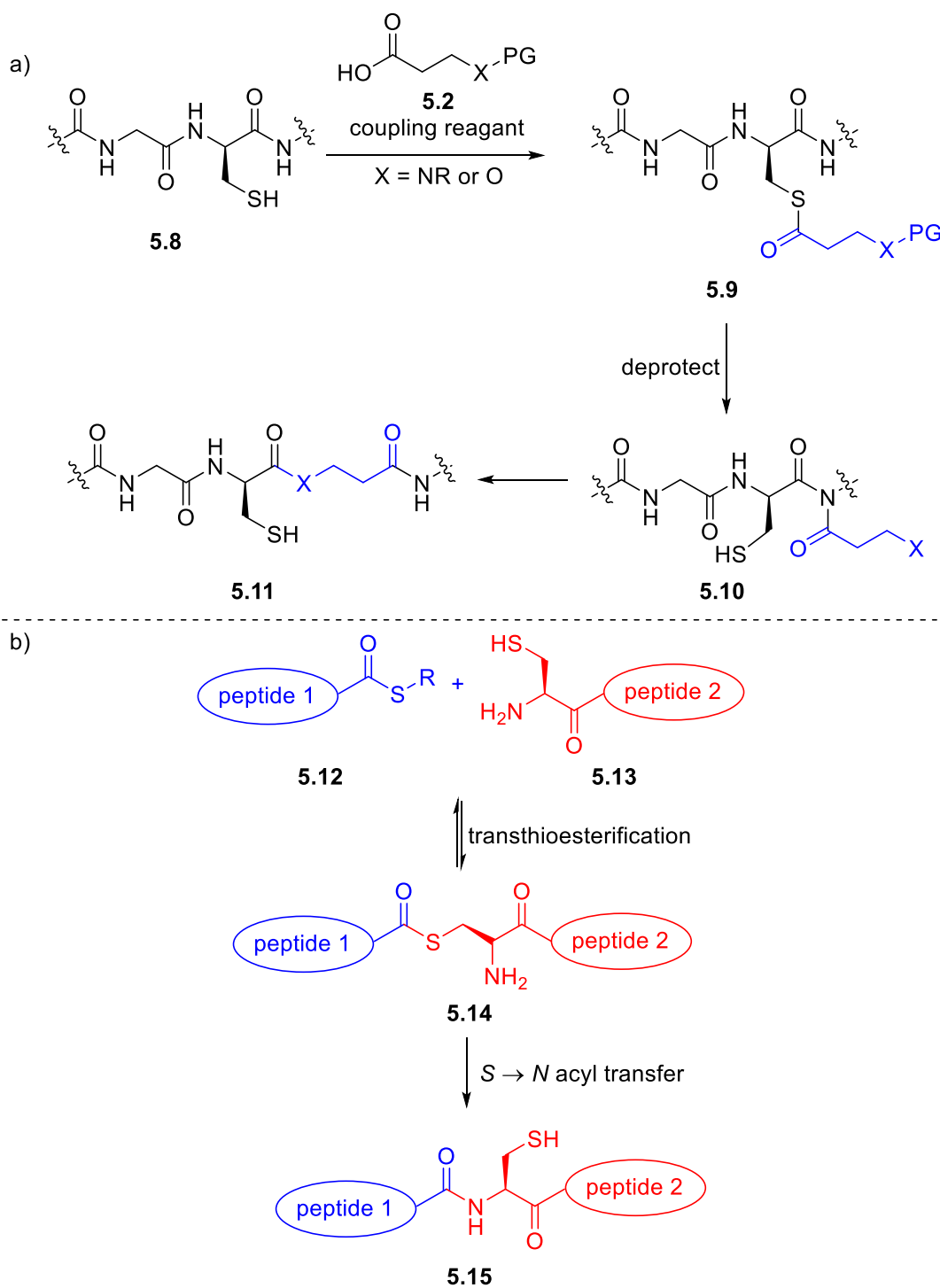


Figure 165. a) Proposed scheme for the insertion of a linear fragment into peptide chains. b) Native chemical ligation reactions used in protein synthesis.

Previous work by Dr Lawer attempted to establish a protocol for the acyl transfer SuRE reaction (e.g. Figure 164), however these attempts were unsuccessful (Figure 166).³⁰⁴ Most of the work was performed using ester derivatives (e.g. **5.16**); however, thioesters (e.g. **5.19**) were tried as well. Increasing the temperature, both with and without additional acidic or basic additives, were all attempted, however, either the products arising from hydrolysis (**5.18** or **5.21**) were isolated, or the starting material remained unreacted.

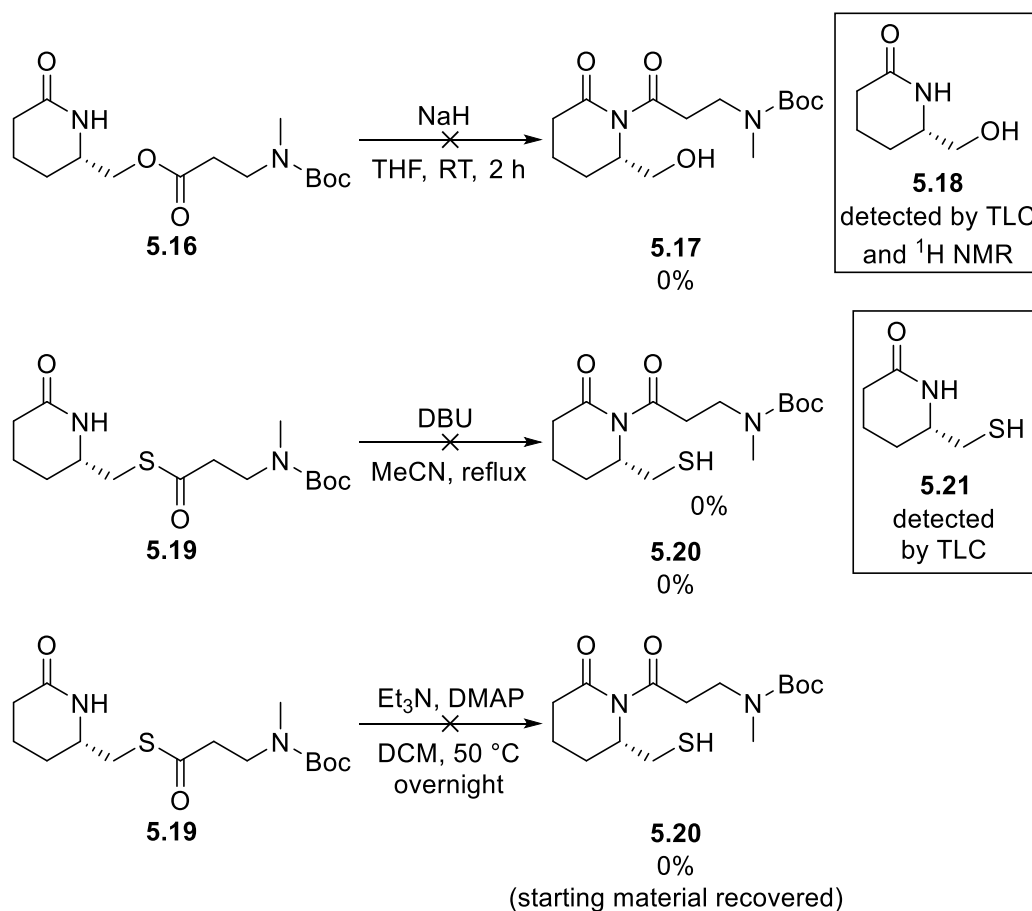


Figure 166. Selected examples of attempted acyl transfer reactions, performed by Dr Lawer.³⁰⁴

The aim of this work was to determine if DFT calculations could provide insight into the acyl transfer reactions, and if so, to develop a procedure to afford the desired, migration products.

5.2 DFT Calculations

Whilst the previous attempts at the acyl transfer SuRE reactions were unsuccessful (Figure 166), there remained an interest in these reactions, and therefore it was proposed that comparing the relative energies of the ester or thioester starting materials (denoted by **XAc**), with the resulting imides (denoted by **NAc**, Figure 167) using DFT, might provide insight into the viability of the acyl transfer reactions.

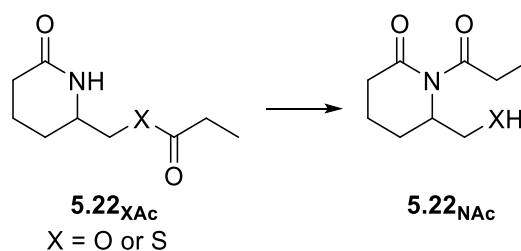


Figure 167. Isomers with which the energies were to be compared using DFT.

The DFT method for calculating the energies previously established (see Section 4.2) was used as this had shown to be successful in modelling other SuRE reactions. Both ester and thioester starting materials were considered in addition to the ring size of the lactam, which previous work by Hutton and co-workers had shown could be a factor in the success of acyl transfer reactions.³⁰⁵

The DFT-calculated energies demonstrated that in all cases studied, the desired imide product (**NAc**) was significantly less thermodynamically favourable than the starting material **XAc** (Table 24). The relative energy difference was lower for the thioester compounds (**5.24** and **5.26**), which was likely due to the reduced stability of the thioester compared to an ester, as discussed previously in the SuRE reaction of thiols (Section 4.2.4).^{291–293,300}

Table 24. DFT-calculated energies for $X \rightarrow N$ acyl migration. Energies are Gibbs energies at 298.15 K at the B3LYP/6-31G* level of theory in a vacuum.

5.23, $n = 1$, $X = O$

5.24, $n = 1$, $X = S$

5.25, $n = 4$, $X = O$

5.26, $n = 4$, $X = S$

Compound	$\Delta G_{\text{rel}} \text{ XAc} /$ kcal mol ⁻¹	$\Delta G_{\text{rel}} \text{ NAc} /$ kcal mol ⁻¹
5.23	0.0	+14.7
5.24	0.0	+3.6
5.25	0.0	+18.6
5.26	0.0	+6.6

Undeterred, articles found during literature searches suggested that acyl migrations can be promoted under acidic or basic conditions.^{306–308} It was therefore proposed that by exploiting the pK_a difference between the amide and alcohols or thiols, a thermodynamic driving force might be provided for the migration to occur. The pK_a values depend on the solvent used, with values reported in water and DMSO, for amides (≈ 15 and ≈ 25 respectively),^{309,310} alcohols (≈ 17 and ≈ 29)^{311,312} and thiols (≈ 11 and ≈ 17)^{312,313}. DFT calculations were performed to compare the relative energies when the isomers were treated as anions and explore this computationally. The B3LYP/6-31+G* level of theory was used, with the inclusion of diffuse basis functions considered preferable for the DFT treatment of anions.^{52,314–316}

The DFT calculations showed that under basic conditions it might be possible to afford the migration of the acyl group in the thioester starting materials (**5.28** and **5.30**, Table 25). The lactam ring size did have a significant effect, with the relative energy difference decreasing upon increasing ring-size. This is suggested to be due to increased steric clashes within the already strained medium-sized ring upon acyl migration.

Table 25. DFT-calculated energies for $X \rightarrow N$ -acyl migration under basic conditions. Energies are Gibbs energies at 298.15 K at the B3LYP/6-31+G* level of theory in a vacuum.

5.27, $n = 1, X = O$
 5.28, $n = 1, X = S$
 5.29, $n = 4, X = O$
 5.30, $n = 4, X = S$

Compound	$\Delta G_{\text{rel}} \text{N}^- /$ kcal mol ⁻¹	$\Delta G_{\text{rel}} \text{X}^- /$ kcal mol ⁻¹
5.27	0.0	+11.0
5.28	0.0	-12.7
5.29	0.0	+27.3
5.30	0.0	-2.5

Whilst the DFT calculations on this anionic system gave an indication that migration of the acyl group could be possible with the thioester derivatives, there was concern that when neutralised the reverse reaction could occur. Therefore, a strategy was proposed in which the thiolate anion (**5.33**), formed after the acyl transfer of **5.32**, would be trapped *in situ* (e.g. by a different acyl chloride **5.34**), preventing the reverse reaction (Figure 168). With this notion in mind, the synthetic experiments were then started.

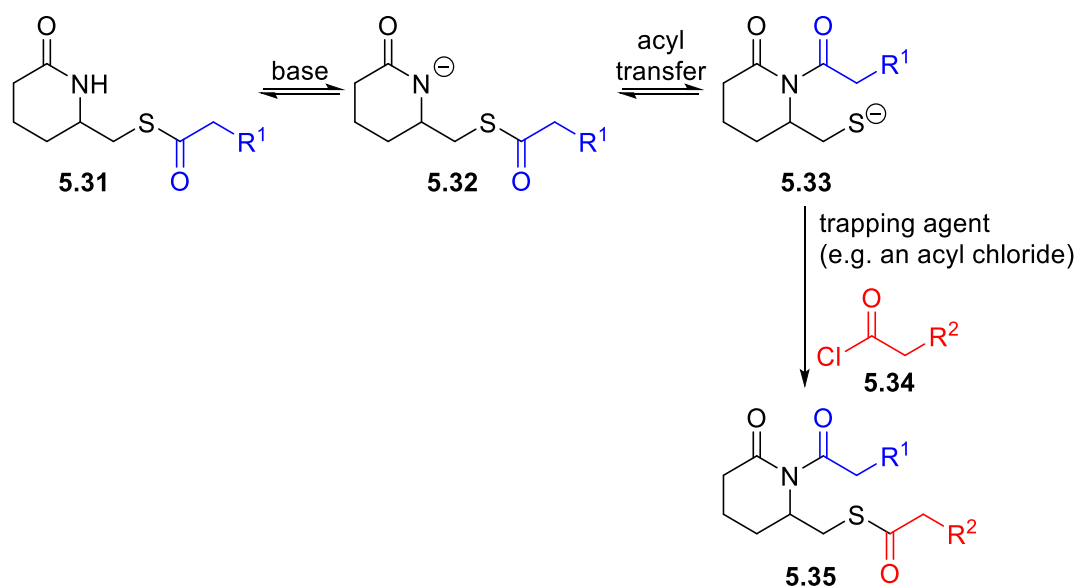


Figure 168. Proposed strategy for $S \rightarrow N$ acyl transfer for imide formation.

5.3 Starting Material Synthesis

Throughout the project, a number of starting materials and reagents were required to be synthesised. This section discusses the synthesis of these molecules, and is structured with the lactam synthesis first, followed by the Michael acceptor synthesis, protected carboxylic acid synthesis and thiol coupling.

Lactam Synthesis

A strategy for the synthesis of 6-membered lactam thiol **5.21** was proposed, using methods reported in the literature. Angle and co-workers reported a 4-step synthesis of alcohol **5.18** from *L*-lysine methyl ester dihydrochloride (**5.36**, Figure 169),³¹⁷ a cheap and readily available starting material.

The Boc-protection of *L*-lysine methyl ester dihydrochloride **5.36** proceeded in high yield. A ruthenium tetroxide (generated *in situ*) oxidation of **5.37** allowed for formation of amide **5.38**. Lactam **5.39** was afforded by treatment of amide **5.38**, which underwent Boc-deprotection followed by intramolecular cyclisation when refluxed in TFA. Finally, ester **5.39** was reduced under unusually mild conditions, with sodium borohydride able to yield the desired product (**5.18**).

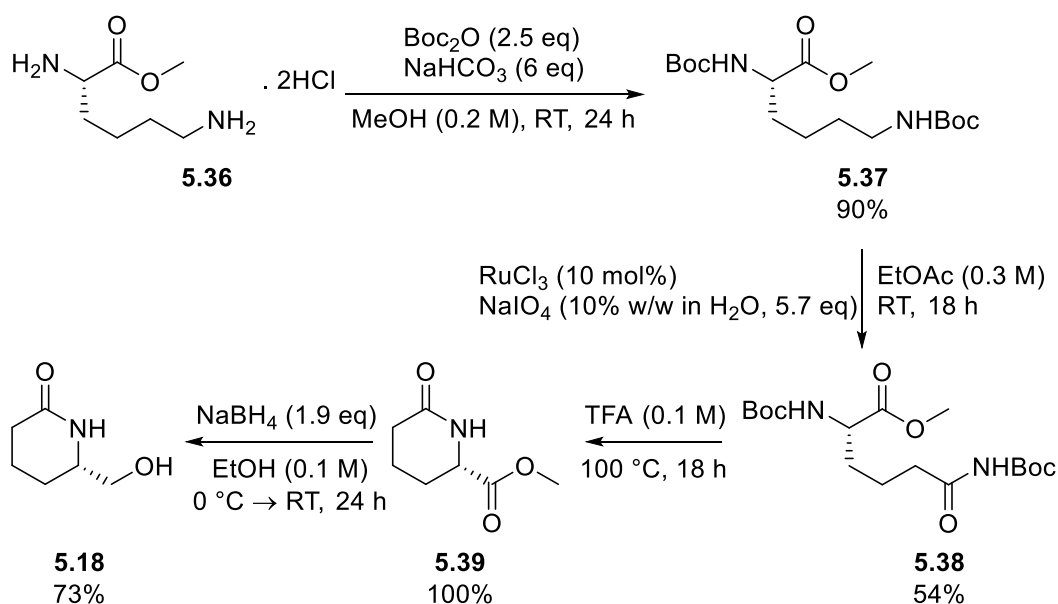


Figure 169. Synthesis of alcohol **5.18** from *L*-lysine methyl ester dihydrochloride **5.36**, using the methods reported by Angle *et al.*³¹⁷

A Mitsunobu reaction between alcohol **5.18** and thioacetic acid **5.40**, afforded thioacetate **5.41** in an 89% yield (Figure 170).³¹⁸

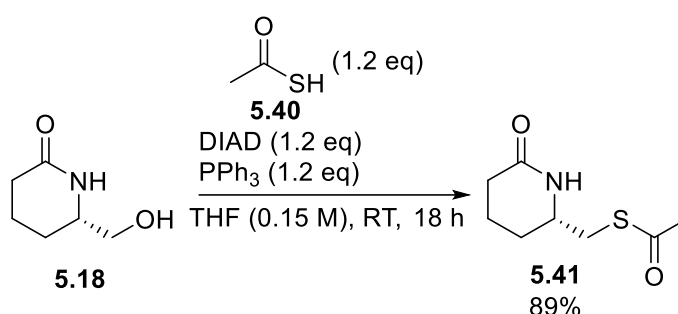


Figure 170. Mitsunobu reaction of alcohol **5.18**, adapted from a patent.³¹⁸

The first attempt at hydrolysis of thioacetate **5.41** was broadly successful with no starting material remaining (Figure 171). However, a disulphide side product (**5.42**) was isolated in addition to the desired product, likely promoted by oxygen.³¹⁹ The formation of the disulphide was suppressed by thoroughly degassing the solutions using nitrogen gas, allowing a higher yield of thiol **5.21** to be achieved.

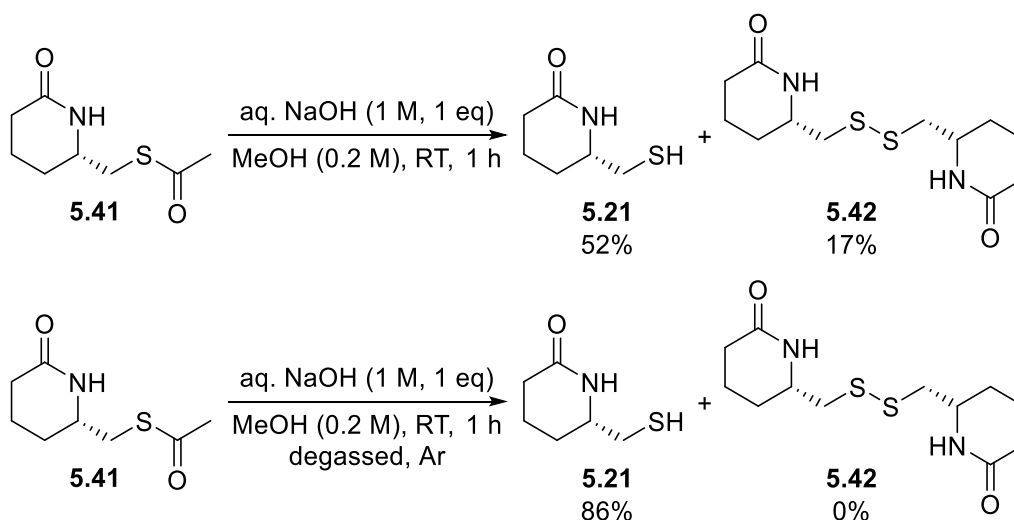


Figure 171. Hydrolysis of thioacetate **5.41**.

A 5-membered thioacetate analogue (**5.46**) was also synthesised using a similar method (Figure 172). Esterification of **5.43** was achieved *via* the formation of an acyl chloride using thionyl chloride.³²⁰ The product (**5.44**) wasn't isolated, and instead was reduced using sodium borohydride to achieve alcohol **5.45** in a 48% yield over 2 steps.³²¹ Finally, a Mitsunobu reaction was again used to afford the desired thioacetate (**5.46**) in a 70% yield.³¹⁸

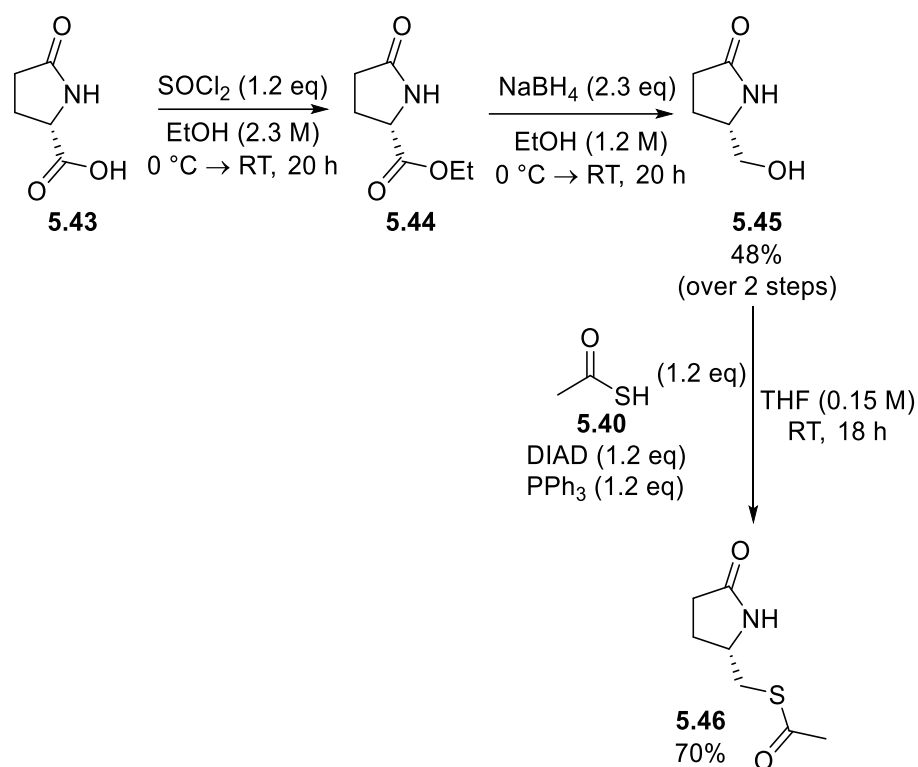


Figure 172. Synthesis of 5-membered thioacetate **5.46**. Using methods reported in the literature.^{318,320,321}

A final lactam that was synthesised was an ethyl-substituted analogue (**5.48**) of thiol **5.21**, to act as a steric mimic for substrate screening (for discussion, see Section 5.4.2). This was achieved following a literature procedure (Figure 173).³²² Grignard addition using ethylmagnesium bromide, followed by an *in situ* reduction using sodium cyanoborohydride yielded the desired product in a 47% yield.

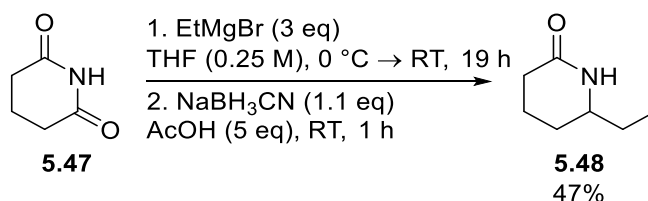


Figure 173. Synthesis of ethyl-substituted lactam **5.48** as reported by Chen *et al.*³²²

Michael Acceptors

To trap the thiolate after acyl migration, Michael acceptors were considered in addition to acyl chlorides. Taking inspiration from biochemical cysteine trapping methods,³²³ a series of substrates were explored (for discussion, see Section 5.4.2). Two compounds that were used needed to be synthesised.

First, an exocyclic maleimide derivate (**5.50**) was made following a literature procedure (Figure 174).³²⁴ A Wittig reaction using *N*-ethyl maleimide **5.49** and benzaldehyde **1.36** afforded the desired product in a 68% yield. Only one stereoisomer was detected in the crude ¹H NMR spectrum, which was consistent with **5.50** having *E*-stereochemistry, as determined and reported by Parmar *et al.*³²⁵

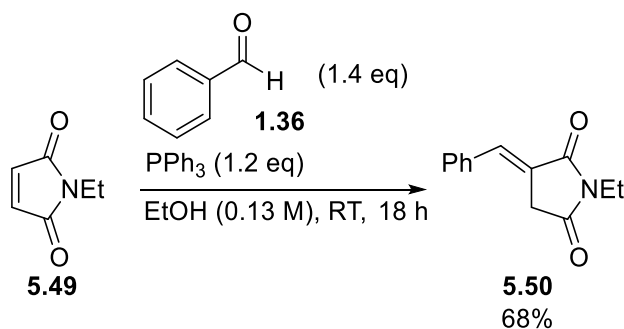


Figure 174. Synthesis of exocyclic maleimide **5.50**, as reported by Yan *et al.*³²⁴

Terminal ynone **5.52** was synthesised according to literature procedures in 2 steps.^{326,327} Grignard addition of ethynylmagnesium bromide **5.51** into benzaldehyde **1.36** afforded propargyl alcohol **1.5** in an 81% yield, which was then able to be oxidised using activated manganese oxide, to give the product ynone **5.52** in a 43% yield.

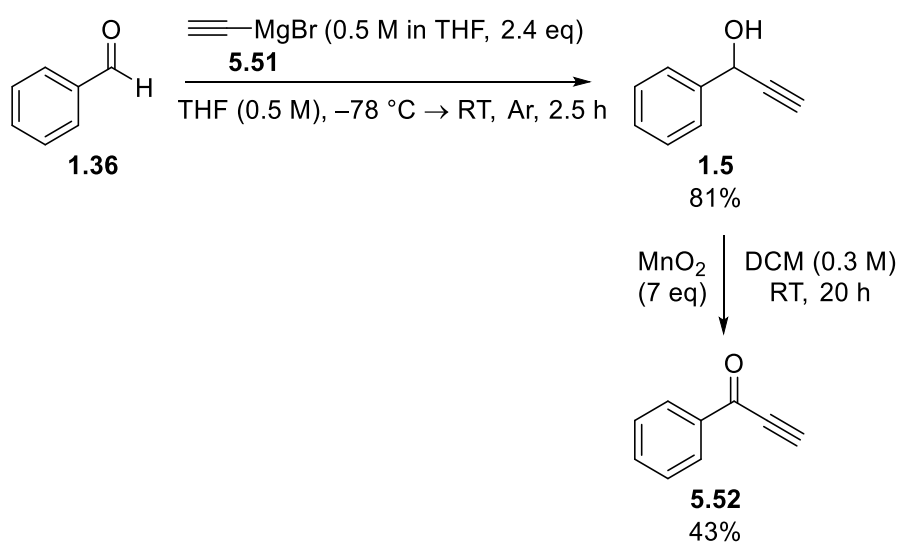


Figure 175. Synthesis of terminal ynone **5.52**, as reported in literature.^{326,327}

Protected Carboxylic Acid Synthesis

Three protected carboxylic acids were used to make different thioester analogues (for more details, see Section 5.4.4). Whilst commonly used protected hydroxyacids and Fmoc-protected

amino acids were available within the Unsworth group inventory. One protected acid had to be made.

N-Boc *N*-methyl β -alanine **5.54** was made following a reported procedure,³²⁸ in which commercially available *N*-Boc β -alanine **5.53** was methylated using an excess of sodium hydride and methyl iodide (Figure 176). An acid/base extraction was able to yield the desired product in a 92% yield.

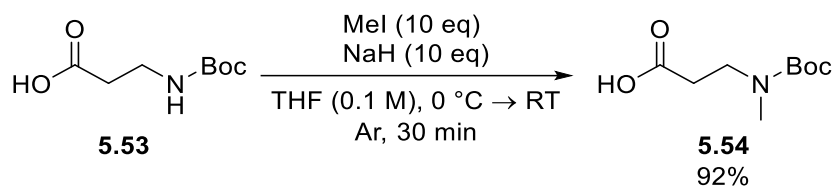


Figure 176. Methylation of *N*-Boc β -alanine **5.53**, as reported in the literature.³²⁸

Thiol Coupling

A series of thioesters were made using 6-membered thiol **5.21**. Initially, HATU was used to couple *N*-benzyl *N*-Fmoc β -alanine (**5.55**), following a procedure developed by Dr Lawer during the previous work.³⁰⁴ The procedure was successful (Figure 177), however, after column chromatography the desired product (**5.56**) was \approx 75% pure (by ^1H NMR analysis), with contamination from tetramethylurea, a by-product formed from the HATU coupling reagent. After taking into account the impurity, the conversion to the coupled product **5.56** was calculated at 57%.

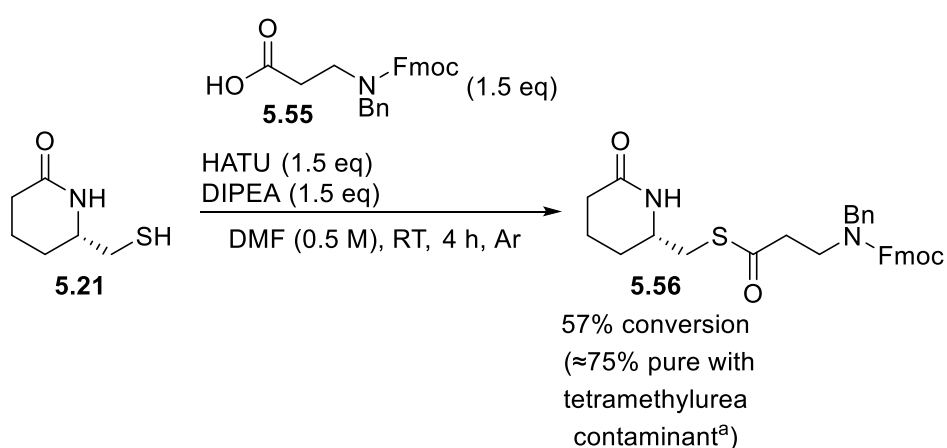


Figure 177. HATU coupling procedure of thiol **5.21** with *N*-benzyl *N*-Fmoc β -alanine **5.55**. ^a Determined by ^1H NMR spectroscopy.

To avoid the problems with tetramethylurea coelution, the coupling reaction between **5.21** and **5.55** using T3P was considered, as the phosphate side products can be removed through an aqueous work-up. A similar yield of 54% was achieved, however this time there were no impurities present (Figure 178).

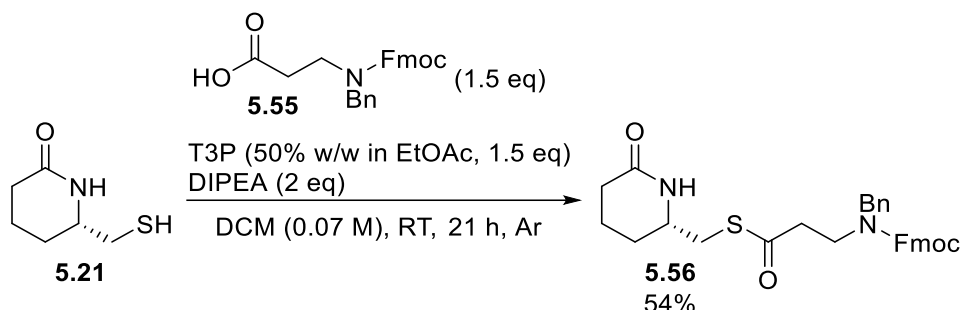


Figure 178. T3P coupling procedure of thiol **5.21** with *N*-benzyl *N*-Fmoc β -alanine **5.56**.

This same procedure was then used for the synthesis of two further thioester derivatives (**5.57** and **5.59**, Figure 179), using *N*-Boc *N*-methyl β -alanine **5.54** and Bn-protected β -hydroxyacid **5.58**. Again, these procedures were successful, however the yields of the product weren't as high as expected. Optimisation could likely improve these yields however it was considered that unless the desired acyl migration was successful, it was not a priority at that time.

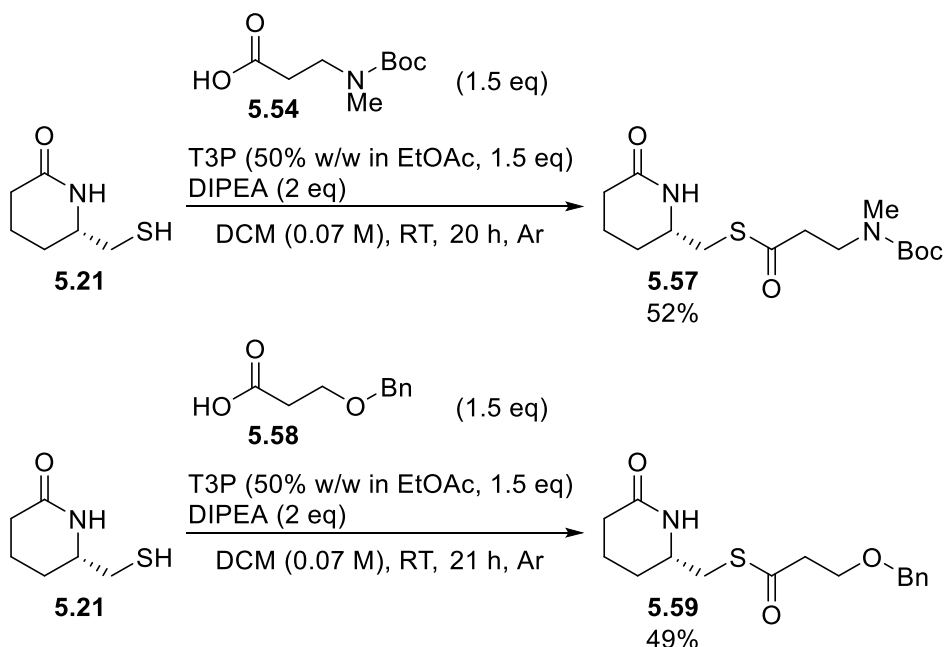


Figure 179. T3P coupling procedure of thiol **5.21** with *N*-Boc *N*-methyl β -alanine **5.54** and Bn-protected β -hydroxyacid **5.58**.

5.4 Acyl-Transfer Studies

5.4.1 Studies using acid chloride trapping

Based on the DFT studies (see Section 5.2), it was first considered that the thiolate anion (*e.g.* **5.62**) formed after migration (**5.61** → **5.62**) could be trapped using an acid chloride (*e.g.* **5.63**, Figure 180). After deprotection this could undergo a SuRE reaction (**5.64** → **5.65**). The primary factor in pursuing this route was that, if successful, the acid chloride used (*e.g.* **5.63**) could ultimately be a linear fragment with which further ring expansion could be achieved. After a final migration, using acetyl chloride (**3.36**) to trap the intermediate could potentially allow for a ring expansion (**5.65** → **5.66**). The acetate-protected thiol could then easily be hydrolysed if desired.

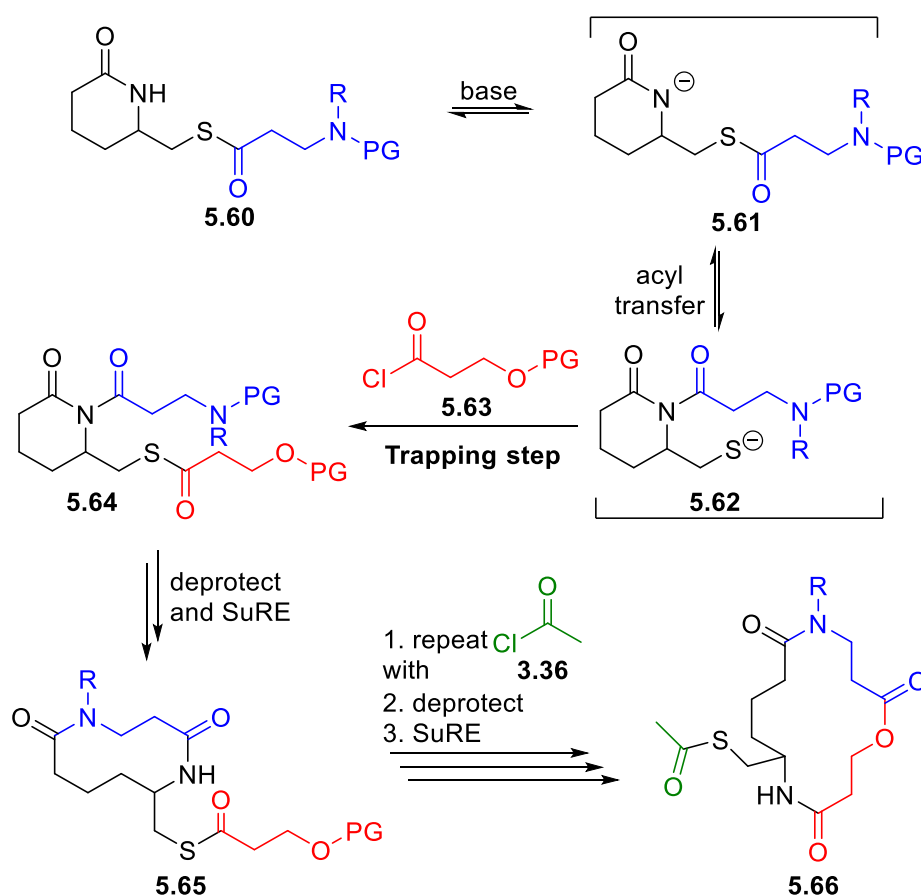


Figure 180. Proposed process for iterative acyl migration and SuRE ring expansion reactions.

Initial studies were performed using simple acetate thioester **5.41**, and propionyl chloride **5.67**, in an attempt to form imide **5.68** (Figure 181). Triethylamine was chosen as a mild, organic base ($pK_{aH} \approx 11$ in H_2O),³²⁹ which based on the general pK_a value of thiols ($pK_a \approx 11$ in H_2O)³¹³ is capable of deprotonating a significant proportion of any thiol that might be formed in the migration reaction, to form the thiolate, which can be subsequently trapped by reacting with the propionyl chloride.

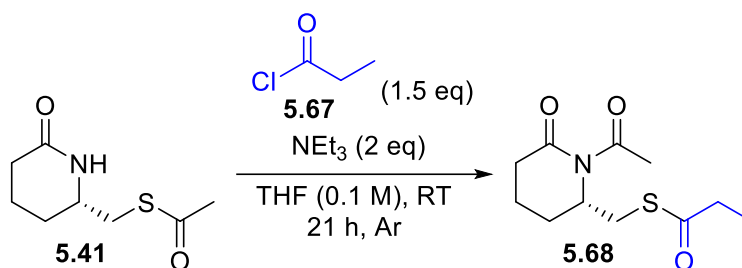


Figure 181. Proposed acyl transfer reaction of thioester **5.41**, trapping with propionyl chloride **5.67**. After 21 hours, TLC analysis showed a variety of new products forming in the reaction, however a vast majority of the starting material ($\approx 75\%$ by ^1H NMR analysis of the crude reaction mixture) also remained. An ESI mass spectrum was recorded of the crude reaction mixture, and whilst an ion consistent with the desired molecular weight was found (*e.g.* **5.69**, Figure 182) another mass peak was also observed at 322.1075, the m/z of which is consistent with an addition of a further propionyl chloride during the reaction, with an example structure shown in Figure 182 (*e.g.* **5.70**). Many products were formed with a similar polarity that were unable to be separated by chromatography, so the exact species were unable to be characterised.

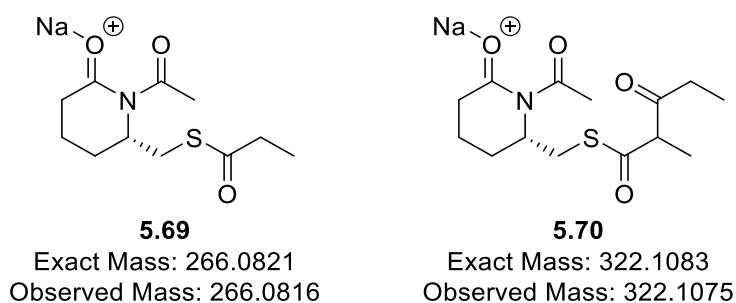


Figure 182. Cations observed in the crude mass spectrum in the attempted acyl transfer reaction of **5.41** using triethylamine. Structures given are examples only, and no characterisation was done.

It was proposed that triethylamine caused enolate-related species to be formed (*e.g.* **5.71** \rightarrow **5.72**), which were then able to react with propionyl chloride (*e.g.* **5.72** \rightarrow **5.73**). The many products observed *via* TLC analysis suggests that this process is unselective. An example mechanism is shown in Figure 183.

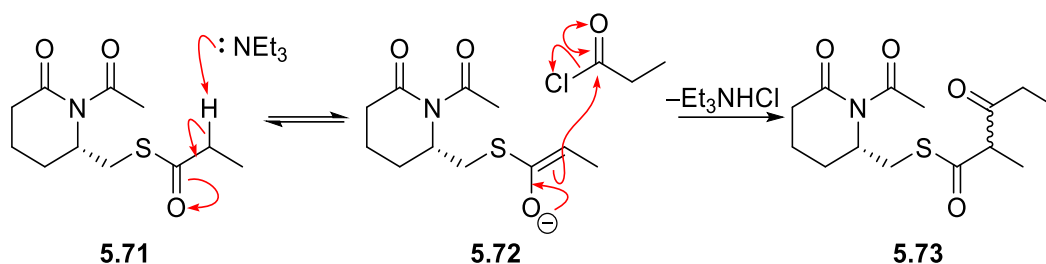


Figure 183. Mechanism highlighting a proposed enolisation and substitution pathway.

To try and suppress the undesired pathways, the reaction was repeated using pyridine, as a weaker base than triethylamine (Figure 184). TLC analysis of the reaction mixture showed only one visible product, and after 22 hours no starting material remained. A mass spectrum of the crude reaction mixture also showed no evidence of the mass peaks for multiple propionyl chloride addition. A product was isolated in a 58% yield (albeit impure with an unknown and inseparable impurity), however the NMR data were instead consistent with direct addition of the propionyl chloride to the amide (5.74).

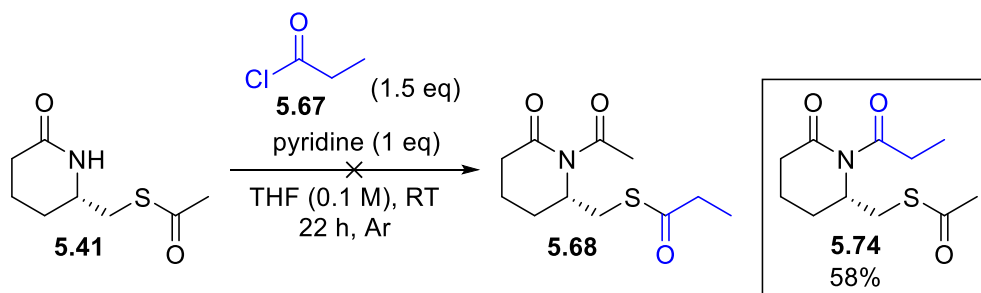


Figure 184. Reaction of thioacetate **5.41** with propionyl chloride **5.67** and pyridine.

HMBC and $^{13}\text{C}\{^1\text{H}\}$ NMR data were the most important for assignment of where the propionyl group was added (Figure 185). A resonance was observed in the $^{13}\text{C}\{^1\text{H}\}$ NMR spectrum at $\delta_{\text{C}} = 194.8$ ppm, which is consistent with the thioester carbonyl. In the HMBC spectra there is a clear crosspeak between the resonance at $\delta_{\text{C}} = 194.8$ ppm and a singlet resonance at $\delta_{\text{H}} = 2.33$ ppm, which was assigned as the acetate methyl group (H^{a}). Additionally, one of the diastereotopic CH_2 protons at $\delta_{\text{H}} = 3.25$ ppm (H^{b}) also has a crosspeak with the same thioester carbonyl resonance. Finally, the triplet resonance at $\delta_{\text{H}} = 1.12$ ppm, which is consistent with the methyl group of the propionyl group (H^{c}), has a crosspeak with one of the imide carbonyls, at $\delta_{\text{C}} = 177.6$ ppm.

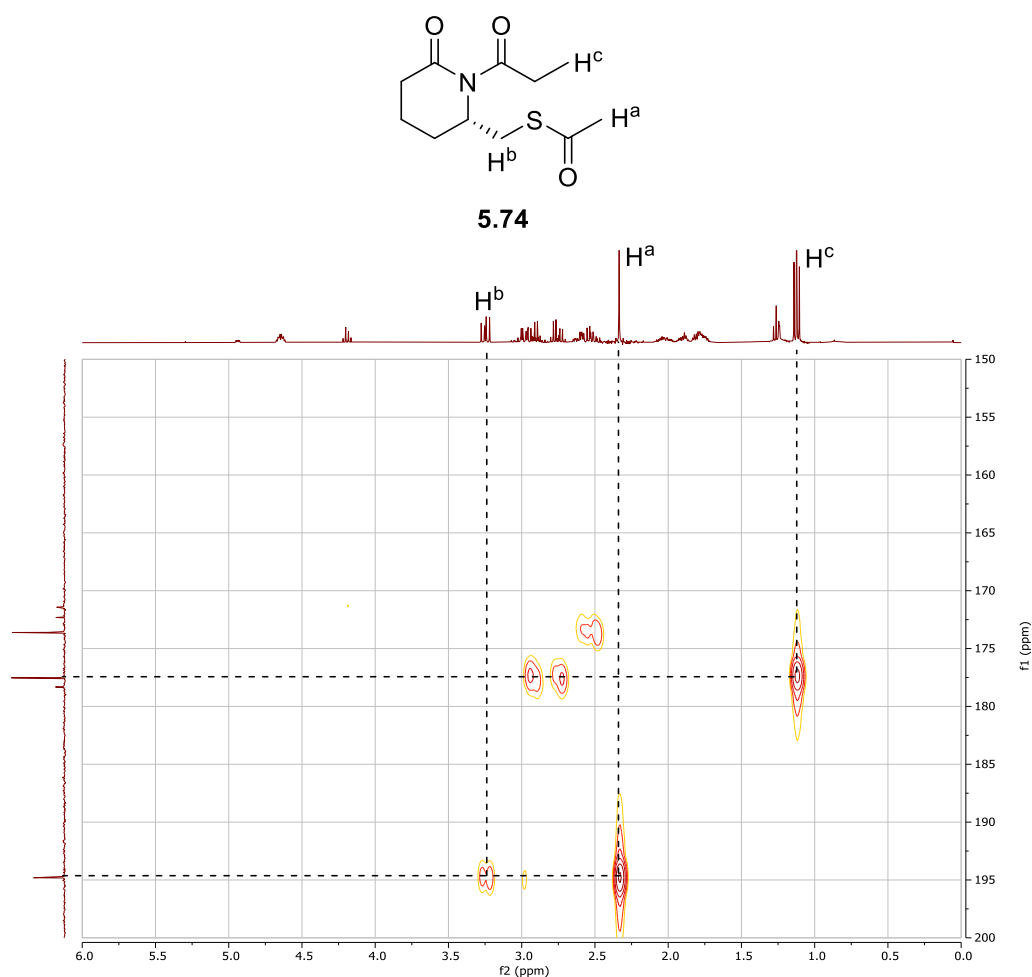


Figure 185. HMBC data with selected assignments used to determine the structure of **5.74**. NMR data recorded on 400 MHz spectrometer, in CDCl₃.

The reaction was repeated using 5-membered lactam analogue **5.46** (Figure 186), and again, instead of the desired migrated product (**5.75**), a product from direct imide formation was instead isolated (**5.76**), in a low 35% yield (starting material was remaining). Assignment of this compound was done using the same key HMBC resonances as previously discussed.

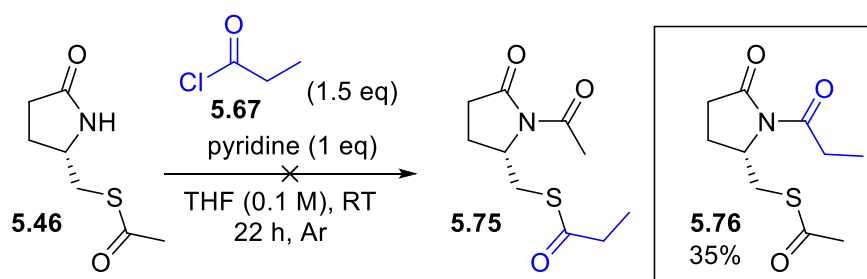


Figure 186. Reaction of thioacetate **5.46** with propionyl chloride **5.67** and pyridine.

5.4.2 Studies using Michael acceptors for trapping

In the attempted acyl-transfer reactions using acyl chlorides as the trapping agent previously discussed (see Section 5.4.1), acylation occurred directly on to the amide nitrogen (Figure 184 and Figure 186), even under the mild conditions used. Taking inspiration from the way in which cysteine amino acid residues are targeted over lysine amino acids in biochemical systems,³²³ Michael acceptors were considered as trapping agents. It was proposed that the amide nitrogen might be unreactive with these softer electrophiles, and that therefore they would react only with the thiolate anion.

Due to the time taken to synthesise thioester compound **5.41**, an alternative approach was devised to screen the Michael acceptors. A binary approach was considered (Figure 187), in which a simpler lactam (**5.48**), and isobutyl mercaptan (**5.77**) could be used to test the reaction. If only the thiol reacted, then this could be a potential substrate to trial. This approach is exemplified in Figure 187 with *N*-ethyl maleimide (**5.49**) as the Michael acceptor.

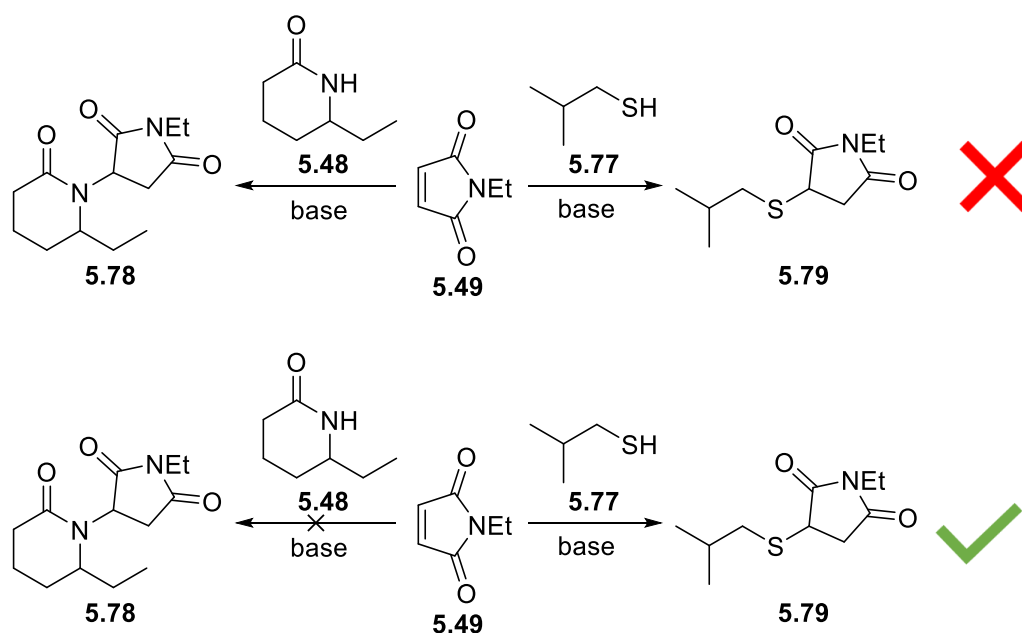


Figure 187. Representation of the Michael acceptor study.

N-ethyl maleimide **5.49** is a widely used substrate within biochemistry for selectively reacting with cysteine residues,^{323,330} and was therefore considered first in this study. A reaction of thiols with maleimides under basic conditions was found in the literature and used as the basis of the conditions used.³³¹

The reaction of isobutyl mercaptan **5.77** and maleimide **5.49** with triethylamine was successful, with clean conversion observed within 30 minutes (Figure 188). A yield wasn't recorded, however in the crude ^1H NMR spectra only the desired product (**5.79**) was observed, with no unreacted maleimide **5.49** present.

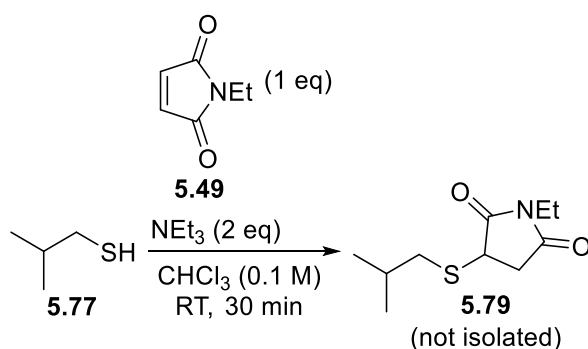


Figure 188. Trial reaction between isobutyl mercaptan **5.77** and *N*-ethyl maleimide **5.49**.

Upon attempting the reaction under the same conditions using ethyl-substituted lactam **5.48**, no product was observed (Figure 189). Whilst this was the desired outcome, it was noted that only the unreacted lactam was present in the crude ^1H NMR spectrum, and the reaction itself went a red colour. It has been reported in the literature that it is possible to polymerise maleimides under basic conditions,^{332–334} with articles also reporting a red solution during the process.^{332,335} This suggested that *N*-ethyl maleimide **5.49** was polymerising under these conditions which could therefore be problematic. Different bases were tested (DBU, DIPEA and K_2CO_3) however the same results were observed.

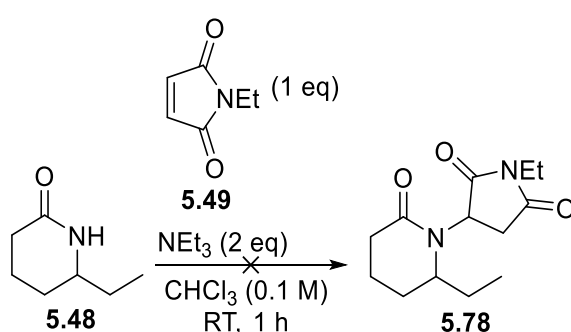


Figure 189. Unsuccessful reaction of ethyl-substituted lactam **5.48** and *N*-ethyl maleimide **5.49**.

The next Michael acceptor that was used, was a phenyl-substituted exocyclic maleimide (**5.50**).^{330,336} The reaction was attempted using similar conditions to those using *N*-ethyl maleimide **5.49**, however in this instance, neither the thiol (**5.77**) nor the lactam (**5.48**) reacted

with **5.50** (Figure 190). The lack of reactivity even with the thiol could be due to the choice of substituent on the alkene, in the future, an alkyl substituent could be more successful.

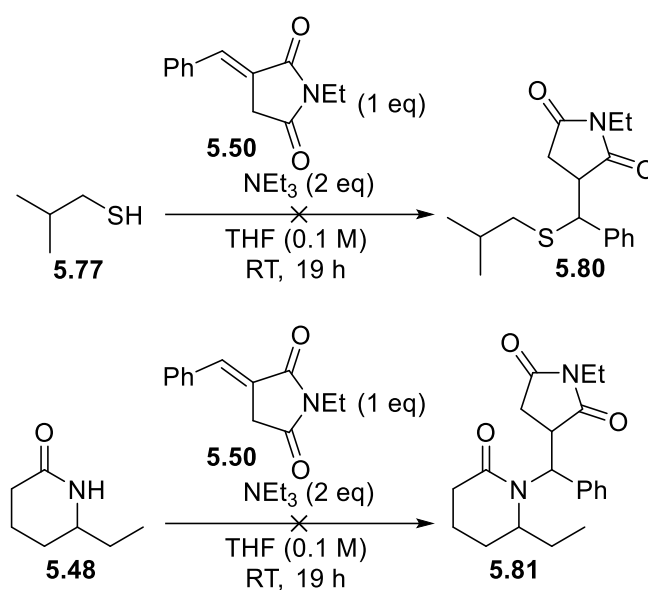


Figure 190. Unsuccessful reaction of thiol **5.79** and **5.48** with phenyl-substituted exocyclic maleimide **5.50**.

Precedent was found which suggested that electron-deficient alkynes have been used to selectively functionalise cysteine residues.^{323,330,337} Ynones were therefore considered as they have been used extensively in part of this project (see Chapter 3). A procedure was found for the reaction of alkyl thiols with phenyl-substituted ynone **3.27**.³³⁸ These conditions were used in the reactions of thiol **5.77** and lactam **5.48**. Clean conversion of the thiol was seen, with only the product **5.82** present in the crude ^1H NMR spectrum. However, no reaction was observed using lactam **5.48**.

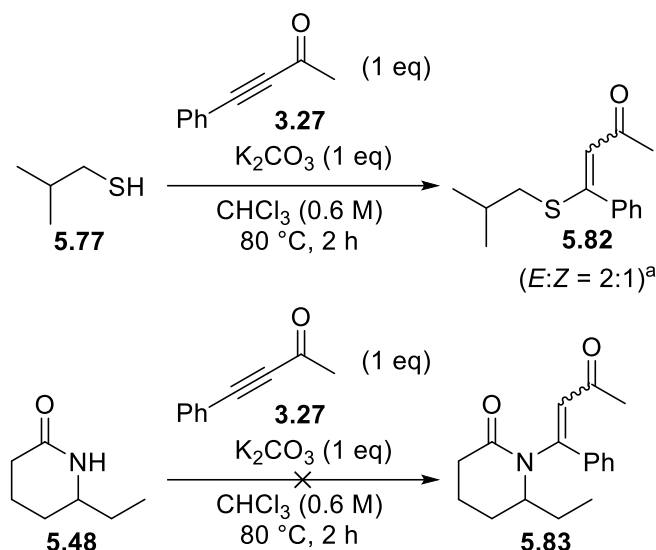


Figure 191. Reactions of thiol **5.77** and lactam **5.48** with phenyl-substituted ynone **3.27**. a) Stereochemistry assigned by comparison of an analogous compound, reported by Nishio *et al.*³³⁹

Encouraged that no lactam functionalisation was observed, even under the high temperature used, the reaction was attempted using the thioacetate lactam **5.41** (Figure 192). Following reaction for 16 hours, starting material was still present, however encouragingly there were two new products on TLC analysis. The crude ¹H NMR spectrum also showed resonances consistent with the alkene protons in **5.82**. Purification yielded a compound, with NMR data which were consistent with the desired, migrated product **5.84** in a 56% yield (slightly impure), and a side product which was identified as a *bis*(acetate) lactam **5.85**.

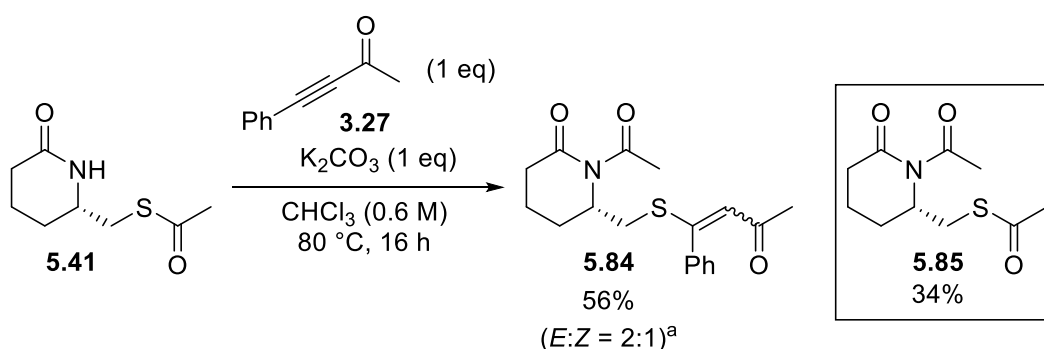


Figure 192. Reactions of thioester **5.41** with phenyl-substituted ynone **3.27**. a) Stereochemistry assigned by comparison of an analogous compound, reported by Nishio *et al.*³³⁹

It was proposed that the *bis*(acetate) side product **5.85** could form from competing thioesterification reactions of the thiolate after migration had occurred (**5.86**, Figure 193), either with other thioacetates (*e.g.* **5.87**), or *via* imide acetates (*e.g.* **5.88**) (reactions of nucleophiles

with imides had been seen in previous SuRE studies).³⁰⁰ Other products were present on TLC analysis of the crude reaction mixture, no further materials could be isolated.

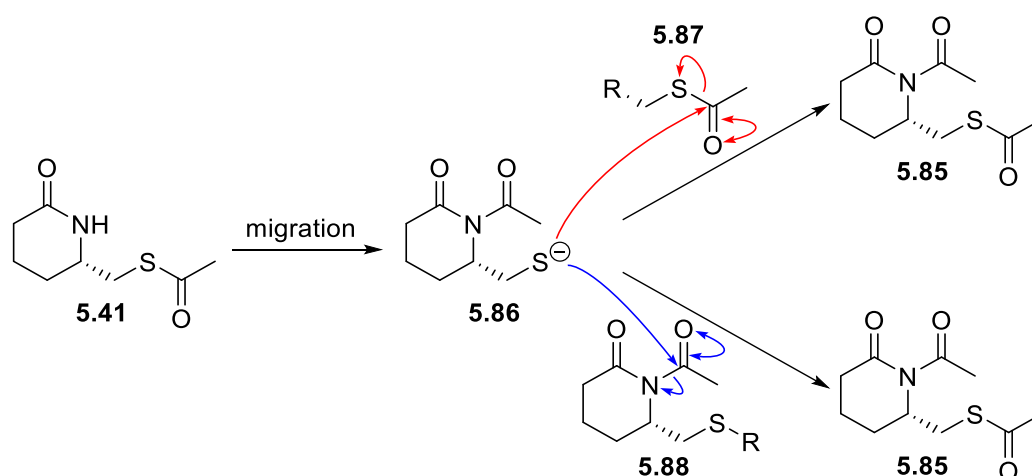


Figure 193. Proposed mechanisms for *bis*(acetate) 5.85 formation.

5.4.3 Optimisation of acyl migration/ynone trapping reaction

Encouraged that acyl migration has been achieved using an ynone to trap the thiolate (Figure 192), work began on optimising the reaction, focused on reducing the amount of starting thioester 5.41, and *bis*(acetate) side product 5.85. First, the reaction was attempted without any added base, but no conversion was observed (Figure 194). This result demonstrates that basic conditions were required, which is in good agreement with the DFT data (Table 25, Section 5.2).

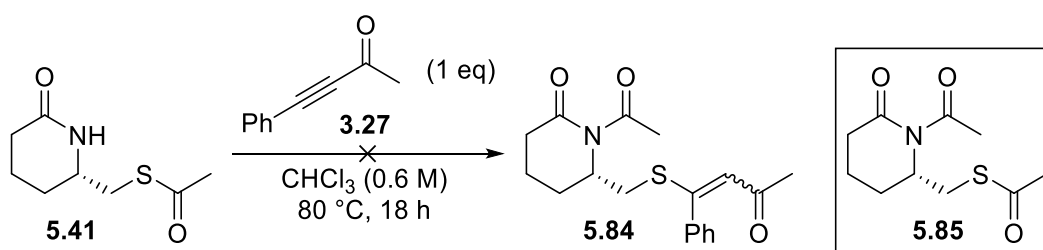


Figure 194. Unsuccessful reactions of thioester 5.41 with phenyl-substituted ynone 3.27 with no base added.

The base was then changed, using triethylamine or pyridine instead of potassium carbonate (Figure 195). With triethylamine trace amounts of 5.84 and 5.85 could be observed *via* TLC analysis, however overall, no significant conversion was observed with either base.

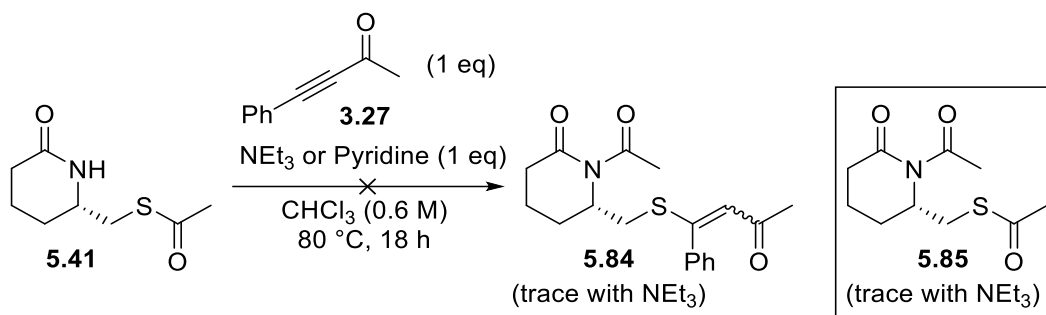


Figure 195. Unsuccessful reactions of thioester **5.41** with phenyl-substituted ynone **3.27** with triethylamine or pyridine added.

A more thorough screening of reaction conditions was then undertaken. Reactions were performed under various conditions, with a known amount of trimethoxybenzene (10 mol%) added as an internal NMR standard (Table 26). Integration of the crude ^1H NMR spectra could give a calculated yield.

First, the effect of changing the solvent was considered (Entries 1–4, Table 26). More polar solvents were used as it was proposed that this might have an impact on the stability of any charged intermediates. More starting material was consumed when THF and acetonitrile were used, however other unidentified side products were found. Neither **5.85** or **5.86** were found with DMF as the solvent, although unidentified side products were formed in low amounts.

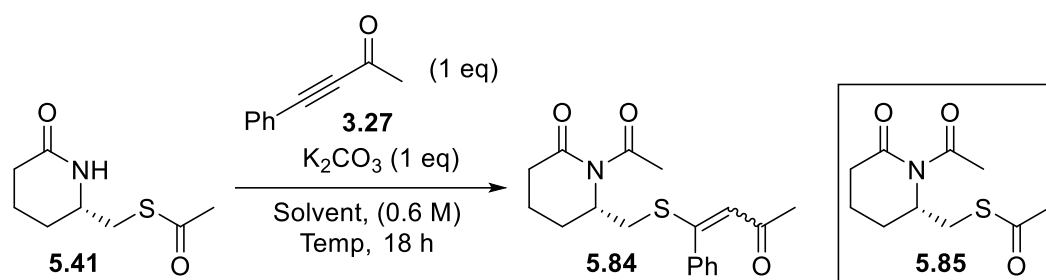
The effects of the reaction temperature were then considered using chloroform (Entries 5 and 6, Table 26) or acetonitrile (Entries 7–9, Table 26) as the solvent. Consumption of the starting material was quickly lowered in chloroform as the temperature decreased. However, in acetonitrile the reaction was still successful at 40°C . Additionally, whilst there was still starting material remaining, less unidentified side products were detected, allowing for isolation of a purer product in a 67% yield.

Finally, it was attempted to push the reaction further to completion with increased equivalents of base or ynone (Entries 10–12, Table 26). When 1.5 equivalents of base and ynone were used (Entry 12, Table 26), there was a large increase in the NMR yield of the product **5.84** (compared to using 1 equivalent of base and ynone, Entry 8, Table 26) however, there was only a small increase in the isolated yield (Entry 12, Table 26). Additionally, there is a large discrepancy between the NMR and isolated yields (Entry 12, Table 26) at 92% and 72% respectively, it is suspected that this is due to inefficiencies in sample transfer and purification at the small (0.2 mmol) scale the reactions were performed at. However, based on the NMR yield, it was decided

that increasing the equivalents of potassium carbonate and ynone to 1.5 (Entry 12, Table 26) would be the standard conditions going forward.

Table 26. Reaction optimisation for the acyl transfer/ynone trapping reaction of thioester **5.41**.

Reactions were performed on a 0.2 mmol scale, and after 18 hours, 100 μ L of a 0.2 M solution of trimethoxybenzene in DCM was added before the reaction was concentrated and a ^1H NMR spectrum recorded. Anhydrous THF, MeCN and DMF were used, and those reactions were performed under an argon atmosphere.



Entry	Solvent	Temp / $^{\circ}\text{C}$	NMR Yield of 5.84 ^a (Isolated Yield) / %	NMR Yield of 5.85 / %	NMR Yield of 5.41 / %
1	CHCl_3	80	57 (56%)	38	20
2	THF ^b	80	55	28	11
3	MeCN ^b	80	66	26	6
4	DMF ^b	80	0	0	80
5	CHCl_3	60	60	34	23
6	CHCl_3	40	45	24	39
7	MeCN	60	80	20	11
8	MeCN	40	81 (67%)	14	9
9	MeCN	RT	69	12	26
10	MeCN ^c	40	84	8	8
11	MeCN ^d	40	85	14	8
12	MeCN ^e	40	92 (72%)	12	8

^a Yield of both stereoisomers. ^b Formation of unknown side products was observed. ^c 1.5 equivalents of **3.27** used. ^d 1.5 equivalents of K_2CO_3 used. ^e 1.5 equivalents of **3.27** and K_2CO_3 used.

The migration and trapping reaction was tested using 5-membered thioacetate **5.46** under the optimised conditions (Figure 196). The reaction was indeed successful, and a 73% yield of the desired product (**5.89**) was isolated.

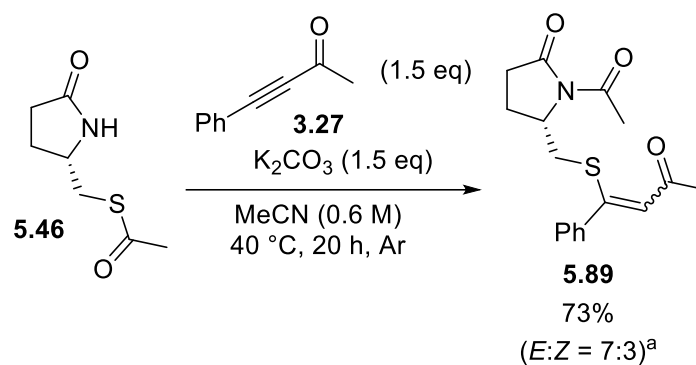


Figure 196. Reactions of thioester **5.46** with phenyl-substituted ynone **3.27**. a) Stereochemistry assigned by comparison of an analogous compound, reported by Nishio et al.³³⁹

The choice of ynone was only very briefly investigated. Terminal ynone **5.52** was tested, due to work reported in the literature demonstrating that a disubstituted internal vinyl thioether moiety was able to be cleaved with the addition of a second thiol.³⁴⁰ The reaction of thioester **5.41** was successful under the standard conditions, albeit in a reduced yield of 49%.

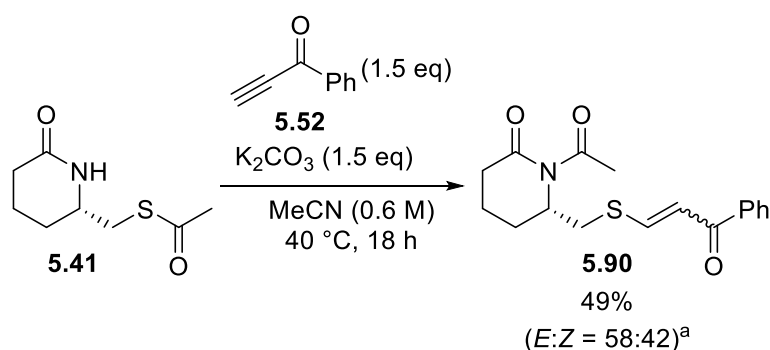


Figure 197. Reactions of thioester **5.41** with terminal ynone **5.52**. a) Stereochemistry was assigned by analysis of the ³*J* alkene coupling constant (15.0 Hz for the *E*-isomer, and 9.5 Hz for the *Z*-isomer).

5.4.4 Nucleophile-tethered acyl migration/ynone trapping

Whilst the acyl migration reaction was optimised with thioester **5.41**, bearing a simple, short acetyl group, and ynone **3.27** (Table 26, Section 5.4.3), it was considered that further optimisation of the migration reaction for more complex thioesters (where the acyl group is longer and contains a protected nucleophile) might be required. However, before any further optimisation of the acyl migration was undertaken, it was decided to first determine if ring expansion of the product imides was possible using SuRE methodologies.

The migration reaction was first attempted using a tethered Fmoc-protected β -alanine thioester derivative **5.56** (Figure 198). There were concerns that an *in situ* Fmoc-deprotection of the amine could cause problems, however the opportunity for a one-pot migration/SuRE reaction also presented itself. After 20 hours, TLC analysis suggested that there was still starting material remaining, but a minor, new product spot was present. Purification was attempted to isolate this product, however the ^1H NMR spectrum showed that this was in fact a mixture of products. An ESI mass spectrum was recorded, and an ion with an m/z consistent with product **5.92** was found, however, this wasn't isolated, nor the structure confirmed.

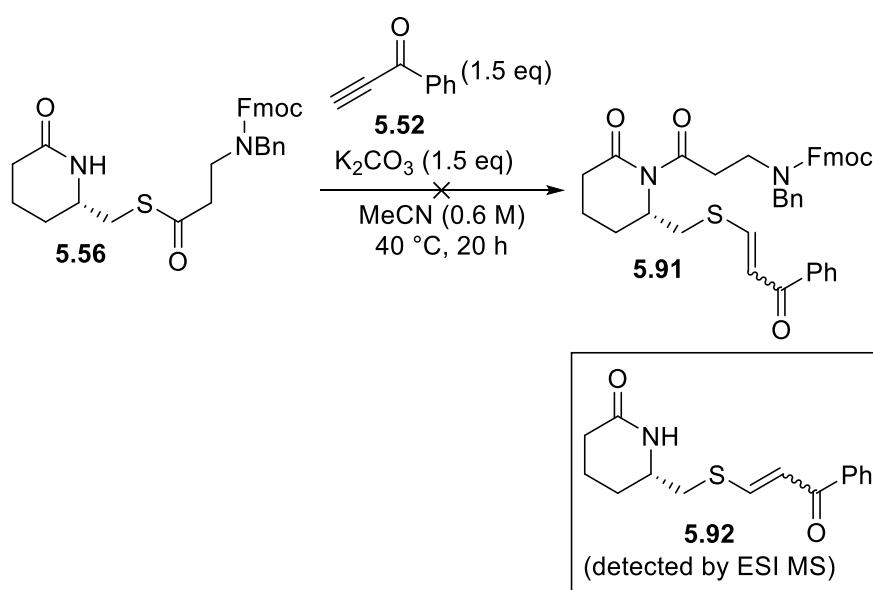


Figure 198. Unsuccessful acyl migration of thioester **5.56** with terminal ynone **5.52**.

It was proposed that under the basic conditions used, an intramolecular cyclisation of the tethered amino acid occurred (**5.93** \rightarrow **5.96**, Figure 199).³⁴¹ After cleavage of the sidechain, the thiolate anion (**5.96**) is then able to undergo conjugate addition with terminal ynone **5.52** (**5.96** \rightarrow **5.97**), which after protonation, would yield the proposed structure **5.92**.

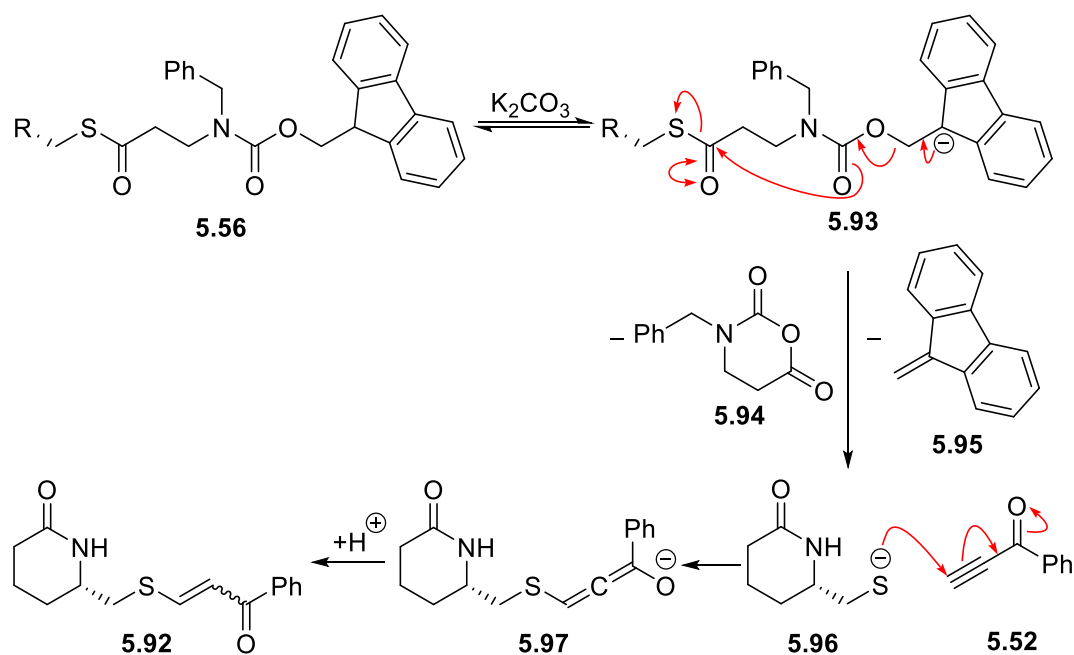


Figure 199. Proposed mechanism of thioester cleavage, for the formation of **5.92** from **5.56**.

To avoid problems caused by the Fmoc-deprotection under the basic conditions used for the acyl-migration, a Boc-protected amino acid sidechain was considered. Thioester **5.57** was therefore treated under the acyl migration reactions (Figure 200). TLC analysis of the reaction mixture showed that the starting material was consumed, with the desired migrated product **5.98** isolated, in a yield of 45%. It was unclear what the fate of the remaining mass balance was, as no other products were able to be isolated.

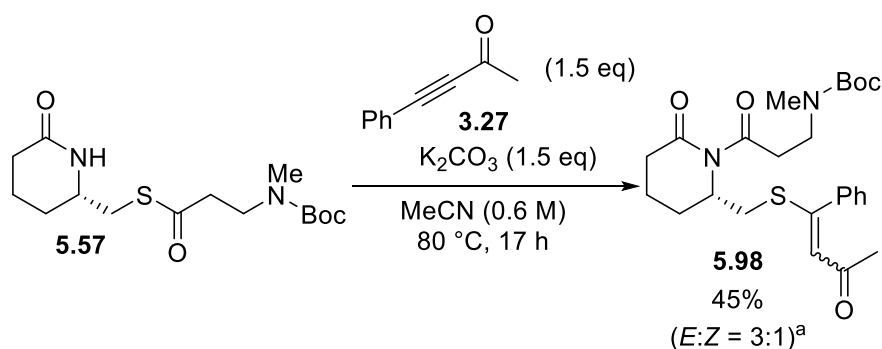


Figure 200. Base-mediated acyl migration of Boc-protected thioester **5.57**.^a Stereochemistry assigned by comparison of an analogous compound, reported by Nishio et al.³³⁹

The ring expansion reaction was then attempted using imide **5.98**, under conditions reported by Yudin *et al.*²⁷² Imide **5.98** was dissolved in a 1:1 mixture of DCM and TFA to cleave the Boc group, after which, an excess of DIPEA was added to promote the ring expansion reaction. No starting material remained after work-up, and TLC analysis showed a new product appeared to have

been formed. The product was isolated, in a 50% yield, and NMR analysis suggested that this was the expected ring expanded product **5.99** (Figure 201).

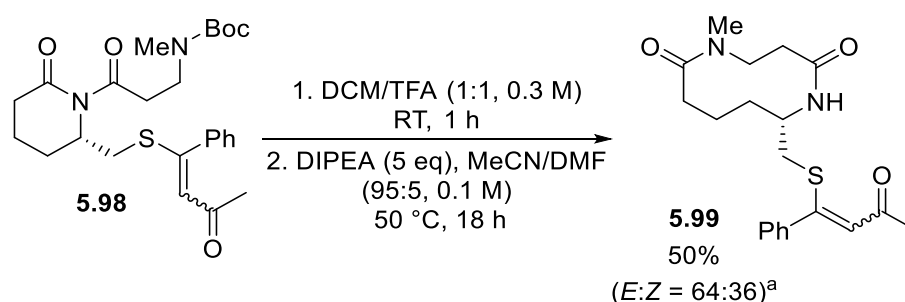


Figure 201. Attempted ring expansion reaction of **5.98**. ^a Stereochemistry assigned by comparison of the ¹³C and ¹H NMR resonances for the enone moiety, with **5.98**.

The ¹³C and HMBC NMR spectra were most useful in determining that ring expansion had occurred, and that the molecule was not the ring opened isomer (**5.99_{RO}**). The HMBC spectrum is shown in Figure 202, with selected crosspeaks to the amide carbonyl resonances assigned, with only the *Z*-stereoisomer discussed here for clarity. The diastereotopic proton resonances H^c and H^d, corresponding to the MeNCH₂ protons, have a crosspeak to both of the amide carbonyls, in contrast to H^f which shows only one crosspeak. Additionally, both H^a and H^b, and H^e, have crosspeaks to different carbonyl resonances. Further evidence that ring expansion had occurred, was the favourable comparison of the ¹³C NMR chemical shifts with data for analogous 10-membered rings available in the literature.²⁹⁹

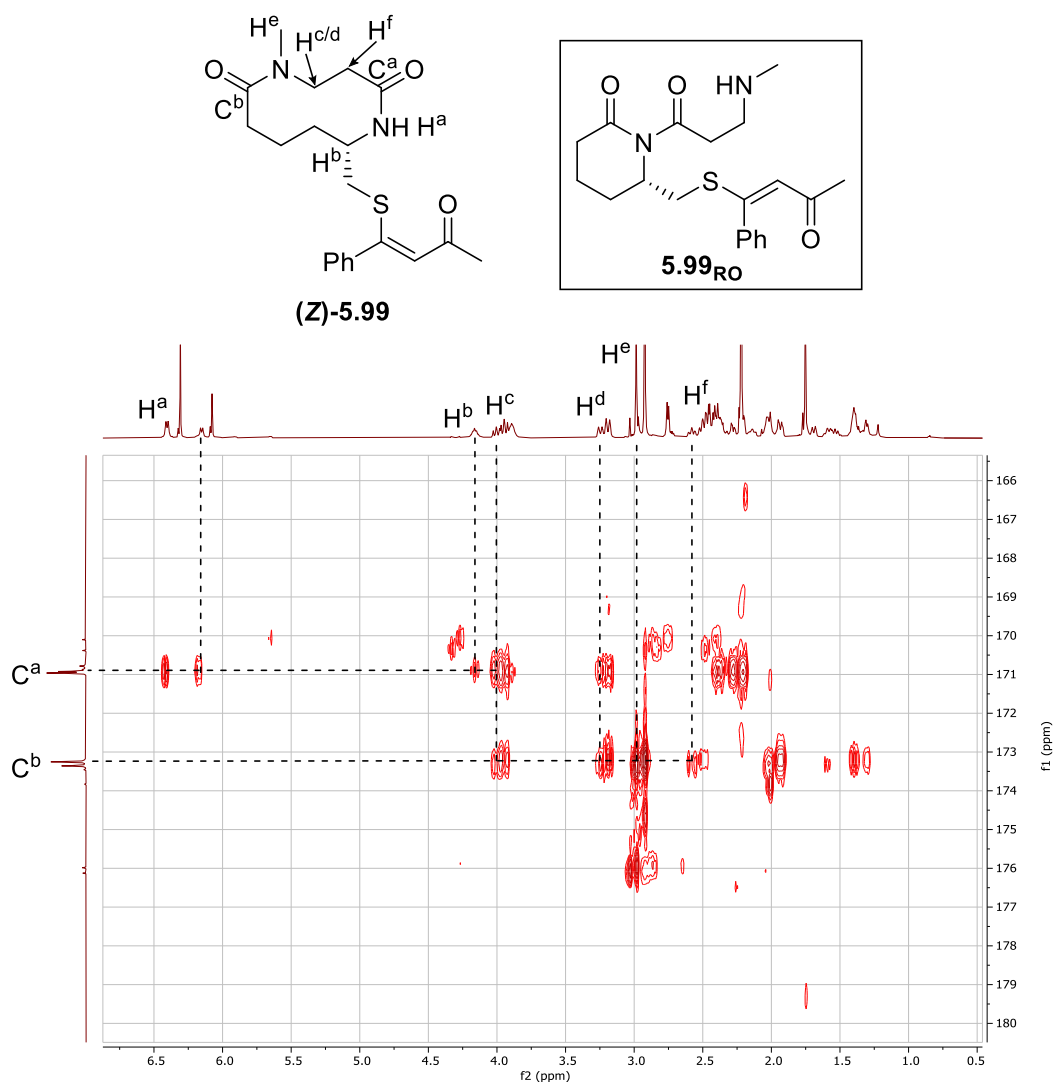


Figure 202. HMBC data with selected assignments used to determine the structure of **5.99**. NMR data recorded on 600 MHz spectrometer, in CDCl₃.

Another common side chain used within SuRE chemistry, is a benzyl-protected β -hydroxy acid.^{279,287} Therefore, the acyl migration of thioester **5.59** was considered using the standard conditions (Figure 203). As with the Boc-protected amine substrate **5.57** previously discussed (Figure 200), no starting material (**5.59**) was remaining by TLC analysis, however, a low yield of the migrated product (**5.100**) was isolated. Again, no further products were able to be found.

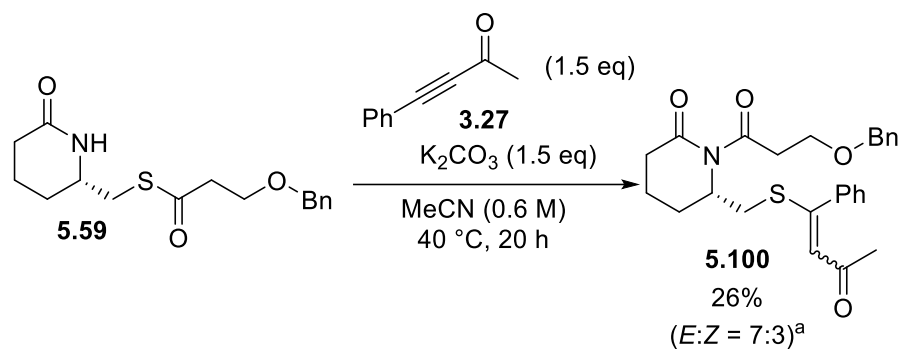


Figure 203. Base-mediated acyl migration of benzyl-protected thioester **5.59**.

Hydrogenation conditions were then used to remove the benzyl protecting group. The reaction was attempted twice, using either Pd/C or Pd(OH)₂/C. Deprotection was found to be unsuccessful under both conditions (Figure 204), with the starting material **5.100** reisolated each time.

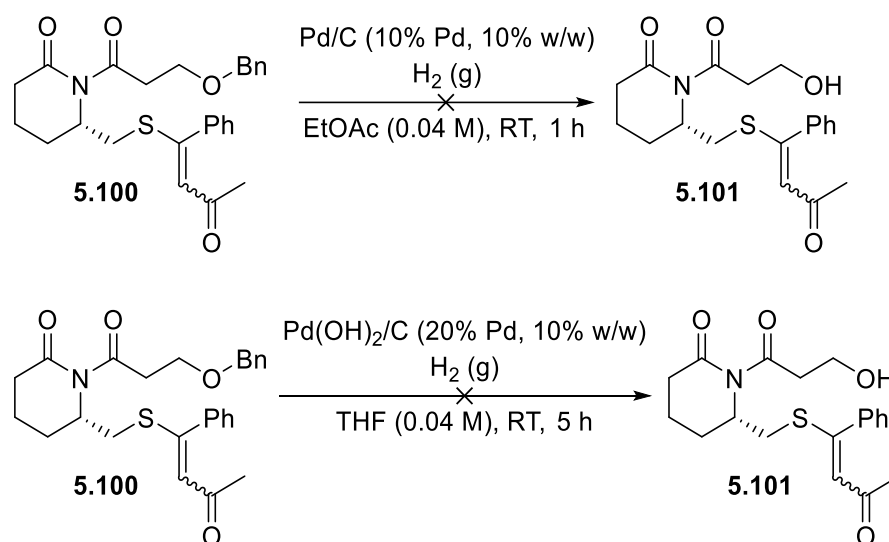


Figure 204. Attempted hydrogenation reactions of imide **5.100**.

Due to the clear difficulties promoting the acyl transfer reaction when using more complex side chains (particularly the *O*-benzyl derivative **5.100**) and the challenges seen with ring expansion, along with external time constraints, it was decided to discontinue the project at this point.

5.4.5 Future Work

Whilst acyl group migration was observed when using thioesters in conjunction with basic conditions and ynones, there was several areas in which further work could be undertaken.

Migration of more complex thioesters was challenging under the conditions employed, with only low to moderate yields of 45% and 26% achieved (with *N*-Boc and *O*-Bn protected tethered side chains respectively). Determining what other products are formed over the course of the acyl transfer reaction would likely be helpful in the optimisation of those reactions.

Next, deprotection of the protecting group for the *O*-containing sidechain (**5.100**) has been challenging. It might be that different protecting groups are needed on the sidechains, which are more compatible with both the conditions used for the migration, and which the deprotection conditions are compatible with the vinyl thioether moiety. However, with the successful ring expansion of Boc-protected amine **5.98**, this does provide evidence that the overall strategy could be further optimised with additional time.

Finally, much of this work was focussed upon using ynone substrates (**3.27** and **5.52**) to trap the migrated products. Changing the Michael acceptor and reoptimizing the conditions for the migration reaction might be necessary for the improvement of the chemistry (and of the previous points mentioned).

5.4.6 Concluding Remarks

Previous work in developing an acyl-transfer reaction by members of the Unsworth group were unsuccessful. DFT calculations were performed to explore the viability of these reactions, and the data suggested that a migration reaction of the acyl group of a thioester, to the nitrogen of a neighbouring amide might be possible under basic conditions. The use of an acyl chloride *in situ* was unsuccessful, with direct acylation of the amide occurring. Instead, a reaction was optimised in which trapping the migrated product with an ynone was successful, with good yields achieved (Figure 205).

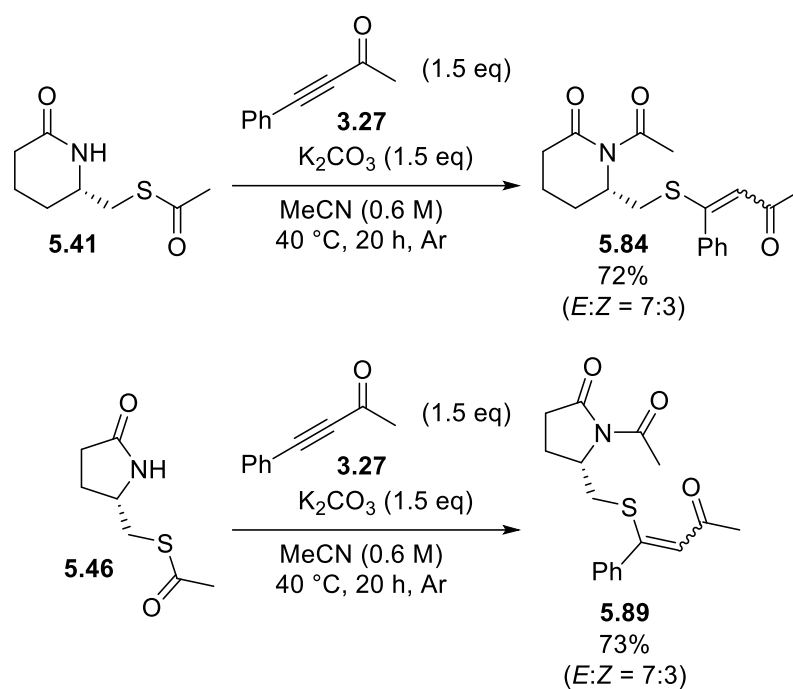


Figure 205. Successful acyl transfer reactions of thioacetate compounds **5.41** and **5.46**, using phenyl-substituted ynone **3.27**.

Upon using more complex thioesters, with protected nucleophiles tethered to the sidechain, the migration reaction became more challenging and lower yields were achieved. Since these thioesters are required for the subsequent ring expansion, this is problematic for the overall efficiency of the acyl-transfer/SuRE process. The subsequent ring expansion of Boc-protected amine **5.98** was successful however and demonstrated a successful realisation of the strategy (Figure 206), with the acyl group introduced as a thioester, in contrast to the typical *N*-acylation method which is used for SuRE reactions. The DFT calculations performed were instrumental in developing the strategy used for the acyl transfer reaction.

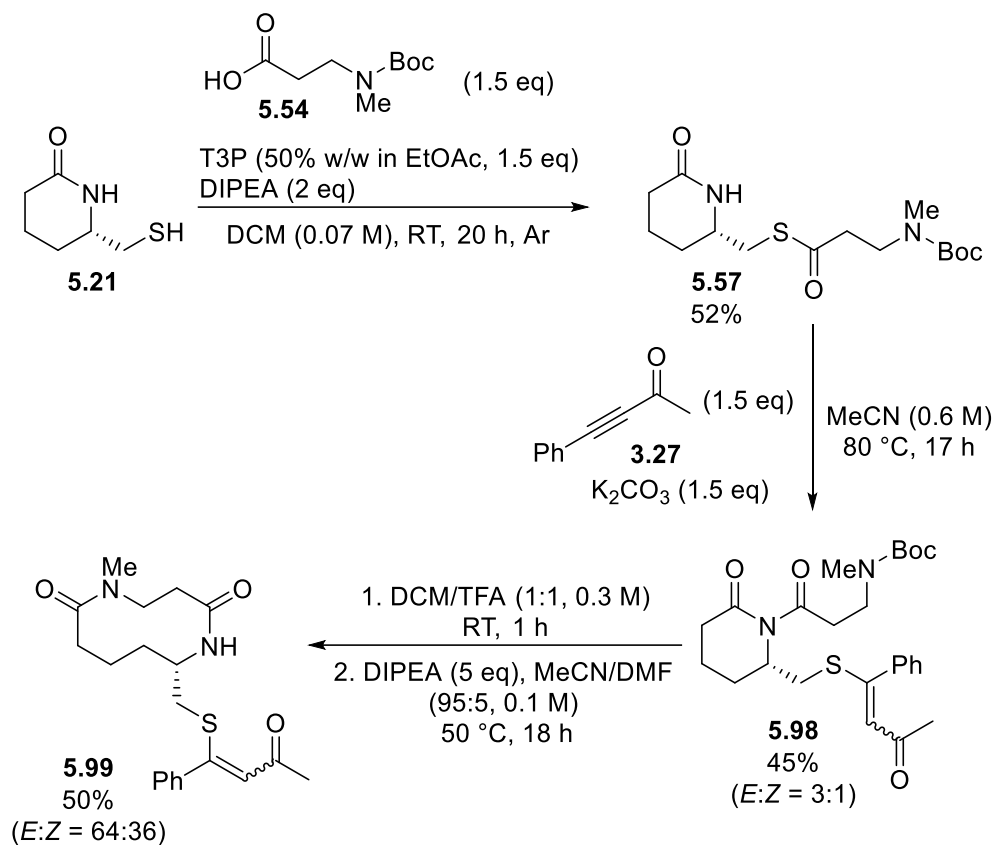


Figure 206. Successful ring expansion process with an acyl-migration step, starting from thiol **5.21**.

Future work was highlighted with which it might be possible to improve upon the reaction, with the work presented in this chapter providing a basis to expand upon.

Chapter 6. Conclusions

Combining experiment and DFT in the study of new reactions allows for a greater understanding of the chemistry, which can then be used to guide further development and optimisation of a process. The work presented in this thesis describes this synergistic approach in the study of a rearrangement of spirocyclic indolenines to quinolines, the gold(I)-catalysed vinylation of indoles, the application of DFT methods in the development of new SuRE ring expansion methods, and the development of an acyl transfer method for lactam acylation.

Previously reported procedures for the rearrangement of spirocyclic indolenines into quinolines using both Brønsted and Lewis acidic reagents was presented (see Section 2.1.2), where it was noted that heat is necessary to promote the reaction, with a preliminary reaction demonstrating that the transformation can occur using stoichiometric LHMDS. The temperatures required for the reactions under acidic and basic conditions were compared (see Section 2.2.2) where it was found that the rearrangement was possible using LHMDS at much lower temperatures. A substrate scope was then performed using LHMDS (Figure 207, see Section 2.2.3), where it was demonstrated that a range of different aryl and alkyl substituents were tolerated.

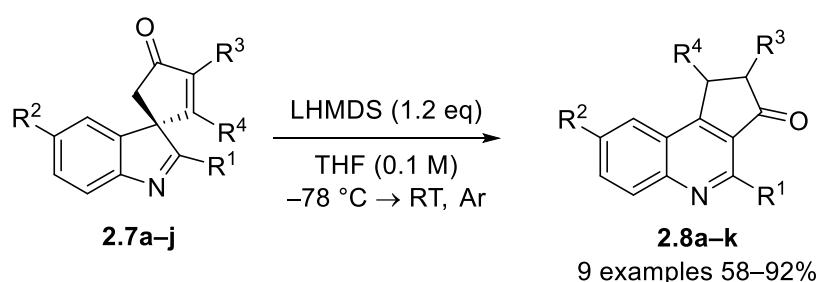


Figure 207. Overview of the substrate scope performed for the LHMDS-mediated quinoline rearrangement of spirocyclic indolenines.

DFT studies (see Section 2.2.4) were then performed to compare the energies of the intermediates and transition states under both the acidic and basic conditions, to determine why heat was generally required for the acidic reactions. Pathways for both sets of conditions were provided, with energies calculated at the D3(BJ)-PBE0/def2-TZVPP//BP86/SV(P) level of theory. Whilst the energies were consistent with the reaction using LHMDS being successful at room temperature, the energies for the reaction using TFA were lower than might be expected. Keto-enol tautomerism is likely required for the quinoline rearrangement to proceed, the kinetics of which were not modelled, it was therefore proposed that it is the keto-enol tautomerism which is rate-limiting under acidic conditions.

Previously reported literature for the gold(I)-catalysed vinylation of indoles showed that isolation of the vinyl indole product is challenging, with trace Brønsted acid which is formed throughout the reaction shown to promote the addition of a second equivalent of indole, forming *bisindole* species (see Sections 3.1.2 and 3.1.3). Previous studies within the Unsworth and Lynam groups demonstrated that the C–C bond forming steps between indoles and ynones are low in energy, and that the subsequent spirocyclic products are resistant to Brønsted acid-catalysed migrations (Figure 208, see Section 3.1.4). The development of a gold(I)-catalysed reaction between indoles and ynones was therefore considered as an opportunity to form vinyl indole species.

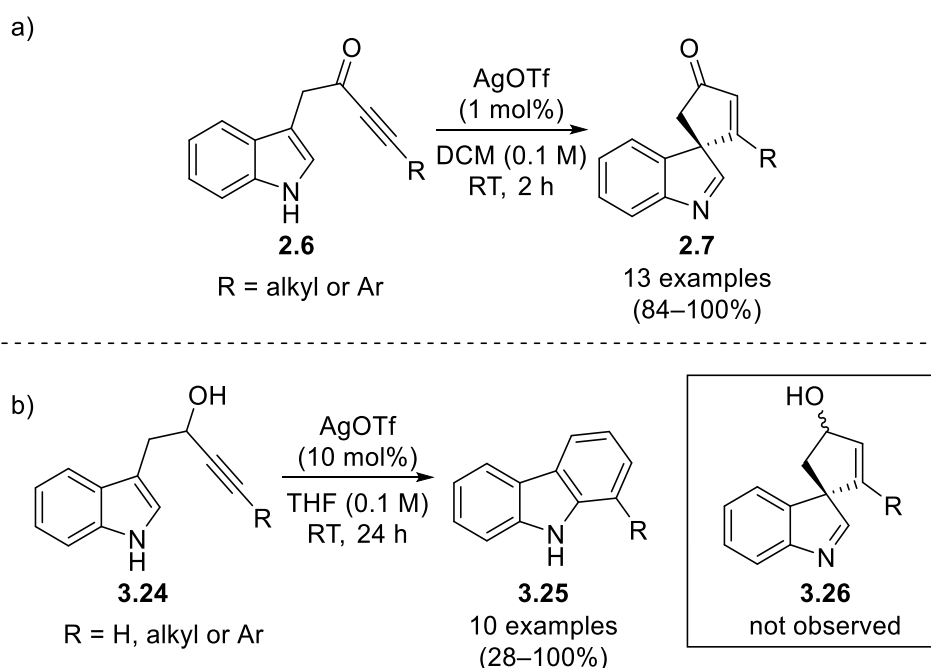


Figure 208. Comparison of the silver triflate catalysed cyclisation of a) indolyl-tethered ynones **2.6** and b) indolyl-tethered propargyl alcohols **3.24**.^{173,200}

The conditions required for the vinylation reaction were successfully optimised (see Section 3.2), with no evidence of the undesired *bisindole* species observed. The reaction proved more challenging for C-3 substituted indoles, with additional substitution of the indole nitrogen required to form the desired C-2 vinyl indole species. A variety of vinyl indole species were able to be synthesised (Figure 209).

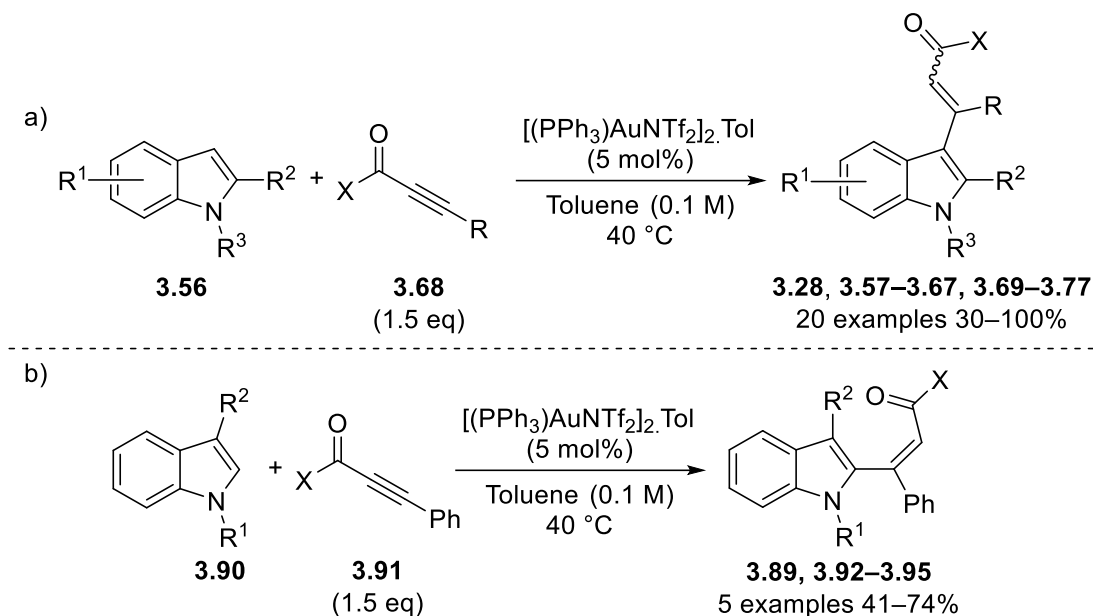


Figure 209. Summary of the substrate scopes performed for the gold(I)-catalysed vinylation of a) indoles **3.56** and b) C-3 substituted indoles **3.90**.

DFT studies were then used to study the vinylation reaction in further detail. Gold(I)-coordination to the indole and ynone were compared, where it was found that the indole is a better ligand for the gold than the ynone, and $^{31}\text{P}\{^1\text{H}\}$ NMR spectra were used to provide experimental evidence of this (see Section 3.3.2). The mechanism of the indole vinylation reaction was also studied, with the computational data suggesting that C-3 substitution occurs for indoles with no C-3 substituent, whilst direct C-2 addition is preferred when the C-3 position is already substituted (see Section 3.3.3). The subsequent acid-promoted formation of bisindole species were then compared with ynones and acetylenes, where it was found that there is no thermodynamic preference for further indole addition with the ynone derivative (Figure 210), and the transition state energies of the addition are higher than the equivalent acetylene derivatives (see Section 3.3.4).

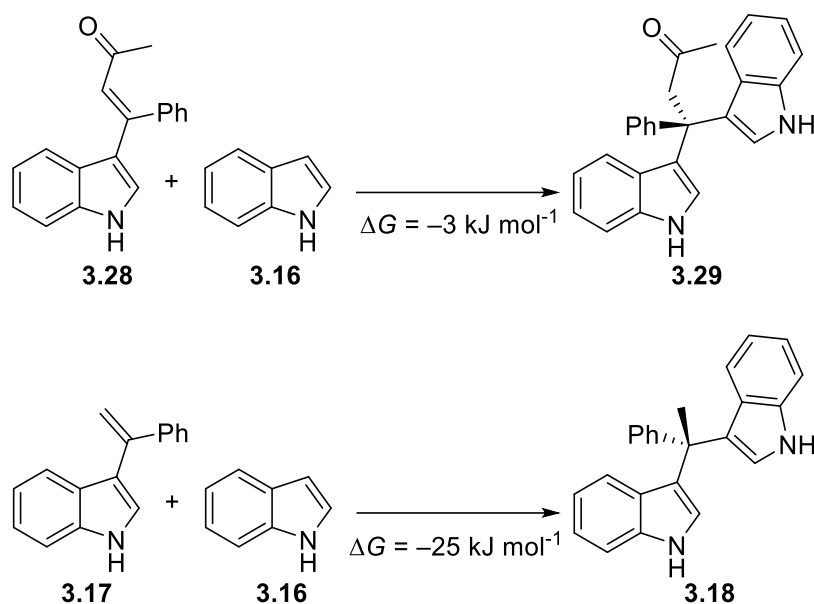


Figure 210. DFT-calculated energy for the formation of *bisindole* compounds **3.29** and **3.18**. Energies are Gibbs energies at 298.15 K at the D3(BJ)-PBE0/def2-TZVPP//BP86/SV(P) level of theory with COSMO solvent correction in toluene.

Further work then focussed on the gold(I)-coordination of the ynone, using both DFT and $^{31}\text{P}\{^1\text{H}\}$ NMR spectroscopy methods (see Section 3.4). It was found that the nature of the carbonyl species and the substituent of the aryl group of the ynone had a large effect on the preference for gold(I)-coordination, and ^{31}P NMR resonances were able to be identified for $\eta^1(\text{O})$ - and $\eta^2(\pi)$ -coordination. During this work, a novel gold(I)-pyrylium complex was identified from ynone dimerisation (Figure 211), when an ynone bearing an electron-donating substituent was used. DFT studies were performed to determine the origin of this species, where the electron-donating group was required to promote the initial C–C bond forming step (see Section 3.4.3).

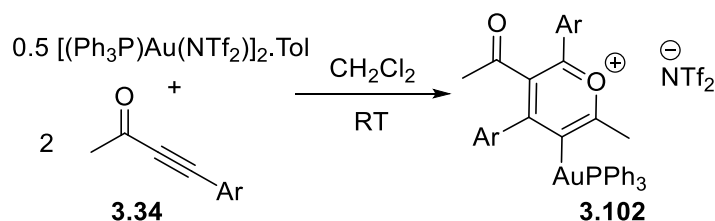


Figure 211. Formation of pyrylium complex **3.102**, from electron-rich ynone **3.34**. Ar = C_6H_4 -4-NMe₂.

In collaboration with Dr Lawer, a previous member of the Unsworth group, a computational method to evaluate the viability of SuRE reactions was validated based on the relative Gibbs energies of the ring-opened (*e.g.* **4.112**) and ring expanded (*e.g.* **4.114**) isomers (Figure 212, see Sections 4.2.2 and 4.2.3). The effects of different functionals, solvation and dispersion were considered, where it was found that B3LYP/6-31G* was the preferred method to study SuRE

reactions. The effects of dispersion with both the Minnesota functionals (M06 and M06-2X) and Grimme's D3 correction were found to be the most detrimental, likely due to the model not appropriately accounting for the dispersion corrections in the ring-opened isomer. The validated method was then applied to other SuRE methodologies that are being developed within the Unsworth group (see Sections 4.2.4 and 4.2.5).

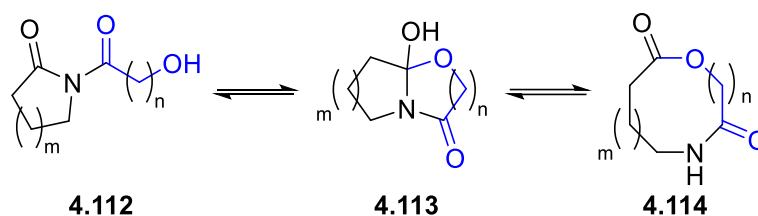


Figure 212. The three isomers considered in the DFT calculations.

One limitation of the SuRE reactions presented is that acylation of the nitrogen of the lactam, required strongly acidic conditions, which therefore might limit the scope of the reaction. Previous work in the Unsworth group attempted to develop an acyl-transfer method, which would allow for the use of milder conditions, however the work was unsuccessful (see Section 5.1).

DFT studies were performed which suggested that the acylation reaction might be possible for thiolactones under basic conditions, however the resulting thiolate anion might require trapping after the migration has occurred (see Section 5.2). The acyl transfer reaction was able to be optimised with an ynone to trap the thiolate *via* Michael addition (see Section 5.4.3). The approach was then applied to an acyl group bearing an *N*-Boc protected amine (Figure 213), and the resulting imide was used in a successful SuRE reaction (see Section 5.4.4).

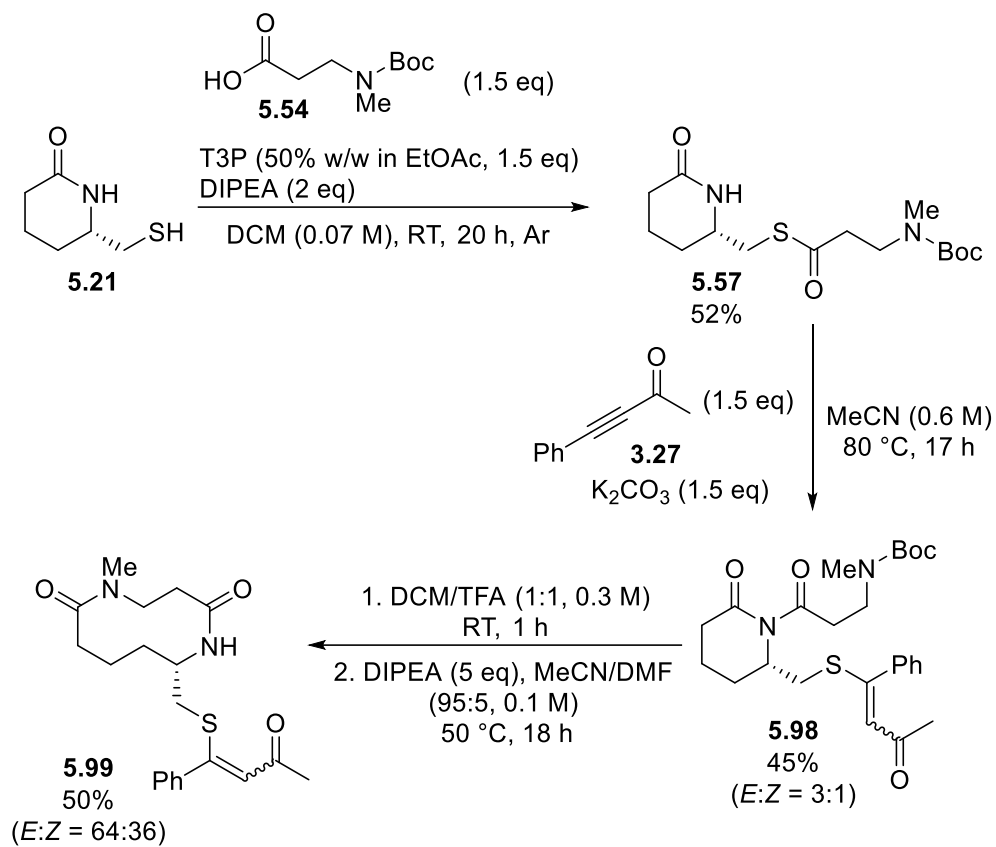


Figure 213. Successful ring expansion process with an acyl-migration step, starting from thiol **5.21**.

Chapter 7. Experimental Data

7.1 General Methods

7.1.1 General Experimental Procedure

Except where stated, all reagents were purchased from commercial sources and used without further purification. Anhydrous THF was obtained from an Innovative Technology Inc. PureSolv[®] solvent purification system. Anhydrous *d*₂-DCM was dried over calcium hydride overnight and degassed with three freeze-pump-thaw cycles before trap-to-trap transfer to ampoules fitted with a PTFE Young's tap. The solvent was then stored under a nitrogen atmosphere and used immediately. ¹H NMR, ¹³C NMR, ¹⁹F NMR and ³¹P NMR spectra were recorded on a JEOL ECX400 or JEOL ECS400 spectrometer, operating at 399.77 MHz, 100.52 MHz, 376.16 MHz and 161.83 MHz respectively, or on a Bruker AVIIIHD 500 operating at 500.23 MHz, 125.80 MHz, 470.64 MHz and 202.49 MHz respectively, or on a Bruker AVIIIHD 600 Widebore spectrometer operating at 600.09 MHz, 150.91 MHz, 564.59 MHz and 242.91 MHz respectively. All spectral data was acquired at 298 K. Chemical shifts (δ) are quoted in parts per million (ppm). The residual solvent peaks; δ_{H} 7.27 and δ_{C} 77.16 for CDCl₃, δ_{H} 5.32 and δ_{C} 53.84 for CD₂Cl₂ and δ_{H} 2.50 and δ_{C} 39.52 for *d*₆-DMSO, were used as a reference. Coupling constants (J) are reported in Hertz (Hz) to the nearest 0.5 Hz. The multiplicity abbreviations used are: s singlet, d doublet, t triplet, q quartet, pent. pentet, sex. sextet, non. nonet, m multiplet, app. apparent, br broad. Signal assignment was achieved by analysis of DEPT, COSY, HMBC and HSQC experiments where required. Infrared (IR) spectra were recorded on a PerkinElmer UATR 2 spectrometer as a thin film dispersed from either CH₂Cl₂ or CDCl₃. Mass-spectra (low and high-resolution) were obtained by the University of York Mass Spectrometry Service, using electrospray ionisation (ESI) on a Bruker Daltonics, Micro-tof spectrometer. Melting points were determined using Gallenkamp apparatus. Thin layer chromatography was carried out on Merck silica gel 60F254 pre-coated aluminium foil sheets and were visualised using UV light (254 nm) and stained with either an acidic solution of vanillin in ethanol (used primarily with indoles), an acidic solution of ninhydrin in ethanol (used primarily with Boc-protected amines) or a basic potassium permanganate solution. Flash column chromatography was carried out using slurry packed Fluka silica gel (SiO₂), 35– 70 μm , 60 Å, under a light positive pressure, eluting with the specified solvent system.

7.1.2 General Computational Information

Throughout this thesis, the Gaussian 09,²⁸⁶ TURBOMOLE V6.4⁵⁹ and Spartan'14²⁸⁵ computational software packages have been used or referenced. Gaussian 09 was primarily used for the work in Chapters 2, 4 and 5 due to its availability on the University of York's high performance computing clusters (YARCC and Viking). Gaussian 09 was also capable of optimising all generated conformations for a particular structure within a single input file. Whilst Dr Lawer used Spartan'14 during their initial work highlighted in Chapter 4, this software was used on a private computer which was no longer accessible for the further work required. In Chapter 3, TURBOMOLE V6.4 was used due to its use on previous related work in studying the divergent gold(I)- and silver(I)-catalysed spirocyclisation reactions (see Section 3.1.4)²⁰¹, so the data could be compared if desired.

Units of kJ mol^{-1} and kcal mol^{-1} have been used throughout this thesis. Whilst units of kJ mol^{-1} were used in Chapter 2 and 3, due to joules being the preferred SI unit for energy, units of kcal mol^{-1} were used in the ring-expansion work (Chapters 4 and 5) to be consistent with the initial studies performed by Dr Lawer, and the previously reported ring expansion DFT calculations (see Section 4.1.4).^{272,275} Where literature data has been reported, the units used by the author have been quoted. A conversion factor of $1 \text{ kcal mol}^{-1} = 4.184 \text{ kJ mol}^{-1}$ can be applied.

The raw output (.out) files for the Gaussian calculations, and a report summarising the output of the TURBOMOLE calculations (which includes energies and xyz coordinates) can be accessed by contacting the supervisors of this work, Jason Lynam (jason.lynam@york.ac.uk) or Will Unsworth (william.unsworth@york.ac.uk).

7.1.3 Computational Procedure for the Quinoline Rearrangement Studies (Chapter 2)

All calculations were performed using the Gaussian 09, Revision D.01 package.²⁸⁶

Initial geometry optimisations were performed at the BP86/SV(P) level,^{32,33,54–56} followed by frequency calculations at the same level. Transition states were located either by using QST2, QST3 methods,^{342,343} or by initially performing a constrained minimisation (by freezing internal coordinates that change most during the reaction) of a structure close to the anticipated transition state. This was followed by a frequency calculation to identify the transition vector to follow during a subsequent transition state optimisation. A final frequency calculation was then performed on the optimised transition-state structure. All minima were confirmed as such by the absence of imaginary frequencies and all transition states were identified by the presence of only one imaginary frequency. Intrinsic Reaction Coordinate (IRC) analysis confirmed that transition states were connected to the appropriate minima. Single-point calculations on the BP86/SV(P) optimised geometries were performed using the hybrid PBE0,^{34–36} meta-hybrid GGA M06-2X,⁴¹ or hybrid ω B7XD functionals,⁴² and the flexible def2-TZVPP basis set.^{56–58} The PBE0/def2-TZVPP, M06-2X/def2-TZVPP and ω B97XD/def2-TZVPP SCF energies were corrected for their zero-point energies, thermal energies and entropies at 298.15 K (obtained from the BP86/SV(P)-level frequency calculations).

Additional calculations for the anionic species were performed using the same method, with initial geometry optimisations and frequency calculations performed at the BP86/6-31+G* level of theory,^{32,33,46–52} followed by single-point calculations at the PBE0/6-311+G* level of theory.^{34–36,51,53} The PBE0/6-311+G* SCF energies were corrected for their zero-point energies, thermal energies and entropies (obtained from the BP86/6-31+G*-level frequency calculations).

Optimisations were performed with *tight* convergence criteria and no symmetry constraints were applied. An *ultrafine* integral grid was used for all calculations. Solvent corrections were applied with the Polarizable Continuum Model (PCM) using the integral equation formalism (IEF) variant,⁶³ and dispersion effects modelled with Grimme's D3 method with Becke–Johnson damping.^{71,75}

Benchmarking studies performed demonstrated that the BP86 and PBE0 functionals are robust and typically perform averagely.^{281,344} These same studies demonstrate that the M06-2X and ω B97XD functionals do often perform better, and single-point calculations were therefore performed using these functionals and the BP86 calculated geometries. Whilst not used in these

studies, it was considered that the effects of dispersion might be easier determined with the D3(BJ) correction applied as a separate correction using the hybrid PBE0 functional, rather than the inherent dispersion that is applied within the M06-2X and ω B97XD functionals.

7.1.4 Computational Procedure for the Indole Vinylation and Gold(I) Speciation Studies (Chapter 3)

All calculations were performed using the TURBOMOLE V6.4 package using the resolution of identity (RI) approximation.^{55,345–352}

Initial optimisations were performed at the (RI-)BP86/SV(P) level,^{32,33,54–56} followed by frequency calculations at the same level. Transition states were located by initially performing a constrained minimisation (by freezing internal coordinates that change most during the reaction) of a structure close to the anticipated transition state. This was followed by a frequency calculation to identify the transition vector to follow during a subsequent transition state optimisation. A final frequency calculation was then performed on the optimised transition-state structure. All minima were confirmed as such by the absence of imaginary frequencies and all transition states were identified by the presence of only one imaginary frequency. Dynamic Reaction Coordinate (DRC) analysis confirmed that transition states were connected to the appropriate minima. Single-point calculations on the (RI-)BP86/SV(P) optimised geometries were performed using the hybrid PBE0 functional,^{34–36} and the flexible def2-TZVPP basis set.^{56–58} The (RI-)PBE0/def2-TZVPP SCF energies were corrected for their zero-point energies, thermal energies and entropies at 298.15 K (obtained from the (RI-)BP86/SV(P)-level frequency calculations). A 60 electron quasi-relativistic ECP replaced the core electrons of Au.⁵⁶

No symmetry constraints were applied during optimisations. Solvent corrections were applied with the COSMO dielectric continuum model,⁶⁵ and dispersion effects modelled with Grimme's D3 method with Becke–Johnson damping.^{71,75}

The above methodology (D3(BJ)-PBE0/def2-TZVPP//BP86/SV(P)) was used due to its use in the previous related work performed by Liddon *et al.*,²⁰¹ to allow for comparisons between the methods to be made if desired. Additionally, the BP86 and PBE0 functionals have both benchmarked favourably in previous studies focused upon gold(I) complexes.^{97–99}

7.1.5 Computational Procedure for Evaluating the Viability of SuRE Reactions (Chapter 4)

Method Development (Sections 4.2.2 and 4.2.3)

All initial calculations performed using the Spartan software package,²⁸⁵ were performed by Dr Aggie Lawer. The method that was used is given here, as reported by Dr Lawer.²⁸⁷ The imides, cyclols and ring expanded products in the selected systems were initially built using Spartan'14,²⁸⁵ and optimised using DFT at the B3LYP/6-31G* level of theory in a vacuum.^{37-40,46-50} Conformational searches of the optimised structures were performed at Molecular Mechanics Force Field (MMFF) level.²⁹⁵ All the generated structures were retained and their energies were calculated using B3LYP/6-31G*. The lowest energy geometry in each case was selected, fully optimised and determined to be minima by the absence of negative vibrational modes, in vacuum using B3LYP/6-31G*. The final geometry optimisations and frequency calculations were also done in vacuum using B3LYP/6-31G*.

Further studies discussed within this thesis for the DFT method development (see Sections 4.2.2 and 4.2.3) were conducted using the Gaussian 09, Revision D.01 package.²⁸⁶

The structures from the Spartan calculations were reoptimized using the stated functional (B3LYP,³⁷⁻⁴⁰ BP86,^{32,33} PBE0,³⁴⁻³⁶ M06⁴¹ and M06-2X⁴¹) and basis set (6-31G*,⁴⁶⁻⁵⁰ SV(P)⁵⁴⁻⁵⁶ or def2-TZVPP⁵⁶⁻⁵⁸), with subsequent frequency calculations. All minima were confirmed as such by the absence of imaginary frequencies. The SCF energies were corrected for their zero-point energies, thermal energies and entropies at 298.15 K (obtained from the frequency calculations). For the D3(BJ)-PBE(0)/def2-TZVPP//BP86/SV(P) energies, single-point calculations on the BP86/SV(P) optimised geometries were performed using the hybrid PBE0 functional and the flexible def2-TZVPP basis set, the thermodynamic corrections were supplied from the BP86/SV(P) calculations, and dispersion effects were modelled with Grimme's D3 method with Becke-Johnson damping.^{71,75}

No symmetry constraints were applied during optimisations. Where used, solvent corrections were applied with the Polarizable Continuum Model (PCM) using the integral equation formalism (IEF) variant.⁶⁴

The functionals used in these benchmarking studies are functionals commonly used and available in various software packages. The studies discussed in Sections 4.2.2 and 4.2.3 validated the use of B3LYP/6-31G* in the study of SuRE reactions.

Thiolactone SuRE (Section 4.2.4) and Dihydroxylation SuRE (Section 4.2.5) Calculations

Conformational analysis of all structures were performed using the PCModel software package,³⁵³ using the Molecular Mechanics Force Field (MMFF) level of theory.²⁹⁵

The structures within 3.5 kcal mol⁻¹ of the lowest energy conformation were retained and the geometry of each optimised in Gaussian 09, Revision D.01,²⁸⁶ at the B3LYP/6-31G* level of theory in the gas phase.^{37,38,52,39,40,46–51} The structure with the lowest calculated electronic energy was then resubmitted for a final geometry optimisation using *tight* convergence criteria, with a subsequent frequency calculation (at the B3LYP/6-31G* level of theory), which confirmed that the structures were minima due to the absence of imaginary frequencies. The B3LYP/6-31G* SCF energies were corrected for their zero-point energies, thermal energies and entropies at 298.15 K (obtained from the frequency calculations). For compound **4.162_{RE}**, where X-ray crystallography data was provided by Dr Kleopas Palate (CCSD 1921223)³⁰⁰ the crystal structure geometry was optimised at the B3LYP/6-31G* level of theory with subsequent frequency calculation, with no initial conformational search performed. No symmetry constraints were applied. An *ultrafine* integral grid was used for all calculations

7.1.6 Computational Procedure for the Acyl Transfer Studies (Chapter 5)

Conformational analysis of all structures were performed using the PCModel software package,³⁵³ using the Molecular Mechanics Force Field (MMFF) level of theory.²⁹⁵

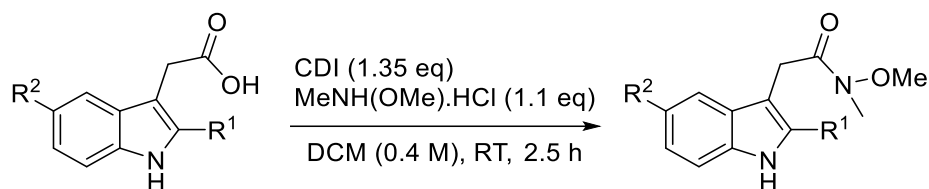
The structures within 3.5 kcal/mol of the lowest energy conformation were retained and the geometry of each optimised in Gaussian 09, Revision D.01,²⁸⁶ at the B3LYP/6-31G*,^{37-40,46-50} or B3LYP/6-31+G* (for the calculations of anions)^{37,38,52,39,40,46-51} level of theory in the gas phase. The structure with the lowest calculated electronic energy was then resubmitted for a final geometry optimisation using *tight* convergence criteria, with a subsequent frequency calculation (using the B3LYP functional with either the 6-31G* or 6-31+G* basis set as appropriate), which confirmed that the structures were minima due to the absence of imaginary frequencies. The SCF energies were corrected for their zero-point energies, thermal energies and entropies at 298.15 K (obtained from the frequency calculations). No symmetry constraints were applied. An *ultrafine* integral grid was used for all calculations.

The B3LYP/6-31G* method was used due to the benchmarking study performed within this thesis for the study of related systems (see Sections 4.2.2 and 4.2.3). The 6-31+G* basis set was used to model the anionic system due to the inclusion of diffuse functions, which are considered necessary when modelling anions.^{52,314-316}

7.2 Quinoline Rearrangement

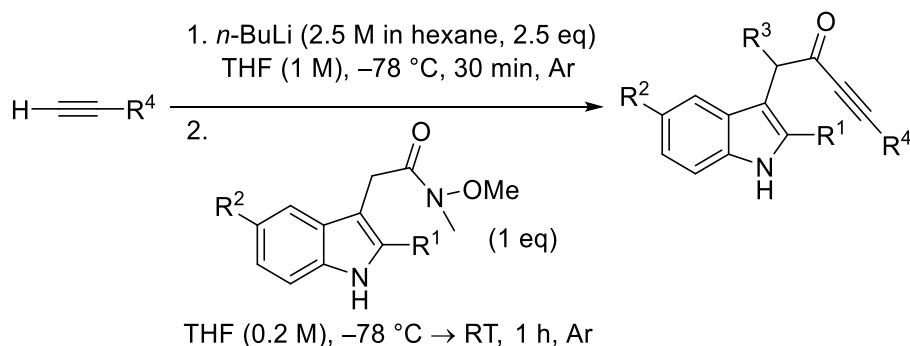
7.2.1 General Procedures

General Procedure A: Weinreb Amide Synthesis



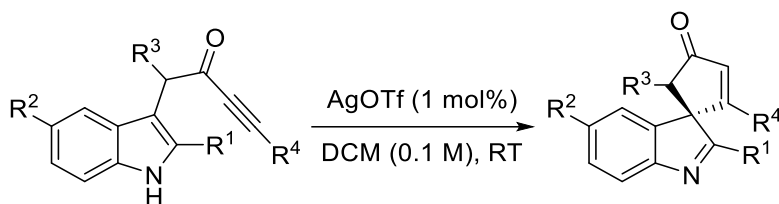
Based on a literature procedure,¹⁷⁶ to a suspension of the given carboxylic acid (1 eq) in DCM (0.4 M), CDI (1.3 eq) was added in portions. The mixture was stirred at room temperature for 1 hour, before adding *N,O*-dimethylhydroxylamine hydrochloride (1.1 eq) in portions and stirring for an additional 1.5 hours. The solution was then poured into deionised water and basified with aq. NaOH (2 M) until the pH was around 10. The organics were then extracted with EtOAc, which were combined and washed with aq. HCl (2 M) and saturated aq. NaCl before drying with MgSO₄ and concentrated *in vacuo* to afford the desired Weinreb amide.

General Procedure B: Ynone Synthesis



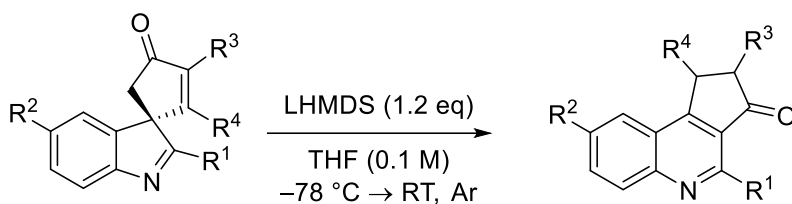
Based on a literature procedure,¹⁷³ to a solution of alkyne (3 eq) in dry THF (1 M) at -78 °C under an atmosphere of argon, *n*-BuLi (2.5 eq) was added. The solution was stirred at -78 °C for 30 minutes, then transferred *via* cannula to a cooled (-78 °C) solution of Weinreb amide (1 eq) in THF (0.2 M). The mixture was stirred for 5 minutes then warmed to room temperature and stirred for a further hour. The reaction was then quenched with saturated aq. NH₄Cl. The mixture was diluted with deionised water and extracted with EtOAc. The organic extracts were combined and dried with MgSO₄, concentrated *in vacuo* and purified by flash column chromatography to afford the ynone product

General Procedure C: Spirocyclic Synthesis



Based on a literature procedure,¹⁷³ to a solution of ynone (1 eq) in DCM (0.1 M), AgOTf (1 mol%) was added and the reaction was stirred at room temperature until complete by TLC analysis. The mixture was then concentrated *in vacuo* and purified by flash column chromatography to afford the spirocyclic indolenine product.

General Procedure D: Quinoline Rearrangement



To a solution of spirocyclic indolenine (0.5 mmol) in THF (2.5 mL), at $-78\text{ }^{\circ}\text{C}$ under an atmosphere of argon, LHMDS (0.6 mL, 0.6 mmol, 1.0 M in THF) was added. The solution was stirred for 5 min at $-78\text{ }^{\circ}\text{C}$ and then warmed to RT. The reaction mixture was stirred at RT until TLC analysis showed the reaction had gone to completion. The reaction was quenched with sat. aq. NH_4Cl (5 mL), diluted with water (5 mL) and extracted with EtOAc (3 x 10 mL). The organics were combined and dried over MgSO_4 , concentrated *in vacuo* and purified by flash column chromatography to afford the quinoline product.

General Procedure E: AlCl_3 Temperature Screens

To a microwave vial containing a solution of spirocycle **2.7a** (0.3 mmol) in *iso*-propanol (3 mL), was added $\text{AlCl}_3 \cdot 6\text{H}_2\text{O}$ (15 μmol). The reaction mixture was heated at the desired temperature for 24 hours. After this time, an aliquot was taken and concentrated *in vacuo* and a ^1H NMR spectrum was recorded in CDCl_3 to analyse the percentage conversion.

General Procedure F: TFA Temperature Screens

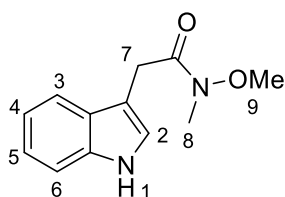
To a microwave vial containing a solution of spirocycle **2.7a** (0.3 mmol) in chloroform (1.5 mL) was added TFA (1.5 mL, 20 mmol). The reaction mixture was heated at the desired temperature for 24 hours. After this time, an aliquot was taken and concentrated *in vacuo* and a ¹H NMR spectrum was recorded in CDCl₃ to analyse the percentage conversion.

General Procedure G: LHMDS Temperature Screens

To a solution of spirocycle **2.7a** (0.75 mmol) in THF (3.75 mL), at -78 °C under an atmosphere of argon, was added LHMDS (0.75 mL, 0.75 mmol, 1 M in THF). The solution was stirred for 5 min, then warmed to the desired temperature with continued stirring, frequently checking for completion by TLC analysis. The reaction was quenched with sat. aq. NH₄Cl (5 mL), diluted with deionised water (5 mL) and extracted with EtOAc (3 x 10 mL). The organics were combined and dried over MgSO₄, concentrated *in vacuo*. A ¹H NMR spectrum was recorded in CDCl₃ to analyse the percentage conversion.

7.2.2 Weinreb Amide Products

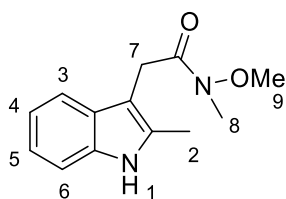
2-(1*H*-Indol-3-yl)-*N*-methoxy-*N*-methylacetamide (2.16a)



2.16a

Synthesised using general procedure A, from indole-3-acetic acid (5.022 g, 28.6 mmol), DCM (70 mL), CDI (6.275 g, 38.7 mmol) and *N,O*-dimethylhydroxylamine hydrochloride (3.098 g, 31.8 mmol). The work up steps required deionised water (100 mL), aq. NaOH (2 M, 20 mL), before extracting with EtOAc (2 x 100 mL). The organics were washed with aq. HCl (2 M, 150 mL) and saturated aq. NaCl (150 mL). After concentrating *in vacuo*, the *title product* was isolated without further purification as a pale, brown powder (5.043 g, 81%). R_f (hexane/ethyl acetate 1:1) 0.25; δ_H (400 MHz; CDCl₃) 3.23 (3 H, s, H-8), 3.67 (3 H, s, H-9), 3.93 (2 H, s, H-7), 7.12 – 7.16 (1 H, m, H-4/5), 7.18 – 7.13 (2 H, m, H-2 and H-4/5), 7.35 – 7.39 (1 H, m, H-6), 7.66 – 7.69 (1 H, m, H-2), 8.09 (1 H, br s, H-1). Spectroscopic data match those reported previously.¹⁷⁵

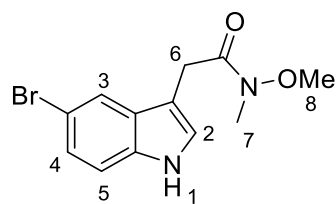
***N*-Methoxy-*N*-methyl-2-(2-methyl-1*H*-indol-3-yl)acetamide (2.16b)**



2.16b

Synthesised using general procedure A, from 2-methyl-3-indoleacetic acid (3.784 g, 20,0 mmol), DCM (48 mL), CDI (4.378 g, 27.0 mmol) and *N,O*-dimethylhydroxylamine hydrochloride (2.146 g, 22.0 mmol). The work up steps required deionised water (100 mL), aq. NaOH (2 M, 20 mL), before extracting with EtOAc (2 x 100 mL). The organics were washed with aq. HCl (2 M, 150 mL) and saturated aq. NaCl (150 mL). After concentrating *in vacuo*, the *title product* was isolated without further purification as a pale, brown powder (4.040 g, 87%). R_f (hexane/ethyl acetate 1:1) 0.27; δ_H (400 MHz; CDCl₃) 2.34, (3 H, s, H-2), 3.20 (3 H, s, H-8), 3.62 (3 H, s, H-9), 3.84 (2 H, s, H-7), 7.05 – 7.12 (2 H, m, H-4,5), 7.18 – 7.23 (1 H, m, H-6), 7.56 – 7.60 (1 H, m, H-3), 8.06 (1 H, br s, H-1). Spectroscopic data match those reported previously.¹⁷⁵

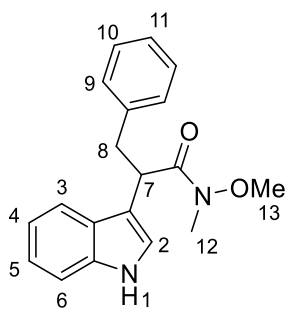
2-(5-Bromo-1*H*-indol-3-yl)-*N*-methoxy-*N*-methylacetamide (2.16c)



2.16c

Synthesised using general procedure A, from 5-bromo-indole-3-acetic acid (1.000 g, 3.9 mmol), DCM (10 mL), CDI (0.863 g, 5.3 mmol) and *N,O*-dimethylhydroxylamine hydrochloride (0.426 g, 4.4 mmol). The work up steps required deionised water (20 mL), aq. NaOH (2 M, 5 mL), before extracting with EtOAc (4 x 30 mL). The organics were washed with aq. HCl (2 M, 30 mL) and saturated aq. NaCl (30 mL). After concentrating *in vacuo*, the *title product* was isolated without further purification as a brown oil (1.077 g, 92%). R_f (hexane/ethyl acetate 1:1) 0.20; δ_H (400 MHz; CDCl₃), 3.24 (3 H, s, H-7), 3.71 (3 H, s, H-8), 3.86 (2 H, s, H-6), 7.06 (1 H, s, H-2), 7.13 (1 H, d, $J = 8.5$, H-5), 7.22 (1 H, dd, $J = 8.5, 2.0$, H-4), 7.73 (1 H, d, $J = 2.0$, H-3), 8.50 (1 H, br s, H-1). Spectroscopic data match those reported previously.¹⁷⁵

2-(1*H*-Indol-3-yl)-*N*-methoxy-*N*-methyl-3-phenylpropanamide (2.16d)

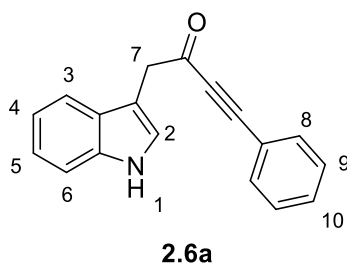


2.16d

Based on a literature procedure,¹⁷⁵ to a solution of diisopropylamine (6.4 mL, 45.6 mmol) in dry THF (23 mL) at 0 °C, under an atmosphere of argon, *n*-BuLi (1.6 M in hexane, 28.5 mL, 45.6 mmol) was added and stirred for 15 minutes before being cooled to -10°C. Indole-3-acetic acid (2.000 g, 11.4 mmol) dissolved in dry THF (12 mL), under an atmosphere of argon, was added and stirred for 2 hours. Benzyl chloride (2.9 mL, 25.2 mmol) was then added and the reaction was brought to room temperature and stirred for 16 hours. The reaction was poured into deionised water (40 mL) and extracted with EtOAc (3 x 40 mL). The organic extracts were combined and dried with MgSO₄ and concentrated *in vacuo*. The crude mixture was dissolved in DCM (43 mL) and *N,O*-dimethylhydroxylamine hydrochloride (1.223 g, 12.5 mmol), *N,N*-diisopropylethylamine (6.0 mL, 34.2 mmol) and T3P (50% w/w in BuOAc, 10.0 mL, 10.881 g, 17.1 mmol) were added sequentially and stirred for 1 hour. The reaction was poured into deionised water (60 mL) and extracted with EtOAc (2 x 60 mL). The organic extracts were washed with aq. HCl (2 M, 2 x 40 mL), aq. NaOH (2 M, 40 mL) and then dried over MgSO₄ before concentrating *in vacuo*. The crude product was purified via flash column chromatography (hexane/ethyl acetate 3:2) to afford the *title product* as a pale, brown solid (0.733 g, 21%). *R_f* (hexane/ethyl acetate 3:2) 0.27; δ_H (400 MHz; CDCl₃) 3.11 (3 H, s, H-12), 3.12 (1 H, dd, *J* = 13.0, 5.5, H-8a), 3.27 (3 H, br s, H-13), 3.52 (1 H, dd, *J* = 13.5, 10.0, H-8b), 4.69 (1 H, br s, H-7), 7.11 – 7.27 (8 H, m, H-Ar), 7.35 – 7.38 (1 H, m, H-6), 7.75 (1 H, d, *J* = 8.0, H-3), 8.20 (1 H, br s, H-1). Spectroscopic data match those reported previously.¹⁷⁵

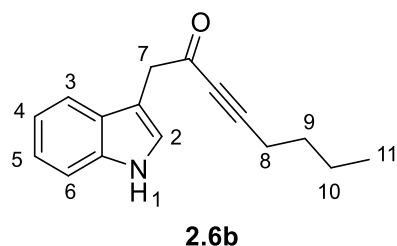
7.2.3 Indolyl-ynone Products

1-(1*H*-Indol-3-yl)-4-phenylbut-3-yn-2-one (2.6a)



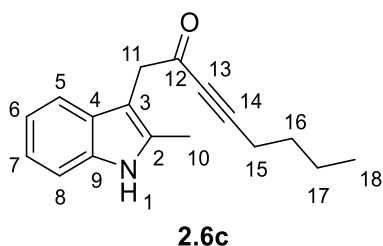
Synthesised using general procedure B, from phenylacetylene (7.077 g, 7.6 mL, 69.3 mmol) in THF (69 mL), *n*-BuLi (2.5 M in hexane, 23.1 mL, 57.8 mmol) and 2-(1*H*-indol-3-yl)-*N*-methoxy-*N*-methylacetamide **2.16a** (5.043 g, 23.1 mmol) with THF (115 mL). The work up required saturated aq. NH₄Cl (100 mL), deionised water (50 mL) and the product was extracted in EtOAc (2 x 50 mL). The crude product was purified via flash column chromatography (hexane/ethyl acetate 9:1 to 5:1) to afford the *title product* as a brown solid (3.823 g, 64%). *R_f* (hexane/ethyl acetate 5:1) 0.24; δ_H (400 MHz; CDCl₃) 4.10 (2 H, d, *J* = 1.0, H-7), 7.16 – 7.20 (1 H, m, H-4), 7.22 – 7.27 (2 H, m, H-2,5), 7.30 – 7.44 (6 H, m, H-6,8,9,10), 7.67 – 7.70 (1 H, m, H-3), 8.17 (1 H, br s, H-1). Spectroscopic data match those reported previously.¹⁷⁵

1-(1*H*-Indol-3-yl)oct-3-yn-2-one (2.6b)



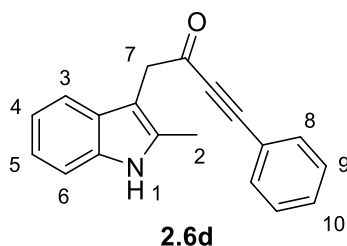
Synthesised using general procedure B, from hex-1-yne (739 mg, 1.0 mL, 9.0 mmol) in THF (9 mL), *n*-BuLi (1.6 M in hexane, 4.7 mL, 7.5 mmol) and 2-(1*H*-indol-3-yl)-*N*-methoxy-*N*-methylacetamide **2.16a** (655 mg, 3.0 mmol) with THF (15 mL). The work up required saturated aq. NH₄Cl (15 mL), deionised water (10 mL) and the product was extracted in EtOAc (3 x 30 mL). The crude product was purified via flash column chromatography (hexane/ethyl acetate 9:1 to 3:1) to afford the *title product* as a brown oil (405 mg, 57%). *R_f* (hexane/ethyl acetate 4:1) 0.34; δ_{H} (400 MHz; CDCl₃) 0.90, (3 H, t, *J* = 7.5, H-11), 1.28 – 1.39 (2 H, m, H-10), 1.42 – 1.51 (2 H, m, H-9), 2.30 (2 H, t, *J* = 7.0, H-8), 4.02 (2 H, d, *J* = 0.5, H-7), 7.06 (1 H, d, *J* = 2.5, H-2), 7.17 (1 H, ddd, *J* = 8.0, 7.0, 1.0, H-4/5), 7.23 (1 H, 8.0, 7.0, 1.5, H-4/5), 7.36 – 7.40 (1 H, m, H-6), 7.62 – 7.65 (1 H, m, H-3), 8.40 (1 H, br s, H-1). Spectroscopic data match those reported previously.¹⁷⁵

1-(2-Methyl-1*H*-indol-3-yl)oct-3-yn-2-one (2.6c)



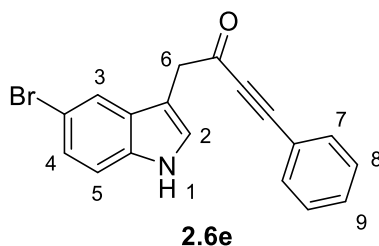
Synthesised using general procedure B, from hex-1-yne (863 mg, 1.2 mL, 10.5 mmol) in THF (11 mL), *n*-BuLi (1.6 M in hexane, 5.5 mL, 8.8 mmol) and *N*-methoxy-*N*-methyl-2-(2-methyl-1*H*-indol-3-yl)acetamide **2.16b** (813 mg, 3.5 mmol) with THF (18 mL). The work up required saturated aq. NH₄Cl (20 mL), deionised water (10 mL) and the product was extracted in EtOAc (3 x 30 mL). The crude product was purified via flash column chromatography (hexane/ethyl acetate 9:1 to 4:1) to afford the *title product* as a yellow oil (414 mg, 47%). *R_f* (hexane/ethyl acetate 1:1) 0.81; ν_{\max} (thin film)/cm⁻¹ 3398, 2957, 2210, 1664, 1462, 740; δ_{H} (400 MHz; CDCl₃) 0.84 (3 H, t, *J* = 7.0, H-18), 1.21 – 1.33 (2 H, m, H-17), 1.34 – 1.44 (2 H, m, H-16), 2.23 (2 H, t, *J* = 7.0, H-15), 2.36 (3 H, s, H-10), 3.86 (2 H, s, H-11), 7.05 – 7.14 (2 H, m, H-6,7), 7.21 – 7.26 (1 H, m, H-8), 7.50 (1 H, d, *J* = 7.5, H-5), 7.98 (1 H, br s, H-1); δ_{C} (100 MHz, CDCl₃) 11.8 (C-10), 13.6 (C-18), 18.7 (C-15), 21.9 (C-17), 29.6 (C-16), 41.3 (C-11), 81.1 (C-13), 95.5 (C-14), 103.5 (C-3), 110.5 (C-8), 118.1 (C-5), 119.6 (C-6/7), 121.3 (C-6/7), 128.7 (C-4), 133.4 (C-2), 135.3 (C-9), 185.8 (C-12); HRMS (ESI⁺) Found: 254.1544; C₁₇H₂₀NO (M+H⁺) Requires 254.1539 (–1.9 ppm error); Found: 276.1363; C₁₇H₁₉NNaO (M+Na) Requires 276.1359 (–1.6 ppm error).

4-Phenyl-1-(2-methyl-1*H*-indol-3-yl)but-3-yn-2-one (2.6d)



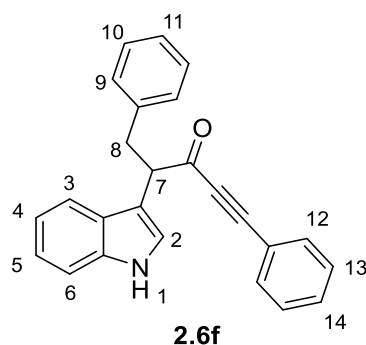
Synthesised using general procedure B, from phenylacetylene (1.072 g, 1.2 mL, 10.5 mmol) in THF (11 mL), *n*-BuLi (1.6 M in hexane, 5.5 mL, 8.8 mmol) and *N*-methoxy-*N*-methyl-2-(2-methyl-1*H*-indol-3-yl)acetamide **2.16a** (0.813 g, 3.5 mmol) with THF (18 mL). The work up required saturated aq. NH₄Cl (20 mL), deionised water (10 mL) and the product was extracted in EtOAc (3 x 30 mL). The crude product was purified via flash column chromatography (hexane/ethyl acetate 9:1 to 4:1) to afford the *title product* as a yellow powder (0.707 g, 74%). *R_f* (hexane/ethyl acetate 1:1) 0.76; δ_{H} (400 MHz; CDCl₃) 2.47 (3 H, s, H-2), 4.00 (2 H, s, H-7), 7.11 – 7.19 (2 H, m, H-4,5), 7.30 – 7.34 (5 H, m, H-6,8,9), 7.38 – 7.43 (1 H, m, H-10), 7.58 – 7.62 (1 H, m, H-3), 7.95 (1 H, br s, H-1). Spectroscopic data match those reported previously.¹⁷⁴

1-(5-Bromo-1*H*-indol-3-yl)-4-phenylbut-3-yn-2-one (2.6e)



Synthesised using general procedure B, from phenylacetylene (1.111 g, 1.2 mL, 10.9 mmol) in THF (11 mL), *n*-BuLi (1.6 M in hexane, 5.7 mL, 9.1 mmol) and 2-(5-bromo-1*H*-indol-3-yl)-*N*-methoxy-*N*-methylacetamide **2.16c** (1.077 g, 3.6 mmol) with THF (18 mL). The work up required saturated aq. NH₄Cl (20 mL), deionised water (10 mL) and the product was extracted in EtOAc (4 x 30 mL). The crude product was purified via flash column chromatography (hexane/ethyl acetate 9:1 to 7:3) to afford the *title product* as a dark, red powder (0.675 g, 55%). *R_f* (hexane/ethyl acetate 7:3) 0.28; δ_{H} (400 MHz; CDCl₃) 4.06 (2 H, s, H-6), 7.24 – 7.39 (5 H, m, H-Ar), 7.41 – 7.47 (3 H, m, H-Ar), 7.83 – 7.85 (1 H, m, H-3), 8.22 (1 H, br s, H-1). Spectroscopic data match those reported previously.¹⁷⁴

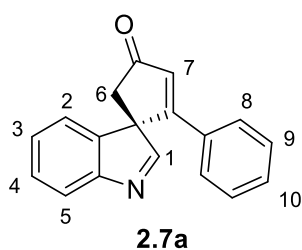
1-Benzyl-1-(1*H*-indol-3-yl)-4-phenylbut-3-yn-2-one (2.6f)



Synthesised using general procedure B, from phenylacetylene (725 mg, 0.8 mL, 7.1 mmol) in THF (7 mL), *n*-BuLi (1.6 M in hexane, 3.7 mL, 5.9 mmol) and 2-(1*H*-indol-3-yl)-*N*-methoxy-*N*-methyl-3-phenylpropanamide **2.16d** (733 mg, 2.4 mmol) with THF (12 mL). The work up required saturated aq. NH₄Cl (20 mL), deionised water (10 mL) and the product was extracted in EtOAc (4 x 30 mL). The crude product was purified via flash column chromatography (hexane/diethyl ether 1:1) to afford the *title product* as an orange oil (497 mg, 59%). *R_f* (hexane/diethyl ether 1:1) 0.34; δ_{H} (400 MHz; CDCl₃) 3.28 (1 H, dd, *J* = 14.0, 7.5, H-8a), 3.68 (1 H, dd, *J* = 14.0, 8.0, H-8b), 4.48 (1 H, dd, *J* = 8.0, 7.5, H-7), 7.14 – 7.26 (8 H, m, H-Ar), 7.28 – 7.34 (2 H, m, H-Ar), 7.37 – 7.43 (4 H, m, H-Ar), 7.74 (1 H, dd, *J* = 8.0, 0.5, H-3), 8.18 (1 H, br s, H-1). Spectroscopic data match those reported previously.¹⁷⁴

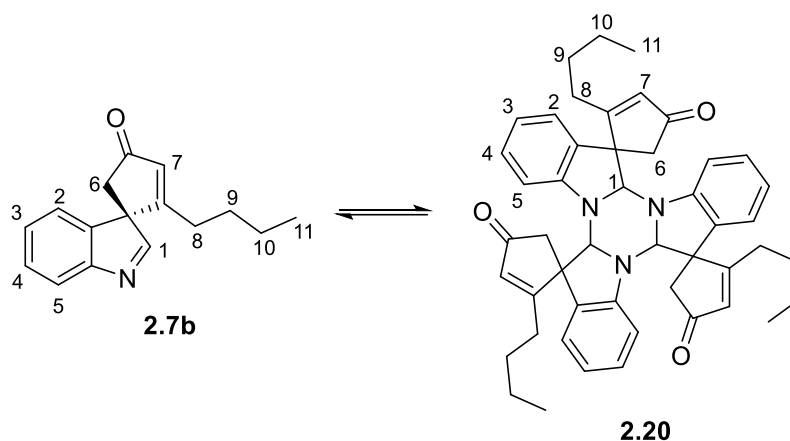
7.2.4 Spirocyclic Indolenine Products

2-Phenylspiro[cyclopent[2]ene-1,3'-indol]-4-one (2.7a)



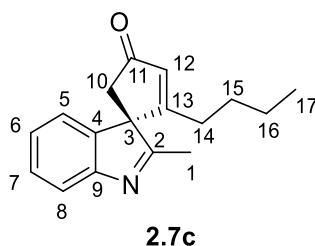
Synthesised using general procedure C, from 1-(1*H*-indol-3-yl)-4-phenylbut-3-yn-2-one **2.6a** (109 mg, 0.4 mmol) in DCM (4 mL) and AgOTf (1 mg, 4 μ mol). The reaction was complete after 2 hours and concentrated *in vacuo*. The crude product was purified by flash column chromatography (hexane/ethyl acetate 3:2) to yield the *title product* as an orange solid (90 mg, 83%). R_f (hexane/ethyl acetate 3:2) 0.50; δ_H (400 MHz; $CDCl_3$) 2.70 (1 H, d, $J = 18.0$, H-6a), 3.06 (1 H, d, $J = 18.0$, H-6b), 6.86 (1 H, s, H-7), 6.96 – 7.01 (2 H, m, H-8), 7.17 – 7.23 (2 H, m, H-9), 7.24 – 7.34 (3 H, m, H-2,3,10), 7.46 (1 H, ddd, $J = 7.5, 7.5, 1.5$, H-4), 7.78 (1 H, d, $J = 8.0$, H-5), 8.22 (1 H, s, H-1). Spectroscopic data match those reported previously.¹⁷⁵

2-Butylspiro[cyclopent[2]ene-1,3'-indol]-4-one (**2.7b**)



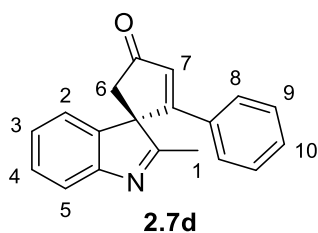
Synthesised using general procedure C, from 1-(1*H*-indol-3-yl)oct-3-yn-2-one **2.6b** (355 mg, 1.5 mmol) in DCM (15 mL) and AgOTf (4 mg, 15 μ mol). The reaction was complete after 3.5 hours and concentrated *in vacuo*. The crude product was purified by flash column chromatography (hexane/ethyl acetate 9:1 to hexane/ethyl acetate 7:3) to yield the *title product* as a brown oil (approximately 1:1.4 ratio of monomer **2.7b**:trimer **2.20**, 345 mg, 97%). R_f (hexane/ethyl acetate 4:1) 0.27 (trimer), 0.17 (monomer); δ_H (400 MHz; $CDCl_3$) 0.67 (3 H, t, $J = 7.0$, H-11, *trimer*), 0.73 – 0.82 (9 H, m, H-17, *monomer + trimer*), 1.04 – 1.24 (8 H, m, H-9/10, *monomer + trimer*), 1.30 – 1.47 (8 H, m, H-9/10, *monomer + trimer*), 1.66 – 1.84 (3 H, m, H-8, *monomer + trimer*), 1.85 – 2.03 (3 H, m, H-8, *monomer + trimer*), 2.14 – 2.25 (1 H, m, H-8, *trimer*), 2.32 – 2.44 (1 H, m, H-8, *trimer*), 2.62 (1 H, d, $J = 19.5$, H-6a, *monomer*), 2.66 (2 H, d, $J = 19.0$, H-6, *trimer*), 2.87 (1 H, d, $J = 19.0$, H-6, *trimer*), 2.93 (1 H, d, $J = 19.0$, H-6, *trimer*), 2.95 (1 H, d, $J = 19.5$, H-6b, *monomer*), 3.03 (1 H, d, $J = 19.0$, H-6, *trimer*), 3.27 (1 H, d, $J = 19.0$, H-6, *trimer*), 4.61 (1 H, s, H-1, *trimer*), 4.83 (1 H, s, H-1, *trimer*), 5.22 (1 H, s, H-1, *trimer*), 5.80 (1 H, d, $J = 8.0$, H-5, *trimer*), 5.85 (1 H, d, $J = 8.0$, H-5, *trimer*), 5.96 (1 H, s, H-7, *trimer*), 6.00 – 6.04 (2 H, m, H-7, *trimer*), 6.30 – 6.31 (1 H, m, H-7, *monomer*), 6.33 (1 H, d, $J = 8.5$, H-5, *trimer*), 6.71 (1 H, ddd, $J = 8.0, 8.0, 1.0$, H-3/4, *trimer*), 6.77 (1 H, t, $J = 7.0$, H-3/4, *trimer*), 6.86 (1 H, t, $J = 7.5$, H-3/4, *trimer*), 6.92 – 6.99 (3 H, m, H-2/3/4, *trimer*), 7.08 – 7.13 (2 H, m, H-2/3/4, *trimer*), 7.20 – 7.24 (2 H, m, H-2, *monomer + trimer*), 7.32 (1 H, t, $J = 7.5$, H-3, *monomer*), 7.44 (1 H, dd, $J = 7.5, 7.5, 1.0$, H-4, *monomer*), 7.72 (1 H, d, $J = 7.0$, H-5, *monomer*), 7.97 (1 H, s, H-1, *monomer*). Spectroscopic data match those reported previously.¹⁷⁵

2-Butyl-2'-methylspiro[cyclopent[2]ene-1,3'-indol]-4-one (2.7c)



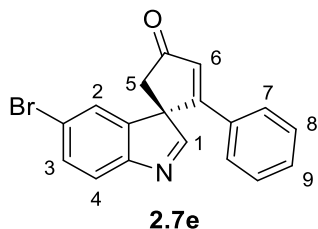
Synthesised using general procedure C, from 1-(2-methyl-1*H*-indol-3-yl)oct-3-yn-2-one **2.6c** (414 mg, 1.6 mmol) in DCM (16 mL) and AgOTf (4 mg, 16 μ mol). The reaction was complete after 1 hour and concentrated *in vacuo*. The crude product was purified by flash column chromatography (hexane/ethyl acetate 1:1) to yield the *title product* as a yellow oil (270 mg, 65%). R_f (hexane/ethyl acetate 1:1) 0.36; ν_{\max} (thin film)/ cm^{-1} 2957, 2930, 2871, 1717, 1693, 1609, 1578, 1456, 755; δ_{H} (400 MHz; CDCl_3) 0.76 (3 H, t, $J = 7.0$, H-17), 1.15 (2 H, sex., $J = 7.0$, H-16), 1.31 – 1.41 (2 H, m, H-15), 1.53 – 1.71 (2 H, m, H-14), 2.17 (3 H, s, H-1), 2.67 (1 H, d, $J = 18.5$, H-10a), 2.72 (1 H, d, $J = 18.5$, H-10b), 6.30 (1 H, t, $J = 1.5$, H-12), 7.13 (1 H, ddd, $J = 7.5, 1.5, 0.5$, H-5), 7.22 (1 H, ddd, $J = 7.5, 7.5, 1.0$, H-6), 7.37 (1 H, ddd, $J = 7.5, 7.5, 1.5$, H-7), 7.57 (1 H, d, $J = 7.5$, H-8); δ_{C} (100 MHz, CDCl_3) 13.7 (C-17), 15.5 (C-1), 22.2 (C-16), 28.2 (C-14), 29.0 (C-15), 42.7 (C-10), 68.6 (C-3), 120.5 (C-8), 121.8 (C-5), 126.3 (C-6), 129.0 (C-7), 131.0 (C-12), 140.2 (C-4), 155.4 (C-9), 181.6 (C-2/13), 181.7 (C-2/13), 206.1 (C-11); HRMS (ESI⁺) Found: 254.1541; $\text{C}_{17}\text{H}_{20}\text{NO}$ ($\text{M}+\text{H}^+$) Requires 254.1539 (–0.5 ppm error); Found: 276.1361; $\text{C}_{17}\text{H}_{19}\text{NNaO}$ ($\text{M}+\text{Na}$) Requires 276.1359 (–0.9 ppm error).

2-Phenyl-2'-methylspiro[cyclopent[2]ene-1,3'-indol]-4-one (2.7d)



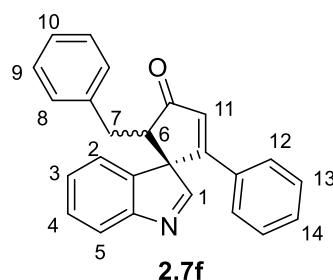
Synthesised using general procedure C, from 4-phenyl-1-(2-methyl-1*H*-indol-3-yl)but-3-yn-2-one **2.6d** (707 mg, 2.6 mmol) in DCM (26 mL) and AgOTf (7 mg, 26 μ mol). The reaction was complete after 1 hour and concentrated *in vacuo*. The crude product was purified by flash column chromatography (hexane/ethyl acetate 1:1) to yield the *title product* as an orange oil (700 mg, 99%). R_f (hexane/ethyl acetate 1:1) 0.39; δ_H (400 MHz; $CDCl_3$) 2.14 (3 H, s, H-1), 2.66 (1 H, d, $J = 18.0$, H-6a), 2.77 (1 H, d, $J = 18.0$, H-6b), 6.83 (1 H, s, H-7), 6.90 – 6.95 (2 H, m, H-8), 7.07 – 7.15 (4 H, m, H-2,9,10), 7.19 – 7.25 (1 H, m, H-3), 7.28 – 7.36 (1 H, m, H-4), 7.60 (1 H, d, $J = 7.5$, H-5). Spectroscopic data match those reported previously.¹⁷⁴

5'-Bromo-2-phenylspiro[cyclopent[2]ene-1,3'-indol]-4-one (2.7e)



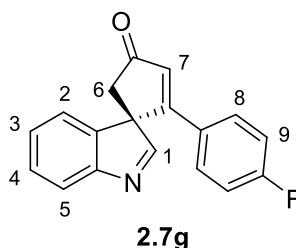
Synthesised using general procedure C, from 1-(5-bromo-1*H*-indol-3-yl)-4-phenylbut-3-yn-2-one **2.6e** (675 mg, 2.0 mmol) in DCM (20 mL) and AgOTf (5 mg, 20 μ mol). The reaction was complete after 1 hour and concentrated *in vacuo*. The crude product was purified by flash column chromatography (hexane/ethyl acetate 7:3 to hexane/ethyl acetate 1:1) to yield the *title product* as a brown powder (468 mg, 69%). R_f (hexane/ethyl acetate 1:1) 0.39; δ_H (400 MHz; $CDCl_3$) 2.68 (1 H, d, $J = 19.0$, H-5a), 3.06 (1 H, d, $J = 19.0$, H-5b), 6.87 (1 H, s, H-6), 6.98 – 7.02 (2 H, m, H-7), 7.21 – 7.26 (2 H, m, H-8), 7.33 – 7.38 (1 H, m, H-9), 7.38 (1 H, dd, $J = 2.0, 0.5$, H-2), 7.58 (1 H, dd, $J = 8.0, 2.0$, H-3), 7.65 (1 H, d, $J = 8.0$, H-4), 8.21 (1 H, s, H-1). Spectroscopic data match those reported previously.¹⁷⁴

5-Benzyl-2-phenylspiro[cyclopentane-1,3'-indol]-2-en-4-one (2.7f)



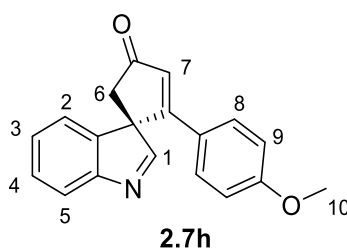
Synthesised using general procedure C, from 1-benzyl-1-(1*H*-indol-3-yl)-4-phenylbut-3-yn-2-one **2.6f** (497 mg, 1.4 mmol) in DCM (14 mL) and AgOTf (4 mg, 1 μ mol). The reaction was complete after 2 hours and concentrated *in vacuo*. The crude product was purified by flash column chromatography (hexane/diethyl ether 7:3 to 4:6) to yield the *title product* as a mixture of diastereoisomers (*major: minor* in a 2:3 ratio) as a brown solid (459 mg, 93%). R_f (hexane/diethyl ether 4:6) 0.24, 0.31; δ_H (400 MHz; $CDCl_3$) 2.11 (1 H, dd, $J = 14.5, 10.5$, H-7a *minor*), 2.54 (1 H, dd, $J = 14.5, 9.0$, H-7a, *major*), 3.18 – 3.30 (2 H, m, H-7b, *major + minor*), 3.49 (1 H, dd, $J = 9.0, 7.0$, H-6, *major*), 3.58 (1 H, dd, $J = 10.5, 4.5$, H-6, *minor*), 6.84 – 6.88 (4 H, m, H-Ar and H-11, *major + minor*), 6.90 – 6.94 (4 H, m, H-Ar, *major + minor*), 7.00 – 7.10 (6 H, m, H-Ar, *major + minor*), 7.12 – 7.21 (6 H, m, H-Ar, *major + minor*), 7.22 – 7.37 (5 H, m, H-Ar, *major + minor*), 7.48 (1 H, ddd, $J = 7.5, 7.5, 1.0$, H-4, *minor*), 7.54 – 7.57, (1 H, m, H-5, *major*), 7.57 – 7.61 (1 H, m, H-5, *minor*), 7.98 (1 H, s, H-1, *minor*), 8.14 (1 H, s, H-1, *major*). Spectroscopic data match those reported previously.¹⁷⁴

2-(4-Fluorophenyl)spiro[cyclopent[2]ene-1,3'-indol]-4-one (2.7g)



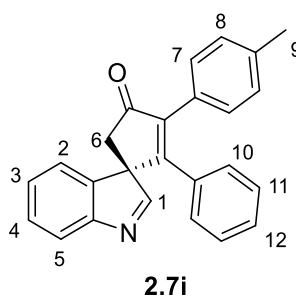
Synthesised using general procedure C, from 1-(1*H*-indol-3-yl)-4-(4-fluorophenyl)but-3-yn-2-one (956 mg, 3.5 mmol) in DCM (35 mL) and AgOTf (9 mg, 34 μ mol). The reaction was complete after 1 hour and concentrated *in vacuo*. The crude product was purified by flash column chromatography (hexane/ethyl acetate 1:1) to yield the *title product* as an orange powder (756 mg, 79%). R_f (hexane/ethyl acetate 1:1) 0.36; δ_H (400 MHz; $CDCl_3$) 2.70 (1 H, d, $J = 18.0$, H-6a), 3.06 (1 H, d, $J = 18.0$, H-6b), 6.80 (1 H, s, H-7), 6.86 – 6.92 (2 H, m, H-9), 6.95 – 7.01 (2 H, m, H-8), 7.24 – 7.26 (1 H, m, H-2), 7.31 (1 H, ddd, $J = 7.5, 7.5, 1.0$, H-3), 7.47 (1 H, ddd, $J = 7.5, 7.5, 1.0$, H-4), 7.67 – 7.80 (1 H, m, H-5), 8.21 (1 H, s, H-1). Spectroscopic data match those reported previously.¹⁷⁴

2-(4-Methoxyphenyl)spiro[cyclopent[2]ene-1,3'-indol]-4-one (2.7h)



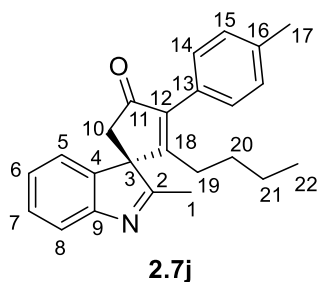
Synthesised using general procedure C, from 1-(1*H*-indol-3-yl)-4-(4-methoxyphenyl)but-3-yn-2-one (355 mg, 1.2 mmol) in DCM (12 mL) and AgOTf (3 mg, 12 μ mol). The reaction was complete after 1.5 hours and concentrated *in vacuo*. The crude product was purified by flash column chromatography (hexane/ethyl acetate 1:1) to yield the *title product* as an orange powder (329 mg, 93%). R_f (hexane/ethyl acetate 1:1) 0.37; δ_H (400 MHz; $CDCl_3$) 2.63 (1 H, d, $J = 18.5$, H-6a), 3.01 (1 H, d, $J = 18.5$, H-6b), 3.71 (3 H, s, H-10), 6.65 – 6.71 (2 H, m, H-9), 6.77 (1 H, s, H-7), 6.91 – 6.97 (2 H, m, H-8), 7.22 – 7.31 (2 H, m, H-2,3), 7.44 (1 H, ddd, $J = 7.5, 7.5, 1.5$, H-4), 7.77 (1 H, d, $J = 7.5$, H-5), 8.20 (1 H, s, H-1). Spectroscopic data match those reported previously.¹⁷⁵

2-Phenyl-5-(4-methylphenyl)spiro[cyclopentane-1,3'-indol]-2-en-4-one (2.7i)



Following a literature procedure,¹⁷⁶ to a dry round-bottomed flask, 1-(1*H*-indol-3-yl)-4-phenylbut-3-yn-2-one **2.6a** (518 mg, 2.0 mmol), 4-iodotoluene (480 mg, 2.2 mmol) and bromobis(triphenylphosphine)(*N*-succinimide)palladium(II) (32 mg, 40 μ mol) were added. The flask was purged with argon and then dry acetonitrile (20 mL) and triethylamine (0.3 mL, 2.1 mmol) were added. The reaction was heated to 60 °C with continuous stirring for 3.5 hours. The mixture was then cooled to room temperature and concentrated *in vacuo*. The crude product was purified by flash column chromatography (hexane/ethyl acetate 9:1 to hexane/ethyl acetate 3:1) to yield the *title product* as a pale, orange solid (307 mg, 44%). R_f (hexane/ethyl acetate 3:1) 0.19; δ_H (400 MHz; CDCl₃) 2.33 (3 H, s, H-9), 2.88 (1 H, d $J = 19.0$, H-6a), 3.22 (1 H, d, $J = 19.0$, H-6b), 6.66 – 6.71 (2 H, m, H-Ar), 7.00 – 7.05 (2 H, m, H-Ar), 7.08 – 7.18 (5 H, m, H-Ar), 7.31 (1 H, ddd, $J = 7.5, 7.5, 1.0$, H-3), 7.36 (1 H, ddd, $J = 7.5, 1.5, 1.0$, H-2), 7.42 (1 H, ddd, $J = 7.5, 7.5, 1.5$, H-4), 7.66 (1 H, ddd, $J = 7.5, 1.0, 1.0$, H-5), 8.19 (1 H, s, H-1). Spectroscopic data match those reported previously.¹⁷⁶

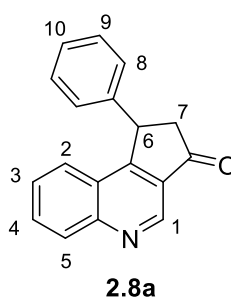
2-Butyl-5-(4-methylphenyl)-2'-methylspiro[cyclopentane-1,3'-indol]-2-en-4-one (2.7j)



Following a literature procedure,¹⁷⁶ to a dry round-bottomed flask, 1-(2-methyl-1*H*-indol-3-yl)oct-3-yn-2-one **2.6c** (529 mg, 2.1 mmol), 4-iodotoluene (501 mg, 2.3 mmol) and bromobis(triphenylphosphine)(*N*-succinimide)palladium(II) (32 mg, 40 μ mol) were added. The flask was purged with argon and then dry acetonitrile (20 mL) and triethylamine (0.3 mL, 2.1 mmol) were added. The reaction was heated to 60 °C with continuous stirring for 4. The mixture was cooled to room temperature and concentrated *in vacuo*. The crude product was purified by flash column chromatography (hexane/ethyl acetate 9:1 to hexane/ethyl acetate 7:3) to yield the *title product* as a pale, yellow oil (489 mg, 71%). R_f (hexane/ethyl acetate 3:1) 0.22; ν_{\max} (thin film)/ cm^{-1} 2957, 1705, 1578, 1408, 755; δ_{H} (400 MHz; CDCl_3) 0.53 (3 H, t, $J = 6.5$, H-22), 0.82 – 1.04 (4 H, m, H-20,21), 1.75 – 1.85 (1 H, m, H-19a), 1.92 – 2.02 (1 H, m, H-19b), 2.24 (3 H, s, H-1), 2.36 (3 H, s, H-17), 2.78 (1 H, d, $J = 19.0$, H-10a), 2.83 (1 H, d, $J = 19.0$, H-10b), 7.19 – 7.26 (6 H, m, H-5,6,14,15), 7.35 – 7.42 (1 H, m, H-7), 7.60 (1 H, d, $J = 7.5$, H-8); δ_{C} (100 MHz; CDCl_3) 13.3 (C-22), 15.9 (C-1), 21.4 (C-17), 22.8 (C-20/21), 28.3 (C-19), 30.0 (C-20/21), 42.7 (C-10), 67.1 (C-3), 120.5 (C-8), 122.3 (C-5/6/14/15), 126.1 (C-5/6/14/15), 128.3 (C-13), 128.8 (C-5/6/14/15), 129.0 (C-5/6/14/15), 129.3 (C-8), 138.3 (C-16), 140.6 (C-12), 143.2 (C-4), 155.6 (C-9), 173.4 (C-18), 182.6 (C-2), 204.8 (C-11); HRMS (ESI⁺) Found: 344.2005; $\text{C}_{24}\text{H}_{26}\text{NO}$ ($\text{M}+\text{H}^+$) Requires 344.2009 (1.0 ppm error); Found: 366.1825; $\text{C}_{24}\text{H}_{25}\text{NNaO}$ ($\text{M}+\text{Na}$) Requires 366.1828 (0.9 ppm error).

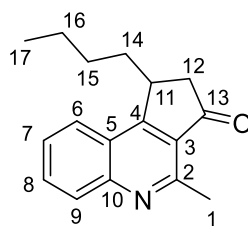
7.2.5 Quinoline Products

1-Phenyl-1,2-dihydro-3H-cyclopenta[c]quinolin-3-one (2.8a)



Following general procedure D, from 2-phenylspiro[cyclopent[2]ene-1,3'-indol]-4-one **2.7a** (194 mg, 0.8 mmol) in THF (3.8 mL) and LHMDS (0.8 mL, 0.8 mmol, 1 M in THF). The reaction was stirred for 30 minutes until complete by TLC analysis. The work up required saturated aq. NH_4Cl (10 mL), deionised water (5 mL) and the product was extracted with EtOAc (5 x 10 mL). The crude product was purified by flash column chromatography (hexane/ethyl acetate 4:1 to 1:1) to yield the *title product* as a pale, brown solid (157 mg, 81%). R_f (hexane/ethyl acetate 1:1) 0.51; δ_{H} (400 MHz; CDCl_3) 2.79 (1 H, dd, $J = 19.0, 3.0$, H-7a), 3.42 (1 H, dd, $J = 19.0, 8.0$, H-7b), 5.05 (1 H, dd, $J = 8.0, 3.0$, H-6), 7.10 – 7.13 (2 H, m, H-8), 7.27 – 7.34 (3 H, m, H-9,10), 7.48 (1 H, ddd, $J = 8.0, 7.0, 1.0$, H-3), 7.71 (1 H, dd, $J = 8.0, 1.0$, H-2), 7.82 (1 H, ddd, $J = 8.0, 7.0, 1.0$, H-4), 8.23 (1 H, d, $J = 8.0$, H-5), 9.31 (1 H, s, H-1). Spectroscopic data match those reported previously.¹⁷³

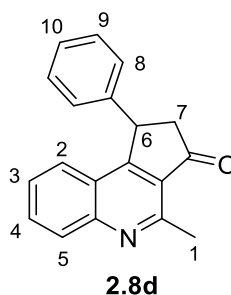
1-Butyl-4-methyl-1,2-dihydro-3H-cyclopenta[c]quinolin-3-one (2.8c)



2.8c

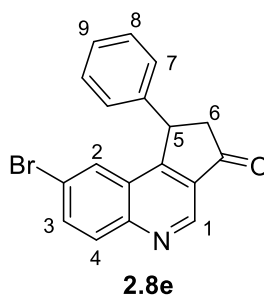
Following general procedure D, from 2-butyl-2'-methylspiro[cyclopent[2]ene-1,3'-indol]-4-one **2.7c** (127 mg, 0.5 mmol) in THF (2.5 mL) and LHMDS (0.6 mL, 0.6 mmol, 1 M in THF). The reaction was stirred for 1 hour until complete by TLC analysis. The work up required saturated aq. NH_4Cl (5 mL), deionised water (5 mL) and the product was extracted with EtOAc (4 x 10 mL). The crude product was purified by flash column chromatography (hexane/ethyl acetate 7:3) to yield the *title product* as a yellow powder (76 mg, 60%). R_f (hexane/ethyl acetate 7:3) 0.31; mp 88 – 89 °C; ν_{max} (thin film)/ cm^{-1} 2929, 2952, 2853, 1708, 1616, 1588, 1417, 773; δ_{H} (400 MHz; CDCl_3) 0.89 (3 H, t, $J = 6.5$, H-17), 1.20 – 1.57 (5 H, m, H-14a,15,16), 2.02 – 2.19 (1 H, m, H-14b), 2.59 (1 H, dd, $J = 19.0, 1.5$, H-12a), 2.94 (1 H, dd, $J = 19.0, 7.0$, H-12b), 2.95 (3 H, s, H-1), 3.78 – 3.87 (1 H, m, H-11), 7.60 (1 H, ddd, $J = 8.5, 7.0, 1.0$, H-7), 7.83 (1 H, ddd, $J = 8.5, 7.0, 1.0$, H-8), 8.04 (1 H, dd, $J = 8.5, 1.0$, H-6), 8.11 (1 H, d, $J = 8.5$, H-9); δ_{C} (100 MHz, CDCl_3) 14.1 (C-17), 22.7 (C-16), 22.8 (C-1), 29.8 (C-15), 36.2 (C-14), 36.9 (C-11), 43.8 (C-12), 124.4 (C-6), 124.4 (C-5), 126.6 (C-7), 128.1 (C-3), 129.9 (C-9), 132.4 (C-8), 149.7 (C-10), 157.4 (C-2), 169.0 (C-4), 205.5 (C-13); HRMS (ESI⁺) Found: 254.1538; $\text{C}_{17}\text{H}_{20}\text{NO}$ ($\text{M}+\text{H}^+$) Requires 254.1539 (0.4 ppm error).

1-Phenyl-4-methyl-1,2-dihydro-3H-cyclopenta[c]quinolin-3-one (2.8d)



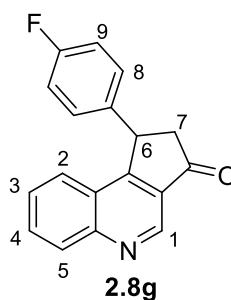
Following general procedure D, from 2-phenyl-2'-methylspiro[cyclopent[2]ene-1,3'-indol]-4-one **2.7d** (137 mg, 0.5 mmol) in THF (2.5 mL) and LHMDS (0.6 mL, 0.6 mmol, 1 M in THF). The reaction was stirred for 1.5 hours until complete by TLC analysis. The work up required saturated aq. NH_4Cl (5 mL), deionised water (5 mL) and the product was extracted with EtOAc (5 x 10 mL). The crude product was purified by flash column chromatography (hexane/ethyl acetate 7:3) to yield the *title product* as an orange powder (97 mg, 71%). R_f (hexane/ethyl acetate 1:1) 0.48; δ_{H} (400 MHz; CDCl_3) 2.75 (1 H, dd, $J = 19.0, 2.5$, H-7a), 3.06 (3 H, s, H-1), 3.38 (1 H, dd, $J = 19.0, 7.5$, H-7b), 4.98 (1 H, dd, $J = 7.5, 2.5$, H-6), 7.09 – 7.13 (2 H, m, H-8), 7.25 – 7.33 (3 H, m, H-9,10), 7.39 (1 H, ddd, $J = 8.5, 7.0, 1.5$, H-3), 7.67 (1 H, ddd, $J = 8.5, 1.5, 0.5$, H-2), 7.77 (1 H, ddd, $J = 8.5, 7.0, 1.5$, H-4), 8.11 (1 H, br d, $J = 8.5$, H-5). Spectroscopic data match those reported previously.¹⁷⁴

8-Bromo-1-phenyl-1,2-dihydro-3H-cyclopenta[c]quinolin-3-one (2.8e)



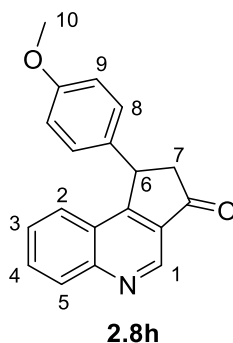
Following general procedure D, from 5'-bromo-2-phenylspiro[cyclopent[2]ene-1,3'-indol]-4-one **2.7e** (169 mg, 0.5 mmol) in THF (2.5 mL) and LHMDS (0.6 mL, 0.6 mmol, 1 M in THF). The reaction was stirred for 30 minutes until complete by TLC analysis. The work up required saturated aq. NH_4Cl (5 mL), deionised water (5 mL) and the product was extracted with EtOAc (4 x 10 mL). The crude product was purified by flash column chromatography (hexane/ethyl acetate 7:3) to yield the *title product* as an orange powder (136 mg, 80%). R_f (hexane/ethyl acetate 7:3) 0.39; δ_{H} (400 MHz; CDCl_3) 2.79 (1 H, dd, $J = 19.5, 3.0$, H-6a), 3.41 (1 H, dd, $J = 19.5, 8.0$, H-6b), 4.99 (1 H, dd, $J = 8.0, 3.0$, H-5), 7.09 – 7.12 (2 H, m, H-7), 7.28 – 7.37 (3 H, m, H-8,9), 7.84 (1 H, dd, $J = 2.0, 0.5$, H-2), 7.87 (1 H, dd, $J = 9.0, 2.0$, H-3), 8.09 (1 H, d, $J = 9.0$, H-4), 9.30 (1 H, s, H-1). Spectroscopic data match those reported previously.¹⁷⁴

1-(4-Fluorophenyl)-1,2-dihydro-3H-cyclopenta[c]quinolin-3-one (2.8g)



Following general procedure D, from 2-(4-fluorophenyl)spiro[cyclopent[2]ene-1,3'-indol]-4-one **2.7g** (139 mg, 0.5 mmol) in THF (2.5 mL) and LHMDS (0.6 mL, 0.6 mmol, 1 M in THF). The reaction was stirred for 30 minutes until complete by TLC analysis. The work up required saturated aq. NH_4Cl (5 mL), deionised water (5 mL) and the product was extracted with EtOAc (4 x 10 mL). The crude product was purified by flash column chromatography (hexane/ethyl acetate 1:1) to yield the *title product* as an orange powder (99 mg, 71%). R_f (hexane/ethyl acetate 1:1) 0.45; δ_{H} (400 MHz; CDCl_3) 2.73 (1 H, dd, $J = 19.5, 3.0$, H-7a), 3.41 (1 H, dd, $J = 19.5, 8.0$, H-7b), 5.04 (1 H, dd, $J = 8.0, 3.0$, H-6), 6.97 – 7.04 (2 H, m, H-9), 7.05 – 7.11 (2 H, m, H-8), 7.50 (1 H, ddd, $J = 8.5, 7.0, 1.5$, H-3), 7.68 (1 H, ddd, $J = 8.5, 1.5, 0.5$, H-2), 7.85 (1 H, ddd, $J = 8.5, 7.0, 1.5$, H-4), 8.25 (1 H, d, $J = 8.5$, H-5), 9.31 (1 H, s, H-1). Spectroscopic data match those reported previously.¹⁷⁴

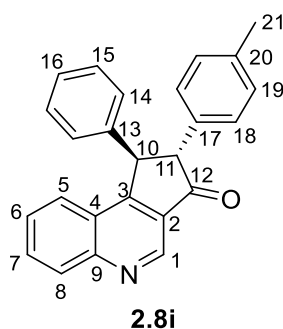
1-(4-Methoxyphenyl)-1,2-dihydro-3H-cyclopenta[c]quinolin-3-one (2.8h)



Following general procedure D, from 2-(4-methoxyphenyl)spiro[cyclopent[2]ene-1,3'-indol]-4-one **2.7h** (145 mg, 0.5 mmol) in THF (2.5 mL) and LHMDS (0.6 mL, 0.6 mmol, 1 M in THF). The reaction was stirred for 30 minutes until complete by TLC analysis. The work up required saturated aq. NH₄Cl (10 mL), deionised water (5 mL) and the product was extracted with EtOAc (3 x 10 mL). The product was purified by flash column chromatography (hexane/ethyl acetate 4:1 to 1:1) to yield the *title product* as an orange powder (133 mg, 92%). *R_f*(hexane/ethyl acetate 1:1) 0.39; δ_H (400 MHz; CDCl₃) 2.72 (1 H, dd, *J* = 19.0, 3.0, H-7a), 3.37 (1 H, dd, *J* = 19.0, 8.0, H-7b), 3.76 (3 H, s, H-10), 4.99 (1 H, dd, *J* = 8.0, 3.0, H-6), 6.80 – 6.84 (2 H, m, H-9), 6.99 – 7.04 (2 H, m, H-8), 7.47 (1 H, ddd, *J* = 8.0, 7.0, 1.0, H-3), 7.73 (1 H, dd, *J* = 8.0, 1.0, H-2), 7.80 (1 H, ddd, *J* = 8.5, 7.0, 1.0, H-4), 8.21 (1 H, d, *J* = 8.5, H-5), 9.27 (1 H, s, H-1). Spectroscopic data match those reported previously.¹⁷³

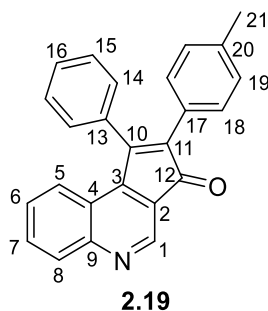
Note that this reaction was performed by Dr Aimee Clarke.

***trans*-1-phenyl-2-(4-methylphenyl)-1,2-dihydro-3*H*-cyclopenta[*c*]quinolin-3-one (2.8i)**



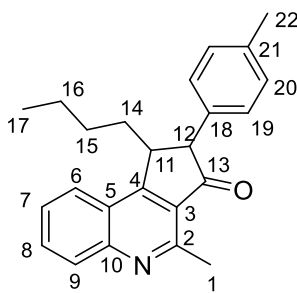
Following general procedure D, from 2-phenyl-3-(4-methylphenyl)spiro[cyclopentane-1,3'-indol]-2-en-4-one **2.7i** (175 mg, 0.5 mmol) in THF (2.5 mL) and LHMDS (0.6 mL, 0.6 mmol, 1 M in THF). The reaction was stirred for 2.5 hours until complete by TLC analysis. The work up required saturated aq. NH_4Cl (5 mL), deionised water (5 mL) and the product was extracted with EtOAc (4 x 10 mL). The crude product was purified by flash column chromatography (hexane/ethyl acetate 9:1 to 3:1) to yield the *title product* as an orange oil (105 mg, 60%). R_f (hexane/ethyl acetate 3:1) 0.33; ν_{max} (thin film)/ cm^{-1} 3028, 1714, 1615, 1574, 1512, 1421; δ_{H} (400 MHz; CDCl_3) 2.34 (3 H, s, H-21), 3.87 (1 H, d, $J = 3.5$, H-11), 4.99 (1 H, d, $J = 3.5$, H-10), 6.99 – 7.03 (2 H, m, H-18/19), 7.05 – 7.09 (2 H, m, H-14), 7.13 – 7.17 (2 H, m, H-18/19), 7.28 – 7.34 (3 H, m, H-15,16), 7.45 (1 H, ddd, $J = 8.5, 7.0, 1.5$, H-6), 7.65 (1 H, ddd, $J = 8.5, 1.5, 0.5$, H-5), 7.82 (1 H, ddd, $J = 8.5, 7.0, 1.5$, H-7), 8.27 (1 H, d, $J = 8.5$, H-8), 9.37 (1 H, s, H-1); δ_{C} (100 MHz; CDCl_3) 21.2 (C-21), 54.4 (C-10), 65.0 (C-11), 125.2 (C, C-Ar), 125.9 (C-5), 127.5 (CH, C-Ar), 127.6 (CH, C-Ar), 127.8 (CH, C-Ar), 127.9 (CH, C-Ar), 129.4 (CH, C-Ar), 129.7 (C-Ar), 129.8 (CH, C-Ar), 130.7 (C-8), 132.5 (C-7), 135.2 (C, C-Ar), 137.3 (C-20), 141.9 (C, C-Ar), 146.0 (C-1), 151.1 (C-9), 164.2 (C, C-Ar), 204.0 (C-12); HRMS (ESI⁺) Found: 350.1532; $\text{C}_{25}\text{H}_{20}\text{NO}$ ($\text{M}+\text{H}^+$) Requires 350.1539 (0.7 ppm error), Found: 372.1351; $\text{C}_{25}\text{H}_{19}\text{NNaO}$ ($\text{M}+\text{Na}$) Requires 372.1539 (2.2 ppm error).

1-Phenyl-2-(4-methylphenyl)-cyclopenta[c]quinolin-3-one (2.19)



Side product formed during the synthesis of **2.8i**. Purification by flash column chromatography (hexane/ethyl acetate 9:1 to 3:1) yielded the *title product* as a red solid (36 mg, 20%). R_f (hexane/ethyl acetate 3:1) 0.40; mp 183 – 187 °C; ν_{\max} (thin film)/ cm^{-1} 2919, 1707, 1618, 1562, 1511, 1488; δ_{H} (400 MHz; CDCl_3) 2.31 (3 H, s, H-21), 7.05 – 7.09 (2 H, m, H-18/19), 7.15 – 7.19 (2 H, m, H-18/19), 7.22 – 7.26 (2 H, m, H-Ar), 7.40 – 7.46 (2 H, m, H-Ar), 7.49 – 7.55 (3 H, m, H-Ar), 7.68 (1 H, ddd, $J = 8.5, 4.5, 4.0$, H-Ar), 8.09 (1 H, ddd, $J = 8.5, 1.0, 1.0$, H-8), 9.05 (1 H, s, H-1); δ_{C} (100 MHz; CDCl_3) 21.5 (C-21), 119.9 (C-3), 122.9 (C, C-Ar), 125.3 (C-14), 126.9 (C, C-Ar), 127.3 (CH, C-Ar), 128.7 (C-18), 129.0 (C-5/6/16), 129.2 (CH, C-Ar), 129.3 (CH, C-Ar), 130.2 (C-19), 130.8 (C-8), 131.8 (CH, C-Ar), 134.2 (C, C-Ar), 134.9 (C, C-Ar), 138.7 (C-20), 142.9 (C-1), 153.2 (C, C-Ar), 153.2 (C-2), 153.8 (C-9), 197.0 (C-12); HRMS (ESI⁺) Found: 348.1377; $\text{C}_{25}\text{H}_{18}\text{NO}$ ($\text{M}+\text{H}^+$) Requires 348.1383 (1.6 ppm error).

1-Butyl-2-(4-methylphenyl)-4-methyl-1,2-dihydro-3H-cyclopenta[c]quinolin-3-one (2.8j)



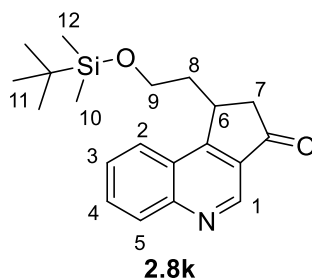
2.8j

Following general procedure D, from 2-butyl-3-(4-methylphenyl)-2'-methylspiro[cyclopentane-1,3'-indol]-2-en-4-one **2.7j** (165 mg, 0.5 mmol) in THF (2.5 mL) and LHMDS (0.6 mL, 0.6 mmol, 1 M in THF). The reaction was stirred for 30 minutes until complete by TLC analysis. The work up required saturated aq. NH_4Cl (10 mL), deionised water (5 mL) and the product was extracted with EtOAc (4 x 10 mL). The product was purified by flash column chromatography (hexane/acetone 99:1 to 95:5) to yield the *title product* as a mixture of diastereoisomers (*major/minor* in a 7:3 ratio) as an orange oil (98 mg, 58%). R_f = (hexane/acetone 95:5) 0.08; ν_{max} (thin film)/ cm^{-1} 2956, 2870, 1706, 1682, 1608, 1578, 755; δ_{H} (400 MHz; CDCl_3) = 0.57 (3 H, t, J = 6.5, H-17, *minor*), 0.89 (3 H, t, J = 7.0, H-17, *major*), 0.82 – 1.02 (4 H, m, H-15,16, *minor*), 1.27 – 1.55 (4 H, m, H-15,16, *major*), 1.55 – 1.62 (2 H, m, H-14, *minor*), 1.62 – 1.73 (1 H, m, H-14a, *major*), 2.17 – 2.25 (1 H, m, H-14b, *major*), 2.30 (3 H, s, H-22, *major*), 2.39 (3 H, s, H-22, *minor*), 2.96 (3 H, s, H-1, *major*), 3.03 (3 H, s, H-1, *minor*), 3.71 (1 H, d, J = 1.5, H-12, *major*), 3.91 (1 H, dt, J = 9.5, 3.0, 1.5, H-11, *major*), 4.15 (1 H, dt, J = 7.0, 4.0, H-11, *minor*), 4.25 (1 H, d, J = 7.0, H-12, *minor*), 6.99 – 7.05 (2 H, m, H-19/20, *major*), 7.08 – 7.14 (2 H, m, H-19/20, *major*), 7.19 – 7.25 (4 H, m, H-19,20, *minor*), 7.60 – 7.67 (2 H, m, H-7, *major* + *minor*), 7.84 – 7.92 (2 H, m, H-8, *major* + *minor*), 8.06 (1 H, d, J = 8.5, H-6, *minor*), 8.10 (1 H, d, J = 8.0, H-6, *major*), 8.14 – 8.19 (2 H, m, H-9, *major* + *minor*); δ_{C} (100 MHz; CDCl_3) 13.7 (C-17, *minor*), 14.1 (C-17, *major*), 21.2 (C-22, *major*), 21.3 (C-22, *minor*), 22.6 (C-16, *minor*), 22.8 (C-1, *major*), 22.8 (C-16, *major* and C-1, *minor*), 29.5 (C-15, *minor*), 30.0 (C-15, *major*), 33.1 (C-14, *minor*), 36.5 (C-14, *major*), 42.8 (C-11, *minor*), 46.6 (C-11, *major*), 59.3 (C-12, *minor*), 60.7 (C-12, *major*), 124.3 (CH, C-Ar, *minor*), 125.0 (CH, C-Ar, *major*), 126.7 (C-7, *minor*), 126.8 (C-6, *major*), 127.3 (C-7, *major*), 127.8 (C, C-Ar, *minor*), 129.3 (C-19/20, *minor*), 129.8 (CH, C-Ar, *major*) 129.8 (C-9, *minor*), 129.9 (CH, C-Ar, *major*), 130.4 (C-19/20, *minor*), 132.5 (C-8, *minor*), 132.6 (C, C-Ar, *minor*), 132.7 (C-8, *major*), 136.6 (C, C-Ar, *major*), 137.1 (C, C-Ar, *minor*), 149.7 (C, C-Ar, *minor*), 149.9 (C, C-Ar, *major*), 157.6 (C, C-Ar, *minor*), 158.1 (C, C-Ar, *major*), 166.9 (C-Ar, *minor*), 168.6 (C-Ar, *major*), 204.6 (C-13,

minor), 205.0 (C-13, *major*); HRMS (ESI⁺) Found: 366.1821; C₂₄H₂₅NONa (M+Na) Requires 366.1828 (-1.9 ppm error).

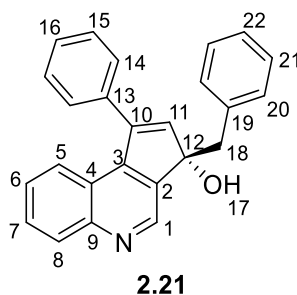
Note that one quaternary carbon resonance for the *minor* isomer, and three quaternary carbon resonances for the *major* could not be found in the ¹³C NMR spectra. It is believed that those resonances are overlapping with other resonances.

1-(2-((*tert*-Butyldimethylsilyl)oxy)ethyl)-1,2-dihydro-3*H*-cyclopenta[*c*]quinolin-3-one (2.8k)



Following general procedure D, from 2-(2-((*tert*-butyldimethylsilyl)oxy)ethyl)spiro[cyclopentane-1,3'-indol]-2-en-4-one (103 mg, 0.3 mmol) in THF (1.5 mL) and LHMDS (0.3 mL, 0.3 mmol, 1 M in THF). The reaction was stirred for 1 hour until complete by TLC analysis. The work up required NH₄Cl (10 mL), deionised water (5 mL) and the product was extracted with EtOAc (4 x 10 mL). The crude product was purified by flash column chromatography (hexane/ethyl acetate 4:1 to 7:3) to yield the *title product* as a brown oil (60 mg, 59%). *R_f* (hexane/ethyl acetate 7:3) 0.33; δ_{H} (400 MHz; CDCl₃) 0.09 (3 H, s, H-10/12), 0.09 (3 H, s, H-10/12), 0.94 (9 H, s, H-11), 1.61 – 1.70 (1 H, m, H-8a), 2.40 – 2.49 (1 H, m, H-8b), 2.70 (1 H, 19.0, 1.5, H-7a), 3.01 (1 H, dd, *J* = 19.0, 7.5, H-7b), 3.73 (1 H, ddd, *J* = 10.5, 9.5, 4.5, H-9a), 3.85 (1 H, ddd, *J* = 10.5, 4.5, 4.5, H-9b), 4.11 – 4.19 (1 H, m, H-6), 7.70 (1 H, ddd, *J* = 8.5, 7.0, 1.5, H-3), 7.90 (1 H, ddd, *J* = 8.5, 7.0, 1.5, H-4), 8.19 (1 H, dd, *J* = 8.5, 1.5, H-2), 8.25 (1 H, d, 8.5, H-5), 9.19 (1 H, s, H-1). Spectroscopic data match those reported previously.¹⁷³

3-Benzyl-1-phenylcyclopenta[c]quinolin-3-ol (2.21)



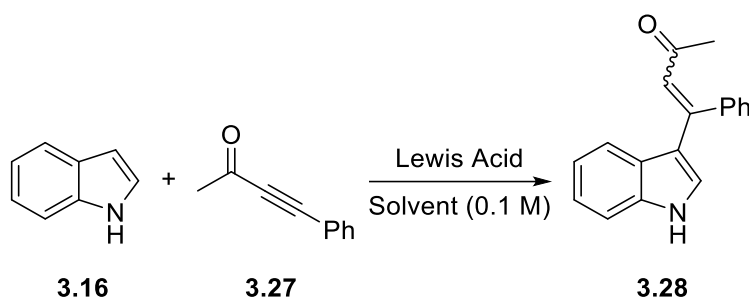
Following general procedure D, from 5-benzyl-2-phenylspiro[cyclopentane-1,3'-indol]-2-en-4-one **2.7f** (175 mg, 0.5 mmol) in THF (2.5 mL) and LHMDS (0.6 mL, 0.6 mmol, 1 M in THF). The reaction was stirred for 1 hour until complete by TLC analysis. The work up required NH₄Cl (5 mL), deionised water (5 mL) and the product was extracted with EtOAc (4 x 10 mL). The crude product was purified by flash column chromatography (hexane/ethyl acetate 6:4) to yield the *title product* as an orange powder (106 mg, 61%). mp 191 – 192 °C; *R_f* (hexane/ethyl acetate 6:4) 0.13; ν_{max} (thin film)/cm⁻¹ 3076, 2328, 1569, 1506, 699; δ_{H} (400 MHz; *d*₆-DMSO) 5.93 (1 H, s, H-17), 6.50 (1 H, s, H-11), 7.02 – 7.11 (5 H, m, H-Ar), 7.20 – 7.35 (4 H, m, H-Ar), 7.45 – 7.51 (3 H, m, H-Ar), 7.60 (1 H, ddd, *J* = 8.5, 7.0, 1.5, H-7), 8.01 (1 H, d, *J* = 8.5, H-8), 8.93 (1 H, s, H-1); δ_{C} (100 MHz; *d*₆-DMSO) 43.7 (C-18), 82.8 (C-12), 122.7 (C-Ar), 123.5 (C-Ar), 125.9 (C-Ar), 126.2 (C-Ar), 127.3 (C-Ar), 128.2 (C-Ar), 128.2 (C-Ar), 128.6 (C-Ar), 128.6 (C-7), 129.9 (C-Ar), 130.2 (C-8), 136.4 (C-Ar), 136.6 (C-Ar), 141.3 (C-10), 142.2 (C-Ar), 144.8 (C-Ar), 145.1 (C-1), 145.5 (C-11), 148.7 (C-Ar); HRMS (ESI⁺) Found: 350.1539; C₂₅H₂₀NO (M+H⁺) Requires 350.1539 (0.1 ppm error).

Note that the benzylic protons (H-18) are overlapping with the residual water peak of the *d*₆-DMSO, as confirmed by ¹³C and HMQC NMR spectra.

7.3 Indole Vinylation

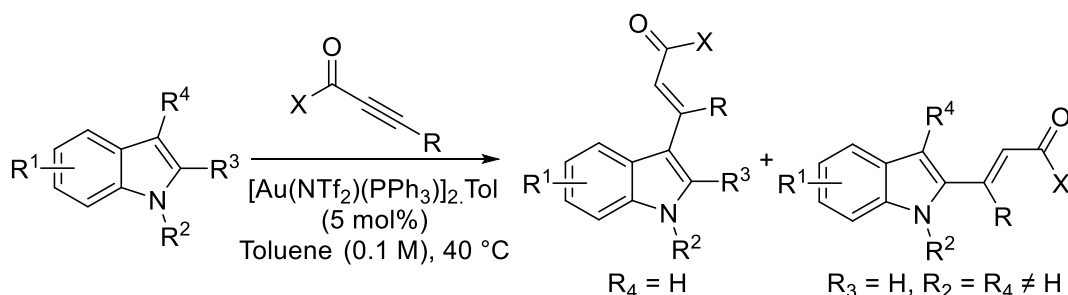
7.3.1 General Procedures

General Procedure H: Indole vinylation Reaction Optimisation



Indole **3.16** (12 mg, 0.1 mmol) was dissolved in the desired solvent (1 mL, 0.1 M), and the desired quantity of 4-phenyl-3-butyne-2-one **3.27** was added, followed by the chosen Lewis acid catalyst. The reaction was stirred at the chosen temperature for the given amount of time before the solvent was concentrated *in vacuo*. ¹H NMR spectra were then recorded to determine the conversion of indole to the desired product.

General Procedure I: Gold-catalysed alkyne addition to indole



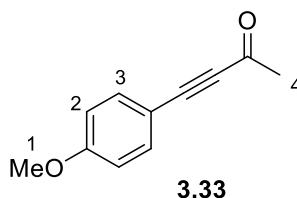
The indole substrate (1 eq) and alkyne (1.5 eq) were dissolved in toluene (0.1 M) and [bis(trifluoromethanesulfonyl)imidate](triphenylphosphine)gold(I) (2:1) toluene adduct (5 mol%) was added. The reaction was then stirred at 40 °C for the reported time. The reaction mixture was then concentrated *in vacuo* and the product was purified *via* flash column chromatography using the reported eluent.

General Procedure J: NMR Studies

To a sample vial, [bis(trifluoromethanesulfonyl)imidate](triphenylphosphine)gold(I) (2:1) toluene adduct (15.7 mg, 0.01 mmol) and the desired amount of substrate were dissolved in *d*₂-DCM (0.6 mL). ¹H and ³¹P{¹H} NMR spectra were then recorded using 16 and 128 scans respectively. For the amide (**3.39** and **3.41**) and ester (**3.43** and **3.44**) alkynes, anhydrous *d*₂-DCM was used. Due to the dimeric nature of the gold catalyst, 1 equivalent of substrate = 0.02 mmol.

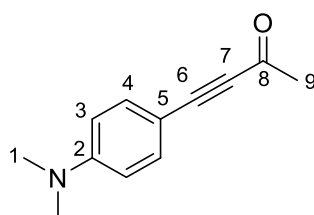
7.3.2 Alkyne Synthesis

4-(4-Methoxyphenyl)-3-butyn-2-one (**3.33**)



Following a literature procedure,²⁰² to a dry round-bottomed flask, 4-methoxyphenyl acetylene **3.30** (397 mg, 0.39 mL, 3.0 mmol) was dissolved in THF (50 mL) under an atmosphere of Ar and cooled to 0 °C. With vigorous stirring, *n*-BuLi (1.32 mL, 2.5 M in hexane, 3.3 mmol) was added and stirred for 15 minutes, at which point the solution was cooled to -78 °C and *N*-methyl *N*-methoxy acetamide **3.32** (356 mg, 0.36 mL, 3.5 mmol) was added slowly over 3 minutes. The reaction was stirred for 30 minutes, before warming to room temperature and stirring for a further 2 hours. The reaction was quenched with aq. HCl (7.5 mL, 2 M) and extracted with DCM (3 x 50 mL). The organic extracts were combined, dried with MgSO₄ and concentrated *in vacuo*. The crude product was purified via flash column chromatography (hexane/ethyl acetate 30:1) to yield the *title product* as a pale, yellow solid (326 mg, 62%). *R_f* (hexane/ethyl acetate 30:1) 0.09; δ_H (400 MHz; CDCl₃) 2.43 (3 H, s, H-4), 3.84 (3 H, s, H-1), 6.87 – 6.92 (2 H, m, H-2), 7.50 – 7.55 (2 H, m, H-3). Spectroscopic data match those reported previously.²⁰²

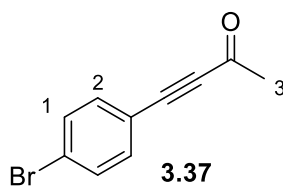
4-(4-(Dimethylamino)phenyl)but-3-yn-2-one (3.34)



3.34

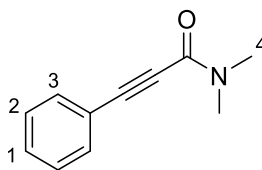
The synthesis was based on a literature procedure.²⁰² To a dry round-bottomed flask, 4-dimethylaminophenyl acetylene **3.31** (499 mg, 3.4 mmol) was dissolved in THF (50 mL) under an atmosphere of Ar and cooled to 0 °C. With vigorous stirring, *n*-BuLi (1.5 mL, 2.5 M in hexane, 3.7 mmol) was added and stirred for 15 minutes, at which point the solution was cooled to -78 °C and *N*-methyl, *N*-methoxy acetamide **3.32** (403 mg, 0.4 mL, 3.9 mmol) was added slowly over 3 minutes. The reaction was stirred for 30 minutes, before warming to room temperature and stirring for a further 2 hours. The reaction was quenched with deionised water (20 mL) and extracted with DCM (3 x 50 mL). The organic extracts were combined, dried with MgSO₄ and concentrated *in vacuo*. The crude product was purified via flash column chromatography (hexane/diethyl ether 7:3) to yield the *title product* as a pale, yellow solid (526 mg, 83%). *R_f* (hexane/diethyl ether 9:1) 0.13; mp 97 – 98 °C; *v*_{max} (thin film)/cm⁻¹ 2905, 2186, 2140, 1656, 816; *δ*_H (400 MHz; CDCl₃) 2.41 (3 H, s, H-9), 3.02 (6 H, s, H-1), 6.59 – 6.64 (2 H, m, H-3), 7.42 – 7.46 (2 H, m, H-4); *δ*_C (100 MHz; CDCl₃) 32.6 (C-9), 40.0 (C-1), 89.2 (C-7), 94.8 (C-6), 105.3 (C-5), 111.6 (C-3), 135.2 (C-4), 151.8 (C-2), 184.7 (C-8); HRMS (ESI⁺) Found: 188.1074; C₁₂H₁₄NO (MH⁺) Requires 188.1070 (-2.0 ppm error); Found: 210.0895; C₁₂H₁₃NNaO (M+Na) Requires 210.0889 (-2.6 ppm error).

4-(4-Bromophenyl)-3-butyne-2-one (3.37)



Following a literature procedure,²⁰² to a dry round-bottomed flask under an atmosphere of argon, ((4-bromophenyl)ethynyl)trimethylsilane **3.35** (203 mg, 0.8 mmol) and freshly distilled acetyl chloride **3.36** (0.06 mL, 57 mg, 0.7 mmol) were dissolved in dry DCM (13 mL) and cooled to 0 °C. Aluminium chloride (298 mg, 2.2 mmol) was added with vigorous stirring. After 30 minutes, the reaction was warmed to room temperature and stirred for a further 30 minutes. The reaction was quenched with aq. HCl (2 mL, 2 M), diluted with deionised water (10 mL) and extracted with DCM (3 x 10 mL). The organic extracts were dried with MgSO₄ and concentrated *in vacuo*. The crude product was purified by flash column chromatography (30:1 hexane/ethyl acetate) to yield the *title product* as a yellow powder (138 mg, 86%). *R_f* (30:1 hexane/ethyl acetate) 0.32; δ_{H} (400 MHz; CDCl₃) 2.46 (3 H, s, H-3), 7.42 – 7.46 (2 H, m, H-1), 7.52 – 7.56 (2 H, m, H-2). Spectroscopic data match those reported previously.²⁰²

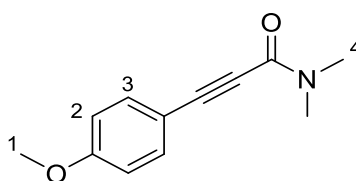
***N,N*-dimethyl-3-phenylpropiolamide (3.39)**



3.39

Following a literature procedure,²⁰³ to a dry-round bottomed flask phenylacetylene **3.13** (204 mg, 0.22 mL, 2.0 mmol) was dissolved in dry THF (1.3 mL) under an atmosphere of argon and cooled to $-78\text{ }^{\circ}\text{C}$. *n*-BuLi (1.0 mL, 2.5 mmol, 2.5 M in hexanes) was added and stirred for 15 minutes before dimethylcarbonyl chloride **3.38** (194 mg, 0.17 mL, 1.8 mmol) was added. The reaction was stirred for 5 minutes then warmed to room temperature and stirred for a further 1.5 hours. The reaction was quenched with saturated aq. ammonium chloride (5 mL), diluted with deionised water (10 mL) and extracted with ethyl acetate (3 x 10 mL). The organic extracts were dried MgSO_4 and concentrated *in vacuo* to yield the crude product. The product was purified via flash column chromatography (hexane/ethyl acetate 2:1) to yield the *title product* as a yellow solid (281 mg, 90%). R_f (2:1 hexane/ethyl acetate) 0.28; δ_{H} (400 MHz; CDCl_3) 3.03 (3 H, s, H-4a), 3.31 (3 H, s, H-4b), 7.34 – 7.45 (3 H, m, H-1 and H-2), 7.53 – 7.58 (2 H, m, H-3). Spectroscopic data match those reported previously.³⁵⁴

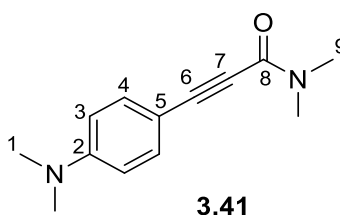
3-(4-(Methoxy)phenyl)-*N,N*-dimethylpropiolamide (3.40)



3.40

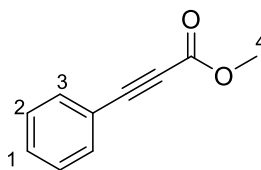
The synthesis was based on a literature procedure.²⁰³ To a dry-round bottomed flask 4-methoxyphenylacetylene **3.30** (0.24 mL, 264 mg, 2.0 mmol) was dissolved in dry THF (1.3 mL) under an atmosphere of argon and cooled to $-78\text{ }^{\circ}\text{C}$. *n*-BuLi (1.0 mL, 2.5 mmol, 2.5 M in hexanes) was added and stirred for 15 minutes before dimethylcarbonyl chloride **3.38** (194 mg, 0.17 mL, 1.8 mmol) was added. The reaction was stirred for 5 minutes then warmed to room temperature and stirred for a further 1.5 hours. The reaction was quenched with deionised water (15 mL) and extracted with ethyl acetate (3 x 10 mL). The organic extracts were dried with Na_2SO_4 and concentrated *in vacuo* to yield the crude product. The product was purified via flash column chromatography (6:4 to 1:1 hexane/ethyl acetate) to yield the *title product* as a pale, yellow powder (363 mg, 99%). R_f (7:3 hexane/ethyl acetate) 0.18; δ_{H} (400 MHz; CDCl_3) 3.04 (3 H, s, H-4a), 3.30 (3 H, s, H-4b), 3.84 (3 H, s, H-1), 6.82 – 6.94 (2 H, m, H-2), 7.44 – 7.56 (2 H, m, H-3). Spectroscopic data match those reported previously.³⁵⁵

3-(4-(Dimethylamino)phenyl)-*N,N*-dimethylpropiolamide (3.41)



The synthesis was based on a literature procedure.²⁰³ To a dry-round bottomed flask 4-ethynyl-*N,N*-dimethylaniline **3.31** (290 mg, 2.0 mmol) was dissolved in dry THF (1.3 mL) under an atmosphere of argon and cooled to $-78\text{ }^{\circ}\text{C}$. *n*-BuLi (1.0 mL, 2.5 mmol, 2.5 M in hexanes) was added and stirred for 15 minutes before dimethylcarbamoyl chloride **3.38** (194 mg, 0.17 mL, 1.8 mmol) was added. The reaction was stirred for 5 minutes then warmed to room temperature and stirred for a further 1.5 hours. The reaction was quenched with deionised water (15 mL) and extracted with ethyl acetate (3 x 10 mL). The organic extracts were dried with MgSO_4 and concentrated *in vacuo* to yield the crude product. The product was purified via flash column chromatography (hexane/ethyl acetate 1:1) to yield the *title product* as a pale, brown solid (339 mg, 87%). R_f (1:1 hexane/ethyl acetate) 0.28; mp $142 - 143\text{ }^{\circ}\text{C}$; ν_{max} (thin film)/ cm^{-1} 2908, 2199, 1608, 1526, 1366, 816; δ_{H} (400 MHz; CDCl_3) 3.00 (6 H, s, H-1), 3.01 (3 H, s, H-9a), 3.28 (3 H, s, H-9b), 6.59 – 6.64 (2 H, m, H-3), 7.39 – 7.44 (2 H, m, H-4); δ_{C} (100 MHz; CDCl_3) 34.2 (C-9a), 38.5 (C-9b), 40.1 (C-1), 80.8 (C-7), 92.8 (C-6), 106.6 (C-5), 111.6 (C-4), 134.0 (C-3), 151.2 (C-2), 155.5 (C-8); HRMS (ESI⁺) Found: 217.1337; $\text{C}_{13}\text{H}_{17}\text{N}_2\text{O}$ (MH^+) Requires 217.1335 (-0.9 ppm error); Found: 239.1157; $\text{C}_{13}\text{H}_{16}\text{N}_2\text{NaO}$ ($\text{M}+\text{Na}$) Requires 239.1155 (-1.0 ppm error).

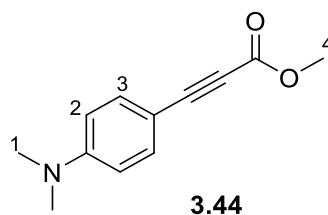
Methyl 3-phenylpropiolate (3.43)



3.43

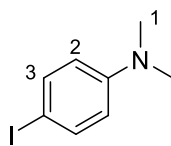
Based off a literature procedure,²⁰³ to a dry round-bottomed flask phenylacetylene **3.13** (613 mg, 6.0 mmol) was dissolved in dry THF (4.0 mL) under an atmosphere of argon and cooled to $-78\text{ }^{\circ}\text{C}$. *n*-BuLi (2.7 mL, 6.8 mmol, 2.5 M in hexanes) was added and stirred for 15 minutes before methyl chloroformate **3.42** (520 mg, 6.0 mmol) was added. The reaction was warmed to room temperature and stirred for 1 hour. The reaction was quenched with deionised water (20 mL) and extracted with ethyl acetate (3 x 20 mL). The organic extracts were dried with MgSO_4 and concentrated *in vacuo* to yield the crude product. The product was purified via flash column chromatography (hexane/ethyl acetate 95:5) to yield the *title product* as a yellow oil (640 mg, 73%). R_f (95:5 hexane/ethyl acetate) 0.35; δ_{H} (400 MHz; CDCl_3) 3.85 (3 H, s, H-4), 7.36 – 7.41 (2 H, m, H-2), 7.44 – 7.49 (1 H, m, H-1), 7.58 – 7.61 (2 H, m, H-3). Spectroscopic data match those reported previously.³⁵⁶

Methyl 3-(4-(dimethylamino)phenyl)propiolate (3.44)



Based off a literature procedure,²⁰³ to a dry round-bottomed flask 4-ethynyl-*N,N*-dimethylaniline (290 mg, 2.0 mmol) was dissolved in dry THF (1.3 mL) under an atmosphere of argon and cooled to $-78\text{ }^{\circ}\text{C}$. *n*-BuLi (1.0 mL, 2.5 mmol, 2.5 M in hexanes) was added and stirred for 15 minutes before methyl chloroformate (170 mg, 0.14 mL, 1.8 mmol) was added. The reaction was warmed to room temperature and stirred for 1 hour. The reaction was quenched with deionised water (15 mL) and extracted with ethyl acetate (3 x 10 mL). The organic extracts were dried with MgSO_4 and concentrated *in vacuo* to yield the crude product. The product was purified via flash column chromatography (hexane/ethyl acetate 9:1) to yield the *title product* as a pale, yellow solid (195 mg, 53%). R_f (9:1 hexane/ethyl acetate) 0.25; δ_{H} (400 MHz; CDCl_3) 3.03 (6 H, s, H-1), 3.82 (3 H, s, H-4), 6.60 – 6.65 (2 H, m, H-2), 7.45 – 7.50 (2 H, m, H-3). Spectroscopic data match those reported previously.³⁵⁶

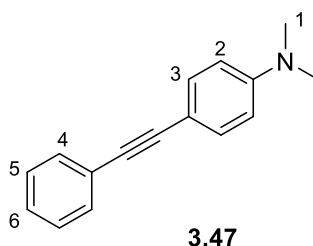
4-Iodo-*N,N*-dimethylaniline (3.46)



3.46

Following a literature procedure,²⁰⁵ to a dry round-bottomed flask, *N,N*-dimethylaniline **3.45** (121 mg, 0.13 mL, 1.0 mmol) and *N*-iodosuccinimide (248 mg, 1.1 mmol) were dissolved in DCM (1 mL) and [*bis*(trifluoromethanesulfonyl)imidate](triphenylphosphine)gold(I) (2:1) toluene adduct (19 mg, 0.01 mmol) was added. The reaction was stirred at room temperature for 19 hours, and then concentrated *in vacuo* to yield the crude product. The product was purified via flash column chromatography (hexane/ethyl acetate 95:5) to yield the *title product* as a white solid (238 mg, 96%). R_f (95:5 hexane/ethyl acetate) 0.50; δ_H (400 MHz; $CDCl_3$) 2.94 (6 H, s, H-1), 6.54 (2 H, br s, H-2), 7.44 – 7.53 (2 H, m, H-3). Spectroscopic data match those reported previously.³⁵⁷

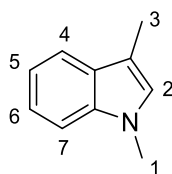
***N,N*-dimethyl-4-(phenylethynyl)aniline (3.47)**



Following a literature procedure,²⁰⁶ to a dry round-bottomed flask, 4-iodo-*N,N*-dimethylaniline **3.46** (25 mg, 0.1 mmol), phenylacetylene **3.13** (13 μ L, 12 mg, 0.1 mmol), *bis*(triphenylphosphine)palladium chloride (0.7 mg, 0.001 mmol) and copper(I) iodide (0.4 mg, 0.002 mmol) were dissolved in thoroughly degassed triethylamine (0.5 mL) under an atmosphere of argon. The reaction was stirred at room temperature overnight for 21 hours, and then concentrated *in vacuo* to yield the crude product. The product was purified via flash column chromatography (hexane to hexane/ethyl acetate 95:5) to yield the *title product* as a pale, yellow solid (22 mg, 98%). R_f (95:5 hexane/ethyl acetate) 0.31; δ_H (400 MHz; $CDCl_3$) 3.01 (6 H, s, H-1), 6.71 (2 H, br s, H-2), 7.28 – 7.36 (3 H, m, H-5 and H-6), 7.43 (2 H, br d, $J = 9.0$, H-3), 7.49 – 7.53 (2 H, m, H-4). Spectroscopic data match those reported previously.³⁵⁸

7.3.3 N-alkylated Indole Synthesis

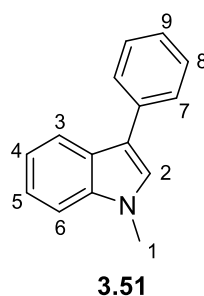
1,3-Dimethylindole (3.49)



3.49

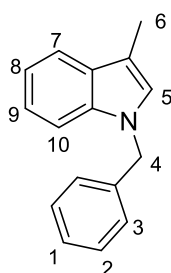
Following a literature procedure,²⁰⁷ to a dry round-bottomed flask, 3-methyl indole **3.48** (131 mg, 1.0 mmol) was dissolved in dry THF (1 mL) under an atmosphere of argon. The solution was cooled to 0 °C and sodium hydride (68 mg, 60% w/w dispersion in mineral oil, 1.7 mmol) was added. The reaction was brought to room temperature and stirred for 30 minutes, then cooled again to 0 °C before methyl iodide (65 μ L, 149 mg, 1.1 mmol) was added and the solution was warmed to room temperature overnight. The reaction was quenched with the addition of deionised water (3 mL), and diluted with ethyl acetate (5 mL). The product was extracted with ethyl acetate (3 x 10 mL). The organic extracts were combined, dried using MgSO₄ and concentrated *in vacuo*. The crude product was purified via flash column chromatography (hexane to hexane/DCM 95:5) to yield the *title product* as a yellow oil (100 mg, 69%). R_f (hexane) 0.15; δ_H (400 MHz; CDCl₃) 2.34 (3 H, s, H-3), 3.75 (3 H, s, H-1), 6.84 (1 H, s, H-2), 7.10 – 7.15 (1 H, m, H-5/6), 7.21 – 7.26 (1 H, m, H-5/6), 7.30 (1 H, d, J = 8.0, H-7), 7.58 (1 H, d, J = 8.0, H-4). Spectroscopic data match those reported previously.³⁵⁹

1-Methyl-3-phenylindole (3.51)



Following a literature procedure,²⁰⁸ to a dry round-bottomed flask, sodium hydride (68 mg, 60% w/w dispersion in mineral oil, 1.7 mmol) was suspended in dry THF (1.6 mL) under an atmosphere of argon, and cooled to 0 °C. A solution of 3-phenyl indole **3.50** (193 mg, 1.0 mmol) in dry THF (1.6 mL) under an atmosphere of argon was added and stirred for 1 hour, before methyl iodide (0.07 mL, 149 mg, 1.1 mmol) was added. The reaction was brought to room temperature and stirred for 1 hour. The reaction was quenched with the addition of deionised water (5 mL), and the product was extracted with DCM (3 x 10 mL). The organic extracts were combined, dried using MgSO₄ and concentrated *in vacuo*. The crude product was purified via flash column chromatography (hexane/ethyl acetate 98:2) to yield the *title product* as a yellow oil (162 mg, 78%). *R_f* (98:2 hexane/ethyl acetate) 0.23; δ_H (400 MHz; CDCl₃) 3.86 (3 H, s, H-1), 7.21 (1 H, ddd, *J* = 8.0, 7.0, 1.5, H-4), 7.26 (1 H, s, H-2), 7.26 – 7.33 (2 H, m, H-Ar), 7.39 (1 H, d, *J* = 8.0, H-6), 7.45 (2 H, dd, *J* = 8.0, 8.0, H-8), 7.67 (2 H, dd, *J* = 8.0, 1.5, H-7), 7.96 (1 H, d, *J* = 8.0, H-3). Spectroscopic data match those reported previously.²⁰⁸

1-Benzyl-3-methylindole (3.52)

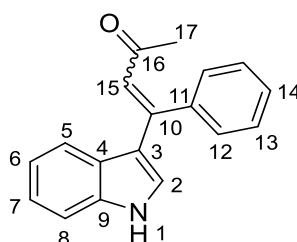


3.52

Following a literature procedure,²⁰⁸ to a dry round-bottomed flask, sodium hydride (80 mg, 60% w/w dispersion in mineral oil, 2.0 mmol) was suspended in dry DMF (0.8 mL) under an atmosphere of argon, and cooled to 0 °C. A solution of 3-methyl indole **3.48** (131 mg, 1.0 mmol) in dry DMF (0.8 mL) under an atmosphere of argon was added, brought to room temperature and stirred for 30 minutes. The solution was cooled to 0 °C before benzyl bromide (0.24 mL, 342 mg, 2.0 mmol) was added. The reaction was brought to room temperature and stirred for 20 hours. The reaction was quenched with the addition of deionised water (10 mL), and saturated aq. NaCl (5 mL) was added. The product was extracted with DCM (3 x 10 mL). The organic extracts were combined, dried using MgSO₄ and concentrated *in vacuo*. The crude product was purified via flash column chromatography (hexane/diethyl ether 99:1), and then further purified *via* recrystallisation from hexane, to yield the *title product* as a white solid (40 mg, 18%). *R_f*(98:2 hexane/ethyl acetate) 0.43; δ_{H} (400 MHz; CDCl₃) 2.35 (3 H, s, H-6), 5.28 (2 H, s, H-4), 6.91 (1 H, s, H-5), 7.09 – 7.15 (3 H, m, H-Ar), 7.15 – 7.20 (1 H, m, H-1), 7.24 – 7.31 (4 H, m, H-Ar), 7.60 (1 H, d, *J* = 8.0, H-7). Spectroscopic data match those reported previously.²⁰⁸

7.3.4 Vinylated-indole Products

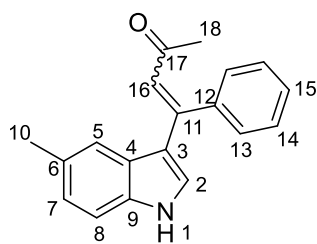
4-(1*H*-Indol-3-yl)-4-phenylbut-3-en-2-one (3.28)



3.28

Synthesised using general procedure I from indole **3.16** (59 mg, 0.50 mmol), 4-phenyl-3-butyne-2-one **3.27** (0.11 mL, 108 mg, 0.75 mmol) and [bis(trifluoromethanesulfonyl)imidate]-(triphenylphosphine)gold(I) (2:1) toluene adduct (40 mg, 0.03 mmol) in toluene (5 mL) for 2 hours at 40 °C. Purification by flash column chromatography (1:1 hexane/diethyl ether) afforded the *title product* as a yellow solid, as a mixture of *E* and *Z* stereoisomers (90 mg, 69%, *E*:*Z* = 74:26). R_f (hexane/diethyl ether 1:1) 0.14; mp 99–105 °C; ν_{\max} (thin film)/ cm^{-1} 3267 (br), 3061, 2928, 1612, 1579, 1554, 1512, 1420, 742; δ_{H} (400 MHz; CDCl_3) 1.88 (3 H, s, H-17, *E*), 1.99 (3 H, s, H-17, *Z*), 6.50 (1 H, s, H-15, *Z*), 6.79 (1 H, d, $J = 3.0$, H-2, *E*), 6.86 (1 H, s, H-15, *E*), 6.96 – 6.98 (2 H, m, H-Ar, *Z*), 7.11 – 7.24 (4 H, m, H-Ar, *E* and *Z*), 7.26 – 7.32 (5 H, m, H-Ar, *E* and *Z*), 7.32 – 7.40 (7 H, m, H-Ar, *E* and *Z*), 7.74 (1 H, d, $J = 8.0$, H-5, *E*), 8.96 (1 H, br s, H-1, *Z*), 9.15 (1 H, br s, H-1, *E*); δ_{C} (100 MHz; CDCl_3) 30.0 (C-17, *Z*), 30.6 (C-17, *E*), 111.8 (CH, C-Ar, *Z*), 112.3 (CH, C-Ar, *E*), 114.2 (C-3, *Z*), 118.4 (C-3, *E*), 120.5 (CH, C-Ar, *Z*), 120.6 (CH, C-Ar, *Z*), 120.8 (CH, C-Ar, *E*), 121.4 (CH, C-Ar, *E*), 122.6 (CH, C-Ar, *Z*), 122.8 (C-15, *E*), 123.1 (CH, C-Ar, *E*), 125.0 (C-4, *E*), 126.4 (C-15, *Z*), 126.8 (C, C-Ar), 128.3 (CH, C-Ar), 128.4 (CH, C-Ar), 128.4 (CH, C-Ar), 128.5 (CH, C-Ar), 129.0 (CH, C-Ar), 129.4 (CH, C-Ar), 129.5 (CH, C-Ar), 130.6 (C-2, *E*), 136.4 (C, C-Ar), 137.5 (C-9, *E*), 140.3 (C-10, *E*), 141.6 (C-10, *Z*), 148.9 (C-11, *Z*), 151.7 (C-11, *E*), 200.6 (C-16, *E*), 201.1 (C-16, *Z*); HRMS (ESI⁺) Found: 262.1228; $\text{C}_{18}\text{H}_{16}\text{NO}$ ($\text{M}+\text{H}^+$) Requires 262.1226 (–0.8 ppm error); Found: 284.1049; $\text{C}_{18}\text{H}_{15}\text{NNaO}$ ($\text{M}+\text{Na}$) Requires 284.1046 (–1.1 ppm error).

4-(5-Methyl-1*H*-indol-3-yl)-4-phenylbut-3-en-2-one (3.57)

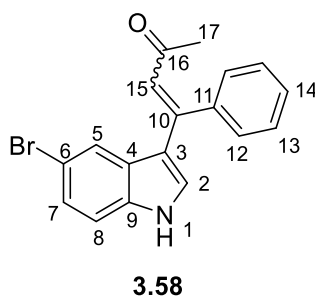


3.57

Synthesised using general procedure I from 5-methylindole (26 mg, 0.20 mmol), 4-phenyl-3-butyne-2-one **3.27** (44 μ L, 43 mg, 0.30 mmol) and [bis(trifluoromethanesulfonyl)imidate]-(triphenylphosphine)gold(I) (2:1) toluene adduct (16 mg, 0.01 mmol) in toluene (2 mL) for 2 hours at 40 °C. Purification by flash column chromatography (6:4 hexane/diethyl ether) afforded the *title product* as a yellow solid, as a mixture of *E* and *Z* stereoisomers (32 mg, 58%, *E*:*Z* = 70:30). R_f (hexane/diethyl ether 6:4) 0.17; mp 133–137 °C; ν_{\max} (thin film)/ cm^{-1} 3263 (br), 3054, 2922, 1619, 1555, 1511, 1420, 720, 699; δ_{H} (400 MHz; CDCl_3) 1.87 (3 H, s, H-18, *E*), 1.99 (3 H, s, H-18, *Z*), 2.31 (3 H, s, H-10, *Z*), 2.48 (3 H, s, H-10, *E*), 6.54 (1 H, s, H-16, *Z*), 6.78 – 6.82 (2 H, m, H-Ar, *E* and *Z*), 6.88 (1 H, s, H-16, *E*), 7.03 (1 H, dd, $J = 8.5, 1.5$, H-7, *Z*), 7.11 (1 H, dd, $J = 8.5, 1.5$, H-7, *E*), 7.29 (1 H, d, $J = 8.5$, H-8, *E*), 7.30 (1 H, d, $J = 8.5$, *Z*), 7.32 – 7.36 (5 H, m, H-Ar, *E* and *Z*), 7.37 – 7.45 (6 H, m, H-Ar, *E* and *Z*), 7.66 (1 H, d, $J = 1.5$, H-5, *E*), 8.60 (1 H, br s, H-1, *Z*), 8.63 (1 H, br s, H-1, *E*); δ_{C} (100 MHz; CDCl_3) 21.6 (C-10, *Z*), 21.8 (C-10, *E*), 29.9 (C-18, *Z*), 30.5 (C-18, *E*), 111.3 (C-8, *Z*), 111.6 (C-8, *E*), 114.1 (C-3, *Z*), 118.5 (C-3, *E*), 120.3 (C-5, *Z*), 120.8 (C-5, *E*), 123.8 (C-16, *E*), 124.5 (C-7, *Z*), 125.0 (C-7, *E*), 125.3 (C, C-Ar), 127.2 (C-16, *Z*), 127.9 (CH, C-Ar), 128.4 (CH, C-Ar), 128.4 (CH, C-Ar), 128.6 (CH, C-Ar), 128.9 (CH, C-Ar), 129.5 (CH, C-Ar), 129.5 (CH, C-Ar), 130.1 (C-6, *Z*), 130.2 (C-2, *E*), 131.1 (C-6, *E*), 134.7 (C-9, *Z*), 135.6 (C-9, *E*), 140.5 (C-11, *E*), 141.5 (C-11, *Z*), 148.3 (C-12, *Z*), 151.0 (C-12, *E*), 200.5 (C-17, *E*), 201.0 (C-17, *Z*); HRMS (ESI⁺) Found: 276.1386; $\text{C}_{19}\text{H}_{18}\text{NO}$ ($\text{M}+\text{H}^+$) Requires 276.1383 (–1.0 ppm error); Found: 298.1201; $\text{C}_{19}\text{H}_{17}\text{NNaO}$ ($\text{M}+\text{Na}$) Requires 298.1202 (0.6 ppm error).

Note that one quaternary carbon resonance could not be found in the ^{13}C NMR spectra, it is believed that it is overlapping with another resonance.

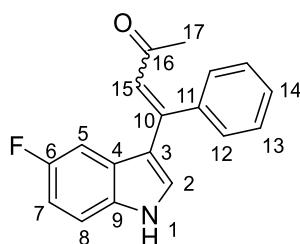
4-(5-Bromo-1*H*-indol-3-yl)-4-phenylbut-3-en-2-one (3.58)



Synthesised using general procedure I from 5-bromo-1*H*-indole (39 mg, 0.20 mmol), 4-phenyl-3-butyne-2-one **3.27** (44 μL , 43 mg, 0.30 mmol) and [bis(trifluoromethanesulfonyl)imidate](triphenylphosphine)gold(I) (2:1) toluene adduct (16 mg, 0.01 mmol) in toluene (2 mL) for 18 hours at 40 °C. Purification by flash column chromatography (9:1 toluene/ethyl acetate) afforded the *title product* as a yellow solid, as a mixture of *E* and *Z* stereoisomers (46 mg, 67%, *E*:*Z* = 73:27). R_f (toluene/ethyl acetate 9:1) 0.18; mp 138–142 °C; ν_{max} (thin film)/ cm^{-1} 3267 (br), 1666, 1628, 1552, 1515, 1456, 1421, 728; δ_{H} (400 MHz; CDCl_3) 1.89 (3 H, s, H-17, *E*), 2.05 (3 H, s, H-17, *Z*), 6.57 (1 H, s, H-15, *Z*), 6.77 (1 H, s, H-15, *E*), 6.90 (1 H, d, $J = 3.0$, H-2, *E*), 7.08 (1 H, br s, H-Ar, *Z*), 7.27 – 7.47 (14 H, m, H-Ar, *E* and *Z*), 7.49 (1 H, d, $J = 2.5$, H-Ar, *Z*), 7.89 (1 H, d, $J = 2.0$, H-5, *E*), 8.52 (1 H, br s, H-1, *E*), 8.57 (1 H, br s, H-1, *Z*); δ_{C} (100 MHz; CDCl_3) 30.5 (C-17, *Z*), 30.7 (C-17, *E*), 113.3 (CH, C-Ar), 113.5 (CH, C-Ar), 113.8 (C-6, *Z*), 113.9 (C-3, *Z*), 114.9 (C-6, *E*), 118.2 (C-3, *E*), 123.1 (C-5, *Z*), 123.4 (C-5, *E*), 123.6 (C-15, *E*), 125.6 (CH, C-Ar), 126.1 (CH, C-Ar), 126.5 (C, C-Ar), 126.7 (C-15, *Z*), 128.5 (CH, C-Ar), 128.6 (CH, C-Ar), 128.8 (CH, C-Ar), 128.8 (CH, C-Ar), 129.2 (CH, C-Ar), 129.4 (CH, C-Ar), 129.8 (CH, C-Ar), 130.8 (C-2, *E*), 135.0 (C-9, *Z*), 136.0 (C-9, *E*), 140.0 (C-10, *E*), 141.2 (C-10, *Z*), 147.9 (C-11, *Z*), 150.5 (C-11, *E*), 200.3 (C-16, *Z*), 200.5 (C-16, *E*); HRMS (ESI⁺) Found: 340.0330; $\text{C}_{18}\text{H}_{15}^{79}\text{BrNO}$ ($\text{M}+\text{H}^+$) Requires 340.0332 (0.5 ppm error); Found: 362.0149; $\text{C}_{18}\text{H}_{14}^{79}\text{BrNNaO}$ ($\text{M}+\text{Na}$) Requires 362.0151 (0.4 ppm error).

Note that one quaternary carbon resonance could not be found in the ^{13}C NMR spectra, it is believed that it is overlapping with another resonance.

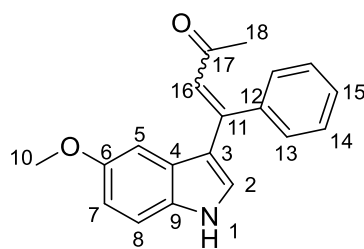
4-(5-Fluoro-1H-indol-3-yl)-4-phenylbut-3-en-2-one (3.59)



3.59

Synthesised using general procedure I from 5-fluoro-1H-indole (27 mg, 0.20 mmol), 4-phenyl-3-butyne-2-one **3.27** (44 μ L, 43 mg, 0.30 mmol) and [bis(trifluoromethanesulfonyl)imidate](triphenylphosphine)gold(I) (2:1) toluene adduct (16 mg, 0.01 mmol) in toluene (2 mL) for 18 hours at 40 °C. Purification by flash column chromatography (9:1 toluene/ethyl acetate) afforded the *title product* as a yellow solid, as a mixture of *E* and *Z* stereoisomers (44 mg, 79%, *E*:*Z* = 72:28). R_f (toluene/ethyl acetate 9:1) 0.19; mp 131–134 °C; ν_{\max} (thin film)/ cm^{-1} 3267 (br), 2924, 1627, 1585, 1554, 1514, 1483, 721; δ_{H} (600 MHz; CDCl_3) 1.92 (3 H, s, H-17, *E*), 2.09 (3 H, s, H-17, *Z*), 6.54 (1 H, s, H-15, *Z*), 6.57 (1 H, dd, $J = 9.5, 2.5$, H-5, *Z*), 6.75 (1 H, s, H-15, *E*), 6.92 (1 H, ddd, $J = 9.5, 9.0, 2.5$, H-7, *Z*), 6.94 (1 H, d, $J = 3.0$, H-2, *E*), 7.00 (1 H, ddd, $J = 9.5, 9.0, 2.5$, H-7, *E*), 7.27 – 7.37 (7 H, m, H-Ar, *E* and *Z*), 7.38 – 7.45 (6 H, m, H-Ar, *E* and *Z*), 7.49 (1 H, d, $J = 2.5$, H-2, *Z*), 8.82 (1 H, br s, H-1, *Z*), 8.88 (1 H, br s, H-1, *E*); δ_{C} (151 MHz; CDCl_3) 30.4 (C-17, *Z*), 30.6 (C-17, *E*), 105.8 (d, $J = 24.5$, C-5, *Z*), 106.3 (d, $J = 25.0$, C-5, *E*), 111.2 (d, $J = 26.5$, C-7, *Z*), 111.6 (d, $J = 26.5$, C-7, *E*), 112.4 (d, $J = 9.5$, C-8), 112.7 (d, $J = 10.0$, C-8), 114.4 (d, $J = 5.0$, C-9, *Z*), 118.9 (d, $J = 4.5$, C-9, *E*), 123.4 (C-15, *E*), 125.6 (d, $J = 10.0$, C-4, *E*), 126.5 (C-15, *Z*), 127.4 (d, $J = 10.0$, C-4), 128.5 (CH, C-Ar), 128.6 (CH, C-Ar), 128.8 (CH, C-Ar), 128.9 (CH, C-Ar), 129.4 (CH, C-Ar), 129.7 (CH, C-Ar), 129.9 (CH, C-Ar), 130.9 (C-2, *E*), 132.8 (C, C-Ar), 133.8 (C, C-Ar), 140.0 (C, C-Ar), 141.3 (C, C-Ar), 147.9 (C, C-Ar), 150.4 (C, C-Ar), 158.3 (d, $J = 236.0$, C-6, *Z*), 158.9 (d, $J = 236.5$, C-6, *E*), 200.1 (C-16, *Z*), 200.2 (C-16, *E*); δ_{F} (565 MHz; CDCl_3); -122.83 (ddd, $J = 9.5, 9.5, 4.5$, *Z*), -121.77 (ddd, $J = 9.5, 9.5, 4.5$, *E*); HRMS (ESI⁺) Found: 280.1132; $\text{C}_{18}\text{H}_{15}\text{FNO}$ ($\text{M}+\text{H}^+$) Requires 280.1132 (0.2 ppm error); Found: 302.0949; $\text{C}_{18}\text{H}_{14}\text{FNNaO}$ ($\text{M}+\text{Na}$) Requires 302.0952 (0.8 ppm error).

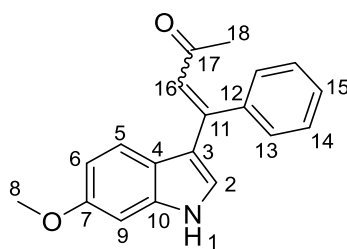
4-(5-Methoxy-1*H*-indol-3-yl)-4-phenylbut-3-en-2-one (3.60)



3.60

Synthesised using general procedure I from 5-methoxy-1*H*-indole (29 mg, 0.20 mmol), 4-phenyl-3-butyne-2-one **3.27** (44 μ L, 43 mg, 0.30 mmol) and [bis(trifluoromethanesulfonyl)imidate](triphenylphosphine)gold(I) (2:1) toluene adduct (16 mg, 0.01 mmol) in toluene (2 mL) for 18 hours at 40 °C. Purification by flash column chromatography (9:1 toluene/diethyl ether), followed by recrystallisation (hexane/diethyl) afforded the *title product* as an orange solid, as a mixture of *E* and *Z* stereoisomers (18 mg, 31%, *E*:*Z* = 76:24). R_f (toluene/diethyl ether 9:1) 0.19; mp 109–112 °C; ν_{\max} (thin film)/ cm^{-1} 3271 (br), 2940, 2831, 1623, 1583, 1554, 1509, 1480, 1212, 720, 699; δ_{H} (400 MHz; CDCl_3) 1.88 (3 H, s, H-18, *E*), 2.04 (3 H, s, H-18, *Z*), 3.61 (3 H, s, H-10, *Z*), 3.80 (3 H, s, H-10, *E*), 6.38 (1 H, d, $J = 2.5$, H-5, *Z*), 6.51 (1 H, s, H-16, *Z*), 6.79 (1 H, s, H-16, *E*), 6.85 (1 H, dd, $J = 9.0, 2.5$, H-7, *Z*), 6.89 – 6.93 (2 H, m, H-Ar, *E*), 7.08 (1 H, d, $J = 2.5$, H-5, *E*), 7.29 (1 H, d, $J = 9.0$, H-8, *E*), 7.29 (1 H, d, $J = 9.0$, H-8, *Z*), 7.32 – 7.37 (4 H, m, H-Ar, *E* and *Z*), 7.39 – 7.46 (7 H, m, H-Ar, *E* and *Z*), 8.56 (2 H, br s, H-1, *E* and *Z*); δ_{C} (100 MHz; CDCl_3) 30.0 (C-18, *Z*), 30.5 (C-18, *E*), 55.6 (C-10, *Z*), 56.0 (C-18, *E*), 101.9 (C-5, *Z*), 103.2 (C-5, *E*), 112.3 (C-8, *Z*), 112.6 (C-8, *E*), 113.0 (C-7, *Z*), 113.2 (C-7, *E*), 114.2 (C-3, *Z*), 118.6 (C-3, *E*), 119.3 (C, C-Ar), 123.4 (C-16, *E*), 125.8 (C-4, *E*), 126.7 (C-16, *Z*), 128.4 (CH, C-Ar), 128.5 (CH, C-Ar), 128.6 (CH, C-Ar), 128.7 (CH, C-Ar), 129.0 (CH, C-Ar), 129.5 (CH, C-Ar), 129.6 (CH, C-Ar), 129.8 (CH, C-Ar), 131.3 (C-9, *Z*), 132.3 (C-9, *E*), 140.4 (C-11, *E*), 141.5 (C-11, *Z*), 148.2 (C, C-Ar, *Z*), 150.9 (C, C-Ar, *E*), 154.8 (C-6, *Z*), 155.4 (C-6, *E*), 200.3 (C-17, *E*), 200.6 (C-17, *Z*); HRMS (ESI⁺) Found: 292.1337; $\text{C}_{19}\text{H}_{18}\text{NO}_2$ ($\text{M}+\text{H}^+$) Requires 292.1332 (–1.7 ppm error); Found: 314.1156; $\text{C}_{19}\text{H}_{17}\text{NNaO}_2$ ($\text{M}+\text{Na}$) Requires 314.1151 (0.8 ppm error).

4-(6-Methoxy-1*H*-indol-3-yl)-4-phenylbut-3-en-2-one (3.61)

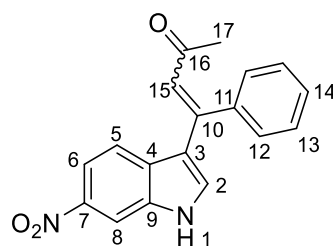


3.61

Synthesised using general procedure I from 6-methoxy-1*H*-indole (29 mg, 0.20 mmol), 4-phenyl-3-butyne-2-one **3.27** (44 μ L, 43 mg, 0.30 mmol) and [bis(trifluoromethanesulfonyl)imidate](triphenylphosphine)gold(I) (2:1) toluene adduct (16 mg, 0.01 mmol) in toluene (2 mL) for 21 hours at room temperature. Purification by flash column chromatography (95:5 to 9:1 toluene/diethyl ether) afforded the *title product* as a yellow solid, as a mixture of *E* and *Z* stereoisomers (18 mg, 30%, *E*:*Z* = 74:26). R_f (toluene/diethyl ether 95:5) 0.12; mp 45–50 °C; ν_{\max} (thin film)/ cm^{-1} 3282 (br), 2931, 1627, 1557, 1519, 1453, 1415, 1238, 1159, 718; δ_{H} (400 MHz; CD_2Cl_2) 1.89 (3 H, s, H-18, *E*), 2.00 (3 H, s, H-18, *Z*), 3.80 (3 H, s, H-8, *Z*), 3.83 (3 H, s, H-8, *E*), 6.48 (1 H, s, H-16), 6.63 (1 H, dd, $J = 9.0, 2.5$, H-6, *Z*), 6.78 (1 H, d, $J = 3.0$, H-2, *E*), 6.79 (1 H, s, H-16, *E*), 6.83 (1 H, dd, $J = 9.0, 2.5$, H-6, *E*), 6.90 (1 H, d, $J = 2.5$, H-9, *E*), 6.91 (1 H, d, $J = 2.5$, H-9, *Z*), 7.29 – 7.36 (5 H, m, H-Ar, *E* and *Z*), 7.37 – 7.44 (7 H, m, H-Ar, *E* and *Z*), 7.62 (1 H, d, $J = 9.0$, H-5, *E*), 8.66 (2 H, br s, H-1, *E* and *Z*); δ_{C} (100 MHz; CD_2Cl_2) 30.1 (C-18, *Z*), 30.8 (C-18, *E*), 55.9 (C-8, *E* and *Z*), 95.0 (C-9, *Z*), 95.5 (C-9, *E*), 110.7 (C-6, *Z*), 111.3 (C-6, *E*), 114.6 (C-3, *Z*), 119.0 (C-3, *E*), 119.6 (C, C-Ar), 121.4 (CH, C-Ar), 121.8 (C-5, *E*), 123.2 (C-16, *E*), 127.2 (CH, C-Ar), 127.2 (CH, C-Ar), 128.4 (CH, C-Ar), 128.6 (CH, C-Ar), 129.1 (CH, C-Ar), 129.2 (CH, C-Ar), 129.6 (CH, C-Ar), 129.8 (CH, C-Ar), 137.5 (C, C-Ar), 138.6 (C, C-Ar), 140.7 (C-11, *E*), 142.1 (C-11, *Z*), 147.9 (C, C-Ar), 150.5 (C, C-Ar), 157.1 (C-7, *Z*), 157.3 (C-7, *E*), 199.4 (C-17, *E*), 200.3 (C-17, *Z*); HRMS (ESI⁺) Found: 292.1321; $\text{C}_{19}\text{H}_{18}\text{NO}_2$ ($\text{M}+\text{H}^+$) Requires 292.1332 (3.6 ppm error); Found: 314.1139; $\text{C}_{19}\text{H}_{17}\text{NNaO}_2$ ($\text{M}+\text{Na}$) Requires 314.1151 (4.1 ppm error).

Note that one quaternary and one methine carbon resonance could not be found in the ^{13}C NMR spectra, it is believed that they are overlapping with other resonances.

4-(6-Nitro-1H-indol-3-yl)-4-phenylbut-3-en-2-one (3.62)

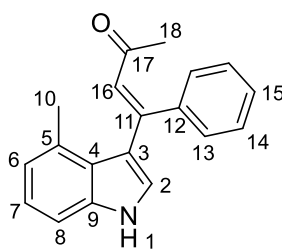


3.62

Synthesised using general procedure I from 6-nitro-1H-indole (32 mg, 0.20 mmol), 4-phenyl-3-butyne-2-one **3.27** (44 μ L, 43 mg, 0.30 mmol) and [bis(trifluoromethanesulfonyl)imidate]-(triphenylphosphine)gold(I) (2:1) toluene adduct (16 mg, 0.01 mmol) in toluene (2 mL) for 24 hours at 100 °C. Purification by flash column chromatography (9:1 to 7:3 toluene/diethyl ether) afforded the *title product* as a yellow solid, as a mixture of *E* and *Z* stereoisomers (42 mg, 69%, *E*:*Z* = 68:32). R_f (toluene/diethyl ether 7:3) 0.22; mp 50–54 °C; ν_{\max} (thin film)/ cm^{-1} 3297 (br), 2925, 1590, 1507, 1337, 1311, 734; δ_{H} (400 MHz; CDCl_3) 1.97 (3 H, s, H-17, *E*), 2.27 (3 H, s, H-17, *Z*), 6.68 (1 H, s, H-15, *Z*), 6.80 (1 H, s, H-15, *E*), 6.92 (1 H, d, $J = 9.0$, H-5, *Z*), 7.22 (1 H, d, $J = 2.5$, H-2, *E*), 7.30 – 7.46 (10 H, m, H-Ar, *E* and *Z*), 7.58 (1 H, d, $J = 9.0$, H-5, *E*), 7.69 (1 H, d, $J = 2.0$, H-2, *Z*), 7.81 (1 H, dd, $J = 9.0, 2.0$, H-6, *Z*), 8.00 (1 H, dd, $J = 9.0, 2.0$, H-6, *E*), 8.20 (1 H, d, $J = 2.0$, H-8, *Z*), 8.33 (1 H, d, $J = 2.0$, H-8, *E*), 9.88 (2 H, br s, H-1, *E* and *Z*); δ_{C} (100 MHz; CDCl_3) 30.7 (C-17, *E*), 31.4 (C-17, *Z*), 108.8 (C-8, *Z*), 109.0 (C-8, *E*), 114.6 (C-3, *Z*), 115.8 (C-6, *Z*), 116.5 (C-6, *E*), 119.2 (C-3, *E*), 120.6 (C-5, *Z*), 120.8 (C-5, *E*), 124.6 (C-15, *E*), 125.9 (C-15, *Z*), 128.7 (CH, C-Ar), 128.9 (CH, C-Ar), 129.2 (CH, C-Ar), 129.4 (CH, C-Ar), 129.8 (C, C-Ar), 130.1 (CH, C-Ar), 131.4 (C, C-Ar), 133.8 (C-2, *Z*), 133.9 (C-2, *E*), 134.9 (C, C-Ar), 136.0 (C, C-Ar), 139.5 (C, C-Ar), 141.3 (C, C-Ar), 143.2 (C-7, *Z*), 143.6 (C-7, *E*), 147.5 (C, C-Ar), 149.6 (C, C-Ar), 199.5 (C-16, *Z*), 200.6 (C-16, *E*); HRMS (ESI⁺) Found: 307.1084; $\text{C}_{18}\text{H}_{15}\text{N}_2\text{O}_3$ ($\text{M}+\text{H}^+$) Requires 307.1077 (–2.1 ppm error); Found: 329.0904; $\text{C}_{18}\text{H}_{14}\text{N}_2\text{NaO}_3$ ($\text{M}+\text{Na}$) Requires 329.0897 (–2.2 ppm error).

Note that one methine carbon resonance could not be found in the ^{13}C NMR spectra, it is believed that it is overlapping with another resonance.

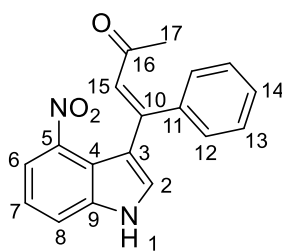
(E)-4-(4-Methyl-1H-indol-3-yl)-4-phenylbut-3-en-2-one (3.63)



3.63

Synthesised using general procedure I from 4-methyl-1H-indole (26 mg, 0.20 mmol), 4-phenyl-3-butyne-2-one **3.27** (44 μ L, 43 mg, 0.30 mmol) and [bis(trifluoromethanesulfonyl)imidate](triphenylphosphine)gold(I) (2:1) toluene adduct (16 mg, 0.01 mmol) in toluene (2 mL) for 2 hours at 40 °C. Purification by flash column chromatography (95:5 toluene/diethyl ether) afforded the *title product* as a yellow solid (39 mg, 71%) as a single geometrical isomer (*E*). R_f (toluene/diethyl ether 95:5) 0.19; mp 45–47 °C; ν_{\max} (thin film)/ cm^{-1} 3300 (br), 2922, 1630, 1589, 1568, 1409, 751, 731; δ_{H} (400 MHz; CDCl_3) 1.84 (3 H, s, H-18), 2.07 (3 H, s, H-10), 6.75 (1 H, s, H-16), 6.85 (1 H, d, $J = 7.0$, H-6), 7.14 (1 H, d, $J = 2.5$, H-2), 7.16 (1 H, d, $J = 7.5$, H-8), 7.29 – 7.36 (4 H, m, H-Ar), 7.38 – 7.42 (2 H, m, H-Ar), 8.66 (1 H, br s, H-1); δ_{C} (100 MHz; CDCl_3) 19.8 (C-10), 29.8 (C-18), 109.4 (CH, C-Ar), 114.6 (C-3), 122.0 (C-6), 123.3 (CH, C-Ar), 125.7 (C-4), 125.8 (C-2), 128.1 (CH, C-Ar), 128.7 (CH, C-Ar), 129.6 (CH, C-Ar), 129.8 (C-16), 131.3 (C-5), 136.9 (C-9), 141.6 (C-11), 149.4 (C-12), 201.9 (C-17); HRMS (ESI⁺) Found: 276.1384; $\text{C}_{19}\text{H}_{18}\text{NO}$ ($\text{M}+\text{H}^+$) Requires 276.1383 (–0.5 ppm error); Found: 298.1203; $\text{C}_{19}\text{H}_{17}\text{NNaO}$ ($\text{M}+\text{Na}$) Requires 298.1202 (–0.2 ppm error).

4-(4-Nitro-1*H*-indol-3-yl)-4-phenylbut-3-en-2-one (3.64)

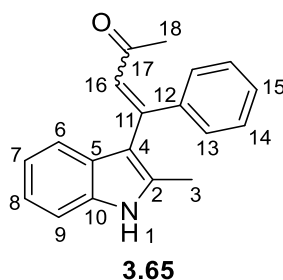


3.64

Synthesised using general procedure I from 4-nitro-1*H*-indole (32 mg, 0.20 mmol), 4-phenyl-3-butyne-2-one **3.27** (44 μ L, 43 mg, 0.30 mmol) and [bis(trifluoromethanesulfonyl)imidate]-(triphenylphosphine)gold(I) (2:1) toluene adduct (16 mg, 0.01 mmol) in toluene (2 mL) for 24 hours at 100 °C. Purification by flash column chromatography (diethyl ether/hexane 7:3 to 8:2) afforded the *title product* as a yellow solid, as a mixture of *E* and *Z* stereoisomers (28 mg, 46%, *E*:*Z* = 97:3). ^1H and ^{13}C NMR data reported for the major *E*-isomer only. R_f (hexane/diethyl ether 3:7) 0.13; mp 182–184 °C; ν_{max} (thin film)/ cm^{-1} 3285 (br), 2924, 1661, 1566, 1515, 1447, 1355, 1332, 736; δ_{H} (400 MHz; d_6 -DMSO) 1.95 (3 H, s, H-17), 6.66 (1 H, s, H-15), 7.23 – 7.36 (6 H, m, H-Ar), 7.68 (1 H, d, $J = 2.5$, H-2), 7.79 (1 H, d, $J = 8.0$, H-8), 7.91 (1 H, d, $J = 8.0$, H-6), 12.32 (1 H, br s, H-1); δ_{C} (100 MHz; d_6 -DMSO) 30.4 (C-17), 111.9 (C-3), 117.2 (C-8), 118.5 (C-4), 118.7 (C-6), 120.9 (CH, C-Ar), 125.8 (C-15), 127.8 (CH, C-Ar), 128.4 (CH, C-Ar), 129.1 (CH, C-Ar), 132.7 (C-2), 138.9 (C-9), 141.7 (C, C-Ar), 141.8 (C, C-Ar), 147.2 (C-10), 198.2 (C-16); HRMS (ESI⁺) Found: 307.1077; $\text{C}_{18}\text{H}_{15}\text{N}_2\text{O}_3$ ($\text{M}+\text{H}^+$) Requires 307.1077 (0.2 ppm error); Found: 329.0894; $\text{C}_{18}\text{H}_{14}\text{N}_2\text{O}_3$ ($\text{M}+\text{Na}$) Requires 329.0897 (0.8 ppm error).

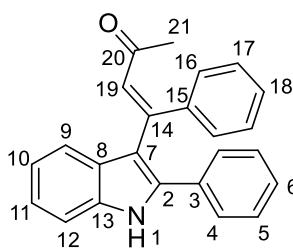
Characteristic NMR resonances for the minor *Z*-isomer can be found at: δ_{H} 6.01 (1 H, s, H-15, *Z*).

4-(2-Methyl-1H-indol-3-yl)-4-phenylbut-3-en-2-one (3.65)



Synthesised using general procedure I from 2-methyl-1H-indole (26 mg, 0.20 mmol), 4-phenyl-3-butyne-2-one **3.27** (44 μ L, 43 mg, 0.30 mmol) and [bis(trifluoromethanesulfonyl)imidate](triphenylphosphine)gold(I) (2:1) toluene adduct (16 mg, 0.01 mmol) in toluene (2 mL) for 19 hours at 40 °C. Purification by flash column chromatography (1:1 hexane/diethyl ether) afforded the *title product* as an orange oil, as a mixture of *E* and *Z* stereoisomers (40 mg, 73%, *E*:*Z* = 77:23). R_f (hexane/diethyl ether 1:1) 0.20; ν_{\max} (thin film)/ cm^{-1} 3284 (br), 3058, 1631, 1585, 1555, 1459, 1429, 743; δ_{H} (400 MHz; CDCl_3) 1.89 (3 H, s, H-18, *E*), 1.96 (3 H, s, H-18, *Z*), 2.12 (3 H, s, H-3, *Z*), 2.26 (3 H, s, H-3, *E*), 6.47 (1 H, s, H-16, *Z*), 6.69 (1 H, s, H-16, *E*), 6.97 – 7.05 (3 H, m, H-Ar, *E* and *Z*), 7.12 – 7.17 (2 H, m, H-Ar, *E* and *Z*), 7.20 (1 H, d, $J = 8.0$, H-Ar, *Z*), 7.28 – 7.44 (12 H, m, H-Ar, *E* and *Z*), 8.16 (1 H, br s, H-1, *Z*), 8.23 (1 H, br s, H-1, *E*); δ_{C} (100 MHz; CDCl_3) 12.7 (C-3, *E*), 13.7 (C-3, *Z*), 29.2 (C-18, *E*), 30.5 (C-18, *Z*), 110.7 (CH, C-Ar), 110.7 (CH, C-Ar), 111.8 (C, C-Ar, *E*), 114.5 (C, C-Ar, *Z*), 119.6 (CH, C-Ar), 119.8 (CH, C-Ar), 120.5 (CH, C-Ar), 120.7 (CH, C-Ar), 121.9 (CH, C-Ar), 122.0 (CH, C-Ar, *Z*), 126.9 (C-16, *Z*), 127.8 (C, C-Ar), 128.3 (CH, C-Ar), 128.5 (CH, C-Ar), 128.5 (CH, C-Ar), 128.6 (C, C-Ar), 128.6 (CH, C-Ar), 129.1 (CH, C-Ar), 129.6 (CH, C-Ar), 130.0 (CH, C-Ar), 135.5 (C, C-Ar), 135.6 (C, C-Ar), 135.9 (C, C-Ar), 137.2 (C, C-Ar), 140.6 (C, C-Ar, *Z*), 141.0 (C, C-Ar), 148.3 (C, C-Ar, *E*), 150.8 (C, C-Ar, *Z*), 200.8 (C-17, *E*), 200.9 (C-17, *Z*); HRMS (ESI⁺) Found: 276.1385; $\text{C}_{19}\text{H}_{18}\text{NO}$ ($\text{M}+\text{H}^+$) Requires 276.1383 (–0.6 ppm error); Found: 298.1202; $\text{C}_{19}\text{H}_{17}\text{NNaO}$ ($\text{M}+\text{Na}$) Requires 298.1202 (0.2 ppm error).

4-Phenyl-4-(2-phenyl-1H-indol-3-yl)but-3-en-2-one (3.66)

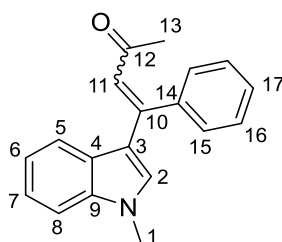


3.66

Synthesised using general procedure I from 2-phenyl-1H-indole (39 mg, 0.20 mmol), 4-phenyl-3-butyne-2-one (44 μ L, 43 mg, 0.30 mmol) and [bis(trifluoromethanesulfonyl)imidate](triphenylphosphine)gold(I) (2:1) toluene adduct (16 mg, 0.01 mmol) in toluene (2 mL) for 19 hours at 40 °C. Purification by flash column chromatography (7:3 to 1:1 hexane/diethyl ether) afforded the *title product* as a yellow solid, as a mixture of *E* and *Z* stereoisomers (55 mg, 81%, *E*:*Z* = 92:8). ^1H and ^{13}C NMR data reported for the major *E*-isomer only. R_f (hexane/diethyl ether 7:3) 0.12; mp 153–155 °C; ν_{max} (thin film)/ cm^{-1} 3295 (br), 2924, 1631, 1449, 1432, 759, 743, 730, 694; δ_{H} (400 MHz; CDCl_3) 1.75 (3 H, s, H-21), 6.75 (1 H, s, H-19), 7.05 – 7.10 (1 H, m, H-Ar), 7.18 – 7.34 (8 H, m, H-Ar), 7.44 (1 H, d, $J = 8.0$, H-9), 7.43 – 7.53 (4 H, m, H-Ar), 8.64 (1 H, br s, H-1); δ_{C} (100 MHz; CDCl_3) 29.0 (C-21), 111.3 (CH, C-Ar), 111.5 (C, C-Ar), 120.0 (CH, C-Ar), 121.1 (CH, C-Ar), 123.2 (CH, C-Ar), 127.2 (CH, C-Ar), 128.2 (CH, C-Ar), 128.3 (CH, C-Ar), 128.7 (CH, C-Ar), 129.1 (CH, C-Ar), 129.2 (C, C-Ar), 129.7 (CH, C-Ar), 130.4 (C-19), 131.7 (C, C-Ar), 136.1 (C, C-Ar), 136.8 (C, C-Ar), 140.5 (C, C-Ar), 147.8 (C, C-Ar), 200.3 (C-20); HRMS (ESI $^+$) Found: 338.1540; $\text{C}_{24}\text{H}_{20}\text{NO}$ ($\text{M}+\text{H}^+$) Requires 338.1539 (–0.1 ppm error); Found: 360.1361; $\text{C}_{24}\text{H}_{19}\text{NNaO}$ ($\text{M}+\text{Na}$) Requires 360.1359 (–0.5 ppm error).

Characteristic NMR resonances for the minor *Z*-isomer can be found at: δ_{H} 1.92 (3 H, s, H-21, *Z*), 6.38 (1 H, s, H-19, *Z*), 8.48 (1 H, br s, H-1, *Z*).

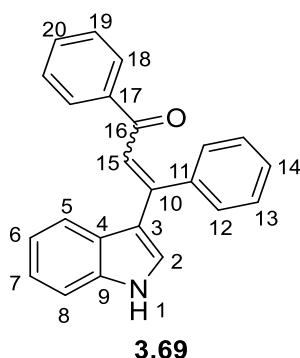
4-(1-Methyl-indol-3-yl)-4-phenylbut-3-en-2-one (3.67)



3.67

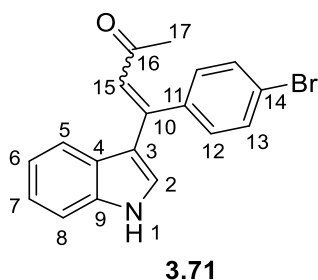
Synthesised using general procedure I from 1-methylindole (66 mg, 0.50 mmol), 4-phenyl-3-butyne-2-one **3.27** (0.11 mL, 108 mg, 0.75 mmol) and [bis(trifluoromethanesulfonyl)imidate](triphenylphosphine)gold(I) (2:1) toluene adduct (40 mg, 0.03 mmol) in toluene (5 mL) for 3 hours at 40 °C. Purification by flash column chromatography (7:3 hexane/diethyl ether) afforded the *title product* as an orange oil, as a mixture of *E* and *Z* stereoisomers (108 mg, 78%, *E*:*Z* = 82:18). R_f (hexane/diethyl ether) 0.17; ν_{\max} (thin film)/ cm^{-1} 3053, 2097, 1633, 1579, 1560, 1521, 1374, 1247, 740, 706; δ_{H} (600 MHz; CDCl_3) 1.89 (3 H, s, H-13, *E*), 2.06 (3 H, s, H-13, *Z*), 3.73 (3 H, s, H-1, *E*), 3.88 (3 H, s, H-1, *Z*), 6.49 (1 H, s, H-11, *Z*), 6.76 (1 H, s, H-2, *E*), 6.88 (1 H, s, H-11, *E*), 6.96 (1 H, ddd, $J = 8.0, 1.0, 1.0$, H-Ar, *Z*), 7.03 (1 H, ddd, $J = 8.0$ Hz, 7.0 Hz, 1.0 Hz, H-Ar, *Z*), 7.23 – 7.28 (2 H, m, H-Ar, *E* + *Z*), 7.31 – 7.39 (7 H, m, H-Ar, *E* + *Z*), 7.40 – 7.42 (1 H, m, H-Ar, *Z*), 7.43 – 7.50 (6 H, m, H-Ar, *E* + *Z*), 7.85 (1 H, d, $J = 8.0$ Hz, H-5, *E*); δ_{C} (151 MHz; CDCl_3) 30.2 (C-13, *Z*), 30.5 (C-13, *E*), 33.2 (C-1, *E*), 33.3 (C-1, *Z*), 109.7 (CH, C-Ar), 110.1 (C, C-Ar), 112.9 (C, C-Ar), 117.4 (C, C-Ar), 120.4 (CH, C-Ar), 121.0 (CH, C-Ar), 121.2 (CH, C-Ar), 121.4 (CH, C-Ar), 122.3 (CH, C-Ar), 123.0 (CH, C-Ar), 123.3 (C-11, *E*), 125.7 (C, C-Ar), 126.3 (C-11, *Z*), 127.7 (C, C-Ar), 128.3 (CH, C-Ar), 128.4 (CH, C-Ar), 128.5 (CH, C-Ar), 129.0 (CH, C-Ar), 129.3 (CH, C-Ar), 129.5 (CH, C-Ar), 132.8 (C-2, *Z*), 134.1 (C-2, *E*), 137.3 (C-9, *Z*), 138.3 (C-9, *E*), 140.5 (C, C-Ar), 142.1 (C, C-Ar), 148.0 (C-10, *Z*), 150.4 (C-10, *E*), 199.8 (C-12, *E*), 200.1 (C-12, *Z*); HRMS (ESI⁺) Found: 276.1373; $\text{C}_{19}\text{H}_{18}\text{NO}$ ($\text{M}+\text{H}^+$) Requires 276.1383 (3.6 ppm error); Found: 298.1192; $\text{C}_{19}\text{H}_{17}\text{NNaO}$ ($\text{M}+\text{Na}$) Requires 298.1202 (3.4 ppm error).

3-(1*H*-Indol-3-yl)-1,3-diphenylprop-2-en-1-one (3.69)



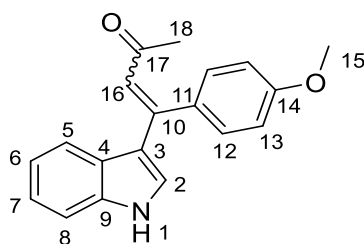
Synthesised using general procedure I from indole **3.16** (23 mg, 0.20 mmol), diphenylpropynone (62 mg, 0.30 mmol) and [bis(trifluoromethanesulfonyl)imidate](triphenylphosphine)gold(I) (2:1) toluene adduct (16 mg, 0.01 mmol) in toluene (2 mL) for 2 hours at 40 °C. Purification by flash column chromatography (9:1 to 7:3 hexane/diethyl ether) afforded the *title product* as a yellow solid, as a mixture of *E* and *Z* stereoisomers (38 mg, 59%, *E*:*Z* = 53:47). R_f (hexane/diethyl ether 7:3) 0.16; mp 170–174 °C; ν_{\max} (thin film)/ cm^{-1} 3284 (br), 3058, 2926, 1637, 1598, 1580, 1547, 1512, 1422, 744, 698; δ_{H} (600 MHz; d_6 -DMSO) 6.67 (1 H, d, $J = 7.5$, H-5, *Z*), 6.81 (1 H, t, $J = 7.5$, H-6, *Z*), 6.99 (1 H, s, H-15, *Z*), 7.02 (1 H, t, $J = 7.5$, H-7, *Z*), 7.09 (1 H, t, $J = 7.5$, H-6, *E*), 7.19 (1 H, t, $J = 7.5$, H-7, *E*), 7.21 – 7.25 (2 H, m, H-Ar, *E*), 7.26 (1 H, d, $J = 3.0$, H-2, *E*), 7.31 – 7.39 (6 H, m, H-Ar, *E* and *Z*), 7.40 – 7.52 (11 H, m, H-Ar, *E* and *Z*), 7.52 (1 H, d, $J = 2.5$, H-2, *Z*), 7.56 (1 H, t, $J = 7.5$, H-Ar, *E*), 7.86 – 7.89 (2 H, m, H-18, *Z*), 7.89 – 7.92 (2 H, m, H-18, *E*), 11.42 (1 H, s, H-1, *Z*), 11.73 (1 H, s, H-1, *E*); δ_{C} (151 MHz; d_6 -DMSO) 111.8 (C-8, *Z*), 112.5 (C-8, *E*), 112.9 (C, C-Ar, *Z*), 116.8 (C-15, *E*), 117.1 (C, C-Ar, *E*), 119.3 (C-6, *Z*), 119.9 (C-5, *Z*), 120.2 (C-5, *E*), 120.7 (C-6, *E*), 121.3 (C-7, *Z*), 121.9 (C-15, *Z*), 122.2 (C-7, *E*), 125.0 (C, C-Ar, *E*), 126.4 (C, C-Ar, *Z*), 127.7 (CH, C-Ar), 127.7 (CH, C-Ar), 128.0 (C-18, *E*), 128.1 (C-18, *Z*), 128.3 (CH, C-Ar), 128.4 (CH, C-Ar), 128.5 (CH, C-Ar), 128.6 (CH, C-Ar), 129.0 (CH, C-Ar), 129.2 (CH, C-Ar), 129.5 (C-2, *Z*), 130.4 (C-2, *E*), 132.1 (CH, C-Ar, *E*), 132.2 (CH, C-Ar, *Z*), 136.2 (C-9, *Z*), 137.4 (C-9, *E*), 138.4 (C, C-Ar), 139.2 (C, C-Ar), 140.4 (C, C-Ar, *E*), 141.9 (C, C-Ar, *Z*), 147.9 (C, C-Ar, *Z*), 151.5 (C, C-Ar), 189.9 (C-16, *E*), 191.5 (C-16, *Z*); HRMS (ESI⁺) Found: 324.1391; $\text{C}_{23}\text{H}_{18}\text{NO}$ ($\text{M}+\text{H}^+$) Requires 324.1383 (–2.6 ppm error); Found: 346.1204; $\text{C}_{23}\text{H}_{17}\text{NNaO}$ ($\text{M}+\text{Na}$) Requires 346.1202 (–0.4 ppm error).

4-(4-Bromophenyl)-4-(1*H*-indol-3-yl)but-3-en-2-one (3.71)



Synthesised using general procedure I from indole **3.16** (29 mg, 0.25 mmol), 4-(4-bromophenyl)but-3-yn-2-one **3.37** (84 mg, 0.38 mmol) and [bis(trifluoromethanesulfonyl)imidate](triphenylphosphine)gold(I) (2:1) toluene adduct (20 mg, 0.01 mmol) in toluene (2.5 mL) for 2 hours at 40 °C. Purification by flash column chromatography (9:1 to 6:4 hexane/diethyl ether) afforded the *title product* as a yellow solid, as a mixture of *E* and *Z* stereoisomers (55 mg, 64%, *E:Z* = 64:36). R_f (hexane/diethyl ether 1:1) 0.14; mp 135–138 °C; ν_{\max} (thin film)/ cm^{-1} 3302 (br), 3061, 2926, 1666, 1552, 1514, 1486, 742; δ_{H} (400 MHz; CDCl_3) 2.02 (6 H, s, H-17, *E* and *Z*), 6.50 (1 H, s, H-15, *Z*), 6.87 (1 H, d, $J = 3.0$, H-2, *E*), 6.89 (1 H, s, H-15, *E*), 6.99 (1 H, d, $J = 8.5$, H-Ar, *Z*), 7.01 – 7.07 (1 H, m, H-Ar, *Z*), 7.19 – 7.23 (3 H, m, H-Ar, *E* and *Z*), 7.23 – 7.26 (1 H, m, H-Ar, *E*), 7.26 – 7.31 (3 H, m, H-Ar, *E* and *Z*), 7.39 – 7.43 (3 H, m, H-Ar, *E* and *Z*), 7.45 – 7.49 (2 H, m, H-12, *Z*), 7.53 – 7.57 (2 H, m, H-12, *E*), 7.79 (1 H, d, $J = 7.5$, H-5, *E*), 8.73 (2 H, br s, H-1, *E* and *Z*); δ_{C} (100 MHz; CDCl_3) 30.1 (C-17, *Z*), 31.1 (C-17, *E*), 111.8 (CH), 112.1 (CH), 113.8 (C-3, *Z*), 118.5 (C-3, *E*), 120.7 (CH), 120.8 (CH), 120.9 (C-5, *E*), 121.7 (CH), 122.8 (C-14, *E*), 122.9 (C-15, *E*), 123.0 (CH), 123.5 (CH), 123.9 (C-14, *Z*), 125.0 (C), 126.7 (C), 127.0 (C-15, *Z*), 128.1 (CH), 129.8 (C-2, *E*), 130.4 (CH), 131.1 (CH), 131.6 (CH), 131.7 (CH), 136.4 (C-9, *Z*), 137.4 (C-9, *E*), 139.3 (C-10, *E*), 140.5 (C-10, *Z*), 146.8 (C-11, *Z*), 149.3 (C-11, *E*), 199.3 (C-16, *E*), 200.6 (C-16, *Z*); HRMS (ESI⁺) Found: 362.0153; $\text{C}_{18}\text{H}_{14}^{79}\text{BrNNaO}$ (M+Na) Requires 362.0151 (–0.5 ppm error); Found: 364.0133; $\text{C}_{18}\text{H}_{14}^{81}\text{BrNNaO}$ (M+Na) Requires 364.0131 (0.5 ppm error).

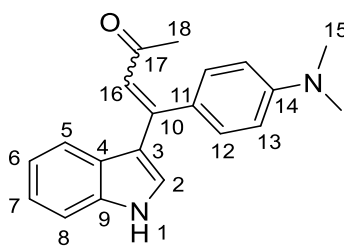
4-(1*H*-Indol-3-yl)-4-(4-methoxyphenyl)but-3-en-2-one (3.72)



3.72

Synthesised using general procedure I from indole **3.16** (29 mg, 0.25 mmol), 4-(4-methoxyphenyl)but-3-yn-2-one **3.33** (65 mg, 0.38 mmol) and [bis(trifluoromethanesulfonyl)imidate](triphenylphosphine)gold(I) (2:1) toluene adduct (20 mg, 0.01 mmol) in toluene (2.5 mL) for 2 hours at 40 °C. Purification by flash column chromatography (1:1 hexane/diethyl ether) afforded the *title product* as a brown solid, as a mixture of *E* and *Z* stereoisomers (64 mg, 88%, *E*:*Z* = 66:34). R_f (hexane/diethyl ether 1:1) 0.09; mp 52–55 °C; ν_{\max} (thin film)/ cm^{-1} 3282 (br), 1605, 1581, 1556, 1508, 1422, 1248, 743; δ_{H} (600 MHz; CDCl_3) 1.91 (3 H, s, H-18, *E*), 1.96 (3 H, s, H-18, *Z*), 3.84 (3 H, s, H-15, *Z*), 3.88 (3 H, s, H-15, *E*), 6.52 (1 H, s, H-16, *Z*), 6.79 (1 H, s, H-16, *E*), 6.84 – 6.88 (2 H, m, H-13, *Z*), 6.94 – 6.97 (2 H, m, H-13, *E*), 6.98 (1 H, d, $J = 3.0$, H-2, *E*), 7.01 – 7.08 (2 H, m, H-Ar, *Z*), 7.18 – 7.23 (2 H, m, H-Ar, *E* and *Z*), 7.25 – 7.30 (3 H, m, H-Ar, *E*), 7.35 – 7.39 (2 H, m, H-12, *Z*), 7.39 – 7.45 (3 H, m, H-Ar, *E* and *Z*) 7.73 (1 H, d, $J = 8.0$, H-5, *E*), 8.53 (1 H, br s, H-1, *E*), 8.57 (1 H, br s, H-1, *Z*); δ_{C} (151 MHz; CDCl_3) 29.9 (C-18, *Z*), 30.5 (C-18, *E*), 55.5 (C-15, *E*), 55.5 (C-15, *Z*), 111.6 (CH, C-Ar, *Z*), 111.9 (CH, C-Ar, *E*), 113.8 (C-13, *E*), 113.9 (C-13, *Z*), 114.8 (C-3, *Z*), 119.4 (C-3, *E*), 120.7 (CH, C-Ar, *Z*), 120.9 (CH, C-Ar, *Z*), 121.1 (C-5, *E*), 121.5 (CH, C-Ar, *E*), 122.8 (CH, C-Ar, *Z*), 123.3 (CH, C-Ar, *E*), 124.1 (C-16, *E*), 125.4 (C-4, *E*), 126.0 (C-16, *Z*), 127.1 (C, C-Ar, *Z*), 127.7 (CH, C-Ar, *Z*), 129.1 (C-2, *E*), 130.3 (C-12, *Z*), 131.2 (C-12, *E*), 132.5 (C-11, *E*), 133.8 (C-10, *Z*), 136.4 (C-9, *Z*), 137.3 (C-9, *E*), 147.7 (C-10, *Z*), 150.2 (C-10, *E*), 160.3 (C-14, *E*), 161.0 (C-14, *Z*), 200.5 (C-17, *E*), 200.6 (C-17, *Z*); HRMS (ESI⁺) Found: 292.1333; $\text{C}_{19}\text{H}_{18}\text{NO}_2$ ($\text{M}+\text{H}^+$) Requires 292.1332 (–0.4 ppm error); Found: 314.1152; $\text{C}_{19}\text{H}_{17}\text{NNaO}_2$ ($\text{M}+\text{Na}$) Requires 314.1151 (–0.3 ppm error).

4-(4-(Dimethylamino)phenyl)-4-(1H-indol-3-yl)but-3-en-2-one (3.73)

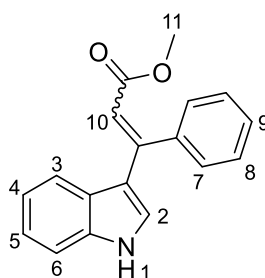


3.73

Synthesised using general procedure I from indole **3.16** (29 mg, 0.25 mmol), 4-(4-(dimethylamino)phenyl)but-3-yn-2-one **3.34** (70 mg, 0.38 mmol) and [bis(trifluoromethanesulfonyl)-imidate](triphenylphosphine)gold(I) (2:1) toluene adduct (20 mg, 0.01 mmol) in toluene (2.5 mL) for 2 hours at 40 °C. Purification by flash column chromatography (1:1 to 3:7 hexane/diethyl ether) afforded the *title product* as a yellow solid, as a mixture of *E* and *Z* stereoisomers (66 mg, 86%, *E*:*Z* = 56:44). R_f (hexane/diethyl ether 1:1) 0.12; mp 62–66 °C; ν_{\max} (thin film)/ cm^{-1} 3254 (br), 2922, 1604, 1561, 1519, 1428, 742; δ_{H} (400 MHz; CDCl_3) 1.91 (3 H, s, H-18, *Z*), 1.93 (3 H, s, H-18, *E*), 3.00 (6 H, s, H-15, *Z*), 3.02 (6 H, s, H-15, *E*), 6.56 (1 H, s, H-16, *Z*), 6.61 – 6.62 (2 H, m, H-13, *Z*), 6.69 – 6.74 (2 H, m, H-13, *E*), 6.70 (1 H, s, H-16, *E*), 7.01 – 7.07 (2 H, m, H-Ar, *E* and *Z*), 7.15 – 7.29 (7 H, m, H-Ar, *E* and *Z*), 7.31 – 7.35 (2 H, m, H-12, *Z*), 7.38 – 7.43 (2 H, m, H-Ar, *E* and *Z*), 7.72 (1 H, d, $J = 8.0$, H-5, *E*), 8.83 (1 H, br s, H-1, *Z*), 8.87 (1 H, br s, H-1, *E*); δ_{C} (100 MHz; CDCl_3) 29.8 (C-18, *Z*), 39.2 (C-18, *E*), 40.3 (C-15, *Z*), 40.4 (C-15, *E*), 111.6 (C-13, *E* and *Z*), 111.9 (CH, C-Ar), 115.1 (C-3, *Z*), 119.5 (C-3, *E*), 120.5 (CH, C-Ar), 120.9 (CH, C-Ar), 121.0 (CH, C-Ar), 121.2 (CH, C-Ar), 122.6 (CH, C-Ar), 123.0 (CH, C-Ar), 123.5 (C-16, *E*), 124.0 (C-16, *Z*), 125.7 (C, C-Ar), 127.3 (C, C-Ar), 127.6 (CH, C-Ar), 128.5 (C, C-Ar), 129.3 (C-2, *E*), 130.3 (C-12, *Z*), 131.4 (C-12, *E*), 136.4 (C-9, *Z*), 137.3 (C-9, *E*), 149.0 (C, C-Ar), 151.1 (C, C-Ar), 151.5 (C, C-Ar), 151.7 (C, C-Ar), 200.7 (C-17, *Z*), 201.3 (C-17, *E*); HRMS (ESI⁺) Found: 305.1646; $\text{C}_{20}\text{H}_{21}\text{N}_2\text{O}$ ($\text{M}+\text{H}^+$) Requires 305.1648 (0.9 ppm error); Found: 327.1465; $\text{C}_{20}\text{H}_{20}\text{N}_2\text{NaO}$ ($\text{M}+\text{Na}$) Requires 327.1468 (1.0 ppm error).

Note that one quaternary and one methine carbon resonance could not be found in the ^{13}C NMR spectra, it is believed that they are overlapping with other resonances.

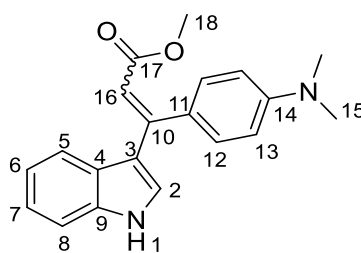
Methyl 3-(1*H*-indol-3-yl)-3-phenylacrylate (**3.74**)



3.74

Synthesised using general procedure I from indole **3.16** (23 mg, 0.20 mmol), methyl phenylpropionate **3.43** (44 μ L, 48 mg, 0.30 mmol) and [bis(trifluoromethanesulfonyl)imidate](triphenylphosphine)gold(I) (2:1) toluene adduct (16 mg, 0.01 mmol) in toluene (2 mL) for 2 hours at 40 °C. Purification by flash column chromatography (7:3 hexane/diethyl ether) afforded the *title product* as a pale, yellow solid, as a mixture of *E* and *Z* stereoisomers (47 mg, 85%, *E*:*Z* = 78:22). R_f (hexane/diethyl ether 7:3) 0.17; δ_H (400 MHz; $CDCl_3$) 3.63 (3 H, s, H-11, *E*), 3.65 (3 H, s, H-11, *Z*), 6.26 (1 H, s, H-10, *Z*), 6.59 (1 H, s, H-10, *E*), 6.89 (1 H, d, $J = 3.0$, H-2, *E*), 6.93 (1 H, d, $J = 8.0$, H-Ar, *Z*), 6.99 (1 H, d, $J = 7.5$, H-Ar, *Z*), 7.14 – 7.19 (1 H, m, H-Ar, *Z*), 7.21 – 7.30 (2 H, m, H-Ar, *E*), 7.31 – 7.36 (4 H, m, H-Ar, *E* and *Z*), 7.37 – 7.44 (8 H, m, *E* and *Z*), 7.55 (1 H, d, $J = 2.5$, H-2, *Z*), 7.82 (1 H, d, $J = 8.5$, H-3, *E*), 8.41 (2 H, br s, H-1, *E* and *Z*). Spectroscopic data match those reported previously.²¹³

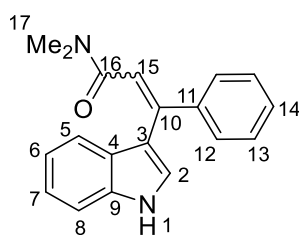
Methyl 3-(4-(dimethylamino)phenyl)-3-(1H-indol-3-yl)acrylate (3.75)



3.75

Synthesised using general procedure I from indole **3.16** (23 mg, 0.20 mmol), methyl 3-(4-(dimethylamino)phenyl)propionate **3.44** (61 mg, 0.30 mmol) and [bis(trifluoromethanesulfonyl)imidate](triphenylphosphine)gold(I) (2:1) toluene adduct (16 mg, 0.01 mmol) in toluene (2 mL) for 2 hours at 40 °C. Purification by flash column chromatography (8:2 to 7:3 hexane/ethyl acetate) afforded the *title product* as a yellow solid, as a mixture of *E* and *Z* stereoisomers (39 mg, 61%, *E*:*Z* = 58:42). R_f (hexane/ethyl acetate 8:2) 0.15, 0.10; mp 58–65 °C; ν_{\max} (thin film)/ cm^{-1} 3327 (br), 2945, 1691, 1607, 1585, 1520, 1155, 819, 744; δ_{H} (600 MHz; CDCl_3) 3.00 (6 H, s, H-15, *E*), 3.00 (6 H, s, H-15, *Z*), 3.63 (3 H, s, H-18, *Z*), 3.68 (3 H, s, H-18, *E*), 6.25 (1 H, s, H-16, *Z*), 6.41 (1 H, s, H-16, *E*), 6.61 – 6.65 (2 H, m, H-13, *Z*), 6.69 – 6.75 (2 H, m, H-13, *E*), 6.98 (1 H, d, $J = 2.5$, H-2, *E*), 7.01 (1 H, ddd, $J = 8.0, 7.0, 1.0$, H-Ar, *Z*), 7.12 (1 H, dd, $J = 8.0, 1.0$, H-Ar, *Z*), 7.13 – 7.19 (2 H, m, H-Ar, *E*), 7.21 – 7.25 (1 H, m, H-Ar, *E*), 7.25 – 7.27 (2 H, m, H-12, *Z*), 7.31 – 7.37 (5 H, m, H-Ar, *E* and *Z*), 7.71 (1 H, dd, $J = 8.0, 1.0$, H-5, *E*), 8.55 (2 H, br s, H-1, *E* and *Z*); δ_{C} (151 MHz; CDCl_3) 40.3 (C-15, *Z*), 40.5 (C-15, *E*), 51.0 (C-18, *E*), 51.1 (C-18, *Z*), 110.6 (C-16, *E*), 111.3 (CH, C-Ar), 111.4 (CH, C-Ar), 111.6 (CH, C-Ar), 111.7 (CH, C-Ar), 111.8 (CH, C-Ar), 114.2 (C-3, *Z*), 119.7 (C-3, *E*), 120.1 (CH, C-Ar), 120.8 (CH, C-Ar), 121.0 (CH, C-Ar), 121.1 (CH, C-Ar), 122.1 (CH, C-Ar), 122.8 (CH, C-Ar), 125.8 (C-4, *E*), 127.3 (C, C-Ar), 127.5 (C, C-Ar), 127.5 (CH, C-Ar), 128.9 (C-2, *E*), 129.4 (C-11, *Z*), 130.2 (C-12, *E*), 130.9 (C-12, *Z*), 136.1 (C-9, *Z*), 137.1 (C-9, *E*), 150.7 (C, C-Ar), 151.3 (C, C-Ar), 151.5 (C, C-Ar), 153.5 (C-11, *E*), 167.6 (C-17, *Z*), 167.8 (C-17, *E*); HRMS (ESI⁺) Found: 321.1584; $\text{C}_{20}\text{H}_{21}\text{N}_2\text{O}_2$ ($\text{M}+\text{H}^+$) Requires 321.1598 (4.2 ppm error); Found: 343.1403; $\text{C}_{20}\text{H}_{20}\text{N}_2\text{NaO}_2$ ($\text{M}+\text{Na}$) Requires 343.1417 (4.0 ppm error); Found: 289.1322; $\text{C}_{19}\text{H}_{17}\text{N}_2\text{O}$ ($\text{M}-\text{OMe}$) Requires 289.1335 (–4.5 ppm error).

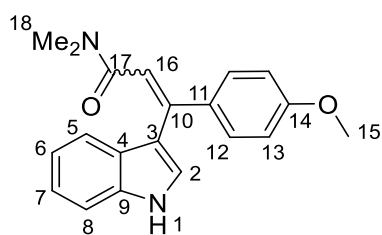
3-(1*H*-Indol-3-yl)-*N,N*-dimethyl-3-phenylacrylamide (3.76)



3.76

Synthesised using general procedure I from indole **3.16** (23 mg, 0.20 mmol), *N,N*-dimethyl-3-phenylpropiolamide **3.39** (52 mg, 0.30 mmol) and [bis(trifluoromethanesulfonyl)imidate]-(triphenylphosphine)gold(I) (2:1) toluene adduct (16 mg, 0.01 mmol) in toluene (2 mL) for 24 hours at 40 °C. Purification by flash column chromatography (7:3 diethyl ether/hexane to ethyl acetate) afforded the *title product* as a pale, brown solid, as a mixture of *E* and *Z* stereoisomers (33 mg, 56%, *E:Z* = 26:74). R_f (hexane/ethyl acetate 3:7) 0.33; mp 124–129 °C; ν_{\max} (thin film)/ cm^{-1} 3218 (br), 2925, 1613, 1494, 1399, 1199, 736; δ_{H} (600 MHz; CDCl_3) 2.78 (3 H, s, H-17a, *Z*), 2.85 (3 H, s, H-17a, *E*), 2.86 (3 H, s, H-17b, *E*), 2.87 (3 H, s, H-17b, *Z*), 6.28 (1 H, s, H-15, *Z*), 6.55 (1 H, s, H-15, *E*), 6.88 (1 H, d, $J = 8.0$, H-5, *Z*), 6.93 (1 H, dd, $J = 8.0, 8.0$, H-6, *Z*), 6.98 (1 H, d, $J = 2.5$, H-2, *E*), 7.14 (2 H, m, H-Ar, *E* and *Z*), 7.23 (1 H, dd, $J = 7.0, 7.0$, H-7, *E*), 7.29 – 7.42 (12 H, m, H-Ar, *E* and *Z*), 7.43 (1 H, d, $J = 2.5$, H-2, *Z*), 7.61 (1 H, d, $J = 8.0$, H-5, *E*), 8.52 (1 H, br s, H-1, *E*), 8.72 (1 H, br s, H-1, *Z*); δ_{C} (151 MHz; CDCl_3) 34.7 (C-17a, *E*), 34.7 (C-17a, *Z*), 38.1 (C-17b, *E*), 38.1 (C-17b, *Z*), 111.5 (CH, C-Ar), 111.8 (CH, C-Ar), 114.1 (C-3, *Z*), 117.7 (C-15, *E*), 118.4 (C-3, *E*), 119.9 (C-15, *Z*), 120.0 (C-6, *Z*), 120.6 (C-5, *E*), 120.7 (C-5, *Z*), 120.8 (C-7, *E*), 122.2 (C-6, *Z*), 122.8 (C-7, *E*), 125.8 (C, C-Ar), 126.2 (C-2, *Z*), 126.4 (C-2, *E*), 126.6 (C, C-Ar), 128.1 (2 x CH, C-Ar), 128.3 (CH, C-Ar), 128.4 (CH, C-Ar), 128.6 (CH, C-Ar), 129.3 (CH, C-Ar), 136.3 (C-9, *Z*), 137.0 (C-9, *E*), 140.2 (C, C-Ar, *E*), 141.2 (C, C-Ar, *Z*), 141.4 (C, C-Ar, *Z*), 142.8 (C, C-Ar, *E*), 169.2 (C-16, *E*), 169.6 (C-16, *Z*); HRMS (ESI⁺) Found: 291.1491; $\text{C}_{19}\text{H}_{19}\text{N}_2\text{O}$ ($\text{M}+\text{H}^+$) Requires 291.1492 (0.2 ppm error); Found: 313.1310; $\text{C}_{19}\text{H}_{18}\text{N}_2\text{NaO}$ ($\text{M}+\text{Na}$) Requires 313.1311 (0.5 ppm error).

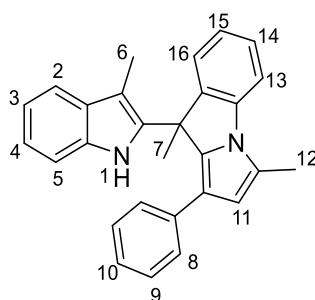
3-(1*H*-Indol-3-yl)-3-(4-methoxyphenyl)-*N,N*-dimethylacrylamide (3.77)



3.77

Synthesised using general procedure I from indole **3.16** (23 mg, 0.20 mmol), 3-(4-methoxyphenyl)-*N,N*-dimethylpropiolamide **3.40** (61 mg, 0.30 mmol) and [bis(trifluoromethanesulfonyl)imidate](triphenylphosphine)gold(I) (2:1) toluene adduct (16 mg, 0.01 mmol) in toluene (2 mL) for 2 hours at 40 °C. Purification by flash column chromatography (1:1 to 2:8 hexane/ethyl acetate) afforded the *title product* as a pale, brown solid, as a mixture of *E* and *Z* stereoisomers (64 mg, 100%, *E:Z* = 45:55). R_f (hexane/ethyl acetate 3:7) 0.23; mp 78–85 °C; ν_{\max} (thin film)/ cm^{-1} 3205 (br), 2927, 1604, 1509, 1457, 1439, 1397, 1247, 742; δ_{H} (600 MHz; CDCl_3) 2.76 (3 H, s, H-18a, *Z*), 2.85 (3 H, s, H-18b, *Z*), 2.86 (3 H, s, H-18a, *E*), 2.91 (3 H, s, H-18b, *E*), 3.78 (3 H, s, H-15, *E*), 3.82 (3 H, s, H-15, *Z*), 6.21 (1 H, s, H-16, *Z*), 6.40 (1 H, s, H-16, *E*), 6.78 – 6.82 (2 H, m, H-13, *E*), 6.82 – 6.85 (2 H, m, H-13, *Z*), 6.90 – 6.94 (3 H, m, H-Ar, *Z* and *E*), 7.06 – 7.10 (2 H, m, H-Ar, *Z* and *E*), 7.16 (1 H, t, $J = 7.5$, H-Ar, *E*), 7.23 – 7.27 (2 H, m, H-12, *E*), 7.30 – 7.33 (3 H, m, H-Ar, *Z*), 7.34 (1 H, d, $J = 8.5$, H-Ar, *Z*), 7.37 (1 H, d, $J = 8.5$, H-Ar, *E*), 7.53 (1 H, d, $J = 8.0$, H-5, *E*), 9.39 (1 H, br s, H-1, *E*), 9.44 (1 H, br s, H-1, *Z*); δ_{C} (151 MHz; CDCl_3) 34.7 (C-18a, *E*), 34.8 (C-18a, *Z*), 38.1 (C-18b, *E*), 38.1 (C-18b, *Z*), 55.3 (C-15, *E*), 55.4 (C-15, *Z*), 111.7 (CH, C-Ar), 112.0 (CH, C-Ar), 113.5 (C-13, *E*), 113.7 (C-13, *Z*), 113.9 (C-3, *Z*), 116.4 (C-16, *E*), 117.8 (C-16, *Z*), 118.0 (C-3, *E*), 119.8 (CH, C-Ar), 120.3 (CH, C-Ar), 120.5 (CH, C-Ar), 121.9 (CH, C-Ar), 122.3 (CH, C-Ar), 125.8 (C-4, *E*), 126.4 (C-2, *E*), 126.6 (C-4, *Z*), 126.8 (C-2, *Z*), 129.4 (C-12, *Z*), 130.6 (C-12, *E*), 132.5 (C, C-Ar), 133.7 (C, C-Ar), 136.5 (C-9, *Z*), 137.1 (C-9, *E*), 141.5 (C, C-Ar), 142.9 (C, C-Ar), 159.6 (C-14, *E*), 160.0 (C-14, *Z*), 169.8 (C-17, *E*), 170.0 (C-17, *Z*); HRMS (ESI⁺) Found: 321.1590; $\text{C}_{20}\text{H}_{21}\text{N}_2\text{O}_2$ ($\text{M}+\text{H}^+$) Requires 321.1598 (2.4 ppm error); Found: 343.1411; $\text{C}_{20}\text{H}_{20}\text{N}_2\text{NaO}_2$ ($\text{M}+\text{Na}$) Requires 343.1417 (1.8 ppm error).

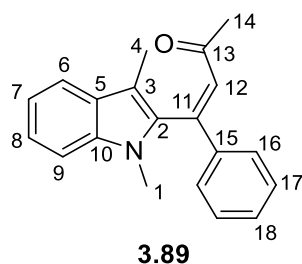
3,9-Dimethyl-9-(3-methyl-1*H*-indol-2-yl)-1-phenyl-9*H*-pyrrolo[1,2- α]indole (3.79)



3.79

Synthesised using general procedure I from 3-methyl-1*H*-indole **3.48** (26 mg, 0.20 mmol), 4-phenyl-3-butyne-2-one **3.27** (44 μ L, 43 mg, 0.30 mmol) and [bis(trifluoromethanesulfonyl)imidate](triphenylphosphine)gold(I) (2:1) toluene adduct (16 mg, 0.01 mmol) in toluene (2 mL) for 24 hours at 40 °C. Purification by flash column chromatography (99:1 to 98:2 hexane/diethyl ether) afforded the *title product* as a brown solid (13 mg, 33%). R_f (hexane/diethyl ether 98:2) 0.08; δ_H (400 MHz; CDCl₃) 2.01 (3 H, s, H-7), 2.09 (3 H, s, H-6), 2.69 (3 H, s, H-12), 6.35 (1 H, s, H-11), 6.99 – 7.08 (2 H, m, H-Ar), 7.09 – 7.13 (5 H, m, H-Ar), 7.15 (1 H, dd, $J = 7.0, 1.5$, H-Ar), 7.21 – 7.25 (1 H, m, H-Ar), 7.25 – 7.29 (2 H, m, H-Ar), 7.42 (1 H, d, $J = 8.0$, H-Ar), 7.51 (1 H, d, $J = 8.0$, H-Ar), 7.98 (1 H, br s, H-1). Spectroscopic data match those reported previously.²¹⁴

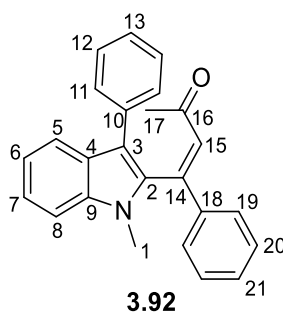
4-(1,3-Dimethyl-indol-2-yl)-4-phenylbut-3-en-2-one (3.89)



Synthesised using general procedure I from 1,3-dimethylindole **3.49** (73 mg, 0.50 mmol), 4-phenyl-3-butyne-2-one **3.27** (0.11 mL, 108 mg, 0.75 mmol) and [bis(trifluoromethanesulfonyl)imidate](triphenylphosphine)gold(I) (2:1) toluene adduct (40 mg, 0.03 mmol) in toluene (5 mL) for 27 hours at 40 °C. Purification by flash column chromatography (9:1 to 8:2 hexane/diethyl ether) afforded the *title product* as an orange oil, as a mixture of *E* and *Z* stereoisomers (107 mg, 74%, *E*:*Z* = 5:95). ¹H and ¹³C NMR data reported for the major *Z*-isomer only. *R_f* (hexane/diethyl ether 8:2) 0.23; *v*_{max} (thin film)/cm⁻¹ 3060, 2919, 1657, 1599, 1573, 1467, 1244, 739; *δ*_H (400 MHz; CDCl₃) 1.89 (3 H, s, H-14), 2.26 (3 H, s, H-4), 3.49 (3 H, s, H-1), 6.95 (1 H, s, H-12), 7.24 (1 H, ddd, *J* = 8.0, 6.5, 1.5, H-Ar), 7.32 – 7.45 (7 H, m, H-Ar), 7.63 (1 H, ddd, *J* = 8.0, 1.0, 1.0, H-Ar); *δ*_C (100 MHz; CDCl₃) 9.3 (C-4), 28.7 (C-14), 30.6 (C-1), 109.4 (CH, C-Ar), 112.4 (C-3), 119.4 (CH, C-Ar), 119.5 (CH, C-Ar), 122.7 (CH, C-Ar), 127.5 (CH, C-Ar), 128.2 (C-5), 129.0 (CH, C-Ar), 130.0 (CH, C-Ar), 131.8 (C-12), 133.0 (C-2), 137.6 (C-10), 138.7 (C-11), 143.5 (C-15), 199.8 (C-13); HRMS (ESI⁺) Found: 290.1530; C₂₀H₂₀NO (M+H⁺) Requires 290.1539 (3.3 ppm error); Found: 312.1349; C₂₀H₁₉NNaO (M+Na) Requires 312.1359 (3.2 ppm error).

Characteristic NMR resonances for the minor *E*-isomer can be found at: *δ*_H 2.14 (3 H, s, H-14, *E*), 2.39 (3 H, s, H-4, *E*), 3.34 (3 H, s, H-1, *E*), 6.37 (1 H, s, H-12, *E*).

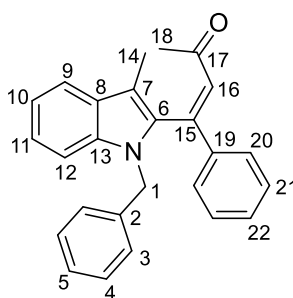
4-(1-Methyl-3-phenyl-indol-2-yl)-4-phenylbut-3-en-2-one (3.92)



Synthesised using general procedure I from 1-methyl-3-phenylindole **3.51** (42 mg, 0.20 mmol), 4-phenyl-3-butyne-2-one **3.27** (44 μ L, 43 mg, 0.30 mmol) and [bis(trifluoromethanesulfonyl)imidate](triphenylphosphine)gold(I) (2:1) toluene adduct (16 mg, 0.01 mmol) in toluene (2 mL) for 24 hours at 40 °C. Purification by flash column chromatography (9:1 to 8:2 hexane/diethyl ether) afforded the *title product* as an orange solid, as a mixture of *E* and *Z* stereoisomers (29 mg, 41%, *E*:*Z* = 2:98). ¹H and ¹³C NMR data reported for the major *Z*-isomer only. *R*_f (hexane/diethyl ether 8:2) 0.19; mp 145–148 °C; ν_{max} (thin film)/cm⁻¹ 3056, 2931, 1690, 1659, 1602, 1465, 772, 760, 747, 699; δ_{H} (400 MHz; CDCl₃) 1.74 (3 H, s, H-17), 3.53 (3 H, s, H-1), 6.82 (1 H, s, H-15), 7.19 – 7.26 (2 H, m, H-Ar), 7.29 – 7.44 (11 H, m, H-Ar), 7.84 (1 H, d, *J* = 8.0, H-Ar); δ_{C} (100 MHz; CDCl₃) 28.9 (C-17), 30.7 (C-1), 109.8 (CH), 118.1 (C, C-Ar), 120.3 (C-5), 120.5 (CH, C-Ar), 123.0 (CH, C-Ar), 126.4 (CH, C-Ar), 126.9 (C, C-Ar), 127.6 (CH, C-Ar), 128.7 (CH, C-Ar), 128.9 (CH, C-Ar), 129.2 (CH, C-Ar), 130.2 (CH, C-Ar), 132.4 (C-15), 133.0 (C-2), 134.5 (C, C-Ar), 137.8 (C-9), 138.9 (C, C-Ar), 142.6 (C, C-Ar), 199.0 (C-16); HRMS (ESI⁺) Found: 352.1699; C₂₅H₂₂NO (M+H⁺) Requires 352.1696 (–0.7 ppm error); Found: 374.1517; C₂₅H₂₁NNaO (M+Na) Requires 374.1515 (–0.4 ppm error).

Characteristic NMR resonances for the minor *E*-isomer can be found at: δ_{H} 1.91 (3H, s, H-17, *E*), 3.36 (3 H, s, H-1, *E*), 6.18 (1 H, s, 15, *E*).

4-(1-Benzyl-3-methyl-indol-2-yl)-4-phenylbut-3-en-2-one (3.93)

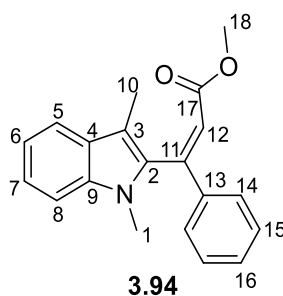


3.93

Synthesised using general procedure I from 1-benzyl-3-methylindole **3.52** (40 mg, 0.18 mmol), 4-phenyl-3-butyne-2-one **3.27** (39 μ L, 39 mg, 0.27 mmol) and [bis(trifluoromethanesulfonyl)imidate](triphenylphosphine)gold(I) (2:1) toluene adduct (14 mg, 0.01 mmol) in toluene (1.8 mL) for 24 hours at 40 °C. Purification by flash column chromatography (9:1 to 8:2 hexane/diethyl ether) afforded the *title product* as an orange solid, as a mixture of *E* and *Z* stereoisomers (41 mg, 62%, *E*:*Z* = 7:93). ^1H and ^{13}C NMR data reported for the major *Z*-isomer only. R_f (hexane/diethyl ether 8:2) 0.30; mp 93–95 °C; ν_{max} (thin film)/ cm^{-1} 3057, 2919, 1689, 1657, 1602, 1462, 1448, 742, 696; δ_{H} (400 MHz; CDCl_3) 1.63 (3 H, s, H-18), 2.23 (3 H, s, H-14), 4.72 (1 H, d, $J = 16.0$, H-1a), 5.12 (1 H, d, $J = 16.0$, H-1b), 6.73 (1 H, s, H-16), 6.97 – 7.02 (2 H, m, H-Ar), 7.13 – 7.39 (11 H, m, H-Ar), 7.67 (1 H, d, $J = 7.5$, H-9); δ_{C} (100 MHz; CDCl_3) 9.5 (C-14), 28.5 (C-18), 47.9 (C-1), 110.2 (CH, C-Ar), 113.9 (C-7), 119.7 (C-9), 123.1 (CH, C-Ar), 127.2 (CH, C-Ar), 127.6 (CH, C-Ar), 127.8 (CH, C-Ar), 128.4 (C, C-Ar), 128.5 (C, C-Ar), 128.6 (CH, C-Ar), 129.0 (CH, C-Ar), 130.0 (CH, C-Ar), 132.0 (C-16), 132.8 (C-6), 137.7 (C, C-Ar), 137.8 (C-13), 139.0 (C-15), 143.4 (C, C-Ar), 199.7 (C-17); HRMS (ESI $^+$) Found: 366.1858; $\text{C}_{26}\text{H}_{24}\text{NO}$ ($\text{M}+\text{H}^+$) Requires 366.1852 (–1.6 ppm error); Found: 388.1677; $\text{C}_{26}\text{H}_{23}\text{NNaO}$ ($\text{M}+\text{Na}$) Requires 388.1672 (–1.2 ppm error).

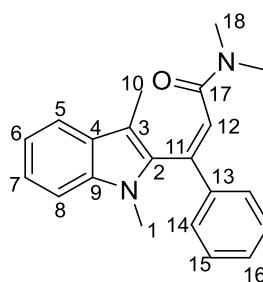
Characteristic NMR resonances for the minor *E*-isomer can be found at: δ_{H} 1.97 (3 H, s, H-18, *E*), 2.29 (3 H, s, H-14, *E*), 4.99 (2 H, s, H-1, *E*), 6.24 (1 H, s, H-16, *E*).

Methyl (Z)-3-(1,3-dimethyl-indol-2-yl)-3-phenylacrylate (3.94)



Synthesised using general procedure I from 1,3-dimethylindole **3.49** (29 mg, 0.20 mmol), methyl phenylpropiolate **3.43** (44 μ L, 48 mg, 0.30 mmol) and [bis(trifluoromethanesulfonyl)imidate](triphenylphosphine)gold(I) (2:1) toluene adduct (16 mg, 0.01 mmol) in toluene (2 mL) for 24 hours at 40 °C. Purification by flash column chromatography (9:1 hexane/diethyl ether) afforded the *title product* as a yellow oil (43 mg, 70%) as a single geometrical isomer (*Z*). R_f (hexane/diethyl ether 9:1) 0.17; ν_{\max} (thin film)/ cm^{-1} 3061, 2950, 1690, 1728, 1623, 1467, 1449, 1260, 741; δ_{H} (400 MHz; CDCl_3) 2.17 (3 H, s, H-10), 3.44 (3 H, s, H-1), 3.64 (3 H, s, H-18), 6.74 (1 H, s, H-12), 7.15 (1 H, ddd, $J = 8.0, 6.5, 1.0$, H-6), 7.24 – 7.28 (1 H, m, H-Ar), 7.29 – 7.43 (6 H, m, H-Ar), 7.63 (1 H, d, $J = 8.0$, H-5); δ_{C} (100 MHz; CDCl_3) 9.3 (C-10), 30.7 (C-1), 51.8 (C-18), 109.3 (CH, C-Ar), 110.7 (C-3), 118.9 (C-6), 119.3 (C-5), 121.1 (C-12), 122.0 (CH, C-Ar), 127.6 (CH, C-Ar), 128.3 (C-4), 129.0 (CH, C-Ar), 130.0 (CH, C-Ar), 133.5 (C-2), 137.6 (C-9), 139.0 (C-11), 146.5 (C-13), 166.0 (C-17); HRMS (ESI⁺) Found: 306.1489; $\text{C}_{20}\text{H}_{20}\text{NO}_2$ ($\text{M}+\text{H}^+$) Requires 306.1489 (0.0 ppm error); Found: 328.1311; $\text{C}_{20}\text{H}_{19}\text{NNaO}_2$ ($\text{M}+\text{Na}$) Requires 328.1308 (–0.9 ppm error); Found: 274.1227; $\text{C}_{19}\text{H}_{16}\text{NO}$ ($\text{M}-\text{OMe}$) Requires 274.1226 (0.4 ppm error).

3-(1,3-Dimethyl-indol-2-yl)-*N,N*-dimethyl-3-phenylacrylamide (3.95)



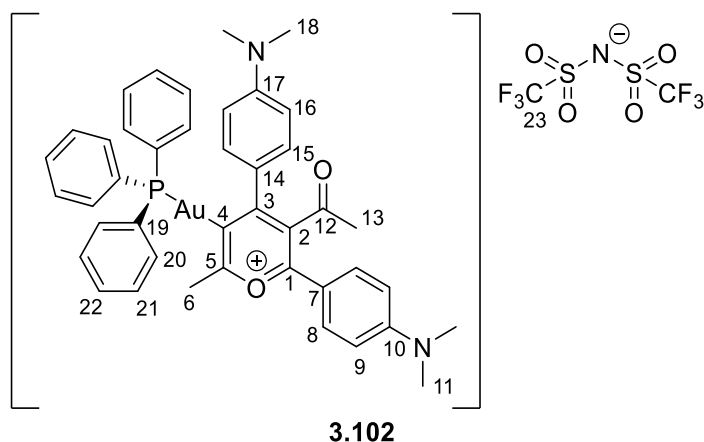
3.95

Synthesised using general procedure I from 1,3-dimethylindole **3.49** (29 mg, 0.20 mmol), *N,N*-dimethyl-3-phenylpropiolamide **3.39** (52 mg, 0.30 mmol) and [bis(trifluoromethanesulfonyl)imidate](triphenylphosphine)gold(I) (2:1) toluene adduct (16 mg, 0.01 mmol) in toluene (2 mL) for 48 hours at 40 °C. Purification by flash column chromatography (8:2 to 2:1 hexane/diethyl ether) afforded the *title product* as a yellow oil, as a mixture of *E* and *Z* stereoisomers (38 mg, 59%, *E:Z* = 7:93). ¹H and ¹³C NMR data reported for the major *Z*-isomer only. *R_f* (hexane/ethyl acetate 2:1) 0.20; *v*_{max} (thin film)/cm⁻¹ 3053, 2924, 1629, 1493, 1469, 1139, 732, 696; δ_{H} (400 MHz; CDCl₃) 2.20 (3 H, s, H-10), 2.93 (6 H, br s, H-18), 3.44 (3 H, s, H-1), 6.89 (1 H, s, H-12), 7.11 – 7.16 (1 H, m, H-6), 7.21 – 7.30 (4 H, m, H-Ar), 7.30 – 7.36 (3 H, m, H-Ar), 7.60 (1 H, d, *J* = 8.0, H-5); δ_{C} (100 MHz; CDCl₃) 9.5 (C-10), 31.0 (C-1), 35.1 (br, C-18a), 37.9 (br, C-18b), 109.4 (CH, C-Ar), 110.4 (C-3), 118.9 (C-6), 119.2 (C-5), 121.9 (CH, C-Ar), 125.8 (C-12), 127.0 (CH, C-Ar), 128.4 (C-4), 128.9 (CH, C-Ar), 129.1 (CH, C-Ar), 133.9 (C-2), 137.6 (C-9), 139.4 (C, C-Ar), 139.4 (C, C-Ar), 167.3 (C-17); HRMS (ESI⁺) Found: 319.1804; C₂₁H₂₃N₂O (M+H⁺) Requires 319.1805 (0.2 ppm error); Found: 341.1624; C₂₁H₂₂N₂NaO (M+Na) Requires 341.1624 (-0.0 ppm error); Found: 278.1228; C₁₉H₁₆NO (M-NMe₂) Requires 278.1226 (0.7 ppm error).

Characteristic NMR resonances for the minor *E*-isomer can be found at: δ_{H} 2.44 (3 H, s, H-10, *E*), 3.30 (3 H, s, H-1, *E*), 6.24 (1 H, s, H-12, *E*).

7.3.5 Gold-pyrylium Complex

3-Acetyl-2,4-bis(4-(dimethylamino)phenyl)-6-methylpyryl-5-yl(triphenylphosphine)gold(I) bis[(trifluoromethane)sulfonyl]azanide (**3.102**)



For the ^1H , ^{19}F and ^{31}P NMR spectra, the clearest data for the *title product* was observed when a more dilute sample was prepared, using 4 equivalents (a 2-fold excess) of the starting ynone. As such, to a sample vial, 4-(4-(dimethylamino)phenyl)but-3-yn-2-one **3.34** (15 mg, 0.08 mmol) was dissolved in d_2 -DCM (0.6 mL), and [bis(trifluoromethanesulfonyl)imidate]-(triphenylphosphine)gold(I) (2:1) toluene adduct (16 mg, 0.01 mmol) was added, which resulted in an immediate colour change to dark red. The sample was transferred to an NMR tube and ^1H , ^{19}F and ^{31}P data were recorded immediately.

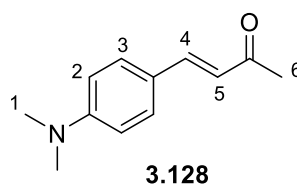
For the ^{13}C NMR spectra, a more concentrated sample was prepared using the same method, with 4-(4-(dimethylamino)phenyl)but-3-yn-2-one **3.34** (78 mg, 0.4 mmol) and [bis(trifluoromethanesulfonyl)-imidate](triphenylphosphine)gold(I) (2:1) toluene adduct (163 mg, 0.1 mmol). After transferring the sample to an NMR tube, ^{13}C NMR data was recorded immediately.

ν_{max} (thin film)/ cm^{-1} 2910, 1705, 1597, 1423, 1348, 1137, 1056; δ_{H} (400 MHz; CD_2Cl_2) 2.05 (3 H, s, H-13), 2.97 (6 H, s, H-11 or H-18), 3.03 (3 H, s, H-6), 3.13 (6 H, s, H-11 or H-18), 6.54 – 6.59 (2 H, m, H-9 or H-16), 6.76 – 6.80 (2 H, m, H-9 or H-16), 7.35 – 7.50 (15 H, m, PPh_3), 7.57 – 7.61 (2 H, m, H-8 or H-15), 7.69 – 7.73 (2 H, m, H-8 or H-15); δ_{C} (100 MHz; CD_2Cl_2) 25.9 (C-13), 32.1 (C-6), 40.1 (C-11 or C-18), 40.2 (C-11 or C-18), 111.5 (C-9 or C-16), 111.2 (C-9 or C-16), 115.7 (C-7 or C-14), 120.3 (q, $^1J_{\text{C-F}} = 322.0$, C-23), 127.2 (C-7 or C-14), 129.6 (d, $^3J_{\text{C-P}} = 11.5$, C-21), 129.8 (d, $^1J_{\text{C-P}} = 55.0$, C-19), 131.0 (d, $^4J_{\text{C-P}} = 4.0$, C-2), 131.7 (C-8 or C-15), 131.8 (C-8 or C-15), 132.2 (d, $^4J_{\text{C-P}} = 2.0$, C-22), 134.4 (d, $^2J_{\text{C-P}} = 13.5$, C-20), 152.4 (C-10 or C-17), 154.1 (C-10 or C-17), 161.4 (d, $^2J_{\text{C-P}} = 111.0$, C-4), 165.5 (C-3), 172.1 (C-1), 175.7 (d, $^3J_{\text{C-P}} = 5.0$, C-5), 202.3 (C-12); δ_{P} (162 MHz; CD_2Cl_2)

41.9; δ_F (376 MHz; CD_2Cl_2) -79.4; HRMS (ESI⁺) Found: 833.2579; $C_{42}H_{41}AuN_2O_2P$ (M^+) Requires 833.2566 (-1.6 ppm error).

Note that toluene is present in the 1H and ^{13}C NMR spectra due to its inclusion in the crystal structure of gold triflimide.

(E)-4-(4-(dimethylamino)phenyl)but-3-en-2-one (3.128)

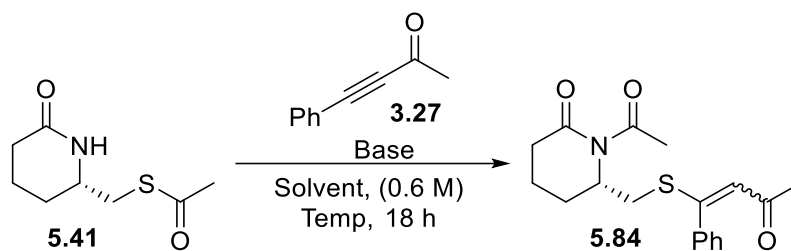


Following a literature procedure,²²⁴ 4-(4-(dimethylamino)phenyl)but-3-yn-2-one **3.34** (37 mg, 0.2 mmol) and [bis(trifluoromethanesulfonyl)imidate](triphenylphosphine)gold(I) (2:1) toluene adduct (8 mg, 0.005 mmol) were dissolved in dry toluene (1 mL) under an atmosphere of argon and diethyl 2,6-dimethyl-1,4-dihydropyridine-3,5-dicarboxylate (HEH, 30 mg, 0.1 mmol) was added. The reaction was stirred at room temperature for 24 hours before being concentrated *in vacuo*. The product was purified via flash column chromatography (9:1 toluene/diethyl ether) to give the *title product* as a mixture with oxidised HEH **3.129** as an orange solid (45 mol% **3.128** by ¹H NMR, 19 mg of mixture, calculated 7 mg of product, 32%). *R*_f(toluene/diethyl ether 9:1) 0.40; δ_H (400 MHz; CDCl₃) 2.35 (3 H, s, H-6), 3.03 (6 H, s, H-1), 6.55 (1 H, d, *J* = 16.0 Hz, H-5), 6.65 – 6.70 (2 H, m, H-2), 7.42 – 7.47 (2 H, m, H-3), 7.47 (1 H, d, *J* = 16.0 Hz, H-4). Spectroscopic data match those reported previously.³⁶⁰

7.4 S-Acyl Transfer

7.4.1 General Procedures

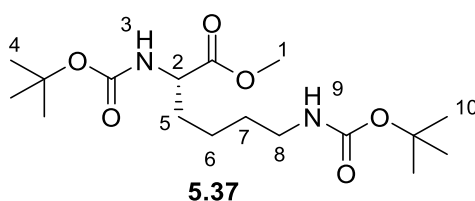
General Procedure K: S-Acyl Transfer Reaction Optimisation



Lactam **5.41** (37 mg, 0.2 mmol) was dissolved in the desired solvent (0.3 mL, 0.6 M), and the desired quantity of 4-phenyl-3-butyne-2-one **3.27** was added, followed by the chosen base. The reaction was stirred at the chosen temperature for 18 hours, then trimethoxybenzene (100 μ L, 0.2 M in DCM) was added before the solvent was concentrated *in vacuo*. ^1H NMR spectra were then recorded to determine the conversion of lactam **5.41** to the desired product **5.84**.

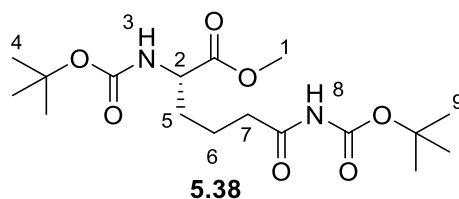
7.4.1 Lactam Synthesis

Methyl N^2,N^6 -bis(*tert*-butoxycarbonyl)-*L*-lysinate (**5.37**)



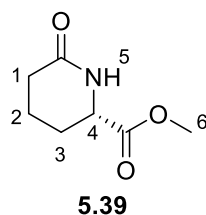
Following a literature procedure,³¹⁷ to a dry round-bottomed flask, (*S*)-lysine methyl ester dihydrochloride salt **5.36** (2.331 g, 10.0 mmol) was dissolved in dry MeOH (50 mL) under an atmosphere of argon. Di-*tert*-butyl dicarbonate (5.456 g, 25.0 mmol) and sodium hydrogen carbonate (5.041 g, 60 mmol) were added, and the mixture was stirred at room temperature for 24 hours. The reaction mixture was filtered and concentrated *in vacuo*. Diethyl ether (150 mL) was added to the residue, and the solution filtered through Celite and concentrated *in vacuo*. The crude product was purified *via* flash column chromatography (hexane/ethyl acetate 3:1) to yield the *title product* as a white solid (3.242 g, 90%). R_f (hexane/ethyl acetate 3:1) 0.34; δ_H (400 MHz; $CDCl_3$) 1.28 – 1.55 (4 H, m, H-6,7), 1.43 (18 H, s, H-4,10), 1.59 – 1.69 (1 H, m, H-5a), 1.73 – 1.83 (1 H, m, H-5b), 3.09 (2 H, app. q, $J = 6.5$, H-8), 3.72 (3 H, s, H-1), 4.22 – 4.31 (1 H, m, H-2), 4.61 (1 H, app. br s, H-9), 5.11 (1 H, br d, $J = 6.5$, H-3). Spectroscopic data match those reported previously.³¹⁷

Methyl (S)-2,6-bis((tert-butoxycarbonyl)amino)-6-oxohexanoate (5.38)



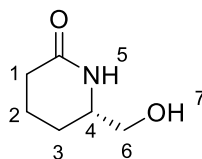
Following a literature procedure,³¹⁷ to a dry round-bottomed flask, **5.37** (3.242 g, 9.0 mmol) was dissolved in ethyl acetate (30 mL). A sodium periodate solution (10% w/w in H₂O, 100 mL) and ruthenium(III) chloride (187 mg, 0.9 mmol) were added, and the biphasic mixture was stirred at room temperature for 18 hours. The reaction mixture was extracted with ethyl acetate (3 x 50 mL). The organic extracts were combined and stirred with *iso*-propanol (20 mL) for 2 hours. The mixture was filtered through Celite and concentrated *in vacuo*. The crude product was purified *via* flash column chromatography (hexane/ethyl acetate 2:1) to yield the *title product* as a yellow oil (1.811 g, 54%). *R_f* (hexane/ethyl acetate 2:1) 0.22; δ_{H} (400 MHz; CDCl₃) 1.45 (9 H, s, H-4/9), 1.49 (9 H, s, H-4/9), 1.63 – 1.76 (3 H, m, H-5a,6), 1.79 – 1.92 (1 H, m, H-5b), 2.66 – 2.83 (2 H, m, H-7), 3.75 (3 H, s, H-1), 4.27 – 4.36 (1 H, m, H-2), 5.12 (1 H, br d, *J* = 8.5, H-3), 7.35 (1 H, br s, H-8). Spectroscopic data match those reported previously.³¹⁷

Methyl (S)-6-oxopiperidine-2-carboxylate (5.39)



Following a literature procedure,³¹⁷ to a dry round-bottomed flask, **5.38** (1.811 g, 4.8 mmol) was dissolved in trifluoroacetic acid (40 mL) and refluxed for 18 hours. The reaction mixture was cooled and concentrated *in vacuo*. The crude product was purified *via* flash column chromatography (ethyl acetate to ethyl acetate/methanol 96:4) to yield the *title product* as a yellow oil (754 mg, 100%). R_f (ethyl acetate/methanol 96:4) 0.25; δ_H (400 MHz; $CDCl_3$) 1.73 – 1.96 (3 H, m, H-Alk), 2.13 – 2.17 (1 H, m, H-Alk), 2.32 – 2.49 (2 H, m, H-Alk), 3.79 (3 H, s, H-6), 4.12 (1 H, dd, $J = 7.5, 6.0$, H-4), 6.50 (1 H, br s, H-5). Spectroscopic data match those reported previously.³¹⁷

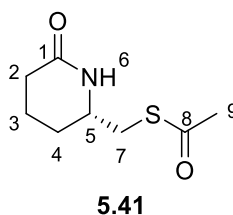
(S)-6-(Hydroxymethyl)piperidin-2-one (5.18)



5.18

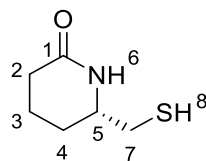
Following a literature procedure,³¹⁷ to a dry round-bottomed flask, **5.39** (754 mg, 4.8 mmol) was dissolved in dry ethanol (48 mL) under an atmosphere of argon and cooled to 0 °C. Sodium borohydride (352 mg, 9.3 mmol) was added and the reaction was brought to room temperature, and stirred for 24 hours. Acetic acid (1 mL) was added, and the reaction was stirred for a further 19 hours. The reaction mixture was concentrated *in vacuo* and the residue was redissolved in DCM (100 mL). The mixture was dried using K₂CO₃, filtered and concentrated *in vacuo*. The crude product was purified *via* flash column chromatography (ethyl acetate/methanol 95:5 to 7:3) to yield the *title product* as a pale, brown solid (554 mg, 73%). *R_f*(ethyl acetate/methanol 7:3) 0.42; δ_{H} (400 MHz; CDCl₃) 1.31 – 1.41 (1 H, m, H-2a), 1.67 – 1.81 (1 H, m, H-Alk), 1.80 – 1.96 (2 H, m, H-Alk), 2.28 (1 H, ddd, *J* = 17.5, 11.0, 6.0, H-3a), 2.42 (1 H, dddd, *J* = 17.5, 5.5, 3.5, 1.5, H-3b), 3.46 (1 H, dd, *J* = 10.5, 8.5, H-6a), 3.50 – 3.58 (1 H, m, H-4), 3.70 (1 H, dd, *J* = 10.5, 3.0, H-6b), 6.96 (1 H, br s, H-5). Spectroscopic data match those reported previously.³¹⁷

(S)-S-((6-Oxopiperidin-2-yl)methyl) ethanethioate (5.41)



Based on a literature procedure,³¹⁸ to a dry round-bottomed flask, triphenylphosphine (1.364 g, 5.2 mmol) and DIAD (1.00 mL, 1.051 g, 5.2 mmol) were dissolved in dry THF (17 mL) under an atmosphere of argon and cooled to 0 °C. The mixture was stirred for 20 minutes before a solution of **5.18** (554 mg, 4.3 mmol) and thioacetic acid (0.36 mL, 393 mg, 5.2 mmol) in dry THF (10 mL) was added (Note: **5.18** is sparingly soluble in THF and required mild heating to fully dissolve). The reaction mixture was brought to room temperature and stirred for 18 hours. The reaction mixture was concentrated *in vacuo*. The crude product was purified *via* flash column chromatography (ethyl acetate to ethyl acetate/methanol 95:5) to yield the *title product* as a pale, brown solid (719 mg, 89%). R_f (ethyl acetate) 0.14; mp 68 – 70 °C; ν_{\max} (thin film)/ cm^{-1} 3212, 2949, 2875, 1689, 1656, 1329, 1306, 625; δ_{H} (400 MHz; CDCl_3) 1.42 – 1.52 (1 H, m, H-4a), 1.65 – 1.77 (1 H, m, H-3a), 1.88 – 2.01 (2 H, m, H-3b,4b), 2.25 – 2.35 (1 H, m, H-2a), 2.36 – 2.44 (1 H, m, H-2b), 2.38 (3 H, s, H-9), 2.84 (1 H, dd, $J = 14.0, 7.0$, H-7a), 3.17 (1 H, dd, $J = 14.0, 5.0$, H-7b), 3.51 – 3.59 (1 H, m, H-5), 5.84 (1 H, br s, H-6); δ_{C} (126 MHz; CDCl_3) 19.3 (C-3), 27.4 (C-4), 30.7 (C-9), 31.2 (C-2), 34.7 (C-7), 52.3 (C-5), 172.4 (C-1), 195.0 (C-8); HRMS (ESI⁺) Found: 188.0741; $\text{C}_8\text{H}_{14}\text{NO}_2\text{S}$ (M+H⁺) Requires 188.0740 (–0.5 ppm error); Found: 210.0561; $\text{C}_8\text{H}_{13}\text{NNaO}_2\text{S}$ (M+Na) Requires 210.0559 (–1.0 ppm error).

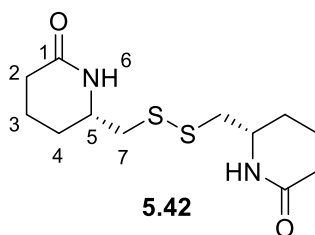
(S)-6-(Mercaptomethyl)piperidin-2-one (5.21)



5.21

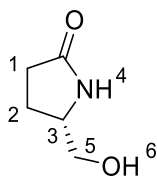
To a dry round-bottomed flask, **5.41** (56 mg, 0.3 mmol) was dissolved in degassed MeOH (1.5 mL) under an atmosphere of argon and a degassed solution of aq. NaOH (1 M, 0.3 mL) was added. The mixture was stirred at room temperature for 1 hour. A solution of aq. HCl (1 M, 0.3 mL) was added, followed by saturated aq. NaCl (10 mL). The product was extracted with ethyl acetate (3 x 10 mL), dried using MgSO₄ and concentrated *in vacuo*. The crude product was purified *via* flash column chromatography (ethyl acetate to ethyl acetate/methanol 95:5) to yield the *title product* as a white solid (38 mg, 86%). *R_f*(ethyl acetate/methanol 95:5) 0.41; mp 74 – 76 °C; ν_{\max} (thin film)/cm⁻¹ 3186, 3077, 2949, 2580, 1650, 1311, 809; δ_{H} (400 MHz; CDCl₃) 1.40 – 1.51 (1 H, m, H-H-3a), 1.44 (1 H, dd, *J* = 10.0, 7.5, H-8), 1.62 – 1.74 (1 H, m, H-4a), 1.83 – 1.91 (1 H, m, H-3b), 1.92 – 2.00 (1 H, m, H-4b), 2.20 – 2.31 (1 H, m, H-2a), 2.36 (1 H, dddd, *J* = 17.5, 5.5, 4.0, 1.5, H-2b), 2.48 (1 H, ddd, *J* = 13.5, 10.0, 7.5, H-7a), 2.70 (1 H, ddd, *J* = 13.5, 7.5, 5.5, H-7b), 3.36 – 3.44 (1 H, m, H-5), 7.00 (1 H, br s, H-6); δ_{C} (100 MHz; CDCl₃) 19.5 (C-3), 27.5 (C-4), 30.8 (C-2), 31.4 (C-7), 55.0 (C-5), 172.7 (C-1); HRMS (ESI⁺) Found: 146.0634; C₆H₁₂NOS (M+H⁺) Requires 146.0634 (0.0 ppm error); Found: 168.0455; C₆H₁₁NNaOS (M+H⁺) Requires 168.0454 (-0.7 ppm error).

(6*S*,6'*S*)-6,6'-(Disulfanediy)bis(methylene))bis(piperidin-2-one) (5.42)



This is a side product formed during the synthesis of **5.21** when the solvents were not degassed, performed at the same scale as described above, with **5.41** (56 mg, 0.3 mmol) in MeOH (1.5 mL) and aq. NaOH (1 M, 0.3 mL). Purification by flash column chromatography ethyl acetate to ethyl acetate/methanol 7:3) yielded the *title product* as a white solid (7 mg, 17%). R_f (ethyl acetate/methanol 7:3) 0.41; mp 130 – 131 °C; ν_{\max} (thin film)/ cm^{-1} 3402, 3193, 2949, 2871, 1652, 1404, 1331, 1308; δ_{H} (400 MHz; CDCl_3) 1.42 – 1.54 (2 H, m, H-H-3a), 1.67 – 1.84 (2 H, m, H-4a), 1.85 – 1.94 (2 H, m, H-3b), 1.94 – 2.02 (2 H, m, H-4b), 2.24 – 2.34 (2 H, m, H-2a), 2.36 – 2.45 (2 H, m, H-2b), 2.63 (2 H, dd, $J = 13.5, 8.5$, H-7a), 2.86 (2 H, dd, $J = 13.5, 4.5$, H-7b), 3.63 – 3.72 (2 H, m, H-5), 6.45 (1 H, br s, H-6); δ_{C} (100 MHz; CDCl_3) 19.6 (C-3), 28.1 (C-4), 31.5 (C-2), 44.7 (C-7), 51.2 (C-5), 172.2 (C-1); HRMS (ESI⁺) Found: 289.1039; $\text{C}_{12}\text{H}_{21}\text{N}_2\text{O}_2\text{S}_2$ (M+H⁺) Requires 289.1039 (–0.1 ppm error); Found: 311.0857; $\text{C}_{12}\text{H}_{20}\text{N}_2\text{NaO}_2\text{S}_2$ (M+Na) Requires 311.0858 (0.3 ppm error).

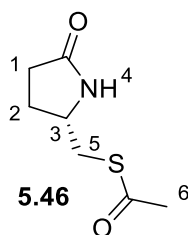
(S)-5-(Hydroxymethyl)pyrrolidin-2-one (5.45)



5.45

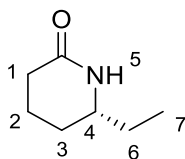
Following a literature procedure,³²¹ (S)-pyroglutamic acid **5.43** (2.581 g, 20.0 mmol) was suspended in dry ethanol (9 mL) under an atmosphere of argon and cooled to 0 °C. Thionyl chloride (1.8 mL, 2.855 g, 24.0 mmol) was added and the reaction was brought to room temperature and stirred for 20 hours. The reaction mixture was concentrated *in vacuo*, and the residue was redissolved in ethyl acetate (50 mL), dried over K₂CO₃, filtered and concentrated *in vacuo*. The crude ethyl ester **5.44** (3.143 g) was dissolved in dry ethanol (16 mL) under an atmosphere of argon and cooled to 0 °C. Sodium borohydride (1.740 g, 46.0 mmol) was added, and the reaction was brought to room temperature and stirred for 20 hours. Acetic acid (6 mL) was added and the reaction was filtered and concentrated *in vacuo*. The crude product was purified *via* flash column chromatography (DCM/methanol 96:4 to 9:1) to yield the *title product* as a brown oil (1.116 g, 48%). *R_f*(DCM/methanol 9:1) 0.31; δ_{H} (400 MHz; CDCl₃) 1.75- 1.89 (1 H, m, H-1/2), 2.13 – 2.27 (1 H, m, H-1/2), 2.28 – 2.47 (2 H, m, H-1/2), 3.43 – 3.55 (1 H, m, H-5a), 3.66 – 3.76 (1 H, m, H-5b), 3.78 – 3.88 (1 H, m, H-3), 6.88 – 7.25 (1 H, br m, H-4). Spectroscopic data match those reported previously.³⁶¹

(S)-S-((5-Oxopyrrolidin-2-yl)methyl) ethanethioate (5.46)



Based on a literature procedure,³¹⁸ to a dry round-bottomed flask, triphenylphosphine (2.990 g, 11.4 mmol) and DIAD (2.2 mL, 2.305 g, 11.4 mmol) were dissolved in dry THF (38 mL) under an atmosphere of argon and cooled to 0 °C. The mixture was stirred for 20 minutes before a solution of **5.45** (1.094 g, 9.5 mmol) and thioacetic acid **5.40** (0.8 mL, 868 mg, 11.4 mmol) in dry THF (21 mL) was added. The reaction mixture was brought to room temperature and stirred for 18 hours. The reaction mixture was concentrated *in vacuo*. The crude product was purified *via* flash column chromatography (ethyl acetate) to yield the *title product* as a yellow oil (1.144 g, 70%). R_f (ethyl acetate) 0.18; δ_H (400 MHz; CDCl₃) 1.75 – 1.87 (1 H, m, H-1/2), 2.25 – 2.49 (3 H, m, H-1,2), 2.38 (3 H, s, H-6), 2.90 (1 H, dd, $J = 14.0, 6.0$, H-5a), 3.18 (1 H, dd, $J = 14.0, 5.0$, H-5b), 3.84 – 3.92 (1 H, m, H-3), 5.92 (1 H, br s, H-4). Spectroscopic data match those reported previously.³¹⁸

6-Ethylpiperidin-2-one (5.48)

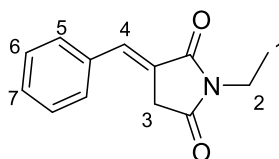


5.48

Following a literature procedure,³²² to a dry round-bottomed flask, piperidine-2,6-dione **5.47** (1.450 g, 12.8 mmol) was dissolved in dry THF (51 mL) under an atmosphere of argon and cooled to 0 °C. Ethyl magnesium bromide (13 mL, 38.5 mmol, 3 M in Et₂O) was added and the reaction was brought to room temperature and stirred for 19 hours. Sodium cyanoborohydride (885 mg, 14.1 mmol) and acetic acid (3.7 mL, 3.843 g, 64.0 mmol) were added and stirred at room temperature for 1 hour. A saturated aq. NaHCO₃ solution (50 mL) was added, and the product was extracted with ethyl acetate (3 x 50 mL), dried using Na₂SO₄ and concentrated *in vacuo*. The crude product was purified *via* flash column chromatography (diethyl ether to diethyl ether/methanol 98:2) to yield the *title product* as a white solid (770 mg, 47%). *R_f* (diethyl ether/methanol 98:2) 0.28; δ_H (500 MHz; CDCl₃) 0.95 (3 H, t, *J* = 7.5, H-7), 1.31 – 1.41 (1 H, m, H-Alk), 1.52 (2 H, pent., *J* = 7.5, H-6), 1.64 – 1.75 (1 H, m, H-Alk), 1.87 – 1.96 (2 H, m, H-Alk), 2.29 (1 H, ddd, *J* = 17.5, 11.0, 6.0, H-1a), 2.36 – 2.44 (1 H, m, H-1b), 3.26 – 3.33 (1 H, m, H-4), 5.85 (1 H, br s, H-5). Spectroscopic data match those reported previously.³²²

7.4.2 Michael Acceptor Synthesis

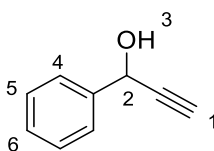
(E)-3-Benzylidene-1-ethylpyrrolidine-2,5-dione (5.50)



5.50

Following a literature procedure,³²⁴ *N*-ethyl maleimide **5.49** (125 mg, 1.0 mmol) and triphenylphosphine (315 mg, 1.2 mmol) were dissolved in ethanol (8 mL) and stirred for 5 minutes. Benzaldehyde **1.36** (0.14 mL, 144 mg, 1.4 mmol) was added and the reaction mixture was stirred at room temperature for 18 hours. The mixture was concentrated *in vacuo* and the crude product was purified *via* flash column chromatography (hexane/ethyl acetate 8:2 to 7:3) to yield the *title product* as a white solid (147 mg, 68%). R_f (hexane/ethyl acetate 8:2) 0.37; δ_H (400 MHz; CDCl₃) 1.26 (3 H, t, $J = 7.5$, H-1), 3.58 (2 H, d, $J = 2.5$, H-3), 3.71 (2 H, q, $J = 7.5$, H-2), 7.40 – 7.53 (5 H, m, H-Ar), 7.63 (1 H, t, $J = 2.5$, H-4). Spectroscopic data match those reported previously.³²⁴

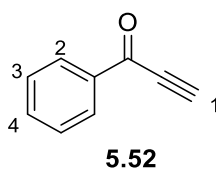
1-Phenylprop-2-yn-1-ol (1.5)



1.5

Following a literature procedure,³²⁷ benzaldehyde **1.36** (1.0 mL, 1.061 g, 1.0 mmol) was dissolved in dry THF (20 mL) under an atmosphere of argon and cooled to -78 °C. Ethynyl magnesium bromide (48 mL, 24.0 mmol, 0.5 M in THF) was added and the reaction mixture was brought to room temperature and stirred for 2.5 hours. The reaction was quenched with saturated aq. NH₄Cl (50 mL) and the product was extracted with DCM (3 x 50 mL). The organic extracts were combined and dried over MgSO₄, filtered and concentrated *in vacuo*. The crude product was purified *via* flash column chromatography (DCM/hexane 4:1) to yield the *title product* as a pale, yellow oil (1.073 g, 81%). R_f (DCM/hexane 4:1) 0.33; δ_H (400 MHz; CDCl₃) 2.19 (1 H, d, $J = 6.5$, H-3), 2.69 (1 H, d, $J = 2.5$, H-1), 5.49 (1 H, dd, $J = 6.5, 2.5$, H-2), 7.33 – 7.43 (3 H, m, H-5,6), 7.55 – 7.99 (2 H, m, H-4). Spectroscopic data match those reported previously.³²⁷

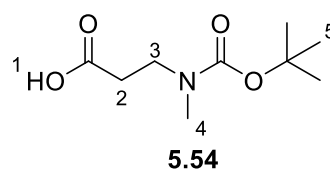
1-Phenylprop-2-yn-1-one (5.52)



Following a literature procedure,³²⁶ 1-phenylprop-2-yn-1-ol **1.5** (1.073 g, 8.1 mmol) was dissolved in DCM (27 mL) and activated magnesium oxide (4.929 g, 56.7 mmol) was added. The reaction mixture was stirred at room temperature for 20 hours, then filtered through Celite and concentrated *in vacuo*. The crude product was purified *via* flash column chromatography (hexane/ethyl acetate 30:1) to yield the *title product* as a pale, brown solid (451 mg, 43%). R_f (hexane/ethyl acetate 30:1) 0.30; δ_H (400 MHz; $CDCl_3$) 3.45 (1 H, s, H-1), 7.49 – 7.55 (2 H, m, H-3), 7.62 – 7.68 (1 H, m, H-4), 8.16 – 8.20 (2 H, m, H-2). Spectroscopic data match those reported previously.³²⁶

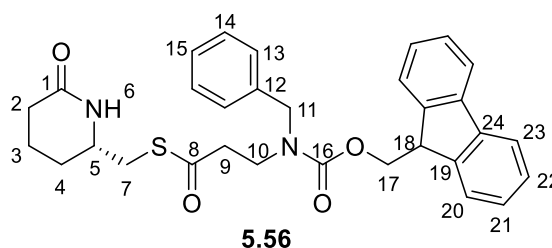
7.4.3 Thiol Coupling

3-((*tert*-Butoxycarbonyl)(methyl)amino)propanoic acid (**5.54**)



Following a literature procedure,³²⁸ to a dry round-bottomed flask, *N*-Boc β-alanine **5.53** (946 mg, 5.0 mmol) and methyl iodide (3.2 mL, 7.097 g, 50.0 mmol) were dissolved in dry THF (50 mL) under an atmosphere of argon. The reaction mixture was cooled to 0 °C and sodium hydride (2.000 g, 50.0 mmol, 60% w/w dispersion in mineral oil) was added. The reaction mixture was stirred for 30 minutes before being brought to room temperature and stirred for a further 17 hours. The reaction was quenched with the addition of deionised water (50 mL) and the organic soluble impurities were extracted with ethyl acetate (4 x 50 mL). The aqueous extract was acidified to pH = 3 with aq. HCl (1 M, 10 mL) and extracted with ethyl acetate (3 x 50 mL). The organic extracts were combined and dried over Na₂SO₄, filtered and concentrated *in vacuo*. The *title product* was isolated as a brown oil without further purification (938 mg, 92%). δ_H (400 MHz; CDCl₃) 1.46 (9 H, s, H-5), 2.59 – 2.67 (2 H, br m, H-2), 2.90 (3 H, s, H-4), 3.53 (2 H, t, *J* = 7.0, H-3). Spectroscopic data match those reported previously.³²⁸

(S)-S-((6-Oxopiperidin-2-yl)methyl) 3-(((9H-fluoren-9-yl)methoxy)carbonyl)(benzyl) amino)propanethioate (5.56)



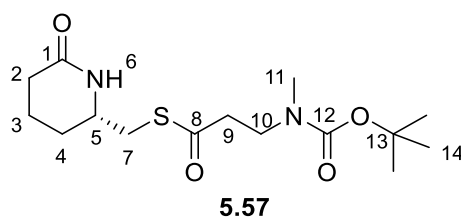
Based on a reported procedure,³⁰⁴ to a dry round-bottomed flask, **5.55** (161 mg, 0.4 mmol), HATU (152 mg, 0.4 mmol) and DIPEA (70 μ L, 52 mg, 0.3 mmol) were dissolved in dry DMF (1 mL) under an atmosphere of argon. To this a solution of **5.21** (44 mg, 0.3 mmol) in dry DMF (1.3 mL) under an atmosphere of argon, was added and the reaction was stirred at room temperature for 4 hours. The reaction was concentrated *in vacuo*, then the residue was dissolved in ethyl acetate (20 mL) and deionised water (10 mL) was added. The product was extracted with ethyl acetate (5 x 10 mL). The organic extracts were combined and washed with sat. aq. NaCl (3 x 20 mL), dried with MgSO₄, filtered, and concentrated *in vacuo*. The crude product was purified *via* flash column chromatography (ethyl acetate) to give the *title product* as a mixture with tetramethylurea as an orange oil (75 mol% **5.56** by ¹H NMR, 98 mg of mixture, calculated 90 mg of product, 57%.)

To avoid the impurity, **5.56** was made using an alternative method. To a dry round-bottomed flask, **5.55** (161 mg, 0.4 mmol), T3P (235 mg, 0.4 mmol, 50% w/w in ethyl acetate) and DIPEA (0.1 mL, 78 mg, 0.6 mmol) were dissolved in dry DCM (4 mL) under an atmosphere of argon. To this a solution of **5.21** (44 mg, 0.3 mmol) in dry DCM (0.6 mL) under an atmosphere of argon, was added and the reaction was stirred at room temperature for 21 hours. The reaction was diluted with deionised water (15 mL) and the product was extracted with ethyl acetate (3 x 15 mL). The organic extracts were dried with MgSO₄, filtered, and concentrated *in vacuo*. The crude product was purified *via* flash column chromatography (ethyl acetate) to yield the *title product* as an orange oil, which exists as a mixture of rotamers in CDCl₃ (denoted as A and B) (86 mg, 54%, A:B = 1.1:1). *R*_f(ethyl acetate) 0.20; ν_{\max} (thin film)/cm⁻¹ 3280, 3065, 2950, 1692, 1660, 1476, 1451, 1419, 736; δ_{H} (400 MHz; CDCl₃) 1.35 – 1.48 (2 H, m, H-4a, A and B), 1.61 – 1.74 (2 H, m, H-3a, A and B), 1.82 – 1.96 (4 H, m, H-3b,4b, A and B), 2.23 – 2.33 (2 H, m, H-2a, A and B), 2.33 – 2.43 (4 H, m, H-2b, A and B, and H-9, B), 2.79 – 2.90 (4 H, m, H-7a, A and B, and H-9, A), 3.03 – 3.13 (2 H, m, H-7b, A and B), 3.21 (2 H, t, *J* = 6.5, H-10, B), 3.44 – 3.51 (2 H, m, H-5, A and B), 3.55

(2 H, t, $J = 6.5$, H-10, A), 4.22 (1 H, t, $J = 6.0$, H-18, A), 4.26 (1 H, t, $J = 5.0$, H-18, B), 4.37 (2 H, s, H-11, A), 4.40 (2 H, s, H-11, B), 4.53 (2 H, d, $J = 6.0$, H-17, A), 4.68 (2 H, d, $J = 5.0$, H-17, B), 6.26 (1 H, br s, H-6, A), 6.30 (1 H, br s, H-6, B), 7.00 – 7.07 (2 H, m, H-Ar, A), 7.10 – 7.16 (2 H, m, H-Ar, B), 7.21 – 7.50 (X H, m, H-Ar, A and B), 7.61 (2 H, d, $J = 7.5$, H-23, B), 7.73 (2 H, d, $J = 7.5$, H-20, A), 7.77 (2 H, d, $J = 7.5$, H-20, B); δ_C (100 MHz; CDCl₃) 19.3 (2 x C-3, A and B), 27.6 (2 x C-4, A and B), 31.3 (2 x C-2, A and B), 34.7 (2 x C-7, A and B), 42.4 (C-9, A or C-10, B), 42.5 (C-9, A or C-10, B), 42.6 (C-9, B), 43.7 (C-10, A), 47.3 (C-18, A or B), 47.6 (C-18, A or B), 51.1 (C-11, A or B), 51.3 (C-11, A or B), 52.3 (C-5, A or B), 52.4 (C-5, A or B), 66.9 (C-17, B), 67.5 (C-17, A), 120.0 (C-20, A or B), 120.1 (C-20, A or B), 124.8 (C-23, A or B), 124.9 (C-23, A or B), 127.1 (CH, C-Ar, A or B), 127.3 (CH, C-Ar, A or B), 127.6 (CH, C-Ar, A or B), 127.7 (CH, C-Ar, A or B), 127.8 (CH, C-Ar, A or B), 127.9 (CH, C-Ar, A or B), 128.7 (CH, C-Ar, A or B), 128.8 (CH, C-Ar, A or B), 137.3 (C-12, A), 137.4 (C-12, B), 141.4 (C, C-19/24, A or B), 141.5 (C, C-19/24, A and B), 143.9 (2 x C, C-19/24, A and B), 156.1 (C-16, A), 156.3 (C-16, B), 172.3 (2 x C-1, A and B), 196.6 (C-8, B), 196.9 (C-8, A); HRMS (ESI⁺) Found: 529.5127; C₃₁H₃₃N₂O₄S (M+H⁺) Requires 529.5216 (–0.3 ppm error); Found: 551.1967; C₃₁H₃₂N₂NaO₄S (M+Na) Requires 551.1975 (1.4 ppm error).

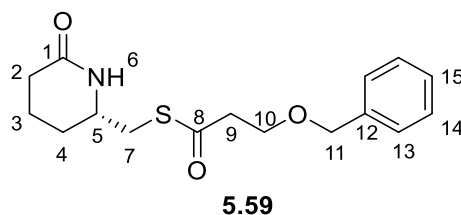
Note that two aromatic CH carbon resonances could not be found in the ¹³C NMR spectra. It is believed that they are overlapping with other resonances.

(S)-S-((6-Oxopiperidin-2-yl)methyl) 3-((tert-butoxycarbonyl)(methyl)amino) propanethioate
(5.57)



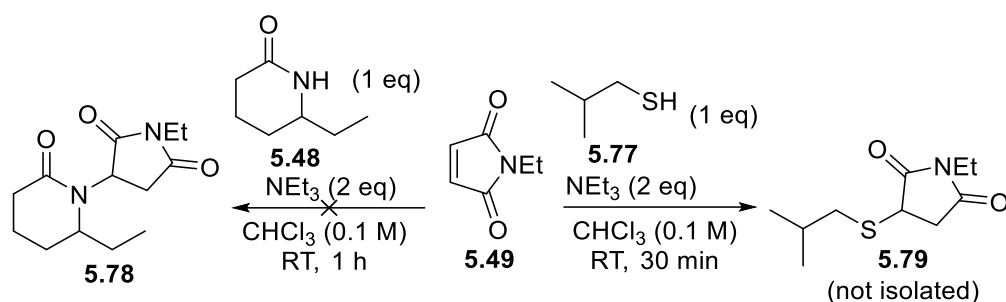
To a dry round-bottomed flask, **5.54** (87 mg, 0.6 mmol), T3P (955 mg, 1.5 mmol, 50% w/w in ethyl acetate) and DIPEA (0.4 mL, 310 mg, 2.4 mmol) were dissolved in dry DCM (15 mL) under an atmosphere of argon. To this a solution of **5.21** (87 mg, 0.6 mmol) in dry DCM (1 mL) under an atmosphere of argon, was added and the reaction was stirred at room temperature for 21 hours. The reaction was diluted with deionised water (5 mL) and the product was extracted with ethyl acetate (3 x 20 mL). The organic extracts were dried with MgSO₄, filtered, and concentrated *in vacuo*. The crude product was purified *via* flash column chromatography (ethyl acetate/acetic acid 98:2) to yield the *title product* as a yellow oil (103 mg, 52%). Note that the ¹³C NMR spectrum showed that the product exists as a mixture of rotamers in CDCl₃ (*A* and *B*). The rotamers are indistinguishable in the ¹H NMR spectrum, however based on the ¹³C NMR spectrum, the rotamers are approximately in a 1:1 ratio. *R_f* (ethyl acetate/acetic acid 98:2) 0.30; *v*_{max} (thin film)/cm⁻¹ 3218, 2933, 1688, 1660, 1480, 1146, 728; δ_{H} (400 MHz; CDCl₃) 1.31 – 1.45 (10 H, m, H-4a,14, *A* and *B*), 1.57 – 1.69 (1 H, m, H-3, *A* and *B*), 1.79 – 1.91 (2 H, m, H-3b,4b, *A* and *B*), 2.17 – 2.27 (1 H, m, H-2a, *A* and *B*), 2.27 – 2.35 (1 H, m, H-2b, *A* and *B*), 2.67 – 2.83 (5 H, m, H-8/9 and 11, *A* and *B*), 2.83 – 2.93 (1 H, m, H-7a, *A* and *B*), 3.06 (1 H, dd, *J* = 14.0, 5.5, H-7b, *A* and *B*), 3.38 – 3.55 (3 H, m, H-5 and 8/9, *A* and *B*), 6.59 (1 H, br s, H-6, *A* and *B*); δ_{C} (100 MHz; CDCl₃) 18.9 (2 x C-3, *A* and *B*), 26.5 (2 x C-4, *A* and *B*), 27.9 (2 x C-14, *A* and *B*), 30.7 (2 x C-2, *A* and *B*), 33.8 (2 x C-7, *A* and *B*), 34.4 (C-11, *A* or *B*), 34.6 (C-11, *A* or *B*), 41.9 (C-9/10, *A* or *B*), 42.3 (C-9/10, *A* or *B*), 44.9 (C-9/10, *A* or *B*), 51.8 (2 x C-5, *A* and *B*), 79.2 (2 x C-13, *A* and *B*), 154.8 (C-12, *A* or *B*), 154.9 (C-12, *A* or *B*), 172.2 (2 x C-1, *A* and *B*), 196.2 (C-8, *A* or *B*), 196.4 (C-8, *A* or *B*); HRMS (ESI⁺) Found: 353.1500; C₁₅H₂₆N₂NaO₄S (M+Na) Requires 353.1505 (1.7 ppm error).

(S)-S-((6-Oxopiperidin-2-yl)methyl) 3-(benzyloxy)propanethioate (5.59)

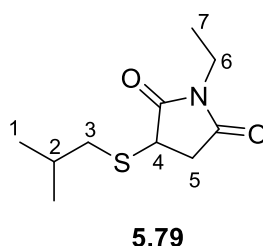


To a dry round-bottomed flask, 3-(benzyloxy)propanoic acid **5.58** (270 mg, 1.5 mmol), T3P (955 mg, 1.5 mmol, 50% w/w in ethyl acetate) and DIPEA (0.4 mL, 310 mg, 2.4 mmol) were dissolved in dry DCM (15 mL) under an atmosphere of argon. To this a solution of **5.21** (87 mg, 0.6 mmol) in dry DCM (1 mL) under an atmosphere of argon, was added and the reaction was stirred at room temperature for 21 hours. The reaction was diluted with deionised water (5 mL) and the product was extracted with ethyl acetate (3 x 20 mL). The organic extracts were dried with MgSO_4 , filtered, and concentrated *in vacuo*. The crude product was purified *via* flash column chromatography (ethyl acetate) to yield the *title product* as a white solid (91 mg, 49%). R_f (ethyl acetate) 0.16; mp 47 – 48 °C; ν_{max} (thin film)/ cm^{-1} 3210, 3063, 2949, 2868, 1688, 1659, 1406, 1306, 1100, 738, 698; δ_{H} (400 MHz; CDCl_3) 1.38 – 1.50 (1 H, m, H-3a/4a), 1.60 – 1.74 (1 H, m, H-3a/4b), 1.82 – 1.97 (2 H, m, H-3b,4b), 2.20 – 2.31 (1 H, m, H-2a), 2.31 – 2.40 (1 H, m, H-2b), 2.87 (2 H, t, $J = 6.0$, H-9), 2.90 (1 H, dd, $J = 14.0, 6.5$, H-7a), 3.14 (1 H, dd, $J = 14.0, 5.5$, H-7b), 3.49 – 3.55 (1 H, m, H-5), 3.75 (3 H, t, $J = 6.0$, H-10), 4.51 (2 H, s, H-11), 6.32 (1 H, br s, H-6), 7.25 – 7.26 (5 H, m, H-Ar); δ_{C} (100 MHz; CDCl_3) 19.4 (C-3), 27.6 (C-4), 31.3 (C-2), 34.7 (C-7), 44.5 (C-9), 52.5 (C-5), 65.6 (C-10), 73.2 (C-11), 127.7 (CH, C-Ar), 127.8 (CH, C-Ar), 128.5 (CH, C-Ar), 137.9 (C-12), 172.3 (C-1), 196.7 (C-8); HRMS (ESI⁺) Found: 308.1312; $\text{C}_{16}\text{H}_{22}\text{NO}_3\text{S}$ ($\text{M}+\text{H}^+$) Requires 308.1315 (1.0 ppm error); Found: 330.1127; $\text{C}_{16}\text{H}_{21}\text{NNaO}_3\text{S}$ ($\text{M}+\text{Na}$) Requires 330.1134 (2.1 ppm error).

7.4.4 Michael Acceptor Screening Nucleophilic Addition to *N*-ethyl maleimide (**5.49**)

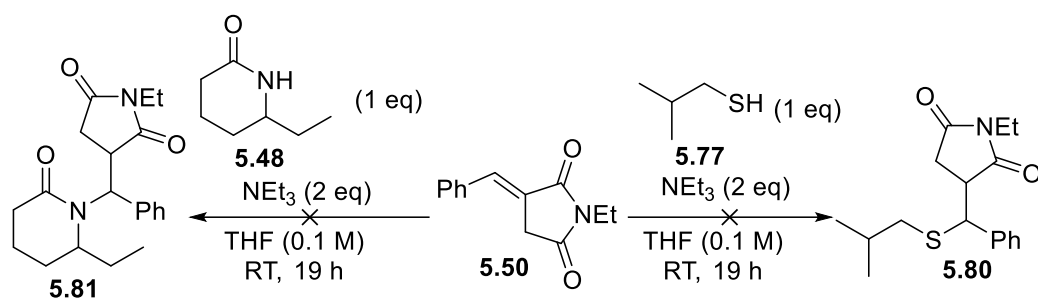


Based on a literature procedure,³³¹ isobutyl mercaptan **5.77** (11 μL , 9 mg, 0.1 mmol) or **5.48** (13 mg, 0.1 mmol) were dissolved in chloroform (1 mL), and *N*-ethyl maleimide **5.49** (12 mg, 0.1 mmol) and triethylamine (29 μL , 20 mg, 0.2 mmol) were added. The reactions were stirred for 1 hour, then concentrated *in vacuo*, and a ^1H NMR spectrum was recorded. No nucleophilic addition to **5.49** was seen when **5.48** was the nucleophile. However, nucleophilic addition was seen when isobutyl mercaptan **5.77** was used, to yield 1-ethyl-3-(isobutylthio)pyrrolidine-2,5-dione (**5.79**), which wasn't isolated. The ^1H NMR data for **5.79** is reported here:



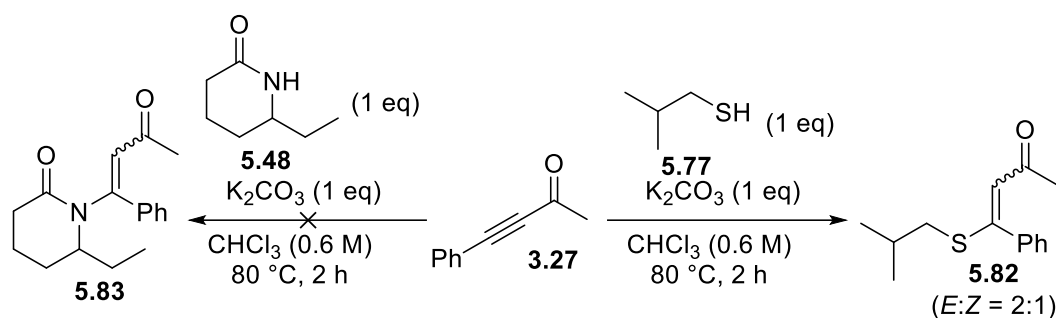
δ_{H} (400 MHz; CDCl_3) 1.01 (6 H, d, $J = 6.5$, H-1), 1.18 (3 H, t, $J = 7.0$, H-7), 1.87 (1 H, m, H-2), 2.64 (1 H, dd, $J = 12.5, 7.5$, H-3a), 2.78 (1 H, dd, $J = 12.5, 6.5$, H-3b), 2.51 (1 H, dd, $J = 18.5, 3.5$, H-5a), 3.11 (1 H, dd, $J = 18.5, 9.0$, H-5b) 3.57 (2 H, q, $J = 7.0$, H-6), 3.67 (1 H, dd, $J = 9.0, 3.5$, H-4).

Nucleophilic Addition to 5.50

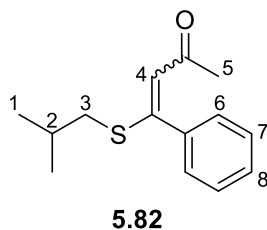


Isobutyl mercaptan **5.77** (11 μL , 9 mg, 0.1 mmol) or **5.48** (13 mg, 0.1 mmol) were dissolved in dry THF (1 mL) under an atmosphere of argon, and **5.50** (21 mg, 0.1 mmol) and triethylamine (29 μL , 20 mg, 0.2 mmol) were added. The reactions were stirred for 19 hours, then concentrated *in vacuo*, and a ^1H NMR spectrum was recorded. No nucleophilic addition to **5.50** was seen with either **5.48** or **5.77** was used as the nucleophile.

Nucleophilic Addition to Ynone 3.27



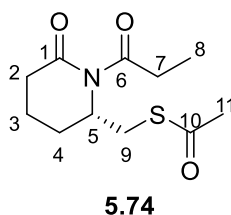
Based on a literature procedure,³³⁸ isobutyl mercaptan **5.77** (22 μL , 18 mg, 0.2 mmol) or **5.48** (25 mg, 0.2 mmol) were dissolved in chloroform (0.3 mL), and 4-phenyl-3-butyne-2-one **3.27** (29 μL , 29 mg, 0.2 mmol) and potassium carbonate (28 mg, 0.2 mmol) were added. The reactions were heated to 80°C and stirred for 1 hour, then concentrated *in vacuo*, and a ^1H NMR spectrum was recorded. No nucleophilic addition to **3.27** was seen when **5.48** was the nucleophile. However, nucleophilic addition was seen when isobutyl mercaptan **5.77** was used, to yield 4-(isobutylthio)-4-phenylbut-3-en-2-one (**5.82**) as a mixture of stereoisomers ($E:Z = 2:1$), which wasn't isolated. The ^1H NMR data for **5.82** is reported here:



δ_{H} (400 MHz; CDCl_3) 0.82 (6 H, d, $J = 7.0$, H-1, *E*), 1.03 (6 H, d, $J = 6.5$, H-1, *Z*), 1.61 (1 H, m, H-2, *E*), 1.77 (3 H, s, H-5, *Z*), 1.95 (1 H, m, H-2, *Z*), 2.24 (2 H, d, $J = 7.0$, H-3, *E*), 2.27 (3 H, s, H-5, *E*), 2.65 (2 H, d, $J = 7.0$, H-3, *Z*), 6.05 (1 H, s, H-4, *Z*), 6.31 (1 H, s, H-4, *Z*), 7.27 – 7.33 (4 H, m, H-Ar, *E* and *Z*), 7.35 – 7.41 (6 H, m, H-Ar, *E* and *Z*).

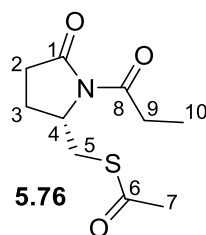
7.4.5 Acyl Transfer Products

(S)-S-((6-Oxo-1-propionylpiperidin-2-yl)methyl) ethanethioate (5.74)



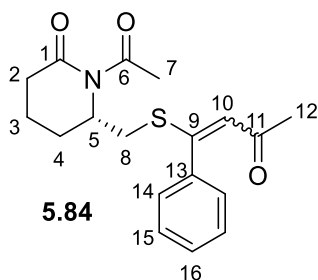
To a dry round-bottomed flask, **5.41** (38 mg, 0.2 mmol) was dissolved in dry THF (2 mL) under an atmosphere of argon, and propionyl chloride **5.67** (26 μ L, 28 mg, 0.3 mmol) and pyridine (16 μ L, 16 mg, 0.2 mmol) were added and the reaction was stirred for 22 hours. The reaction was diluted with deionised water (10 mL) and the product was extracted with ethyl acetate (4 x 10 mL). The organic extracts were combined, dried over MgSO_4 , filtered, and concentrated *in vacuo*. The crude product was purified *via* flash column chromatography (hexane/ethyl acetate 8:2) to yield the *title product* as a pale, yellow oil (28 mg, 58%). R_f (hexane/ethyl acetate 8:2) 0.23; ν_{max} (thin film)/ cm^{-1} 3288, 2926, 1690, 1662, 1352, 1166, 626; δ_{H} (400 MHz; CDCl_3) 1.12 (3 H, t, $J = 7.5$, H-8), 1.70 – 1.85 (2 H, m, H-3a,4a), 1.85 – 1.95 (1 H, m, H-3b/4b), 1.85 – 2.10 (1 H, m, H-3b/4b), 2.34 (3 H, s, H-11), 2.51 (1 H, ddd, $J = 18.0, 9.5, 7.0$, H-2a), 2.57 – 2.67 (1 H, m, H-2b), 2.75 (1 H, dd, $J = 18.0, 7.5$, H-7a), 2.92 (1 H, dd, $J = 18.0, 7.5$, H-7b), 2.98 (1 H, dd, $J = 13.5, 4.5$, H-9a), 3.25 (1 H, dd, $J = 13.5, 9.0$, H-9b), 4.64 (1 H, dq, $J = 9.0, 4.5$, H-5), δ_{C} (100 MHz; CDCl_3) 9.4 (C-8), 17.0 (C-3/4), 25.0 (C-3/4), 30.6 (C-11), 31.3 (C-2), 32.9 (C-7), 34.6 (C-9), 52.5 (C-5), 173.6 (C-1/6), 177.6 (C-1/6), 194.8 (C-10); HRMS (ESI⁺) Found: 266.0826; $\text{C}_{11}\text{H}_{17}\text{NNaO}_3\text{S}$ (M+Na) Requires 266.0821 (–1.7 ppm error).

(S)-S-((5-Oxo-1-propionylpyrrolidin-2-yl)methyl) ethanethioate (5.76)



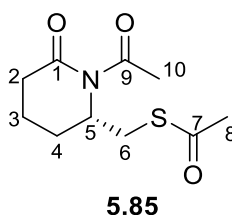
To a dry round-bottomed flask, **5.46** (35 mg, 0.2 mmol) was dissolved in dry THF (2 mL) under an atmosphere of argon, and propionyl chloride **5.67** (26 μ L, 28 mg, 0.3 mmol) and pyridine (16 μ L, 16 mg, 0.2 mmol) were added and the reaction was stirred for 22 hours. The reaction was diluted with deionised water (10 mL) and the product was extracted with ethyl acetate (4 x 10 mL). The organic extracts were combined, dried over MgSO_4 , filtered, and concentrated *in vacuo*. The crude product was purified *via* flash column chromatography (hexane/ethyl acetate 8:2) to yield the *title product* as a pale, yellow oil (16 mg, 35%). R_f (hexane/ethyl acetate 8:2) 0.21; ν_{max} (thin film)/ cm^{-1} 2980, 2941, 1739, 1695, 1364, 1226, 625; δ_{H} (600 MHz; CDCl_3) 1.15 (3 H, t, $J = 7.5$, H-10), 1.83 (1 H, ddt, $J = 13.5, 9.5, 2.0$, H-3a), 2.11 (1 H, dq, $J = 13.5, 10.0$, H-3b), 2.37 (3 H, s, H-7), 2.49 (1 H, ddd, $J = 18.0, 10.0, 2.0$, H-2a), 2.81 (1 H, ddd, $J = 18.0, 10.0, 9.5$, H-2b), 2.90 (2 H, q, $J = 7.5$, H-9), 3.20 (1 H, dd, $J = 14.0, 3.0$, H-5a), 3.37 (1 H, dd, $J = 14.0, 7.5$, H-5b), 4.56 (1 H, dddd, $J = 9.5, 7.5, 3.0, 2.0$, H-4); δ_{C} (151 MHz; CDCl_3) 8.4 (C-10), 21.7 (C-3), 30.7 (C-7/9), 30.9 (C-7/9), 31.4 (C-5), 32.4 (C-2), 56.3 (C-4), 175.1 (C-1/8), 175.5 (C-1/8), 195.0 (C-6); HRMS (ESI⁺) Found: 252.0670; $\text{C}_{10}\text{H}_{15}\text{NNaO}_3\text{S}$ (M+Na) Requires 252.0665 (2.0 ppm error).

(S)-1-Acetyl-6-(((3-oxo-1-phenylbut-1-en-1-yl)thio)methyl)piperidin-2-one (5.84)



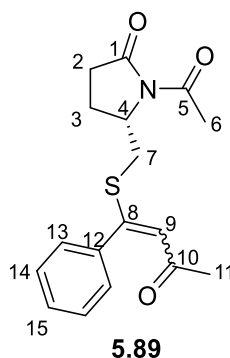
To a dry round-bottomed flask, **5.41** (26 mg, 0.1 mmol) and 4-phenyl-3-butyne-2-one **3.27** (29 μ L, 29 mg, 0.2 mmol) were dissolved in dry acetonitrile (0.2 mL) under an atmosphere of argon, and potassium carbonate (29 mg, 0.2 mmol) was added. The reaction mixture was stirred at 40 $^{\circ}$ C for 18 hours. The mixture was concentrated *in vacuo* and the crude product was purified *via* flash column chromatography (hexane/ethyl acetate 9:1 to 7:3) to yield the *title product* as a yellow oil, as a mixture of *E* and *Z* stereoisomers (34 mg, 72%, *E:Z* = 7:3). R_f (hexane/ethyl acetate 7:3) 0.15; ν_{\max} (thin film)/ cm^{-1} 3280, 3058, 2952, 1693, 1657, 1538, 1365, 1235, 1174, 762, 730, 700; δ_{H} (400 MHz; CDCl_3) 1.60 – 1.74 (4 H, m, H-Alk, *E* and *Z*), 1.78 – 1.89 (2 H, m, H-Alk, *E* and *Z*), 1.89 (3 H, s, H-12, *Z*), 2.06 – 2.11 (1 H, m, H-Alk, *E*), 2.18 – 2.24 (1 H, m, H-Alk, *Z*), 2.27 (3 H, s, H-12, *E*), 2.34 (3 H, s, H-7, *E*), 2.40 – 2.44 (2 H, m, H-2, *E*), 2.48 (3 H, s, H-7, *Z*), 2.49 – 2.52 (1 H, m, H-8a, *E*), 2.55 – 2.58 (2 H, m, H-2, *Z*), 2.68 (1 H, dd, $J = 13.0, 4.5$, H-8b, *E*), 2.76 (1 H, dd, $J = 13.5, 10.0$, H-8a, *Z*), 3.16 (1 H, dd, $J = 13.5, 4.0$, H-8b, *Z*), 4.44 – 4.49 (1 H, m, H-5, *E*), 4.78 – 4.84 (1 H, m, H-5, *Z*), 6.37 (1 H, s, H-10, *E*), 6.42 (1 H, s, H-10, *Z*), 7.28 – 7.37 (4 H, m, H-Ar, *E* and *Z*), 7.35 – 7.42 (6 H, m, H-Ar, *E* and *Z*); δ_{C} (100 MHz; CDCl_3) 16.9 (C-3, *Z*), 16.9 (C-3, *E*), 24.7 (C-4, *E*), 25.0 (C-4, *Z*), 27.5 (C-7, *E*), 27.6 (C-7, *Z*), 30.6 (C-12, *Z*), 30.8 (C-12, *E*), 34.3 (C-2, *E*), 34.4 (C-2, *Z*), 34.6 (C-8, *Z*), 34.9 (C-8, *E*), 51.2 (C-5, *Z*), 52.5 (C-5, *E*), 122.4 (C-10, *Z*), 124.9 (C-10, *E*), 128.2 (CH, C-Ar, *E*), 128.5 (CH, C-Ar, *Z*), 128.7 (CH, C-Ar, *Z*), 128.8 (CH, C-Ar, *E*), 129.3 (CH, C-Ar, *Z*), 129.6 (CH, C-Ar, *E*), 137.2 (C-13, *Z*), 138.3 (C-13, *E*), 156.0 (C-9, *Z*), 158.1 (C-9, *E*), 173.0 (C-1/6, *E*), 173.3 (C-1/6, *Z*), 173.4 (C-1/6, *E*), 173.7 (C-1/6, *Z*), 195.9 (C-11, *Z*), 196.1 (C-11, *E*); HRMS (ESI⁺) Found: 354.1127; $\text{C}_{18}\text{H}_{21}\text{NNaO}_3\text{S}$ (M+Na) Requires 354.1134 (–2.0 ppm error).

(S)-S-((1-Acetyl-6-oxopiperidin-2-yl)methyl) ethanethioate (5.85)



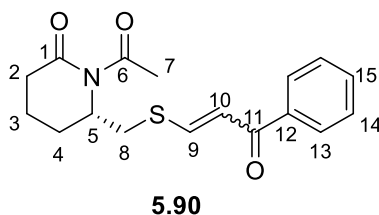
Isolated as a side-product from the acyl transfer reaction of **5.41**, using the unoptimised conditions. **5.41** (37 mg, 0.2 mmol) and 4-phenyl-3-butyne-2-one **3.27** (29 μ L, 29 mg, 0.2 mmol) were dissolved in chloroform (0.3 mL), and potassium carbonate (28 mg, 0.2 mmol) was added and the reaction mixture was stirred at 80 °C for 18 hours. The mixture was concentrated *in vacuo* and the crude product was purified *via* flash column chromatography (hexane/ethyl acetate 9:1 to 7:3) to yield the *title product* as a pale, yellow oil (8 mg, 34%). R_f (hexane/ethyl acetate 7:3) 0.41; ν_{\max} (thin film)/ cm^{-1} 3376, 2922, 2851, 1691, 1380, 1367, 1244; δ_{H} (400 MHz; CDCl_3) 1.75 – 1.85 (2 H, m, H-3a and H-4a), 1.89 – 1.85 (1 H, m, H-4b), 2.00 – 2.11 (1 H, m, H-3b), 2.35 (3 H, s, H-8), 2.48 (3 H, s, H-10), 2.50 – 2.57 (1 H, m, H-2a), 2.60 – 2.66 (1 H, m, H-2b), 3.00 (1 H, dd, $J = 13.5, 4.0$, H-6a), 3.27 (1 H, dd, $J = 13.5, 9.0$, H-6b), 4.67 (1 H, dddd, $J = 9.0, 4.5, 4.0, 4.0$, H-5); δ_{C} (100 MHz; CDCl_3) 17.1 (C-3), 25.0 (C-4), 27.7 (C-10), 30.6 (C-8), 31.3 (C-6), 34.6 (C-2), 52.4 (C-5), 173.5 (C, C-1 or C-10), 173.8 (C, C-1 or C-10), 194.8 (C-7); HRMS (ESI⁺) Found: $\text{C}_{10}\text{H}_{16}\text{NO}_3\text{S}$; 230.0841 ($\text{M}+\text{H}^+$) Requires 230.0845 (–1.7 ppm error); Found: $\text{C}_{10}\text{H}_{15}\text{NNaO}_3\text{S}$; 252.0655 ($\text{M}+\text{Na}$) Requires 252.0665 (–4.3 ppm error).

(S)-1-Acetyl-5-(((3-oxo-1-phenylbut-1-en-1-yl)thio)methyl)pyrrolidin-2-one (5.89)



To a dry round-bottomed flask, **5.46** (52 mg, 0.30 mmol) and 4-phenyl-3-butyne-2-one **3.27** (65 μ L, 65 mg, 0.45 mmol) were dissolved in dry acetonitrile (1 mL) under an atmosphere of argon, and potassium carbonate (62 mg, 0.45 mmol) was added. The reaction mixture was stirred at 40 $^{\circ}$ C for 20 hours. The mixture was concentrated *in vacuo* and the crude product was purified *via* flash column chromatography (hexane/ethyl acetate 1:1) to yield the *title product* as an orange oil, as a mixture of *E* and *Z* stereoisomers (70 mg, 73%, *E*:*Z* = 7:3). R_f (hexane/ethyl acetate 1:1) 0.32; ν_{\max} (thin film)/ cm^{-1} 3301, 3059, 2932, 1737, 1692, 1658, 1538, 1359, 1288, 1269, 762, 700; δ_{H} (600 MHz; CDCl_3) 1.89 (3 H, s, H-11, *Z*), 1.94 – 2.08 (4 H, m, H-Alk, *E* and *Z*), 2.26 (3 H, s, H-11, *E*), 2.35 (3 H, s, H-6, *E*), 2.35 – 2.41 (1 H, m, H-2a, *E*), 2.48 (3 H, s, H-6, *Z*), 2.50 – 2.58 (2 H, m, H-2a, *E* and *Z*), 2.65 (1 H, dd, $J = 13.5, 8.0$, H-7a, *E*), 2.68 – 2.74 (1 H, m, H-2b, *Z*), 2.80 (1 H, dd, $J = 13.5, 9.0$, H-7a, *Z*), 2.84 (1 H, dd, $J = 13.5, 3.5$, H-7b, *E*), 3.28 (1 H, dd, $J = 13.5, 3.0$, H-7b, *Z*), 4.30 (1 H, dddd, $J = 9.0, 8.5, 3.0, 2.0$, H-4, *E*), 4.58 – 4.63 (1 H, m, H-4, *Z*), 6.38 (1 H, s, H-9, *E*), 6.46 (1 H, s, H-9, *Z*), 7.26 – 7.30 (4 H, m, H-Ar, *E* and *Z*), 7.34 – 7.41 (6 H, m, H-Ar, *E* and *Z*); δ_{C} (151 MHz; CDCl_3) 21.6 (C-3, *E*), 22.0 (C-3, *Z*), 25.3 (2 x C-6, *E* and *Z*), 30.6 (C-11, *Z*), 30.9 (C-11, *E*), 31.6 (C-2, *Z*), 31.7 (C-2, *E*), 34.6 (C-7, *Z*), 34.8 (C-7, *E*), 54.9 (C-4, *Z*), 56.2 (C-4, *E*), 122.1 (C-9, *Z*), 125.0 (C-9, *E*), 128.2 (CH, C-Ar, *E*), 128.5 (CH, C-Ar, *Z*), 128.6 (CH, C-Ar, *Z*), 128.9 (CH, C-Ar, *E*), 129.4 (CH, C-Ar, *E*), 129.6 (CH, C-Ar, *Z*), 137.0 (C-12, *Z*), 138.0 (C-12, *E*), 155.7 (C-8, *Z*), 157.9 (C-8, *E*), 170.6 (C-1/5, *E*), 171.2 (C-1/5, *Z*), 175.1 (C-1/5, *Z*), 175.3 (C-1/5, *E*), 195.8 (C-10, *Z*), 196.0 (C-10, *E*); HRMS (ESI⁺) Found: 318.1157; $\text{C}_{17}\text{H}_{20}\text{NO}_3\text{S}$ ($\text{M}+\text{H}^+$) Requires 318.1158 (0.5 ppm error); Found: 340.0974; $\text{C}_{17}\text{H}_{19}\text{NNaO}_3\text{S}$ ($\text{M}+\text{Na}$) Requires 340.0978 (1.2 ppm error).

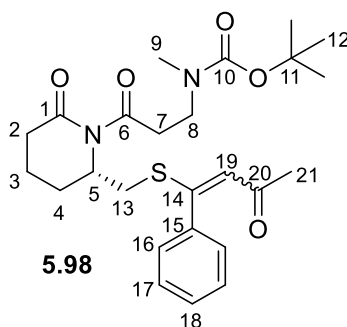
(S)-1-Acetyl-6-(((3-oxo-3-phenylprop-1-en-1-yl)thio)methyl)piperidin-2-one (5.90)



To a dry round-bottomed flask, **5.41** (37 mg, 0.2 mmol) and **5.52** (39 mg, 0.3 mmol) were dissolved in dry acetonitrile (0.3 mL) under an atmosphere of argon, and potassium carbonate (42 mg, 0.3 mmol) was added. The reaction mixture was stirred at 40 °C for 18 hours. The mixture was concentrated *in vacuo* and the crude product was purified *via* flash column chromatography (hexane/ethyl acetate 9:1 to 7:3) to yield the *title product* as an orange solid, as a mixture of *E* and *Z* stereoisomers (31 mg, 49%, *E:Z* = 58:42). R_f (hexane/ethyl acetate 7:3) 0.27, 0.20; mp 53 – 58 °C; ν_{\max} (thin film)/ cm^{-1} 3060, 2954, 2925, 1689, 1640, 1531, 1378, 1367, 1237, 733, 694; δ_{H} (400 MHz; CDCl_3) 1.72 – 1.92 (6 H, m, H-3,4a, *E* and *Z*), 2.21 – 2.29 (1 H, m, H-4b, *E*), 2.29 – 2.36 (1 H, m, H-4b, *Z*), 2.52 (3 H, s, H-7, *Z*), 2.52 (3 H, s, H-7, *E*), 2.55 – 2.66 (4 H, m, H-2, *E* and *Z*), 2.72 – 2.87 (2 H, m, H-8a, *E* and *Z*), 2.99 – 3.06 (1 H, m, H-8b, *Z*), 3.38 (1 H, dd, $J = 14.0, 3.5$, H-8b, *E*), 4.61 (1 H, ddt, $J = 11.5, 6.0, 3.0, 3.0$, H-5, *Z*), 4.81 (1 H, ddd, $J = 11.0, 5.5, 3.5$, H-5, *E*), 7.17 (1 H, d, $J = 10.0$, H-10, *Z*), 7.42 (1 H, d, $J = 15.0$, H-10, *E*), 7.44 – 7.59 (6 H, m, H-Ar, *E* and *Z*), 7.69 (1 H, d, $J = 10.0$, H-9, *Z*), 7.88 (1 H, d, $J = 15.0$, H-9, *E*), 7.94 – 7.99 (2 H, m, H-13, *Z*), 8.07 – 8.13 (2 H, m, H-13, *E*); δ_{C} (100 MHz; CDCl_3) 16.8 (C-3, *E* or *Z*), 16.9 (C-3, *E* or *Z*), 23.7 (C-4, *Z*), 24.5 (C-4, *E*), 27.8 (C-7, *E* or *Z*), 28.0 (C-7, *E* or *Z*), 33.8 (C-8, *E*), 34.6 (C-2, *E* or *Z*), 34.6 (C-2, *E* or *Z*), 38.1 (C-8, *Z*), 51.8 (C-5, *E*), 54.4 (C-5, *Z*), 117.6 (C-10, *Z*), 119.5 (C-10, *E*), 128.2 (CH, C-Ar, *E* or *Z*), 128.7 (CH, C-Ar, *E* or *Z*), 128.8 (CH, C-Ar, *E* or *Z*), 132.7 (C-15, *E* or *Z*), 132.8 (C-15, *E* or *Z*), 137.9 (C-12, *E* or *Z*), 137.9 (C-12, *E* or *Z*), 146.1 (C-9, *E*), 151.2 (C-9, *Z*), 173.4 (C-1/6, *E* or *Z*), 174.0 (C-1/6, *E* or *Z*), 174.2 (C-1/6, *E* or *Z*), 186.9 (C-11, *E*), 189.3 (C-11, *Z*); HRMS (ESI⁺) Found: 318.1162; $\text{C}_{17}\text{H}_{20}\text{NO}_3\text{S}$ ($\text{M}+\text{H}^+$) Requires 318.1158 (–1.0 ppm error); Found: 340.0978; $\text{C}_{17}\text{H}_{20}\text{NNaO}_3\text{S}$ ($\text{M}+\text{Na}$) Requires 340.0978 (–0.1 ppm error).

Note that two quaternary carbon resonances could not be found in the ^{13}C NMR spectra. It is believed that those resonances are for an imide carbonyl, and an aromatic C–H, which are overlapping with other resonances.

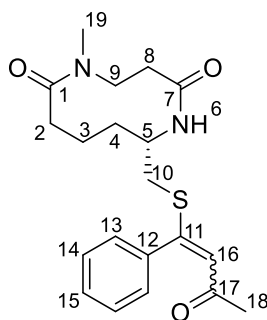
***tert*-Butyl (S)-methyl(3-oxo-3-(2-oxo-6-(((3-oxo-1-phenylbut-1-en-1-yl)thio)methyl)piperidin-1-yl)propyl)carbamate (5.98)**



To a dry round-bottomed flask, **5.57** (253 mg, 0.8 mmol) and 4-phenyl-3-butyne-2-one **3.27** (0.16 mL, 159 mg, 1.1 mmol) were dissolved in dry acetonitrile (1.3 mL) under an atmosphere of argon, and potassium carbonate (159 mg, 1.2 mmol) was added. The reaction mixture was stirred at 80 °C for 24 hours. The mixture was concentrated *in vacuo* and the residue was dissolved in DCM (10 mL). Deionised water (10 mL) was added and the product was extracted with DCM (2 x 10 mL). The organic extracts were combined, dried using MgSO₄, then filtered and concentrated *in vacuo*. The crude product was purified *via* flash column chromatography (hexane/ethyl acetate 9:1 to 7:3) to yield the *title product* as an orange oil, as a mixture of *E* and *Z* stereoisomers (162 mg, 45%, *E*:*Z* = 3:1). Note that the ¹³C NMR spectrum showed that the *Z* stereoisomer product exists as a mixture of rotamers in CDCl₃ (*A* and *B* The rotamers are indistinguishable in the ¹H NMR spectrum, however based on the ¹³C NMR spectrum, the rotamers are approximately in a 1:1 ratio. *R_f*(hexane/ethyl acetate 7:3) 0.19; *v*_{max} (thin film)/cm⁻¹ 2972, 2936, 1683, 1541, 1391, 1365, 1163, 1141, 723, 701; *δ*_H (600 MHz; CDCl₃) 1.42 (9 H, s, H-12, *E*), 1.43 (9 H, s, H-12, *Z*), 1.65 – 1.76 (3 H, m, H-3a,4a, *E* and H-3a, *Z*), 1.79 – 1.93 (6 H, m, H-3b, *E* and H-3b,4a,21, *Z*), 2.03 – 2.09 (1 H, m, H-4b, *E*), 2.15 – 2.22 (1 H, m, H-4b, *Z*), 2.27 (3 H, s, H-21, *E*), 2.36 – 2.44 (2 H, m, H-2, *E*), 2.50 (1 H, dd, *J* = 13.0, 10.0, H-13a, *E*), 2.56 – 2.58 (2 H, m, H-2, *Z*), 2.62 – 2.69 (1 H, m, H-13b, *Z*), 2.73 – 2.82 (4 H, m, H-9, *E* and H-13a, *Z*), 2.86 (3 H, s, H-9, *Z*), 2.92 – 3.00 (2 H, m, H-7, *E*), 3.07 – 3.18 (3 H, m, H-7,13b, *Z*), 3.34 – 3.46 (2 H, m, H-8, *E*), 3.46 – 3.60 (2 H, m, H-8, *Z*), 4.37 – 4.50 (1 H, m, H-5, *E*), 4.70 – 4.82 (1 H, m, H-5, *Z*), 6.36 (1 H, s, H-19, *E*), 6.42 (1 H, br s, H-19, *Z*), 7.27 – 7.32 (4 H, m, H-Ar, *E* and *Z*), 7.34 – 7.42 (6 H, m, H-Ar, *E* and *Z*); *δ*_C (151 MHz; CDCl₃) 16.8 (C-3, *E*), 16.8 (C-3, *Z*, *A* and *B*), 24.7 (C-4, *E*), 24.9 (C-4, *Z*, *A* and *B*), 28.5 (C-12, *E* and *Z*, *A* and *B*), 30.6 (C-21, *Z*, *A* and *B*), 30.8 (C-21, *E*), 34.3 (C-2, *E*), 34.4 (C-2, *Z*, *A* and *B*), 34.6 (C-13, *Z*, *A* and *B*), 34.7 (C-9, *E*), 34.8 (C-9, *Z*, *A* and *B*), 35.0 (C-13, *E*), 37.5 (C-7, *E*), 38.1 (C-7, *Z*, *A* and *B*), 44.9 (C-8, *E*), 45.1 (C-8, *Z*, *A* or *B*), 45.3 (C-8, *Z*, *A* or *B*), 51.4 (C-5, *Z*, *A* and *B*), 52.8 (C-5, *E*), 79.5 (C-11, *E* and

Z, A and B), 122.1 (C-19, Z, A or B), 122.5 (C-19, Z, A or B), 124.8 (C-19, E), 128.2 (CH, C-Ar, E), 128.5 (CH, C-Ar, Z, A and B), 128.7 (CH, C-Ar, Z, A and B), 128.8 (CH, C-Ar, E), 129.3 (CH, C-Ar, E), 129.6 (CH, C-Ar, Z, A and B), 137.2 (C-15, Z, A and B), 138.3 (C-15, E), 155.7 (C-10, E), 155.7 (C-10, Z, A or B), 155.7 (C-10, Z, A or B), 156.1 (C-14, Z, A and B), 158.1 (C-14, E), 173.3 (C-1/6, Z, A and B), 173.4 (C-1/6, E), 174.3 (C-1/6, E), 174.9 (C-1/6, Z, A and B), 195.9 (C-20, Z, A and B), 196.1 (C-20, E); HRMS (ESI⁺) Found: 475.2266; C₂₅H₃₅N₂O₅S (M+H⁺) Requires 475.2261 (-1.0 ppm error); Found: 497.2077; C₂₅H₃₅N₂NaO₅S (M+Na) Requires 497.2081 (0.7 ppm error).

(S)-5-Methyl-10-(((3-oxo-1-phenylbut-1-en-1-yl)thio)methyl)-1,5-diazecane-2,6-dione (5.99)



5.99

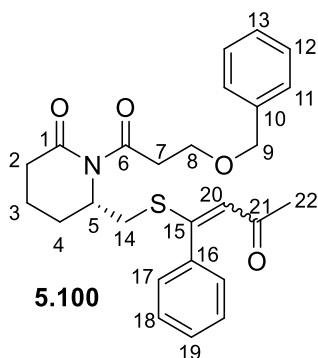
Following a literature procedure,²⁷² to a dry round-bottomed flask **5.98** (162.6 mg, 0.3 mmol) was dissolved in DCM (1.7 mL) and TFA (1.7 mL). The reaction was stirred at room temperature for 1 hour, and the solvent removed *in vacuo*. The crude residue was dissolved in acetonitrile (3.2 mL) and DMF (0.2 mL), and DIPEA (221 mg, 0.3 mL, 1.7 mmol) was added. The reaction was stirred at 50 °C for 18 hours, and the solvent removed *in vacuo*. The crude product was purified *via* flash column chromatography (ethyl acetate to ethyl acetate/methanol 98:2 to 95:5 to 9:1). A sticky, yellow solid (112 mg) was isolated, however the ¹³C NMR spectrum suggested the compound was formed as, or was contaminated with, a TFA salt. The compound was dissolved in ethyl acetate (10 mL) and washed with aq. NaOH (10% w/w, 3 x 10 mL), dried with Na₂SO₄, filtered and concentrated *in vacuo*. The crude product was purified *via* flash column chromatography (ethyl acetate/methanol 98:2 to 9:1) to yield the *title product* as a yellow solid, as a mixture of *E* and *Z* stereoisomers (64 mg, 50%, *E*:*Z* = 64:36). Note that the ¹H NMR spectrum showed that the *E* stereoisomer product exists as a mixture of rotamers in CDCl₃ (*A*:*B* = 9:1), and the *Z* stereoisomer product also exists as a mixture of rotamers in CDCl₃ (*C*:*D* = 3:1). ¹H and ¹³C NMR data reported for the major rotamer of the *E*- and *Z*-isomers only. *R_f* (ethyl acetate/methanol 9:1) 0.50; mp 46 – 52 °C; δ_H (600 MHz; CDCl₃) 1.28 – 1.45 (3 H, m, H-3a,4, *E*), 1.48 – 1.64 (2 H, m, H-3a,4a, *Z*), 1.69 (1 H, ddd, *J* = 14.0, 3.0, 3.0, H-4b, *Z*), 1.75 (3 H, s, H-18, *Z*), 1.90 – 1.98 (1 H, m, H-2a, *E*), 1.98 – 2.06 (2 H, m, H-3b, *E* and H-2a, *Z*), 2.10 – 2.18 (1 H, m, H-3b, *Z*), 2.19 – 2.25 (4 H, m, H-8a,18, *E*), 2.28 (1 H, dd, *J* = 12.5, 3.5, H-8a, *Z*), 2.34 – 2.54 (5 H, m, H-2b,8b,10, *E* and H-8b, *Z*), 2.58 (1 H, ddd, *J* = 16.0, 12.5, 4.0, H-2b, *Z*), 2.75 (2 H, d, *J* = 7.0, H-10, *Z*), 2.92 (3 H, s, H-19, *E*), 2.99 (3 H, s, H-19, *Z*), 3.19 (1 H, ddd, *J* = 15.5, 3.5, 3.5, H-9a, *E*), 3.25 (1 H, ddd, *J* = 15.5, 3.5, 3.5, H-9a, *Z*), 3.84 – 4.04 (3 H, m, H-5,8b, *E* and H-8b, *Z*), 4.11 – 4.20 (1 H, m, H-5, *Z*), 6.08 (1 H, s, H-16, *Z*), 6.15 (1 H, d, *J* = 10.0, H-6, *Z*), 6.31 (1 H, s, H-16, *E*), 6.40 (1 H, d, *J* = 9.5, H-6, *E*), 7.21 – 7.30 (5 H, m, H-Ar, *E* and *Z*), 7.31 – 7.39 (5 H, m, H-Ar, *E* and *Z*); δ_C (151

MHz; CDCl₃) 23.3 (C-3, *E*), 23.3 (C-3, *Z*), 27.5 (C-2, *E*) 27.6 (C-2, *Z*), 30.2 (C-18, *Z*), 30.6 (C-4, *E*), 30.8 (C-4, *Z*), 30.9 (C-18, *E*), 34.2 (C-19, *E*), 34.3 (C-19, *Z*), 37.1 (2 x C-8, *E* and *Z*), 38.8 (C-10, *Z*), 39.3 (C-C-10, *E*), 47.9 (2 x C-9, *E* and *Z*), 48.5 (C-5, *Z*), 49.5 (C-5, *E*), 122.4 (C-16, *Z*), 124.2 (C-16, *E*), 128.2 (CH, C-Ar, *E* or *Z*), 128.5 (CH, C-Ar, *E* or *Z*), 128.6 (CH, C-Ar, *E* or *Z*), 129.1 (CH, C-Ar, *E* or *Z*), 129.5 (CH, C-Ar, *E* or *Z*), 137.2 (C-12, *Z*), 138.3 (C-12, *E*), 157.7 (C-11, *Z*), 159.7 (C-11, *E*), 170.9 (C-7, *Z*), 171.0 (C-7, *E*), 173.3 (C-1, *E*), 173.4 (C-1, *Z*), 196.2 (C-17, *Z*), 196.6 (C-17, *E*); HRMS (ESI⁺) Found: 397.1562; C₂₀H₂₆N₂NaO₃S (M+Na) Requires 397.1556 (-1.4 ppm error).

Note that one aromatic CH carbon resonance could not be found in the ¹³C NMR spectra. It is believed that this resonance is overlapping with other resonances.

Characteristic NMR resonances for the minor *E*-rotamer (*B*) can be found at: δ_H 6.32 (1 H, s, H-16, *E*), and characteristic NMR resonances for the minor *Z*-rotamer (*D*) can be found at: δ_H 1.77 (3 H, s, H-18, *Z*), 6.09 (1 H, s, H-16, *Z*).

(S)-1-(3-(Benzyloxy)propanoyl)-6-(((3-oxo-1-phenylbut-1-en-1-yl)thio)methyl)piperidin-2-one
(5.100)



To a dry round-bottomed flask, **5.59** (57 mg, 0.2 mmol) and 4-phenyl-3-butyne-2-one **3.27** (39 μ L, 39 mg, 0.3 mmol) were dissolved in dry acetonitrile (0.3 mL) under an atmosphere of argon, and potassium carbonate (37 mg, 0.3 mmol) was added. The reaction mixture was stirred at 40 $^{\circ}$ C for 21 hours. The mixture was concentrated *in vacuo* and the residue was dissolved in DCM (5 mL). Deionised water (5 mL) was added and the organic extract was separated and dried using MgSO_4 , then filtered and concentrated *in vacuo*. The crude product was purified *via* flash column chromatography (hexane/ethyl acetate 7:3) to yield the *title product* as a yellow oil, as a mixture of *E* and *Z* stereoisomers (21 mg, 26%, *E*:*Z* = 7:3). R_f (hexane/ethyl acetate 7:3) 0.17; ν_{max} (thin film)/ cm^{-1} 3029, 2951, 2870, 1694, 1542, 1365, 1170, 697; δ_{H} (400 MHz; CDCl_3) 1.54 – 1.79 (4 H, m, H-Alk, *E* and *Z*), 1.78 – 1.89 (2 H, m, H-Alk, *E* and *Z*), 1.91 (3 H, s, H-22, *Z*), 2.04 – 2.13 (1 H, m, H-Alk, *E*), 2.15 – 2.23 (1 H, m, H-Alk, *Z*), 2.29 (3 H, s, H-22, *E*), 2.36 – 2.42 (2 H, m, H-2, *E*), 2.48 – 2.56 (3 H, m, H-2, *Z* and H-14a, *E*), 2.69 (1 H, dd, $J = 13.0, 4.0$, H-14b, *E*), 2.77 (1 H, dd, $J = 13.5, 10.0$, H-14a, *Z*), 3.05 (2 H, t, $J = 6.0$, H-7, *E*), 3.13 – 3.21 (3 H, m, H-7,14b, *Z*), 3.62 – 3.88 (4 H, m, H-8, *E* and *Z*), 4.46 – 4.55 (5 H, m, H-5, *E* and H-9, *E* and *Z*), 4.78 – 4.85 (1 H, m, H-5, *Z*), 6.38 (1 H, s, H-20, *E*), 6.41 (1 H, s, H-20, *Z*), 7.28 – 7.42 (20 H, m, H-Ar, *E* and *Z*); δ_{C} (100 MHz; CDCl_3) 16.9 (2 x C-3, *E* and *Z*), 24.7 (C-4, *E*), 25.0 (C-4, *Z*), 30.7 (C-22, *Z*), 30.9 (C-22, *E*), 34.4 (C-2, *E*), 34.5 (C-2, *Z*), 34.7 (C-14, *Z*), 35.0 (C-14, *E*), 39.8 (C-7, *E*), 39.9 (C-7, *Z*), 51.5 (C-5, *Z*), 52.9 (C-5, *E*), 65.8 (C-8, *E*), 65.9 (C-8, *Z*), 73.2 (C-9, *E*), 73.3 (C-9, *Z*), 122.3 (C-20, *Z*), 124.8 (C-20, *E*), 127.7 (CH, C-Ar, *E* or *Z*), 127.8 (CH, C-Ar, *E* or *Z*), 127.9 (CH, C-Ar, *E* or *Z*), 127.9 (CH, C-Ar, *E* or *Z*), 128.3 (CH, C-Ar, *E* or *Z*), 128.5 (CH, C-Ar, *E* or *Z*), 128.5 (CH, C-Ar, *E* or *Z*), 128.6 (CH, C-Ar, *E* or *Z*), 128.7 (CH, C-Ar, *E* or *Z*), 128.9 (CH, C-Ar, *E* or *Z*), 129.3 (CH, C-Ar, *E* or *Z*), 129.6 (CH, C-Ar, *E* or *Z*), 137.3 (C-16, *Z*), 138.2 (C, C-Ar, *E* or *Z*), 138.4 (C, C-Ar, *E* or *Z*), 156.1 (C-15, *Z*), 158.2 (C-15, *E*), 173.4 (C-1/6, *Z*), 173.5 (C-1/6, *E*), 174.0 (C-1/6, *E*), 174.7 (C-1/6, *Z*), 196.0 (C-2, *Z*), 196.2 (C-21, *E*); HRMS (ESI⁺) Found:

452.1893; $C_{26}H_{30}NO_4S$ ($M+H^+$) Requires 452.1890 (0.7 ppm error); Found: 474.1709;
 $C_{26}H_{29}NNaO_4S$ ($M+Na$) Requires 474.1710 (-0.2 ppm error).

Note that one quaternary aromatic carbon resonance could not be found in the ^{13}C NMR spectra.
It is believed that this resonance is overlapping with other resonances.

References

- 1 T. Tsuneda, *Density Functional Theory in Quantum Chemistry*, Springer Japan, Tokyo, First Edit., 2014.
- 2 D. Johnson, PhD Thesis, University of York, 2013.
- 3 C. J. Cramer, *Essentials of Computational Chemistry*, John Wiley & Sons, Ltd, Chichester, Second Edi., 2004.
- 4 P. Nava, *Density Functional Theory Calculations on Palladium Clusters and on an AgInS Semiconductor Compound*, Cuvillier Verlag, Göttingen, First Edit., 2005.
- 5 G. H. Grant and W. G. Richards, *Computational Chemistry*, Oxford University Press Inc., New York, First Edit., 1995.
- 6 D. O. Hayword, *Quantum Mechanics for chemists*, The Royal Society of Chemistry, Cambridge, First Edit., 2002.
- 7 E. Rutherford, *Philos. Mag.*, 1911, **21**, 669–688.
- 8 N. Bohr, *Philos. Mag.*, 1913, **26**, 1–25.
- 9 N. Bohr, *Philos. Mag.*, 1913, **26**, 476–502.
- 10 W. Wilson, *Philos. Mag.*, 1915, **29**, 795–802.
- 11 L. De Broglie, *Ann. Phys.*, 1925, **10**, 22–128.
- 12 C. J. Davisson and L. H. Germer, *Proc. Natl. Acad. Sci. U.S.A.*, 1928, **14**, 317–322.
- 13 C. J. Davisson, *Bell Labs Tech. J.*, 1928, **7**, 90–105.
- 14 G. P. Thomson and A. Reid, *Nature*, 1927, **119**, 890–890.
- 15 E. Schrödinger, *Phys. Rev.*, 1926, **28**, 1049–1070.
- 16 M. Born, *Zeitschrift für Phys.*, 1926, **37**, 863–867.
- 17 M. Born and R. Oppenheimer, *Ann. Phys. (Berl.)*, 1927, **389**, 457–484.

- 18 D. R. Hartree, *Math. Proc. Camb. Philos. Soc.*, 1928, **24**, 89–110.
- 19 D. R. Hartree, *Math. Proc. Camb. Philos. Soc.*, 1928, **24**, 426–437.
- 20 D. R. Hartree, *Math. Proc. Camb. Philos. Soc.*, 1929, **25**, 310–314.
- 21 D. R. Hartree, *Math. Proc. Camb. Philos. Soc.*, 1928, **24**, 111–132.
- 22 J. C. Slater, *Phys. Rev.*, 1930, **35**, 210–211.
- 23 V. Fock, *Zeitschrift für Phys.*, 1930, **61**, 126–148.
- 24 W. Pauli, *Zeitschrift für Phys.*, 1925, **31**, 765–783.
- 25 W. Heisenberg, *Zeitschrift für Phys.*, 1927, **43**, 172–198.
- 26 J. C. Slater, *Phys. Rev.*, 1929, **34**, 1293–1322.
- 27 D. R. Hartree and W. Hartree, *Proc. R. Soc. A*, 1935, **150**, 9–33.
- 28 L. H. Thomas, *Math. Proc. Camb. Philos. Soc.*, 1927, **23**, 542–548.
- 29 E. Fermi, *Rend. Lincei*, 1927, **6**, 602–607.
- 30 P. Hohenberg and W. Kohn, *Phys. Rev.*, 1964, **136**, B864–B871.
- 31 W. Kohn and L. J. Sham, *Phys. Rev.*, 1965, **140**, A1133–A1138.
- 32 A. D. Becke, *Phys. Rev. A*, 1988, **38**, 3098–3100.
- 33 J. P. Perdew, *Phys. Rev. B*, 1986, **33**, 8822–8824.
- 34 J. P. Perdew, K. Burke and M. Ernzerhof, *Phys. Rev. Lett.*, 1996, **77**, 3865–3868.
- 35 J. P. Perdew, K. Burke and M. Ernzerhof, *Phys. Rev. Lett.*, 1997, **78**, 1396–1396.
- 36 C. Adamo and V. Barone, *J. Chem. Phys.*, 1999, **110**, 6158–6170.
- 37 A. D. Becke, *J. Chem. Phys.*, 1993, **98**, 5648–5652.
- 38 C. Lee, W. Yang and R. G. Parr, *Phys. Rev. B*, 1988, **37**, 785–789.

- 39 S. H. Vosko, L. Wilk and M. Nusair, *Can. J. Phys.*, 1980, **58**, 1200–1211.
- 40 P. J. Stephens, F. J. Devlin, C. F. Chabalowski and M. J. Frisch, *J. Phys. Chem.*, 1994, **98**, 11623–11627.
- 41 Y. Zhao and D. G. Truhlar, *Theor. Chem. Acc.*, 2008, **120**, 215–241.
- 42 J.-D. Chai and M. Head-Gordon, *Phys. Chem. Chem. Phys.*, 2008, **10**, 6615.
- 43 J. C. Slater, *Phys. Rev.*, 1930, **36**, 57–64.
- 44 S. F. Boys, *Proc. R. Soc. A*, 1950, **200**, 542–554.
- 45 A. L. Magalhães, *J. Chem. Educ.*, 2014, **91**, 2124–2127.
- 46 R. Ditchfield, W. J. Hehre and J. A. Pople, *J. Chem. Phys.*, 1971, **54**, 724–728.
- 47 W. J. Hehre, R. Ditchfield and J. A. Pople, *J. Chem. Phys.*, 1972, **56**, 2257–2261.
- 48 P. C. Hariharan and J. A. Pople, *Theor. Chim. Acta*, 1973, **28**, 213–222.
- 49 M. S. Gordon, J. S. Binkley, J. A. Pople, W. J. Pietro and W. J. Hehre, *J. Am. Chem. Soc.*, 1982, **104**, 2797–2803.
- 50 M. M. Francl, W. J. Pietro, W. J. Hehre, J. S. Binkley, M. S. Gordon, D. J. DeFrees and J. A. Pople, *J. Chem. Phys.*, 1982, **77**, 3654–3665.
- 51 T. Clark, J. Chandrasekhar, G. W. Spitznagel and P. V. R. Schleyer, *J. Comput. Chem.*, 1983, **4**, 294–301.
- 52 G. W. Spitznagel, T. Clark, P. von Ragué Schleyer and W. J. Hehre, *J. Comput. Chem.*, 1987, **8**, 1109–1116.
- 53 R. Krishnan, J. S. Binkley, R. Seeger and J. A. Pople, *J. Chem. Phys.*, 1980, **72**, 650–654.
- 54 A. Schäfer, H. Horn and R. Ahlrichs, *J. Chem. Phys.*, 1992, **97**, 2571–2577.
- 55 K. Eichkorn, F. Weigend, O. Treutler and R. Ahlrichs, *Theor. Chem. Acc.*, 1997, **97**, 119–124.

- 56 D. Andrae, U. Häußermann, M. Dolg, H. Stoll and H. Preuß, *Theor. Chim. Acta*, 1990, **77**, 123–141.
- 57 F. Weigend, M. Häser, H. Patzelt and R. Ahlrichs, *Chem. Phys. Lett.*, 1998, **294**, 143–152.
- 58 F. Weigend and R. Ahlrichs, *Phys. Chem. Chem. Phys.*, 2005, **7**, 3297–3305.
- 59 *TURBOMOLE User's Manual (Version 6.4)*, TURBOMOLE GmbH, 2012.
- 60 J. W. Ochterski, *Thermochemistry in Gaussian*, Gaussian, Inc., 2000.
- 61 J. W. Ochterski, *Vibrational Analysis in Gaussian*, Gaussian, Inc., 1999.
- 62 J. Zhang, H. Zhang, T. Wu, Q. Wang and D. van der Spoel, *J. Chem. Theory Comput.*, 2017, **13**, 1034–1043.
- 63 J. Tomasi, B. Mennucci and R. Cammi, *Chem. Rev.*, 2005, **105**, 2999–3094.
- 64 J. Tomasi and M. Persico, *Chem. Rev.*, 1994, **94**, 2027–2094.
- 65 A. Klamt and G. Schüürmann, *J. Chem. Soc., Perkin Trans. 2*, 1993, 799–805.
- 66 A. Klamt, *J. Phys. Chem.*, 1995, **99**, 2224–2235.
- 67 F. London, *Trans. Faraday Soc.*, 1937, **33**, 8b – 26.
- 68 J. P. Wagner and P. R. Schreiner, *Angew. Chem. Int. Ed.*, 2015, **54**, 12274–12296.
- 69 P. R. Schreiner, L. V. Chernish, P. A. Gunchenko, E. Y. Tikhonchuk, H. Hausmann, M. Serafin, S. Schlecht, J. E. P. Dahl, R. M. K. Carlson and A. A. Fokin, *Nature*, 2011, **477**, 308–311.
- 70 A. A. Fokin, L. V. Chernish, P. A. Gunchenko, E. Y. Tikhonchuk, H. Hausmann, M. Serafin, J. E. P. Dahl, R. M. K. Carlson and P. R. Schreiner, *J. Am. Chem. Soc.*, 2012, **134**, 13641–13650.
- 71 S. Grimme, J. Antony, S. Ehrlich and H. Krieg, *J. Chem. Phys.*, 2010, **132**, 154104.
- 72 A. D. Becke and E. R. Johnson, *J. Chem. Phys.*, 2005, **123**, 154101.
- 73 A. D. Becke and E. R. Johnson, *J. Chem. Phys.*, 2005, **122**, 154104.

- 74 E. R. Johnson and A. D. Becke, *J. Chem. Phys.*, 2006, **124**, 174104.
- 75 S. Grimme, S. Ehrlich and L. Goerigk, *J. Comput. Chem.*, 2011, **32**, 1456–1465.
- 76 N. Mardirossian and M. Head-Gordon, *Mol. Phys.*, 2017, **115**, 2315–2372.
- 77 J. Sirirak, N. Lawan, M. W. Van der Kamp, J. N. Harvey and A. J. Mulholland, *PeerJ Phys. Chem.*, 2020, **2**, e8.
- 78 A. P. Bento, M. Solà and F. M. Bickelhaupt, *J. Comput. Chem.*, 2005, **26**, 1497–1504.
- 79 É. Brémond, M. Savarese, N. Q. Su, Á. J. Pérez-Jiménez, X. Xu, J. C. Sancho-García and C. Adamo, *J. Chem. Theory Comput.*, 2016, **12**, 459–465.
- 80 R. G. Epton, W. P. Unsworth and J. M. Lynam, *Isr. J. Chem.*,
DOI:10.1002/ijch.202200033.
- 81 A. S. K. Hashmi, *Chem. Rev.*, 2021, **121**, 8309–8310.
- 82 L. Ciano, N. Fey, C. J. V. Halliday, J. M. Lynam, L. M. Milner, N. Mistry, N. E. Pridmore, N. S. Townsend and A. C. Whitwood, *Chem. Commun.*, 2015, **51**, 9702–9705.
- 83 N. Hidalgo, J. J. Moreno, M. Pérez-Jiménez, C. Maya, J. López-Serrano and J. Campos, *Organometallics*, 2020, **39**, 2534–2544.
- 84 R. L. LaLonde, W. E. Brenzovich, Jr., D. Benitez, E. Tkatchouk, K. Kelley, W. A. Goddard, III and F. D. Toste, *Chem. Sci.*, 2010, **1**, 226.
- 85 Y. Zhu, W. Zhou, E. M. Petryna, B. R. Rogers, C. S. Day and A. C. Jones, *ACS Catal.*, 2016, **6**, 7357–7362.
- 86 K. L. Toups, G. T. Liu and R. A. Widenhoefer, *J. Organomet. Chem.*, 2009, **694**, 571–575.
- 87 L. Lempke, T. Fischer, J. Bell, W. Kraus, K. Rurack and N. Krause, *Org. Biomol. Chem.*, 2015, **13**, 3787–3791.
- 88 R. Dorel and A. M. Echavarren, *Chem. Rev.*, 2015, **115**, 9028–9072.
- 89 A. Fürstner and P. W. Davies, *Angew. Chem. Int. Ed.*, 2007, **46**, 3410–3449.

- 90 Y. Yamamoto, *J. Org. Chem.*, 2007, **72**, 7817–7831.
- 91 D. J. Gorin, B. D. Sherry and F. D. Toste, *Chem. Rev.*, 2008, **108**, 3351–3378.
- 92 Z. Lu, T. Li, S. R. Mudshinge, B. Xu and G. B. Hammond, *Chem. Rev.*, 2021, **121**, 8452–8477.
- 93 W. M. C. Sameera and F. Maseras, *WIREs Comput. Mol. Sci.*, 2012, **2**, 375–385.
- 94 C. J. Cramer and D. G. Truhlar, *Phys. Chem. Chem. Phys.*, 2009, **11**, 10757.
- 95 P. Sit and L. Zhang, in *Heterogeneous Catalysts*, Wiley, 2021, pp. 405–418.
- 96 O. N. Faza, R. Á. Rodríguez and C. S. López, *Theor. Chem. Acc.*, 2011, **128**, 647–661.
- 97 P. Nava, D. Hagebaum-Reignier and S. Humbel, *ChemPhysChem*, 2012, **13**, 2090–2096.
- 98 R. Kang, W. Lai, J. Yao, S. Shaik and H. Chen, *J. Chem. Theory Comput.*, 2012, **8**, 3119–3127.
- 99 G. Ciancaleoni, S. Rampino, D. Zuccaccia, F. Tarantelli, P. Belanzoni and L. Belpassi, *J. Chem. Theory Comput.*, 2014, **10**, 1021–1034.
- 100 K. P. Kepp, *J. Phys. Chem. A*, 2017, **121**, 2022–2034.
- 101 M. Bandini, A. Bottoni, M. Chiarucci, G. Cera and G. Pietro Miscione, *J. Am. Chem. Soc.*, 2012, **134**, 20690–20700.
- 102 Y. Li and X. Zhao, *ChemCatChem*, 2020, **12**, 6265–6271.
- 103 Y. Yang, J. Li, R. Zhu, C. Liu and D. Zhang, *ACS Catal.*, 2018, **8**, 9252–9261.
- 104 A. A. Hussein and H. S. Ali, *J. Org. Chem.*, 2020, **85**, 12682–12691.
- 105 L. Zhou, Y. Zhang, R. Fang and L. Yang, *ACS Omega*, 2018, **3**, 9339–9347.
- 106 R. Fang, L. Zhou, P. C. Tu, A. M. Kirillov and L. Yang, *Organometallics*, 2018, **37**, 1927–1936.
- 107 B. Alcaide, P. Almendros, I. Fernández, R. Martín-Montero, F. Martínez-Peña, M. P. Ruiz and M. R. Torres, *ACS Catal.*, 2015, **5**, 4842–4845.

- 108 Y. Li, J. Zhang, X. Zhao and Y. Wang, *Mol. Catal.*, 2022, **519**, 112154.
- 109 B. Ranieri, I. Escofet and A. M. Echavarren, *Org. Biomol. Chem.*, 2015, **13**, 7103–7118.
- 110 Z. Lu, G. B. Hammond and B. Xu, *Acc. Chem. Res.*, 2019, **52**, 1275–1288.
- 111 Z. Lu, J. Han, O. E. Okoromoba, N. Shimizu, H. Amii, C. F. Tormena, G. B. Hammond and B. Xu, *Org. Lett.*, 2017, **19**, 5848–5851.
- 112 J. H. Teles, S. Brode and M. Chabanas, *Angew. Chem. Int. Ed.*, 1998, **37**, 1415–1418.
- 113 E. Mizushima, T. Hayashi and M. Tanaka, *Org. Lett.*, 2003, **5**, 3349–3352.
- 114 S. Gaillard, J. Bosson, R. S. Ramón, P. Nun, A. M. Z. Slawin and S. P. Nolan, *Chem. Eur. J.*, 2010, **16**, 13729–13740.
- 115 Z. Lu, J. Han, G. B. Hammond and B. Xu, *Org. Lett.*, 2015, **17**, 4534–4537.
- 116 D. Wang, R. Cai, S. Sharma, J. Jirak, S. K. Thummanapelli, N. G. Akhmedov, H. Zhang, X. Liu, J. L. Petersen and X. Shi, *J. Am. Chem. Soc.*, 2012, **134**, 9012–9019.
- 117 R. S. Paton and F. Maseras, *Org. Lett.*, 2009, **11**, 2237–2240.
- 118 A. S. K. Hashmi, S. Pankajakshan, M. Rudolph, E. Enns, T. Bander, F. Rominger and W. Frey, *Adv. Synth. Catal.*, 2009, **351**, 2855–2875.
- 119 T. Fan, X. Chen, J. Sun and Z. Lin, *Organometallics*, 2012, **31**, 4221–4227.
- 120 J. Jiang, Y. Liu, C. Hou, Y. Li, Z. Luan, C. Zhao and Z. Ke, *Org. Biomol. Chem.*, 2016, **14**, 3558–3563.
- 121 X. Zhang and Z. Geng, *RSC Adv.*, 2016, **6**, 62099–62108.
- 122 B. Herlé, P. M. Holstein and A. M. Echavarren, *ACS Catal.*, 2017, **7**, 3668–3675.
- 123 C. Wang, Q. Cui, Z. Zhang, Z. Yao, S. Wang and Z. Yu, *Chem. Eur. J.*, 2019, **25**, 9821–9826.
- 124 A. A. Ogunlana and X. Bao, *Chem. Commun.*, 2019, **55**, 11127–11130.
- 125 M. Jia and M. Bandini, *ACS Catal.*, 2015, **5**, 1638–1652.

- 126 J. Schießl, J. Schulmeister, A. Doppiu, E. Wörner, M. Rudolph, R. Karch and A. S. K. Hashmi, *Adv. Synth. Catal.*, 2018, **360**, 3949–3959.
- 127 A. Zhdanko and M. E. Maier, *ACS Catal.*, 2014, **4**, 2770–2775.
- 128 D. Zuccaccia, L. Belpassi, F. Tarantelli and A. Macchioni, *J. Am. Chem. Soc.*, 2009, **131**, 3170–3171.
- 129 N. Salvi, L. Belpassi, D. Zuccaccia, F. Tarantelli and A. Macchioni, *J. Organomet. Chem.*, 2010, **695**, 2679–2686.
- 130 D. Zuccaccia, L. Belpassi, L. Rocchigiani, F. Tarantelli and A. Macchioni, *Inorg. Chem.*, 2010, **49**, 3080–3082.
- 131 G. Ciancaleoni, L. Biasiolo, G. Bistoni, A. Macchioni, F. Tarantelli, D. Zuccaccia and L. Belpassi, *Organometallics*, 2013, **32**, 4444–4447.
- 132 D. Sorbelli, J. Segato, A. Del Zotto, L. Belpassi, D. Zuccaccia and P. Belanzoni, *Dalton Trans.*, 2021, **50**, 5154–5160.
- 133 A. Macchioni, *Chem. Rev.*, 2005, **105**, 2039–2074.
- 134 J. R. Pliego, *Org. Biomol. Chem.*, 2021, **19**, 1900–1914.
- 135 Y. Ma, H. S. Ali and A. A. Hussein, *Catal. Sci. Technol.*, 2022, **12**, 674–685.
- 136 A. S. K. Hashmi, J. P. Weyrauch, W. Frey and J. W. Bats, *Org. Lett.*, 2004, **6**, 4391–4394.
- 137 A. Cervantes-Reyes, F. Rominger, M. Rudolph and A. S. K. Hashmi, *Chem. Eur. J.*, 2019, **25**, 11745–11757.
- 138 A. Cervantes-Reyes, F. Rominger, M. Rudolph and A. S. K. Hashmi, *Adv. Synth. Catal.*, 2020, **362**, 2523–2533.
- 139 C. M. Krauter, A. S. K. Hashmi and M. Pernpointner, *ChemCatChem*, 2010, **2**, 1226–1230.
- 140 P. M. Stein, M. Rudolph and A. S. K. Hashmi, *Adv. Synth. Catal.*, 2021, **363**, 4264–4271.

- 141 J. C. Timmerman, B. D. Robertson and R. A. Widenhoefer, *Angew. Chem. Int. Ed.*, 2015, **54**, 2251–2254.
- 142 A. Couce-Rios, A. Lledós, I. Fernández and G. Ujaque, *ACS Catal.*, 2019, **9**, 848–858.
- 143 N. Fey and J. M. Lynam, *WIREs Comput. Mol. Sci.*, 2022, **12**, 1–23.
- 144 Z. Zhang, S. Du Lee and R. A. Widenhoefer, *J. Am. Chem. Soc.*, 2009, **131**, 5372–5373.
- 145 Z. Dong, C.-H. Liu, Y. Wang, M. Lin and Z.-X. Yu, *Angew. Chem. Int. Ed.*, 2013, **52**, 14157–14161.
- 146 A. D. Patil, A. J. Freyer, L. Killmer, P. Offen, B. Carte, A. J. Jurewicz and R. K. Johnson, *Tetrahedron*, 1997, **53**, 5047–5060.
- 147 F. Marion, D. E. Williams, B. O. Patrick, I. Hollander, R. Mallon, S. C. Kim, D. M. Roll, L. Feldberg, R. Van Soest and R. J. Andersen, *Org. Lett.*, 2006, **8**, 321–324.
- 148 S. Panichanun and I. Ralph C. Bick, *Tetrahedron*, 1984, **40**, 2685–2689.
- 149 S. J. Pastine, S. W. Youn and D. Sames, *Org. Lett.*, 2003, **5**, 1055–1058.
- 150 Y. Yamamoto, S. Kuwabara, Y. Ando, H. Nagata, H. Nishiyama and K. Itoh, *J. Org. Chem.*, 2004, **69**, 6697–6705.
- 151 H. Yamamoto, I. Sasaki, H. Imagawa and M. Nishizawa, *Org. Lett.*, 2007, **9**, 1399–1402.
- 152 R. S. Menon and M. G. Banwell, *Org. Biomol. Chem.*, 2010, **8**, 5483.
- 153 S. Aikonen, M. Muuronen, T. Wirtanen, S. Heikkinen, J. Musgreave, J. Burés and J. Helaja, *ACS Catal.*, 2018, **8**, 960–967.
- 154 M. Kreuzahler and G. Haberhauer, *Angew. Chem. Int. Ed.*, 2020, **59**, 17739–17749.
- 155 M. Kreuzahler, A. Daniels, C. Wölper and G. Haberhauer, *J. Am. Chem. Soc.*, 2019, **141**, 1337–1348.
- 156 M. Kreuzahler and G. Haberhauer, *Angew. Chem. Int. Ed.*, 2020, **59**, 9433–9437.
- 157 M. Kreuzahler and G. Haberhauer, *J. Org. Chem.*, 2019, **84**, 8210–8224.

- 158 M. E. de Orbe, M. Zanini, O. Quinonero and A. M. Echavarren, *ACS Catal.*, 2019, **9**, 7817–7822.
- 159 K. Krafts, E. Hempelmann and A. Skórska-Stania, *Parasitol. Res.*, 2012, **111**, 1–6.
- 160 A. Lilienkampf, J. Mao, B. Wan, Y. Wang, S. G. Franzblau and A. P. Kozikowski, *J. Med. Chem.*, 2009, **52**, 2109–2118.
- 161 P. S. Kharkar, M. N. Deodhar and V. M. Kulkarni, *Med. Chem. Res.*, 2009, **18**, 421–432.
- 162 J. Ghosh, V. Swarup, A. Saxena, S. Das, A. Hazra, P. Paira, S. Banerjee, N. B. Mondal and A. Basu, *Int. J. Antimicrob. Agents*, 2008, **32**, 349–354.
- 163 T. Ohyama, Y. Li, T. Utsugi, S. Irie, Y. Yamada and T. Sato, *Jpn. J. Cancer Res.*, 1999, **90**, 691–698.
- 164 S. Kumar, S. Bawa and H. Gupta, *Mini Rev. Med. Chem.*, 2010, **9**, 1648–1654.
- 165 A. Marella, O. P. Tanwar, R. Saha, M. R. Ali, S. Srivastava, M. Akhter and M. Shaquiquzzaman, *Saudi Pharm. J.*, 2013, **21**, 1–12.
- 166 R. H. Manske, *Chem. Rev.*, 1942, **30**, 113–144.
- 167 Z. H. Skraup, *Monatsh. Chem.*, 1880, **1**, 316–318.
- 168 O. Doebner and W. v. Miller, *Ber. Dtsch. Chem. Ges.*, 1881, **14**, 2812–2817.
- 169 M. Conrad and L. Limpach, *Ber. Dtsch. Chem. Ges.*, 1887, **20**, 944–948.
- 170 P. Friedlaender, *Ber. Dtsch. Chem. Ges.*, 1882, **15**, 2572–2575.
- 171 P. Friedländer and C. F. Gohring, *Ber. Dtsch. Chem. Ges.*, 1883, **16**, 1833–1839.
- 172 W. Pfitzinger, *J. Prakt. Chem.*, 1888, **38**, 582–584.
- 173 J. T. R. Liddon, M. J. James, A. K. Clarke, P. O'Brien, R. J. K. Taylor and W. P. Unsworth, *Chem. Eur. J.*, 2016, **22**, 8777–8780.
- 174 P. Fedoseev and E. Van Der Eycken, *Chem. Commun.*, 2017, **53**, 7732–7735.

- 175 M. J. James, J. D. Cuthbertson, P. O'Brien, R. J. K. Taylor and W. P. Unsworth, *Angew. Chem. Int. Ed.*, 2015, **54**, 7640–7643.
- 176 H. E. Ho, T. C. Stephens, T. J. Payne, P. O. Brien, R. J. K. Taylor and W. P. Unsworth, *ACS Catal.*, 2018, **9**, 504–510.
- 177 M. J. Robins, V. Samano and M. D. Johnson, *J. Org. Chem.*, 1990, **55**, 410–412.
- 178 S. F. Martin, J. A. Dodge, L. E. Burgess and M. Hartmann, *J. Org. Chem.*, 1992, **57**, 1070–1072.
- 179 M. Hiscock and G. B. Porter, *J. Chem. Soc. B Phys. Org.*, 1971, 1631.
- 180 A. H. Jackson and A. E. Smith, *Tetrahedron*, 1965, **21**, 989–1000.
- 181 T. Aggarwal, S. Sushmita and A. K. Verma, *Org. Biomol. Chem.*, 2019, **17**, 8330–8342.
- 182 R. G. Epton, A. K. Clarke, R. J. K. Taylor, W. P. Unsworth and J. M. Lynam, *Eur. J. Org. Chem.*, 2019, **31–32**, 5563–5571.
- 183 R. Sunberg, in *The Chemistry of Indoles*, ed. R. Sunberg, Academic Press, Inc., New York, 1st edn., 1970, pp. 1–92.
- 184 A. M. Venkatesan, O. Dos Santos, J. Ellingboe, D. A. Evrard, B. L. Harrison, D. L. Smith, R. Scerni, G. A. Hornby, L. E. Schechter and T. H. Andree, *Bioorg. Med. Chem. Lett.*, 2010, **20**, 824–827.
- 185 M. W. Robinson, J. H. Overmeyer, A. M. Young, P. W. Erhardt and W. A. Maltese, *J. Med. Chem.*, 2012, **55**, 1940–1956.
- 186 H. Hasegawa, Y. Yamada, K. Komiyama, M. Hayashi, M. Ishibashi, T. Sunazuka, T. Izuhara, K. Sugahara, K. Tsuruda, M. Masuda, N. Takasu, K. Tsukasaki, M. Tomonaga and S. Kamihira, *Blood*, 2007, **110**, 1664–1674.
- 187 D. Kumar, N. M. Kumar, K. Akamatsu, E. Kusaka, H. Harada and T. Ito, *Bioorg. Med. Chem. Lett.*, 2010, **20**, 3916–3919.

- 188 E. Dolušić, P. Larrieu, L. Moineaux, V. Stroobant, L. Pilotte, D. Colau, L. Pochet, B. Van den Eynde, B. Masereel, J. Wouters and R. Frédérick, *J. Med. Chem.*, 2011, **54**, 5320–5334.
- 189 C. Steuer, C. Gege, W. Fischl, K. H. Heinonen, R. Bartenschlager and C. D. Klein, *Bioorg. Med. Chem.*, 2011, **19**, 4067–4074.
- 190 C. Ferrer, C. H. M. Amijs and A. M. Echavarren, *Chem. Eur. J.*, 2007, **13**, 1358–1373.
- 191 C. Luo, H. Yang, R. Mao, C. Lu and G. Cheng, *New J. Chem.*, 2015, **39**, 3417–3423.
- 192 J. Schießl, M. Rudolph and A. S. K. Hashmi, *Adv. Synth. Catal.*, 2017, **359**, 639–653.
- 193 E. B. McLean, F. M. Cutolo, O. J. Cassidy, D. J. Burns and A.-L. Lee, *Org. Lett.*, 2020, **22**, 6977–6981.
- 194 T. Mehrabi and A. Ariaifard, *Chem. Commun.*, 2016, **52**, 9422–9425.
- 195 T. T. Dang, F. Boeck and L. Hintermann, *J. Org. Chem.*, 2011, **76**, 9353–9361.
- 196 M. J. James, P. O'Brien, R. J. K. Taylor and W. P. Unsworth, *Chem. Eur. J.*, 2016, **22**, 2856–2881.
- 197 C. M. Dobson, *Nature*, 2004, **432**, 824–828.
- 198 C. Lipinski and A. Hopkins, *Nature*, 2004, **432**, 855–861.
- 199 Y. Zheng, C. M. Tice and S. B. Singh, *Bioorg. Med. Chem. Lett.*, 2014, **24**, 3673–3682.
- 200 M. J. James, R. E. Clublely, K. Y. Palate, T. J. Procter, A. C. Wyton, P. O'Brien, R. J. K. Taylor and W. P. Unsworth, *Org. Lett.*, 2015, **17**, 4372–4375.
- 201 J. T. R. Liddon, J. A. Rossi-Ashton, A. K. Clarke, J. M. Lynam, R. J. K. Taylor and W. P. Unsworth, *Synth.*, 2018, **50**, 4829–4836.
- 202 T. Schubert, W. Hummel, M.-R. Kula and M. Müller, *Eur. J. Org. Chem.*, 2001, **2001**, 4181.
- 203 F. Mo, H. N. Lim and G. Dong, *J. Am. Chem. Soc.*, 2015, **137**, 15518–15527.

- 204 Y. Zi, F. Schömberg, F. Seifert, H. Görls and I. Vilotijevic, *Org. Biomol. Chem.*, 2018, **16**, 6341–6349.
- 205 D. Leboeuf, J. Ciesielski and A. Frontier, *Synlett*, 2013, **25**, 399–402.
- 206 J. Tasseroul, M. M. Lorenzo-Garcia, J. Dosso, F. Simon, S. Velari, A. De Vita, P. Tecilla and D. Bonifazi, *J. Org. Chem.*, 2020, **85**, 3454–3464.
- 207 S. Islam and I. Larrosa, *Chem. Eur. J.*, 2013, **19**, 15093–15096.
- 208 R. B. Bedford, N. Fey, M. F. Haddow and R. F. Sankey, *Chem. Commun.*, 2011, **47**, 3649.
- 209 C. Shao, G. Shi, Y. Zhang, S. Pan and X. Guan, *Org. Lett.*, 2015, **17**, 2652–2655.
- 210 J. A. Rossi-Ashton, A. K. Clarke, J. R. Donald, C. Zheng, R. J. K. Taylor, W. P. Unsworth and S. L. You, *Angew. Chem. Int. Ed.*, 2020, **59**, 7598–7604.
- 211 Y. D. Shao, X. S. Wu and S. K. Tian, *Eur. J. Org. Chem.*, 2012, 1590–1596.
- 212 X. Zeng, Z. Lu, S. Liu, G. B. Hammond and B. Xu, *J. Org. Chem.*, 2017, **82**, 13179–13187.
- 213 M. N. Godoi, F. de Azambuja, P. D. G. Martinez, N. H. Morgon, V. G. Santos, T. Regiani, D. Lesage, H. Dossmann, R. B. Cole, M. N. Eberlin and C. R. D. Correia, *Eur. J. Org. Chem.*, 2017, **2017**, 1794–1803.
- 214 K. Xu, W. Chen, J. Lin, G. Chen, B. Wang and X. Tian, *Chem. Commun.*, 2019, **55**, 14613–14616.
- 215 M. Orbach, S. Shankar, O. V. Zenkina, P. Milko, Y. Diskin-Posner and M. E. van der Boom, *Organometallics*, 2015, **34**, 1098–1106.
- 216 N. P. Yahaya, K. M. Appleby, M. Teh, C. Wagner, E. Troschke, J. T. W. Bray, S. B. Duckett, L. A. Hammarback, J. S. Ward, J. Milani, N. E. Pridmore, A. C. Whitwood, J. M. Lynam and I. J. S. Fairlamb, *Angew. Chem. Int. Ed.*, 2016, **55**, 12455–12459.
- 217 A. T. Balaban and V. Wray, *Org. Magn. Reson.*, 1977, **9**, 16–22.
- 218 D. Fărcașiu and M. Kizirian, *J. Heterocycl. Chem.*, 1990, **27**, 2041–2045.

- 219 C. Croix, A. Balland-Longeau, H. Allouchi, M. Giorgi, A. Duchêne and J. Thibonnet, *J. Organomet. Chem.*, 2005, **690**, 4835–4843.
- 220 R. Kazem Shiroodi, M. Soltani and V. Gevorgyan, *J. Am. Chem. Soc.*, 2014, **136**, 9882–9885.
- 221 L. Chen, K. Chen and S. Zhu, *Chem*, 2018, **4**, 1208–1262.
- 222 D. Malhotra, L.-P. Liu, M. S. Mashuta and G. B. Hammond, *Chem. Eur. J.*, 2013, **19**, 4043–4050.
- 223 N. Asao, K. Takahashi, S. Lee, T. Kasahara and Y. Yamamoto, *J. Am. Chem. Soc.*, 2002, **124**, 12650–12651.
- 224 E. Tomás-Mendivil, C. F. Heinrich, J.-C. Ortuno, J. Starck and V. Michelet, *ACS Catal.*, 2017, **7**, 380–387.
- 225 R. G. Epton, W. P. Unsworth and J. M. Lynam, *Organometallics*, 2022, **41**, 497–507.
- 226 R. M. Kohli, C. T. Walsh and M. D. Burkart, *Nature*, 2002, **418**, 658–661.
- 227 E. Marsault and M. L. Peterson, *J. Med. Chem.*, 2011, **54**, 1961–2004.
- 228 A. K. Yudin, *Chem. Sci.*, 2015, **6**, 30–49.
- 229 E. H. Flynn, M. V. Sigal, P. F. Wiley and K. Gerzon, *J. Am. Chem. Soc.*, 1954, **76**, 3121–3131.
- 230 N. Naruse, O. Tenmyo, K. Kawano, K. Tomita, N. Ohgusa, T. Miyaki, M. Konishi and T. Oki, *J. Antibiot.*, 1991, **44**, 733–740.
- 231 C. Festa, S. De Marino, V. Sepe, M. V. D’Auria, G. Bifulco, C. Débitus, M. Bucci, V. Vellecco and A. Zampella, *Org. Lett.*, 2011, **13**, 1532–1535.
- 232 H. Zhang, S. Qiu, P. Tamez, G. T. Tan, Z. Aydogmus, N. Van Hung, N. M. Cuong, C. Angerhofer, D. Doel Soejarto, J. M. Pezzuto and H. H. S. Fong, *Pharm. Biol.*, 2002, **40**, 221–224.

- 233 A. Evidente, R. Lanzetta, R. Capasso, M. Vurro and A. Botralico, *Phytochemistry*, 1993, **34**, 999–1003.
- 234 F. L. Cook, C. W. Bowers and C. L. Liotta, *J. Org. Chem.*, 1974, **39**, 3416–3418.
- 235 D. Wynn, *Talanta*, 1984, **31**, 1036–1040.
- 236 Y. Demizu, N. Yamagata, S. Nagoya, Y. Sato, M. Doi, M. Tanaka, K. Nagasawa, H. Okuda and M. Kurihara, *Tetrahedron*, 2011, **67**, 6155–6165.
- 237 T. Ema, D. Tanida and T. Sakai, *J. Am. Chem. Soc.*, 2007, **129**, 10591–10596.
- 238 G. Illuminati and L. Mandolini, *Acc. Chem. Res.*, 1981, **14**, 95–102.
- 239 M. A. Casadei, C. Galli and L. Mandolini, *J. Am. Chem. Soc.*, 1984, **106**, 1051–1056.
- 240 M. B. Smith and J. March, *March's Advanced Organic Chemistry*, John Wiley & Sons, Inc., Hoboken, NJ, USA, 2006.
- 241 J. Clayden, N. Greeves and S. Warren, *Organic Chemistry*, Oxford University Press, New York, 2nd edn., 2001.
- 242 C. J. White and A. K. Yudin, *Nat. Chem.*, 2011, **3**, 509–524.
- 243 V. D. Bock, R. Perciaccante, T. P. Jansen, H. Hiemstra and J. H. Van Maarseveen, *Org. Lett.*, 2006, **8**, 919–922.
- 244 J. Lécaillon, P. Gilles, G. Subra, J. Martinez and M. Amblard, *Tetrahedron Lett.*, 2008, **49**, 4674–4676.
- 245 Y. Li, A. Yongye, M. Giulianotti, K. Martinez-Mayorga, Y. Yu and R. A. Houghten, *J. Comb. Chem.*, 2009, **11**, 1066–1072.
- 246 Y. Li, M. Giulionatti and R. A. Houghten, *Org. Lett.*, 2010, **12**, 2250–2253.
- 247 J. A. Camarero and T. W. Muir, *Chem. Commun.*, 1997, 1369–1370.
- 248 W. S. Horne, C. A. Olsen, J. M. Beierle, A. Montero and M. R. Ghadiri, *Angew. Chem. Int. Ed.*, 2009, **48**, 4718–4724.

- 249 L. T. Scott, J. Rebek, L. Ovsyanko and C. L. Sims, *J. Am. Chem. Soc.*, 1977, **99**, 625–626.
- 250 S. Mazur and P. Jayalekshmy, *J. Am. Chem. Soc.*, 1979, **101**, 677–683.
- 251 K. Haas, W. Ponikwar, H. Nöth and W. Beck, *Angew. Chem. Int. Ed.*, 1998, **37**, 1086–1089.
- 252 H. Fu, H. Chang, J. Shen, L. Yu, B. Qin, K. Zhang and H. Zeng, *Chem. Commun.*, 2014, **50**, 3582–3584.
- 253 C. B. Reese and H. P. Sanders, *Synthesis*, 1981, **4**, 276–278.
- 254 A. Eschenmoser, D. Felix and G. Ohloff, *Helv. Chim. Acta*, 1967, **50**, 708–713.
- 255 J. Schreiber, D. Felix, A. Eschenmoser, M. Winter, F. Gautschi, K. H. Schulte-Elte, E. Sundt, G. Ohloff, J. Kalovoda, H. Kaufmann, P. Wieland and G. Anner, *Helv. Chim. Acta*, 1967, **50**, 2101–2108.
- 256 P. Dowd and S. C. Choi, *J. Am. Chem. Soc.*, 1987, **109**, 6548–6549.
- 257 A. L. J. Beckwith, R. Kazlauskas and M. R. Syner-Lyons, *J. Org. Chem.*, 1983, **48**, 4718–4722.
- 258 J. R. Donald and W. P. Unsworth, *Chem. Eur. J.*, 2017, **23**, 8780–8799.
- 259 S. Bäurle, T. Blume, A. Mengel, C. Parchmann, W. Skuballa, S. Bäsler, M. Schäfer, D. Sülzle and H. P. Wrona-Metzinger, *Angew. Chem. Int. Ed.*, 2003, **42**, 3961–3964.
- 260 S. Bäurle, T. Blume, J. Günther, D. Henschel, R. C. Hillig, M. Husemann, A. Mengel, C. Parchmann, E. Schmid and W. Skuballa, *Bioorg. Med. Chem. Lett.*, 2004, **14**, 1673–1677.
- 261 J. P. Krieger, G. Ricci, D. Lesuisse, C. Meyer and J. Cossy, *Angew. Chem. Int. Ed.*, 2014, **53**, 8705–8708.
- 262 F. Kopp, C. F. Stratton, L. B. Akella and D. S. Tan, *Nat. Chem. Biol.*, 2012, **8**, 358–365.
- 263 R. Schmid and H. Schmid, *Helv. Chim. Acta*, 1977, **60**, 1361–1366.
- 264 U. Kramer, A. Guggisberg, M. Hesse and H. Schmid, *Angew. Chem. Int. Ed.*, 1977, **16**, 861–862.

- 265 U. Kramer, A. Guggisberg, M. Hesse and H. Schmid, *Helv. Chim. Acta*, 1978, **61**, 1342–1352.
- 266 R. Wälchli and M. Hesse, *Helv. Chim. Acta*, 1982, **65**, 2299–2301.
- 267 R. Wälchli, A. Guggisberg and M. Hesse, *Helv. Chim. Acta*, 1984, **67**, 2178–2185.
- 268 E. Stephanou, A. Guggisberg and M. Hesse, *Helv. Chim. Acta*, 1979, **62**, 1932–1943.
- 269 U. Kramer, A. Guggisberg, M. Hesse and H. Schmid, *Angew. Chem. Int. Ed.*, 1978, **17**, 200–202.
- 270 C. Jenny and M. Hesse, *Helv. Chim. Acta*, 1981, **64**, 1807–1811.
- 271 E. J. Corey, D. J. Brunelle and K. C. Nicolaou, *J. Am. Chem. Soc.*, 1977, **99**, 7359–7360.
- 272 R. Mendoza-Sanchez, V. B. Corless, Q. N. N. Nguyen, M. Bergeron-Brlek, J. Frost, S. Adachi, D. J. Tantillo and A. K. Yudin, *Chem. Eur. J.*, 2017, **23**, 13319–13322.
- 273 A. Sapegin, A. Osipyan and M. Krasavin, *Org. Biomol. Chem.*, 2017, **15**, 2906–2909.
- 274 A. Osipyan, A. Sapegin, A. S. Novikov and M. Krasavin, *J. Org. Chem.*, 2018, **83**, 9707–9717.
- 275 E. Reutskaya, A. Osipyan, A. Sapegin, A. S. Novikov and M. Krasavin, *J. Org. Chem.*, 2019, **84**, 1693–1705.
- 276 C. Kitsiou, J. J. Hindes, P. l'Anson, P. Jackson, T. C. Wilson, E. K. Daly, H. R. Felstead, P. Hearnshaw and W. P. Unsworth, *Angew. Chem. Int. Ed.*, 2015, **54**, 15794–15798.
- 277 L. G. Baud, M. A. Manning, H. L. Arkless, T. C. Stephens and W. P. Unsworth, *Chem. Eur. J.*, 2017, **23**, 2225–2230.
- 278 T. C. Stephens, M. Lodi, A. M. Steer, Y. Lin, M. T. Gill and W. P. Unsworth, *Chem. Eur. J.*, 2017, **23**, 13314–13318.
- 279 T. C. Stephens, A. Lawer, T. French and W. P. Unsworth, *Chem. Eur. J.*, 2018, **24**, 13947–13953.
- 280 S. F. Sousa, P. A. Fernandes and M. J. Ramos, *J. Phys. Chem. A*, 2007, **111**, 10439–10452.

- 281 L. Goerigk, A. Hansen, C. Bauer, S. Ehrlich, A. Najibi and S. Grimme, *Phys. Chem. Chem. Phys.*, 2017, **19**, 32184–32215.
- 282 M. Torrent-Sucarrat, S. Navarro, F. P. Cossío, J. M. Anglada and J. M. Luis, *J. Comput. Chem.*, 2017, **38**, 2819–2828.
- 283 P. Hao, J. Sun, B. Xiao, A. Ruzsinszky, G. I. Csonka, J. Tao, S. Glindmeyer and J. P. Perdew, *J. Chem. Theory Comput.*, 2013, **9**, 355–363.
- 284 A. Brakestad, P. Wind, S. R. Jensen, L. Frediani and K. H. Hopmann, *J. Chem. Phys.*, 2021, **154**, 214302.
- 285 *Spartan'14*, Wavefunction, Inc., Irvine, CA.
- 286 M. J. Frisch, G. W. Trucks, H. B. Schlegel, G. E. Scuseria, J. R. Robb, J. R. Cheeseman, G. Scalmani, V. Barone, G. A. Petersson, H. Nakatsuji, X. Li, M. Caricato, A. Marenich, J. Bloino, B. G. Janesko, R. Gomperts, B. Mennucci, H. P. Hratchian, J. V. Ortiz, A. F. Izmaylov, L. Sonnenberg, D. Williams-Young, F. Ding, F. Lipparini, F. Egidi, J. Goings, B. Peng, A. Petrone, T. Henderson, D. Ranasinghe, V. G. Zakrzewski, J. Gao, N. Rega, G. Zheng, W. Liang, M. Hada, M. Ehara, K. Toyota, R. Fukuda, J. Hasegawa, M. Ishida, T. Nakajima, Y. Honda, O. Kitao, H. Nakai, T. Vreven, K. Throssell, J. A. Montgomery Jr., J. E. Peralta, F. Ogliaro, M. Bearpark, J. J. Heyd, E. Brothers, K. N. Kudin, V. N. Staroverov, T. Keith, R. Kobayashi, J. Normand, K. Raghavachari, A. Rendell, J. C. Burant, S. S. Iyengar, J. Tomasi, M. Cossi, J. M. Millam, M. Klene, C. Adamo, R. Cammi, J. W. Ochterski, R. L. Martin, K. Morokuma, O. Farkas, J. B. Foresman and D. J. Fox, *Gaussian 09, Revision D.01*, Gaussian, Inc., Wallingford CT, 2016.
- 287 A. Lawer, R. G. Epton, T. C. Stephens, K. Y. Palate, M. Lodi, E. Marotte, K. J. Lamb, J. K. Sangha, J. M. Lynam and W. P. Unsworth, *Chem. – A Eur. J.*, 2020, **26**, 12674–12683.
- 288 J. W. Skiles, J. T. Suh, B. E. Williams, P. R. Menard, J. N. Barton, B. Loev, H. Jones, E. S. Neiss and A. Schwab, *J. Med. Chem.*, 1986, **29**, 784–796.
- 289 D. V. Ferraris, P. Majer, C. Ni, C. E. Slusher, R. Rais, Y. Wu, K. M. Wozniak, J. Alt, C. Rojas, B. S. Slusher and T. Tsukamoto, *J. Med. Chem.*, 2014, **57**, 243–247.
- 290 C.-L. J. Wang and J. . Salvino, *Tetrahedron Lett.*, 1984, **25**, 5243–5246.

- 291 A. M. M. El-Aasar, C. P. Nash, L. L. Ingraham, A. M. M. El-Assar, C. P. Nash and L. L. Ingraham, *Biochemistry*, 1982, **21**, 1972–1976.
- 292 W. Yang and D. G. Drueckhammer, *J. Am. Chem. Soc.*, 2001, **123**, 11004–11009.
- 293 C. M. Hall and J. Wemple, *J. Org. Chem.*, 1977, **42**, 2118–2123.
- 294 A. Lawer, R. G. Epton, T. C. Stephens, K. Y. Palate, M. Lodi, E. Marotte, K. J. Lamb, J. K. Sangha, J. M. Lynam and W. P. Unsworth, *Chem. Eur. J.*, 2020, **26**, 12674–12683.
- 295 T. a Halgren, *J. Comput. Chem.*, 1996, **17**, 490–519.
- 296 L. J. Mathias and D. R. Moore, *J. Am. Chem. Soc.*, 1985, **107**, 5817–5818.
- 297 D. R. Moore and L. J. Mathias, *Macromolecules*, 1986, **19**, 1530–1536.
- 298 D. R. Moore and L. J. Mathias, *J. Org. Chem.*, 1987, **52**, 1599–1601.
- 299 K. Y. Palate, Z. Yang, A. C. Whitwood and W. P. Unsworth, *RSC Chem. Biol.*, 2022, **3**, 334–340.
- 300 K. Y. Palate, R. G. Epton, A. C. Whitwood, J. M. Lynam and W. P. Unsworth, *Org. Biomol. Chem.*, 2021, **19**, 1404–1411.
- 301 T. C. Stephens, PhD Thesis, University of York, 2019.
- 302 A. C. Conibear, E. E. Watson, R. J. Payne and C. F. W. Becker, *Chem. Soc. Rev.*, 2018, **47**, 9046–9068.
- 303 S. Wang, Y. A. Thopate, Q. Zhou and P. Wang, *Chinese J. Chem.*, 2019, **37**, 1181–1193.
- 304 A. Lawer, Unpublished Work, 2018.
- 305 J. Shang, V. J. Thombare, C. L. Charron, U. Wille and C. A. Hutton, *Chem. – A Eur. J.*, 2021, **27**, 1620–1625.
- 306 G. Fodor and J. Kiss, *J. Am. Chem. Soc.*, 1950, **72**, 3495–3497.
- 307 A. M. Fureby, C. Virto, P. Adlercreutz and B. Mattiasson, *Biocatal. Biotransformation*, 1996, **14**, 89–111.

- 308 K. K.-C. Liu, K. Nozaki and C. H. Wong, *Biocatal. Biotransformation*, 1990, **3**, 169–177.
- 309 D. H. B. Ripin, in *Practical Synthetic Organic Chemistry*, John Wiley & Sons, Inc., Hoboken, NJ, USA, 2011, pp. 771–803.
- 310 F. G. Bordwell and H. E. Fried, *J. Org. Chem.*, 1991, **56**, 4218–4223.
- 311 P. Ballinger and F. A. Long, *J. Am. Chem. Soc.*, 1960, **82**, 795–798.
- 312 F. G. Bordwell, *Acc. Chem. Res.*, 1988, **21**, 456–463.
- 313 J. P. Danehy and K. N. Parameswaran, *J. Chem. Eng. Data*, 1968, **13**, 386–389.
- 314 G. W. Spitznagel, T. Clark, J. Chandrasekhar and P. V. R. Schleyer, *J. Comput. Chem.*, 1982, **3**, 363–371.
- 315 T. J. Lee and H. F. Schaefer, *J. Chem. Phys.*, 1985, **83**, 1784–1794.
- 316 A. D. Boese, J. M. L. Martin and N. C. Handy, *J. Chem. Phys.*, 2003, **119**, 3005–3014.
- 317 S. R. Angle, X. L. Qian, A. A. Pletnev and J. Chinn, *J. Org. Chem.*, 2007, **72**, 2015–2020.
- 318 WO2012138678A1, 2012.
- 319 D. Witt, *Synthesis*, 2008, **2008**, 2491–2509.
- 320 J. Zaminer, C. Brockmann, P. Huy, R. Opitz, C. Reuter, M. Beyermann, C. Freund, M. Müller, H. Oschkinat, H. G. Schmalz and R. Kühne, *Angew. Chem. Int. Ed.*, 2010, **49**, 7111–7115.
- 321 A. Kamimura, Y. Nagata, A. Kadowaki, K. Uchida and H. Uno, *Tetrahedron*, 2007, **63**, 11856–11861.
- 322 M. Chen and G. Dong, *J. Am. Chem. Soc.*, 2017, **139**, 7757–7760.
- 323 O. Boutureira and G. J. L. Bernardes, *Chem. Rev.*, 2015, **115**, 2174–2195.
- 324 L. Yan, W. Yang, L. Li, Y. Shen and Z. Jiang, *Chinese J. Chem.*, 2011, **29**, 1906–1910.
- 325 S. Parmar, S. P. Pawar, R. Iyer and D. Kalia, *Chem. Commun.*, 2019, **55**, 14926–14929.

- 326 Y. Matsuya, A. Koiwai, D. Minato, K. Sugimoto and N. Toyooka, *Tetrahedron Lett.*, 2012, **53**, 5955–5957.
- 327 V. K. Vyas, R. C. Knighton, B. M. Bhanage and M. Wills, *Org. Lett.*, 2018, **20**, 975–978.
- 328 WO2014032801A1, 2014.
- 329 M. R. Crampton and I. A. Robotham, *J. Chem. Res.*, 1997, 22–23.
- 330 J. M. J. M. Ravasco, H. Faustino, A. Trindade and P. M. P. Gois, *Chem. Eur. J.*, 2019, **25**, 43–59.
- 331 S. H. Frayne, R. R. Murthy and B. H. Northrop, *J. Org. Chem.*, 2017, **82**, 7946–7956.
- 332 B. A. Abel and C. L. McCormick, *Macromolecules*, 2016, **49**, 6193–6202.
- 333 X. Ji, W. Tian, K. Jin, H. Diao, X. Huang, G. Song and J. Zhang, *Nat. Commun.*, 2022, **13**, 3717.
- 334 M. Azechi, N. Toyota, K. Yamabuki, K. Onimura and T. Oishi, *Polym. Bull.*, 2011, **67**, 631–640.
- 335 U. S. Sahu and S. N. Bhadani, *Makromol. Chem., Rapid Commun.*, 1982, **3**, 103–107.
- 336 D. Kalia, P. V. Malekar and M. Parthasarathy, *Angew. Chem. Int. Ed.*, 2016, **55**, 1432–1435.
- 337 B. Trofimov, A. Mal'kina, O. Shemyakina, V. Nosyreva, A. Borisova, S. Khutsishvili and L. Krivdin, *Synthesis*, 2009, **2009**, 3136–3142.
- 338 K. Hideg, O. Hideg-Hankovszky and P. Sohár, *Chem. Ber.*, 1974, **107**, 2079–2083.
- 339 T. Nishio and Y. Omote, *J. Chem. Soc. Perkin Trans. 1*, 1981, 934–938.
- 340 H. Y. Shiu, T. C. Chan, C. M. Ho, Y. Liu, M. K. Wong and C. M. Che, *Chem. Eur. J.*, 2009, **15**, 3839–3850.
- 341 L. A. Carpino, H. G. Chao, M. Beyermann and M. Bienert, *J. Org. Chem.*, 1991, **56**, 2635–2642.

- 342 C. Peng and H. Bernhard Schlegel, *Isr. J. Chem.*, 1993, **33**, 449–454.
- 343 C. Peng, P. Y. Ayala, H. B. Schlegel and M. J. Frisch, *J. Comput. Chem.*, 1996, **17**, 49–56.
- 344 L. Goerigk and S. Grimme, *Phys. Chem. Chem. Phys.*, 2011, **13**, 6670.
- 345 P. Császár and P. Pulay, *J. Mol. Struct.*, 1984, **114**, 31–34.
- 346 R. Ahlrichs, M. Bär, M. Häser, H. Horn and C. Kölmel, *Chem. Phys. Lett.*, 1989, **162**, 165–169.
- 347 P. Deglmann, F. Furche and R. Ahlrichs, *Chem. Phys. Lett.*, 2002, **362**, 511–518.
- 348 P. Deglmann, K. May, F. Furche and R. Ahlrichs, *Chem. Phys. Lett.*, 2004, **384**, 103–107.
- 349 K. Eichkorn, O. Treutler, H. Öhm, M. Häser and R. Ahlrichs, *Chem. Phys. Lett.*, 1995, **240**, 283–290.
- 350 O. Treutler and R. Ahlrichs, *J. Chem. Phys.*, 1995, **102**, 346–354.
- 351 M. von Arnim and R. Ahlrichs, *J. Chem. Phys.*, 1999, **111**, 9183–9190.
- 352 F. Weigend, *Phys. Chem. Chem. Phys.*, 2006, **8**, 1057.
- 353 K. E. Gilbert, *PCModel 10.075*, Serena Software, Bloomington, IN, 2020.
- 354 Z. Liu, J. Zhang, S. Chen, E. Shi, Y. Xu and X. Wan, *Angew. Chem. Int. Ed.*, 2012, **51**, 3231–3235.
- 355 D. García-López, M. G. Civit, C. M. Vogels, J. M. Ricart, S. A. Westcott, E. Fernández and J. J. Carbó, *Catal. Sci. Technol.*, 2018, **8**, 3617–3628.
- 356 T. Wendling, E. Risto, T. Krause and L. J. Gooßen, *Chem. Eur. J.*, 2018, **24**, 6019–6024.
- 357 G. S. Kottas, T. Brotin, P. F. H. Schwab, K. Gala, Z. Havlas, J. P. Kirby, J. R. Miller and J. Michl, *Organometallics*, 2014, **33**, 3251–3264.
- 358 D. Zhao, C. Gao, X. Su, Y. He, J. You and Y. Xue, *Chem. Commun.*, 2010, **46**, 9049.
- 359 T. Torigoe, T. Ohmura and M. Sugimoto, *Angew. Chem. Int. Ed.*, 2017, **56**, 14272–14276.

- 360 S. Dhuru, D. Bhedi, D. Gophane, K. Hirbhagat, V. Nadar, D. More, S. Parikh, R. Dalal, L. C. Fonseca, F. Kharas, P. Y. Vadnal, R. A. Vishwakarma and H. Sivaramakrishnan, *Bioorg. Med. Chem. Lett.*, 2011, **21**, 3784–3787.
- 361 S. Paul, W. B. Schweizer, G. Rugg, H. M. Senn and R. Gilmour, *Tetrahedron*, 2013, **69**, 5647–5659.

Medium-Sized Rings

Deutsche Ausgabe: DOI: 10.1002/ange.201907206
Internationale Ausgabe: DOI: 10.1002/anie.201907206

Internal Nucleophilic Catalyst Mediated Cyclisation/Ring Expansion Cascades for the Synthesis of Medium-Sized Lactones and Lactams

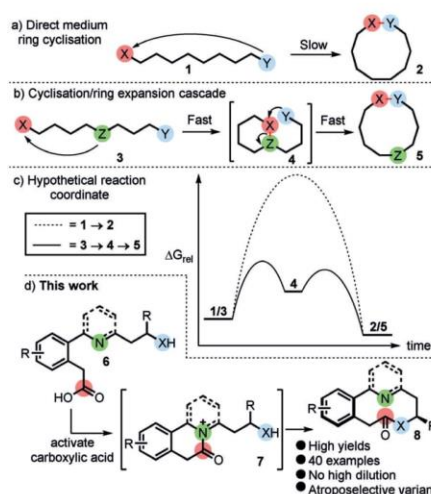
Aggie Lawer, James A. Rossi-Ashton[†], Thomas C. Stephens[†], Bradley J. Challis, Ryan G. Epton, Jason M. Lynam und William P. Unsworth*

Abstract: A strategy for the synthesis of medium-sized lactones and lactams from linear precursors is described in which an amine acts as an internal nucleophilic catalyst to facilitate a novel cyclisation/ring expansion cascade sequence. This method obviates the need for the high-dilution conditions usually associated with medium-ring cyclisation protocols, as the reactions operate exclusively via kinetically favourable „normal“-sized cyclic transition states. This same feature also enables biaryl-containing medium-sized rings to be prepared with complete atroposelectivity by point-to-axial chirality transfer.

Introduction

Medium-sized rings have much promise in medicinal chemistry^[1,2] but are difficult to prepare by conventional cyclisation methods.^[3] Destabilising transannular interactions and loss of entropy during cyclisation mean that medium-ring cyclisation reactions of the type 1→2 (Scheme 1a) typically suffer from competing intermolecular reactions or other side processes.^[4,5] Synthetic routes to access medium-sized rings that avoid end-to-end cyclisation are therefore desirable, and ring expansion reactions have proven to be especially useful in this context.^[6,7]

In this manuscript, a new process is described by which medium-sized rings can be accessed directly from simple linear precursors. The avoidance of medium-sized cyclic transition states is key to our design principle, in which we use a nucleophilic catalyst built into the linear starting material to promote a cyclisation/ring expansion cascade. For example, while the direct synthesis of ten-membered ring 2 from a hypothetical linear precursor 1 (Scheme 1a) is usually a slow/difficult process,^[4] we reasoned that similar medium-sized ring frameworks would be more effectively synthesised from alternative linear precursors of the form 3, in which a reactive motif „Z“ built into the linear starting material mediates a cyclisation/ring expansion cascade (3→4→5, Scheme 1b).^[8,9] By designing the reactions so that both



Scheme 1. a) Direct medium ring cyclisation. b) Cyclisation/ring expansion. c) Hypothetical reaction coordinates. d) This work: Internal nucleophilic catalyst mediated cyclisation/ring expansion cascade reactions.

discrete cyclisation reactions proceed via „normal“-sized cyclic transition states (especially if they are 5- or 6-membered), it is reasonable to expect that a kinetically more favourable reaction course will be followed, as illustrated in the stylised reaction coordinate for these two scenarios depicted in Scheme 1c. By allowing this lower-energy pathway to operate, medium-sized ring transition states can be avoided, which should help to reduce side reactions and obviate the need for impractical high-dilution/pseudo-high-dilution conditions that are common in typical medium-sized ring and macrocycle cyclisation reactions.^[10]

The realisation of this strategy is reported herein. Thus a method based on the formation (6→7) and spontaneous expansion (7→8) of reactive acyl-ammonium ion intermediates is described that enables nitrogen-containing medium-sized rings to be prepared from simple linear precursors (Scheme 1d). Using these cascade reactions, we show that a wide range of functionalised medium-sized lactones and lactams (40 examples, 31–100% yield) can be prepared under mild, practical reaction conditions. Furthermore, in suitably designed cases, biaryl-containing medium-sized rings can also

[*] Dr. A. Lawer, J. A. Rossi-Ashton,^[†] T. C. Stephens,^[†] B. J. Challis, R. G. Epton, Dr. J. M. Lynam, Dr. W. P. Unsworth
University of York
York, YO10 5DD (UK)
E-Mail: william.unsworth@york.ac.uk

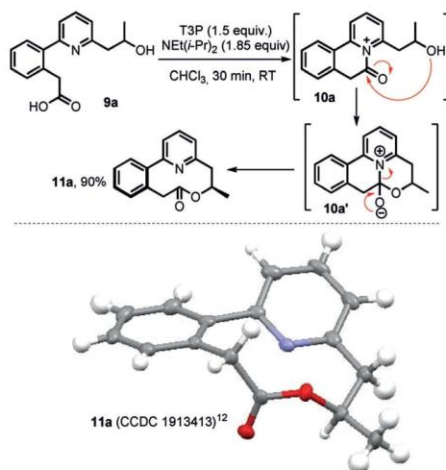
[†] These authors contributed equally to this work.

Supporting information and the ORCID identification number(s) for the author(s) of this article can be found under:
<https://doi.org/10.1002/anie.201907206>.

be formed with complete atroposelectivity by a new type of point-to-axial chirality transfer reaction.^[11]

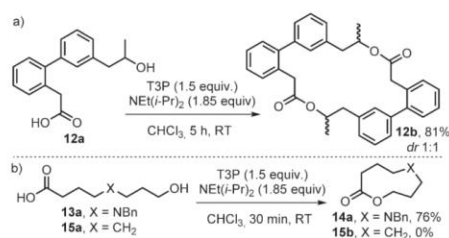
Results and Discussion

We started by examining pyridine-containing linear precursor **9a** (see the Supporting Information for its synthesis). The plan was that activation of carboxylic acid **9a** would initiate a cyclisation (**9a**→**10a**) and ring expansion (**10a**→**11a**) cascade. Thus, carboxylic acid **9a** was treated with T3P (propanephosphonic acid anhydride) and NEt(*i*-Pr)₂ in chloroform,^[12] and after stirring for just 30 min at room temperature, the desired ten-membered lactone **11a** was formed and isolated in 90% yield. Of further interest, **11a** was formed exclusively as the single atropisomer shown, with the structural and stereochemical assignment supported by X-ray crystallographic data^[13] (Scheme 2: the atroposelectivity aspects of this reaction, including data that confirms that atropisomerisation by free rotation is not an energetically feasible process for this system, are discussed later in the manuscript).



Scheme 2. Cyclisation/ring expansion cascade synthesis of **11a**.

Given the known challenges of forming ten-membered ring lactones,^[13a-d] the efficiency of this reaction was highly encouraging, especially as it was performed under mild conditions at standard dilution. Nonetheless, to discount the possibility that this is simply an unusually efficient ten-membered-ring lactonisation, hydroxy acid **12a** (analogous to **9a** but lacking the pyridine nitrogen atom) was reacted under the same conditions used to make **11a** (with a 5 h reaction time; Scheme 3 a). As expected, none of the analogous ten-membered lactone was formed, with dimeric 20-membered lactone **12b** the only tractable product isolated from this



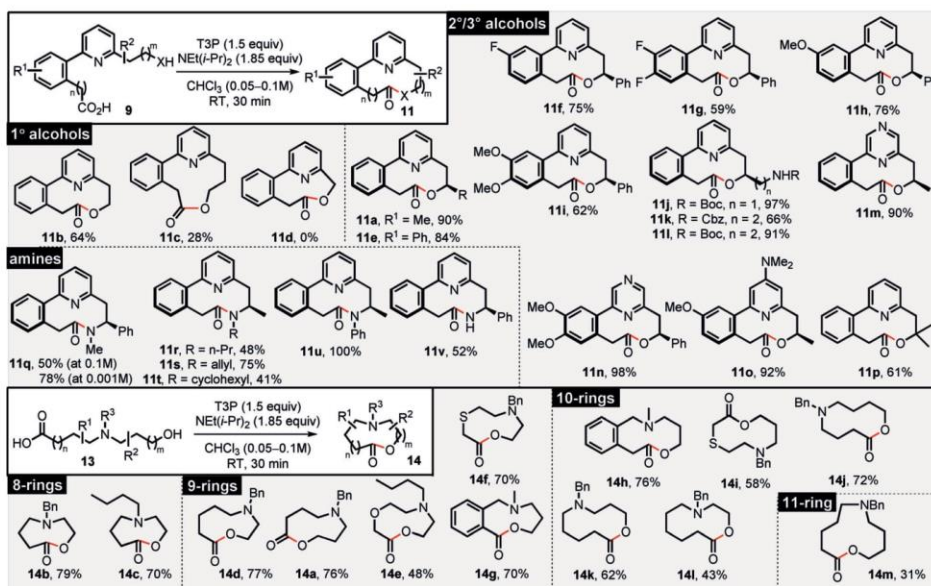
Scheme 3. a) Formation of 20-membered head-to-tail dimer **12b**. b) Cyclisation/ring expansion cascade synthesis of **14a** and failed synthesis of **15b**.

reaction, corroborating the importance of the pyridine nitrogen atom in mediating the synthesis of **11a**. Furthermore, our novel cyclisation/ring expansion cascade also works well using an aliphatic tertiary amine as the internal nucleophilic catalyst in place of the pyridine; thus, linear hydroxy acid **13a** was converted into nine-membered lactone **14a** in 76% yield (T3P, 30 min, RT), whilst an intractable mixture of products resulted when the analogous nitrogen-free hydroxy acid **15a** was reacted under the same conditions (Scheme 3 b).

The scope of the reaction is broad and is summarised in Scheme 4. Ten-membered lactone **11b** was formed without problem using the standard method, whilst the homologous eleven-membered lactone **11c** was also prepared, albeit in lower yield, which is likely to be a result of this example proceeding via a less favourable seven-membered transition state. Conversely, the synthesis of the smaller nine-membered product **11d** failed, presumably because of too much strain in the sp²-rich scaffold. Next, a range of secondary-alcohol-based systems were tested, and the reactions worked well in all cases; functionality at various positions of the starting material, protected amine handles, diazine and DMAP-like tethers, and tertiary alcohols were all well-tolerated, with lactones **11e–p** isolated in consistently high yields.

The same strategy can also be used to make medium-sized lactams using unprotected-amine-based nucleophiles. Using the standard protocol, lactam **11q** was formed in 50% yield; competing intermolecular amide bond formation likely accounts for the decreased yield, which is supported by the observation that a significantly higher yield was obtained when the same reaction was performed at increased dilution (78%). Other secondary-amine-based systems performed similarly under the standard undiluted conditions (**11r–v**). Pleasingly, aniline-based lactam **11u** was formed in quantitative yield; presumably, this system did not suffer from competing intermolecular reaction in view of the lower nucleophilicity of the aniline nucleophile relative to aliphatic amines. Finally, we found that primary-amine-derived lactam **11v** could be formed in 52% yield using the standard conditions.^[14]

Medium-sized lactones **14a–m** were also prepared from aliphatic tertiary-amine-containing hydroxy acids **13a–m**. The yields were generally good across this series, with broad scope demonstrated; it is especially noteworthy that the cascade



Scheme 4. Cyclisation/ring expansion cascade reactions of pyridine- and tertiary-amine-containing hydroxy acids and amino acids.

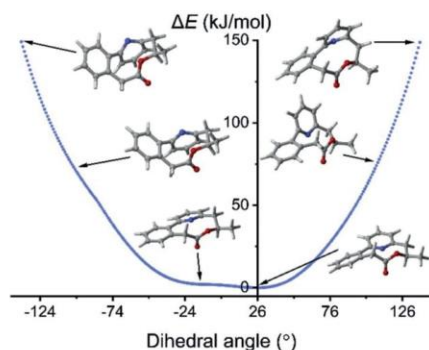
reactions can be used to prepare lactones right across the „medium-sized“ ring range, with eight- to eleven-membered lactones all being prepared using the standard protocol. The utility of the cyclisation/ring expansion cascade has therefore been well demonstrated by the synthesis of 34 medium-sized lactones or lactams using a simple and mild synthetic method, without requiring high dilution conditions.

An important feature of these reactions is the observation that in all examples containing two stereochemical units, the products were exclusively formed as single diastereoisomers (**11a**, **11e–o**, and **11q–v**; all contain a point stereogenic centre and an unsymmetrical biaryl unit with axial chirality). Thus the point chirality of the secondary nucleophile is able to fully control the formed atropisomer in the medium-sized cyclic biaryl product in all of these cases, via what is, to the best of our knowledge, an unprecedented type of point-to-axial chirality transfer.^[11] Atropisomerism can play a vital role in mediating ligand–target interactions in biology,^[15] but while synthetic methods able to impart exquisite levels of control over stereogenic centres on a single atom (usually referred to as point chirality) are very well established, methods designed to control other chirality elements (e.g., planar, axial, and helical chirality)^[16] are less well developed.^[17] Atroposelective methods capable of delivering medium-sized rings or macrocycles are particularly rare,^[18] which encouraged us to examine the atroposelectivity of our cascade reactions in more detail.

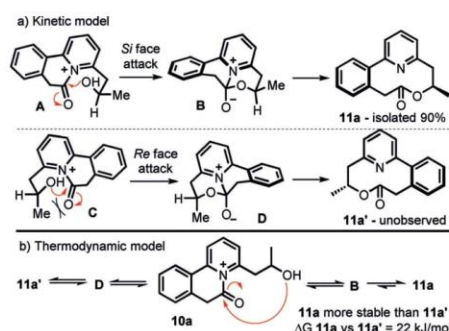
First, we confirmed that the biaryl unit in the medium-sized ring products is unable to undergo free rotation. Based

on its geometry and ring size, we predicted that the sp²-rich medium-ring scaffold **11a** would be relatively rigid and that rotation about the biaryl C–C single bond is unlikely to be kinetically accessible; indeed, to the best of our knowledge, compound **11a** is the smallest ring system based on an unbridged 1,2-disubstituted and 1,3-disubstituted biaryl framework in the literature. Related larger macrocyclic scaffolds containing similar biaryl motifs have also been shown to exist as stable atropisomers at room temperature,^[19,20] nonetheless, for additional support, we modelled the energy required to rotate about this bond by DFT (Scheme 5). Starting from the crystal structure of **11a**, this was optimised at the BP86/SV(P) level of theory, and scans were performed whilst rotating the biaryl dihedral angle in both directions, reoptimising the structure at each step. No minima were found from these calculations, and the energies calculated increased steeply to give values that can be considered chemically inaccessible, strongly suggesting that the biaryl unit is indeed unable to rotate freely (see the Supporting Information for tabulated data).

One hypothesis for the excellent stereoselectivity, which is depicted in Scheme 6 for prototypical substrate **11a**, is a kinetic argument that hinges on the stereochemistry-determining step operating via a six-membered transition state. The observed stereochemical outcome is consistent with the alcohol attacking the prochiral intermediate *N*-acyl ammonium ion with the methyl group in a pseudo-equatorial orientation in a chair/boat-like conformation (see **A**→**B**, Scheme 6a). Conversely, to generate the unobserved isomer



Scheme 5. Calculated BP86/SV(P) electronic energies for **11a** with a SCRF solvent correction in CHCl_3 . The energies given are for geometry-optimised structures at fixed biaryl dihedral angles.

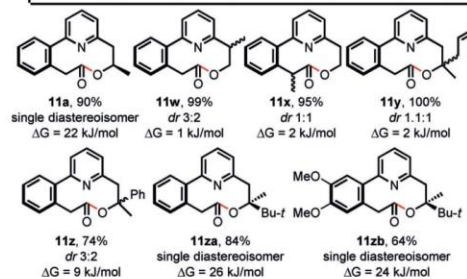
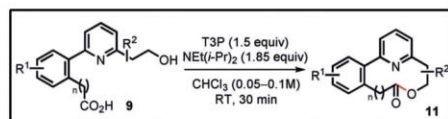


Scheme 6. Proposed atroposelectivity models. a) A kinetic model based on diastereoselective attack into prochiral *N*-acyliminium ion (**A**→**B**). b) A thermodynamic model based on reversible ring expansion/ring contraction.

11a', attack on the opposite face of the *N*-acyl ammonium ion is required, which necessitates that the methyl group be oriented in a pseudo-axial conformation, the transition state for which (**C**→**D**) is likely to be higher in energy.^[21]

An alternative explanation is that the reactions are reversible and under thermodynamic control (Scheme 6b). This model is supported by DFT calculations of the ground-state energies of **11a** and **11a'**; thus, the Gibbs free energy of the observed and unobserved atropisomers **11a** and **11a'** were calculated at the M06-2X/6-311G* level of theory (see the Supporting Information for full details),^[22] and the observed isomer **11a** was calculated to be 22 kJ mol^{-1} lower in free energy than the unobserved isomer **11a'**. Such a large energy difference would provide a clear driving force for the selective formation of **11a** if the reactions are reversible.

The atroposelectivity was also probed experimentally (Scheme 7). Thus substrates with the methyl substituent transposed α to both the phenyl and pyridyl rings were



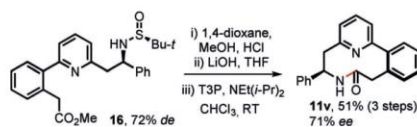
Scheme 7. Cyclisation/ring expansion cascade reactions of pyridine-containing substrates with point stereogenic centres, and the calculated free energy difference between the two atropisomeric forms.

prepared and tested in the cyclisation/ring expansion cascade (**11w** and **11x**). Both reactions worked very well in terms of conversion and yield, but the atroposelectivity was low compared with that for **11a**. This suggests that the position α to the nucleophile is special in terms of its ability to control the biaryl stereochemistry. Therefore, we next examined the steric influence of this position using unsymmetrical tertiary alcohol nucleophiles (**11y**–**zb**). Interestingly, a clear trend of increasing atroposelectivity was observed as the alcohol substituents become more different in size; low atroposelectivity was observed for **11y** (methyl vs. allyl), modest atroposelectivity for **11z** (methyl vs. phenyl), and complete atroposelectivity was restored for **11za** and **11zb** (methyl vs. *tert*-butyl).

This atroposelectivity trend is consistent with the kinetic argument outlined in Scheme 6a (with the large substituent presumably adopting the pseudo-equatorial conformation). However, the thermodynamic model cannot be ruled out either, especially as DFT calculations of the relative free energies of the two possible atropisomers in each case correlate well with the observed atroposelectivity; a large difference in free energy was calculated for the atroposelective examples (**11a**, **11za**, **11zb**, $\Delta G = 22\text{--}26 \text{ kJ mol}^{-1}$) whereas the least selective examples can be considered isoenergetic at this level of theory (**11x**, **11y**, $\Delta G = 2 \text{ kJ mol}^{-1}$). This arguably favours the thermodynamic model, but caution should be exercised when interpreting these results, as the calculated difference in free energies of the products may simply serve as an approximation for the difference in free energy of the analogous transition states that lead to their formation (especially given that the products and transition states might be expected to have reasonably similar geometries). Indeed, it may be that either/both models operate in different examples. Ascertaining which operates in any given reaction system is therefore difficult; however, what is clear is that for high atroposelectivity to be achieved synthetically, the

key is having either a secondary nucleophile or an unsymmetrical tertiary nucleophile with a significant size difference between its substituents.

Finally, as the point-to-axial chirality transfer is a diastereoselective process, it is straightforward to prepare enantioenriched biaryl products simply by using an enantioenriched nucleophile. Thus, as a simple proof of concept, enantioenriched (ca. 71% *ee*) lactam **11v** was formed in 51% overall yield from **16** (72% *de*) following acidic cleavage of the Ellman's auxiliary, ester hydrolysis, and cyclisation/expansion in the usual way (Scheme 8).^[23]



Scheme 8. Synthesis of enantioenriched planar chiral lactam **11v**.

Conclusion

In summary, a cyclisation/ring expansion cascade reaction has been developed for the synthesis of ten-membered cyclic biaryl systems from simple pyridyl-based linear carboxylic acids. The novel strategy simultaneously addresses two important synthetic challenges: 1) achieving efficient and reliable end-to-end cyclisations of medium-sized rings from linear precursors; 2) effectively controlling atroposelectivity in the resulting cyclic products in biaryl-based systems. The cyclisation/ring expansion cascade strategy is also applicable to simple tertiary amine containing hydroxy acids to make eight- to eleven-membered lactones, which greatly extends its scope and potential utility. Thus the synthetic methods reported should facilitate the practical and selective synthesis of biologically important medium-sized rings, whilst a new strategy for generating planar chiral medium-sized rings by point-to-axial chirality transfer has also been introduced.

Experimental Section

Exemplar synthetic procedure for the cyclisation/ring expansion cascade to generate ten-membered lactone **11a**: To a stirring solution of 2-(2-(6-(2-hydroxypropyl)pyridin-2-yl)phenyl)acetic acid **9a** (44.0 mg, 0.163 mmol) in chloroform (3 mL) was added diisopropylethylamine (50.0 μ L, 0.302 mmol), followed by the addition of T3P (78.0 mg, 0.284 mmol, 156 mg of a 50% solution in ethyl acetate). Upon addition of T3P, the solution rapidly changed from a colourless to an orange solution. After stirring for 30 min at room temperature, the solution was concentrated, and the product purified by flash column chromatography (SiO₂, 1:1 ethyl acetate/hexane) to afford **11a** as a pale yellow solid (37 mg, 90%).

Acknowledgements

We thank the EPSRC (EP/P029795/1, A.L.), the Leverhulme Trust (for an Early Career Fellowship, ECF-2015-013, for W.P.U.) and the University of York (T.C.S., J.A.R., R.G.E.,

W.P.U.) for financial support. We are also grateful for the provision of an Eleanor Dodson Fellowship (to W.P.U.) by the Department of Chemistry, University of York, and the EPSRC for a contribution to the DTA studentships of T.C.S. (1792616). Finally, we thank Dr. Adrian C. Whitwood (University of York) for X-ray crystallography.

Conflict of interest

The authors declare no conflict of interest.

Stichwörter: Atropisomere · Axiale Chiralität · Mittlere Ringe · Pyridine · Ringerweiterungen

Zitierweise: *Angew. Chem. Int. Ed.* **2019**, *58*, 13942–13947
Angew. Chem. **2019**, *131*, 14080–14085

- [1] For medium-sized rings in medicinal chemistry, see: a) K. R. Romines, K. D. Watenpaugh, P. K. Tomich, W. J. Howe, J. K. Morris, K. D. Lovasz, A. M. Mulichak, B. C. Finze, J. C. Lynn, M.-M. Horng, F. J. Schwende, M. J. Ruwart, G. L. Zipp, K.-T. Chong, L. A. Dolak, L. N. Toth, G. M. Howard, B. D. Rush, K. F. Wilkinson, P. L. Possert, R. J. Dalga, R. R. Hinshaw, *J. Med. Chem.* **1995**, *38*, 1884; b) T. P. Majhi, B. Achari, P. Chattopadhyay, *Heterocycles* **2007**, *71*, 1011; c) F. Kopp, C. F. Stratton, L. B. Akella, D. S. Tan, *Nat. Chem. Biol.* **2012**, *8*, 358; d) R. A. Bauer, T. A. Wenderski, D. S. Tan, *Nat. Chem. Biol.* **2013**, *9*, 21.
- [2] For macrocycles in medicinal chemistry, see: a) E. M. Driggers, S. P. Hale, J. Lee, N. K. Terrett, *Nat. Rev. Drug Discovery* **2008**, *7*, 608; b) E. Marsault, M. L. Peterson, *J. Med. Chem.* **2011**, *54*, 1961; c) F. Giordanetto, J. Kihlberg, *J. Med. Chem.* **2014**, *57*, 278; d) A. K. Yudin, *Chem. Sci.* **2015**, *6*, 30.
- [3] a) M. A. Casadei, C. Galli, L. Mandolini, *J. Am. Chem. Soc.* **1984**, *106*, 1051; b) A. Hussain, S. K. Yousof, D. Mukherjee, *RSC Adv.* **2014**, *4*, 43241.
- [4] G. Illuminati, L. Mandolini, *Acc. Chem. Res.* **1981**, *14*, 95.
- [5] a) J. Fastrez, *J. Phys. Chem.* **1989**, *93*, 2635; b) J. C. Collins, K. James, *MedChemComm* **2012**, *3*, 1489.
- [6] For recent examples of ring expansion reactions in medium-sized ring synthesis, see Refs. [1c] and [1d] and: a) C. Kitsiou, J. J. Hindes, P. F. Anson, P. Jackson, T. C. Wilson, E. K. Daly, H. R. Felstead, P. Hearnshaw, W. P. Unsworth, *Angew. Chem. Int. Ed.* **2015**, *54*, 15794; *Angew. Chem.* **2015**, *127*, 16020; b) L. Li, Z.-L. Li, F.-L. Wang, Z. Guo, Y.-F. Cheng, N. Wang, X.-W. Dong, C. Fang, J. Liu, C. Hou, B. Tan, X.-Y. Liu, *Nat. Commun.* **2016**, *7*, 13852; c) J. E. Hall, J. V. Matlock, J. W. Ward, J. Clayden, *Angew. Chem. Int. Ed.* **2016**, *55*, 11153; *Angew. Chem.* **2016**, *128*, 11319; d) Z.-L. Li, X.-H. Li, N. Wang, N.-Y. Yang, X.-Y. Liu, *Angew. Chem. Int. Ed.* **2016**, *55*, 15100; *Angew. Chem.* **2016**, *128*, 15324; e) L. G. Baud, M. A. Manning, H. L. Arkless, T. C. Stephens, W. P. Unsworth, *Chem. Eur. J.* **2017**, *23*, 2225; f) T. C. Stephens, M. Lodi, A. Steer, Y. Lin, M. Gill, W. P. Unsworth, *Chem. Eur. J.* **2017**, *23*, 13314; g) R. Mendoza-Sanchez, V. B. Corless, Q. N. N. Nguyen, M. Bergeron-Brlek, J. Frost, S. Adachi, D. J. Tantillo, A. K. Yudin, *Chem. Eur. J.* **2017**, *23*, 13319; h) R. Costil, O. Lefebvre, J. Clayden, *Angew. Chem. Int. Ed.* **2017**, *56*, 14602; *Angew. Chem.* **2017**, *129*, 14794; i) D. R. Loya, A. Jean, M. Cormier, C. Fressigné, S. Nejrrotti, J. Blanchet, J. Maddaluno, M. De Paolis, *Chem. Eur. J.* **2018**, *24*, 2080; j) T. C. Stephens, A. Lawer, T. French, W. P. Unsworth, *Chem. Eur. J.* **2018**, *24*, 13947; k) Y. Zhou, Y.-L. Wei, J. Rodriguez, Y. Coquerel, *Angew. Chem. Int. Ed.* **2019**, *58*, 456; *Angew. Chem.* **2019**, *131*, 466; l) E.

- Reutskaya, A. Osipyan, A. Sapegin, A. S. Novikov, M. Krasavin, *J. Org. Chem.* **2019**, *84*, 1693.
- [7] For reviews on ring expansion chemistry, see: a) M. Hesse in *Ring Enlargement in Organic Chemistry*, Wiley-VCH, Weinheim, **1991**; b) W. P. Unsworth, J. R. Donald, *Chem. Eur. J.* **2017**, *23*, 8780; for a review on consecutive ring expansion reactions, see: c) T. C. Stephens, W. P. Unsworth, *Synlett* **2019**, <https://doi.org/10.1055/s-0037-1611500>.
- [8] For rare examples of conceptually related ring expansion cascade processes, see: a) H. Wu, W. Zi, G. Li, H. Lu, F. D. Toste, *Angew. Chem. Int. Ed.* **2015**, *54*, 8529; *Angew. Chem.* **2015**, *127*, 8649; b) B. Zhou, L. Li, X.-Q. Zhu, J.-Z. Yan, Y.-L. Guo, L.-W. Ye, *Angew. Chem. Int. Ed.* **2017**, *56*, 4015; *Angew. Chem.* **2017**, *129*, 4073. For ring expansion cascades, see Ref. [7c].
- [9] For important studies on acyl transfer processes that operate via transient covalent catalysis and bear analogy with the new reactions described in this manuscript, see: a) D. S. Kemp, *Biopolymers* **1981**, *20*, 1793; b) D. S. Kemp, D. J. Kerkman, S.-L. Leung, G. Hanson, *J. Org. Chem.* **1981**, *46*, 490; c) S. B. H. Kent, *Chem. Soc. Rev.* **2009**, *38*, 338; d) J. P. Tam, C. T. T. Wong, *J. Biol. Chem.* **2012**, *287*, 27020.
- [10] See Ref. [2] and: a) Y. H. Lau, P. de Andrade, Y. Wu, D. R. Spring, *Chem. Soc. Rev.* **2015**, *44*, 91; b) A. P. Treder, J. L. Hickey, M.-C. J. Tremblay, S. Zaretsky, C. C. G. Scully, J. Mancuso, A. Doucet, A. K. Yudin, E. Marsault, *Chem. Eur. J.* **2015**, *21*, 9249.
- [11] The terminology „point-to-axial“ chirality transfer refers to the fact that the point chirality of the linear starting material controls the axial chirality of the biaryl unit. As the medium-sized ring products overall exhibit planar chirality, we arguably could have used the terminology „point-to-planar“ chirality transfer but chose the former as we believe that it is more intuitive to consider the individual stereogenic units. For selected examples of point-to-axial chirality transfer in synthesis, see: a) T. Qin, S. L. Skraba-Joiner, Z. G. Khalil, R. P. Johnson, R. J. Capon, J. A. Porco, Jr., *Nat. Chem.* **2015**, *7*, 234; b) R. J. Armstrong, M. Nandakumar, R. M. P. Dias, A. Noble, E. L. Myers, V. K. Aggarwal, *Angew. Chem. Int. Ed.* **2018**, *57*, 8203; *Angew. Chem.* **2018**, *130*, 8335; c) A. Link, C. Sparr, *Angew. Chem. Int. Ed.* **2018**, *57*, 7136; *Angew. Chem.* **2018**, *130*, 7254; d) H. Li, W. Fan, X. Hong, *Org. Biomol. Chem.* **2019**, *17*, 1916.
- [12] T3P was chosen as the activating agent in view of precedent for its use for the N-acylation of cyclic imines; see: a) W. P. Unsworth, C. Kitsiou, R. J. K. Taylor, *Org. Lett.* **2013**, *15*, 258; b) W. P. Unsworth, G. Coulthard, C. Kitsiou, R. J. K. Taylor, *J. Org. Chem.* **2014**, *79*, 1368; c) W. P. Unsworth, R. J. K. Taylor, *Synlett* **2016**, *27*, 2051.
- [13] CCDC 1913413 (**11 a**) contains the supplementary crystallographic data for this paper. These data can be obtained free of charge from The Cambridge Crystallographic Data Centre.
- [14] Compounds **11 q**, **11 u**, and **11 v** exist as concentration-dependent mixtures of rotamers about the newly formed amide bond in CDCl₃ solution.
- [15] For the importance of atropisomerism in drug discovery, see: a) J. Clayden, W. J. Moran, P. J. Edwards, S. R. L. LaPlante, *Angew. Chem. Int. Ed.* **2009**, *48*, 6398; *Angew. Chem.* **2009**, *121*, 6516; b) S. R. L. LaPlante, L. D. Fader, K. R. Fandrick, D. R. Fandrick, O. Hucke, R. Kemper, S. P. F. Miller, P. J. Edwards, *J. Med. Chem.* **2011**, *54*, 7005; c) J. E. Smyth, N. M. Butler, P. A. Keller, *Nat. Prod. Rep.* **2015**, *32*, 1562; d) P. W. Glunz, L. Mueller, D. L. Cheney, V. Ladziata, Y. Zou, N. R. Wurtz, A. Wei, P. C. Wong, R. R. Wexler, E. S. Priestley, *J. Med. Chem.* **2016**, *59*, 4007; e) P. W. Glunz, *Bioorg. Med. Chem. Lett.* **2018**, *28*, 53.
- [16] For excellent reviews in which these chirality elements are discussed, see: a) E. M. G. Jamieson, F. Modicom, S. M. Goldup, *Chem. Soc. Rev.* **2018**, *47*, 5266; b) A. Link, C. Sparr, *Chem. Soc. Rev.* **2018**, *47*, 3804; c) R. M. Witzig, D. Lotter, V. C. Fäseke, C. Sparr, *Chem. Eur. J.* **2017**, *23*, 12960; d) D. C. Harrowven, S. L. Kostiuik, *Nat. Prod. Rep.* **2012**, *29*, 223.
- [17] For prominent examples of the stereoselective synthesis of compounds with axial, planar, and helical chirality, see: a) M. R. Crittall, H. S. Rzepa, D. R. Carbery, *Org. Lett.* **2011**, *13*, 1250; b) N. Di Iorio, P. Righi, A. Mazzanti, M. Mancinelli, A. Ciogli, G. Bencivenni, *J. Am. Chem. Soc.* **2014**, *136*, 10250; c) A. Link, C. Sparr, *Angew. Chem. Int. Ed.* **2014**, *53*, 5458; *Angew. Chem.* **2014**, *126*, 5562; d) V. C. Fäseke, C. Sparr, *Angew. Chem. Int. Ed.* **2016**, *55*, 7261; *Angew. Chem.* **2016**, *128*, 7378; e) B. Zilatte, A. Castrogiovanni, C. Sparr, *ACS Catal.* **2018**, *8*, 2981; f) D. Lotter, A. Castrogiovanni, M. Neuburger, C. Sparr, *ACS Cent. Sci.* **2018**, *4*, 656; g) C. G. Newton, E. Braconi, J. Kuziola, M. D. Wodrich, N. Cramer, *Angew. Chem. Int. Ed.* **2018**, *57*, 11040; *Angew. Chem.* **2018**, *130*, 11206; h) Y. Wang, W. Ju, H. Tian, S. Sun, X. Li, W. Tian, J. Gui, *J. Am. Chem. Soc.* **2019**, *141*, 5021.
- [18] For atroposelective syntheses of medium-sized rings and macrocycles, see: a) H. Tabata, H. Suzuki, K. Akiba, H. Takahashi, H. Natsugari, *J. Org. Chem.* **2010**, *75*, 5984; b) E. Van Den Berge, J. Pospisil, T. Trieu-Van, L. Collard, R. Robiette, *Eur. J. Org. Chem.* **2011**, 6649; c) I. Mutule, B. Joo, T. Medne, T. Kalnins, E. Vedejs, E. Suna, *J. Org. Chem.* **2015**, *80*, 3058.
- [19] See Ref. [18b] and: P. S. Baran, N. Z. Burns, *J. Am. Chem. Soc.* **2006**, *128*, 3908.
- [20] For the rotation of 1,3-disubstituted pyridines, see: I. R. Lahoz, A. Navarro-Vázquez, A. L. Llamas-Saiz, J. L. Alonso-Gómez, M. M. Cid, *Chem. Eur. J.* **2012**, *18*, 13836.
- [21] We attempted to corroborate this model by DFT calculations (see the Supporting Information for full details), but unfortunately were unable to convincingly find transition state structures for either scenario, which may be a consequence of these fast reactions operating via very shallow transition states. We are therefore unable to comment in a quantitative fashion on kinetic control in these reactions.
- [22] To compare the energies of the possible diastereoisomers, the structures were optimised at the M06-2X/6-311G* level of theory, followed by frequency calculations at the same level. These structures were confirmed as minima by the absence of imaginary frequencies. The M06-2X/6-311G* SCF energies were corrected for their zero-point energies, thermal energies, and entropies obtained from the frequency calculations. Optimisations were performed with tight convergence criteria, and no symmetry constraints were applied. An ultrafine integral grid was used for all calculations. Solvent corrections were applied with the polarisable continuum model (PCM) using the integral equation formalism variant (IEFPCM0). Energies in Hartrees and xyz coordinates are reported in the Supporting Information.
- [23] Enantiomer ratios were determined by HPLC analysis on a chiral stationary phase (see the Supporting Information). Partial overlap of signals means that there may be a small amount of error in the absolute ee value assigned, but what is clear is that qualitatively, the chirality transfer was successful. Further studies will be needed to build on these preliminary data in the future.

Manuskript erhalten: 10. Juni 2019
Veränderte Fassung erhalten: 23. Juli 2019
Akzeptierte Fassung online: 24. Juli 2019
Endgültige Fassung online: 13. August 2019

Rearrangements



Synthetic and Mechanistic Studies into the Rearrangement of Spirocyclic Indolenines into Quinolines

Ryan G. Epton,^[a] Aimee K. Clarke,^[a] Richard J. K. Taylor,^[a] William P. Unsworth*^[a] and Jason M. Lynam*^[a]

Abstract: A Density functional theory (DFT) approach has been used to shed light on the mechanism of a recently discovered rearrangement reaction for the conversion of spirocyclic indolenines into cyclopentanone-fused quinolines. A new base-mediated variant of this unusual rearrangement reaction has also been developed, that operates at much lower tempera-

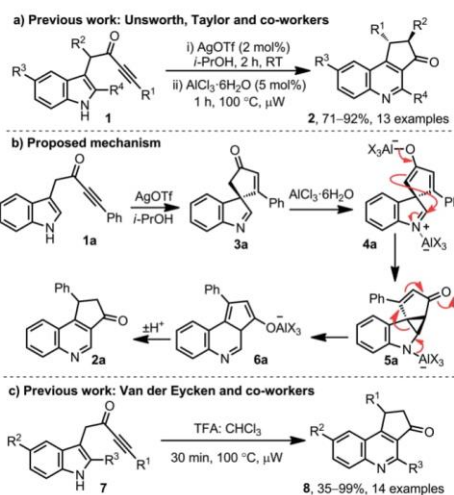
tures than those required in the analogous acidic reactions. The DFT study suggests that both the acid and base-mediated variants proceed via an enol/enolate intermediate, and the ease with which this key intermediate forms appears to be crucial in explaining the kinetic outcomes.

Introduction

The quinoline core is of great historical^[1] and current^[2] importance in the field of heterocyclic chemistry in view of the many useful applications of quinoline-containing molecules; for example, quinolines can be found in medicines, agrochemicals, dyes, ligands, catalysts, materials and electronic devices.^[1,2] Consequently, many powerful methods for the synthesis of quinolines have been developed over the years.^[3,4] Classical named-reactions such as the Skraup, Friedlander, Doebner-von Miller, Conrad-Limbach, Combes and Pfitzinger reactions are rightly held in high regard^[3] and modified/improved quinoline syntheses continue to be actively developed.^[4]

We recently reported^[5] a new way to access cyclopentanone-fused quinolines **2**^[6] from indole-tethered ynones **1** (Scheme 1a). The proposed mechanism for this one-pot process is illustrated by the conversion of ynone **1a** into quinoline **2a** (Scheme 1b). First, ynone **1a** is converted into spirocyclic indolenine^[7] **3a** via a dearomatizing spirocyclisation reaction^[8–10] upon reaction with π -acidic silver(I) triflate^[11] in *i*PrOH at room temperature. Then, the addition of $\text{AlCl}_3 \cdot 6\text{H}_2\text{O}$ directly to this reaction mixture and heating to 100 °C in a microwave was found to promote a hitherto unprecedented rearrangement into quinoline **2a**; the rearrangement was tentatively proposed to proceed via an enolisation (**3a** \rightarrow **4a**), cyclopropanation (**4a** \rightarrow **5a**), ring expansion (**5a** \rightarrow **6a**) and tautomerisation (**6a** \rightarrow **2a**) cascade sequence, as shown in Scheme 1b, although it

should be stressed that no evidence was obtained in support of this mechanism. Later, Van der Eycken and co-workers went on to develop a transition metal-free variant of this transformation,^[12,13] using trifluoroacetic acid (TFA) to promote the same overall transformation, enabling a broad range of quinolines to be prepared using a simple, single step protocol that also benefitted from reduced reaction times (**7** \rightarrow **8**, Scheme 1c). The authors proposed broadly the same mechanism as that shown in Scheme 1b for this metal-free variant, although again,



Scheme 1. Ynone to indolenine to quinoline rearrangements.

[a] Department of Chemistry, University of York, York, YO10 5DD, United Kingdom
E-mail: william.unsworth@york.ac.uk
jason.lynam@york.ac.uk

Supporting information and ORCID(s) from the author(s) for this article are available on the WWW under <https://doi.org/10.1002/ejoc.201900798>.

no evidence was obtained in its support. Most recently, Song, Liu and co-workers observed a closely related transformation unexpectedly during a silver(I)-catalysed trifluoromethylation cascade process and the same mechanism was again proposed.^[14]

To the best of our knowledge, this indolenine to quinoline rearrangement reaction is without precedent outside of these studies.^[5,12,14] Therefore, we believe that more convincingly ascertaining the mechanism of this unusual ring expansion rearrangement reaction is important,^[15] and our attempts to do so are reported in this manuscript using a density functional theory (DFT) approach.^[16] Additional synthetic studies performed to support the computational aspects have also led to a new base-mediated variant of this reaction being established, that operates at much lower temperatures than those used in the previous studies. The DFT results obtained support the mechanism proposed in the earlier synthetic studies and the ease with which a key enol/enolate reactive is formed appears to play a major role in explaining the surprising kinetic outcomes of the different variants.

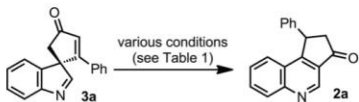
Results and Discussion

The optimal conditions used in our previous work,^[5a] and in the Van der Eycken study,^[12] utilised microwave heating and reaction temperatures of 100 °C, which enabled the quinoline target molecules **2/8** to be prepared in high yields within 1 hour. Before embarking on the DFT study, it was decided to gauge whether such vigorous heating is strictly necessary; we reasoned that having a clearer idea of the minimum temperature required to promote rearrangement would be helpful later when interpreting the computational results. Thus, simple model spirocycle **3a** (which had already been shown in the literature to be a good substrate in both the $\text{AlCl}_3 \cdot 6\text{H}_2\text{O}$ and TFA promoted reaction systems,^[5,12] (Table 1, entries 1–2) was chosen as a model system to test the limits of the rearrangement step by switching from microwave to conventional heating and lowering the temperature until the reactions begin to shut down (Table 1).

Starting with the use of $\text{AlCl}_3 \cdot 6\text{H}_2\text{O}$ in *i*PrOH, it was found that full conversion of spirocycle **3a** into quinoline **2a** can still be achieved at 80 °C, partial conversion (38 %) is observed at 50 °C and the reactions only shut down completely when the temperature is reduced to 40 °C (Table 1, entries 3–5). Thus, the reaction is viable at much lower temperatures than those used in the published synthetic study. The same was found when examining Van der Eycken's TFA-mediated variant; indeed, full conversion into **2a** was observed right down to 40 °C using these conditions, with partial conversion (54 %) at room temperature.^[17,18] The knowledge that these reactions can be performed at lower temperatures if required is likely to be useful when more sensitive functional groups are present in the substrates.

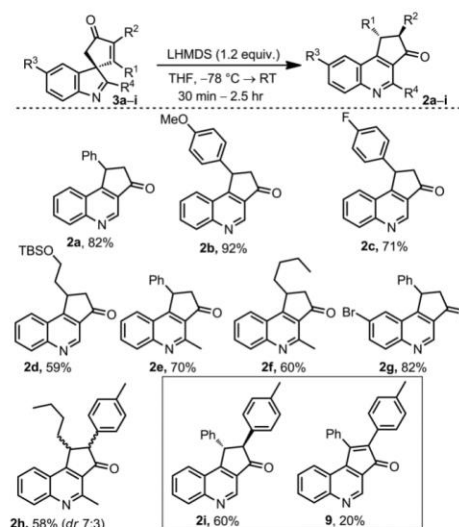
We also decided to examine the analogous base-mediated rearrangement of **3a** into **2a** (Table 1, entries 10–13). We already knew from initial screening during our earlier work^[5a] that lithium hexamethyldisilazide (LHMDS) can also promote

Table 1. Temperature limits for the rearrangement of spirocycle **3a** into quinoline **2a**.



Entry	Conditions	Temp/°C	Time/h	Conversion ^[a]
1	See ref. ^[5a] ($\text{AlCl}_3 \cdot 6\text{H}_2\text{O}$)	100	1	100
2	See ref. ^[12] (TFA)	100	0.5	100
3	$\text{AlCl}_3 \cdot 6\text{H}_2\text{O}$ (5 mol%), <i>i</i> PrOH, (0.1 M), heating	80	24	100
4		50	24	38
5		40	24	0
6	1:1 TFA/ CHCl_3 (0.1 M)	60	24	100
7		50	24	100
8		40	24	100 ^[b]
9		rt.	24	54
10	LHMDS (1 equiv.), THF (0.2 M)	rt.	0.5	100
11		0	0.5	100
12		-20	1.5	100
13		-46	3	58
14	LHMDS (1 equiv.), TMEDA (2 equiv.), THF (0.2 M)	rt.	0.5	100

[a] Conversion is based on integration of signals corresponding to **3a** and **2a** in the ^1H NMR spectra of the unpurified reaction mixture. [b] All of **3a** was consumed but the product formed contained unidentified impurities. TMEDA = tetramethylethylenediamine.

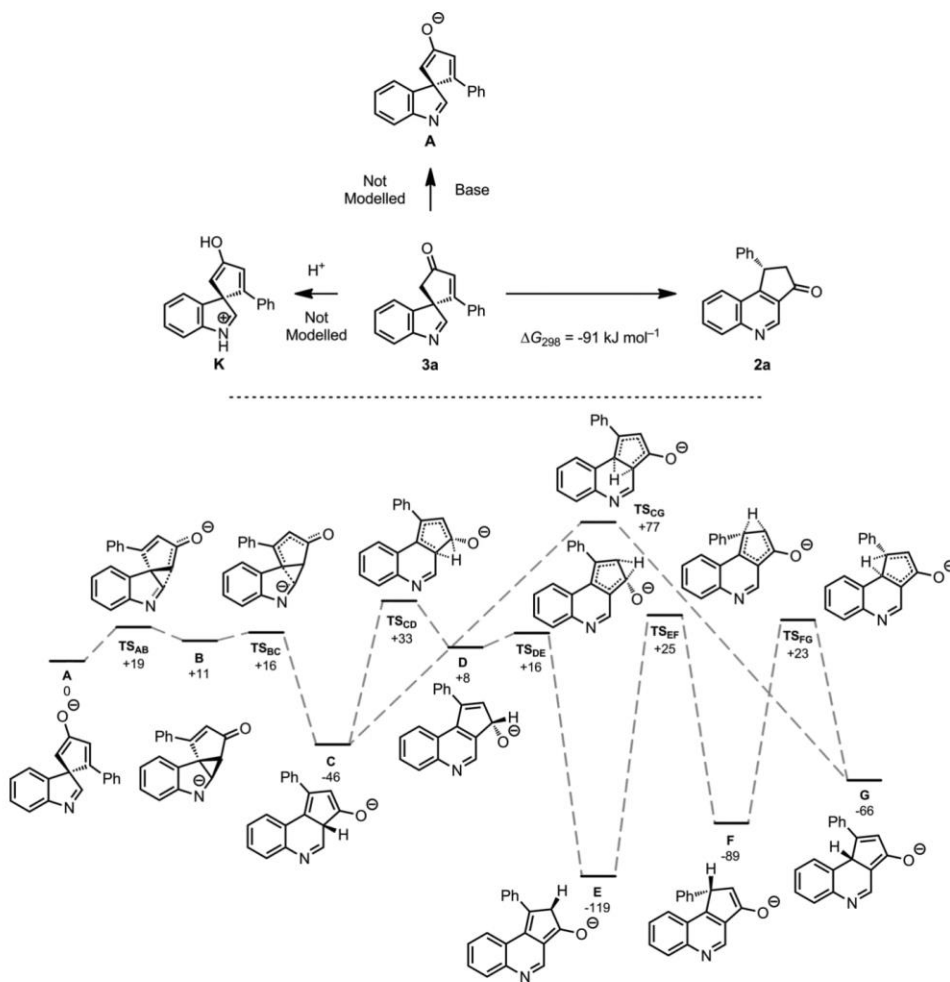


Scheme 2. LHMDS-mediated rearrangement of spirocycles **3a-i** into quinolines **2a-i** and **9**.

this rearrangement, but this base-mediated variant was not examined in synthetic studies. Thus, we examined the conversion of **3a** into **2a** using 1 equivalent of LHMDS in THF at various temperatures and found that these basic conditions promote the rearrangement at temperatures as low as $-46\text{ }^{\circ}\text{C}$ (i.e. much lower than either of the $\text{AlCl}_3\cdot 6\text{H}_2\text{O}$ or TFA variants).

The ability to conduct these reactions under these mild and complementary basic conditions could have useful synthetic

implications. Therefore, we tested the LHMDS-mediated conditions on a range of spirocycles **3a-i**, and pleasingly, the expected quinolines **2a-i** were isolated in each case. The reaction of spirocycle **3i** is noteworthy in that alongside the expected quinoline **2i**, a minor oxidised side product **9** was also isolated; this system presumably was more prone to undergo spontaneous oxidation as result of the extra conjugation in the product (Scheme 2).^[14]



Next, the ring expansion process (under both acidic and basic conditions) was modelled using density functional theory. Geometries were optimised at the BP86/SV(P) level of theory and confirmed as minima or transition states through analysis of the calculated vibrational modes. The energies of the resulting geometries were then obtained using the hybrid PBE0 functional with the triple zeta def2-TZVPP basis set.^[19] The Gibbs energies were obtained by combining these electronic energies with thermal corrections from the BP86/SV(P) level at 298 K. This method allows for an accurate description of the electronic structure of the molecule but saves on the computational expense of determining the thermal corrections at the PBE0/def2-TZVPP level. Dispersion effects were modelled with Grimme's D3 method with Becke–Johnson damping.^[20] The effects of solvation on the reaction were modelled with a PCM model in THF (for the base-promoted reaction) and CHCl_3 (acid-promoted) simulating the reaction conditions. This was the method used in our previous work on ynone cyclisations.^[16]

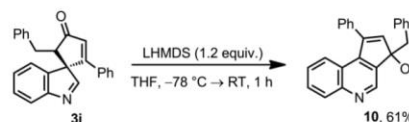
In order to ensure that the diffusion effects of modelling an anionic pathway were being effectively captured, the surface was also calculated using the 6-311+G* basis set with the PBE0 functional. The resulting energies show no significant differences from those at the PBE0/def2-TZVPP level (see Supporting Information). The effect of different density functionals on the relative energies of the calculated states was also investigated. The energies of all the intermediate species showed negligible method effects. Although, when compared to the relative energies at the PBE0 functional, the transition states energies were systematically lower when BP86 was used and higher at the M06-2X and ω B97XD level (see Supporting Information).

The formation of **2a** from **3a** was found to be exergonic by 91 kJ mol^{-1} , demonstrating that, as expected, the formation of the quinoline products is thermodynamically favourable (Figure 1a). Two mechanistic pathways were then considered for this transformation as, on the basis of experimental results, the reaction could be either base- or acid-promoted.

Considering the base-promoted reaction first (Figure 1b). In order to model the ring-opening reaction, the most acidic protons in **3a** were considered to be those in the α -position to the carbonyl group. The addition of TMEDA to sequester Li^+ did not affect the outcome of the experimental reaction (Table 1 Entry 14) indicating that the cations were not playing a role in the transformation and were hence excluded from the calculations. Therefore, the starting point for the calculations was anion **A** in which the deprotonation event had already occurred: this was also taken as the reference state for the potential energy surface (Figure 1b). Compound **B** (+11 kJ mol^{-1}) can be formed from **A** through a low-lying transition state TS_{AB} (+19 kJ mol^{-1}) and this process corresponds to formal nucleophilic attack by the enolate at the 2-position of the indolenine unit. Opening of the cyclopropyl group in **B** proceeds through TS_{BC} (+16 kJ mol^{-1}) to give **C** (−46 kJ mol^{-1}) via a fragmentation reaction. Compound **C** may interconvert to **D**, **E**, **F** and **G** through a series of formal 1,5 hydride shifts. From **C**, the lowest energy 1,5 hydride shift is through TS_{CD} (+33 kJ mol^{-1}) to give

the highest energy isomer of the ring-expanded annulated product compound (**D** = +8 kJ mol^{-1}). However, the subsequent 1,5-hydride shift from **D** gives the lowest energy isomer **E** (−119 kJ mol^{-1}) through a low-lying transition state (TS_{DE}). Given that all the other transition states are higher in energy, and that **E** is the lowest energy isomer, we would expect **E** to be the dominant form in solution, which on acid work up would be protonated to give **2a**.

As an aside, based on this hydride migration mechanism, we briefly examined the effect of replacing the hydrogen atom that undergoes migration with a benzyl group that might have been expected to migrate similarly. Thus, indolenine **3j** was prepared and reacted with LHMDS in the usual way. Rearrangement into a quinoline product was indeed observed, although in this case, following the first 1,5-migration (analogous to the conversion of **C** into **D** into Figure 1) the usual sequence was interrupted, allowing tertiary alcohol quinoline derivative **10** to be isolated in 61% yield (Scheme 3).



Scheme 3. LHMDS-mediated rearrangement of spirocycle **3j** into quinoline **10**.

Returning to the DFT studies, we also considered the acid-promoted reaction (Figure 2). As the opening of the spirocycle operates through both Lewis and Brønsted conditions we elected to model the acid-promoted reaction by simply investigating the effects of protonation. It was considered that the indole nitrogen in **3a** would be the most basic site. Protonation of this nitrogen would give **J**, which was taken as the reference state. The isomeric form **J'**, in which protonation has occurred at the carbonyl oxygen, lies +37 kJ mol^{-1} higher in energy, supporting this argument that addition of H^+ to the nitrogen is the thermodynamically preferred site of protonation. All attempts to find transition states which resulted in the formation of cyclopropyl derivative **L** from **J** were unsuccessful. However, it was found that **L** could be formed directly from **K** (+40 kJ mol^{-1}), which is the enol tautomer of **J**, through TS_{KL} (+46 kJ mol^{-1}). Opening of the cyclopropyl group in **L** proceeds through TS_{LM} (+60 kJ mol^{-1}) to give **M** (+26 kJ mol^{-1}). As was the case for the base-catalysed reaction, **M** may convert to a series of isomers through formal 1,5-hydride shifts. Isomers **N**, **O**, **P**, and **Q** are all at lower energy than **J**, with **O** being the thermodynamically preferred isomer (−64 kJ mol^{-1}). Considering that the reaction may be performed with a large excess of TFA, the possibility of the substrate being doubly protonated cannot be discounted. However, all attempts to locate a transition state for the opening of the spirocycle from a dicationic intermediate have been unsuccessful.

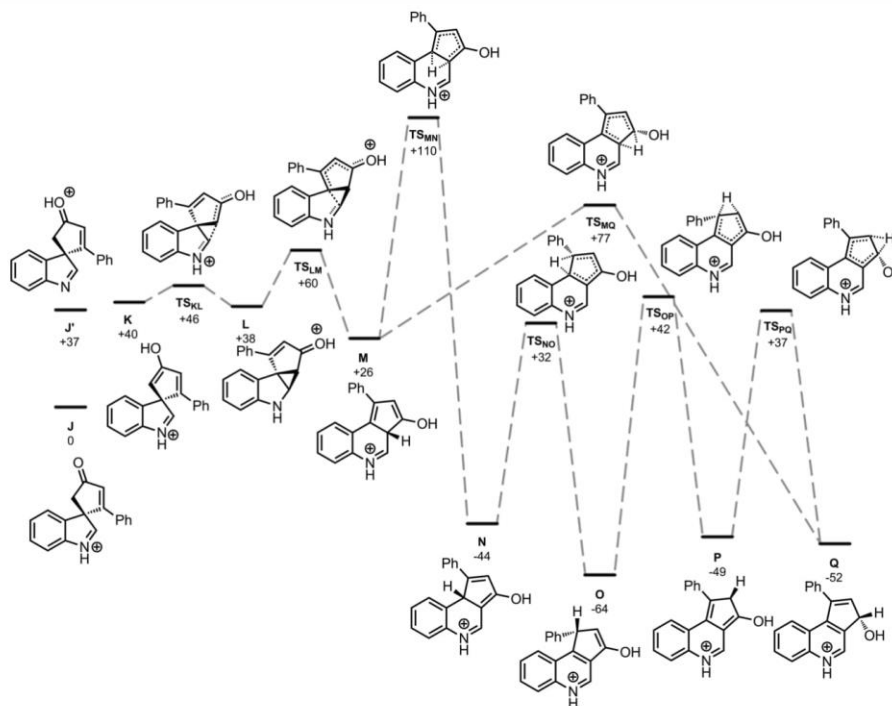


Figure 2. DFT-calculated energies for ring-expansion and 1,5-hydride shifts corresponding to the base-promoted formation of **2a** from **3a**. Energies are Gibbs energies at 298 K in kJ mol^{-1} at the D3BJ-PBE0/def2-TZVPP//BP86/SV(P) level with SCRFF solvent correction in CHCl_3 .

Conclusions

In summary, convincing computational support has been obtained for the mechanism of rearrangement for the conversion of cyclopentenone-based spirocyclic indolenines into fused quinolines. The DFT results support the mechanisms proposed in the earlier synthetic studies and provide additional insight into the likely pathway by which the 1,5-hydride shifts operate. A base-catalysed variant of the rearrangement has also been established that works at significantly lower temperatures than those used in the analogous acid-catalysed reactions.

The calculations demonstrate that the barriers to the opening of the spirocycle through cyclopropyl **B** (base-promoted) or **L** (acid promoted) are low. In the base-promoted case, TS_{BC} lies at $+16 \text{ kJ mol}^{-1}$ relative to the reference state **A** which (when taken with the fact that TS_{AB} lies at -19 kJ mol^{-1}) indicates that the ring-opening process will be rapid when deprotonation has occurred. This is the case for all computational methods investigated. These data are consistent with the observation that the reaction between **3a** and LHMDs is efficient even at -46°C .

In the case of the acid-promoted reaction, the energetic span for ring opening of the spirocycle (difference in energy between **J** and TS_{LM}) is 60 kJ mol^{-1} , higher than the corresponding bar-

rier in the base-promoted case. However, the reaction generally required elevated temperatures (80°C) and long reaction times (24 h). The barrier of 60 kJ mol^{-1} would indicate that, if these states were rate controlling, then ring-opening would be complete under far less forcing conditions. However, it is important to stress that it was not possible to locate a transition state for ring-opening from **J** and that tautomerisation to **K** is a requirement for opening of the spirocycle. The conversion of **J** to **K** is almost certainly a bimolecular process and, as the nature of such an intermolecular deprotonation/re-protonation is complex, this step was not modelled. However, our data indicate that it is this process which is controlling the reaction rather than the C–C bond migration needed to open the spirocycle. As such, slow enol formation (under acidic conditions) in contrast with rapid enolate formation when using strong base is likely the key contributing factor to the stark difference in rate of the two processes.

Experimental Section

General Procedure A: AlCl_3 Temperature Screens: To a microwave vial containing a solution of spirocycle (0.3 mmol) in isoprop-

anol (3 mL), was added $\text{AlCl}_3 \cdot 6\text{H}_2\text{O}$ (15 μmol). The reaction mixture was heated at the desired temperature for 24 hours. After this time, an aliquot was taken and concentrated in vacuo and a ^1H NMR spectrum was recorded in CDCl_3 to analyse the percentage conversion.

General Procedure B: TFA Temperature Screens: To a microwave vial containing a solution of spirocycle (0.3 mmol) in chloroform (1.5 mL) was added TFA (1.5 mL, 20 mmol). The reaction mixture was heated at the desired temperature for 24 hours. After this time, an aliquot was taken and concentrated in vacuo and a ^1H NMR spectrum was recorded in CDCl_3 to analyse the percentage conversion.

General Procedure C: LHMDS Temperature Screens: To a solution of spirocycle (0.75 mmol) in THF (3.75 mL), at -78°C under an atmosphere of argon, was added LHMDS (0.75 mL, 0.75 mmol, 1 M in THF). The solution was stirred for 5 min, then warmed to the desired temperature with continued stirring, frequently checking for completion by TLC analysis. The reaction was quenched with sat. aq. NH_4Cl (5 mL), diluted with water (5 mL) and extracted with EtOAc (3 \times 10 mL). The organics were combined and dried with MgSO_4 , concentrated in vacuo. A ^1H NMR spectrum was recorded in CDCl_3 to analyse the percentage conversion.

General Procedure D: LHMDS Mediated Rearrangement: To a solution of spirocycle (0.5 mmol) in THF (2.5 mL), at -78°C under an atmosphere of argon, was added LHMDS (0.6 mL, 0.6 mmol, 1.0 M in THF). The solution was stirred for 5 min at -78°C and then warmed to r.t. The reaction mixture was stirred at r.t. until TLC analysis showed the reaction had gone to completion. The reaction was quenched with sat. aq. NH_4Cl (5 mL), diluted with water (5 mL) and extracted with EtOAc (3 \times 10 mL). The organics were combined and dried with MgSO_4 , concentrated in vacuo and purified by flash column chromatography to afford the quinoline product.

1-Phenyl-1,2-dihydro-3H-cyclopenta[c]quinolin-3-one (2a): Synthesised using general procedure D (30 minutes reaction time) from 2-phenylspiro[cyclopent[2]ene-1,3'-indol]-4-one **3a** (194 mg, 0.75 mmol). Purification by flash column chromatography (4:1 to 1:1 hexane/EtOAc) afforded the titled product **2a** as a pale brown solid (157 mg, 81 %). $R_f = 0.51$ (hexane/EtOAc, 1:1); ^1H NMR (400 MHz, CDCl_3): $\delta = 9.32$ (s, 1H), 8.24 (d, $J = 8.0$ Hz, 1H), 7.82 (ddd, $J = 8.0, 7.0, 1.0$ Hz, 1H), 7.73 (dd, $J = 8.0, 1.0$ Hz, 1H), 7.49 (ddd, $J = 8.0, 7.0, 1.0$ Hz, 1H), 7.36–7.25 (m, 3H), 7.16–7.12 (m, 2H), 5.05 (dd, $J = 8.0, 3.0$ Hz, 1H), 3.42 (dd, $J = 19.0, 8.0$ Hz, 1H), 2.78 ppm (dd, $J = 19.0, 3.0$ Hz, 1H). Spectroscopic data matched those reported in the literature.^[5]

LHMDS-Mediated Rearrangement of 3a with TMEDA: To a solution of 2-phenylspiro[cyclopent[2]ene-1,3'-indol]-4-one **3a** (77 mg, 0.3 mmol) and distilled TMEDA (0.1 mL, 0.6 mmol) in THF (1.5 mL), at -78°C under an atmosphere of argon, was added LHMDS (0.3 mL, 0.3 mmol, 1 M in THF). The solution was stirred for 5 min, then warmed to room temperature with continued stirring for 30 minutes. The reaction was quenched with sat. aq. NH_4Cl (10 mL), diluted with water (5 mL) and extracted with EtOAc (3 \times 10 mL). The organics were combined, washed with sat. aq. NaCl (10 mL), dried with MgSO_4 and concentrated in vacuo. A ^1H NMR spectrum was recorded in CDCl_3 to analyse the reaction mixture and this confirmed that ynone **3a** was fully and cleanly converted into quinoline **2a**, as was the case in the analogous reaction without TMEDA.

1-(4-Methoxyphenyl)-1,2-dihydro-3H-cyclopenta[c]quinolin-3-one (2b): Synthesised using general procedure D (30 minutes reaction time) from 2-(4-methoxyphenyl)spiro[cyclopent[2]ene-1,3'-indol]-4-one **3b** (145 mg, 0.5 mmol). Purification by flash column

chromatography (1:1 hexane/EtOAc) afforded the titled product **2b** as an orange solid (133 mg, 92 %). $R_f = 0.39$ (hexane/EtOAc, 1:1); ^1H NMR (400 MHz, CDCl_3): $\delta = 9.27$ (s, 1H), 8.21 (d, $J = 8.5$ Hz, 1H), 7.80 (ddd, $J = 8.5, 7.0, 1.5$ Hz, 1H), 7.73 (dd, $J = 8.0, 1.0$ Hz, 1H), 7.47 (ddd, $J = 8.5, 7.0, 1.0$ Hz, 1H), 7.04–6.99 (m, 2H), 6.84–6.80 (m, 2H), 4.99 (dd, $J = 8.0, 3.0$ Hz, 1H), 3.76 (s, 3H), 3.37 (dd, $J = 19.0, 8.0$ Hz, 1H), 2.72 ppm (dd, $J = 19.0, 3.0$ Hz, 1H). Spectroscopic data matched those reported in the literature.^[5]

1-(4-Fluorophenyl)-1,2-dihydro-3H-cyclopenta[c]quinolin-3-one (2c): Synthesised using general procedure D (30 minutes reaction time) from 2-(4-fluorophenyl)spiro[cyclopent[2]ene-1,3'-indol]-4-one **3c** (139 mg, 0.5 mmol). Purification by flash column chromatography (1:1 hexane/EtOAc) afforded the titled product **2c** as an orange solid (99 mg, 71 %). $R_f = 0.45$ (hexane/EtOAc, 1:1); ^1H NMR (400 MHz, CDCl_3): $\delta = 9.31$ (s, 1H), 8.25 (d, $J = 8.0$ Hz, 1H), 7.85 (ddd, $J = 8.5, 7.0, 1.5$ Hz, 1H), 7.68 (ddd, $J = 8.5, 1.5, 0.5$ Hz, 1H), 7.50 (ddd, $J = 8.5, 7.0, 1.5$ Hz, 1H), 7.11–7.05 (m, 2H), 7.04–6.97 (m, 2H), 5.04 (dd, $J = 8.0, 3.0$ Hz, 1H), 3.41 (dd, $J = 19.5, 8.0$ Hz, 1H), 2.73 ppm (dd, $J = 19.5, 3.0$ Hz, 1H). ^{19}F NMR (376 MHz, CDCl_3): $\delta = -114.5$ ppm. Spectroscopic data matched those reported in the literature.^[12]

1-[2-((tert-Butyldimethylsilyloxy)ethyl)-1,2-dihydro-3H-cyclopenta[c]quinolin-3-one (2d): Synthesised using general procedure D (1 hour reaction time) from 2-[2-((tert-butylidimethylsilyloxy)ethyl)spiro[cyclopentane-1,3'-indol]-2-en-4-one **3d** (103 mg, 0.3 mmol). Purification by flash column chromatography (4:1 to 7:3 hexane/EtOAc) afforded the titled product **2d** as a brown oil (60 mg, 59 %). $R_f = 0.33$ (hexane/EtOAc, 7:3); ^1H NMR (400 MHz, CDCl_3): $\delta = 9.15$ (s, 1H), 8.22 (d, $J = 8.5$ Hz, 1H), 8.16 (d, $J = 8.5$ Hz, 1H), 7.87 (ddd, $J = 8.5, 7.0, 1.5$ Hz, 1H), 7.68 (ddd, $J = 8.5, 7.0, 1.5$ Hz, 1H), 4.15–4.08 (m, 1H), 3.82 (dt, $J = 10.5, 4.5$ Hz, 1H), 3.71 (td, $J = 10.5, 4.5$ Hz, 1H), 2.98 (dd, $J = 19.0, 7.5$ Hz, 1H), 2.67 (dd, $J = 19.0, 1.5$ Hz, 1H), 2.49–2.41 (m, 1H), 1.63 (tdd, $J = 14.0, 10.0, 4.5$ Hz, 1H), 0.91 (s, 9H), 0.07 (s, 3H), 0.06 ppm (s, 3H). Spectroscopic data matched those reported in the literature.^[5]

4-Methyl-1-phenyl-1,2-dihydro-3H-cyclopenta[c]quinolin-3-one (2e): Synthesised using general procedure D (1.5 hour reaction time) from 2-phenyl-2'-methylspiro[cyclopent[2]ene-1,3'-indol]-4-one **3e** (137 mg, 0.5 mmol). Purification by flash column chromatography (7:3 hexane/EtOAc) afforded the titled product **2e** as an orange solid (97 mg, 71 %). $R_f = 0.48$ (hexane/EtOAc, 1:1); ^1H NMR (400 MHz, CDCl_3): $\delta = 8.11$ (d, $J = 8.5$ Hz, 1H), 7.77 (ddd, $J = 8.5, 7.0, 1.5$ Hz, 1H), 7.67 (ddd, $J = 8.5, 1.5, 0.5$ Hz, 1H), 7.39 (ddd, $J = 8.5, 7.0, 1.5$ Hz, 1H), 7.33–7.25 (m, 3H), 7.13–7.09 (m, 2H), 4.98 (dd, $J = 7.5, 2.5$ Hz, 1H), 3.38 (dd, $J = 19.0, 7.5$ Hz, 1H), 3.06 (s, 3H), 2.75 ppm (dd, $J = 19.0, 2.5$ Hz, 1H). Spectroscopic data matched those reported in the literature.^[12]

1-Butyl-4-methyl-1,2-dihydro-3H-cyclopenta[c]quinolin-3-one (2f): Synthesised using general procedure D (1 hour reaction time) from 2-butyl-2'-methylspiro[cyclopent[2]ene-1,3'-indol]-4-one **3f** (127 mg, 0.5 mmol). Purification by flash column chromatography (7:3 hexane/EtOAc) afforded the titled product **2f** as a yellow solid (76 mg, 60 %). $R_f = 0.31$ (hexane/EtOAc, 7:3); m.p. 88–89 $^\circ\text{C}$; ^1H NMR (400 MHz, CDCl_3): $\delta = 8.11$ (d, $J = 8.5$ Hz, 1H), 8.04 (dd, $J = 8.5, 1.0$ Hz, 1H), 7.83 (ddd, $J = 8.5, 7.0, 1.0$ Hz, 1H), 7.60 (ddd, $J = 8.5, 7.0, 1.0$ Hz, 1H), 3.87–3.78 (m, 1H), 2.95 (s, 3H), 2.94 (dd, $J = 19.0, 7.0$ Hz, 1H), 2.59 (dd, $J = 19.0, 1.5$ Hz, 1H), 2.19–2.02 (m, 1H), 1.57–1.20 (m, 5H), 0.89 ppm (t, $J = 6.5$ Hz, 3H); ^{13}C NMR (100 MHz, CDCl_3): $\delta = 205.5$ (C=O), 169.0 (C), 157.4 (C), 149.7 (C), 132.4 (CH), 129.9 (CH), 128.1 (C), 126.6 (CH), 124.4 (C), 124.4 (CH), 43.8 (CH₂), 36.9 (C), 36.2 (CH₂), 29.8 (CH₂), 22.8 (CH₃), 22.7 (CH₂), 14.1 ppm (CH₃); IR (thin film): $\tilde{\nu}_{\text{max}} = 1708$ (s, C=O), 1616 (C=C), 1588 (C=C) cm^{-1} ; HRMS (ESI): m/z calcd. for $\text{C}_{17}\text{H}_{20}\text{NONa}^+$: 254.1539 [M + Na]⁺, found 254.1538.

8-Bromo-1-phenyl-1,2-dihydro-3H-cyclopenta[*c*]quinolin-3-one (2g): Synthesised using general procedure D (30 minutes reaction time) from 5'-bromo-2-phenylspiro[cyclopent[2]ene-1,3'-indol]-4-one **3g** (169 mg, 0.5 mmol). Purification by flash column chromatography (7:3 hexane/EtOAc) afforded the *titled product 2g* as a yellow solid (136 mg, 80%). $R_f = 0.39$ (hexane/EtOAc, 7:3); $^1\text{H NMR}$ (400 MHz, CDCl_3): $\delta = 9.30$ (s, 1H), 8.09 (d, $J = 9.0$ Hz, 1H), 7.87 (dd, $J = 9.0, 2.0$ Hz, 1H), 7.84 (d, $J = 2.0$ Hz, 1H), 7.37–7.28 (m, 3H), 7.12–7.09 (m, 2H), 4.99 (dd, $J = 8.0, 3.0$ Hz, 1H), 3.41 (dd, $J = 19.5, 8.0$ Hz, 1H), 2.79 ppm (dd, $J = 19.5, 3.0$ Hz, 1H). Spectroscopic data matched those reported in the literature.^[12]

trans-2-(4-Methylphenyl)-1-phenyl-1,2-dihydro-3H-cyclopenta[*c*]quinolin-3-one (2i): Synthesised using general procedure D (2.5 hour reaction time) from 3-(4-methylphenyl)-2-phenylspirocyclopentane-1,3'-indol]-2-en-4-one **3i** (175 mg, 0.5 mmol). Purification by flash column chromatography (9:1 to 3:1 hexane/EtOAc) afforded the *titled product 2i* as an orange oil (105 mg, 60%). $R_f = 0.33$ (hexane/EtOAc, 3:1); $^1\text{H NMR}$ (400 MHz, CDCl_3): $\delta = 9.37$ (s, 1H), 8.27 (br. d, $J = 8.5$ Hz, 1H), 7.82 (ddd, $J = 8.5, 7.0, 1.5$ Hz, 1H), 7.65 (ddd, $J = 8.5, 1.5, 0.5$ Hz, 1H), 7.45 (ddd, $J = 8.5, 7.0, 1.5$ Hz, 1H), 7.34–7.28 (m, 3H), 7.17–7.13 (m, 2H), 7.09–7.05 (m, 2H), 7.03–6.99 (m, 2H), 4.99 (d, $J = 3.5$ Hz, 1H), 3.87 (d, $J = 3.5$ Hz, 1H), 2.34 ppm (s, 3H); $^{13}\text{C NMR}$ (100 MHz, CDCl_3): $\delta = 204.0$ (C), 164.2 (C), 151.1 (C), 146.0 (CH), 141.9 (C), 137.3 (C), 135.2 (C), 132.5 (CH), 130.7 (CH), 129.8 (CH), 129.7 (C), 129.4 (CH), 127.9 (CH), 127.8 (CH), 127.6 (CH), 127.5 (CH), 125.9 (CH), 125.2 (C), 65.0 (CH), 54.4 (CH), 21.2 ppm (CH₃); IR (thin film): $\tilde{\nu}_{\text{max}} = 1714$ (s, C=O), 1615 (C=C), 1574 (C=C) cm^{-1} ; HRMS (ESI): m/z calcd. for $\text{C}_{25}\text{H}_{19}\text{NONa}^+$: 372.1539 [M + Na]⁺, found 372.1351.

2-(4-Methylphenyl)-1-phenyl-cyclopenta[*c*]quinolin-3-one (9): Side product formed from the reaction of 3-(4-methylphenyl)-2-phenylspirocyclopentane-1,3'-indol]-2-en-4-one **3i** using general procedure D. Purification by flash column chromatography (9:1 to 3:1 hexane/EtOAc) afforded the *titled product 9* as a red solid (36 mg, 20%). $R_f = 0.40$ (hexane/EtOAc, 3:1); m.p. 183–187 °C; $^1\text{H NMR}$ (400 MHz, CDCl_3): $\delta = 9.05$ (s, 1H), 8.09 (dd, $J = 8.5, 1.0$ Hz, 1H), 7.68 (ddd, $J = 8.5, 4.5, 4.0$ Hz, 1H), 7.55–7.49 (m, 3H), 7.46–7.40 (m, 2H), 7.26–7.22 (m, 2H), 7.17 (d, $J = 8.5$ Hz, 2H), 7.07 (d, $J = 8.5$ Hz, 2H), 2.31 ppm (s, 3H); $^{13}\text{C NMR}$ (100 MHz, CDCl_3): $\delta = 197.0$ (C), 153.8 (C), 153.2 (C), 153.2 (C), 142.9 (CH), 138.7 (C), 134.9 (C), 134.2 (C), 131.8 (CH), 130.8 (CH), 130.2 (CH), 129.3 (CH), 129.2 (CH), 129.0 (CH), 128.7 (CH), 127.3 (CH), 126.9 (C), 125.3 (CH), 122.9 (C), 119.9 (C), 21.5 ppm (CH₃); IR (thin film): $\tilde{\nu}_{\text{max}} = 1707$ (s, C=O), 1618 (C=C), 1562 (C=C) cm^{-1} ; HRMS (ESI): m/z calcd. for $\text{C}_{25}\text{H}_{18}\text{NO}^+$: 348.1383 [M + H]⁺, found 348.1377.

3-Benzyl-1-phenylcyclopenta[*c*]quinolin-3-ol (10): Synthesised using general procedure D (1 hour reaction time) from a 1:1 mixture of diastereoisomers of 5-benzyl-2-phenylspiro[cyclopentane-1,3'-indol]-2-en-4-one **3j** (175 mg, 0.5 mmol). Purification by flash column chromatography (6:4 hexane/EtOAc) afforded the *titled product 10* as an orange solid (106 mg, 61%). $R_f = 0.13$ (hexane/EtOAc, 6:4); m.p. 191–192 °C; $^1\text{H NMR}$ (400 MHz, $(\text{CD}_3)_2\text{SO}$): $\delta = 8.93$ (s, 1H), 8.01 (d, $J = 8.5$ Hz, 1H), 7.60 (ddd, $J = 8.5, 7.0, 1.5$ Hz, 1H), 7.51–7.45 (m, 3H), 7.35–7.20 (m, 4H), 7.11–7.02 (m, 5H), 6.50 (s, 1H), 5.93 ppm (s, 1H); $^{13}\text{C NMR}$ (100 MHz, $(\text{CD}_3)_2\text{SO}$): $\delta = 148.7$ (C), 145.5 (CH), 145.1 (CH), 144.8 (C), 142.2 (C), 141.3 (C), 136.6 (C), 136.4 (C), 130.2 (CH), 129.9 (CH), 128.6 (CH), 128.6 (CH), 128.2 (CH), 128.2 (CH), 127.3 (CH), 126.2 (CH), 125.9 (CH), 123.5 (CH), 122.7 (C), 82.8 (C), 43.7 ppm (CH₂); IR (thin film): $\tilde{\nu}_{\text{max}} = 1569$ (C=C), 1506 (C=C) cm^{-1} ; HRMS (ESI): m/z calcd. for $\text{C}_{25}\text{H}_{20}\text{NO}^+$: 350.1539 [M + H]⁺, found 350.1539. Note: In $(\text{CD}_3)_2\text{SO}$ some proton signals are obscured by the residual water signal; these are observed in CDCl_3 at 3.45 (d, $J = 13.5$ Hz, 1H) and 3.30 (d, $J = 13.5$ Hz, 1H) for the CH₂ of the benzyl group.

1-Butyl-2-(4-methylphenyl)-4-methyl-1,2-dihydro-3H-cyclopenta[*c*]quinolin-3-one (2h): Synthesised using general procedure D from 2-butyl-3-(4-methylphenyl)-2'-methylspirocyclopentane-1,3'-indol]-2-en-4-one **3h** (165 mg, 0.5 mmol). Purification by flash column chromatography (99:1 to 95:5 hexane/acetone) afforded the *titled product 2h* as an orange oil as a 7:3 mixture of diastereoisomers (98 mg, 58%). $R_f = 0.08$ (hexane/acetone, 95:5); $^1\text{H NMR}$ (400 MHz, CDCl_3): $\delta = 8.19$ –8.14 (m, 2H), 8.12–8.04 (m, 2H), 7.92–7.84 (m, 2H), 7.67–7.60 (m, 2H), 7.25–7.19 (m, 4H), 7.14–7.08 (m, 2H), 7.05–6.99 (m, 2H), 4.25 (d, $J = 7.0$ Hz, 1H), 4.15 (m, 1 H), 3.91 (ddd, $J = 9.5, 3.0, 1.5$ Hz, 1H), 3.71 (d, $J = 1.5$ Hz, 1H), 3.04 (s, 3H), 2.96 (3H), 2.33 (s, 3H), 2.30 (s, 3H), 2.25–2.17 (m, 1H), 1.68–1.27 (m, 8H), 1.03–0.81 (m, 2H), 0.89 (t, $J = 7.0$ Hz, 3H), 0.60–0.48 (m, 1H), 0.57 ppm (t, $J = 6.5$ Hz, 3H); $^{13}\text{C NMR}$ (100 MHz, CDCl_3): $\delta = 205.0$ (C), 204.7 (C), 168.6 (C), 166.9 (C), 158.1 (C), 157.5 (C), 149.9 (C), 149.7 (C), 139.3 (C), 137.1 (C), 136.6 (C), 136.4 (C), 132.7 (CH), 132.6 (C), 132.5 (CH), 130.4 (CH), 130.0 (CH), 129.9 (CH), 129.8 (CH), 129.4 (C), 129.3 (CH), 127.8 (C), 127.3 (CH), 126.8 (CH), 126.7 (CH), 125.0 (C), 124.5 (CH), 124.3 (CH), 60.7 (CH), 59.3 (CH), 46.6 (CH), 42.8 (CH), 36.5 (CH₂), 33.1 (CH₂), 30.0 (CH₂), 29.5 (CH₂), 22.9 (CH₃), 22.8 (CH₂), 22.8 (CH₃), 22.6 (CH₂), 21.3 (CH₃), 21.2 (CH₃), 14.1 (CH₃), 13.7 ppm (CH₃); IR (thin film): $\tilde{\nu}_{\text{max}} = 1710$ (s, C=O), 1615 (C=C), 1590 (C=C), 1565 (C=C), 1512 (C=C); HRMS (ESI): m/z calcd. for $\text{C}_{24}\text{H}_{25}\text{NONa}^+$: 366.1828 [M + Na]⁺, found 366.1821.

1-(2-Methyl-1H-indol-3-yl)oct-3-yn-2-one: To a solution of hex-1-yne (1.2 mL, 10.5 mmol) in THF (10.5 mL), at -78 °C under an atmosphere of argon, was added *n*BuLi (5.5 mL, 8.8 mmol, 1.6 M in hexane). The mixture was stirred for 30 min at -78 °C then transferred via cannula to a solution of *N*-methoxy-*N*-methyl-2-(2-methyl-1H-indol-3-yl)acetamide (813 mg, 3.5 mmol) in THF (17.5 mL) which was also cooled to -78 °C under an atmosphere of argon. The resulting mixture was stirred for 5 min and then warmed to r.t. with continued stirring for 1 h. The reaction was quenched with sat. aq. NH_4Cl (20 mL), diluted with water (10 mL) and extracted with EtOAc (3 × 30 mL). The organics were combined and dried with MgSO_4 , concentrated in vacuo and purified by flash column chromatography (9:1 to 4:1 hexane/EtOAc) to afford the *titled product 51* as a yellow oil (414 mg, 47%). $R_f = 0.81$ (hexane/EtOAc, 1:1); $^1\text{H NMR}$ (400 MHz, CDCl_3): $\delta = 7.92$ (br. s, 1H), 7.51 (d, $J = 7.5$ Hz, 1H), 7.30–7.27 (m, 1H), 7.16–7.07 (m, 2H), 3.87 (s, 2H), 2.42 (s, 3H), 2.25 (t, $J = 7.0$ Hz, 2H), 1.45–1.37 (m, 2H), 1.33–1.22 (m, 2H), 0.85 ppm (t, $J = 7.0$ Hz, 3H); $^{13}\text{C NMR}$ (100 MHz, CDCl_3): $\delta = 185.6$ (C), 135.3 (C), 133.3 (C), 128.8 (C), 121.5 (CH), 119.8 (CH), 118.3 (CH), 110.4 (CH), 103.9 (C), 95.4 (C), 81.1 (C), 41.4 (CH₂), 29.6 (CH₂), 21.9 (CH₂), 18.8 (CH₂), 13.6 (CH₃), 12.0 ppm (CH₃); IR (thin film): $\tilde{\nu}_{\text{max}} = 2210$ (C=C), 1664 (C=O) cm^{-1} ; HRMS (ESI): m/z calcd. for $\text{C}_{17}\text{H}_{19}\text{NONa}^+$: 276.1359 [M + Na]⁺, found 276.1363.

2-Butyl-2'-methylspiro[cyclopent[2]ene-1,3'-indol]-4-one (3f): To a solution of 1-(2-methyl-1H-indol-3-yl)oct-3-yn-2-one (414 mg, 1.6 mmol) in DCM (16 mL) was added AgOTf (4.2 mg, 16 μmol) at r.t. The reaction mixture was stirred for 1 h and then concentrated in vacuo. Purification by flash column chromatography (1:1 hexane/EtOAc) afforded the *titled product 3f* as a yellow oil (270 mg, 55%). $R_f = 0.36$ (hexane/EtOAc, 1:1); $^1\text{H NMR}$ (400 MHz, CDCl_3): $\delta = 7.57$ (d, $J = 7.5$ Hz, 1H), 7.37 (ddd, $J = 7.5, 1.5, 1.5$ Hz, 1H), 7.22 (ddd, $J = 7.5, 1.0, 1.0$ Hz, 1H), 7.13 (ddd, $J = 7.5, 1.5, 1.0$ Hz, 1H), 6.30 (t, $J = 1.5$ Hz, 1H), 2.72 (d, $J = 18.5$ Hz, 1H), 2.67 (d, $J = 18.5$ Hz, 1H), 2.17 (s, 3H), 1.71–1.53 (m, 2H), 1.41–1.31 (m, 2H), 1.15 (sext., $J = 7.0$ Hz, 2H), 0.76 ppm (t, $J = 7.0$ Hz, 3H); $^{13}\text{C NMR}$ (100 MHz, CDCl_3): $\delta = 206.1$ (C), 181.7 (C), 181.6 (C), 155.4 (C), 140.2 (C), 131.0 (CH), 129.0 (CH), 126.3 (CH), 121.8 (CH), 120.5 (CH), 68.6 (C), 42.7 (CH₂), 29.0 (CH₂), 28.2 (CH₂), 22.2 (CH₂), 15.5 (CH₃), 13.7 ppm (CH₃); IR (thin

film): $\nu_{\max} = 1717$ (s, C=O), 1693 (C=C), 1609 (C=C) cm^{-1} ; HRMS (ESI): m/z calcd. for $\text{C}_{17}\text{H}_{19}\text{NONa}^+$: 276.1359 [M + Na] $^+$, found 276.1361.

2-Butyl-5-(4-methylphenyl)-2'-methylspiro[cyclopentane-1,2'-indol]-2-en-4-one (3h): To a dry round-bottomed flask, 1-(2-methyl-1*H*-indol-3-yl)oct-3-yn-2-one **S1** (529 mg, 2.1 mmol), 4-iodotoluene (501 mg, 2.3 mmol) and bromobis(triphenylphosphine)-(N-succinimide)palladium(II) (32 mg, 40 μmol) were added. The flask was purged with argon and then dry acetonitrile (20 mL) and triethylamine (0.3 mL, 2.1 mmol) were added. The reaction was heated to 60 °C with continuous stirring for 4 h. The mixture was then cooled to r.t. and concentrated in vacuo. Purification by flash column chromatography (9:1 to 7:3 hexane/EtOAc) afforded the titled product **3h** as a pale yellow oil (489 mg, 71 %). $R_f = 0.22$ (hexane/EtOAc, 7:3); ^1H NMR (400 MHz, CDCl_3): $\delta = 7.63$ (d, $J = 7.5$ Hz, 1H), 7.45–7.38 (m, 1H), 7.29–7.22 (m, 6H), 2.86 (d, $J = 19.0$ Hz, 1H), 2.81 (d, $J = 19.0$ Hz, 1H), 2.39 (s, 3H), 2.27 (s, 3H), 2.05–1.95 (m, 1H), 1.88–1.78 (m, 1H), 1.06–0.85 (m, 4H), 0.56 ppm (t, $J = 6.0$ Hz, 3H); ^{13}C NMR (100 MHz, CDCl_3): $\delta = 204.8$ (C), 182.6 (C), 173.4 (C), 155.6 (C), 143.2 (C), 140.6 (C), 138.3 (C), 129.3 (CH), 129.0 (CH), 128.8 (CH), 128.3 (C), 126.1 (CH), 122.3 (CH), 120.5 (CH), 67.1 (C), 42.7 (CH₂), 30.0 (CH₂), 28.3 (CH₂), 22.8 (CH₂), 21.4 (CH₃), 15.9 (CH₃), 13.3 ppm (CH₃); IR (thin film): $\nu_{\max} = 1706$ (s, C=O), 1609 (C=C), 1578 (C=C) cm^{-1} ; HRMS (ESI): m/z calcd. for $\text{C}_{24}\text{H}_{25}\text{NONa}^+$: 366.1828 [M + Na] $^+$, found 366.1825.

Acknowledgments

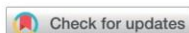
The authors thank the EPSRC (A. K. C. EP/R013748/1), the Leverhulme Trust (for an Early Career Fellowship, ECF-2015-013, for W. P. U.) and the University of York (R. G. E., W. P. U.) for financial support. We are also grateful for the provision of an Eleanor Dodson Fellowship (to W. P. U.) by the Department of Chemistry, University of York. We also thank the EPSRC (grants EP/H011455/1 and EP/K031589/1) for funding the computational resources used in this study.

Keywords: Quinolines · Spirocycles · Indolenines · Rearrangement · Density functional calculations

- [1] R. H. Manske, *Chem. Rev.* **1942**, *30*, 113–144.
- [2] For reviews and perspective on the applications and uses of quinolines, see: a) S. M. Prajapati, K. D. Patel, R. H. Vekariya, S. N. Panchal, H. D. Patel, *RSC Adv.* **2014**, *4*, 24463–24476; b) A. Marella, O. P. Tanwar, R. Saha, M. R. Ali, S. Srivastava, M. Akhter, M. Shaquiquzaman, *Saudi Pharm. J.* **2013**, *21*, 1–12; c) Jaina V. Chandra, P. Kumar Jain, K. Pathak, D. Pathak, A. Vaidy, *Arabian Journal of Chemistry*. **2016**, <https://doi.org/10.1016/j.arabjoc.2016.10.009> and references cited therein.
- [3] For classical quinoline syntheses, see reference 1 and: a) R. H. F. Manske, M. Kulka, *Org. React.* **1953**, *7*, 59–98; b) P. A. Claret, *Compr. Org. Chem.* **1979**, *4*, 155–203; c) J. J. Eisch, T. Dluzniewski, *J. Org. Chem.* **1989**, *54*, 1269–1274; d) M. Conrad, L. Limpach, *Ber. Dtsch. Chem. Ges.* **1891**, *24*, 2999–2992;
- [4] For more recent developments in quinoline synthesis, see reference 2a and: a) V. V. Kouznetsov, L. Y. Mendez, C. M. Gomez, *Curr. Org. Chem.* **2005**, *9*, 141–161; b) V. F. Batista, D. C. G. A. Pinto, A. M. S. Silva, *ACS Sustainable Chem. Eng.* **2016**, *4*, 4064–4078; c) M. Mastali, M. Glatz, E. Pittenauer, G. Allmaier, K. Kirchner, *J. Am. Chem. Soc.* **2016**, *138*, 15543–15546; d) H. Su, M. Bao, J. Huang, Li. Qiu, X. Xu, *Adv. Synth. Catal.* **2018**, *361*, 826–831; e) J. V. Jun, E. J. Petersson, D. M. Chenoweth, *J. Am. Chem. Soc.* **2018**, *140*, 9486–9493; f) C. Wang, J. Yang, X. Meng, Y. Sun, X. Man, J. Li, F. Sun, *Dalton Trans.* **2019**, *48*, 4474–4478.
- [5] For the original study, see: a) J. T. R. Liddon, M. J. James, A. K. Clarke, P. O'Brien, R. J. K. Taylor, W. P. Unsworth, *Chem. Eur. J.* **2016**, *22*, 8777–8780.
- For a follow up study involving halogenated derivatives, see: b) J. T. R. Liddon, A. K. Clarke, R. J. K. Taylor, W. P. Unsworth, *Org. Lett.* **2016**, *18*, 6328–6331.
- [6] For bioactive cyclopentanone-fused quinolines, see: V. V. Kouznetsov, C. Ochoa Puentes, A. R. Romero Bohórquez, S. A. Zaccchino, M. Sortino, M. Gupta, Y. Vázquez, A. Bahsas, J. Amaro-Luis, *Lett. Org. Chem.* **2006**, *3*, 300–304.
- [7] For a review on the chemistry of spirocyclic indolenines, see: M. J. James, P. O'Brien, R. J. K. Taylor, W. P. Unsworth, *Chem. Eur. J.* **2016**, *22*, 2856–2881 and references cited therein.
- [8] For related dearomatizing spirocyclisation reactions of ynones, see: a) W. P. Unsworth, J. D. Cuthbertson, R. J. K. Taylor, *Org. Lett.* **2013**, *15*, 3306–3309; b) M. J. James, J. Cuthbertson, P. O'Brien, R. J. K. Taylor, W. P. Unsworth, *Angew. Chem. Int. Ed.* **2015**, *54*, 7640–7643; *Angew. Chem.* **2015**, *127*, 7750; c) A. K. Clarke, M. J. James, P. O'Brien, R. J. K. Taylor, W. P. Unsworth, *Angew. Chem. Int. Ed.* **2016**, *55*, 13798–13802; *Angew. Chem.* **2016**, *128*, 14002; d) M. J. James, N. D. Grant, P. O'Brien, R. J. K. Taylor, W. P. Unsworth, *Org. Lett.* **2016**, *18*, 6256–6259; e) A. K. Clarke, J. T. R. Liddon, J. D. Cuthbertson, R. J. K. Taylor, W. P. Unsworth, *Org. Biomol. Chem.* **2017**, *15*, 233–245; f) H. E. Ho, M. J. James, P. O'Brien, R. J. K. Taylor, W. P. Unsworth, *Org. Lett.* **2018**, *20*, 1439–1443; g) H. E. Ho, T. C. Stephens, T. J. Payne, P. O'Brien, R. J. K. Taylor, W. P. Unsworth, *ACS Catal.* **2019**, *9*, 504–510.
- [9] For indole dearomatization reactions with other tethered functional groups, see: a) K.-J. Wu, L. X. Dai, S.-L. You, *Org. Lett.* **2012**, *14*, 3772; b) M. J. James, R. E. Clubley, K. Y. Palate, T. J. Procter, A. C. Wytton, P. O'Brien, R. J. K. Taylor, W. P. Unsworth, *Org. Lett.* **2015**, *17*, 4372–4375; c) S. J. Chambers, G. Coulthard, W. P. Unsworth, P. O'Brien, R. J. K. Taylor, *Chem. Eur. J.* **2016**, *22*, 6496–6500; d) V. Magné, F. Blanchard, A. Marinetti, A. Voituriez, X. Guinchard, *Adv. Synth. Catal.* **2016**, *358*, 3355–3361; e) M. J. James, P. O'Brien, R. J. K. Taylor, W. P. Unsworth, *Angew. Chem. Int. Ed.* **2016**, *55*, 9671–9675; *Angew. Chem.* **2016**, *128*, 9823; f) Y. Wang, C. Zheng, S.-L. You, *Angew. Chem. Int. Ed.* **2017**, *56*, 15093–15097; *Angew. Chem.* **2017**, *129*, 15289; g) D. Ryzhakov, M. Jarret, R. Guillot, C. Kouklovsky, G. Vincent, *Org. Lett.* **2017**, *19*, 6336–6339; h) J. T. R. Liddon, J. A. Rossi-Ashton, R. J. K. Taylor, W. P. Unsworth, *Org. Lett.* **2018**, *20*, 3349–3353; i) C. Zheng, S.-L. You, *Nat. Prod. Rep.* **2019**, DOI: <https://doi.org/10.1039/C8NP00098K>.
- [10] For reviews on dearomatization, see: a) X.-W. Liang, C. Zheng, S.-L. You, *Chem. Eur. J.* **2016**, *22*, 11918; b) S. P. Roche, J.-J. Youe Tendoung, B. Tréguier, *Tetrahedron* **2015**, *71*, 3549; c) C.-X. Zhuo, W. Zhang, S.-L. You, *Angew. Chem. Int. Ed.* **2012**, *51*, 12662; *Angew. Chem.* **2012**, *124*, 12834; d) C. X. Zhuo, C. Zheng, C. S.-L. You, *Acc. Chem. Res.* **2014**, *47*, 2558; e) C. Zheng, S.-L. You, *Chem* **2016**, *1*, 830.
- [11] For reviews on silver-catalysed alkyne activation, see: a) G. Fang, X. Bi, *Chem. Soc. Rev.* **2015**, *44*, 8124; b) A. K. Clarke, H. E. Ho, J. A. Rossi-Ashton, R. J. K. Taylor, W. P. Unsworth, *Chem. Asian J.* **2019** DOI: <https://doi.org/10.1002/asia.201900309>.
- [12] P. Fedoseev, E. Van Der Eycken, *Chem. Commun.* **2017**, *53*, 7732–7735.
- [13] For related works from the same group, see: a) F. Schröder, U. Sharma, M. Mertens, F. Devred, D. Debecker, R. Luque, E. V. Van der Eycken, *ACS Catal.* **2016**, *6*, 8156; b) Y. He, Z. Li, K. Robeyns, L. Van Meervelt, E. V. Van der Eycken, *Angew. Chem. Int. Ed.* **2018**, *57*, 272; *Angew. Chem.* **2018**, *130*, 278.
- [14] G. Han, L. Xue, L. Zhao, T. Zhu, J. Hou, Y. Song, Y. Liu, *Adv. Synth. Catal.* **2019**, *361*, 678. This interesting cascade process also proceeded with concomitant additional oxidation of the cyclopentenone ring.
- [15] For indole to quinoline ring expansion reactions, see: a) P. C. Magnanini, *Ber. Dtsch. Chem. Ges.* **1887**, *20*, 2608; b) F. De Angelis, A. Inesi, M. Feroci, R. Nicoletti, *J. Org. Chem.* **1995**, *60*, 445–447. For a recent general review of ring expansion reactions, see c) W. P. Unsworth, J. R. Donald, *Chem. Eur. J.* **2017**, *23*, 8780.
- [16] For other DFT studies, including information on related reaction systems, by the Unsworth and Lynam groups, see: a) A. K. Clarke, J. M. Lynam, R. J. K. Taylor, W. P. Unsworth, *ACS Catal.* **2018**, *8*, 6844–6850; b) J. T. R. Liddon, J. A. Rossi-Ashton, A. K. Clarke, J. M. Lynam, R. J. K. Taylor, W. P. Unsworth, *Synthesis* **2018**, *50*, 4829–4836; c) A. Lawer, J. A. Rossi-Ashton, T. C. Stephens, B. J. Challis, R. G. Epton, J. M. Lynam, W. P. Unsworth, *Angew. Chem. Int. Ed.* **2019**, DOI: <https://doi.org/10.1002/anie.201907206>.

- [17] Van der Eycken and co-workers also showed that partial formation of **2a** is possible at r.t. but settled on higher temperatures for their optimal synthetic procedure, see reference 12.
- [18] Note that the work-up/purification of the TFA-mediated reactions is typically more straightforward than those using $AlCl_3 \cdot 6H_2O$ (in which precipitate formation can sometimes complicate isolation of the product).
- [19] F. Weigend, M. Häser, H. Patzelt, R. Ahlrichs, *Chem. Phys. Lett.* **1998**, *294*, 143.
- [20] S. Grimme, S. Ehrlich, L. Goerigk, *J. Comput. Chem.* **2011**, *32*, 1456–65.

Received: May 31, 2019



Cite this: *Chem. Sci.*, 2020, 11, 1353

All publication charges for this article have been paid for by the Royal Society of Chemistry

Received 21st October 2019
Accepted 12th December 2019

DOI: 10.1039/c9sc05311e

rsc.li/chemical-science

Visible-light-induced intramolecular charge transfer in the radical spirocyclisation of indole-tethered yrones†

Hon Eong Ho,^a Angela Pagano,^b James A. Rossi-Ashton,^a James R. Donald,^b Ryan G. Epton,^a Jonathan C. Churchill,^a Michael J. James,^a Peter O'Brien,^a Richard J. K. Taylor^{*a} and William P. Unsworth^{†a}

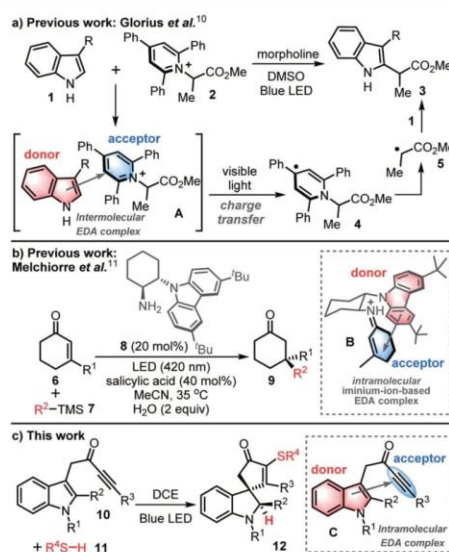
Indole-tethered yrones form an intramolecular electron donor–acceptor complex that can undergo visible-light-induced charge transfer to promote thiyl radical generation from thiols. This initiates a novel radical chain sequence, based on dearomatising spirocyclisation with concomitant C–S bond formation. Sulfur-containing spirocycles are formed in high yields using this simple and mild synthetic protocol, in which neither transition metal catalysts nor photocatalysts are required. The proposed mechanism is supported by various mechanistic studies, and the unusual radical initiation mode represents only the second report of the use of an intramolecular electron donor–acceptor complex in synthesis.

Introduction

The use of visible-light-mediated photochemistry in synthesis has grown enormously in recent years,^{1,2} triggered by dramatic progress in the fields of photoredox catalysis,³ energy transfer⁴ and atom transfer processes.⁵ This has led to a renaissance in the use of single electron transfer (SET) processes in chemical synthesis, including renewed interest in the study of charge transfer in electron donor–acceptor (EDA) complexes.

The phenomenon of charge transfer was first postulated in the 1950s,^{6,7} but received relatively little attention in synthetic chemistry⁸ until a surge in interest in the last decade,⁹ with an illustrative example recently reported by Glorius and co-workers summarised in Scheme 1a.¹⁰ In this study, it was shown that the coupling of indoles **1** and pyridinium salt acceptors **2** can be performed in the absence of a transition metal catalyst or photocatalyst. Key to this process is the formation of an intermolecular EDA complex **A** between an indole (the donor) and a pyridinium salt (the acceptor); the EDA complex can then absorb visible light to promote charge transfer to form radical **4**, that can then fragment to give electrophilic radical **5** and couple with indole **1** to afford C-2 functionalised indole **3** via a radical chain process.

This report and others,^{9,10} highlight the value of *intermolecular* EDA-mediated charge transfer for the construction of challenging chemical bonds. However, until a 2018 report by



Scheme 1 EDA complexes in synthetic chemistry (a, b = previous work, c = this work). DCE = 1,2-dichloroethane. LED = light emitting diode.

^aDepartment of Chemistry, University of York, York, YO10 5DD, UK. E-mail: richard.taylor@york.ac.uk; william.unsworth@york.ac.uk

^bDepartment of Chemistry and Industrial Chemistry, University of Genova, via Dodecaneso, 31, 16146 Genova, Italy

† Electronic supplementary information (ESI) available. CCDC 1945620, 1945621, 1945618, 1945619 and 1945660. For ESI and crystallographic data in CIF or other electronic format see DOI: 10.1039/c9sc05311e



Melchiorre and co-workers,^{11,12} there were no reports of the use of photon-absorbing *intramolecular* EDA complexes being used in synthesis. In this seminal study, an enantioselective radical conjugate addition reaction is described that relies on visible-light-excitation of a chiral iminium-ion based intramolecular EDA complex **B**, itself formed *in situ* from a ketone **6** and organocatalyst **8** (Scheme 1b).¹¹

Herein, a new synthetic method based on *intramolecular* EDA complexation and charge transfer is reported for only the second time. Thus, a novel radical dearomatising spirocyclisation¹³ of indole-tethered ynones **10** (ref. 14) and thiols **11** is described for the formation of spirocyclic indolines **12** with concomitant C-S bond formation (Scheme 1c).¹⁵ The reactions are catalyst-free and proceed *via* a thiyl radical-based chain process, that is thought to be self-initiated by the ynone starting material **10**, through visible-light-induced charge transfer of an intramolecular EDA complex **C**. A wide range of sulfur-containing spirocycles **12** have been prepared using this mild, high yielding synthetic procedure. This unusual photocatalyst-free method to initiate radical chemistry was discovered by serendipity, and could easily have gone unnoticed, if not for the recent surge in interest in the study of charge transfer in electron donor-acceptor (EDA) complexes.

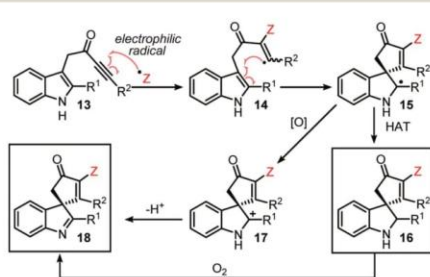
Results and discussion

The original aim of this project was to develop a radical spirocyclisation protocol based on more well-established methods for radical generation. We postulated that indole-tethered ynones **13** would react with electrophilic radicals *via* regioselective addition to the alkyne group (**13** → **14**), before cyclising on to the indole at its 3-position to form a spirocyclic radical intermediate (**14** → **15**). Radical **15** could then go on to form either spirocyclic indoline **16** *via* hydrogen atom transfer (HAT), or spirocyclic indolenine **18** *via* single electron oxidation followed by proton loss (Scheme 2). Oxidation of **16** to **18** in the presence of molecular oxygen, or other oxidants, was also predicted to be viable. Confidence in this general idea was raised by reports of radical-based dearomative processes involving phenol- and anisole-tethered alkynes.^{16,17} These studies confirm that electrophilic radicals can react with ynones with the

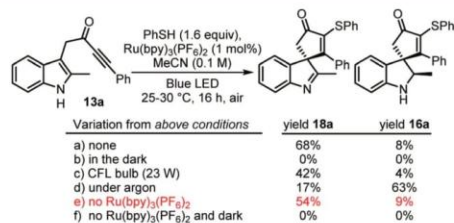
desired regioselectivity, and that the so-formed radical species can go on to react with tethered aromatics; however, to the best of our knowledge, such a strategy had not been applied to indole-tethered alkynes prior to this report.

This study began by examining the reaction of ynone **13a** with a thiyl radical generated from thiophenol *in situ*. Thiyl radicals are versatile reactive intermediates in synthetic radical chemistry¹⁸ and we reasoned that the derived products could be relevant in drug discovery, in view of the prevalence of vinyl sulfides in bioactive compounds.¹⁹ A photoredox catalysis approach originally was chosen to generate the thiyl radical,²⁰ which led to the development of the conditions summarised in Scheme 3 (see ESI† for full optimisation). Thus, the combination of thiophenol, catalytic Ru(bpy)₃(PF₆)₂ and irradiation with a blue LED lamp ($\lambda_{\text{max}} = 455 \text{ nm}$, 60 W) at rt under air, enabled the conversion of indole-tethered ynone **13a** into spirocyclic indolenine²¹ **18a** in reasonable yield *via* an overall oxidative dearomative process (Scheme 3, a). Product **18a** was synthesised along with indoline **16a** as minor side-product, with **16a** believed to be an intermediate on the route to indolenine **18a**.²² Control experiments revealed that oxygen is required for the efficient formation of **18a** (indoline **16a** is the major product in the absence of oxygen, Scheme 3, d) and more intriguingly, a mixture of both products **18a** and **16a** is formed even *in the absence of any photocatalyst* (Scheme 3, e). In the absence of light, no reaction occurs (Scheme 3, f). This indolenine-forming reaction was also found to work on other ynone starting materials (5 examples, see ESI† page S8 for details).

The unexpected discovery that spirocyclisation can be achieved without Ru(bpy)₃(PF₆)₂ was intriguing, both from a mechanistic standpoint, and in view of the clear practical and environmental benefits of avoiding metal-based photocatalysts. We therefore decided to explore this process in more detail and started by establishing whether the photocatalyst-free reaction conditions could be applied to other substrates. Additional optimisation was performed at this point (see ESI†), and based on this, the decision was made to prioritise the synthesis of indoline products **16/19** (*via* overall redox neutral reactions, *c.f.* Scheme 3, d) rather than indolenines **18** (overall oxidative processes, *c.f.* Scheme 3, a).²³ Thus, the reactions were performed under argon rather than air; another change to the



Scheme 2 Planned reaction courses.



Scheme 3 Control reactions; all yields are based on comparison to an internal standard in the ¹H NMR spectrum of the unpurified reaction mixture except for 'a' which is an isolated yield. CFL = compact fluorescent lamp.



conditions was to switch the solvent from acetonitrile to 1,2-dichloroethane (see ESI† for further optimisation details).

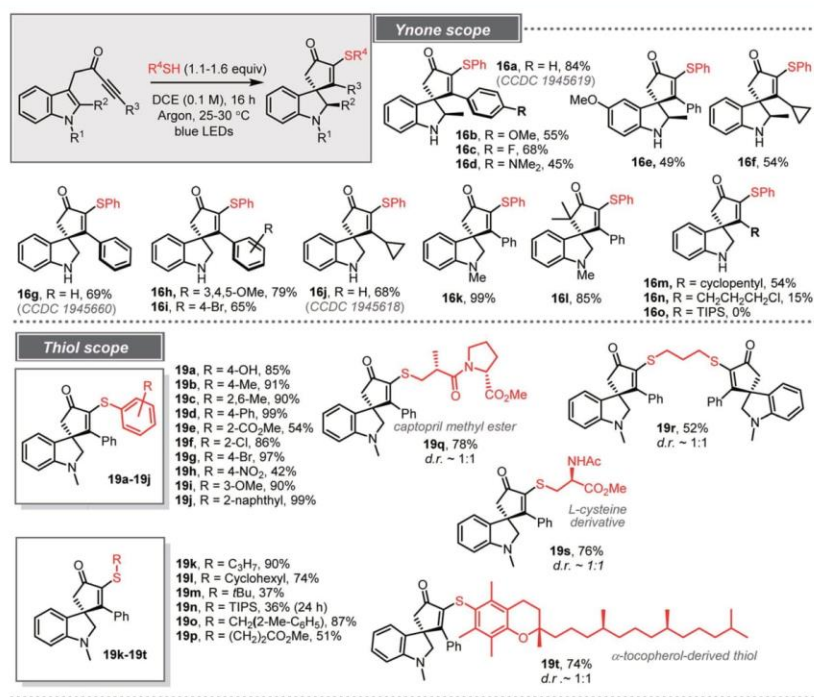
The optimised conditions were then tested across a range of indole-tethered ynone and thiols, and the results summarised in Scheme 4 confirm that the reaction is broad in scope. Changes to the substituent on the indole nitrogen (NH and NMe), the indole 2-position and the ynone terminus (R^3) were all tolerated (**16a–n**, 15–99%), with bulky TIPS-substituted ynone **13o** (to form **16o**) the only unsuccessful example. In cases where the indole C-2 position is substituted (**16a–f**) the products were isolated as the single diastereoisomer shown, with the assignment of relative stereochemistry based on X-ray crystallographic data for **16a**.^{24,25}

The reactions also work well with a range of thiols (20 examples, **19a–19t**, 36–99%). Various electronically diverse, substituted arylthiols were well-tolerated (**19a–19j**), with the more electron-rich examples typically the highest yielding. We were also pleased to observe that aliphatic thiols are compatible with the standard procedure (**19k–19p**); the S–H bond dissociation energy (BDE) for alkyl thiols (~ 87 kcal mol⁻¹) is usually higher than related aryl thiols (72–82 kcal mol⁻¹), which can adversely affect their reactivity in radical reactions.¹⁸ More

complex thiols have also been shown to work well using the standard procedure, including 1,3-propanedithiol (to make dimeric product **19r**), a protected cysteine derivative and a peptide-like thiol (to make **19q** and **19s**) and an α -tocopherol-derived thiol (to make **19t**).

Having established the synthetic method, attention then turned to understanding how the reactions operate in the absence of photocatalyst. We reasoned that visible-light activation of one of the starting materials must play a key role. Based on precedent, several possibilities could be envisaged:^{26,27} (1) light-induced homolytic cleavage of the thiol S–H bond to generate a thiyl radical would account for the observed reactivity, as this could start a radical chain reaction, as outlined earlier in Scheme 2; (2) similar reactivity could also originate from homolytic S–S bond cleavage of trace disulfides present in the thiol reagent; (3) photoexcitation of the alkyne to its triplet state could form an open-shell species theoretically capable of initiating radical chemistry.

Although we considered all of these scenarios to be unlikely under the influence of blue light (based on the energy typically needed to homolyse S–H/S–S bonds or to electronically excite alkynes),^{18,27} control experiments were nonetheless designed to



Scheme 4 Light induced charge-transfer radical spirocyclisation. Isolated yields following column chromatography are given.

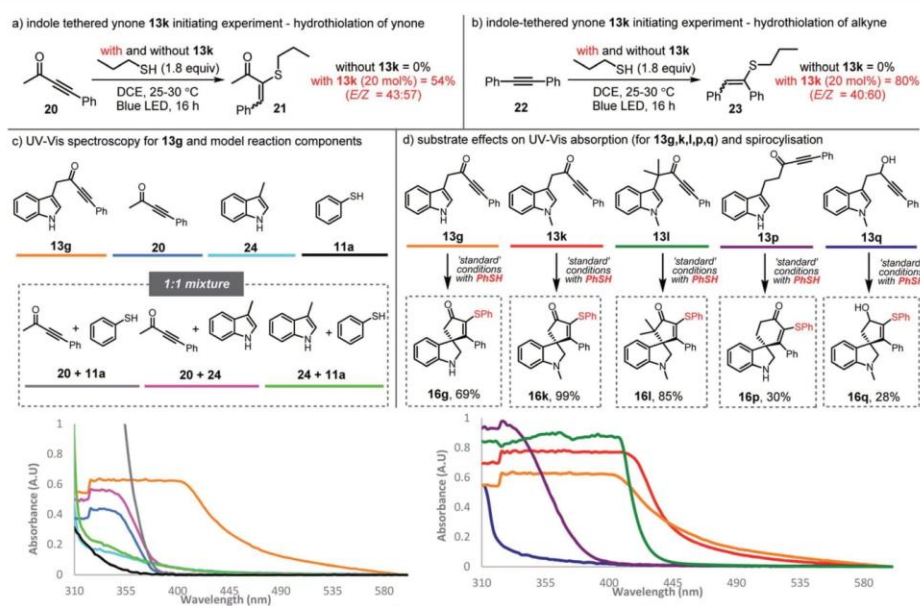


examine these possibilities. The experiments were based on the hydrothiolation of simple alkynes; thus, each of alkynes **20** and **22** were reacted with *n*-propane thiol under blue LED irradiation at RT, but no conversion into vinyl sulfides **21** and **23** was observed, with the alkynes fully recovered in each case (Schemes 5a and 5b). The lack of hydrothiolation in these experiments supports the idea that the initiation mechanisms suggested above are invalid; thiyl radicals seem not to be formed directly from the thiol reagent (or trace amounts of disulfides) in the presence of either of these alkynes, and the lack of reactivity observed with ynone starting material **20**, appears to rule out simple triplet excitation of the ynone functionality under blue light radiation. Instead, these results suggest that the indole-tethered ynone moiety **13** itself is critical to the observed reactivity. Indeed, compelling evidence that supports the involvement of the ynone in initiating thiyl radical chemistry was obtained when alkynes **20** and **22** were again reacted with *n*-propane thiol, but this time with the addition of sub-stoichiometric (20 mol%) ynone **13k**; under these conditions, hydrothiolation products **21** and **23** were obtained in 54% and 80% yields, respectively.

Normally, neither ynones nor 3-substituted indoles would be expected to absorb visible light wavelength photons. However, the ynones **13** used in this study tend to be yellow in colour, and indeed, ynone **13g** was found to absorb relatively strongly at

around 455 nm (the λ_{max} of the light source) when analysed using UV-Vis spectroscopy (orange line, Scheme 5c; for the emission spectra of **13g** see the ESI†). In contrast, model ynone **20** (blue line), 3-substituted indole **24** (cyan line), and thio-phenol **11a** (black line) displayed little/no absorption in the same region. Equimolar mixtures of these compounds (**20** + **11a** in grey, **20** + **24** in pink and **24** + **11a** in green) did absorb in the visible region when measured at 0.02 M, although interestingly, when mixed at much higher concentration (>0.5 M) a significant bathochromic shift was observed for a mixture of ynone **20** and indole **24**, indicating that the intermolecular interaction of these components can influence their absorption properties, albeit at concentrations well above those used in the synthetic reactions (see ESI, Scheme S3†). The addition of thiol **11a** does not appear to influence the absorbance, with near-identical UV-Vis spectra obtained for both ynone **13k** and a mixture of **20** and **24**, with and without the inclusion of **11a** (see ESI Scheme S4†).

The ability of the indole ynone starting materials **13** to absorb visible light around 455 nm appears to correlate well with the success of the radical cascade processes, as illustrated by the data presented in Scheme 5d. For example, alkynes **13p** and **13q**, showed low absorption at 455 nm (purple and blue lines respectively) and both the conversion and yields for these reactions were much lower than those for the standard substrates (*c.f.* Scheme 4).²⁸ In contrast, ynones **13g**, **13k** and



Scheme 5 (a) Hydrothiolation of ynone **20**; (b) Hydrothiolation of alkyne **22**; (c) UV-Vis spectroscopy studies of indole-tethered ynone **13g** compared with model reaction components; (d) UV-Vis spectroscopy of indole-tethered ynones (**13g**, **13k**, **13l**, **13p**) and propargylic alcohol **13q**. All UV-Vis experiments were performed in anhydrous 1,2-dichloroethane (0.02 M).



13l, which all reacted efficiently to form **16g**, **16k** and **16l** with full conversion and in good yields, show a clear red-shift into the visible region (orange, red and green lines respectively).²⁹

We postulate that through-space interactions explain the enhanced visible light absorption of the reactive ynone systems, *via* formation of an intramolecular EDA complex of the form **C** (Scheme 6a) that enables the ynone to absorb relatively long wavelength visible light and initiate thiyl radical chemistry. A through bond process (*i.e.* involving conjugation *via* enolate formation)³⁰ was also considered as a possible explanation for the red shift of typical ynone substrates, but was ruled out on the basis of the UV-Vis data and successful reaction of non-enolisable ynone **13l**. The formation of an intramolecular EDA complex is also supported by time-dependent density functional theory (TDDFT) calculations performed on ynone **13k**, which predicted a peak at 441 nm with an oscillator strength of 0.050 (Scheme 6b). This peak is composed entirely of a charge transfer excitation between the π orbitals of the indole HOMO and ynone LUMO (Scheme 6b).

Thus, a mechanism is proposed in which the formation of an EDA complex **C** is followed by visible light absorption to form a photoexcited state, loosely represented as charge transfer complex **25**. This species may simply relax to reform EDA complex **C** *via* back electron transfer, or alternatively, the open shell excited state **25** could abstract a hydrogen atom from the thiol **11**, thus generating the thiyl radical needed to start a radical cascade (Scheme 6a).³¹ At this point, a more typical

radical chain process can operate (Scheme 6c), which likely proceeds by the addition of thiyl radical to the ynone (**10** \rightarrow **26**), spirocyclisation (**26** \rightarrow **27**) and hydrogen atom abstraction from thiol **11** (**27** \rightarrow **12**), thus enabling chain propagation. Quantum yield measurements ($\phi = 19.8$)³² support operation through a chain process.^{33,34}

Conclusions

In summary, a new dearomative method for the synthesis of sulfur-containing spirocyclic indolines is described, based on the reaction of indole-tethered yrones with thiyl radicals generated *in situ* from thiols. The reactions are promoted by visible light, operate at RT under mild reaction conditions and need neither a transition metal catalyst nor added photocatalyst to proceed efficiently across a wide range of substrates. The reaction is thought to be self-initiated³⁵ with visible-light-mediated photoexcitation of an intramolecular EDA complex formed between the indole and ynone moieties in the starting material leading to the formation of an open shell excited charge-transfer complex, capable of abstracting a hydrogen atom from the thiol and initiating radical chain propagation.

To the best of our knowledge, this is only the second report that details the use of intramolecular EDA complexes in synthesis. This rare radical activation mode was uncovered entirely by serendipity,³⁶ and this is a feature of the discovery that we are keen to highlight, as we believe that intramolecular EDA complexes likely play key roles in other synthetic methods, but can go (or have gone) unnoticed.^{36d} As awareness of the value of charge transfer processes in synthetic chemistry grows, we believe that many important new methods of this type will be discovered, both through design and by serendipity.

Conflicts of interest

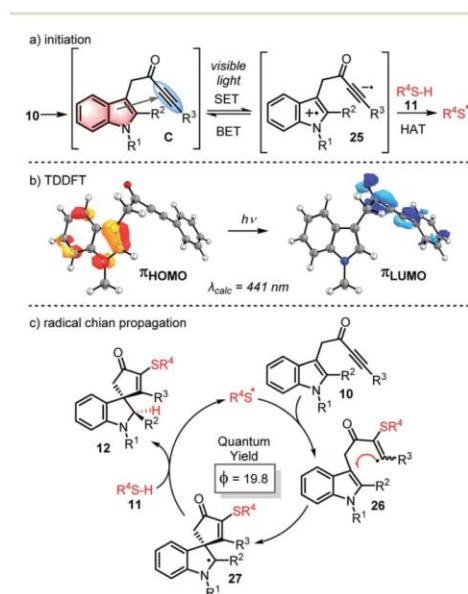
There are no conflicts to declare.

Acknowledgements

The authors would like to thank the EPSRC (H. E. H. EP/N035119/1), the University of York, the Leverhulme Trust (for Early Career Fellowships, ECF-2015-013, W. P. U. and ECF-2019-135, M. J. J.) and Erasmus+ (for Angela Pagano) for financial support. We are also grateful for the provision of an Eleanor Dodson Fellowship (to W. P. U.) by the Department of Chemistry, University of York. Dr Adrian C. Whitwood and Rachel Parker are thanked for X-ray crystallography. We would also like to thank Prof. Giovanni Petrillo (University of Genova) Dr Alison Parkin and Prof. Neil Hunt (both University of York) for helpful discussions.

Notes and references

- (a) H. Trommsdorff, *Ann. Pharm.*, 1834, **11**, 190; (b) H. D. Roth, *Angew. Chem., Int. Ed.*, 1989, **28**, 1193.
- For selected reviews of visible light photocatalysis, see: (a) T. P. Yoon, M. A. Ischay and J. Du, *Nat. Chem.*, 2010, **2**,



Scheme 6 (a) Proposed mechanism for initiation; (b) TDDFT calculations; (c) proposed propagation cycle.



- 527; (b) D. P. Hari and B. König, *Angew. Chem., Int. Ed.*, 2013, **52**, 4734; (c) M. D. Kärkäs, J. A. Porco Jr and C. R. J. Stephenson, *Chem. Rev.*, 2016, **116**, 9683; (d) D. Ravelli, S. Protti and M. Fagnoni, *Chem. Rev.*, 2016, **116**, 9850; (e) T. Hering, A. U. Meyer and B. König, *J. Org. Chem.*, 2016, **81**, 6927; (f) L. Marzo, S. K. Pagire, O. Reiser and B. König, *Angew. Chem., Int. Ed.*, 2018, **57**, 10034.
- 3 For selected reviews of photoredox catalysis, see: (a) C. K. Prier, D. A. Rankic and D. W. C. MacMillan, *Chem. Rev.*, 2013, **113**, 5322; (b) J. D. Nguyen, E. M. D'Amato, J. M. Narayanam and C. R. J. Stephenson, *Nat. Chem.*, 2012, **4**, 854; (c) M. H. Shaw, J. Twilton and D. W. C. MacMillan, *J. Org. Chem.*, 2016, **81**, 6898; (d) J. Xuan and W.-J. Xiao, *Angew. Chem., Int. Ed.*, 2012, **51**, 6828.
- 4 For information on visible-light-induced organic photochemical reactions that proceed via energy-transfer pathways, see: Q.-Q. Zhou, Y.-Q. Zou, L.-Q. Lu and W.-J. Xiao, *Angew. Chem., Int. Ed.*, 2019, **58**, 1586 and references cited therein.
- 5 T. Courant and G. Masson, *J. Org. Chem.*, 2016, **81**, 6945.
- 6 R. S. Mulliken, *J. Am. Chem. Soc.*, 1952, **74**, 811.
- 7 For photophysical studies see: S. V. Rosokha and J. K. Kochi, *Acc. Chem. Res.*, 2008, **41**, 641 and references cited therein.
- 8 For early synthetic examples, see: (a) M. A. Fox, J. Younathan and G. E. Fryxell, *J. Org. Chem.*, 1983, **48**, 3109; (b) S. Sankararaman, W. A. Haney and J. K. Kochi, *J. Am. Chem. Soc.*, 1987, **109**, 7824; (c) T. Gotoh, A. B. Padias and J. H. K. Hall, *J. Am. Chem. Soc.*, 1991, **113**, 1308; (d) R. Rathore and J. K. Kochi, *Adv. Phys. Org. Chem.*, 2000, **35**, 193.
- 9 For a useful review of this area, see: (a) C. G. S. Lima, T. Lima, M. Duarte, I. D. Jurberg and M. W. Paixão, *ACS Catal.*, 2016, **6**, 1389. For selected recent research articles, see: (b) M. Tobisu, T. Furukawa and N. Chatani, *Chem. Lett.*, 2013, **42**, 1203; (c) J. Davies, S. G. Booth, S. Essafi, R. A. W. Dryfe and D. Leonori, *Angew. Chem., Int. Ed.*, 2015, **54**, 14017; (d) Y. Cheng, X. Yuan, J. Ma and S. Yu, *Chem.-Eur. J.*, 2015, **21**, 8355; (e) M. L. Spell, K. Deveaux, C. G. Bresnahan, B. L. Bernard, W. Sheffield, R. Kumar and J. R. Ragains, *Angew. Chem., Int. Ed.*, 2016, **55**, 6515; (f) V. Quint, F. Morlet-Savary, J.-F. Lohier, J. Lalevée, A.-C. Gaumont and S. Lakhdar, *J. Am. Chem. Soc.*, 2016, **138**, 7436; (g) A. Böhm, T. Bach and T. Chem, *Chem.-Eur. J.*, 2016, **22**, 15921; (h) L. Marzo, S. Wang and B. König, *Org. Lett.*, 2017, **19**, 5976; (i) J. Zhang, Y. Li, R. Xu and Y. Chen, *Angew. Chem., Int. Ed.*, 2017, **56**, 12619; (j) B. Liu, C.-H. Lim and G. M. Miyake, *J. Am. Chem. Soc.*, 2017, **139**, 13616; (k) H.-H. Zhang and S. Yu, *Org. Lett.*, 2019, **21**, 3711; (l) Q.-Q. Ge, J.-S. Qian and J. Xu, *J. Org. Chem.*, 2019, **84**, 8691; (m) K. Liang, N. Li, Y. Zhang, T. Li and C. Xia, *Chem. Sci.*, 2019, **10**, 3049; (n) M.-C. Fu, R. Shang, B. Zhao, B. Wang and Y. Fu, *Science*, 2019, **363**, 1429; (o) Y. Liu, X.-L. Chen, K. Sun, X.-Y. Li, F.-L. Zeng, X.-C. Liu, L.-B. Qu, Y.-F. Zhao and B. Yu, *Org. Lett.*, 2019, **21**, 4019; (p) J. J. Wu, L. He, A. Noble and V. K. Aggarwal, *J. Am. Chem. Soc.*, 2018, **140**, 10700.
- 10 M. J. James, F. Strieth-Kalthoff, F. Sandfort, F. J. R. Klauck, F. Wagener and F. Glorius, *Chem.-Eur. J.*, 2019, **25**, 8240.
- 11 Z.-Y. Cao, T. Ghosh and P. Melchiorre, *Nat. Comm.*, 2018, **9**, 3274.
- 12 For important contributions from the same group that involve intermolecular EDA complexes, see: (a) E. Arceo, I. D. Jurberg, A. Álvarez-Fernández and P. Melchiorre, *Nat. Chem.*, 2013, **5**, 750; (b) E. Arceo, A. Bahamonde, G. Bergonzini and P. Melchiorre, *Chem. Sci.*, 2014, **5**, 2438; (c) M. Nappi, G. Bergonzini and P. Melchiorre, *Angew. Chem., Int. Ed.*, 2014, **53**, 4921; (d) S. R. Kandukuri, A. Bahamonde, I. Chatterjee, I. D. Jurberg, E. C. Escudero-Adán and P. Melchiorre, *Angew. Chem., Int. Ed.*, 2015, **54**, 1485; (e) Ł. Woźniak, J. J. Murphy and P. Melchiorre, *J. Am. Chem. Soc.*, 2015, **137**, 5678; (f) A. Bahamonde and P. Melchiorre, *J. Am. Chem. Soc.*, 2016, **138**, 8019.
- 13 For recent reports of radical dearomatizing reactions of indoles, see: (a) J. Wu, Y. Dou, R. Guillot, C. Kouklovsky and G. Vincent, *J. Am. Chem. Soc.*, 2019, **141**, 2832; (b) J. Wu, R. K. Nandi, R. Guillot, C. Kouklovsky and G. Vincent, *Org. Lett.*, 2018, **20**, 1845; (c) J.-H. Ye, L. Zhu, S.-S. Yan, M. Miao, X.-C. Zhang, W.-J. Zhou, J. Li, Y. Lan and D.-G. Yu, *ACS Catal.*, 2017, **7**, 8324.
- 14 For transition metal (non-radical) transformations of indole-tethered ynones of this type, see: (a) M. J. James, J. Cuthbertson, P. O'Brien, R. J. K. Taylor and W. P. Unsworth, *Angew. Chem., Int. Ed.*, 2015, **54**, 7640; (b) M. J. James, R. E. Clubley, K. Y. Palate, T. J. Procter, A. C. Wyton, P. O'Brien, R. J. K. Taylor and W. P. Unsworth, *Org. Lett.*, 2015, **17**, 4372; (c) J. T. R. Liddon, M. J. James, A. K. Clarke, P. O'Brien, R. J. K. Taylor and W. P. Unsworth, *Chem.-Eur. J.*, 2016, **22**, 8777; (d) A. K. Clarke, M. J. James, P. O'Brien, R. J. K. Taylor and W. P. Unsworth, *Angew. Chem., Int. Ed.*, 2016, **55**, 13798; (e) J. T. R. Liddon, A. K. Clarke, R. J. K. Taylor and W. P. Unsworth, *Org. Lett.*, 2016, **18**, 6328; (f) A. K. Clarke, J. M. Lynam, R. J. K. Taylor and W. P. Unsworth, *ACS Catal.*, 2018, **8**, 6844; (g) H. E. Ho, T. C. Stephens, T. J. Payne, P. O'Brien, R. J. K. Taylor and W. P. Unsworth, *ACS Catal.*, 2019, **9**, 504.
- 15 For selected indole dearomatization methods, see: (a) K.-J. Wu, L. X. Dai and S.-L. You, *Org. Lett.*, 2012, **14**, 3772; (b) S. J. Chambers, G. Coulthard, W. P. Unsworth, P. O'Brien and R. J. K. Taylor, *Chem.-Eur. J.*, 2016, **22**, 6496; (c) V. Magné, F. Blanchard, A. Marinetti, A. Voituriez and X. Guinchard, *Adv. Synth. Catal.*, 2016, **358**, 3355; (d) M. J. James, P. O'Brien, R. J. K. Taylor and W. P. Unsworth, *Angew. Chem., Int. Ed.*, 2016, **55**, 9671; (e) Y. Wang, C. Zheng and S.-L. You, *Angew. Chem., Int. Ed.*, 2017, **56**, 15093; (f) D. Ryzhakov, M. Jarret, R. Guillot, C. Kouklovsky and G. Vincent, *Org. Lett.*, 2017, **19**, 6336; (g) J. T. R. Liddon, J. A. Rossi-Ashton, R. J. K. Taylor and W. P. Unsworth, *Org. Lett.*, 2018, **20**, 3349.
- 16 For examples of radical-based dearomative processes involving phenol- and anisole-tethered alkynes, see: (a) W. Wei, H. Cui, D. Yang, H. Yue, C. He, Y. Zhang and H. Wang, *Green Chem.*, 2017, **19**, 5608; (b) Y. Zhang,



- J. Zhang, B. Hu, M. Ji, S. Ye and G. Zhu, *Org. Lett.*, 2018, **20**, 2988; (c) C. R. Reddy, S. Yarlagadda, B. Ramesh, M. R. Reddy, B. Sridhar and B. V. S. Reddy, *Eur. J. Org. Chem.*, 2017, 2332; (d) Y. Liu, Q.-L. Wang, C.-S. Zhou, B.-Q. Xiong, P.-L. Zhang, C. Yang and K.-W. Tang, *J. Org. Chem.*, 2018, **83**, 2210; (e) L.-J. Wang, A.-Q. Wang, Y. Xia, X.-X. Wu, X.-Y. Liu and Y.-M. Liang, *Chem. Commun.*, 2014, **50**, 13998; (f) X.-H. Ouyang, R.-J. Song, B. Liu and J.-H. Li, *Chem. Commun.*, 2016, **52**, 2573; (g) D.-P. Jin, P. Gao, D.-Q. Chen, S. Chen, J. Wang, X.-Y. Liu and Y.-M. Liang, *Org. Lett.*, 2016, **18**, 3486; (h) H. Cui, W. Wei, D. Yang, J. Zhang, Z. Xu, J. Wen and H. Wang, *RSC Adv.*, 2015, **5**, 84657; (i) H.-L. Hua, Y.-T. He, Y.-F. Qiu, Y.-X. Li, B. Song, P. Gao, X.-R. Song, D.-H. Guo, X.-Y. Liu and Y.-M. Liang, *Chem.–Eur. J.*, 2015, **21**, 1468. For selected examples of metal-free radical-cyclisation of alkyne: (j) J. Wen, W. Wei, S. Xue, D. Yang, Y. Lou, C. Gao and H. Wang, *J. Org. Chem.*, 2015, **80**, 4966; (k) X.-H. Ouyang, R.-J. Song, Y. Li, B. Liu and J.-H. Li, *J. Org. Chem.*, 2014, **79**, 4582; (l) H. Sahoo, A. Mandal, S. Dana and M. Baidya, *Adv. Synth. Catal.*, 2018, **260**, 1099; (m) X.-H. Yang, X.-H. Ouyang, W.-T. Wei, R.-J. Song and J.-H. Li, *Adv. Synth. Catal.*, 2015, **357**, 1161; (n) C. Pan, B. Fang, W. Hu, X. Feng and J.-T. Yu, *J. Org. Chem.*, 2016, **81**, 2087; (o) W. Wei, L. Wang, H. Yue, Y.-Y. Jiang and D. Yang, *Org. Biomol. Chem.*, 2018, **16**, 8379.
- 17 For a relevant process based on a visible light mediated thyl radical annulation of alkyne-tethered quinolinones, see: K. Kim, H. Choi, D. Kang and S. Hong, *Org. Lett.*, 2019, **21**, 3417. EDA complex activation in the ground state was ruled out in this study.
- 18 For a review on thyl radicals in organic synthesis, see (a) F. Dénès, M. Pichowicz, G. Povie and P. Renaud, *Chem. Rev.*, 2014, **114**, 2587. For the bond dissociation energies of thiols and disulfides, see (b) N. A. Romero and D. A. Nicewicz, *J. Am. Chem. Soc.*, 2014, **136**, 17024.
- 19 (a) M. Feng, B. Tang, S. Liang and X. Jiang, *Curr. Top. Med. Chem.*, 2016, **16**, 1200; (b) E. A. Ilardi, E. Vitaku and J. T. Njardarson, *J. Med. Chem.*, 2014, **57**, 2832; (c) A. Gangjee, Y. Zeng, T. Talreja, J. J. McGuire, R. L. Kisliuk and S. F. Queener, *J. Med. Chem.*, 2007, **50**, 3046; (d) B. Le Grand, C. Pignier, R. Létienne, F. Cuisiat, F. Rolland, A. Mas and B. Vacher, *J. Med. Chem.*, 2008, **51**, 3856.
- 20 For a recent example of thyl radicals being used in photoredox mediated cross coupling, see: M. S. Oderinde, M. Frenette, D. W. Robbins, B. Aquila and J. W. Johannes, *J. Am. Chem. Soc.*, 2016, **138**, 1760.
- 21 For a review on spirocyclic indolenines, see: M. J. James, P. O'Brien, R. J. K. Taylor and W. P. Unsworth, *Chem.–Eur. J.*, 2016, **22**, 2856.
- 22 Re-subjecting an isolated sample of **16a** to the reaction conditions led to full conversion into indolenine **18a** over time, with atmospheric oxygen the likely oxidant (see ESI† for further details).
- 23 We reasoned that running the reactions under argon rather than air would lead to a more reproducible procedure, and we also know that spiroindolenines can be easily prepared

by oxidation of the corresponding spiroindolenines if required (see ESI†).

- 24 CCDC 1945619 (**16a**), 1945618 (**16j**), 1945660 (**16g**), 1645620 (**13g**), and 1645621 (**13k**) contain the crystallographic data, see ESI†.
- 25 When an analogous ynone substrate (**13r**) bearing a phenyl group at the indole C-2 position was tested, an inseparable mixture of indolenine product **18r** and indoline **16r** was obtained, as well as other minor impurities (the yields quoted below are based on NMR against an internal standard). The increased stability of the doubly benzylic radical that this reaction proceeds by, as well as the fact that this radical would be expected to undergo oxidation more easily, both account for the contrasting reactivity of this substrate compared with its alkyl substituted analogues. Although this reaction is not useful synthetically, the small amount of **16r** produced did appear to be formed as a single diastereoisomer, most likely with the same relative stereochemistry as that obtained for products **16b–f**.



- 26 See ref. *2d* and R. K. Mohamed, P. W. Peterson and I. V. Alabugin, *Chem. Rev.*, 2013, **113**, 7089.
- 27 For radical hydrothiolation, see ref. *18a*, and: (a) J. Healy, T. Rasmussen, S. Miller, I. R. Booth and S. J. Conway, *Org. Chem. Front.*, 2016, **3**, 439; (b) I. H. Rosa, M. L. B. Peixoto, G. R. Rosa, B. Godoi, F. Z. Galetto, M. G. M. D'Oca and M. Godoi, *Tetrahedron Lett.*, 2017, **58**, 3777; (c) J. József, L. L. Juhász and L. Somsák, *New J. Chem.*, 2019, **43**, 5670; (d) V. V. Levin, N. D. Zelinsky and A. D. Dilman, *J. Org. Chem.*, 2019, **84**, 8337.
- 28 The structural features of **13p** and **13q** (the elongated tether in **13p** and reduction of the carbonyl group in **13q**) were designed to disrupt formation of the EDA complex that is proposed to enable charge transfer and the resulting reaction.
- 29 The blue LED spectral output is a bell curve centred at 455 nm, with sufficient irradiance in the 400–420 nm range to trigger slow radical initiation from substrates **13p** and **13q**. We believe these substrates to be competent thyl radical chain carriers, as exemplified by the fact that an increase in yield for the conversion of **13q** → **16q**, from 28 to 65%, was observed upon the addition of 20 mol% of ynone **13k**, a substrate with a significantly higher absorbance at 455 nm.
- 30 L. Dell'Amico, A. Vega-Peñaloza, S. Cuadros and P. Melchiorre, *Angew. Chem., Int. Ed.*, 2016, **55**, 3313.
- 31 Unfortunately, we have been unable to obtain clear structural information on the fate of the initiator species **25** following HAT. Analysis of the unpurified reaction a typical reaction between ynone **13l** and thiophenol using



- ESI mass spectrometry led to the detection of peak representing a reduced version of the starting material (ynone **131** + H₂ + H⁺), but no identifiable products could be isolated from the reaction.
- 32 For more details on the method used to calculate quantum yield, see ESI page S9,† and for important background on such methods, see: (a) M. A. Cismesia and T. P. Yoon, *Chem. Sci.*, 2015, **6**, 5426; (b) K. Liang, N. Li, Y. Zhang, T. Li and C. Xia, *Chem. Sci.*, 2019, **10**, 3049.
- 33 The proposed mechanism is further supported by deuterium labelling studies in which the reaction of ynone **131** with PhSD was performed, with the expected deuterated product (**161**†, see ESI, pages S12 and S13†) being obtained. No significant difference in rate of reaction was observed when comparing this reaction with the analogous reaction with PhSH, suggesting that the HAT step is not rate determining (also see ESI, pages S12 and S13†).
- 34 Attempts to provide additional evidence for the existence of the EDA complex using cyclic voltammetry were inconclusive (see ESI pages S15 and S16†).
- 35 For useful perspective on catalysis of radical reactions, including especially relevant discussion of the concept of 'smart initiation', see: A. Studer and D. P. Curran, *Angew. Chem., Int. Ed.*, 2016, **55**, 58.
- 36 For examples and discussion of the importance of serendipity for discovery in synthetic chemistry, see: (a) S. Z. Zard, *Chem. Commun.*, 2002, 1555; (b) R. N. Grimes, *J. Organomet. Chem.*, 2013, **747**, 4; (c) M. Kazim, M. A. Siegler and T. Lectka, *Org. Lett.*, 2019, **21**, 2326. For useful discussion on the discovery of unforeseen energy-transfer-based transformations, see: (d) J. Ma, F. Strieth-Kalthoff, C. Henkel, M. Teders, A. Kahnt, W. Knolle, A. Gómez-Suárez, K. Dirian, W. Alex, K. Bergander, C. G. Daniliuc, B. Abel, D. M. Guldi and F. Glorius, *Chem*, 2019, **5**, 2183.



Paper 4 – Evaluating the Viability of Successive Ring-Expansions Based on Amino Acid and Hydroxyacid Side-Chain Insertion

Chemistry—A European Journal

Full Paper
doi.org/10.1002/chem.202002164

Chemistry
Europe
European Chemical
Societies Publishing

Macrocycles | Hot Paper |

Evaluating the Viability of Successive Ring-Expansions Based on Amino Acid and Hydroxyacid Side-Chain Insertion

Aggie Lawer,^[a] Ryan G. Epton,^[a] Thomas C. Stephens,^[a] Kleopas Y. Palate,^[a] Mahendar Lodi,^[a] Emilie Marotte,^[b] Katie J. Lamb,^[a] Jade K. Sangha,^[a] Jason M. Lynam,^{*,[a]} and William P. Unsworth^{*,[a]}

Abstract: The outcome of ring-expansion reactions based on amino/hydroxyacid side-chain insertion is strongly dependent on ring size. This manuscript, which builds upon our previous work on Successive Ring Expansion (SuRE) methods, details efforts to better define the scope and limitations of these reactions on lactam and β -ketoester ring systems with respect to ring size and additional functionality. The synthetic results provide clear guidelines as to which substrate classes are more likely to be successful and are

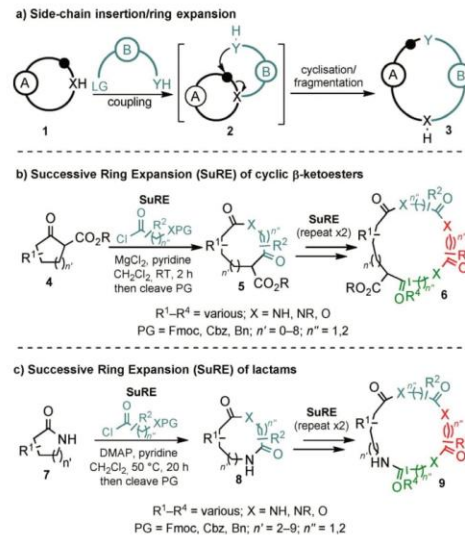
supported by computational results, using a density functional theory (DFT) approach. Calculating the relative Gibbs free energies of the three isomeric species that are formed reversibly during ring expansion enables the viability of new synthetic reactions to be correctly predicted in most cases. The new synthetic and computational results are expected to support the design of new lactam- and β -ketoester-based ring-expansion reactions.

Introduction

Rearrangements that allow ring-enlarged products to be prepared from smaller cyclic systems have much utility in synthetic chemistry.^[1,2] Ring expansions are particularly useful for the synthesis of medium-sized rings (8- to 11-membered) and macrocycles (12+ membered), as alternatives to direct end-to-end cyclisations.^[3] End-to-end cyclisations can be difficult and unpredictable processes due to competing intermolecular coupling and other side reactions, and they often necessitate the use of impractical high-dilution (or pseudo-high-dilution) conditions.^[4] In contrast, high dilution can often be avoided completely in well-designed ring-expansion systems.^[1,2,5]

Side-chain insertion ring-expansion reactions (Scheme 1 a) are a useful sub-class of ring expansion, as the requisite precursors are generally straightforward to prepare. Various methods in which the ring expansion is accompanied by concomi-

tant C–O, C–N and C–C bond formation are known, and this topic has been recently reviewed.^[1(a)] Amongst this class of reaction, our group has developed a series side-chain insertion ring expansion processes that can be performed iteratively. These methods, which we have termed “Successive Ring Expansion”



Scheme 1. Side-chain insertion ring-expansion reactions and Successive Ring Expansion (SuRE).

[a] A. Lawer, R. G. Epton, Dr. T. C. Stephens, K. Y. Palate, Dr. M. Lodi, Dr. K. J. Lamb, J. K. Sangha, Dr. J. M. Lynam, Dr. W. P. Unsworth
Department of Chemistry, University of York
York, YO10 5DD (UK)
E-mail: jason.lynam@york.ac.uk
william.unsworth@york.ac.uk

[b] E. Marotte
ENSICAEN, 6 Boulevard Maréchal Juin
CS 45053 14050, Caen Cedex 04 (France)

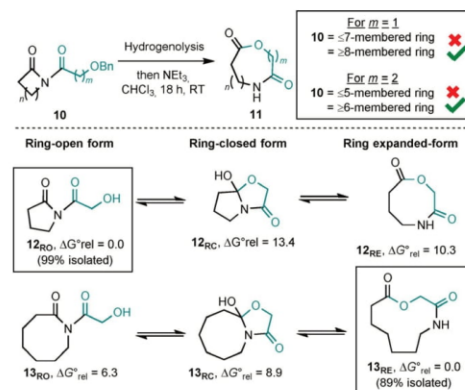
Supporting information and the ORCID identification numbers for the authors of this article can be found under:
<https://doi.org/10.1002/chem.202002164>.

© 2020 The Authors. Published by Wiley-VCH GmbH. This is an open access article under the terms of the Creative Commons Attribution License, which permits use, distribution and reproduction in any medium, provided the original work is properly cited.

(SuRE) reactions,^[5] enable the controlled, iterative insertion of amino acid or hydroxyacid-derived linear sequences into cyclic β -ketoesters (**4**→**6**, Scheme 1b)^[5a,b] or lactams (**7**→**9**, Scheme 1c).^[5c,d]

In our experience, the most important factor in determining the outcome of new ring-expansion reactions of the types summarised in Scheme 1b and c is ring size. This is well demonstrated by the outcomes of our published lactone-forming ring expansions of imides of the form **10** (Scheme 2).^[5d] Thus, for both α - and β -hydroxyacid derived linear fragments (3- and 4-atom ring expansions, respectively), there is a clear point at which ring expansion “switches on”; the reactions work for starting materials with rings that are eight-membered or more for three-atom expansions ($m=1$) and rings that are six-membered or more for four-atom expansions ($m=2$). The analogous reactions fail for smaller ring variants. We have previously postulated that these reactions are under thermodynamic control, and hence that the reaction outcomes depend on the relative Gibbs free energies of the three isomeric forms that the substrate must pass through for ring expansion to occur. This idea is supported by calculations performed at the DFT/B3LYP/6-31G* level of theory;^[5d,6-8] thus, five-membered ring-open imide **12_{RO}** (RO=ring-opened) was calculated to be significantly lower in Gibbs free energy than its isomeric ring-closed (**12_{RC}**, RC=ring-closed) and ring-expanded forms (**12_{RE}**, RE=ring-expanded), and this was replicated in the synthetic results, with imide **12_{RO}** being isolated in 99% yield following hydrogenolysis of the parent benzyl protected imide (**10**, where $n=2$, $m=1$). Conversely, in the case of the analogous eight-membered starting material (**10**, where $n=5$, $m=1$), the ring-expanded form **13_{RE}** was calculated to be the most stable isomer, and upon testing the reaction, **13_{RE}** was isolated in 89% yield, meaning that the calculations again were in line with the synthetic results.

These calculations, which drew inspiration from a similar approach used by Yudin and co-workers,^[2d] were done primarily

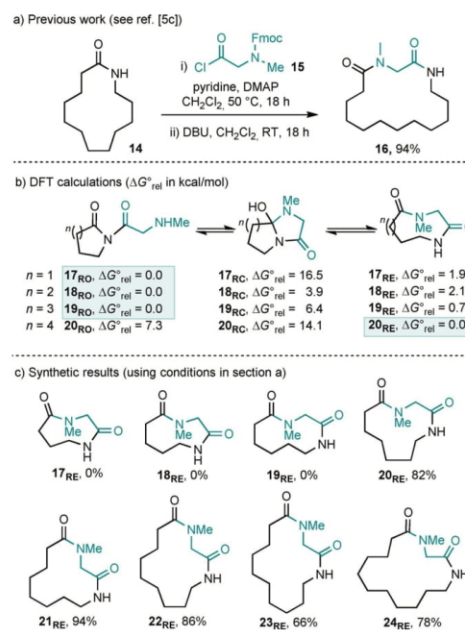


Scheme 2. Ring-size dependency on the outcome of the ring expansion of imides into aza-lactones. ΔG°_{rel} values are given in kcal mol⁻¹.

to validate our ideas about the reactions being under thermodynamic control. In this work, we have explored the validity of using calculations of this type predictively. As we continue to develop this research programme, having a reliable predictive tool to inform the likelihood of new SuRE variants working before committing to labour-intensive synthetic efforts will be of value. The utility of this approach is demonstrated herein; in total, 52 new ring-expansion reactions have been attempted, with 48 successfully furnishing the desired ring-expanded product. Our DFT/B3LYP/6-31G* method correctly predicted the reaction outcome in almost all cases, and compared favourably when benchmarked against other alternative methods, including those that model solvation and dispersion interactions. Thus, we believe that this widely available DFT/B3LYP/6-31G* approach will be useful to help assess the viability of new ring-expansion reactions before committing to synthetic efforts.

Results and Discussion

We started by examining the ring expansion of simple lactams with sarcosine derivative **15**. We had already shown that this acid chloride is compatible with our standard lactam ring expansion method (**14**→**16**, Scheme 3a), but prior to this work, 13-membered lactam **14** was the smallest aliphatic lactam on



Scheme 3. Ring-size dependency on the outcome of the ring expansion of imides with N-methyl sarcosine derivatives. ΔG°_{rel} values are given in kcal mol⁻¹ with thermal corrections at 298 K.

which we have reported a successful ring expansion with any linear α -amino acid chloride.

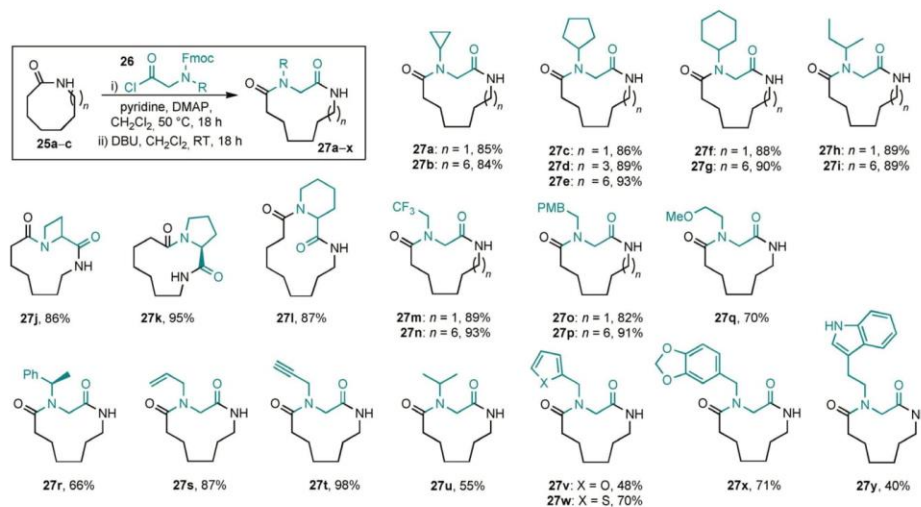
Prior to doing the synthetic chemistry, we ran DFT calculations based on the method used in our earlier study. To summarise this method, each of the three components of the equilibria deriving from five- to eight-membered ring imide precursors **17_{RO}**–**20_{RO}** were optimised at the DFT/B3LYP/6-31G* level of theory in vacuum.^[6–8] Conformational searches of the optimised structures were performed at the Molecular Mechanics Force Field level. All the generated structures were retained, and their energies were calculated using DFT/B3LYP/6-31G*. The lowest energy geometry in each case was selected, fully optimised and determined to be minima by the absence of negative vibrational modes, in vacuum using DFT/B3LYP/6-31G*. In each case, the relative free energies of the imide (**17_{RO}**–**20_{RO}**), ring-closed (**17_{RC}**–**20_{RC}**), and ring-expanded (**17_{RE}**–**20_{RE}**) isomers were calculated, with ΔG_{rel}^\ddagger values quoted in kcal mol⁻¹ (Scheme 3b). More information about the choice of this method and method effects are included later in the manuscript,^[7] until then, the discussion will focus on the synthetic aspects and DFT/B3LYP/6-31G* calculations.

In the five- to seven-membered series, the imide isomers **17_{RO}**–**19_{RO}** were calculated to be the most stable, thus suggesting that ring expansion is unlikely to proceed in these examples. This prediction was verified by synthetic results; thus, none of the ring-expanded products **17_{RO}**–**19_{RO}** were obtained when attempts were made to prepare them using the standard conditions, with no tractable products isolated from these reactions (**17_{RO}**–**19_{RO}**, Scheme 3c). Conversely, the ring-expanded isomer **20_{RE}** was calculated to be the lowest in free energy in the eight-membered ring series, and this again was borne out in the synthetic results, with **20_{RE}** isolated in 82%

yield. Thus, the use of an eight-membered ring starting material (or larger) appears to be the 'switch on' point for this series, as it was for the analogous lactone systems in Scheme 2. This is supported by the high yielding (66–94%) ring expansions of 9–12-membered lactam systems to form products **21_{RE}**–**24_{RE}** under the standard conditions.

Medicinal interest in medium-sized rings and macrocycles has increased significantly in the last decade,^[9] and the reaction variant described in Scheme 3 appears to be well suited for use in the preparation of peptoid-containing macrocycles,^[10] as long as the starting lactam is an eight-membered ring or larger. Thus, to better demonstrate its potential utility, we went on to investigate the range of N-substituents that can be tolerated on the linear unit **26**, with these results summarised in Scheme 4. In total, 24 new ring-expansion reactions of this type have been performed, to make **27a–y** (**27k** was described previously)^[5c] using various functionalised amino acid-derived linear fragments (**26**). Most of the reactions proceeded in high yield (the yield quoted is for the full N-acylation/protecting group cleavage/rearrangement sequence) under the standard reaction conditions, significantly expanding the range and diversity of amino acid derivatives that have been demonstrated in the SuRE method to date.

All the new SuRE reactions presented in Scheme 4 worked (at least to some degree), although there were a few outliers that were lower yielding (e.g., furan-derivative **27v**). In these cases, we believe that the lower yield is not caused by an inherent difference in the thermodynamics of the ring expansion equilibrium (i.e., the relative free energies of the analogous isomers **27_{RO}**, **27_{RC}** and **27_{RE}** are in line with those for the methyl analogue **20**, see SI for full details)^[11] but can be explained by substrate-dependent side reactions or problems

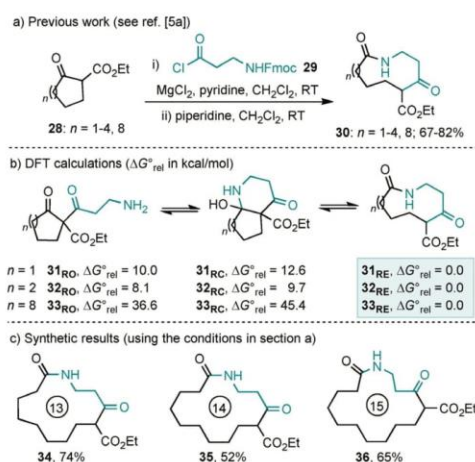


Scheme 4. Scope of lactam ring-expansion reactions with N-functionalised amino acids.

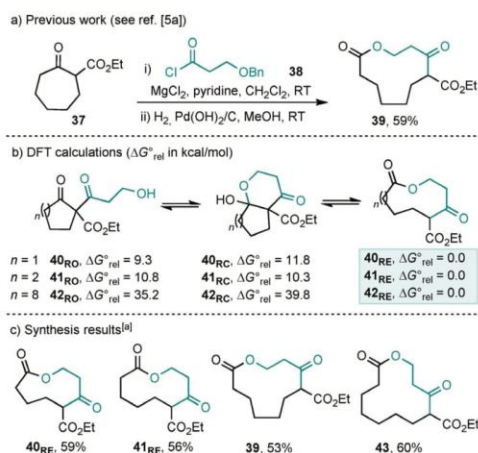
with the preceding N-acylation step. For example, in the case of furan derivative **27**, the lower yield is largely due to incomplete N-acylation (step i), which in turn is likely to be a consequence of the relative instability of the acid-sensitive furan motif. Unexpected side reactions/degradation also cannot be ruled out during the ring-expansion reaction (step ii) in cases where more reactive functional groups are involved.

Next, we examined the ring expansions of cyclic β -ketoesters. These reactions were the subject of our first two publications in this area,^[5a,b] which focused mainly on the insertion of β -amino acid derived linear fragments; for example, five- to eight- and 12-membered cyclic β -ketoesters (**28**) were all found to undergo smooth ring expansion (to form products of the type **30**) upon reaction under the reported conditions with β -alanine derived acid chloride **29** (Scheme 5a).^[5a] DFT/B3LYP/6-31G* calculations were performed to measure the energies of the equilibrating isomers of the five-, six-, and 12-membered ring systems **31–33** as before. Pleasingly, the calculations suggest that the ring-expanded isomers are lowest in energy by a clear margin, suggesting that there is a strong thermodynamic driving force for ring expansion in this series (Scheme 5b). To complete the synthetic series, we went on to perform the ring expansion of nine- to 11-membered β -ketoesters for the first time, with these new synthetic reactions proceeding well, affording lactams **34–36** (52–74%, Scheme 5c).

The hydroxyacid-based analogue of this cyclic β -ketoester ring expansion was less well developed, with the expansion of seven-membered **37** the only example of this type featured in our previous publications to have been performed on a simple cyclic β -ketoester (Scheme 6a). Given the importance of macrocyclic lactones in medicinal chemistry,^[12] we decided to test whether the scope of this variant could be expanded. As was



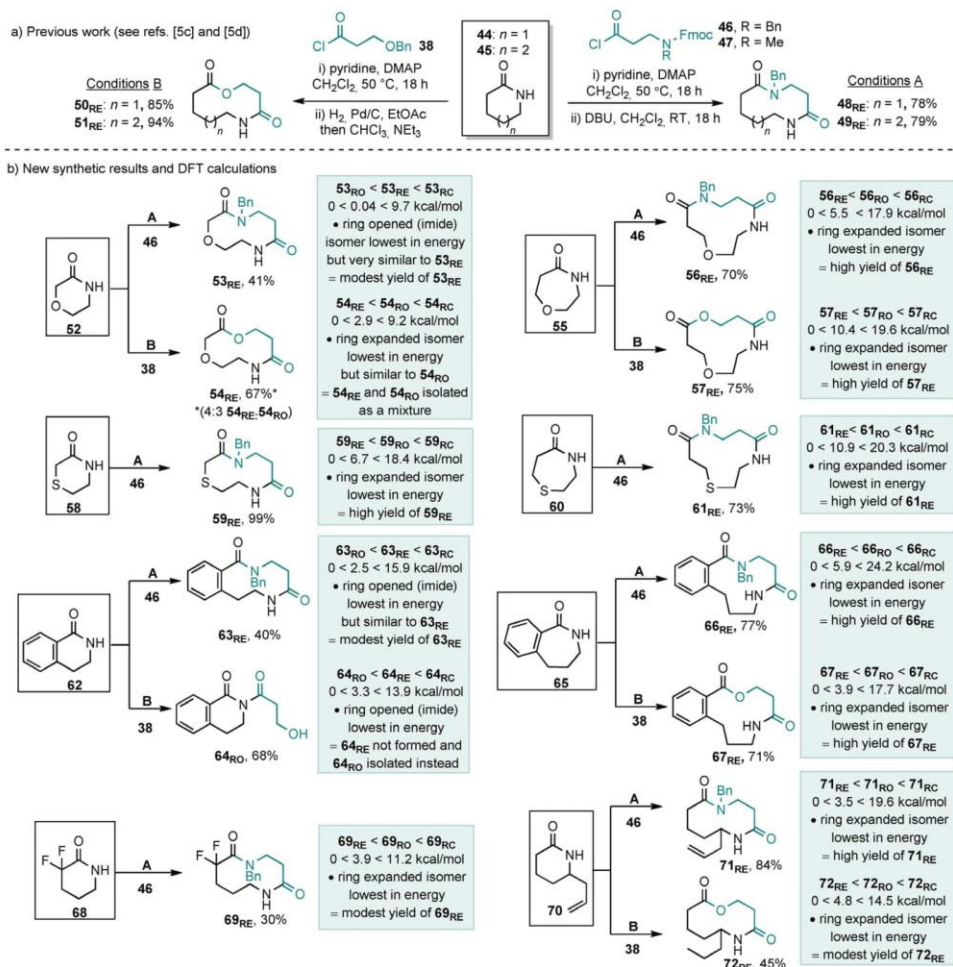
Scheme 5. Ring-size dependency of the outcome of the ring expansion of β -ketoesters with β -alanine-derived acid chloride **29**. ΔG_{rel}^\ddagger values are given in kcal mol⁻¹.



Scheme 6. Ring-size dependency of the outcome of the ring expansion of β -ketoesters with β -hydroxy acid chloride **38**. ΔG_{rel}^\ddagger values are given in kcal mol⁻¹. i) β -ketoester, **38**, MgCl₂, pyridine, CH₂Cl₂, RT; ii) Pd/C H₂, EtOAc, 3 h, RT; NEt₃, CHCl₃, RT, 18 h.

done for the analogous amino acid system, DFT/B3LYP/6-31G* calculations were performed to measure the energies of the equilibrating isomers of the five-, six-, and 12-membered ring systems **40–42** (Scheme 6b), which again suggested that there is a clear thermodynamic driving force for ring expansion. Pleasingly, the corresponding synthetic experiments all worked well, with five- to eight-membered β -ketoesters undergoing C-acylation, hydrogenolysis and ring expansion to give ring-expanded lactones **39**, **40**_{RE}, **41**_{RE} and **43** all in comparable yields (Scheme 6c). In a small change to the published conditions shown in Scheme 6a, we found that performing the hydrogenolysis in ethyl acetate (rather than methanol) and then stirring with triethylamine in chloroform led to superior reaction yields. The main reason the isolated yields are in the 50–60% range (and not higher) is due to loss of material during the C-acylation step (especially the work-up, during which the magnesium salts can cause problems with phase separation) and these results are in line with typical yields in our previous papers.^[5a,b]

We then went on to test other lactam-based ring expansion systems with additional functionality present in the starting lactams. Hydroxyacid and amino acid derivatives **38** and **46** were used to exemplify the synthetic reactions, and in the calculations for **46**, a simplified N-methyl (rather than N-benzyl) derivative was used (i.e., from **47**) as this significantly reduced the computational time but was found to have very little impact on the calculations.^[13] Thus, we started by examining lactams containing α -heteroatoms (**52**, **55**, **58** and **60**) with amino acid and hydroxyacid derivatives **38** and **46**. The analogous heteroatom-free variants of these reactions had been tested in our earlier work (Scheme 7a) and were shown to be high yielding. Therefore, based purely on our chemical intu-

Scheme 7. Lactam ring-expansion reactions and DFT calculations. $\Delta G_{rel}^{\ddagger}$ values are given in kcal mol⁻¹.

ition at this stage, we did not expect to see much variation upon switching to these new systems. However, starting from six-membered lactam **52**, a much lower isolated yield (41%) of the ring-expanded product 53_{RE} was obtained in the amino acid series, while the ring-expanded lactone 54_{RE} was isolated as an inseparable mixture with its ring-opened imide form 54_{RO} . The calculations give clues as to why these reactions did not proceed well; for example, the ring-opened and ring-expanded isomers 53_{RO} and 53_{RE} were calculated to have very similar Gibbs free energies, thus suggesting that both may be formed in this reaction, although only the relatively non-polar

product 53_{RE} was isolated after chromatography, in modest yield. Compounds 54_{RO} and 54_{RE} were also calculated to be similar in free energy and in this case a mixture of products was isolated. Conversely, upon moving to seven-membered starting material **55**, a clear preference for the ring-expanded isomer was predicted by the calculations, which manifested in much improved synthetic yields for the desired ring-expanded isomers (**70** and **75%** for 56_{RE} and 57_{RE} respectively).

In contrast to oxygen-containing **52** and **55**, sulfur-containing lactams **58** and **60** both performed well in the synthetic ring-expansion reactions with **46**;^[14] ring-expanded products

59_{RE} and **61_{RE}** were each formed in good yield. This was again mirrored in the calculations, with **59_{RE}** and **61_{RE}** calculated to be the lowest energy isomers in each case by clear margins. The difference in reactivity between **52** and **58**, which is presumably a result of some relatively subtle stereoelectronic effects and/or differences in bond lengths, is not something that we would have predicted without the calculations.

We also examined benzannulated, fluorinated and branched lactam starting materials **62**, **65**, **68** and **70**, and as before, the predictive ability of the calculations was retained. Indeed, the ability to predict when reactions will fail completely is also important; for example, the ring-opened imide isomer **64_{RO}** was calculated to be the most stable isomer in this series, and this was corroborated by the synthetic results.

In general, we have found that for systems in which the ring-expanded isomer is calculated to be the lowest in energy by more than 3 kcal mol⁻¹, then the reactions tend to work reliably. In cases where the free energy difference is less than 3 kcal mol⁻¹, the reaction outcomes are less predictable, often giving low yields of ring-expanded products and/or mixtures. The reactions to form ring-expanded products **69_{RE}** and **72_{RE}**, which were isolated in modest 30 and 45% yields, respectively, are outliers in terms of yield, but the lower yields in these cases simply reflect the fact that the N-acylation step did not proceed to completion in either case. Indeed, an important caveat to keep in mind when using this DFT/B3LYP/6-31G* method is that it only gives an indication of the chances of achieving a favourable equilibrium. It does not account for the efficiency of the synthetic steps that take place before the equilibrium, the possibility of off-equilibrium side reactions or other kinetic effects.

As all the ring-expanded products described in this manuscript were made using SuRE methods, they are all, in theory, potential starting materials for further ring-expansion reactions. Representative examples of products (**73–77**) that have been expanded for a second time in our earlier work are shown in Figure 1, with the second linear fragment inserted highlighted in red. After undergoing one ring expansion, the rings should all be large enough that they are beyond the “switch on” point for any of the ring-expansion reaction types that we

have studied and calculated (not withstanding any effects resulting from the additionally added functional groups) and should therefore be thermodynamically favourable. This is corroborated by our work to date in which several successful successive ring-expansion reactions are reported. This does not mean that performing additional iterations is always routine (e.g., in some cases, the acylation reactions can be more difficult on these more functionalised systems, sometimes requiring additional equivalents of acid chloride),^[5c-d] but once acylation has been achieved, ring expansion is typically straightforward. Three new examples of doubly ring-expanded products (**78–80**, see the Supporting Information for reaction conditions), based on new substrates made for the first time in this manuscript, have been performed and are reported here for completeness.

Computational chemistry: Method evaluation

The DFT/B3LYP/6-31G* methodology used has demonstrated, in both this and previous work,^[5d] good success in predicting the outcome of SuRE reactions. Calculations at the B3LYP/6-31G* level are relatively computationally efficient, but do not take into consideration effects such as solvation and dispersion. These additions are typically used to improve the accuracy of such calculations, therefore, we decided to benchmark their effects, along with a range of functionals, in order to determine any potential method-effects in the calculations.

For this study general gradient approximation, GGA (BP86), hybrid (B3LYP and PBE0) and meta-hybrid (M06 and M06-2X) functionals were used. Solvation effects were applied using a PCM model with either dichloromethane or chloroform as relevant to simulate the reaction conditions. The effects of dispersion are inherently taken into consideration by the M06 and M06-2X functionals.^[15] They were also applied using the Grimme's D3 method with Becke-Johnson damping^[16] to a PBE0/def2-TZVPP single-point calculation, using the geometry and thermodynamic corrections from a BP86/SV(P) calculation; this method has been used successfully by our groups in previous projects,^[17] and also tests the effect of a large triple zeta basis set.^[18]

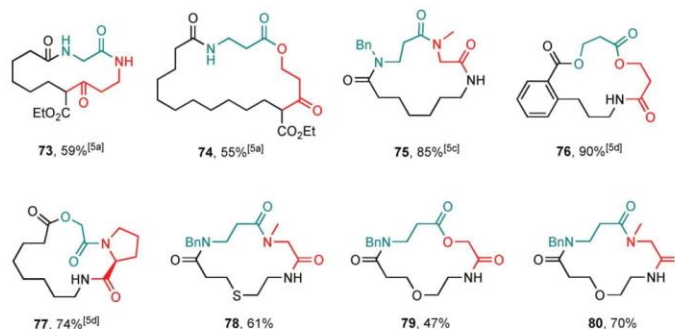


Figure 1. Successive ring expansion products.

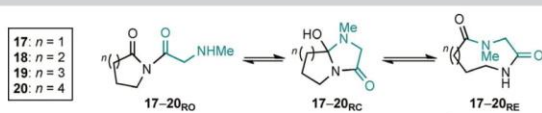
Initially, a wide range of methods were benchmarked against structures **17–20**, by reoptimising the structures from the B3LYP/6-31G* calculations and comparing the relative energies with the experimental outcomes (Table 1). Structures with which the ring-closed isomer has a larger energy than the ring-opened or ring-expanded isomers (**17**, **19** and **20**), produced the most comparable results, with there being little difference when using GGA or hybrid functionals with the 6-31G* basis set.

Modelling the effects of solvation also had little effect on the relative energy differences when using the hybrid B3LYP functional. Comparable results are observed both with and without solvent corrections. However, this does not extend to the BP86/SV(P) calculations, with more significant relative energy differences observed when compared to the standard B3LYP/6-31G* calculations, which appears to come from greater stabilisation of the ring-closed and ring-expanded isomers than the ring-opened when solvent is included.

The effects of dispersion had the greatest impact on the expected outcomes of the experiments, with the M06, M06-2X and D3(BJ)-PBE0 calculations showing lower relative energies for the ring-closed and ring-expanded isomers, predicting that ring expansion should be comparatively more thermodynamically favourable in these examples, and in some cases contradicting the experimental results. We believe that due to the side chain present in the ring-opened structures being directed away from the ring, there are fewer stabilising interactions present than compared to the ring-closed or expanded isomers. As a consequence of these different molecule geometries, it appears that modelling the dispersion interactions may result in the stability of the ring-expanded isomer being over-predicted when compared to the ring-opened form. This alters the expected reaction outcome where the B3LYP/6-31G* calculations predict these isomers to be similar in energy.

With dispersion effects having a large effect on the relative energy differences and the predicted thermodynamic out-

Table 1. Relative difference of Gibbs energies at 298 K for structures **17–20** at different levels of theory. Solvent corrections were applied using a PCM model. * Geometry from the BP86/SV(P) level.



Compound	Functional	Basis set	Solvent correction	Empirical dispersion correction	RO [kcal mol ⁻¹]	RC [kcal mol ⁻¹]	RE [kcal mol ⁻¹]	Yield RE [%]
17 (n=1)	B3LYP	6-31G*	N	N	0.0	16.5	1.9	0
	B3LYP	6-31G*	PCM	N	0.0	14.9	0.2	
	BP86	6-31G*	N	N	0.0	14.9	1.6	
	PBE0	6-31G*	N	N	0.0	14.1	1.2	
	M06	6-31G*	PCM	N	0.0	10.8	-2.1	
	M06-2X	6-31G*	PCM	N	0.0	8.7	-1.6	
	BP86	SV(P)	PCM	N	0.0	11.5	-2.1	
	PBE0*	def2-TZVPP	PCM	D3(BJ)	0.0	9.2	-3.3	
	18 (n=2)	B3LYP	6-31G*	N	N	0.0	3.9	
B3LYP		6-31G*	PCM	N	0.0	2.2	-1.1	
BP86		6-31G*	N	N	0.0	0.5	-1.1	
PBE0		6-31G*	N	N	0.0	-0.6	-1.6	
M06		6-31G*	PCM	N	0.0	-3.0	-3.8	
M06-2X		6-31G*	PCM	N	0.0	-4.5	-4.1	
BP86		SV(P)	PCM	N	0.0	-1.2	-3.0	
PBE0*		def2-TZVPP	PCM	D3(BJ)	0.0	-3.0	-5.3	
19 (n=3)		B3LYP	6-31G*	N	N	0.0	6.4	0.7
	B3LYP	6-31G*	PCM	N	0.0	6.2	-0.3	
	BP86	6-31G*	N	N	0.0	5.5	-0.4	
	PBE0	6-31G*	N	N	0.0	4.4	-1.3	
	M06	6-31G*	PCM	N	0.0	1.1	-3.8	
	M06-2X	6-31G*	PCM	N	0.0	-0.5	-3.4	
	BP86	SV(P)	PCM	N	0.0	2.7	-1.8	
	PBE0*	def2-TZVPP	PCM	D3(BJ)	0.0	0.7	-5.0	
	20 (n=4)	B3LYP	6-31G*	N	N	7.3	14.1	0.0
B3LYP		6-31G*	PCM	N	9.9	16.1	0.0	
BP86		6-31G*	N	N	8.3	13.8	0.0	
PBE0		6-31G*	N	N	8.8	13.3	0.0	
M06		6-31G*	PCM	N	12.2	12.8	0.0	
M06-2X		6-31G*	PCM	N	11.4	10.5	0.0	
BP86		SV(P)	PCM	N	11.1	13.6	0.0	
PBE0*		def2-TZVPP	PCM	D3(BJ)	13.4	14.0	0.0	

comes on these examples, the study was extended to include these effects to several other systems, using the M06-2X/6-31G* methodology. A comparison between this method and B3LYP/6-31G* is presented in Table 2. As observed with structures 17–20 (Table 1), the main difference between the two methods is that, when compared to the ring-expanded form, the relative energies of the ring-closed forms are lower at the M06-2X/6-31G* level ($\Delta_{\text{ave}} = -5.2 \text{ kcal mol}^{-1}$), and ring-opened isomers increased ($\Delta_{\text{ave}} = 3.1 \text{ kcal mol}^{-1}$). In most instances this doesn't change the expected outcome of the reaction, however, where there is a smaller difference in the energy of the ring-opened and ring-expanded isomers (see 53, 63 and 64), this does result in ring expansion being predicted to be favourable. Notably in some examples the intermediate ring-closed isomer becomes lower in energy than the ring-opened, however, this does not seem to correlate to any observable difference in how well the reaction proceeds experimentally (see 32, 40 and 69 for examples).

Thus, for either method, both the B3LYP and M06-2X functionals correctly predicts the expected reaction outcomes in the majority of cases, although on average, it is the B3LYP method that more closely correlates with the experimental findings, despite the fact that the M06-2X functional usually performs better for organic molecules due to the inclusion of dispersion corrections.^[15,19] Therefore, we believe that these results clearly demonstrate that the B3LYP/6-31G* methodology is suitable as an aid for predicting the outcome of SuRE reactions, balancing computational efficiency with good prediction of reaction outcome. The observation that a greater than 3 kcal mol^{-1} energy difference between ring-opened and ring-expanded isomers is needed to more confidently predict the outcome of the reaction, is based upon the inherent computational accuracy of these calculations

Conclusions

In summary, we have significantly expanded the scope of various classes of SuRE reaction, and have shown that the reaction outcomes can be predicted based on the relative Gibbs free energies of three isomeric species in equilibrium by using DFT calculations.^[20] Useful conclusions can also be drawn from the significantly expanded synthetic scoping reactions and a total of 48 new ring-expanded products are reported in this manuscript. In most cases, the isomer calculated to be lowest in energy was the major product obtained in the corresponding synthetic results.

Of course, any computational predictive method of this type will never be 100% accurate, especially given how difficult it is to model the properties and conformations of relatively flexible systems like macrocycles.^[21] In view of this, the approximations involved in the calculations and the possibility that kinetic effects might prevent equilibrium being reached in some reaction systems, we do not recommend using the calculations to make quantitative predictions on reaction yields or the Boltzmann distribution of the isomers in the presumed equilibria. The guideline that a free energy difference of more than 3 kcal mol^{-1} in favour of the ring-expanded isomer when using

Table 2. Relative difference of Gibbs energies at 298 K. Solvent corrections were applied using a PCM model with either dichloromethane or chloroform as relevant for the M06-2X/6-31G* calculations. See the Supporting Information for absolute energies. Blue numbers denotes the most significant differences between the two methods $> 3 \text{ kcal mol}^{-1}$. Δ_{ave} is defined as the mean value of the energy at M06-2X/6-31G*—energy at B3LYP/6-31G*.

Compound	Functional/ basis set	RO [kcal mol ⁻¹]	RC [kcal mol ⁻¹]	RE [kcal mol ⁻¹]	Yield RE [%]
31	B3LYP/6-31G*	10.0	12.6	0.0	67 ^[5a]
	M06-2X/6-31G*	12.5	10.2	0.0	
32	B3LYP/6-31G*	8.1	9.7	0.0	82 ^[5a]
	M06-2X/6-31G*	10.5	3.7	0.0	
33	B3LYP/6-31G*	36.6	45.4	0.0	80 ^[5a]
	M06-2X/6-31G*	38.0	34.7	0.0	
40	B3LYP/6-31G*	9.3	11.8	0.0	59
	M06-2X/6-31G*	11.7	8.1	0.0	
41	B3LYP/6-31G*	10.8	10.3	0.0	56
	M06-2X/6-31G*	10.3	3.7	0.0	
42	B3LYP/6-31G*	35.2	39.8	0.0	–
	M06-2X/6-31G*	32.6	30.5	0.0	
53	B3LYP/6-31G*	0.0	9.7	0.0	41
	M06-2X/6-31G*	6.9	7.1	0.0	
54	B3LYP/6-31G*	2.9	9.2	0.0	67 ^[6a]
	M06-2X/6-31G*	5.0	4.5	0.0	
56	B3LYP/6-31G*	5.5	17.9	0.0	70
	M06-2X/6-31G*	11.7	13.8	0.0	
57	B3LYP/6-31G*	10.4	19.6	0.0	75
	M06-2X/6-31G*	11.2	13.8	0.0	
59	B3LYP/6-31G*	6.7	18.4	0.0	99
	M06-2X/6-31G*	12.0	13.1	0.0	
61	B3LYP/6-31G*	10.9	20.3	0.0	73
	M06-2X/6-31G*	14.5	15.1	0.0	
63	B3LYP/6-31G*	–2.5	13.4	0.0	40
	M06-2X/6-31G*	2.8	10.0	0.0	
64	B3LYP/6-31G*	–3.3	10.6	0.0	0
	M06-2X/6-31G*	0.5	6.8	0.0	
66	B3LYP/6-31G*	5.9	24.2	0.0	77
	M06-2X/6-31G*	9.4	19.1	0.0	
67	B3LYP/6-31G*	3.9	17.7	0.0	71
	M06-2X/6-31G*	6.0	12.8	0.0	
69	B3LYP/6-31G*	3.9	11.2	0.0	30
	M06-2X/6-31G*	9.2	5.7	0.0	
71	B3LYP/6-31G*	3.5	19.6	0.0	84
	M06-2X/6-31G*	9.8	14.5	0.0	
72	B3LYP/6-31G*	4.8	14.5	0.0	45
	M06-2X/6-31G*	6.6	9.2	0.0	
	Δ_{ave}	3.1	–5.2	0.0	

[a] Isolated as a mixture (54_{rel}/54_{no} 4:3).

the B3LYP/6-31G* methodology usually leads to a successful reaction is a qualitative observation, that this was true in all such cases tested in which the preceding acylation step was efficient. It should not be considered a hard rule. However, as a guide to assessing the viability of new ring-expansion reactions before embarking on synthetic effort, we do believe that this DFT/B3LYP/6-31G* method, which is widely implemented across the vast majority of computational chemistry packages, has practical utility and will be useful in directing future synthetic efforts, in our group and others.

Acknowledgements

The authors thank the Leverhulme Trust (for an Early Career Fellowship, ECF-2015-013, for W. P. U.) the University of York (T. C. S., K. Y. P., J. K. S., W. P. U.) and the EPSRC (EP/P029795/1, A. L., and for the computational equipment used in this study, grants EP/H011455/1 and EP/K031589/1) for financial support. We are also grateful to the Science and Engineering Research Board, Department of Science & Technology, Government of India for an overseas postdoctoral fellowship for M. L., to Erasmus+ for supporting E. M., and the Department of Chemistry, University of York for the provision of an Eleanor Dodson Fellowship (to W. P. U.). Finally, thanks also go to Prof Paul Clarke (University of York) for assistance with Spartan.

Conflict of interest

The authors declare no conflict of interest.

Keywords: density functional theory · macrocycles · rearrangement · ring expansion · ring systems

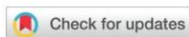
- [1] For recent reviews on ring-expansion reactions, see: a) J. R. Donald, W. P. Unsworth, *Chem. Eur. J.* **2017**, *23*, 8780; b) D. Reyes Loya, M. De Paolis, *Chem. Eur. J.* **2019**, *25*, 1842; c) T. C. Stephens, W. P. Unsworth, *Synlett* **2020**, *31*, 133; d) A. K. Clarke, W. P. Unsworth, *Chem. Sci.* **2020**, *11*, 2876. For an excellent, detailed account of classical ring expansion approaches, see: e) M. Hesse, *Ring Enlargement in Organic Chemistry*, Wiley-VCH, Weinheim, **1991**.
- [2] For selected recent examples, see: a) J. E. Hall, J. V. Matlock, J. W. Ward, J. Clayden, *Angew. Chem. Int. Ed.* **2016**, *55*, 11153; *Angew. Chem.* **2016**, *128*, 11319; b) Z.-L. Li, X.-H. Li, N. Wang, N.-Y. Yang, X.-Y. Liu, *Angew. Chem. Int. Ed.* **2016**, *55*, 15100; *Angew. Chem.* **2016**, *128*, 15324; c) L. Li, Z.-L. Li, F.-L. Wang, Z. Guo, Y.-F. Cheng, N. Wang, X.-W. Dong, C. Fang, J. Liu, C. Hou, B. Tan, X.-Y. Liu, *Nat. Commun.* **2016**, *7*, 13852; d) R. Mendoza-Sanchez, V. B. Corless, Q. N. N. Nguyen, M. Bergeron-Briek, J. Frost, S. Adachi, D. J. Tantillo, A. K. Yudin, *Chem. Eur. J.* **2017**, *23*, 13319; e) R. Costil, G. Lefebvre, J. Clayden, *Angew. Chem. Int. Ed.* **2017**, *56*, 14602; *Angew. Chem.* **2017**, *129*, 14794; f) D. R. Loya, A. Jean, M. Cormier, C. Fressigné, S. Nejrrotti, J. Blanchet, J. Maddaluno, M. De Paolis, *Chem. Eur. J.* **2018**, *24*, 2080; g) T. Guney, T. A. Wenderski, M. W. Boudreau, D. S. Tan, *Chem. Eur. J.* **2018**, *24*, 13150; h) A. Osipyan, A. Sapegin, A. S. Novikov, M. Krasavin, *J. Org. Chem.* **2018**, *83*, 9707; i) N. Wang, Q.-S. Gu, Z.-L. Li, Z. Li, Y.-L. Guo, Z. Guo, X.-Y. Liu, *Angew. Chem. Int. Ed.* **2018**, *57*, 14225; *Angew. Chem.* **2018**, *130*, 14421; j) Y. Zhou, Y.-L. Wei, J. Rodriguez, Y. Coquerel, *Angew. Chem. Int. Ed.* **2019**, *58*, 456; *Angew. Chem.* **2019**, *131*, 466; k) A. Lawer, J. A. Rossi-Ashton, T. C. Stephens, B. J. Challis, R. G. Epton, J. M. Lynam, W. P. Unsworth, *Angew. Chem. Int. Ed.* **2019**, *58*, 13942; *Angew. Chem.* **2019**, *131*, 14080; l) C. Zhao, Z. Ye, Z.-X. Ma, S. A. Wildman, S. A. Blaszczyk, L. Hu, I. A. Guizei, W. Tang, *Nat. Commun.* **2019**, *10*, 4015; m) E. Reutskaya, A. Osipyan, A. Sapegin, A. S. Novikov, M. Krasavin, *J. Org. Chem.* **2019**, *84*, 1693; n) Y. Xia, S. Ochi, G. Dong, J. Am. Chem. Soc. **2019**, *141*, 13038; o) Y. Yuan, Z. Guo, Y. Mu, Y. Wang, M. Xu, Y. Li, *Adv. Synth. Catal.* **2020**, *362*, 1298; p) Z. Xu, Z. Huang, Y. Li, R. Kunyil, C. Zhang, L. Ackermann, Z. Ruan, *Green Chem.* **2020**, *22*, 1099; q) X. Li, S. Wang, H. Wang, W. Wang, L. Liu, W. Chang, J. Li, *Adv. Synth. Catal.* **2020**, *362*, 1525.
- [3] For information on macrocyclisation strategies in general, see: a) A. Parenty, X. Moreau, J.-M. Campagne, *Chem. Rev.* **2006**, *106*, 911; b) R. Hill, V. Rai, A. K. Yudin, *J. Am. Chem. Soc.* **2010**, *132*, 2889; c) C. J. White, A. K. Yudin, *Nat. Chem.* **2011**, *3*, 509; d) A. P. Treder, J. L. Hickey, M.-C. J. Tremblay, S. Zaretsky, C. C. G. Scully, J. Mancuso, A. Doucet, A. K. Yudin, E. Marsault, *Chem. Eur. J.* **2015**, *21*, 9249; e) F. Saito, J. W. Bode, *Nat. Chem.* **2016**, *8*, 1085; f) *Practical Medicinal Chemistry with Macrocycles* (Eds.: E. Marsault, M. L. Peterson), Wiley, **2017**; g) S. Roesner, G. J. Saunders, I. Wilkening, E. Jayawant, J. V. Geden, P. Kerby, A. M. Dixon, R. Notman, M. Shipman, *Chem. Sci.* **2019**, *10*, 2465; h) K. T. Mortensen, T. J. Osberger, T. A. King, H. F. Sore, D. R. Spring, *Chem. Rev.* **2019**, *119*, 10288.
- [4] See refs. [1] and [2] for various discussion on the challenges of medium-sized ring and macrocyclisation reactions. For information on the influence of ring size and dilution effects in cyclisation reactions, see: a) G. Illuminati, L. Mandolini, *Acc. Chem. Res.* **1981**, *14*, 95; b) J. Fastrez, *J. Phys. Chem.* **1989**, *93*, 2635; c) J. C. Collins, K. James, *Med. Chem. Commun.* **2012**, *3*, 1489; d) S. Mazur, P. Jayalekshmy, *J. Am. Chem. Soc.* **1979**, *101*, 677; e) C. Rosenbaum, H. Waldmann, *Tetrahedron Lett.* **2001**, *42*, 5677; f) A.-C. Bédard, S. K. Collins, *J. Am. Chem. Soc.* **2011**, *133*, 19976; g) H. Kurouchi, T. Ohwada, *J. Org. Chem.* **2020**, *85*, 876.
- [5] a) C. Kitsiou, J. J. Hindes, P. l'Anson, P. Jackson, T. C. Wilson, E. K. Daly, H. R. Felstead, P. Hearnshaw, W. P. Unsworth, *Angew. Chem. Int. Ed.* **2015**, *54*, 15794; *Angew. Chem.* **2015**, *127*, 16020; b) L. G. Baud, M. A. Manning, H. L. Arkless, T. C. Stephens, W. P. Unsworth, *Chem. Eur. J.* **2017**, *23*, 2225; c) T. C. Stephens, M. Lodi, A. Steer, Y. Lin, M. Gill, W. P. Unsworth, *Chem. Eur. J.* **2017**, *23*, 13314; d) T. C. Stephens, A. Lawer, T. French, W. P. Unsworth, *Chem. Eur. J.* **2018**, *24*, 13947. See also ref. [2j] for examples of SuRE reactions being used by another group.
- [6] The DFT/B3LYP/6-31G* method was chosen as it is well known, implemented across the vast majority of computational chemistry packages, and it performs well in various settings, including in our earlier work (ref. [5d]).
- [7] B3LYP, BP86, PBE0, M06 and M06-2X functionals and 6-31G*, SV(P) and def2-TZVPP basis sets have all been evaluated in this study. See Tables 1 and 2, the Supporting Information and the associated discussion for details.
- [8] The energy calculations, final optimisations and frequency calculations were all done in a vacuum. In our previous study (ref. [5d]), all the calculations were run using a solvated model system (non-polar solvent) as well as in vacuum, and there was little difference in the free energy values obtained between the two methods, therefore it was decided to use vacuum calculations in this study, given that they are less demanding computationally.
- [9] For medium-sized rings and macrocycles in medicinal chemistry, see: a) E. M. Driggers, S. P. Hale, J. Lee, N. K. Terrett, *Nat. Rev. Drug Discovery* **2008**, *7*, 608; b) E. Marsault, M. L. Peterson, *J. Med. Chem.* **2011**, *54*, 1961; c) F. Kopp, C. F. Stratton, L. B. Akella, D. S. Tan, *Nat. Chem. Biol.* **2012**, *8*, 358; d) R. A. Bauer, T. A. Wenderski, D. S. Tan, *Nat. Chem. Biol.* **2013**, *9*, 21; e) F. Giordanetto, J. Kihlberg, *J. Med. Chem.* **2014**, *57*, 278; f) A. Grossmann, S. Bartlett, M. Janecsek, J. T. Hodgkinson, D. R. Spring, *Angew. Chem. Int. Ed.* **2014**, *53*, 13093; *Angew. Chem.* **2014**, *126*, 13309; g) A. K. Yudin, *Chem. Sci.* **2015**, *6*, 30; h) I. B. Seiple, Z. Zhang, P. Jakubec, A. Langlois-Mercier, P. M. Wright, D. T. Hog, K. Yabu, S. R. Allu, T. Fukuzaki, P. N. Carlsen, Y. Kitamura, X. Zhou, M. L. Condakes, F. T. Szczypiński, W. D. Green, A. G. Myers, *Nature* **2016**, *533*, 338; i) S. Collins, S. Bartlett, F. Nie, H. F. Sore, D. R. Spring, *Synthesis* **2016**, *48*, 1457; j) S. Javed, M. Bodugam, J. Torres, A. Ganguly, P. Hanson, *Chem. Eur. J.* **2016**, *22*, 6755; k) M. Dow, F. Marchetti, K. A. Abrahams, L. Vaz, G. S. Besra, S. Warriner, A. Nelson, *Chem. Eur. J.* **2017**, *23*, 7207; l) W. Xu, Y. H. Lau, G. Fischer, Y. S. Tan, A. Chattopadhyay, M. de la Roche, M. Hyyönen, C. Verma, D. R. Spring, L. S. Itzhaki, *J. Am. Chem. Soc.* **2017**, *139*, 2245.
- [10] a) S. B. Y. Shin, B. Yoo, L. J. Todor, K. Kirshenbaum, *J. Am. Chem. Soc.* **2007**, *129*, 3218; b) A. M. Webster, S. L. Cobb, *Tetrahedron Lett.* **2017**, *58*, 1010; c) A. M. Webster, S. L. Cobb, *Chem. Eur. J.* **2018**, *24*, 7560.

- [11] $\Delta G_{\text{rel}}^{\ddagger}$ values for **27v** calculated using the standard DFT/B3LYP/6-31G* method (see the Supporting Information for full details): **27v_{im}** (imide) = 8.1 kcal mol⁻¹; **27v_{RC}** (cyclo) = 16.7 kcal mol⁻¹; **27v_{RE}** (ring-expanded) = 0.0 kcal mol⁻¹.
- [12] a) J. M. McGuire, R. I. Bunch, R. C. Anderson, H. E. Boaz, E. H. Flynn, H. M. Powell, J. W. Smith, *Antibiot. Chemother.* **1952**, *2*, 281; b) G. M. Bright, A. A. Nagel, J. Bordner, K. A. Desai, J. N. Dibrino, J. Nowakowska, L. Vincent, R. M. Watrous, F. C. Sciavolino, A. R. English, J. A. Retsema, M. R. Anderson, L. A. Brennan, R. J. Borovoy, C. R. Cimochoowski, J. A. Faiella, A. E. Girard, D. Girard, C. Herbert, M. Manousosa, R. Mason, *J. Antibiot.* **1988**, *41*, 1029; c) C. Khosla, *Chem. Rev.* **1997**, *97*, 2577; d) D. E. Cane, C. T. Walsh, C. Khosla, *Science* **1998**, *282*, 63; e) S. R. Park, A. R. Han, Y. H. Ban, Y. J. Yoo, E. J. Kim, Y. J. Yoon, *Appl. Microbiol. Biotechnol.* **2010**, *85*, 1227; f) Q. Li, I. B. Seiple, *J. Am. Chem. Soc.* **2017**, *139*, 13304.
- [13] To test whether this simplification is valid, we calculated the energies of isomers **53** using the parent system (i.e., with Nbn rather than NMe) and all three of the calculated $\Delta G_{\text{rel}}^{\ddagger}$ values were within 0.7 kcal mol⁻¹ of the simplified analogues: $\Delta G_{\text{rel}}^{\ddagger}$ values for **53** calculated using the standard DFT/B3LYP/6-31G* method: **53_{im}** (imide) = 0.0 kcal mol⁻¹; **53_{RC}** (cyclo) = 10.4 kcal mol⁻¹; **53_{RE}** (ring-expanded) = 0.3 kcal mol⁻¹.
- [14] Ring expansion of **58** and **60** with hydroxyacid derivative **38** was not possible due to incompatibility of the S-containing starting material with hydrogenolysis.
- [15] Y. Zhao, D. G. Truhlar, *Theor. Chem. Acc.* **2008**, *120*, 215.
- [16] S. Grimme, S. Ehrlich, L. Goerigk, *J. Comput. Chem.* **2011**, *32*, 1456.
- [17] a) A. K. Clarke, J. M. Lynam, R. J. K. Taylor, W. P. Unsworth, *ACS Catal.* **2018**, *8*, 6844; b) J. T. R. Liddon, J. A. Rossi-Ashton, A. K. Clarke, J. M. Lynam, R. J. K. Taylor, W. P. Unsworth, *Synthesis* **2018**, *50*, 4829; c) R. G. Epton, A. K. Clarke, R. J. K. Taylor, W. P. Unsworth, J. M. Lynam, *Eur. J. Org. Chem.* **2019**, 5563.
- [18] F. Weigend, M. Häser, H. Patzelt, R. Ahlrichs, *Chem. Phys. Lett.* **1998**, *294*, 143.
- [19] a) S. Luo, Y. Zhao, D. G. Truhlar, *Phys. Chem. Chem. Phys.* **2011**, *13*, 13683–13689; b) Y. Minenkov, H. Wang, Z. Wang, S. M. Sarathy, L. Cavallo, *J. Chem. Theory Comput.* **2017**, *13*, 3537–3560; c) P. Stewart, L. Rodriguez, D. H. Ess, *J. Phys. Org. Chem.* **2011**, *24*, 1222–1228; d) H. Valdes, K. Pluháčková, M. Pitonák, J. Řezáč, P. Hobza, *Phys. Chem. Chem. Phys.* **2008**, *10*, 2747–2757; e) N. Mardirossian, M. Head-Gordon, *J. Chem. Theory Comput.* **2016**, *12*, 4303–4325.
- [20] See the Supporting Information for computational details.
- [21] a) V. Štepanić, S. Koštrun, I. Malnar, M. Hlevnjak, K. Butković, I. Čaleta, M. Dukšić, G. Kragol, O. Makaruha-Stegić, L. Mikac, J. Ralić, I. Tatić, B. Tavčar, K. Valko, S. Zulfikari, V. Munić, *J. Med. Chem.* **2011**, *54*, 719; b) S. D. Appavoo, S. Huh, D. B. Diaz, A. K. Yudin, *Chem. Rev.* **2019**, *119*, 9724; c) I. V. Smolyar, A. K. Yudin, V. G. Nenajdenko, *Chem. Rev.* **2019**, *119*, 10032.

Manuscript received: May 1, 2020

Accepted manuscript online: May 20, 2020

Version of record online: September 11, 2020



Synthesis of macrocyclic and medium-sized ring thiolactones *via* the ring expansion of lactams†

Cite this: *Org. Biomol. Chem.*, 2021, **19**, 1404

Kleopas Y. Palate,^{1b} Ryan G. Epton, Adrian C. Whitwood,^{1b} Jason M. Lynam^{1b} and William P. Unsworth^{1b*}

Received 15th December 2020,
Accepted 17th January 2021

DOI: 10.1039/d0ob02502j

rsc.li/obc

A side chain insertion method for the ring expansion of lactams into macrocyclic thiolactones is reported, that can also be incorporated into Successive Ring Expansion (SuRE) sequences. The reactions are less thermodynamically favourable than the analogous lactam- and lactone-forming ring expansion processes (with this notion supported by DFT data), but nonetheless, three complementary protecting group strategies have been developed to enable this challenging transformation to be achieved.

Introduction

Thioesters are amongst the most important class of small molecules in biology, with thioesters such as acetyl coenzyme A playing central roles in countless biosynthetic processes.¹ The biochemistry of thioesters has also inspired the development of methods in synthetic chemistry, for example in the native chemical ligation of peptides and during protein splicing.² Thiolactones (the cyclic analogues of thioesters, Fig. 1) also have important biological functions; for example, homocysteine thiolactone **1** is involved in the post translational modification of proteins,^{3a} acts as an allosteric Dopamine D2 receptor antagonist^{3b} and may have played a role in the development of life on Earth.^{3c} Thiolactones are also relevant in medicinal chemistry; *e.g.* as antibiotics (thiolactomycin **2**), or as pro-drugs, where the relative ease with which they undergo hydrolysis⁴ is important in revealing the bioactive form *in vivo* (*e.g.* **3** and **4**).⁵ Indeed, the ability of thiolactones to undergo ring-opening *via* reaction with water, and other nucleophiles, is often key to their use as reagents in synthetic chemistry⁶ and in polymer science.⁷

Macrocyclic and medium-sized ring thiolactones are relatively rare in the literature. Of those that are known, most are prepared *via* the condensation of an activated linear thiol-tethered carboxylic acid derivative *via* an end-to-end cyclisation reaction (**5** → **6**, Scheme 1a).⁸ As is common for larger ring cyclisation processes of this type,^{9,10} these methods are often low yielding and usually require high dilution conditions and/or slow addition of reagents to afford the thiolactone products.⁸

Ring expansion represents an attractive alternative strategy for macrocycle/medium sized ring synthesis, as the inefficient end-to-end cyclisation step can be replaced with a more kinetically favourable rearrangement reaction.^{11,12} However, published ring expansion approaches to make macrocyclic and medium-sized ring thiolactones are limited to only a handful of examples.^{13,14} To the best of our knowledge, the first was reported by Mahajan and Araujo in 1978, and is based on the oxidative cleavage of cyclic vinyl sulfides **7** to form ring expanded thiolactones **8** (Scheme 1b).^{13a,b} In addition to two papers on the synthesis of medium-sized thiolactones *via* sigmatropic rearrangements,^{13c,d} the work most closely related to the present study was reported by Zhang and co-workers in 2014 (Scheme 1c).^{13e} This study was based on classical side chain insertion of thiol-tethered cyclic nitro ketone **9a** to form thiolactone **10**, using a method conceptually related to previous works by Hesse and co-workers.¹⁵

Our main contribution to the ring expansion field is through the development of an iterative ring expansion strategy known as Successive Ring Expansion (SuRE).¹⁶ As is illustrated in Scheme 2d, a key aspect of SuRE reactions is that the motif present in the starting material (*e.g.* the lactam in **11**) is regenerated upon ring expansion (**11** → **13**),^{16c,d} thus enabling additional iterations of the same reaction to be performed to expand the ring further (*e.g.* 2 more iterations enable the conversion of **13** → **14**). To date, our research has focused on

Department of Chemistry, University of York, Heslington, York, YO10 5DD, UK.

E-mail: william.unsworth@york.ac.uk

† Electronic supplementary information (ESI) available. CCDC 1921223, 2040346 and 2040347. For ESI and crystallographic data in CIF or other electronic format see DOI: 10.1039/d0ob02502j

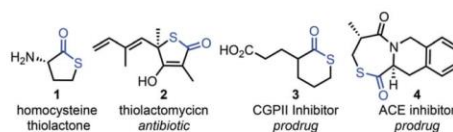
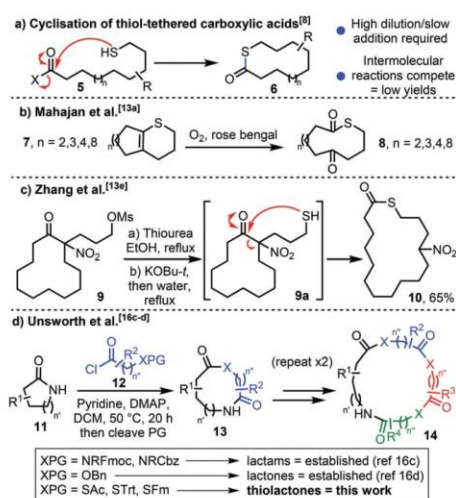
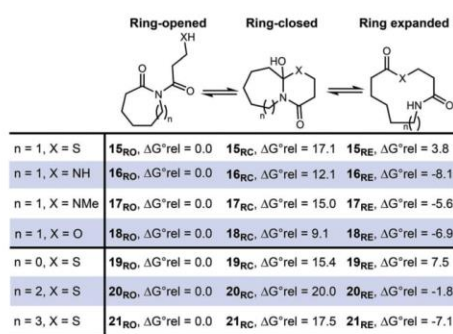


Fig. 1 Biologically important thiolactones 1–4.





Scheme 1 Strategies to make medium-sized and macrocyclic thiolactones. (a) End-to-end cyclisation; (b) ring expansion via oxidative cleavage; (c) ring expansion via side-chain insertion; (d) successive ring expansion (SuRE).



Scheme 2 Relative energies of isomeric species in SuRE-type rearrangement of imides using a DFT/B3LYP/6-31G* approach. ΔG[‡]rel values at 298 K are given in kcal mol⁻¹.

SuRE reactions based on the use of amino acid (**12**, where XPG = NRFmoc or NRCbz)^{13c} or hydroxy acid (**12**, where XPG = OBn)^{13d} derivatives, to form ring expanded lactams and lactones respectively. In this manuscript, we describe our efforts to extend this concept to include S-nucleophiles. For various reasons outlined herein, these reactions were considerably more challenging to develop than the analogous processes involving N- and O-nucleophiles. Nonetheless, the successful synthesis of macrocyclic and medium-sized thiolactones via

the ring expansion of lactams with thiol-tethered carboxylic acid derivatives has been achieved and is described here for the first time.

Results and discussion

Computational chemistry

In our earlier work, we shied away from using thiol derivatives in SuRE, as we thought the reactions would be less thermodynamically favourable than analogous reactions with amino/hydroxy acids (and hence might be harder to develop). This notion was based on a consideration of the ring expansion as an equilibrium of the type depicted in Scheme 2; we reasoned that there would be a lower thermodynamic driving force for ring expansion based on the formation of a thioester (when X = S) than there is for the formation of comparatively more stable lactams/lactones (when X = NR or O), which benefit from greater resonance stabilisation. Indeed, this idea is supported by DFT studies; using a computational method recently established by our groups to assess the viability of SuRE-type reactions,^{17,18} the relative free energies isomers **15_{RO}**, **15_{RC}**, **15_{RE}** were calculated at the DFT/B3LYP/6-31G* level for a potential 7 → 11-membered ring expansion to form **15_{RE}**. The calculations give a clear steer that this reaction is unlikely to proceed, as the ring opened isomer **15_{RO}** was calculated to be lower in energy than the ring expanded isomer **15_{RE}** by a significant margin (3.8 kcal mol⁻¹).¹⁹ This is in contrast with calculations for the analogous 7 → 11-membered ring expansion reactions based on lactam and lactone formation (**16–18**), where the ring expanded isomers were calculated to be lower in energy in each case; indeed, these reactions have been shown to work well in our previous synthetic work.^{16c,d}

When compared to the S-containing system **15**, the desired ring expanded isomer is 9.4–11.9 kcal mol⁻¹ more stable in the N/O-containing analogues **16–18**. This clearly illustrates the significant additional challenge of accessing thiolactones using the SuRE method; for a more visual representation of the stark difference in the S-containing system **15**, see the simplified potential energy surfaces depicted in Fig. 2.

Nonetheless, additional calculations on the higher homologues of sulfur-containing systems gave hope that the approach may still be feasible; for example, S-containing systems **19–21** were treated in the same way, and it was calculated that the ring expanded product is the lowest energy isomer for 8- and 9-membered ring starting materials, suggesting that these larger ringed variants are viable and have a higher chance of success. Therefore, it was decided to focus on larger ring starting materials, starting with readily available 8- and 13-membered ring lactams.

Protecting group strategy selection

A key decision was the choice of protecting group for the thiol. Three complementary strategies were explored, the first based on S-acetate protection. Thus, 8- and 13-membered lactams **21a** and **21b** were both reacted with acid chloride **22** using our



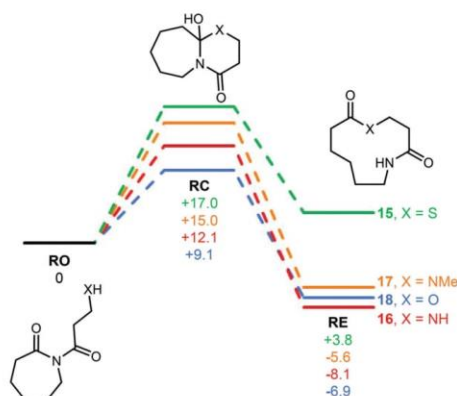
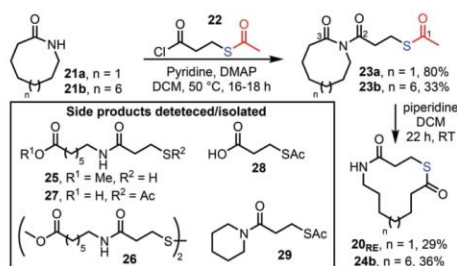


Fig. 2 Simplified potential energy surfaces for 15–18 calculated using a DFT/B3LYP/6-31G* approach. $\Delta G_{\text{rel}}^{\ddagger}$ values at 298 K are given in kcal mol⁻¹. Note that this diagram depicts the calculated relative Gibbs free energies of the ground states of the three isomeric species in the ring expansion equilibrium only. Transition state energies were not calculated.

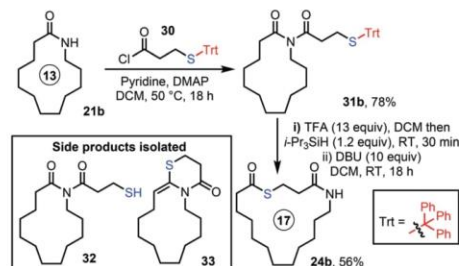
published *N*-acylation conditions to form imides **23a** and **23b** (Scheme 3). We then explored cleavage of the acetyl protecting group *via* the addition of various nucleophilic reagents, in the hope that this would result in concomitant ring expansion to form thiolactones. Of the conditions surveyed, stirring imides **23a** and **23b** with piperidine at RT in DCM were the most effective, forming thiolactones **20_{RE}** and **24b** in 29% and 36% yield respectively. However, chemoselectivity was a significant challenge using this approach; in particular, we were unable to fully discriminate between the three carbonyl groups of **23a**. For example, unwanted reaction at the cyclic carbonyl C-3 (*e.g.* to form linear products **25–27**) and/or unwanted C-2 attack (to form **28/29** and reform **21a**) led to a reduction in yield for the desired product in all cases (see ESI, Table S1† for a full list of conditions trialled, reaction outcomes and synthetic details).



Scheme 3 SuRE using an S-Ac protecting group strategy.

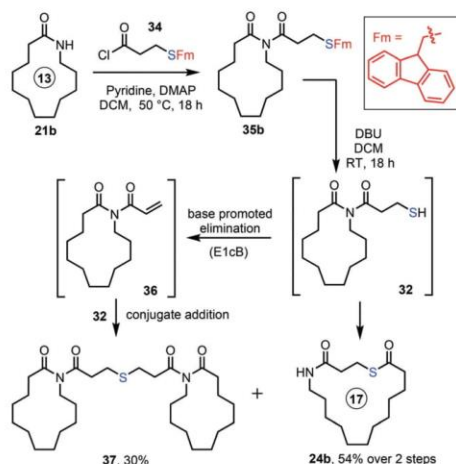
With the S-Ac method proving difficult, we instead turned to an acid-labile trityl (Trt) protecting group strategy.²⁰ Exploratory studies focused on 13-membered ring lactam **21b**, which was converted into imide **31b** *via* our standard method, using acid chloride **30**. Various combinations of acids and trityl scavenger reagents were then trialled, to cleave the Trt protecting group and promote ring expansion into **24b** (see ESI, Table S2† for a full list of conditions, reaction outcomes and synthetic details). The best conditions found were those summarised in Scheme 4, in which the Trt group was first cleaved using excess TFA in the presence of a silane scavenger reagent. This was then followed by aqueous workup and finally, stirring the product mixture overnight with an excess of DBU in DCM at RT, which promoted ring expansion to form the desired thiolactone product **24b**. The yield was much-improved (56%) compared to the S-Ac strategy, but side product formation was still not fully avoided, with a new condensation side product **33** observed under some of the conditions tested (likely as a result of the switch to acidic conditions), and thiol **32** was also isolated in some cases.²¹

Finally, a third protecting group strategy based on the use of the fluorenylmethyl (Fm) group was explored. The Fm protecting group is used relatively infrequently in organic synthesis (certainly compared to the related Fmoc protecting group) but it has attractive properties for the protections of thiols.²² The deprotection of Fm-protected thiols is typically done under conditions similar to those used to cleave Fmoc protecting groups from amines (*e.g.* using organic amine bases at RT). Given that such conditions were effective in our earlier work on SuRE using Fmoc-protected amino acid derivatives,^{16c,d} we reasoned that this approach might reduce side product formation in the present study. Thus, the *N*-acylation of lactam **21b** with S-Fm-containing acid chloride **34** was performed to form imide **35b** (Scheme 5), which was taken directly onto the next step without purification. A non-nucleophilic base (DBU) was chosen to cleave the Fm protecting group, and pleasingly this promoted concomitant protecting group cleavage/ring expansion to form **24b** in 54% yield over the overall 2 step telescoped sequence from **21b**. Frustratingly however, the product was accompanied by formation of another side product not observed in using the



Scheme 4 SuRE using an S-Trt protecting group strategy.





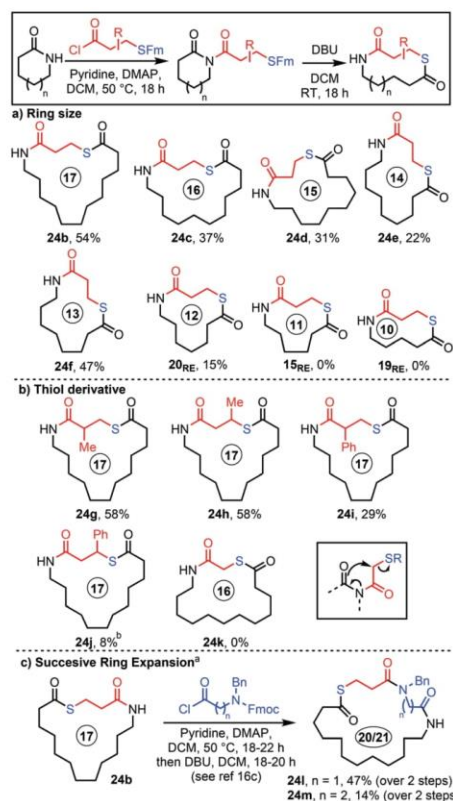
Scheme 5 SuRE using an S-Fm protecting group strategy.

other protecting group strategies, in this case dimer 37. We presume that 37 is formed *via* base promoted elimination of 32 (or 35b) to form acrolein derivative 36, which then reacts with another molecule of thiol 32 *via* conjugate addition.

Reaction scope

Despite not being able to fully suppress all side reactions, we were satisfied with the overall yield of 24b (54% over 2 steps) achievable using the S-Fm protocol. Therefore, this approach was taken forward onto the reaction scoping phase of the project. We started by examining the effect of varying the lactam ring size, with 6–13-membered lactams all tested, using S-Fm-tethered acid chloride 34 and the procedure in Scheme 6. Pleasingly, the ring expanded thiolactone products were obtained for all the 8–13-membered parent lactams (24b–f and 20_{RE}, 15–54%, Scheme 6a). Overall yields for the telescoped acylation/Fm cleavage/ring expansion sequence were generally modest, with the lowest yield obtained for the 8 → 12-membered ring transformation to form 20_{RE}, which is not surprising given that the DFT results discussed earlier (Scheme 2) predicted this to be a borderline case thermodynamically. Conversely, the 10- and 11-membered ring products 15_{RE} and 19_{RE} were not formed at all, which was expected given that the ring opened imide isomers were calculated to be significantly lower in energy than the ring-expanded products for these examples.

Branching is tolerated on the linear fragment, with thiolactones 24g–j all being formed using the standard protocol (Scheme 6b). The yields were comparatively low for the phenyl-substituted systems, likely due to competing elimination reactions; for example, in forming 24j, a significant quantity of a cinnamyl side product (resulting from base-promoted

Scheme 6 Scope of the SuRE method using thiol-tethered carboxylic acid derivatives. ^a Using our published method (ref. 16c). ^b *N*-Acylation step performed at RT (see ESI† for full details).

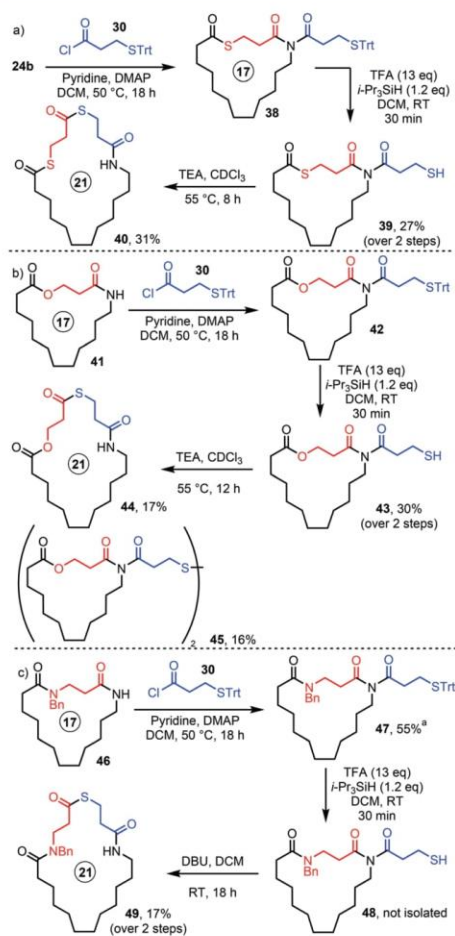
S-elimination, *c.f.* Scheme 5) was observed in the reaction mixtures, even upon reducing the temperature for the *N*-acylation step.²³ Unfortunately, we were unable to form 16-membered thiolactone 24k in the same way, using a shorter α -substituted homologue of the S-Fm-tethered acid chloride, with substrate degradation *via* a pathway known to lead to polymerisation (Scheme 6b box) proposed to be the main problem in this case.²⁴

We also confirmed that thiolactone-containing lactams are able to undergo further ring expansion *via* SuRE with amino acid chloride derivatives, with doubly expanded macrocycles 24l and 24m both prepared from 24b using our published method (Scheme 6c). The yields were lower than those of typical amino acid SuRE reactions, which is likely to be a consequence of the relatively reactive thiolactone enabling side reactions of the type already described, but nonetheless we



were pleased to learn that thiolactones can be incorporated into larger macrocycles as part of iterative ring expansion sequences.

Other attempts to use the new method as part of longer sequences were more challenging however; for example, we were unable to form a doubly expanded product *via* the sequential insertion of two thiolactones (*e.g.* **40**, Scheme 7) using the standard protocol. Thankfully, we were able to develop a reasonable work-around by using the S-Trt protecting group strategy and adding purification steps at intermediate points in the synthesis (Scheme 7). For example,



Scheme 7 Successive ring expansion - special cases. ^a Contains trace impurities (see ESI†).

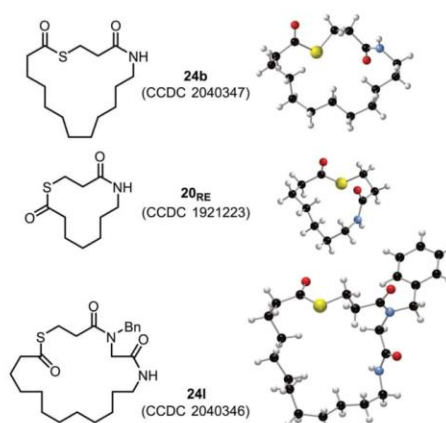


Fig. 3 X-ray crystal structures for **24b**, **20_{RE}** and **24I**.

N-acylation of thiolactone-containing lactam **24b** with acid chloride **30**, followed by cleavage of the Trt protecting group furnished imide thiol **39**, with chromatographic purification used after each step. Triethylamine was then used to promote the ring expansion, which was done in CDCl_3 to aid reaction monitoring, thus affording bis-thiolactone **40** in modest yield (Scheme 7a).

Macrocycle **44**, a product which contains a lactam, a lactone, and a thiolactone group, was also prepared using a similar strategy, starting from a previously reported lactone SuRE product **41** (Scheme 7b).^{16d} Another previously unobserved side product was isolated in this case, disulfide **45**, presumably as a result of oxidation of **43** by adventitious oxygen; incidentally, we believe that disulfide formation may also be a minor side reaction in other reactions featured in this manuscript, although this was the only case where it was confirmed *via* isolation of a pure product. Finally, macrocycle **49** was prepared, starting from bis-lactam **46**;^{16c} in this case, the ring expansion step was performed in DCM using DBU as the base (Scheme 7c).

To add additional support to the structural assignments made in this study, X-ray crystal structures were obtained for macrocyclic lactones **24b**, **20_{RE}** and **24I** (Fig. 3).²⁵

Conclusions

Ascertaining whether thiol-derivatives can be used in SuRE reactions was a major reason for undertaking this study. In this manuscript we have shown that they can, despite the transformation being more challenging than previous SuRE variants; while yields of >90% are common in our *N*- and *O*-SuRE processes, we have been unable to replicate this



level of synthetic efficiency in the thiolactone-forming SuRE variants. The reduced thermodynamic driving force (supported by the DFT studies, see Scheme 2 and Fig. 2) for ring expansion is likely to be a significant factor that contributes to this difference; the DFT calculations as performed do not directly probe the reaction kinetics, but given the shift in calculated Gibbs free energy change for ring expansion in the S-containing cases, it is reasonable to predict that there would also be an associated increase in transition state energies (e.g. considering Hammond's postulate).²⁶ A reduced reaction rate is not necessarily a problem when considered in isolation, but it is when kinetically accessible side reactions compete with the desired transformation, which we have clearly demonstrated to be the case for this system.²⁷

More positively, thiolactone-forming ring expansion processes are rare in the literature,^{13,14} and we are pleased to learn that thiolactones can be incorporated into ring-expanded lactams using SuRE. Three complementary protecting group strategies have been explored and 15 novel macrocyclic thiolactones have been prepared using the new methods, which generally proceed in good overall yield (up to 58%) over the telescoped *N*-acylation/protecting group cleavage/ring expansion sequence (≈83% per transformation). Although we are happy to acknowledge that this study was frustrating at times, observing and appreciating the various unexpected side reactions encountered will certainly help to inform future work on SuRE, as well as related studies on side chain insertion ring expansion reactions.

Experimental

Full synthetic details and spectroscopic data for all compounds are provided in the ESI.† A general synthetic procedure for the S-fluorenylmethyl (S-Fm) method (including *N*-acylation, S-Fm cleavage and ring expansion) is provided here: a mixture of lactam (0.5 mmol), DMAP (0.05 mmol) and pyridine (3.0 mmol) in DCM (7 mL) under an argon atmosphere was stirred at RT for 30 min. Next, a solution of acid chloride **34** (1.5 mmol) in DCM (3 mL) was added and the resulting mixture was heated at reflux (50 °C heating block temperature) for 18 h. The mixture was then diluted with DCM (10 mL) and washed with 10% aq. HCl (10 mL). The aqueous layer was then extracted with DCM (3 × 10 mL) and the combined organic extracts dried over MgSO₄ and concentrated *in vacuo*. The crude material was then re-dissolved in DCM (10 mL) and DBU (5.00 mmol) was added, followed by stirring at RT for 18 h, before the solvent was removed *in vacuo* and the ring-expanded product purified by flash column chromatography.

Conflicts of interest

There are no conflicts to declare.

Acknowledgements

The authors thank the EPSRC for the computational equipment used in this study (EP/H011455/1 and EP/K031589/1) and the Department of Chemistry, University of York for the provision of an Eleanor Dodson Fellowship (to W. P. U.) and for supporting K. Y. P. and R. G. E. with PhD studentships. Thanks also go to Zhongzhen Yang for help with preliminary studies and to Sam Hart for X-ray crystallography.

Notes and references

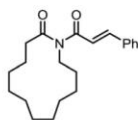
- For a review, see: F. Pietrocola, L. Galluzzi, J. M. Bravo-San Pedro, F. Madeo and G. Kroemer, *Cell Metab.*, 2015, **21**, 805.
- (a) P. E. Dawson, T. W. Muir, I. Clark-Lewis and S. B. Kent, *Science*, 1994, **266**, 776 For useful perspective on N → S acyl transfer in peptide thioester synthesis (conceptually related to the methodology described in this manuscript), see: (b) D. Macmillan, A. Adams and B. Premdjee, *Isr. J. Chem.*, 2011, **51**, 885.
- (a) M. Sibrian-Vazquez, J. O. Escobedo, S. Lim, G. K. Samoei and R. M. Strongin, *Proc. Natl. Acad. Sci. U. S. A.*, 2010, **107**, 551; (b) L. F. Agnati, S. Ferré, S. Genedani, G. Leo, D. Guidolin, M. Filafarro, P. Carriba, V. Casadó, C. Lluís, R. Franco, A. S. Woods and K. Fuxe, *J. Proteome Res.*, 2006, **5**, 3077; (c) Y. Vallee, I. Shalayel, K.-D. Ly, K. V. R. Rao, G. de Paëpe, K. Märker and A. Millet, *Int. J. Dev. Biol.*, 2017, **61**, 471.
- For a classical study comparing the rates of hydrolysis of lactones and thiolactones, see: C. M. Stevens and D. S. Tarbell, *J. Org. Chem.*, 1954, **19**, 1996.
- (a) C.-L. J. Wang and J. M. Salvino, *Tetrahedron Lett.*, 1984, **25**, 5243; (b) D. V. Ferraris, P. Majer, C. Ni, C. E. Slusher, R. Rais, Y. Wu, K. M. Wozniak, J. Alt, C. Rojas, B. S. Slusher and T. Tsukamoto, *J. Med. Chem.*, 2014, **57**, 243; (c) D. H. Kim, C. J. Guinosso, G. C. Buzby Jr., D. R. Herbst, R. J. McCaully, T. C. Wicks and R. L. Wendt, *J. Med. Chem.*, 1983, **26**(3), 394.
- For a review that includes a useful and detailed account of the synthesis and reactivity of thiolactones, see: (a) Z. Paryzek and I. Skiera, *Org. Prep. Proced. Int.*, 2007, **39**, 203 For selected more recent applications of thiolactones in synthetic chemistry, see: (b) J. Huang, F. Xiong, Z.-H. Wang and F.-E. Chen, *Helv. Chim. Acta*, 2009, **92**, 1445; (c) D. Frank, P. Espeel, S. Classens, E. Mes and F. E. Du Prez, *Tetrahedron*, 2016, **72**, 6616.
- (a) P. Espeel and F. E. Du Prez, *Eur. Polym.*, 2015, **62**, 247; (b) H. R. Kricheldorf, S. M. Weidner and F. Scheliga, *Polym. Chem.*, 2017, **8**, 1589; (c) P. Espeel, F. Goethals and F. E. Du Prez, *J. Am. Chem. Soc.*, 2011, **133**, 1678; (d) S. Martens, A. Landuyt, P. Espeel, B. Devreese, P. Dawyndt and F. Du Prez, *Nat. Commun.*, 2018, **9**, 4451.





- 8 (a) K. Steliou, P. Salama and J. Corriveau, *J. Org. Chem.*, 1985, **50**, 4969; (b) D. Bhar and S. Chandrasekaran, *Tetrahedron*, 1997, **53**, 11835.
- 9 For papers on the importance of ring size in end-to-end cyclisation reactions of larger rings, see: (a) G. Illuminati and L. Mandolini, *Acc. Chem. Res.*, 1981, **14**, 95; (b) J. Fastrez, *J. Phys. Chem.*, 1989, **93**, 2635; (c) J. C. Collins and K. James, *MedChemComm*, 2012, **3**, 1489; (d) H. Kurouchi and T. Ohwada, *J. Org. Chem.*, 2020, **85**, 876.
- 10 For general perspective on macrocycle synthesis, see: (a) E. Marsault and M. L. Peterson, *J. Med. Chem.*, 2011, **54**, 1961; (b) A. K. Yudin, *Chem. Sci.*, 2015, **6**, 30; (c) K. T. Mortensen, T. J. Osberger, T. A. King, H. F. Sore and D. R. Spring, *Chem. Rev.*, 2019, **119**, 10288; (d) *Practical Medicinal Chemistry with Macrocycles*, ed. E. Marsault and M. L. Peterson, Wiley, 2017; (e) S. D. Appavoo, S. Huh, D. B. Diaz and A. K. Yudin, *Chem. Rev.*, 2019, **119**, 9724; (f) I. V. Smolyar, A. K. Yudin and V. G. Nenajdenko, *Chem. Rev.*, 2019, **119**, 10032; (g) I. Saridakis, D. Kaiser and N. Maulide, *ACS Cent. Sci.*, 2020, **6**, 1869.
- 11 For reviews of ring expansion chemistry, see: (a) M. Hesse, in *Ring Enlargement in Organic Chemistry*, Wiley-VCH, Weinheim, 1991; (b) W. P. Unsworth and J. R. Donald, *Chem. – Eur. J.*, 2017, **23**, 8780; (c) K. Prantz and J. Mulzer, *Chem. Rev.*, 2010, **110**, 3741; (d) T. C. Stephens and W. P. Unsworth, *Synlett*, 2020, **31**, 133; (e) A. K. Clarke and W. P. Unsworth, *Chem. Sci.*, 2020, **11**, 2876.
- 12 (a) L. Li, Z.-L. Li, F.-L. Wang, Z. Guo, Y.-F. Cheng, N. Wang, X.-W. Dong, C. Fang, J. Liu, C. Hou, B. Tan and X.-Y. Liu, *Nat. Commun.*, 2016, **7**, 13852; (b) J. E. Hall, J. V. Matlock, J. W. Ward and J. Clayden, *Angew. Chem., Int. Ed.*, 2016, **55**, 11153; (c) Z.-L. Li, X.-H. Li, N. Wang, N.-Y. Yang and X.-Y. Liu, *Angew. Chem., Int. Ed.*, 2016, **55**, 15100; (d) R. Mendoza-Sanchez, V. B. Corless, Q. N. N. Nguyen, M. Bergeron-Brlek, J. Frost, S. Adachi, D. J. Tantillo and A. K. Yudin, *Chem. – Eur. J.*, 2017, **23**, 13319; (e) R. Costil, Q. Lefebvre and J. Clayden, *Angew. Chem., Int. Ed.*, 2017, **56**, 14602; (f) D. R. Loya, A. Jean, M. Cormier, C. Fressigné, S. Nejrroti, J. Blanchet, J. Maddaluno and M. De Paolis, *Chem. – Eur. J.*, 2018, **24**, 2080; (g) N. Wang, Q.-S. Gu, Z.-L. Li, Z. Li, Y.-L. Guo, Z. Guo and X.-Y. Liu, *Angew. Chem., Int. Ed.*, 2018, **57**, 14225; (h) Y. Zhou, Y.-L. Wei, J. Rodriguez and Y. Coquerel, *Angew. Chem., Int. Ed.*, 2019, **58**, 456; (i) E. Reutskaya, A. Osipyan, A. Sapegin, A. S. Novikov and M. Krasavin, *J. Org. Chem.*, 2019, **84**, 1693; (j) A. Lawer, J. A. Rossi-Ashton, T. C. Stephens, B. J. Challis, R. G. Epton, J. M. Lynam and W. P. Unsworth, *Angew. Chem., Int. Ed.*, 2019, **58**, 13942; (k) S. Grintsevich, A. Sapegin, E. Reutskaya, S. Peintner, M. Erdélyi and M. Krasavin, *Eur. J. Org. Chem.*, 2020, 5664.
- 13 (a) H. C. De Araújo and J. R. Mahajan, *Synthesis*, 1978, 228; (b) J. R. Mahajan and H. C. De Araújo, *Synthesis*, 1980, 64; (c) R. Malherbe, G. Rist and D. Bellus, *J. Org. Chem.*, 1982, **48**, 860; (d) E. Vedejs, J. M. Dolphin and H. Mastalerz, *J. Am. Chem. Soc.*, 1983, **105**, 127; (e) C. Meng, J.-J. Li, X.-M. Liang, J.-J. Zhang and D.-Q. Wang, *Phosphorus, Sulfur Silicon Relat. Elem.*, 2014, **189**, 1529.
- 14 Thiolactones are also involved in ring expansion cascade reactions (known as 'thia zip reactions'), although are intermediates and not the final products in these reactions, see: J. P. Tam, Y.-A. Lu and Q. Yu, *J. Am. Chem. Soc.*, 1999, **121**, 4316.
- 15 (a) Y. Nakashita and M. Hesse, *Angew. Chem.*, 1981, **93**, 1077; (b) S. Stanchev and M. Hesse, *Helv. Chim. Acta*, 1989, **72**, 1052.
- 16 (a) C. Kitsiou, J. J. Hindes, P. I'Anson, P. Jackson, T. C. Wilson, E. K. Daly, H. R. Felstead, P. Hearnshaw and W. P. Unsworth, *Angew. Chem., Int. Ed.*, 2015, **54**, 15794; (b) L. G. Baud, M. A. Manning, H. L. Arkless, T. C. Stephens and W. P. Unsworth, *Chem. – Eur. J.*, 2017, **23**, 2225; (c) T. C. Stephens, M. Lodi, A. Steer, Y. Lin, M. Gill and W. P. Unsworth, *Chem. – Eur. J.*, 2017, **23**, 13314; (d) T. C. Stephens, A. Lawer, T. French and W. P. Unsworth, *Chem. – Eur. J.*, 2018, **24**, 13947 For the application of SuRE reactions in the work of another group, see: (e) C. Zhao, Z. Ye, Z.-X. Ma, S. A. Wildman, S. A. Blaszczyk, L. Hu, I. A. Guizei and W. Tang, *Nat. Commun.*, 2019, **10**, 4015, DOI: 10.1038/s41467-019-11976-2.
- 17 This method was introduced by our group in ref. 16d, and more fully explored and benchmarked against other computational methods in: A. Lawer, R. G. Epton, T. C. Stephens, K. Y. Palate, M. Lodi, E. Marotte, K. J. Lamb, J. K. Sangha, J. Lynam and W. P. Unsworth, *Chem. – Eur. J.*, 2020, **26**, 12674 See ESI for full details of the new computational chemistry results reported in this paper.†
- 18 For computational chemistry studies on related ring expansion processes, see ref. 12d and i.
- 19 A guideline established in our earlier work (ref. 17) is that the ring expanded isomer should be the most stable by >3kcal mol⁻¹ for ring expansion to be the predicted outcome.
- 20 P. Majer, P. F. Jackson, G. Delahanty, B. S. Grella, Y.-S. Ko, W. Li, Q. Liu, K. M. Maclin, J. Poláková, K. A. Shaffer, D. Stoermer, D. Vitharana, E. Y. Wang, A. Zakrzewski, C. Rojas, B. S. Slusher, K. M. Wozniak, E. Burak, T. Limsakun and T. Tsukamoto, *J. Med. Chem.*, 2003, **46**, 1989.
- 21 Another important consideration when using this approach is that in our hands, the *N*-acylation step (*i.e.* **21b** → **31b**) was somewhat capricious, which we think is a consequence of the requirement to form an acid chloride in the presence of an acid labile protecting group. Efficient *N*-acylation can still be achieved by forming and reacting acid chloride **30** quickly, but compared with other SuRE variants, this is an additional complication.
- 22 (a) M. Ruiz-Gayo, F. Albericio, E. Pedrosa and E. J. Giralt, *Chem. Soc., Chem. Commun.*, 1986, 1501; (b) E. J. Corey, D. Y. Gin and R. S. Kania, *J. Am. Chem. Soc.*, 1996, **118**, 9202; (c) B. Ponsati, E. Giralt and D. Andreu, *Tetrahedron*, 1990, **46**, 8255.

23 Under the standard conditions, the following cinnamyl imide product was obtained and isolated in 70% yield (see ESI compound **S6**):†



24 (a) D. R. Moore and L. J. Mathias, *J. Org. Chem.*, 1987, **52**, 1599; (b) L. J. Mathias and D. R. Moore, *J. Am. Chem. Soc.*, 1985, **107**, 5817.

25 CCDC 2040347 (**24b**), 1921223 (**20RE**) and 2040346 (**24I**) contain the crystallographic data for these macrocyclic thiolactones, see: †.

26 This is also supported qualitatively by the observation that free-thiol containing imides (*e.g.*, **20RO**, **32**, **39**, and **43**) were found to be isolable, kinetically stable species, while the analogous amine containing systems cannot be isolated as they ring expand spontaneously at RT (see ref. 16c).

27 In total, six mechanistically distinct side reactions were observed during this study: (1) nucleophilic attack at the C-3 carbonyl leading to lactam opening (*e.g.*, **25–27**); (2) nucleophilic attack at the C-2 carbonyl leading to cleavage of the external imide C–N bond (*e.g.* **28**, **29**); (3) condensation (*e.g.* **33**); (4) β -elimination of S (*e.g.* Scheme 5 and **24j**); (5) dimerisation via conjugate addition (*e.g.* Scheme 5); (6) disulfide formation (*e.g.* **45**, Scheme 7).



Paper 6 – Indole-ynones as Privileged Substrates for Radical Dearomatizing Spirocyclization Cascades



pubs.acs.org/OrgLett

Letter

Indole-ynones as Privileged Substrates for Radical Dearomatizing Spirocyclization Cascades

Nantachai Inprung, Hon Eong Ho, James A. Rossi-Ashton, Ryan G. Epton, Adrian C. Whitwood, Jason M. Lynam, Richard J. K. Taylor, Michael J. James,* and William P. Unsworth*

Cite This: *Org. Lett.* 2022, 24, 668–674

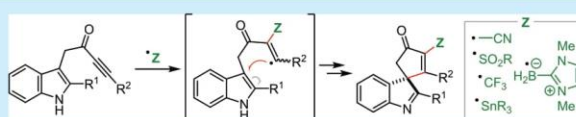
Read Online

ACCESS |

Metrics & More

Article Recommendations

Supporting Information



ABSTRACT: Indole-ynones have been established as general substrates for radical dearomatizing spirocyclization cascade reactions. Five distinct and varied synthetic protocols have been developed—cyanomethylation, sulfonation, trifluoromethylation, stannylation and borylation—using a variety of radical generation modes, ranging from photoredox catalysis to traditional AIBN methods. The simple and easily prepared indole-ynones can be used to rapidly generate diverse, densely functionalized spirocycles and have the potential to become routinely used to explore radical reactivity. Experimental and computational investigations support the proposed radical cascade mechanism and suggest that other new methods are now primed for development.

Compound classes that expedite access to privileged biologically active scaffolds are highly prized in synthetic chemistry.¹ For example, *N*-arylacrylamides **1** are prominent precursors for the synthesis of biologically important 3,3-disubstituted oxindoles,² with a number of elegant (and asymmetric) metal-catalyzed strategies known (**1** → **2** → **3**, Scheme 1A).³ Complementary radical-based strategies (**1** → **4** → **5**, Z = various, Scheme 1A) have also been developed.⁴ Indeed, these methods are so well established that *N*-arylacrylamide-based radical addition–cyclization cascades have become a “go-to” system with which to probe radical mechanisms and benchmark new (and old) methods for the reactions of radicals.⁵

The identification of new scaffolds with the utility of *N*-arylacrylamides therefore has great potential in synthetic and medicinal chemistry—both for their ability to facilitate the exploration of novel biologically relevant chemical space and as testing grounds for new methodologies. Indole-ynones (**6**) are an emerging class of compounds that rival the versatile reactivity of *N*-arylacrylamides, most notably for the synthesis of spirocyclic indolenines.^{6,7} A number of synthetic methods have been reported, by our groups and others, based on the reaction of the electron-rich indole moieties with a tethered ynone group, promoted by alkyne activation with various reagent classes, including π -acids,⁸ Brønsted acids,⁹ palladium(II) complexes,¹⁰ electrophilic halogenation reagents,¹¹ and others^{12,13} (**6** → **7** → **8**, Scheme 1B).

These previous studies focused on two-electron processes, but in 2020, our group published the first radical-based spirocyclization of an indole-ynone. In this work, thyl radicals generated *in situ* were shown to promote dearomatizing

spirocyclization with concomitant C–S bond formation (**6** → **9** → **10**, Scheme 1B) via a hydrogen atom transfer based radical chain process.^{14,15} Interestingly, the thyl radical formation that initiates this process was shown to be promoted by visible-light-mediated photoexcitation of an intramolecular electron donor–acceptor (EDA) complex, formed between the indole and alkyne moieties in the indole-ynone **6**.^{16,17} Soon afterward, related radical spirocyclization methods began to emerge from other groups. For example, Liu, Han and co-workers reported an efficient Cu(I)-catalyzed trifluoromethylation protocol, which proceeds via the formation of trifluoromethyl radicals from Togni's reagent (Z = CF₃).^{18a} A similar cascade was also reported by Xu, Pan, Ma and co-workers; in this case, dearomatizing spirocyclization was promoted by selenyl radicals, formed via the homolysis of diselenides (Z = SeR).^{18b}

We postulated that in addition to being versatile precursors for two-electron processes,^{8,13,19} indole-ynones **6** may be similarly privileged substrates for radical cascade reactions.²⁰ Thus, herein we describe efforts to fully establish indole-ynones as general precursors for radical dearomatizing spirocyclization reactions. In total, five efficient, novel synthetic protocols have been established for dearomative cyanomethy-

Received: December 6, 2021

Published: January 5, 2022



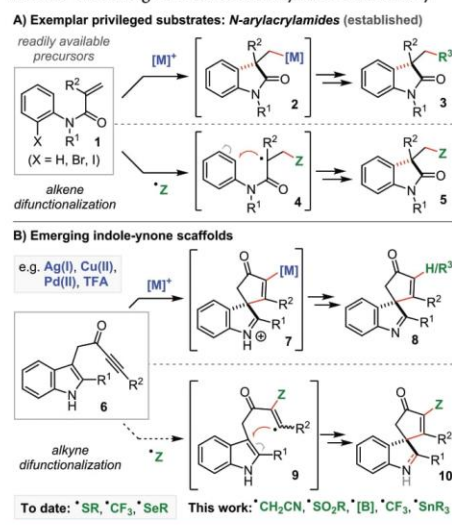
ACS Publications

© 2022 American Chemical Society

668

https://doi.org/10.1021/acs.orglett.1c04098
Org. Lett. 2022, 24, 668–674

Scheme 1. Privileged Substrates in Synthetic Chemistry



lation, sulfonylation, trifluoromethylation, stannylation, and borylation. Demonstrating that spirocyclization can be achieved using a range of radical generation methods was also an important goal, and the new methods developed rely on various radical reaction modes ranging from traditional AIBN homolysis to more modern photoredox catalysis and EDA complex activation.

The first radical class utilized were cyanomethyl radicals.²¹ Cyanomethyl radicals can be generated from bromoacetonitrile **11** via known photoredox catalysis methods.^{22,23} Optimization results for the conversion of indole-ynone **6a** into spirocyclic indolenine **12a** are included in Table 1. Optimal conditions (entry 1) were identified based on the use of catalytic Ir(*p*-F-ppy)₃ (1 mol %) and 2,6-lutidine in DCE with blue light irradiation (25–30 °C, fan cooling). Light is essential for reactivity (entry 2), and the reaction is shut down by the addition of TEMPO (entry 3), which taken together strongly indicates that a light-promoted radical process operates. Changes to the quantity and identity of base led to inferior conversion (entries 4–7). Other photocatalysts were trialed (entries 8–11), but only Ir(III) catalysts resulted in satisfactory conversion into **12a**, with the relatively reducing catalyst Ir(*p*-F-ppy)₃ being the most effective. Interestingly, modest conversion into **12a** was also observed in the absence of an added photocatalyst (entry 12), indicating that electron-donor–acceptor (EDA) complexes may also be photoexcited to initiate dearomative spirocyclization,¹⁴ albeit with lower efficiency than the reaction with Ir(*p*-F-ppy)₃.

Next, the generality of the cyanomethylation reaction was explored (Scheme 2A).²⁴ A selection of indole-tethered ynones **6a–g** were prepared and tested using the optimized conditions, and all were converted into spirocyclic indolenines **12a–g** in 44–75% yield; this series includes 2-halo substituted systems, which furnished synthetically useful spirocyclic indoleninyl halides **12e–g**.^{8d} Attempts to perform the reaction

Table 1. Cyanomethylation Optimization^a

entry	deviation from standard conditions ^a	12a (%) ^b	6a (%) ^b
1	none	75 ^c	12 ^c
2	without light	0	99
3	with TEMPO (2 equiv)	0	99
4	without 2,6-lutidine	13	52
5	2,6-lutidine (1 equiv)	40	42
6	2,4,6-collidine (2 equiv)	60	15
7	K ₂ CO ₃ (2 equiv)	40	42
8	Ir(ppy) ₃ (1 mol %)	60	6
9	Ru(bpy) ₃ (PF ₆) ₂ (1 mol %)	0	74
10	Eosin Y (1 mol %)	0	80
11	10-phenyl phenothiazine (1 mol %)	7	93
12	without photocatalyst	31	56

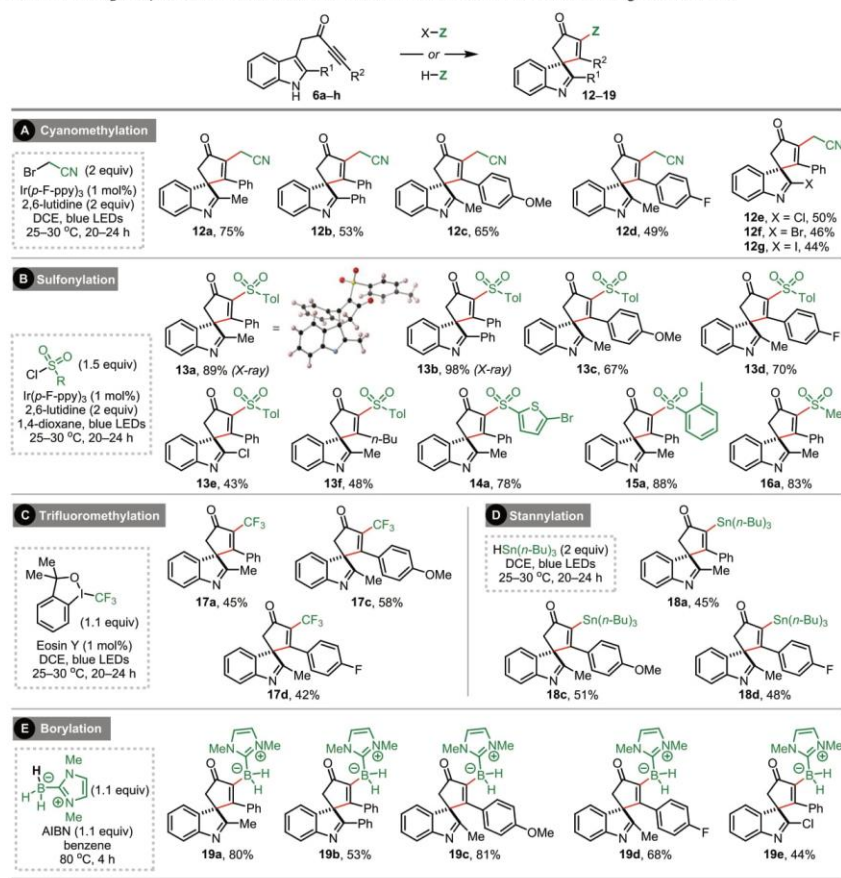
^aStandard conditions: Ir(*p*-F-ppy)₃ (1 mol %), 2,6-lutidine (2 equiv), DCE (0.1 M), rt, blue LED, on 0.2 mmol scale. ^bYields based on ¹H NMR analysis of the unpurified reaction mixture using CH₂Br₂ as an internal standard unless stated. ^cIsolated yield following column chromatography.

on indole-ynones without a 2-substituent (i.e., R¹ = H in the general scheme) were not successful however, with these reactions complicated by competing radical addition to the indole ring.

Attention then turned toward the development of reactions based on other radical types. In total, four additional distinct reaction classes have been developed (Scheme 2B–E), with additional synthetic and optimization details included in the Supporting Information. First, known photoredox-catalyzed methods for the generation of sulfonyl radicals using sulfonyl chlorides²⁵ were adapted and used to prepare sulfonylated spirocycles **13–16** in good to excellent yields (9 examples, 43–98%, Scheme 2B).²⁶ This series confirms that switching to other reactive radical species can be achieved remarkably easily, with high yields obtained.²⁷ A transition-metal-free method for the synthesis of trifluoromethylated spirocycles was also developed that complements the copper-catalyzed reaction reported by Liu, Han and co-workers featured in Scheme 1B.^{18a} Here, Togni's reagent was used with the photoredox catalyst Eosin Y to form trifluoromethylated spirocycles **17a,c–d** in 42–65% yield (Scheme 2C). Note that, in this system, control reactions show that product **17a** could be obtained in reduced yield in the absence of an added photocatalyst, or in the dark, indicating that EDA complex activation^{14,28} may also enable trifluoromethyl radical formation alongside the Eosin Y catalyzed pathway.

In addition, a remarkable additive-free stannylation dearomatizing spirocyclization reaction was developed, which can be performed simply by irradiating a mixture of the indole-ynone and tributyltin hydride in DCE with blue LEDs (Scheme 2D). Using these mild conditions, stannylation spirocyclic indolenines **18a,c–d** were formed in 45–51% yield. In line with our previous work with thiols,¹⁴ we propose that these reactions were initiated either via a hydrogen atom transfer or an electron transfer event between the photoexcited indole-ynone and tributyltin hydride to generate a tributyltin

Scheme 2. Radical Spirocyclization Cascades with Diverse Radicals Generated via a Range of Methods

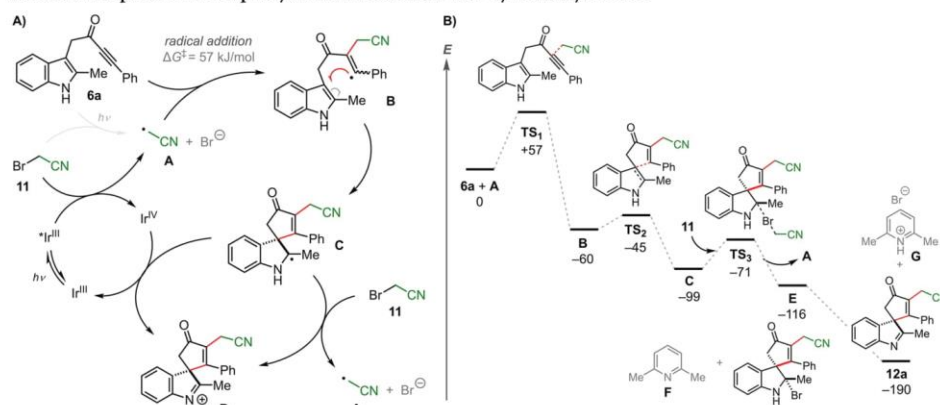


radical. The potential to develop other unconventional additive-free dearomatizing spirocyclization reactions of this type highlights the still relatively untapped synthetic utility of this substrate class. Finally, we have also shown that similar reactivity can be promoted using classical thermal radical generation conditions. AIBN in refluxing benzene was used to generate *N*-heterocyclic carbene (NHC) boryl radicals²⁹ that go on to form borylated spirocycles **19a–e** in 44–81% yield (Scheme 2E). Diversification of these products was also briefly explored, in which we confirmed that borylated spirocycle **19a** could be converted into a pinacol ester and undergo subsequent Suzuki–Miyaura cross-coupling (see Supporting Information).

A proposed mechanism, exemplified on the initial cyanomethylation system, is presented in Scheme 3A. First, it is known that photoexcited Ir(III) complexes such as Ir(*p*-F-ppy)₃ are able to reduce bromoacetonitrile **11** to form cyanomethyl radical **A**,²³ which we presume initiates the

radical cascade.³⁰ This is supported by Stern–Volmer luminescence quenching studies, which show that the photocatalyst Ir(*p*-F-ppy)₃ excited state is quenched by bromoacetonitrile (see Supporting Information). Next, we propose that cyanomethyl radical **A** reacts with the ynone moiety of **6a** to form vinylic radical **B**, which cyclizes quickly to form α -amino alkyl radical **C**. Intermediate **C** may then either (i) be oxidized by an Ir(IV) species to regenerate the Ir(III) photoredox catalyst and form the spirocyclic product **D** (which is deprotonated in the presence of 2,6-lutidine) or (ii) propagate a radical chain by reacting with **11** via halogen-atom transfer³¹ or electron transfer³² to form cyanomethyl radical **A** and spirocyclic product **D**.

To gauge whether steps subsequent to radical formation could be limiting the reaction, DFT calculations of the individual steps were undertaken (Scheme 3B). Of these steps, the addition of the cyanomethyl radical is the slowest step (TS₁) and the calculated ΔG^\ddagger of 57 kJ/mol is accessible for a

Scheme 3. Proposed Radical Spirocyclization Mechanism with Cyanomethyl Radical^a

^aEnergies are Gibbs energies in kJ/mol and were calculated using the D3-B3LYP/def2-TZVPP//B3LYP/def2-SVP level of theory at 298 K with COSMO solvent correction in DCE.

room temperature reaction. The analogous energy barrier was also calculated for each of the other four radical classes featured in this manuscript (i.e., sulfonyl, trifluoromethyl, stannyl, and boryl radical addition to indole-ynone **6a**), as well as for the previously reported thyl¹⁴ and selenyl^{18b} radical systems (Table 2; see the Supporting Information for further

Table 2. Calculated Activation Barriers^a for the Addition of Radicals ($\cdot Z$) to Indole-ynone **6a**

$\cdot Z$	ΔG^\ddagger
$\cdot\text{CN}$	57 kJ/mol
$\cdot\text{Ts}$	42 kJ/mol
$\cdot\text{CF}_3$	44 kJ/mol
$\cdot\text{SnMe}_3$	34 kJ/mol
$\cdot\text{H}_2\text{B}^+\text{-NHC}^-$	35 kJ/mol
$\cdot\text{SPh}$	15 kJ/mol
$\cdot\text{SePh}$	17 kJ/mol

^aGibbs energies calculated using the D3-B3LYP/def2-TZVPP//B3LYP/def2-SVP level of theory at 298 K with appropriate COSMO solvent corrections.

details). In all cases, this barrier was calculated to be lower in energy than that of the cyanomethyl system, strongly indicating that the radical addition step is not only viable, but likely to be facile across a range of radical species. For cyanomethylation, the subsequent radical spirocyclization through TS_2 and bromine abstraction leading to chain propagation via TS_3 have low free energies of activation and are therefore probably not rate controlling.

Based on the above, we consider it likely that all reaction series developed herein operate via the same general mechanism; the exact nature of the oxidative step ($\text{C} \rightarrow \text{D}$ in Scheme 3A) will vary depending on the reagents used and reaction conditions on a case-by-case basis, and of course the radical initiation modes differ in each series. For clarity, full proposed mechanisms for each of the reactions in Scheme 2B–E are included in the Supporting Information. Having demonstrated the feasibility of the radical cascades using diverse reagents and conditions, both experimentally and computationally, it is likely that variants based on various other radical intermediates will also be feasible, and new methods will emerge in time. The development of any new radical spirocyclization of these types could be facilitated by virtual screening of the radical addition step for proposed radical species, using the DFT method established in this study. Of course, the ability of indole-ynones to undergo facile two-electron cyclization reactions means that it will be important to test for this possibility when developing new methods. Further, the opportunity to develop novel catalyst-free activation modes should also be possible based on photoexcitation of the indole-ynone itself.

In closing, we have demonstrated that indole-ynones are general precursors for radical dearomatizing spirocyclization cascades through the development of five different synthetic protocols. These easily prepared reagents can be used to provide expedient access to libraries of densely functionalized spirocycles with rich biological potential. Our mechanistic studies indicate that many other cascade protocols of comparable/higher efficiency should be feasible using other radical classes and/or initiation modes. Moreover, we anticipate that these findings will facilitate the development and identification of other privileged substrate systems based on other heterocycle-ynone frameworks.

■ ASSOCIATED CONTENT

Supporting Information

The Supporting Information is available free of charge at <https://pubs.acs.org/doi/10.1021/acs.orglett.1c04098>.

Experimental procedures, characterization data, computational details, and copies of ^1H , ^{13}C , ^{11}B , and ^{19}F NMR spectra for all compounds featured in this manuscript. (PDF)

Accession Codes

CCDC 2087802 and 2087806 contain the supplementary crystallographic data for this paper. These data can be obtained free of charge via www.ccdc.cam.ac.uk/data_request/cif, or by emailing data_request@ccdc.cam.ac.uk, or by contacting The Cambridge Crystallographic Data Centre, 12 Union Road, Cambridge CB2 1EZ, UK; fax: +44 1223 336033.

■ AUTHOR INFORMATION

Corresponding Authors

Michael J. James – Department of Chemistry, University of York, Heslington, York YO10 5DD, U.K.; orcid.org/0000-0003-2591-0046; Email: michael.james@york.ac.uk

William P. Unsworth – Department of Chemistry, University of York, Heslington, York YO10 5DD, U.K.; orcid.org/0000-0002-9169-5156; Email: william.unsworth@york.ac.uk

Authors

Nantachai Inprung – Department of Chemistry, University of York, Heslington, York YO10 5DD, U.K.

Hon Eong Ho – Department of Chemistry, University of York, Heslington, York YO10 5DD, U.K.; orcid.org/0000-0003-1037-2505

James A. Rossi-Ashton – Department of Chemistry, University of York, Heslington, York YO10 5DD, U.K.; orcid.org/0000-0002-0989-2506

Ryan G. Epton – Department of Chemistry, University of York, Heslington, York YO10 5DD, U.K.; orcid.org/0000-0001-7717-7339

Adrian C. Whitwood – Department of Chemistry, University of York, Heslington, York YO10 5DD, U.K.; orcid.org/0000-0002-5132-5468

Jason M. Lynam – Department of Chemistry, University of York, Heslington, York YO10 5DD, U.K.; orcid.org/0000-0003-0103-9479

Richard J. K. Taylor – Department of Chemistry, University of York, Heslington, York YO10 5DD, U.K.

Complete contact information is available at: <https://pubs.acs.org/doi/10.1021/acs.orglett.1c04098>

Notes

The authors declare no competing financial interest.

■ ACKNOWLEDGMENTS

The authors would like to thank the Development and Promotion of Science and Technology Talents Project (DPST), Royal Thai Government. (N.I. EP/N035119/1), the University of York, and the Leverhulme Trust (for an Early Career Fellowship, ECF-2019-135, M.J.J.) for financial support. We are also grateful to the University of York for the provision of an Eleanor Dodson Fellowship (to W.P.U.).³⁰

■ REFERENCES

- (1) (a) Morton, D.; Leach, S.; Cordier, C.; Warriner, S.; Nelson, A. Synthesis of Natural-Product-Like Molecules with Over Eighty Distinct Scaffolds. *Angew. Chem., Int. Ed.* **2009**, *48*, 104–109. (b) Davison, E. K.; Brimble, M. A. Natural Product Derived Privileged Scaffolds in Drug Discovery. *Curr. Opin. Chem. Biol.* **2019**, *52*, 1–8.
- (2) (a) Rottmann, M.; McNamara, C.; Yeung, B. K. S.; Lee, M. C. S.; Zou, B.; Russell, B.; Seitz, P.; Plouffe, D. M.; Dharia, N. V.; Tan, J.; Cohen, S. B.; Spencer, K. R.; González-Páez, G. E.; Lakshminarayana, S. B.; Goh, A.; Suwanarusk, R.; Jegla, T.; Schmitt, E. K.; Beck, H.-P.; Brun, R.; Nosten, F.; Renia, L.; Dartois, V.; Keller, T. H.; Fidock, D. A.; Winzeler, E. A.; Diagona, T. T. Spiroindolones, a Potent Compound Class for the Treatment of Malaria. *Science* **2010**, *329*, 1175–1180.
- (3) For review(s), see: (a) Klein, J. E. M. N.; Taylor, R. J. K. Transition-Metal-Mediated Routes to 3,3-Disubstituted Oxindoles through Anilide Cyclisation. *Eur. J. Org. Chem.* **2011**, *2011*, 6821–6841. (b) Marchese, A. D.; Larin, E. M.; Mirabi, B.; Lautens, M. Metal-Catalyzed Approaches toward the Oxindole Core. *Acc. Chem. Res.* **2020**, *53*, 1605–1619. For selected recent examples, see: (c) Pan, Q.; Ping, Y.; Wang, Y.; Guo, Y.; Kong, W. Ni-Catalyzed Ligand-Controlled Regiodivergent Reductive Dicarboxylation of Alkenes. *J. Am. Chem. Soc.* **2021**, *143*, 10282–10291. (d) Chen, X.-W.; Yue, J.-P.; Wang, K.; Gui, Y.-Y.; Niu, Y.-N.; Liu, J.; Ran, C.-K.; Kong, W.; Zhou, W.-J.; Yu, D.-G. Nickel-Catalyzed Asymmetric Reductive Carbo-Carboxylation of Alkenes with CO₂. *Angew. Chem., Int. Ed.* **2021**, *60*, 14068–14075.
- (4) For review(s), see: (a) Chen, J.-R.; Yu, X.-Y.; Xiao, W.-J. Tandem Radical Cyclization of N-Arylacrylamides: An Emerging Platform for the Construction of 3,3-Disubstituted Oxindoles. *Synthesis* **2015**, *47*, 604–629. (b) Song, R.-J.; Liu, Y.; Xie, Y.-X.; Li, J.-H. Difunctionalization of Acrylamides through C–H Oxidative Radical Coupling: New Approaches to Oxindoles. *Synthesis* **2015**, *47*, 1195–1209. For selected recent examples, see: (c) Liu, Z.; Zhong, S.; Ji, X.; Deng, G.-J.; Huang, H. Hydroarylation of Activated Alkenes Enabled by Proton-Coupled Electron Transfer. *ACS Catal.* **2021**, *11*, 4422–4429. (d) Lu, Y.; Fang, C.-Z.; Liu, Q.; Li, B.-L.; Wang, Z.-X.; Chen, X.-Y. Donor–Acceptor Complex Enables Cascade Radical Cyclization of N-Arylacrylamides with Katritzky Salts. *Org. Lett.* **2021**, *23*, 5425–5429. (e) Lai, X.-L.; Shu, X.-M.; Song, J.; Xu, H.-C. Electrophotocatalytic Decarboxylative C–H Functionalization of Heteroarenes. *Angew. Chem., Int. Ed.* **2020**, *59*, 10626–10632. (f) Hell, S. M.; Meyer, C. F.; Laudadio, G.; Misale, A.; Willis, M. C.; Noël, T.; Trabanco, A. A.; Gouverneur, V. Silyl Radical-Mediated Activation of Sulfonyl Chlorides Enables Direct Access to Aliphatic Sulfonamides from Alkenes. *J. Am. Chem. Soc.* **2020**, *142*, 720–725.
- (5) Based on a Reaxys search using the input below (G = any group), an approximate total of 7,284 N-arylacrylamide cyclization reactions have been reported in the literature to date (accessed September 7, 2021).



- (6) James, M. J.; O'Brien, P.; Taylor, R. J. K.; Unsworth, W. P. Synthesis of spirocyclic indolenines. *Chem.—Eur. J.* **2016**, *22*, 2856–2881.

- (7) For spirocycles in medicinal chemistry, see: (a) Zheng, Y.; Tice, C. M.; Singh, S. B. The use of spirocyclic scaffolds in drug discovery. *Bioorg. Med. Chem. Lett.* **2014**, *24*, 3673. (b) Müller, G.; Berkenbosch, T.; Benningshof, J. C. J.; Stumpfe, D.; Bajorath, J. Charting Biologically Relevant Spirocyclic Compound Space. *Chem.—Eur. J.* **2017**, *23*, 703. (c) Zheng, Y.-J.; Tice, C. M. The utilization of spirocyclic scaffolds in novel drug discovery. *Expert Opin. Drug Discovery* **2016**, *11*, 831. (d) Griggs, S. D.; Thompson, N.; Tape, D. T.; Fabre, M.; Clarke, P. A. A Two-Step Synthesis of 2-Spiropiperidines. *Chem.—Eur. J.* **2017**, *23*, 9262.

- (8) (a) James, M. J.; Cuthbertson, J. D.; O'Brien, P.; Taylor, R. J. K.; Unsworth, W. P. Silver(I)- or Copper(II)-Mediated Dearomatization of Aromatic Yrones: Direct Access to Spirocyclic Scaffolds. *Angew. Chem., Int. Ed.* **2015**, *54*, 7640–7643. (b) Liddon, J. T. R.; James, M. J.; Clarke, A. K.; O'Brien, P.; Taylor, R. J. K.; Unsworth, W. P. Catalyst-Driven Scaffold Diversity: Selective Synthesis of Spirocycles, Carbazoles and Quinolines from Indolyl Yrones. *Chem.—Eur. J.* **2016**, *22*, 8777–8780. (c) Clarke, A. K.; James, M. J.; O'Brien, P.; Taylor, R. J. K.; Unsworth, W. P. Silica-Supported Silver Nitrate as a Highly Active Dearomatizing Spirocyclization Catalyst: Synergistic Alkyne Activation by Silver Nanoparticles and Silica. *Angew. Chem., Int. Ed.* **2016**, *55*, 13798–13802. (d) Liddon, J. T. R.; Clarke, A. K.; Taylor, R. J. K.; Unsworth, W. P. Preparation and Reactions of Indoleninyl Halides: Scaffolds for the Synthesis of Spirocyclic Indole Derivatives. *Org. Lett.* **2016**, *18*, 6328–6331. (e) Liddon, J. T. R.; Rossi-Ashton, J. A.; Clarke, A. K.; Lynam, J. M.; Taylor, R. J. K.; Unsworth, W. P. Divergent reactivity of indole tethered yrones with silver(I) and gold(I) catalysis: a combined synthetic and computational study. *Synthesis* **2018**, *50*, 4829–4836. (f) Han, G.; Xue, L.; Zhao, L.; Zhu, T.; Hou, J.; Song, Y.; Liu, Y. Access to CF₃-Containing Cyclopentaquinolone Derivatives from Indolyl-yrones via Silver-Catalyzed One-pot Reaction. *Adv. Synth. Catal.* **2019**, *361*, 678–682.
- (9) (a) Fedoseev, P.; Van Der Eycken, E. Temperature switchable Brønsted acid-promoted selective syntheses of spiro-indolenines and quinolines. *Chem. Commun.* **2017**, *53*, 7732–7735. (b) Inprung, N.; James, M. J.; Taylor, R. J. K.; Unsworth, W. P. A Thiol-Mediated Three-Step Ring Expansion Cascade for the Conversion of Indoles into Functionalized Quinolines. *Org. Lett.* **2021**, *23*, 2063–2068.
- (10) Ho, H. E.; Stephens, T. C.; Payne, T. J.; O'Brien, P.; Taylor, R. J. K.; Unsworth, W. P. Merging π -acid and Pd catalysis: Dearomatizing spirocyclisation cross-coupling cascade reactions of alkyne tethered aromatics. *ACS Catal.* **2019**, *9*, 504–510.
- (11) Fedoseev, P.; Coppola, G.; Ojeda, G. M.; Van der Eycken, E. V. Synthesis of Spiroindolenines by Intramolecular Ipso-Iodocyclization of Indol Yrones. *Chem. Commun.* **2018**, *54*, 3625–3628.
- (12) Ekebergh, A.; Börje, A.; Mårtensson, J. Total Synthesis of Nostodione A, a Cyanobacterial Metabolite. *Org. Lett.* **2012**, *14*, 6274–6277.
- (13) For related works based on yrones tethered to heterocycles other than indole, see: (a) Unsworth, W. P.; Cuthbertson, J. D.; Taylor, R. J. K. Total Synthesis of Spirobacillene A. *Org. Lett.* **2013**, *15*, 3306–3309. (b) Ho, H. E.; James, M. J.; O'Brien, P.; Taylor, R. J. K.; Unsworth, W. P. Ag(I)-catalysed synthesis of azabicyclic alkaloid frameworks from ketimine-tethered yrones: total synthesis of indolizidine 209D. *Org. Lett.* **2018**, *20*, 1439–1443. (c) Clarke, A. K.; Lynam, J. M.; Taylor, R. J. K.; Unsworth, W. P. 'Back to front' indole synthesis using silver(I) catalysis: unexpected C-3 pyrrole activation mode supported by DFT. *ACS Catal.* **2018**, *8*, 6844–6850. (d) Rossi-Ashton, J. A.; Clarke, A. K.; Taylor, R. J. K.; Unsworth, W. P. Modular Synthesis of Polycyclic Alkaloid Scaffolds via an Enantioselective Dearomative Cascade. *Org. Lett.* **2020**, *22*, 1175–1181.
- (14) Ho, H. E.; Pagano, A.; Rossi-Ashton, J. A.; Donald, J. R.; Epton, R. G.; Churchill, J. C.; James, M. J.; O'Brien, P.; Taylor, R. J. K.; Unsworth, W. P. Visible-light-induced intramolecular charge transfer in the radical spirocyclisation of indole-tethered yrones. *Chem. Sci.* **2020**, *11*, 1353–1360.
- (15) For selected radical-based dearomative processes involving phenol- and anisole-tethered alkynes, see: (a) Wang, L.-J.; Wang, A.-Q.; Xia, Y.; Wu, X.-X.; Liu, X.-Y.; Liang, Y.-M. Silver-catalyzed carbon–phosphorus functionalization of N-(p-methoxyaryl)-propiolamides coupled with dearomatization: access to phosphorylated aza-decenones. *Chem. Commun.* **2014**, *50*, 13998–14001. (b) Ouyang, X.-H.; Song, R.-J.; Li, Y.; Liu, B.; Li, J.-H. Metal-Free Oxidative Ipso-Carboacylation of Alkynes: Synthesis of 3-Acylspiro[4.5]trienones from N-Arylpropiolamides and Aldehydes. *J. Org. Chem.* **2014**, *79*, 4582–4589. (c) Cui, H.; Wei, W.; Yang, D.; Zhang, J.; Xu, Z.; Wen, J.; Wang, H. Silver-catalyzed direct spirocyclization of alkynes with thiophenols: a simple and facile approach to 3-thioazaspiro[4.5]trienones. *RSC Adv.* **2015**, *5*, 84657–84661. (d) Wen, J.; Xue, S.; Yang, D.; Lou, Y.; Gao, C.; Wang, H.; Wei, W. Metal-Free Oxidative Spirocyclization of Alkynes with Sulfonylhydrazides Leading to 3-Sulfonated Azaspiro[4.5]trienones. *J. Org. Chem.* **2015**, *80*, 4966–4972. (e) Zhang, Y.; Zhang, J.; Hu, B.; Ji, M.; Ye, S.; Zhu, G. Synthesis of Difluoromethylated and Phosphorated Spiro[5.5]trienones via Dearomative Spirocyclization of Biaryl Yrones. *Org. Lett.* **2018**, *20*, 2988–2992.
- (16) Cao, Z.-Y.; Ghosh, T.; Melchiorre, P. *Nat. Commun.* **2018**, *9*, 3274.
- (17) For instructive reviews on the use of EDA complexes in synthetic chemistry, see: (a) Lima, C. G. S.; Lima, T.; Duarte, M.; Jurberg, I. D.; Paixão, M. W. Organic Synthesis Enabled by Light-Irradiation of EDA Complexes: Theoretical Background and Synthetic Applications. *ACS Catal.* **2016**, *6*, 1389. (b) Crisena, G. E. M.; Mazzarella, D.; Melchiorre, P. Synthetic methods driven by the photoactivity of electron donor-acceptor complexes. *J. Am. Chem. Soc.* **2020**, *142*, 5461–5476.
- (18) (a) Li, C.; Xue, L.; Zhou, J.; Zhao, Y.; Han, G.; Hou, J.; Song, Y.; Liu, Y. Copper-Catalyzed Trifluoromethylation of Yrones Coupled with Dearomatizing Spirocyclization of Indoles: Access to CF₃-Containing Spiro[cyclopentane-1,3'-indole]. *Org. Lett.* **2020**, *22*, 3291–3296. (b) Zhou, X.-J.; Liu, H.-Y.; Mo, Z.-Y.; Ma, X.-L.; Chen, Y.-Y.; Tang, H.-T.; Pan, Y.-M.; Xu, Y.-L. Visible-Light-Promoted Selenylative Spirocyclization of Indolyl-yrones toward the Formation of 3-Selenospiroindolenine Anticancer Agents. *Chem.—Asian J.* **2020**, *15*, 1536–1539.
- (19) For other examples of indole dearomatization using yrones see (a) Fedoseev, P.; Van der Eycken, E. V. Temperature switchable Brønsted acid-promoted selective syntheses of spiro-indolenines and quinolines. *Chem. Commun.* **2017**, *53*, 7732–7735. (b) Gan, P.; Pitzen, J.; Qu, P.; Snyder, S. A. Total Synthesis of the Caged Indole Alkaloid Arboridinine Enabled by *aza*-Prins and Metal-Mediated Cyclizations. *J. Am. Chem. Soc.* **2018**, *140*, 919–925. For related examples based on other electron deficient alkynes, see: (c) Schröder, F.; Sharma, U.; Mertens, M.; Devred, F.; Debecker, D.; Luque, R.; Van der Eycken, E. V. Silver-Nanoparticle-Catalyzed Dearomatization of Indoles toward 3-Spiroindolenines via a 5-*exo-dig* Spirocyclization. *ACS Catal.* **2016**, *6*, 8156–8161. (d) He, Y.; Li, Z.; Robeyns, K.; Van Meervelt, L.; Van der Eycken, E. V. A Gold-Catalyzed Domino Cyclization Enabling Rapid Construction of Diverse Polyheterocyclic Frameworks. *Angew. Chem., Int. Ed.* **2018**, *57*, 272–276.
- (20) (a) Wille, U. Radical Cascades Initiated by Intermolecular Radical Addition to Alkynes and Related Triple Bond Systems. *Chem. Rev.* **2013**, *113*, 813–853. (b) Sebren, L. J.; James, J.; Devery, I.; Stephenson, C. R. J. Catalytic Radical Domino Reactions in Organic Synthesis. *ACS Catal.* **2014**, *4*, 703–716.
- (21) For information on other radical cyanomethylation methods, see: Donald, J. R.; Berrell, S. L. Radical cyanomethylation via vinyl azide cascade-fragmentation. *Chem. Sci.* **2019**, *10*, 5832–5836. and references therein.
- (22) (a) Welin, E. R.; Warkentin, A. A.; Conrad, J. C.; MacMillan, D. W. C. Enantioselective α -Alkylation of Aldehydes by Photoredox Organocatalysis: Rapid Access to Pharmacophore Fragments from β -Cyanaldehydes. *Angew. Chem., Int. Ed.* **2015**, *54*, 9668–9672. (b) Chang, Q.; Liu, Z.; Liu, P.; Sun, P. Visible-Light-Induced Regioselective Cyanomethylation of Imidazopyridines and Its Application in Drug Synthesis. *J. Org. Chem.* **2017**, *82*, 5391–5397. (c) O'Brien, C. J.; Droegge, D. G.; Jiu, A. Y.; Gandhi, S. S.; Paras, N. A.; Olson, S. H.; Conrad, J. Photoredox Cyanomethylation of Indoles: Catalyst Modification and Mechanism. *J. Org. Chem.* **2018**, *83*, 8926–8935.
- (23) For useful background on the reduction of haloacetonitriles, see: Isse, A. A.; Gennaro, A. Homogeneous Reduction of Haloacetonitriles by Electrogenerated Aromatic Radical Anions: Determination of the Reduction Potential of $\bullet\text{CH}_2\text{CN}$. *J. Phys. Chem. A* **2004**, *108*, 4180–4186.
- (24) Note that a 20–24 h reaction time was used in most of the substrate scoping phase of this study for convenience and consistency,

but reduced reaction times may be possible in some cases (see page 9 of the Supporting Information).

(25) Chaudhary, R.; Natarajan, P. Visible Light Photoredox Activation of Sulfonyl Chlorides: Applications in Organic Synthesis. *ChemistrySelect* **2017**, *2*, 6458–6479.

(26) CCDC 2087802 and 2087806 contain the crystallographic data for compounds **13a** and **13b**.

(27) An interesting and complementary sulfonylative spirocyclization method was published as we were finalizing this paper for submission, based on the generation of sulfonyl radicals from DABCO-(SO₂)₂ and aryldiazonium salts. See: Chen, Z.; Zhang, H.; Zhou, S.-F.; Cui, X. Metal-Free Sulfonylative Spirocyclization of Indolyl-ynones via Insertion of Sulfur Dioxide: Access to Sulfonated Spiro[cyclopentenone-1,3'-indoles]. *Org. Lett.* **2021**, *23*, 7992.

(28) Cheng, Y.; Yuan, X.; Ma, J.; Yu, S. Direct Aromatic C–H Trifluoromethylation via an Electron-Donor–Acceptor Complex. *Chem.–Eur. J.* **2015**, *21*, 8355–8359.

(29) (a) Ueng, S.-H.; Solovyev, A.; Yuan, X.; Geib, S. J.; Fensterbank, L.; Lacôte, E.; Malacria, M.; Newcomb, M.; Walton, J. C.; Curran, D. P. N-Heterocyclic Carbene Boryl Radicals: A New Class of Boron-Centered Radical. *J. Am. Chem. Soc.* **2009**, *131*, 11256–11262. (b) Taniguchi, T. Advances in Chemistry of N-Heterocyclic Carbene Boryl Radicals. *Chem. Soc. Rev.* **2021**, *50*, 8995–9021.

(30) Based on the reported redox potentials of the *Ir(III) excited state ($E_{1/2}^{IV/*III} = -1.91$ V vs SCE) and bromoacetonitrile ($E_{1/2}^{red} = -0.69$ V vs SCE) it is highly likely that this step is thermodynamically favorable. For redox potentials, see ref 23 and also: Teegardin, K.; Day, J. I.; Weaver, J. Advances in Photocatalysis: A Microreview of Visible Light Mediated Ruthenium and Iridium Catalyzed Organic Transformations. *Org. Process Res. Dev.* **2016**, *20*, 1156–1163.

(31) Constantin, T.; Zanini, M.; Regni, A.; Sheikh, N. S.; Juliá, F.; Leonori, D. Aminoalkyl radicals as halogen-atom transfer agents for activation of alkyl and aryl halides. *Science* **2020**, *367*, 1021–1026.

(32) Alvarez, E. M.; Karl, T.; Berger, F.; Torkowski, L.; Ritter, T. Late-Stage Heteroarylation of Hetero(Aryl)Sulfonium Salts Activated by α -Amino Alkyl Radicals. *Angew. Chem., Int. Ed.* **2021**, *60*, 13609–13613.

Recommended by ACS

Modular Counter-Fischer–Indole Synthesis through Radical–Enolate Coupling

Hyunho Chung, Hong Geun Lee, *et al.*

JANUARY 08, 2021
ORGANIC LETTERS

READ 

Selectivity, Speciation, and Substrate Control in the Gold-Catalyzed Coupling of Indoles and Alkynes

Ryan G. Epton, Jason M. Lynam, *et al.*

FEBRUARY 10, 2022
ORGANOMETALLICS

READ 

Divergent Annulative C–C Coupling of Indoles Initiated by Manganese-Catalyzed C–H Activation

Bingxian Liu, Xingwei Li, *et al.*

AUGUST 31, 2018
ACS CATALYSIS

READ 

Tandem Construction of Indole-Fused Phthalazines from (2-Alkynylbenzylidene)hydrazines under Metal-Free Conditions

Zhaojiang Shi, Xiuling Cui, *et al.*

FEBRUARY 07, 2020
THE JOURNAL OF ORGANIC CHEMISTRY

READ 

Get More Suggestions >

Selectivity, Speciation, and Substrate Control in the Gold-Catalyzed Coupling of Indoles and Alkynes

Ryan G. Epton, William P. Unsworth,* and Jason M. Lynam*

Cite This: *Organometallics* 2022, 41, 497–507

Read Online

ACCESS |

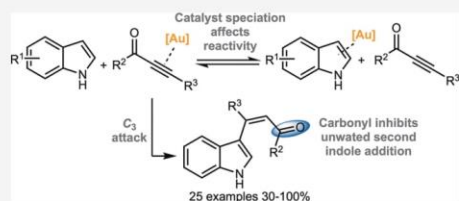
Metrics & More

Article Recommendations

Supporting Information

Downloaded via UNIV OF YORK on July 12, 2022 at 16:08:03 (UTC). See https://pubs.acs.org/sharingguidelines for options on how to legitimately share published articles.

ABSTRACT: A convenient and mild protocol for the gold-catalyzed intermolecular coupling of substituted indoles with carbonyl-functionalized alkynes to give vinyl indoles is reported. This reaction affords 3-substituted indoles in high yield, and in contrast to the analogous reactions with simple alkynes which give bisindolemethanes, only a single indole is added to the alkyne. The protocol is robust and tolerates substitution at a range of positions of the indole and the use of ester-, amide-, and ketone-substituted alkynes. The use of 3-substituted indoles as substrates results in the introduction of the vinyl substituent at the 2-position of the ring. A combined experimental and computational mechanistic study has revealed that the gold catalyst has a greater affinity to the indole than the alkyne, despite the carbon–carbon bond formation step proceeding through an $\eta^2(\pi)$ -alkyne complex, which helps to explain the stark differences between the intra- and intermolecular variants of the reaction. This study also demonstrated that the addition of a second indole to the carbonyl-containing vinyl indole products is both kinetically and thermodynamically less favored than in the case of more simple alkynes, providing an explanation for the observed selectivity. Finally, a highly unusual gold-promoted alkyne dimerization reaction to form a substituted gold pyrrolium salt has been identified and studied in detail.



INTRODUCTION

Gold-catalyzed carbon–carbon and carbon–heteroatom bond formation reactions are powerful and synthetically versatile transformations. Coordination of an unsaturated substrate, such as an alkene or alkyne to an electrophilic Au(I) or Au(III) center, results in activation toward nucleophilic attack, and this has been exploited in a wide range of intra- and intermolecular coupling reactions.^{1,2}

We have recently demonstrated how gold(I) catalysts promote intramolecular C–C bond formation in ynone-tethered indoles **1** to afford carbazoles **3** (Scheme 1A).³ Alternative catalysts such as AgOTf result in the formation of spirocycles **4**.^{4–7} DFT calculations suggest that carbon–carbon bond formation proceeds by nucleophilic attack onto a gold- or silver-bound alkyne (**1** → **2**).^{8,9} The calculations indicate that the spirocycle **4** is a kinetic product, formed through indole C₃-attack onto the activated alkyne, and carbazole **3** is the thermodynamic product, formed through the corresponding C₂-addition when the spirocyclization step is reversible. In all cases the calculated transition states for carbon–carbon bond formation are located at low energy (<41 kJ mol⁻¹ with respect to the reference state) and the C–C bond formation (**1** → **2**) step was calculated to be almost barrierless. These results, and others,^{10–17} demonstrate the synthetic versatility of **1** as a framework to access a range of important structural motifs.

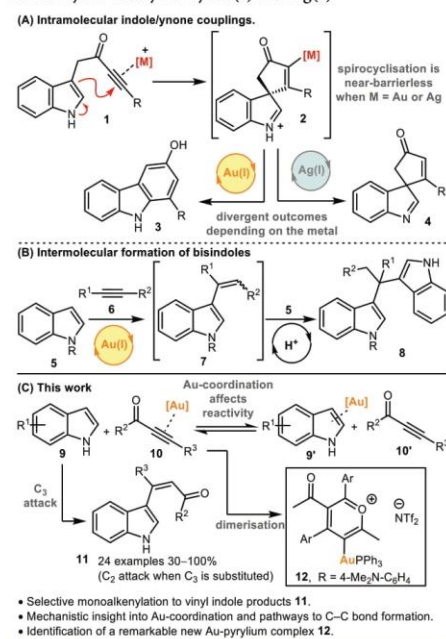
The ease with which ynone-tethered indoles **1** can be converted into scaffolds **3** and **4** provided encouragement that hitherto unknown intermolecular variants could be developed to

enable the facile C–H alkenylation of simple, unfunctionalized indoles.^{18–21} 3-Vinyl indoles (e.g., **7**, Scheme 1B) are highly important molecules, both as synthetic building blocks for biologically significant indole-based drugs and natural products, and in their own right, with various biologically active 3-vinyl indoles and methods to synthesize them known.^{22–27} However, making 3-vinyl indoles via the gold-catalyzed coupling of indoles and alkynes is challenging; while the required coupling reaction (**6** → **7**, Scheme 1B) can be promoted using gold catalysis, the vinyl indole products **7** undergo rapid reaction with a second molecule of indole to form bisindolemethanes **8**.^{28–30} It is possible to inhibit the second indole addition by designing systems in which the monofunctionalized intermediate is trapped in situ (e.g., in a cyclization with a tethered nucleophile),^{28,31} but this approach does not allow access to vinyl indoles like **7**. Recently, Lee and co-workers have shown that vinyl indoles can be prepared in excellent yield from the reaction of 2-substituted indoles with an excess of alkyne at low gold catalyst loadings, although with indole itself, bisindolemethanes were still generated.³² While this could be circum-

Received: January 19, 2022

Published: February 10, 2022



Scheme 1. Intra- and Intermolecular Reactions of Indoles with Alkynes Catalyzed by Au(I) and Ag(I)


vented through the use of a 2-boryl-substituted indole and subsequent deprotection, the selective monoalkenylation of unsubstituted indole remains an unsolved challenge.

The formation of the *bisindolemethanes* follows an interesting mechanistic pathway. Both experimental³³ and computational³⁴ data with indole and pyrrole nucleophiles indicate that the initial coupling with the alkyne is gold-catalyzed, whereas the subsequent addition of the second heterocycle to vinyl 7 is Brønsted acid-catalyzed. Protonation occurs at the alkene group of the vinyl indole to give a carbocation which is then attacked by another molecule of indole; even in cases where no Brønsted acidic reagents are used, trace acid formed in situ is usually sufficient to promote this transformation.^{5,35} Avoiding *bisindolemethane* formation is therefore a significant challenge, but one we were confident could be overcome by harnessing the unique reactivity of ynone.^{3,5,8,9,11,13} In our previous work, we have shown that the electron-withdrawing carbonyl group of the ynone moiety can significantly enhance the reactivity of the alkyne when treated with a Au(I) catalyst. This enables ynone to be coupled with indoles under very mild conditions. Furthermore, the same carbonyl group has been shown to suppress Brønsted acid-catalyzed migration reactions in the resulting products—both features were postulated to promote the selective formation of the desired vinylindoles 11 in this study (Scheme 1C).

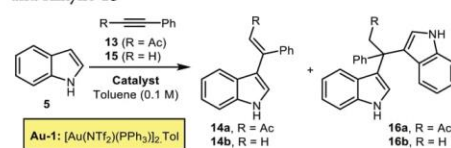
The successful realization of this strategy is reported herein. A simple method for the synthesis of a range of vinyl indoles 11 has been established, using a cationic gold(I) catalyst to promote the coupling of indoles and ynone, as well as other electron

deficient ester- and amide-based alkyne derivatives (Scheme 1C). Our theory that the carbonyl group can enhance the first vinylation reaction but suppress subsequent reactions appears to be valid, given that reactions proceed under mild conditions and *bisindolemethane* formation is completely avoided. A series of mechanistic and computational experiments have also been performed that enable a deeper understanding of the nature of the states involved in C–C bond formation, and help to explain how the site of Au-coordination both influences the regioselectivity of the vinylindole formation and accounts for the stark difference in reactivity between the intermolecular and intramolecular variants. An investigation into the speciation of the gold catalyst is also presented, which enabled the identification of a novel gold pyriliun complex 12, arising from the dimerization of two ynone.

RESULTS AND DISCUSSION

Catalyst Optimization and Synthetic Scope. Our initial experiments focused on assessing the intermolecular addition of indole 5 to ynone 13, as a like-for-like comparison with the intramolecular cyclization of 1: the results are summarized in Table 1. First, AgOTf, Cu(OTf)₂ and SnCl₂·2H₂O were tested,

Table 1. Intermolecular Reaction of Indole 5 with Ynone 13 and Alkyne 15

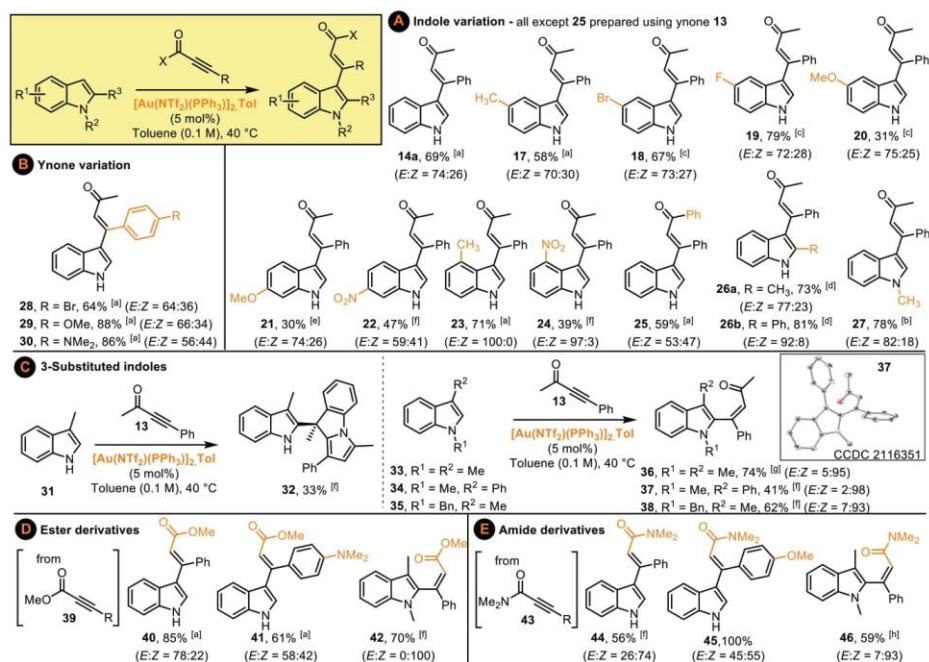


entry	alkyne ^a	catalyst	temp (°C)	time (h)	product ^b (E/Z)
1	13	AgOTf (10 mol %)	RT	24	–
2	13	Cu(OTf) ₂ (10 mol %)	RT	24	–
3	13	SnCl ₂ ·2H ₂ O (10 mol %)	RT	24	–
4	13	Au-1 (5 mol %)	RT	24	14a, 90% (73:27)
5	13 ^c	Au-1 (5 mol %)	40	2	14a, 100% (71:29)
6	15 ^d	Au-1 (5 mol %)	40	2	16b, 81%
7	15 ^d	Au-1 (5 mol %) C ₂ CO ₃ (10 mol %)	40	16	16b trace
8	15 ^d	Au-1 (5 mol %) NEt ₃ (10 mol %)	40	16	–

^a1.0 equiv unless stated. ^bConversion determined by the ratio of remaining indole to both geometrical isomers of 14 by ¹H NMR spectroscopy. ^c1.5 equiv of 13 was used. ^d1.5 equiv of 15 was used.

as these reagents were found to be excellent catalysts for the intramolecular spirocyclization of indoles 1 into 4 in our previous work (Scheme 1A). However, all were ineffective in this reaction; no consumption of either 5 or 13 was observed when analyzed using ¹H NMR spectroscopy. A more reactive catalyst was therefore sought, and the Gagosz catalyst [Au(NTf₂)(PPh₃)₂]₂·Tol (Au-1) was chosen for its well-known activity and ready availability.³⁶ Pleasingly, Au-1 effectively catalyzed the coupling, promoting 90% conversion into vinyl indole 14a at room temperature (entry 4) at 5 mol % catalyst loading, with further optimization enabling complete conversion into 14a at 40 °C over 2 h (entry 5; for additional optimization experiments see the Supporting Information). The vinyl indole

Scheme 2. Selective Gold-Catalyzed Monovinylolation of Indoles with Electron Deficient Alkynes



^a2 h reaction time. ^b3 h reaction time. ^c18 h reaction time. ^d19 h reaction time. ^e21 h reaction time at room temperature. ^f24 h reaction time. ^g27 h reaction time. ^h48 h reaction time.

product 14 was formed as a mixture of *E*- and *Z*-isomers, which are believed to equilibrate in solution. The formal electrophilic addition occurred at the C₃-position of the indole as expected, and pleasingly, no evidence for the formation bisindolemethane product 16a was obtained. This contrasts starkly to the reaction outcome when indole 5 was reacted with phenyl acetylene 15 under the same conditions; in this case the only product observed was bisindolemethane 16b.

Attempts to suppress the formation of 16b by adding basic additives to quench trace Brønsted acid formation were unsuccessful with the basic additives inhibiting the reaction (entries 7–8).

With conditions for intermolecular indole-ynone coupling established, attention next moved to exploring the scope of the reaction. Variation of the indole coupling partner was first examined, with a range of indoles bearing electronically diverse substituents around the benzenoid portion tested, and all performed well under the standard conditions (14–25 Scheme 2A). Pleasingly, functionalization on the pyrrole ring of the indole is also tolerated, with indoles bearing C₂- and N₁-substituents formed in good yields (26a, 26b, 27, Scheme 2A). The ynone coupling partner can also be varied, which is noteworthy given that the electronic properties of the ynone can have a major influence on reaction efficiencies in related processes (28–30, Scheme 2B).

We were also keen to examine the reactivity of an indole substrate in which the more reactive C₃-position is blocked, and therefore ynone 13 was reacted with skatole 31 (Scheme 2C). Either C₂-vinylation or dearomative C₃-difunctionalisation were considered to be the two most likely outcomes in this case, but neither of these products were isolated; instead, the dominant component of the reaction mixture was the three-component reaction product 32. This product presumably formed via an initial C₂-vinylation, followed by a cascade process, analogous to that previously observed by Tian and co-workers for a related system treated under Brønsted acid-catalyzed conditions.³⁷ The formation of 32 was encouraging nonetheless, as it demonstrated that C₂-addition to skatole was occurring, but a subsequent condensation reaction did not allow isolation of the desired vinylindole product. Pleasingly, the introduction of an *N*-substituent prevented the three-component coupling, with indoles 33–35 all being converted into vinylindoles 36–38 in good yields, with selective vinylation at the indole C₃-position. Finally, we tested whether other electron deficient alkynes may react similarly to ynone, and pleasingly, ester- (40–42, Scheme 2D) and amide-based (44–46, Scheme 2E) products were formed in good to excellent yields in the same way. These reactions are practically very simple to perform, and across all reaction series, the only change needed to the standard method was to vary the reaction time (based on TLC analysis). Most products were isolated as mixtures of geometrical isomers, with

the observed *E/Z* ratios believed to be thermodynamic outcomes, resulting from facile alkene isomerism enabled by conjugation of the electron-rich indole into the carbonyl. For products formed via vinylation at the indole C_3 -position, the *E* isomer tends to predominate, based on chemical shift trends, nOe studies, and comparisons to literature NMR data (see Supporting Information).³⁸ In C_2 -vinylation examples (36–38, 42, 46) the *Z* isomer is formed as the major geometrical isomer, with the assignment of product 37 based on X-ray crystallographic data³⁹ and the others by analogy.

Experimental and Computational Mechanistic Studies. The results from the synthetic studies raised a number of mechanistic questions about the pathways underpinning the formation of the substituted indole compounds. These were as follows:

- What is the origin of the selectivity for a 1:1 coupling in these reactions, compared to the more conventional addition of two molecules of indole to the alkyne to give a bisindolemethane?
- What factors influence the stark difference in the relative ease of the intra- and intermolecular variants of the coupling between an indole and ynone?
- What controls the C_2 versus C_3 regioselectivity addition to the indole, especially when the C_3 position is substituted?

A combined experimental and computational mechanistic study was undertaken to address these questions. In the first instance, the interactions between the gold catalyst $[\text{Au}(\text{NTf}_2)(\text{PPh}_3)]_2 \cdot \text{Tol}$ and the individual alkyne and heterocyclic substrates were investigated; the idea here was that a better understanding of gold speciation with respect to both reaction components would shed light on the observed reactivity, both in the intra- and intermolecular variants. $^{31}\text{P}\{^1\text{H}\}$ NMR spectroscopy was therefore used to study the speciation, and these experimental data were compared to calculations using density functional theory (DFT). Full details of the computational methods are provided in the Supporting Information, and all energies quoted are Gibbs energies in kJ mol^{-1} at 298.15 K. In the calculations the gold catalyst was treated as $[\text{Au}(\text{PPh}_3)]^+$. Experimentally, there is evidence of solvent-dependent ion-pairing in these systems,^{40–42} and we have investigated the potential effects computationally (see Supporting Information).

The interaction between a range of substituted alkynes and $[\text{Au}(\text{PPh}_3)]^+$ was studied first. As shown in Figure 1a, the gold has the potential to exhibit either $\eta^1(\text{O})$ -binding, A, or $\eta^2(\pi)$ binding, B, to the alkynes. It was reasoned that the energy balance between these different binding modes would be influenced by changes to the substituents on the phenyl-ring of the alkyne, and whether a ketone, amide, or ester substituent was present.

The energy balance between states A and B was evaluated by DFT for a range of substituted alkynes (Figure 1a). Two important trends were evident in the data. First, using an amide-substituted alkyne (see 48 and 49) is predicted to increase the relative stability of the O-bound form, A. Second, the introduction of an electron-donating NMe_2 -group into the 4-position of the alkyne should have the opposite effect and increase the affinity of the $\eta^2(\pi)$ -bound form, C (see 47, 49, and 51).

These predictions were supported by experimental data which used $^{31}\text{P}\{^1\text{H}\}$ NMR spectroscopy to probe the speciation of the gold complex in solution. Experiments performed with DMF and $\text{PhC}_2\text{C}_6\text{H}_4\text{-4-NMe}_2$ provided reference spectra for $\eta^1(\text{O})$

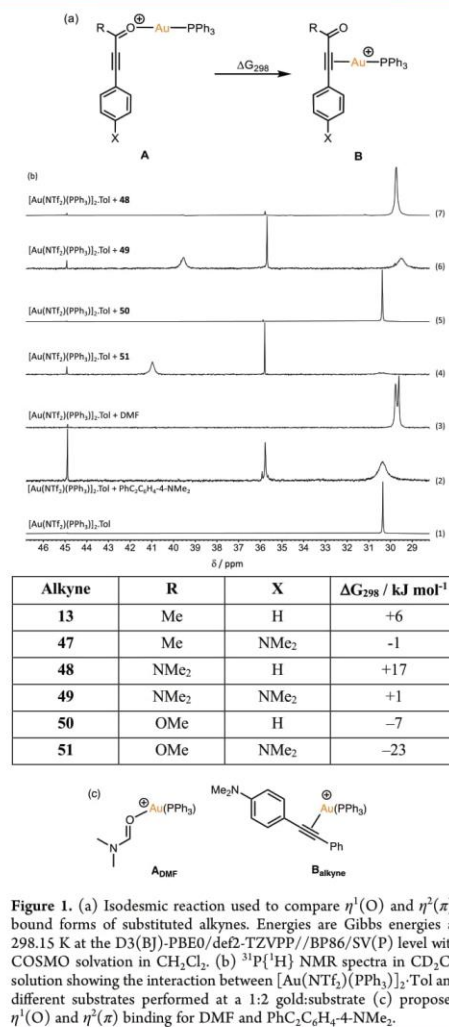


Figure 1. (a) Isodesmic reaction used to compare $\eta^1(\text{O})$ and $\eta^2(\pi)$ -bound forms of substituted alkynes. Energies are Gibbs energies at 298.15 K at the D3(BJ)-PBE0/def2-TZVPP//BP86/SV(P) level with COSMO solvation in CH_2Cl_2 . (b) $^{31}\text{P}\{^1\text{H}\}$ NMR spectra in CD_2Cl_2 solution showing the interaction between $[\text{Au}(\text{NTf}_2)(\text{PPh}_3)]_2 \cdot \text{Tol}$ and different substrates performed at a 1:2 gold:substrate (c) proposed $\eta^1(\text{O})$ and $\eta^2(\pi)$ binding for DMF and $\text{PhC}_2\text{C}_6\text{H}_4\text{-4-NMe}_2$.

(A_{DMF}) and $\eta^2(\pi)$ binding (B_{alkyne}), respectively (Figure 1b, spectra (2) and (3), Figure 1c). Spectrum (4), obtained after treatment of a CH_2Cl_2 solution of $[\text{Au}(\text{NTf}_2)(\text{PPh}_3)]_2 \cdot \text{Tol}$ with 51, exhibited a sharp resonance at δ 35.8, consistent with the $\eta^2(\pi)$ -alkyne coordination mode, B, being the dominant form. A resonance at δ 41.0 was assigned to the formation of a product arising from alkyne dimerization which will be discussed in detail later. An analogous reaction with 50, which lacks the NMe_2 -group on the aryl ring, did not show any change when compared with $[\text{Au}(\text{NTf}_2)(\text{PPh}_3)]_2 \cdot \text{Tol}$, spectrum (5). However, spectrum (7), obtained from a reaction with amide 48, was dominated by a sharp single resonance at δ 29.7, consistent

with binding mode A. Using amide **49**, which also possessed a NMe₂ substituent on the aryl group, showed evidence for both $\eta^1(\text{O})$ and $\eta^2(\pi)$ binding, spectrum (6). Several spectra exhibited a resonance at δ_p 45.5, which is likely due to $[\text{Au}(\text{PPh}_3)_2]^+$ on the basis of a comparison with an authentic sample.

Next, the relative affinity of the gold cation toward the triple bonds of a range of alkynes was evaluated through a series of calculated isodesmic reactions (Figure 2). The change in free

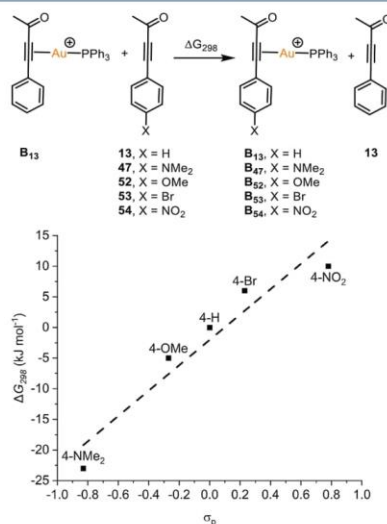


Figure 2. Isodesmic reaction used to calculate affinity of alkynes for gold. Energies are Gibbs energies at 298.15 K at the D3(BJ)-PBE0/def2-TZVPP//BP86/SV(P) level with COSMO solvation in CH₂Cl₂ (top). Linear free energy relationship between the calculated change in free energy against Hammett parameter σ_p (bottom). Dashed line shows fit to a least mean squares linear regression ($R^2 = 0.92$).

energy for alkyne substitution of the parent complex B₁₃ by alkynes with various substituents in the 4-position of the phenyl ring was calculated using DFT. These data demonstrate the presence of a linear free energy relationship between the relative energy change on binding to the gold and the Hammett (σ_p) parameter of the aryl substituent. The positive slope indicates that electron-donating groups favor $\eta^2(\pi)$ -alkyne coordination to the gold cation. This is consistent with alkyne binding being a net donor to the gold with π -backdonation to the vacant π^* -orbitals on the ligand (a key factor affecting the stability of midtransition metal alkyne complexes) not being a dominant effect.^{43,44}

The predicted enhanced affinity for the gold cation by electron-rich alkynes was supported by ³¹P{¹H} NMR spectroscopy. Reaction of $[\text{Au}(\text{NTf}_2)(\text{PPh}_3)_2]\text{Tol}$ with 10 equiv of bromine-substituted alkyne **53** resulted in little change to the ³¹P{¹H} NMR spectrum (Figure 3, spectrum (4)) with only a small amount of starting material consumed.⁴⁵ The corresponding reaction with **13** resulted in a complex series of resonances in the region between δ 40 and 45: the resonance for $[\text{Au}(\text{NTf}_2)$

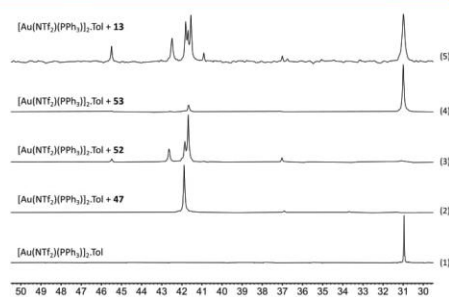


Figure 3. ³¹P{¹H} NMR spectra of a mixture of $[\text{Au}(\text{NTf}_2)(\text{PPh}_3)_2]\text{Tol}$ and ynones in a 1:10 gold:substrate ratio in CD₂Cl₂ solution.

$[\text{PPh}_3]_2\text{Tol}$ was still present (spectrum (5)). In contrast, in spectrum (3) when the 4-OMe-substituted alkyne, **52**, was used almost all of the starting material was consumed and again a series of new resonances between δ 40 and 45 were observed. A resonance at δ 37.0 was also present which, by analogy of the results in Figure 2, may represent a complex with an $\eta^2(\pi)$ -bound alkyne. Reaction between $[\text{Au}(\text{NTf}_2)(\text{PPh}_3)_2]\text{Tol}$ and 10 equiv of NMe₂-substituted **47** resulted in a single new resonance at δ_p 41.9. The chemical shift of this resonance is markedly different from those assigned to the $\eta^1(\text{O})$ and $\eta^2(\pi)$ -alkyne (Figure 2), which typically appear at δ_p 29 and 35, respectively. The species responsible for the resonance at δ_p 41.9 was identified as a gold-substituted pyrylium salt and is discussed later.

These results demonstrate that the gold cation may readily coordinate to the alkyne and that electronic effects have a significant influence on the binding mode (i.e., $\eta^1(\text{O})$ versus $\eta^2(\pi)$ -alkyne), with electron-donating substituents on the aryl substituent favoring the required $\eta^2(\pi)$ -alkyne binding.

Next, potential gold coordination to the indole component was examined. Although the carbon–carbon bond formation step in the vinylation reaction was expected to occur through nucleophilic attack of the indole onto a gold-coordinated alkyne, we reasoned that the indoles could also be suitable ligands for the Au(I) cations themselves, and thus compete for the catalyst with the ynone. Experimental evidence for this interaction between the gold and heterocycle was obtained through a series of titrations between $[\text{Au}(\text{NTf}_2)(\text{PPh}_3)_2]\text{Tol}$ and indole, **5**, or skatole, **31**, in CD₂Cl₂ solution, monitored by ³¹P{¹H} NMR spectroscopy. In both cases, the appearance of the spectra was concentration-dependent (Figure 4). For indole, a broad resonance was observed at all $[\text{Au}(\text{NTf}_2)(\text{PPh}_3)_2]\text{Tol}:\text{S}$ ratios, with a shift to lower field of ca. 4.3 ppm when moving from a 1:1 to a 1:10 ratio. For skatole, a single sharp resonance was observed, which exhibited a smaller concentration-dependent change in chemical shift.

These ³¹P{¹H} NMR studies support the suggestion that the heterocycles may indeed bind to the gold cation. DFT calculations allowed for the relative binding affinity of $[\text{Au}(\text{PPh}_3)]^+$ toward indole **5** and skatole **31** when compared to the alkyne **13** to be evaluated (Scheme 3). Binding of the $[\text{Au}(\text{PPh}_3)]^+$ to the five-membered ring of **5** and **31** was successfully modeled as states C₅ and C₃₁ respectively. These were taken as the reference states for the calculations with the addition of one molecule of ynone **13**. Coordination of the

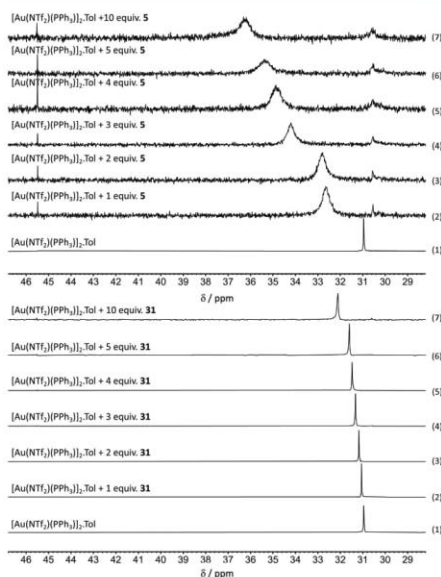
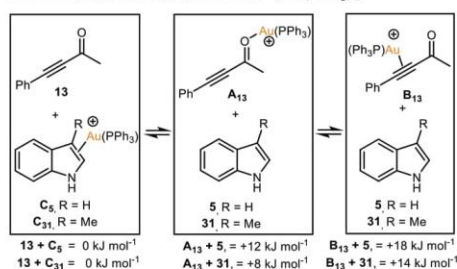


Figure 4. $^{31}\text{P}\{^1\text{H}\}$ NMR spectra of $[\text{Au}(\text{NTf}_2)(\text{PPh}_3)]_2 \cdot \text{Tol}$ with different ratios of **5** (top) and **31** (bottom) in CD_2Cl_2 .

Scheme 3. Relative Changes in Free Energy on Coordination of Indole, 5, Skatole, 31, and 13 to $[\text{Au}(\text{PPh}_3)]^{+a}$

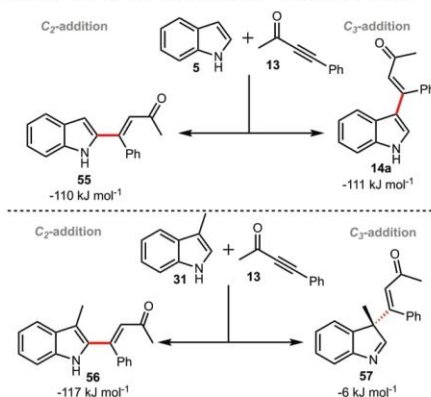


^aEnergies are Gibbs energies at 298.15 K at the D3(BJ)-PBE0/def2-TZVPP//BP86/SV(P) level with COSMO solvation in toluene.

$[\text{Au}(\text{PPh}_3)]^+$ to the carbonyl group of the ynone is endergonic (+12 and +8 kJ mol^{-1} for indole and skatole, respectively), whereas $\eta^2(\pi)$ -coordination of the alkyne lies at +18 and +14 kJ mol^{-1} for indole and skatole, respectively. This is a remarkable prediction as the prevailing mechanistic view of gold-catalyzed reactions of this type is that the metal activates the alkyne toward nucleophilic addition via $\eta^2(\pi)$ -coordination of the alkyne.

The pathways controlling the formation of the vinyl indoles were investigated next. In the first instance, the thermodynamic preference for C_2 - and C_3 -addition of the alkyne to indole and skatole were calculated. (Scheme 4). For indole, the experimentally observed C_3 -addition to produce **14** is exergonic

Scheme 4. DFT-Calculated Changes in Energy for Products Arising from C_2 - and C_3 -Addition to Indole and Skatole^a



^aEnergies are Gibbs energies at 298.15 K at the D3(BJ)-PBE0/def2-TZVPP//BP86/SV(P) level with COSMO solvation in toluene.

by -111 kJ mol^{-1} : the thermodynamic driving force for C_2 -addition to produce **55** is essentially identical (-110 kJ mol^{-1}). The C_3 -regioselectivity of the reaction between **5** and **13** is therefore predicted to be kinetic in nature. In the skatole case, C_3 -addition will produce **57**, which is the intermolecular analogue of the spirocycle **4** (Scheme 1). As a consequence of the methyl group at the site of substitution, **57** is not able to rearomatize, which is reflected in the fact it lies at only -6 kJ mol^{-1} with respect to **31** and **13**. The C_2 -addition product, **56**, which has rearomatized following a formal proton migration, is exergonic by -117 kJ mol^{-1} , broadly in line with the addition to indole **5**.

With these data strongly indicating that the C_3 -selectivity for the reaction is kinetic in nature, transition states for C–C bond formation were sought to support this using DFT. States for the addition of the indole to a gold-coordinated alkyne, **B**, could be readily located; however, the corresponding pathways associated with the addition of the ynone to a coordinated indole (C_5) could not be found. A pathway for the addition of indole to the O-coordinated alkyne, **A**, was located, but at much higher energy than the pathway via **B** (see Supporting Information). These data support the supposition that the reaction proceeds via addition of indole to an $\eta^2(\pi)$ gold-coordinated ynone, despite the heterocycle being a better ligand for the metal.

Transition states for C_3 - and C_2 -addition of **5** to **B** were located ($\text{TS}_{\text{BD-H}}$ and $\text{TS}_{\text{BF-H}}$) at +59 and +67 kJ mol^{-1} , respectively (Figure 5). Although the difference in energy is small, C_3 -addition through $\text{TS}_{\text{CD-H}}$ was found to be the lower energy pathway at all levels of theory employed (see Supporting Information). A Dynamic Reaction Coordinate (DRC) analysis indicated that $\text{TS}_{\text{BD-H}}$ connected state B_H with Wheland-type intermediate D_H . Attempts to optimize the geometry of D_H resulted in E_H in which a hydrogen atom had migrated to the oxygen of the ynone, resulting in rearomatization of the indole. This may indicate that D_H sits in a shallow minimum and, similarly, attempts to optimize F_H (which DRC predicts connects to **B** via $\text{TS}_{\text{BF-H}}$) resulted in G_H .

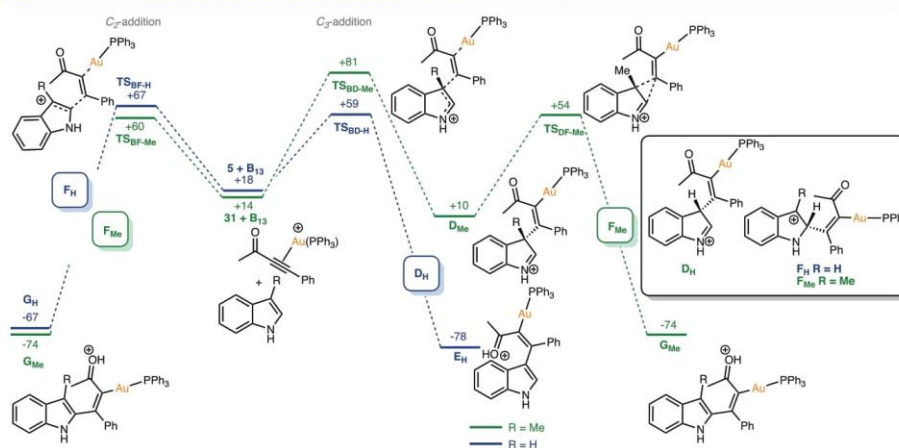


Figure 5. DFT-calculated pathways for the addition of **5** or **31** to gold-coordinated alkyne complex **B**₁₃. Energies are Gibbs energies in kJ mol^{-1} at 298.15 K at the D3(BJ)-PBE0/def2-TZVPP//BP86/SV(P) level with COSMO solvation in toluene.

For skatole **31** the kinetic preference for the site of attack was reversed. Here, C_2 -addition via $\text{TS}_{\text{BF-Me}}$ lies at $+60 \text{ kJ mol}^{-1}$, whereas $\text{TS}_{\text{BE-Me}}$ was located at $+81 \text{ kJ mol}^{-1}$. Again, attempts to optimize F_{Me} resulted in G_{Me} . However, in the case of C_3 -addition via $\text{TS}_{\text{BD-Me}}$ it was possible to optimize the corresponding states D_{Me} ($+10 \text{ kJ mol}^{-1}$), presumably as hydrogen migration is not possible in this Wheland intermediate. Instead, a transition state for vinyl migration was located ($\text{TS}_{\text{DF-Me}}$) at $+54 \text{ kJ mol}^{-1}$. This leads to G_{Me} , again presumably via F_{Me} . A transition state for methyl migration was also obtained, but this was at higher energy (see Supporting Information). These data therefore indicate that both C_2 - and C_3 -addition pathways for addition to skatole will lead to **32**, although the former route is kinetically preferred.

The data also provide an explanation for the difference in reactivity between the intra- and intermolecular systems. There is clearly a greater entropic penalty in the case of the intermolecular coupling reaction; however, the stronger binding of the gold cation to the indole when compared to the alkyne will also inhibit access to the product-forming pathways. Binding to the indole is still possible in the case of the intramolecular pathway; however, the preorganized structure of the substrate may enable low energy π -slippage events^{46–48} leading to alkyne coordination without the necessity for loss of the metal. In the intermolecular case, this is not possible and decoordination of the gold followed by re-coordination in the thermodynamically less preferred binding mode is required.

With the origin of the site-selectivity of the reaction established, the factors controlling single versus double addition of the indole to alkynes were then investigated. In the case of the system derived from the ynone substrate, the relative thermodynamic free energy change for the formation of **16a** from **14a** and **5** (Scheme 5a) was calculated to be -3 kJ mol^{-1} . In the case of the corresponding system based on phenylacetylene, the formation of **16b** from **15b** and **5** was found to have much greater change in free energy ($\Delta G_{298} = -25 \text{ kJ mol}^{-1}$, Scheme 5b). These data indicate that in the case of the ynone

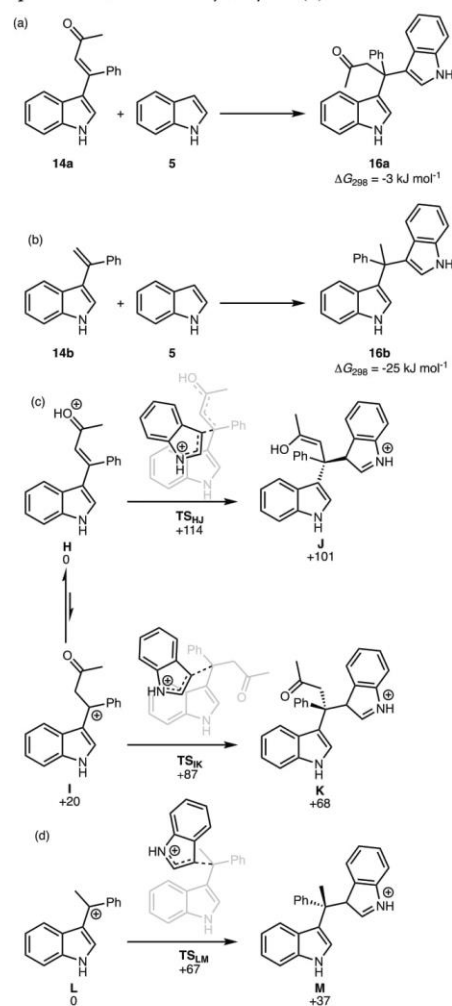
system there is, at best, only a very small thermodynamic driving force for the addition of a second indole to **14a**.

The kinetic factors controlling this difference in reactivity between the two systems were also investigated. As previous experimental and computational work had established that the addition of a second indole molecule to vinyl indoles was acid-catalyzed,^{33,34} analogous processes were calculated for the addition of a second molecule of indole to vinyl indole **14** (Scheme 5c). Protonation of **14** could be envisaged to occur at either the carbonyl groups to give **H** or the alkene to give **I**. Cation **H**, which was taken as the reference state for this series of calculations, was found to be 20 kJ mol^{-1} more stable than **I**. Transition states for the addition of indole to both **H** and **I** (TS_{IH} and TS_{IK}) were located at $+114$ and $+87 \text{ kJ mol}^{-1}$ respectively. The transition state for the analogous phenylacetylene-derived product (TS_{LM} , Scheme 5d) lies at $+67 \text{ kJ mol}^{-1}$ with respect to the cation precursor and the coupled product **M** lies at lower energy than those derived from **14** ($+101$ and $+68 \text{ kJ mol}^{-1}$ for **J** and **K**, respectively).

The precise putative pathway for the addition of the second indole in the ynone system will depend on the relative rate of proton transfer between **H** and **I** (if this is rapid and an equilibrium concentration of **I** is present, then the energetic span will be 87 kJ mol^{-1} , otherwise it will be 114 kJ mol^{-1}). However, it is evident the addition of a second indole to either cation of the ynone-derived system has a higher barrier than for the phenylacetylene derivative. In the ynone case, the resulting cationic intermediates **J** and **K** lie at a significantly higher relative energy than in the phenylacetylene case, **M**.

At the start of this study, we postulated that the introduction of the carbonyl group on the alkynes might reduce the proclivity of the vinylindole product to undergo additional reactions with indole, and this notion was borne out in the synthetic reactions featured in Scheme 2. Further, it is supported by the DFT data, with the carbonyl-based system facing significantly higher kinetic barriers for the addition of a second indole compared to the analogous simple alkyne system, and there is a negligible thermodynamic driving force for this process.

Scheme 5. DFT-Calculated Pathways for the Acid Catalyst Addition to Vinylindole **14** (a) and the Corresponding Species Derived from Phenylacetylene (b)^a

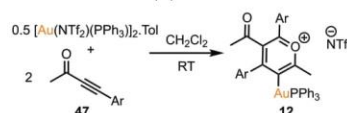


^aEnergies are Gibbs energies at 298.15 K (in kJ mol^{-1} for (c) and (d)) at the D3(BJ)-PBE0/def2-TZVPP//BP86/SV(P) level with COSMO solvation in CH_2Cl_2 .

Identification of a Novel Gold-Coordinated Pyrylium Salt from Alkyne Coupling. The NMR studies designed to investigate the interaction of substituted ynone with $[\text{Au}(\text{NTf}_2)(\text{PPh}_3)_2]\text{Tol}$ had demonstrated that a selective reaction occurred when **47** was employed. Specifically, the addition of 2 equiv of **47** to a CD_2Cl_2 solution of Au^{I} complex $[\text{Au}(\text{NTf}_2)$

$(\text{PPh}_3)_2]\text{Tol}$ resulted in an immediate change in color to deep red and the formation of **12**, as shown by the resonance in the $^{31}\text{P}\{^1\text{H}\}$ NMR spectrum at δ_{p} 41.9. Although all attempts to isolate **12** from the reaction mixture were unsuccessful, a combination of spectroscopic methods demonstrated that the product was a gold-substituted pyrylium salt,⁴⁹ arising from the dimerization of two ynone (Scheme 6).

Scheme 6. Formation of Pyrylium Salt **12**^a



^aAr = C_6H_4 -4-NMe₂.

The ESI mass spectrum of the solution exhibited a peak at $m/z = 833.2579$ consistent with **12** having the composition $[\text{Au}(\text{47})_2(\text{PPh}_3)]^+$; that is, 2 equiv of the alkyne had been incorporated into the coordination sphere of the metal. The $^{13}\text{C}\{^1\text{H}\}$ NMR spectrum (Figure 6) exhibited a series of

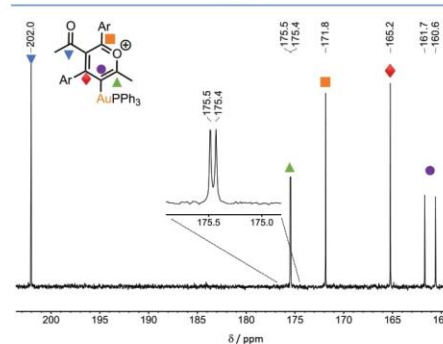


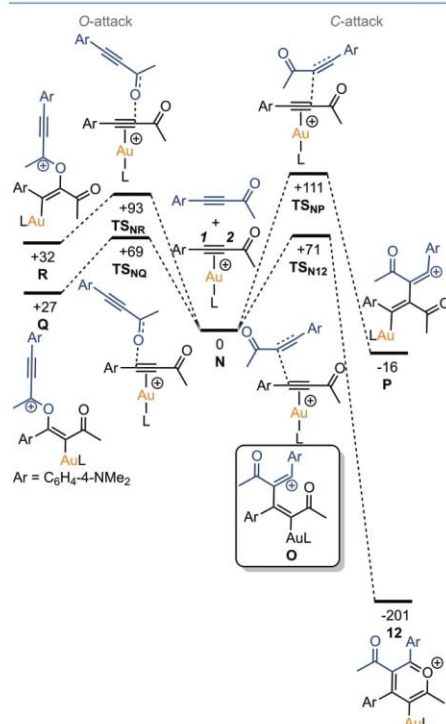
Figure 6. Expansion of a $^{13}\text{C}\{^1\text{H}\}$ NMR spectrum of **12** in CD_2Cl_2 solution. Ar = C_6H_4 -4-NMe₂.

resonances consistent with the formulation of **12** as a pyrylium complex. For example, a doublet resonance at δ 161.4 ($^2J_{\text{PC}} = 111.2 \text{ Hz}$) is consistent with a gold-bound carbon atom and compares favorably with the corresponding resonance in $[\text{Au}(\text{C}_6\text{H}_2\text{-}2,4,6\text{-Me}_3)(\text{PPh}_3)]$ (δ 169.8, $^2J_{\text{PC}} = 111.2 \text{ Hz}$).⁵⁰ A doublet resonance at δ 175.5 ($^3J_{\text{PC}} = 5.4 \text{ Hz}$) and singlets at δ 171.8 and 165.2 were observed whose chemical shifts are characteristic of carbon atoms in the 2, 4, and 6 positions of a pyrylium salt. Two resonances for the NMe₂ groups were observed, indicating that two ynone had been incorporated into **12** but in different environments. Moreover, only a single resonance was observed in the carbonyl region at δ 202.0, indicating that one acyl group had been modified significantly during the reaction, which is again consistent with pyrylium formation.

The gold-mediated intramolecular coupling of alkynes is a common reaction pathway. However, corresponding intermolecular routes are scarce.^{51–53} Establishing the mechanistic pathways that lead to **12** is therefore important in understanding

this unusual product formation. The initial dimerization step was anticipated to occur through nucleophilic attack at an $\eta^2(\pi)$ -coordinated complex of ynone **47**, by either the carbonyl (O-attack) or C \equiv C group (C-attack) of another molecule of ynone **47**.

DFT calculations were used to distinguish between these possibilities and the results are shown in Figure 7. The alkyne complex **B**₄₇ and a molecule of ynone **47** was taken as the reference state for the calculations, collectively referred to as **N**. Considering first C-attack, transition state **TS**_{N12} (located at +71 kJ mol⁻¹) involves addition of the carbonyl-substituted carbon of **47** onto the aryl-substituted carbon (C1) of the gold-



Ar	L	TS _{N12}	TS _{NQ}	Q	12
C ₆ H ₄ -4-NMe ₂	PPh ₃	+71	+69	+27	-201
C ₆ H ₅	PPh ₃	+75	+63	+23	-224
C ₆ H ₄ -4-OMe	PPh ₃	+69	+61	+20	-220
C ₆ H ₄ -4-NMe ₂	PMe ₃	+61	+70	+33	-197
C ₆ H ₄ -4-NMe ₂	IPr	+77	+77	+33	-198
C ₆ H ₄ -4-NMe ₂	JohnPhos	+70	+75	+37	-199

Figure 7. DFT-calculated pathways for the gold-mediated dimerization of alkynes. All energies are Gibbs energies at 298.15 K in kJ mol⁻¹ at the D3(BJ)-PBE0/def2-TZVPP//BP86/SV(P) level with COSMO solvation in CH₂Cl₂.

coordinated alkyne. Attempts to optimize structure **O** (the expected state arising from **TS**_{N12}) were unsuccessful: in all cases, pyrylium complex **12** was obtained. This may indicate that **O** either sits in a very shallow minimum or that **TS**_{N12} is a bifurcated transition state proceeding directly to **12**. The transition state for C-attack at C2 proceeds through **TS**_{NP}, which is at much higher energy (+111 kJ mol⁻¹) than **TS**_{N12} so is uncompetitive.

The alternative O-attack by **47** onto **CI** of **B**₄₇ proceeds to give alkenyl complex **Q** through **TS**_{NQ} (+69 kJ mol⁻¹), which lies at a similar energy to **TS**_{N12} (+71 kJ mol⁻¹). As with the C-attack pathway, addition to C2 lies at considerably higher energy in the O-attack case (**TS**_{NR} + 93 kJ mol⁻¹) and therefore can be discounted. On the basis of the energies of **TS**_{NQ} and **TS**_{N12} it is likely that both O- and C-attack pathways operate, but it appears that pyrylium complex formation can only take place via C-attack, as all attempts to find a pathway by which **Q** might itself rearrange into **12** were unsuccessful. In this case, it is likely that **Q** is an off-cycle complex in equilibrium with the starting materials **N**, and because **Q** lies at higher energy than the reference state (and **12** much lower), the irreversible formation of **12** through **TS**_{N12} predominates.

We were also interested to learn why in the synthetic NMR experiments described earlier (Figure 3), selective pyrylium formation was only observed when using electron rich ynone **47**. Therefore, the calculations were repeated for the two lowest energy O- and C- attack pathways to evaluate the effects of different substituents on the ynone and the ligand on gold (Figure 7). Overall, the ligand effects are small, but the most notable observation is that in the case of the C₆H₅-substituted ynone **13**, the corresponding transition state leading to the pyrylium complex **TS**_{N12} lies at 12 kJ mol⁻¹ higher in energy than the O-attack pathway. This need not rule out selective pyrylium formation if the reaction remains under thermodynamic control, but side reactions resulting from **Q** are also possible. For example, **Q** could potentially be converted into a cyclic complex, via a mechanism related to that observed in the gold-catalyzed 1,3-O-transposition of ynone (see Supporting Information for details).⁵⁴ Thus, the experimental observation that the reaction of C₆H₅-substituted ynone **13** is much less selective than it is for the C₆H₄-4-NMe₂-substituted case is likely a consequence of an increased kinetic preference for **Q** resulting in more side-reactions.

CONCLUSIONS

The use of carbonyl-substituted alkynes as coupling partners in the gold-catalyzed coupling with indoles has unlocked a well-controlled pathway enabling selective monovinylation to give vinyl indoles. DFT calculations reveal that there is both a kinetic and thermodynamic component to the observed selectivity, with the carbonyl group destabilizing the intermediate carbocations and related transition states for C–C addition when compared to more conventional substrates. It is clear that the outcome of the reaction is controlled by the nature of the alkyne substrate, with control reactions with phenylacetylene giving the expected bisindolemethane.

To account for the difference between the intra-^{3,5,7,8} and intermolecular variants of the coupling reaction, there is presumably an entropic component, but also important is the somewhat surprising observation that the gold catalyst shows a thermodynamic preference for binding to the indole, rather than the alkyne. This may also explain the lack of activity of other Lewis acid catalysts in the intermolecular reactions as it is not

unreasonable to expect that the most potent nucleophile in the reaction is also the best ligand for the metal.

The observation of a product arising from the coupling of two alkynes within the coordination sphere of gold is remarkable. Although related pyrylium salts have been frequently proposed in the gold-catalyzed intramolecular coupling of alkynes with tethered carbonyl groups,^{55,56} and may be isolated,⁵⁷ the observation of **12** is a unusual example of an intermolecular addition and may offer the potential for future synthetic findings.

■ ASSOCIATED CONTENT

Supporting Information

The Supporting Information is available free of charge at <https://pubs.acs.org/doi/10.1021/acs.organomet.2c00035>.

Structure data (XYZ)

Experimental details and spectroscopic data for the compounds prepared in this work; Details of the computational methodology employed, an evaluation of anion effects, and collated energies and coordinates (PDF)

Accession Codes

CCDC 2116351 contains the supplementary crystallographic data for this paper. These data can be obtained free of charge via www.ccdc.cam.ac.uk/data_request/cif, or by emailing data_request@ccdc.cam.ac.uk, or by contacting The Cambridge Crystallographic Data Centre, 12 Union Road, Cambridge CB2 1EZ, UK; fax: +44 1223 336033.

■ AUTHOR INFORMATION

Corresponding Authors

William P. Unsworth – Department of Chemistry, University of York, York YO10 5DD, U.K.; orcid.org/0000-0002-9169-5156; Email: william.unsworth@york.ac.uk

Jason M. Lynam – Department of Chemistry, University of York, York YO10 5DD, U.K.; orcid.org/0000-0003-0103-9479; Email: jason.lynam@york.ac.uk

Author

Ryan G. Epton – Department of Chemistry, University of York, York YO10 5DD, U.K.; orcid.org/0000-0001-7717-7339

Complete contact information is available at:

<https://pubs.acs.org/doi/10.1021/acs.organomet.2c00035>

Notes

The authors declare no competing financial interest.

■ ACKNOWLEDGMENTS

We are grateful to the University of York (Ph.D. studentship to R.G.E. and the provision of an Eleanor Dodson Fellowship to W.P.U.) and the EPSRC (EP/H011455/1 and EP/K031589/1) for funding computational equipment used in this study. We thank Dr. Michael James (University of York) for insightful comments on this manuscript. We are grateful to Dr. Adrian Whitwood for the single crystal X-ray structure of **37**.

■ REFERENCES

- (1) Campeau, D.; León Rayo, D. F.; Mansour, A.; Muratov, K.; Gagosz, F. Gold-catalyzed reactions of specially activated alkynes, allenes, and alkenes. *Chem. Rev.* **2021**, *121*, 8756–8867.
- (2) Halliday, C. J. V.; Lynam, J. M. Gold-alkynyls in catalysis: Alkyne activation, gold cumulenes and nuclearity. *Dalton Trans.* **2016**, *45*, 12611–12626.

- (3) Liddon, J. T. R.; Rossi-Ashton, J. A.; Clarke, A. K.; Lynam, J. M.; Taylor, R. J. K.; Unsworth, W. P. Divergent reactivity of indole-tethered ynones with silver(I) and gold(I) catalysts: A combined synthetic and computational study. *Synthesis* **2018**, *50*, 4829–4836.

- (4) James, M. J.; Cuthbertson, J. D.; O'Brien, P.; Taylor, R. J.; Unsworth, W. P. Silver(I)- or copper(II)-mediated dearomatization of aromatic ynones: Direct access to spirocyclic scaffolds. *Angew. Chem., Int. Ed. Engl.* **2015**, *54*, 7640–7643.

- (5) James, M. J.; Clubley, R. E.; Palate, K. Y.; Procter, T. J.; Wyton, A. C.; O'Brien, P.; Taylor, R. J. K.; Unsworth, W. P. Silver(I)-catalyzed dearomatization of alkyne-tethered indoles: Divergent synthesis of spirocyclic indolenines and carbazoles. *Org. Lett.* **2015**, *17*, 4372–4375.

- (6) Clarke, A. K.; James, M. J.; O'Brien, P.; Taylor, R. J. K.; Unsworth, W. P. Silica-supported silver nitrate as a highly active dearomatizing spirocyclization catalyst: Synergistic alkyne activation by silver nanoparticles and silica. *Angew. Chem., Int. Ed.* **2016**, *55*, 13798–13802.

- (7) Liddon, J. T. R.; James, M. J.; Clarke, A. K.; O'Brien, P.; Taylor, R. J. K.; Unsworth, W. P. Catalyst-driven scaffold diversity: Selective synthesis of spirocycles, carbazoles and quinolines from indolyl ynones. *Chem. Eur. J.* **2016**, *22*, 8777–8780.

- (8) Clarke, A. K.; Lynam, J. M.; Taylor, R. J. K.; Unsworth, W. P. "Back-to-front" indole synthesis using silver(I) catalysis: Unexpected C-3 pyrrole activation mode supported by DFT. *ACS Catal.* **2018**, *8*, 6844–6850.

- (9) Epton, R. G.; Clarke, A. K.; Taylor, R. J. K.; Unsworth, W. P.; Lynam, J. M. Synthetic and mechanistic studies into the rearrangement of spirocyclic indolenines into quinolines. *Eur. J. Org. Chem.* **2019**, *2019*, 5563–5571.

- (10) James, M. J.; O'Brien, P.; Taylor, R. J. K.; Unsworth, W. P. Selective synthesis of six products from a single indolyl α -diazocarbonyl precursor. *Angew. Chem., Int. Ed.* **2016**, *55*, 9671–9675.

- (11) Rossi-Ashton, J. A.; Clarke, A. K.; Taylor, R. J. K.; Unsworth, W. P. Modular synthesis of polycyclic alkaloid scaffolds via an enantioselective dearomative cascade. *Org. Lett.* **2020**, *22*, 1175–1181.

- (12) Inprung, N.; James, M. J.; Taylor, R. J. K.; Unsworth, W. P. A thiol-mediated three-step ring expansion cascade for the conversion of indoles into functionalized quinolines. *Org. Lett.* **2021**, *23*, 2063–2068.

- (13) Ho, H. E.; Pagano, A.; Rossi-Ashton, J. A.; Donald, J. R.; Epton, R. G.; Churchill, J. C.; James, M. J.; O'Brien, P.; Taylor, R. J. K.; Unsworth, W. P. Visible-light-induced intramolecular charge transfer in the radical spirocyclisation of indole-tethered ynones. *Chem. Sci.* **2020**, *11*, 1353–1360.

- (14) Han, G. F.; Xue, L.; Zhao, L. L.; Zhu, T. Z.; Hou, J. L.; Song, Y. G.; Liu, Y. P. Access to CF₃-containing cyclopentaquinolone derivatives from indolyl-ynones via silver-catalyzed one-pot reaction. *Adv. Synth. Catal.* **2019**, *361*, 678–682.

- (15) Fedoseev, P.; Coppola, G.; Ojeda, G. M.; Van der Eycken, E. V. Synthesis of spiroindolenines by intramolecular ipso-iodocyclization of indol ynones. *Chem. Commun.* **2018**, *54*, 3625–3628.

- (16) Fedoseev, P.; Van der Eycken, E. Temperature switchable bronsted acid-promoted selective syntheses of spiro-indolenines and quinolines. *Chem. Commun.* **2017**, *53*, 7732–7735.

- (17) Inprung, N.; Ho, H. E.; Rossi-Ashton, J. A.; Epton, R. G.; Whitwood, A. C.; Lynam, J. M.; Taylor, R. J. K.; James, M. J.; Unsworth, W. P. Indole-ynones as privileged substrates for radical dearomatizing spirocyclization cascades. *Org. Lett.* **2022**, *24*, 668–674.

- (18) Grimster, N. P.; Gauntlett, C.; Godfrey, C. R.; Gaunt, M. J. Palladium-catalyzed intermolecular alkenylation of indoles by solvent-controlled regioselective C–H functionalization. *Angew. Chem., Int. Ed.* **2005**, *44*, 3125–3129.

- (19) Gorsline, B. J.; Wang, L.; Ren, P.; Carrow, B. P. C–H alkenylation of heteroarenes: Mechanism, rate, and selectivity changes enabled by thioether ligands. *J. Am. Chem. Soc.* **2017**, *139*, 9605–9614.

- (20) Gemoets, H. P.; Hessel, V.; Noel, T. Aerobic C–H olefination of indoles via a cross-dehydrogenative coupling in continuous flow. *Org. Lett.* **2014**, *16*, 5800–3.

- (21) Chen, W. L.; Gao, Y. R.; Mao, S.; Zhang, Y. L.; Wang, Y. F.; Wang, Y. Q. Palladium-catalyzed intermolecular C3 alkenylation of indoles using oxygen as the oxidant. *Org. Lett.* **2012**, *14*, 5920–5923.

- (22) Kumar, D.; Kumar, N. M.; Akamatsu, K.; Kusaka, E.; Harada, H.; Ito, T. Synthesis and biological evaluation of indolyl chalcones as antitumor agents. *Bioorg. Med. Chem. Lett.* **2010**, *20*, 3916–3919.
- (23) Dolusic, E.; Larrieu, P.; Moineaux, L.; Stroobant, V.; Pilotte, L.; Colau, D.; Pochet, L.; Van den Eynde, B.; Masereel, B.; Wouters, J.; Frederick, R. Tryptophan 2,3-dioxygenase (TDO) inhibitors. 3-(2-(pyridyl)ethenyl)indoles as potential anticancer immunomodulators. *J. Med. Chem.* **2011**, *54*, 5320–5334.
- (24) Robinson, M. W.; Overmeyer, J. H.; Young, A. M.; Erhardt, P. W.; Maltese, W. A. Synthesis and evaluation of indole-based chalcones as inducers of methuosis, a novel type of nonapoptotic cell death. *J. Med. Chem.* **2012**, *55*, 1940–1956.
- (25) Venkatesan, A. M.; Dos Santos, O.; Ellingboe, J.; Evrard, D. A.; Harrison, B. L.; Smith, D. L.; Scerni, R.; Hornby, G. A.; Schechter, L. E.; Andree, T. H. Novel benzofuran derivatives with dual 5-HT_{1A} receptor and serotonin transporter affinity. *Bioorg. Med. Chem. Lett.* **2010**, *20*, 824–827.
- (26) Steuer, C.; Gege, C.; Fischl, W.; Heinonen, K. H.; Bartschlagler, R.; Klein, C. D. Synthesis and biological evaluation of alpha-ketoamides as inhibitors of the dengue virus protease with antiviral activity in cell culture. *Bioorg. Med. Chem.* **2011**, *19*, 4067–4074.
- (27) For recent discussion of 3-vinylindole synthesis via methods other than C–H alkenylation, see: Barbero, M.; Dughera, S.; Alberti, S.; Ghigo, G. A simple, direct synthesis of 3-vinylindoles from the carbocation-catalyzed dehydrative cross-coupling of ketones and indoles. A combined experimental and computational study. *Tetrahedron* **2019**, *75*, 363–373 and references cited therein.
- (28) Ferrer, C.; Amijs, C. H. M.; Echavarren, A. M. Intra- and intermolecular reactions of indoles with alkynes catalyzed by gold. *Chem. Eur. J.* **2007**, *13*, 1358–1373.
- (29) Li, Z.; Shi, Z.; He, C. Addition of heterocycles to electron deficient olefins and alkynes catalyzed by gold(III). *J. Organomet. Chem.* **2005**, *690*, 5049–5054.
- (30) Luo, C.; Yang, H.; Mao, R.; Lu, C.; Cheng, G. An efficient Au(I) catalyst for double hydroarylation of alkynes with heteroarenes. *New J. Chem.* **2015**, *39*, 3417–3423.
- (31) Leseurre, L.; Chao, C.-M.; Seki, T.; Genin, E.; Touillet, P. Y.; Genêt, J.-P.; Michelet, V. Synthesis of functionalized carbo- and heterocycles via gold-catalyzed cycloisomerization reactions of enynes. *Tetrahedron* **2009**, *65*, 1911–1918.
- (32) McLean, E. B.; Cutolo, F. M.; Cassidy, O. J.; Burns, D. J.; Lee, A.-L. Selectivity control in gold-catalyzed hydroarylation of alkynes with indoles: Application to unsymmetrical bis(indolyl)methanes. *Org. Lett.* **2020**, *22*, 6977–6981.
- (33) Schiefl, J.; Rudolph, M.; Hashmi, A. S. K. The gold-catalyzed hydroarylation of alkynes with electron-rich heteroarenes – a kinetic investigation and new synthetic possibilities. *Adv. Synth. Catal.* **2017**, *359*, 639–653.
- (34) Mehrabi, T.; Ariafard, A. The different roles of a cationic gold(I) complex in catalysing hydroarylation of alkynes and alkenes with a heterocycle. *Chem. Commun.* **2016**, *52*, 9422–9425.
- (35) Dang, T. T.; Boeck, F.; Hintermann, L. Hidden bronsted acid catalysis: Pathways of accidental or deliberate generation of triflic acid from metal triflates. *J. Org. Chem.* **2011**, *76*, 9353–9361.
- (36) Mezailes, N.; Ricard, L.; Gagosz, F. Phosphine gold(I) bis-(trifluoromethanesulfonyl)imidate complexes as new highly efficient and air-stable catalysts for the cycloisomerization of enynes. *Org. Lett.* **2005**, *7*, 4133–6. The catalyst used in this study was purchased from Sigma Aldrich and is formulated as [Au(NTf₂)(PPh₃)₂]₂·Toluene. The catalytic amounts used are based on this stoichiometry, and therefore the mol % of [Au(NTf₂)(PPh₃)] is double this amount.
- (37) Xu, K.; Chen, W.; Lin, J.; Chen, G.; Wang, B.; Tian, X. Facile synthesis of 9H-pyrrolo[1,2-a]indoles via Brønsted acid catalyzed cascade reactions. *Chem. Commun.* **2019**, *55*, 14613–14616.
- (38) Godoi, M. N.; de Azambuja, F.; Martinez, P. D. G.; Morgon, N. H.; Santos, V. G.; Regiani, T.; Lesage, D.; Dossmann, H.; Cole, R. B.; Eberlin, M. N.; Correia, C. R. D. Revisiting the intermolecular Fujiwara hydroarylation of alkynes. *Eur. J. Org. Chem.* **2017**, *2017*, 1794–1803.
- (39) CCDC 2116351 (compound 37) contains the crystallographic data for compounds, see: www.ccdc.cam.ac.uk/data_request/cif.
- (40) Pickup, O. J. S.; Khazal, I.; Smith, E. J.; Whitwood, A. C.; Lynam, J. M.; Bolaky, K.; King, T. C.; Rawe, B. W.; Fey, N. Computational discovery of stable transition-metal vinylidene complexes. *Organometallics* **2014**, *33*, 1751–1761.
- (41) Ciano, L.; Fey, N.; Halliday, C. J. V.; Lynam, J. M.; Milner, L. M.; Mistry, N.; Pridmore, N. E.; Townsend, N. S.; Whitwood, A. C. Dispersion, solvent and metal effects in the binding of gold cations to alkynyl ligands: Implications for Au(I) catalysis. *Chem. Commun.* **2015**, *51*, 9702–9705.
- (42) Given the similarity in chemical shift between the η¹(O)-bound complex, **A**, and [Au(NTf₂)(PPh₃)₂]₂·Tol, the possibility that the observed resonances could be assigned to binding mode **A** cannot be excluded.
- (43) Lu, Z.; Han, J.; Okoromoba, O. E.; Shimizu, N.; Amii, H.; Tormena, C. F.; Hammond, G. B.; Xu, B. Predicting counterion effects using a gold affinity index and a hydrogen bonding basicity index. *Org. Lett.* **2017**, *19*, 5848–5851.
- (44) Lu, Z.; Li, T.; Mudshinge, S. R.; Xu, B.; Hammond, G. B. Optimization of catalysts and conditions in gold(I) catalysis-counterion and additive effects. *Chem. Rev.* **2021**, *121*, 8452–8477.
- (45) Zuccaccia, D.; Belpassi, L.; Tarantelli, F.; Macchioni, A. Ion pairing in cationic olefin-gold(I) complexes. *J. Am. Chem. Soc.* **2009**, *131*, 3170–3171.
- (46) Orbach, M.; Shankar, S.; Zenkina, O. V.; Milko, P.; Diskin-Posner, Y.; van der Boom, M. E. Generation of mono- and bimetallic palladium complexes and mechanistic insight into an operative metal ring-walking process. *Organometallics* **2015**, *34*, 1098–1106.
- (47) Hammarback, L. A.; Clark, I. P.; Sazanovich, I. V.; Towrie, M.; Robinson, A.; Clarke, F.; Meyer, S.; Fairlamb, I. J. S.; Lynam, J. M. Mapping out the key carbon-carbon bond-forming steps in Mn-catalyzed C–H functionalization. *Nat. Catal.* **2018**, *1*, 830–840.
- (48) Yahya, N. P.; Appleby, K. M.; Teh, M.; Wagner, C.; Troschke, E.; Bray, J. T. W.; Duckett, S. B.; Hammarback, L. A.; Ward, J. S.; Milani, J.; Pridmore, N. E.; Whitwood, A. C.; Lynam, J. M.; Fairlamb, I. J. S. Manganese(I)-catalyzed C–H activation: The key role of a 7-membered manganacycle in H-transfer and reductive elimination. *Angew. Chem., Int. Ed.* **2016**, *55*, 12455–12459.
- (49) Balaban, A. T.; Wray, V. ¹³C N.M.R. Spectra of some pyrylium salts and related compounds. *Org. Mag. Res.* **1977**, *9*, 16–22.
- (50) Croix, C.; Ballard-Longeau, A.; Allouchi, H.; Giorgi, M.; Duchêne, A.; Thibonnet, J. Organogold(I) complexes: Synthesis, X-ray crystal structures and aurophilicity. *J. Organomet. Chem.* **2005**, *690*, 4835–4843.
- (51) García-Fernández, P. D.; Iglesias-Sigüenza, J.; Rivero-Jerez, P. S.; Díez, E.; Gómez-Bengoa, E.; Fernández, R.; Lassaletta, J. M. AuI-catalyzed hydroalkynylation of haloalkynes. *J. Am. Chem. Soc.* **2020**, *142*, 16082–16089.
- (52) Kreuzahler, M.; Haberhauer, G. Cyclopropenylmethyl cation: A concealed intermediate in gold(I)-catalyzed reactions. *Angew. Chem., Int. Ed.* **2020**, *59*, 17739–17749.
- (53) Kreuzahler, M.; Haberhauer, G. Gold(I)-catalyzed haloalkynylation of aryl alkynes: Two pathways, one goal. *Angew. Chem., Int. Ed.* **2020**, *59*, 9433–9437.
- (54) Aikonen, S.; Muuronen, M.; Wirtanen, T.; Heikkinen, S.; Musgreave, J.; Burés, J.; Helaja, J. Gold(I)-catalyzed 1,3-O-transposition of ynones: Mechanism and catalytic acceleration with electron-rich aldehydes. *ACS Catal.* **2018**, *8*, 960–967.
- (55) Guo, B.; Zhou, Y.; Zhang, L.; Hua, R. Brønsted acid-promoted one-pot synthesis of chrysenes derivatives via isochromenylium intermediate formed in situ. *J. Org. Chem.* **2015**, *80*, 7635–7641.
- (56) Zhang, C.; Wang, G.; Zhan, L.; Yang, X.; Wang, J.; Wei, Y.; Xu, S.; Shi, M.; Zhang, J. Gold(I) or gold(III) as real intermediate species in gold-catalyzed cycloaddition reactions of enynal/enynone? *ACS Catal.* **2020**, *10*, 6682–6690.
- (57) Tomás-Mendivil, E.; Heinrich, C. F.; Ortuno, J.-C.; Starck, J.; Michelet, V. Gold-catalyzed access to 1H-isochromenes: Reaction development and mechanistic insight. *ACS Catal.* **2017**, *7*, 380–387.

DFT Studies of Au(I) Catalysed Reactions: Anion Effects and Reaction Selectivity

Ryan G. Epton,^{*,[a]} William P. Unsworth,^[a] and Jason M. Lynam^{*,[a]}

Abstract: Density functional theory (DFT) is a powerful tool that can aid in the exploration and development of synthetic chemistry, and its use is often applied in the chemistry of gold(I) catalysis. In this review, we discuss two different facets of these calculations – namely, the exploration and explanation of anion effects, and the regioselectivity and speciation of gold(I)-catalysed reactions. The research described herein clearly shows the importance of including

the anion in DFT studies of Au(I)-catalysed reactions, especially when using low polarity solvents, or where hydrogen-bonding is prevalent. Additionally, we show that whilst using DFT to study the selectivity of reactions can be successful, benchmarking the computational results against experimental data is vitally important for ensuring that the model is accurately describing the observed results.

Keywords: catalysis · gold · DFT · anion effects · π -acids

1. Introduction

Interest in gold catalysis has increased exponentially over the last 20 years.^[1] Primarily, the catalytic applications of gold(I) are based on its ability to act as a π -acid. Au(I) complexes are able to coordinate to and activate unsaturated C–C bonds, particularly alkynes,^[2] although similar reactivity has also been observed with alkenes^[3] and allenes.^[4] The typical mechanism proposed for gold(I)-catalysed reactions involves the coordination of the gold(I) complex to the unsaturated C–C bond, forming an $\eta^2(\pi)$ complex, which activates the π -system to undergo attack by a nucleophile (1→2). Protodemetalation then occurs (2→3), regenerating the Au(I) catalyst and allowing further reactions to take place (Figure 1).^[5]

The nature of the gold catalyst used, and its coordination environment, can have a significant effect on reaction outcomes. This may be by simply increasing the reaction yield, but in many cases, it can also alter the reaction selectivity and change the ratio of products that are formed. The ligand used can also influence the reaction outcomes, with phosphine or *N*-heterocyclic carbene (NHC) ligands being the most common, and the counterion used is also often altered during reaction optimisation.^[6]

Computational chemistry utilising density functional theory (DFT) is frequently used in studies of catalytic

reactions.^[7] DFT offers a good balance of calculation time versus accuracy and is, therefore, often the method of choice to explore the mechanism of transition metal catalysed reactions.

Papers benchmarking the success of DFT calculations to study gold(I) complexes have been published, which provide recommendations on the level of theory best employed for studying reactions using gold(I) catalysis.^[8] The double-hybrid B2PLYP functional performed well across multiple studies, with BP86,^[8b,d] PBE0,^[8c] wB97X^[8c] and M06^[8a,b] functionals also shown to be successful at modelling the energies and geometries of gold(I) complexes. Ahlrichs' def2 basis sets generally performed well, with a triple- ζ type basis set with polarisation recommended.^[8d] Electrostatic core potentials (ECPs) such as LANL2DZ or SDD are commonly used on the gold atom to account for relativistic effects.

In this review paper, we highlight potential considerations when using DFT to explore gold(I) catalysis. Recent examples of the use of DFT to explore reaction processes are provided, focussing on the effects of including the anions used in the reaction, and studying how DFT can be used to explore the selectivity of gold(I)-catalysed reactions. With a wide range of literature available, it was not possible to review them all, however other papers which were instructive are highlighted.^[9]

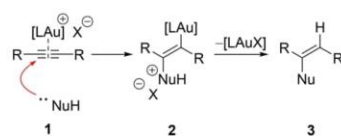


Figure 1. Typical scheme for alkyne activation by gold(I) cations.

[a] R. G. Epton, Dr. W. P. Unsworth, Dr. J. M. Lynam
Department of Chemistry, University of York
Heslington, York, YO10 5DD (UK)
E-mail: rge500@york.ac.uk
jason.lynam@york.ac.uk

© 2022 The Authors. Israel Journal of Chemistry published by Wiley-VCH GmbH. This is an open access article under the terms of the Creative Commons Attribution License, which permits use, distribution and reproduction in any medium, provided the original work is properly cited.

Review

Note, throughout this review, we use numbers to indicate compounds, whereas DFT calculated states are denoted by letters.

2. Using DFT to Explain the Effects of the Anion on the Reaction Mechanism

In reactions utilising gold(I) catalysts, typically a ligated gold(I) chloride (LAuCl) precatalyst is used, which is then activated by a metal salt containing a weakly coordinating anion. This results in salt metathesis, enabling the formation of an active Lewis acidic cationic gold(I) species (LAu⁺) in solution which is catalytically active.^[10] Other activation methods, such as protonolysis of an alkylgold and hydroxide species,^[11] or via sonication and centrifugation,^[12] have been used to avoid any competing “silver effects”.^[12,13]

Many studies utilising DFT methods have successfully captured the experimental reaction outcomes by focussing solely on the cationic gold-based component of the catalyst system without consideration of the counteranion.^[14] However, recent papers have detailed instances where optimising the counterion has been important for the course of the reaction.^[6,15]

In 2009, Tarantelli, Macchioni and co-workers studied ion pairing in cationic olefin-gold(I) complexes.^[16] Two 4-Me-styryl gold(I) complexes were synthesised with either a triphenylphosphine (**4PPh₃**) or NHC ligand (**4NHC**, NHC = 1,3-bis(di-*iso*-propylphenyl)-imidazol-2-ylidene) (Figure 2). Both complexes had a tetrafluoroborate anion which enabled the use of ¹⁹F,¹H-HOESY NMR experiments to study the preferred orientation of the anion with respect to the gold complex under low temperature conditions.

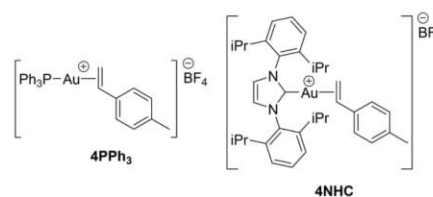


Figure 2. 4-Me-styryl gold(I) complexes studied by Zuccaccia *et al.*^[16]

These NMR studies showed that the choice of ligand influenced the ion-pairing (Figure 3), with strong contacts observed between the olefinic protons and the tetrafluoroborate anion in complex **4PPh₃**. In contrast, for complex **4NHC**, contacts were observed primarily with the imidazole protons furthest away from the styrene.

The observed NMR data were further supported by DFT calculations. Geometry optimisations (at the BLYP/ZORA/TZ2P level of theory) of varying configurations were performed, and these confirmed that the lowest energy arrangement of the complexes agreed with the NMR experiments (Figure 4).

This effect was rationalised by analysing the charge distribution and the Coulomb potential of both the styrene cationic complexes (Figure 5). The olefinic protons of the coordinated styrene and, in the case of complex **4NHC**, the imidazolium protons at the back of the complex were shown to have the greatest positive charge within the complex (denoted as a blue colour on the isodensity surface), and therefore be the most attractive points for counterion coordination.

Further studies examined the effects of changing both the ligand and the unsaturated hydrocarbon coordinated to the



Ryan G. Epton received his Masters' degree in 2018 at the University of Leicester, completing his Masters' research project under the supervision of Dr Sandeep Handa. Ryan then joined the University of York under the joint supervision of Dr William P Unsworth and Dr Jason M Lynam, where he is now in the final year of his Ph.D. studies. His current research interests are in the use of computational chemistry in organic synthesis and transition metal catalysis.



William P. Unsworth is a Senior Lecturer in Organic Chemistry at the University of York. His group's research interests include ring expansion approaches for the synthesis of medium-sized rings and macrocycles and the development of new catalytic methods, using metal-based catalysts, photochemical activation and biocatalysis. He has published over 60 peer reviewed papers to date won the RSC

Hickinbottom Award for his work on the synthesis of spirocycles and macrocycles.



Jason M. Lynam is a Reader in Inorganic Chemistry at the University of York. His group's research interests are focussed on mechanistic aspects of organometallic chemistry. This includes the application of computational chemistry and time-resolved spectroscopy to the study of metal-catalysed reactions. He has published over 110 peer reviewed papers and was a principal investigator in the team that was awarded the 2021 RSC Horizon Prize in Physical Organic Chemistry for work on unveiling the mechanistic steps in Mn-catalysed reactions.

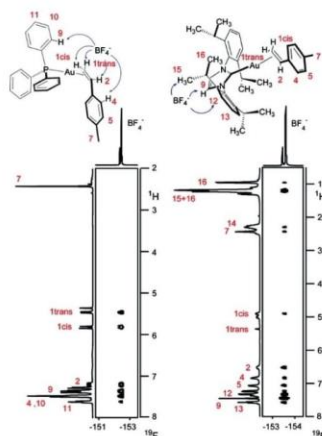


Figure 3. Low temperature ^{19}F , ^1H -HOESY spectra of **4PPh₃** (left) and **4NHC** (right). Key ion-pairing contacts have been highlighted with assignments made by Zuccaccia *et al.* Reprinted with permission from ref [16]. Copyright 2009 American Chemical Society.

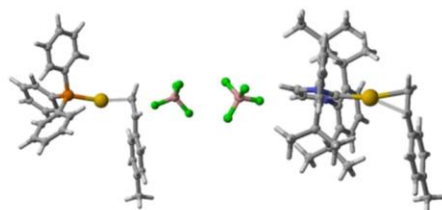


Figure 4. Lowest energy arrangements of **4PPh₃** (left) and **4NHC** (right) as calculated by DFT by Zuccaccia *et al.*, calculated at the BLYP/ZORA/TZ2P level of theory. Structures reproduced using coordinates located in the original paper's ESI.

gold(I) cation, which highlighted that the anion coordination depends greatly on the ligands in the cationic unit, with coordination most likely observed around the most acidic protons, rather than the gold centre.^[17–19]

This body of work has demonstrated that the location of the anion with respect to the catalytically active cation can be predicted and is often near the most positively charged sites within the complex, providing a starting point for other researchers to consider when including the counterion in their DFT calculations.

In 2021, an extensive report by Sorbelli *et al.* on the gold(I)-catalysed Meyer-Schuster rearrangement of 1-phenyl-2-propyn-1-ol **5** was published, particularly focused upon the effects of both the solvent and the counteranion on the

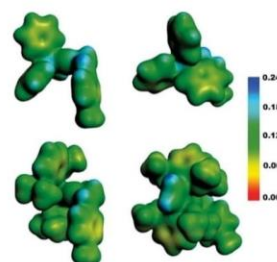


Figure 5. Side (left) and back (right) views of the DFT calculated structures of **4PPh₃** (top) and **4NHC** (bottom), without counterion. Coulomb potential is mapped on an electronic isodensity surface ($\rho = 0.007 \text{ e}/\text{\AA}^3$). Coulomb potential in au. Reprinted with permission from ref [16]. Copyright 2009 American Chemical Society.

turnover frequency (TOF) of the reaction.^[20] Experimentally, clear trends were found in the turnover frequency (TOF) of the reaction, with the efficiency of the reaction decreasing with increasing polarity of the solvent, and the specific counterion used ($\text{TfO}^- > \text{TsO}^- > \text{BF}_4^- > \text{TFA}^-$). Selected optimisation results are shown in Table 1.

The authors used DFT studies to rationalise these data. Formation of $\eta^2(\pi)$ -alkyne complex **B** from the uncoordinated species (**5** and **7**) was considered. Intermediates involved during de-coordination of the counterion demonstrated that the anion interacts with both the gold atom and the hydrogen of the terminal alkyne (Figure 6).

Whereas both the tosylate and triflate anions ($\text{X}^- = \text{TsO}^-$ and TfO^- , Figure 6) were predicted to be able to form complex

Table 1. NHCAuX catalysed Meyer-Schuster rearrangement of 1-phenyl-2-propyn-1-ol **5** to cinnamaldehyde **6** at 50 °C.

Entry	Solvent	Catalytic System ^[a]	Conv. ^[b] /%	TOF ^[c] /h ⁻¹
1	<i>p</i> -Cymene	NHCAuOTf	91	394
2	<i>p</i> -Cymene	NHCAuCl/ AgOTf ^[d]	11	44
3	<i>p</i> -Cymene	NHCAuCl/ AgTFA ^[d]	0.4	2
4	<i>p</i> -Cymene	NHCAuCl/ AgBF ₄ ^[d]	7	28
5	<i>p</i> -Cymene	NHCAuCl/ AgOTf ^[d]	30	115
6	γ -Valerolactone	NHCAuOTf	23	105

[a] NHCAuOTf (0.0025 mmol), **5** (0.5 mmol), solvent (200 μL). [b] Determined by the average value of three measurements after 30 minutes by ^1H NMR. [c] $\text{TOF} = (\text{mol}_{\text{product}}/\text{mol}_{\text{catalyst}})/t$ calculated after 30 minutes. [d] 1.1 eq of silver salt used. NHC = 1,3-bis(*di*-isopropylphenyl)-imidazol-2-ylidene

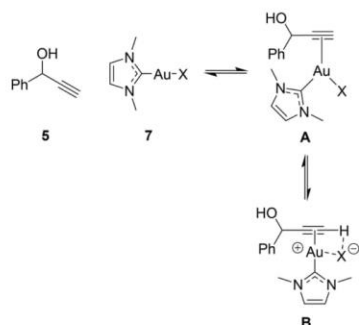


Figure 6. Proposed intermediate structures calculated for the formation of $\eta^2(\pi)$ -alkyne complex **B** from the uncoordinated species **5** and **7**.

B, a low-lying transition state (+4.2 kcal mol⁻¹ from **5** and **7** at the BP86/ZORA/B2PLYP/CPCM level of theory) was found when trifluoroacetate was calculated as the anion (X=TFA, Figure 6), in which the alkyne was deprotonated, resulting in σ -bonded gold alkynyl complex **8** (Figure 7). It was postulated that this was the reason behind the poorest efficiency observed in the experiments using AgTFA as the co-catalyst.

The proposed mechanism for the Meyer-Schuster rearrangement, and the intermediates studied, are shown in Figure 8. To explain the difference in reactivity when using the other anions (namely OTf⁻, OTs⁻ and BF₄⁻), the energies of the proposed transition states and intermediates involved in

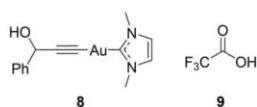


Figure 7. σ -Bonded gold alkynyl complex **8** with the formation of acid **9**, calculated by DFT when trifluoroacetate was the counterion.

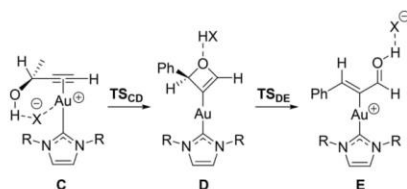


Figure 8. Intermediates studied in the Meyer-Schuster rearrangement of **5**. X=OTs, OTf or BF₄. A simplified NHC was used in the calculations (R=Me).

the catalytic cycle were calculated (BP86/ZORA/D3//B2PLYP/CPCM), with the anion proposed to coordinate to the alcohol of the starting material. The authors found that the first transition state (**TS_{CD}**), corresponding to attack of the alcohol into the gold-coordinated alkyne, was the highest energy, and the relative energies for the three counterions were consistent with the experimental data, in which the triflate was fastest (+32.6 kcal mol⁻¹ relative to **C**), followed by the tosylate (+34.3 kcal mol⁻¹) and then the tetrafluoroborate (+36.9 kcal mol⁻¹). The authors proposed that the main factors in the energy of transition state (**TS_{CD}**) were the hydrogen-accepting ability of the anion, and how well the anion coordinates to the gold atom.

Finally, the effect of solvent polarity was also considered. In low polarity media it is understood that an ion pair is formed due to the solvent's inability to strongly coordinate the cation and anion. In more polar solvents, solvation of the cation and anion is efficient, separating the ions.^[21] This effect was studied by explicitly modelling a molecule of γ -valerolactone to coordinate to the alcohol. Whilst a structure for the equivalent oxetene intermediate (**D**, Figure 8) couldn't be found, the transition state for a one-step process was calculated (**F**, Figure 9) which showed a higher energy than the triflate-assisted process (+33.4 vs +31.6 kcal mol⁻¹ in the gas phase at the BP86/ZORA/D3//B2PLYP level of theory), which is consistent with the experimental observations.

Overall, the study demonstrates how DFT enables the rationalisation of the reaction rates with different anions, in both the formation of the active catalytic species, and then also in the key intramolecular cyclisation step of the catalytic cycle. Insight from computational chemistry was also able to rationalise the solvent effects, in that higher polarity solvents restrict the ability for the anion to participate, with higher energy transition states observed.

In 2021, Hussein and co-workers described the impact of different ring-sized NHC ligands on the gold(I)-catalysed cyclisation of propargylic amide **10** to give methylene-3-oxazoline **11** (Figure 10a).^[22] As part of this work, DFT was used to study the mechanism of the reaction, to address the role of the counterion in the reaction. It was proposed that the

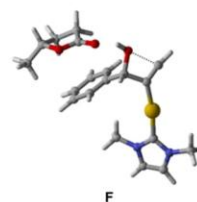


Figure 9. DFT-calculated transition state structure for the Meyer-Schuster rearrangement, in which γ -valerolactone is modelled coordinating to the hydroxyl group. Structures reproduced using coordinates located in the original paper's ESI.

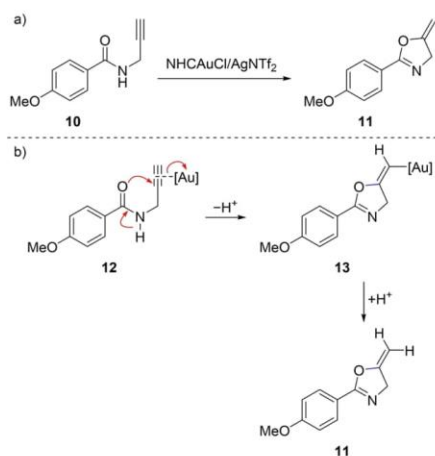


Figure 10. a) Reaction studied by Ma *et al.*,^[22] the cyclisation of propargylic amide **10**, resulting in methylene-3-oxazoline **11**, first reported by Hashmi *et al.* and then used as a standard reaction when comparing different NHC ligands.^[22,23] b) Mechanism proposed by Hashmi *et al.* for the formation of **11**.^[23]

reaction occurs via nucleophilic attack of the amide carbonyl, aided by the lone pair of the adjacent nitrogen (Figure 10b).^[23]

The authors first considered different coordination binding modes, both with and without the anion. The $\eta^2(\pi)$ alkyne gold(I) complex with hydrogen bonding of the triflimide anion (**H**, Figure 11a) was found to be the lowest energy bound complex at +9.6 kcal mol⁻¹ energy higher than the separate species at the SMD(CHCl₃)-PBE0-D3BJ/def2-TZVP,6-311+G(d,p)/PBE0-D3BJ/SDD,6-31G(d) level of theory. Other coordination modes were studied, including *O*-coordinated gold species, with (**I**, Figure 11b) and without deprotonation of the amide nitrogen (**J** and **K**, Figure 11b), however these complexes were much higher in energy.

Considering again the gold(I) alkyne complex with hydrogen bonding anion (**H**), transition states for the possible cyclisations were found (Figure 12). *5-exo-dig* cyclisation (**L**) was calculated to be energetically preferred over *6-endo-dig* cyclisation (**M**) by 4.6 kcal mol⁻¹ (+16.1 vs +20.7 kcal mol⁻¹), which was consistent with the experimentally observed outcome.

When gold(I)-coordination was considered without the anion, the energy of the intermediate was greatly increased at +16.7 kcal mol⁻¹ (**N**, Figure 13). Transition states for the cyclisation of **N** were; however, higher in energy than the equivalent triflimide-coordinated transition states, at +25.5 and +27.2 kcal mol⁻¹ for the *5-exo-* (**O**) and *6-endo-dig* (**P**) cyclisations respectively, strongly suggesting that the triflimide anion does indeed play an active role in the reaction.

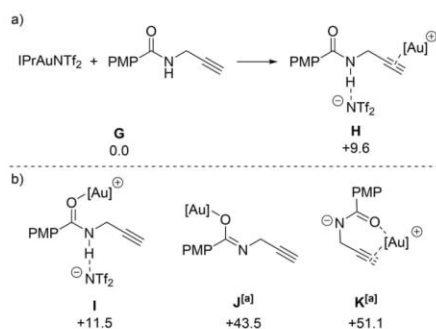


Figure 11. DFT-calculated structures at the SMD(CHCl₃)-PBE0-D3BJ/def2-TZVP,6-311+G(d,p)/PBE0-D3BJ/SDD,6-31G(d) level of theory. Energies are Gibbs energies in kcal mol⁻¹. [Au]=IPrAu⁺. a) Preferred configuration of gold(I)-coordination to **10**. b) Other calculated configurations of higher energy. [a] States resulting from loss of HNTf₂ from **I**.

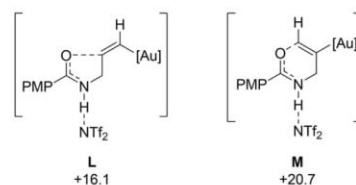


Figure 12. DFT-calculated energies for the transition states of *5-exo-dig* (**L**) and *6-endo-dig* (**M**) cyclisations of **H**. Energies are Gibbs energies at the SMD(CHCl₃)-PBE0-D3BJ/def2-TZVP,6-311+G(d,p)/PBE0-D3BJ/SDD,6-31G(d) level of theory in kcal mol⁻¹ with **G** as the reference point. [Au]=IPrAu⁺. PMP = *p*-methoxyphenyl.

Whilst the cyclised oxazoline intermediate (**Q**, Figure 14a) is calculated to be lower in energy than **H**, the calculated energies when neutral triflimide has dissociated (**R**) are significantly higher at +19 kcal mol⁻¹, prompting further DFT studies on the possible proton-migration processes.

Following reports that water clusters can aid in proton transfer,^[24] the possibility of a water-assisted mechanism was considered for the protodemetalation, however, the calculations predicted this to be higher in energy. Generation of the protonated product **T** and vinyl-gold species **S** by participation of the basic nitrogen of oxazole ring in the product was therefore also considered (Figure 15). Transition state **TS_{OS}** (+10.4 kcal mol⁻¹) was found at a much lower energy than the triflimide-promoted pathway. The transition state of protodemetalation was then calculated as **TS_{SH}** (+13.7 kcal mol⁻¹) resulting in two units of the product **11**. Overall, this process was calculated to be lower in energy than the equivalent triflimide anion-assisted process, with the rate-limiting step

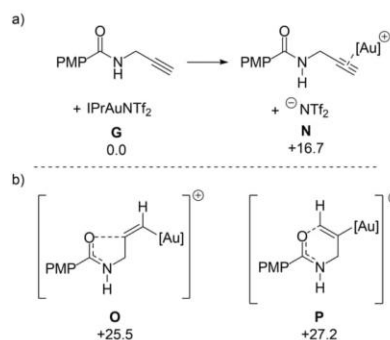


Figure 13. DFT-calculated structures at the SMD(CHCl₃)-PBE0-D3B/def2-TZVP,6-311+G(d,p)//PBE0-D3B/SDD,6-31G(d) level of theory. Energies are Gibbs energies in kcal mol⁻¹. [Au]=IPrAu⁺. a) Ion-separated-coordination of Au(I) to **10**. b) Transition states energies of 5-*exo-dig* (O) and 6-*endo-dig* (P) cyclisations of N.

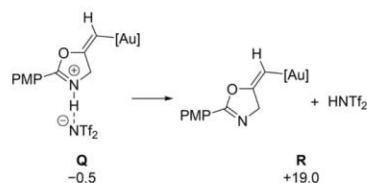


Figure 14. DFT-calculated structures at the SMD(CHCl₃)-PBE0-D3B/def2-TZVP,6-311+G(d,p)//PBE0-D3B/SDD,6-31G(d) level of theory. Energies are Gibbs energies in kcal mol⁻¹. [Au]=IPrAu⁺. Energies of the intermediate gold(I)-oxazoline species, before and after the removal of triflimide.

predicted to be the initial cyclisation (L) at 16.1 kcal mol⁻¹ in energy.

The DFT data enabled a catalytic cycle to be proposed (Figure 16). First, an initiation cycle, in which cyclisation occurs via a 5-*exo-dig* cyclisation (L) promoted by initial coordination of the gold(I) NHC complex to propargylic amide **10**, with hydrogen bonding of the triflimide anion to the amide nitrogen (H). A triflimide-assisted proton-migration then occurs resulting in the product (**11**). After initiation, an iterative cycle is predicted to take place, where the oxazole product (**11**) deprotonates intermediate Q: this was calculated to be a lower energy pathway than deprotonation by NTf₂⁻.

The authors demonstrated that coordination of the anion can be important when discussing reaction mechanisms, potentially changing the viability of a predicted mechanism. In this reaction the product itself is predicted to take part in the catalysis. Product participation in this manner could have a pronounced effect on the observed kinetics, and without

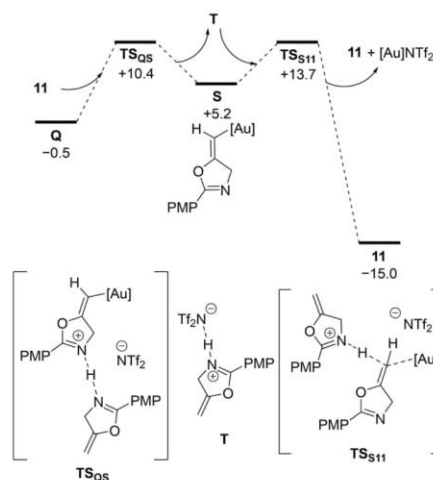


Figure 15. DFT-calculated pathway for oxazoline-assisted proton-migration of Q. Energies are Gibbs energies at the SMD(CHCl₃)-PBE0-D3B/def2-TZVP,6-311+G(d,p)//PBE0-D3B/SDD,6-31G(d) level of theory in kcal mol⁻¹. [Au]=IPrAu⁺.

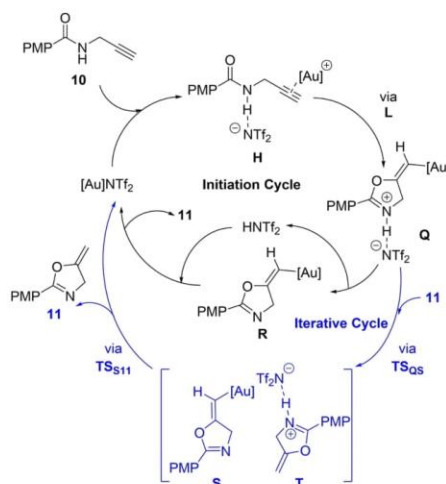


Figure 16. Catalytic cycle proposed by Ma *et al.* for propargylic amide cyclisation. The anion plays a role in the reaction process throughout. Reproduced with permission from ref [22]. Copyright 2022 Royal Society of Chemistry.

considering the anion effects, the rationale for this could be missed.

The handful of papers discussed here only shows a small subset of the studies within the field of gold(I) chemistry where anion effects have been studied by computational chemistry. It is hoped that highlighting these recent examples brings to light the importance of considering the anion when beginning to study a process theoretically. Ligand, substrate, anion, and solvent all should be considered, with the studies herein demonstrating that ion pairing is more notable in less polar solvents, with coordination then present often in areas of greater positive charge density, and through hydrogen bonding of substrates.

3. Using DFT to Explore the Regioselectivity and Coordination in Gold(I) Catalysis

DFT has been used extensively to provide evidence and understanding to observed experimental results, with a view that by understanding reaction mechanism, then improvements or further development can then take place. This has been useful in gold chemistry, in the study of reaction regioselectivity, due to either carbon atom of the gold-coordinated unsaturated C–C bond being potential options for nucleophilic attack.

Amongst the simplest gold-catalysed reactions of alkenes and alkynes, are their hydration and hydroamination reactions, which typically progress via Markovnikov addition. However, methodologies are being published which accomplish the less-common anti-Markovnikov addition.

Timmerman *et al.* reported a gold(I)-catalysed hydroamination reaction of alkylidenecyclopropanes **13** (ACP derivatives which resulted in the anti-Markovnikov addition of imidazolidone **14** (Figure 17).^[25] Couce-Rios and co-authors used DFT to explore the origins of the observed regioselectivity.^[26]

First, DFT was used to calculate the energies of the intermediates and transition states for the proposed mechanism, using the $\eta^2(\pi)$ gold(I)-coordinated benzyl-substituted

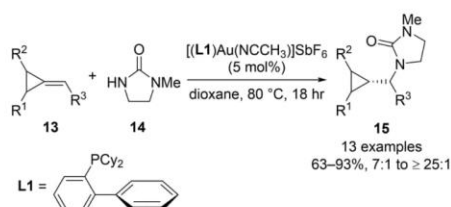


Figure 17. Gold(I)-catalysed hydroamination of ACP derivatives **13** with 1-methyl-imidazolidin-2-one **14** as reported by Timmerman *et al.*^[25]

ACP derivative (**U**) as the reference compound. Energies (calculated at the M06/6-31G(d,p)&SDD(f) level of theory) of +21.7 and +21.0 kcal mol⁻¹, were calculated for the transition states of Markovnikov (**TS_{UW}**) and anti-Markovnikov (**TS_{UV}**) addition respectively (Figure 18).

When considering the relative energy difference between pathways, it is important to note that due to the logarithmic relationship between the calculated energy and both the equilibrium and rate constants, a small difference in energy can contribute to a significant difference in the predicted outcome.^[27] In this instance, whilst the calculated energies of the transition states are similar, and a mixture of products might be predicted, the formation of **15** was seen predominantly via lower energy transition state **TS_{UV}**, highlighting the need to consider both the experiments and calculations together.

The energies for the possible protodemetalation pathways were also calculated, which suggested that the initial nucleophilic addition was the rate-determining step. The height of the energy barriers is consistent with the elevated temperature required for these reactions to occur.

Next, alkenes bearing various substituents were considered to compare the geometries of the $\eta^2(\pi)$ -alkene gold(I) complex and the transition state energies for Markovnikov and anti-Markovnikov addition (Table 2). These data were then compared to the experimental results where available. It should be noted that all the calculations use CyJohnPhos (**L1**) as the ligand, however the experimental results of ethylene, styrene and isobutene were only available for TrixiePhos (**L2**).^[28] Most of the experimental results match the predicted outcomes.^[25,28] Alkenes **16a**, **16e**, **16g** and **16h** proceeded with Markovnikov addition, and alkene **16f** is the previously discussed benzyl-substituted ACP derivative, which occurred

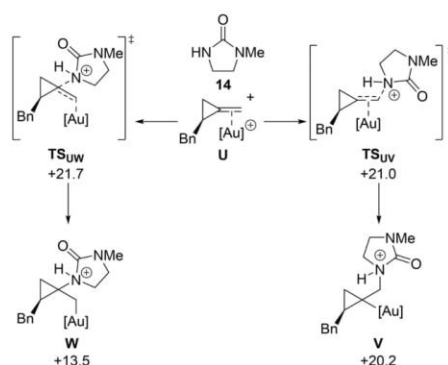


Figure 18. DFT-calculated transition state energies for Markovnikov and anti-Markovnikov addition into gold(I)-coordinated ACP **U**. Energies are Gibbs energies in kcal mol⁻¹ at 298 K, calculated at the M06/6-31G(d,p)&SDD(f) level of theory with SMD solvent correction in 1,4-dioxane.

Table 2. Transition state energies for Markovnikov (ΔG_M^\ddagger) and anti-Markovnikov (ΔG_{AM}^\ddagger) addition of **14** catalysed by (L1)Au⁺, and geometrical parameters for the initial $\eta^2(\pi)$ -alkene gold(I) complexes. All data were computed at the M06/6-31G(d,p)&SDD(f) level of theory.

Substrate	ΔG_M^\ddagger / kcal mol ⁻¹	ΔG_{AM}^\ddagger / kcal mol ⁻¹	$\Delta\Delta G^\ddagger$ / kcal mol ⁻¹	$d_1 - d_2$ / Å	17:18 Ratio
16a	+15.4	–	–	–0.002	100:0 ^[c]
16b	+23.2	+8.1	+15.1	0.007	–
16c	+19.0	+10.6	+8.4	–0.002	–
16d	+23.5	+16.1	+7.4	–0.105	–
16e	+21.4	+19.4	+2.0	–0.154	100:0 ^[c]
16f	+21.7	+21.0	+0.7	–0.119	0:100 ^[b]
16g	+20.4	+27.4	–7.0	–0.257	100:0 ^[c]
16h	+20.0	+27.3	–7.3	–0.256	100:0 ^[d]

[a] $d_1 = \text{Au}-\text{C}_{\text{terminal}}$ distance; $d_2 = \text{Au}-\text{C}_{\text{internal}}$ distance. [b] Conditions 1 were used. [c] Conditions 2 were used. [d] Conditions 1 were used at 100 °C.

with anti-Markovnikov addition. Styrene (**16e**) was the only example which the experimental outcome doesn't match the predicted outcome.

A trend was observed in which the energy difference between the Markovnikov and anti-Markovnikov addition could be related to the degree that the gold(I) catalyst has slipped across the alkene (Figure 19). Additional work by the group showed that strain from the disfavoured addition was significantly higher than the favoured addition, which further highlighted the importance of the initial geometry of the gold-coordinated alkene.

A similar substituent-directed effect was studied in the gold(I)-catalysed cyclisation of β -yne furans, reported by Dong *et al.*, as a method to make cyclohexafuran and cycloheptafuran derivatives.^[29] The cycloheptafuran skeleton is found in natural products,^[30] but their synthesis is challenging using conventional methods.

With β -yne furans (*e.g.* **19**), nucleophilic attack can take place into the $\eta^2(\pi)$ -alkyne gold(I)-coordinated complex (Figure 20), either through a 6-*exo* cyclisation (**19**→**22**) resulting in cyclohexafuran species **23**, or alternatively, attack can occur on the other carbon via a 7-*endo* cyclisation (**19**→**20**), giving cycloheptafuran derivatives **21**.

Typically, cyclohexafuran analogues are formed when reacting β -yne furans with transition metal catalysts (Figure 21a).^[31] However, it was proposed by Dong *et al.* that tuning the electronic properties of the alkyne may allow for better control of the regioselectivity. Using internal alkyne **26**, it was possible to optimise for the formation of the desired cycloheptafuran product **27** using gold(I) catalysis (Figure 21b).

To explore the mechanism using DFT (at the B3LYP/SDD-6-31G(d) level of theory), transition states for the 7-*endo* (TS_{XZ}) and 6-*exo* (TS_{XZ}) pathways were calculated (Figure 22), from $\eta^2(\pi)$ -alkyne gold(I) complex **X**, for different

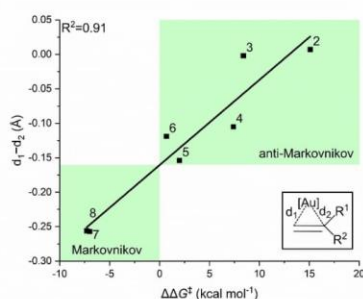


Figure 19. Plot of the difference in transition state energy between Markovnikov and anti-Markovnikov addition ($\Delta\Delta G^\ddagger$) against the difference in distance of the gold centre from the terminal (d_1) and internal (d_2) carbons. Values refer to the entries in Table 2. Adapted with permission from ref [26]. Copyright 2019 American Chemical Society.

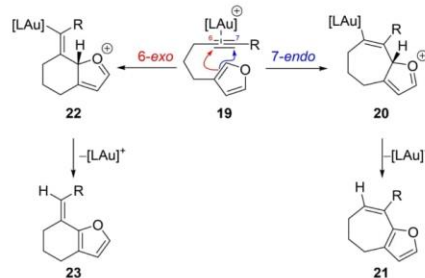


Figure 20. Proposed 6-*exo* and 7-*endo* cyclisations of β -yne furan derivative **19**.

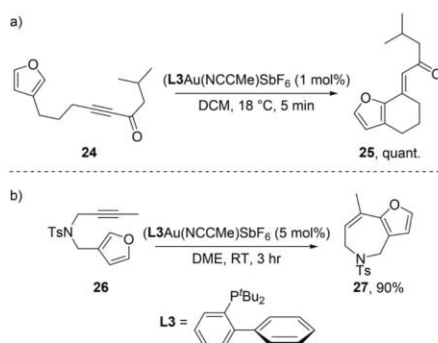


Figure 21. Synthesis of cyclohexafuran **20** as reported by Menon *et al.* in their total synthesis of furansesquiterpenes.^[31d] b) Optimised conditions for the 7-*endo*-dig cyclisation of β -yne furan **21**.

substituents. This was successful at matching the experimental outcomes, with the terminal alkyne favouring the 6-*exo* transition state by 2.3 kcal mol⁻¹, and the methyl- and phenyl-substituted pathways favouring the 7-*endo* transition state by 3.1 and 4.8 kcal mol⁻¹ respectively.

To determine the reasons between the difference in reaction outcome, natural population analysis (NPA) was used to compare the charges of the alkyne carbon atoms. This demonstrated that the different alkyne substituents affected the charge density of the alkyne, with nucleophilic attack then occurring onto the most 'positively' charged carbon of the alkyne. This then highlighted further ways the scope of the reaction could be expanded (Figure 23).

Firstly, introduction of a ketone on the tether to make an internal ynone moiety **28** still resulted in formation of the cycloheptafuran product **29**, which was proposed to be due to the synergistic effects of the substituents. Secondly, the calculations highlighted that substituting the alkyne with an

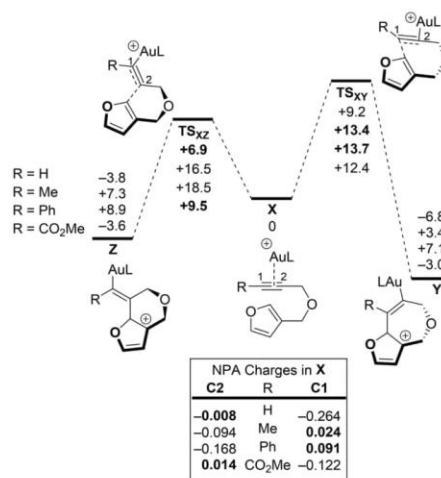


Figure 22. DFT-calculated energies for 6-*exo* and 7-*endo* cyclisation of β -yne furans. Energies are Gibbs energies at 298 K in kcal mol⁻¹ at the B3LYP/SDD-6-31G(d) level of theory. Calculated NPA charges for the alkyne carbons of **X** are given. L=PMe₃. Reproduced with permission from ref [29]. Copyright 2013 Wiley-VCH.

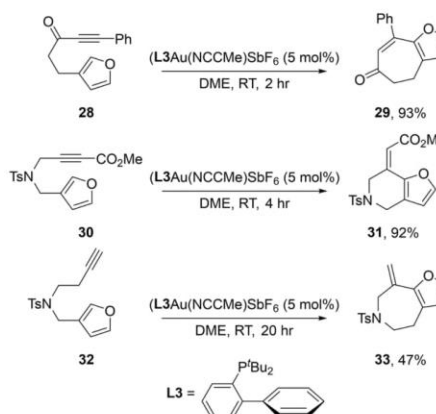


Figure 23. Additional reactions to explore the substrate scope following the DFT analysis.

ester functionality (**30**) would promote formation of the 6-*exo* products, which was observed experimentally (**31**). Finally, by extending the tether (**32**), 7-*exo* cyclisation could be achieved

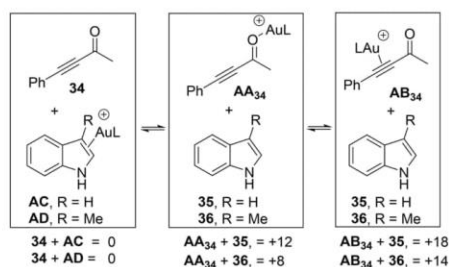


Figure 24. Energies are Gibbs energies at 298.15 K at the D3(BJ)-PBE0/def2-TZVPP//BP86/SV(P) level of theory with COSMO solvent correction in toluene. Energies are in kJ mol^{-1} . L=PPh₃.

with terminal alkynes (33). This highlights well the power of DFT to inform new directions for synthesis.

In our own groups, we have used DFT to explore the selectivity of gold(I) coordination in a study exploring the formation of 3-vinylindole species using alkynes with electron-withdrawing functionalities.^[32] First, the relative energy difference between coordination to indoles (35 and 36) and ynone (34) species were compared (Figure 24). Coordination to both the ketone (AA) and alkyne (AB) of the ynone was considered. It was found that the indole gold(I)-coordinated species (AC and AD) was calculated to be the lowest energy-binding mode (at the D3(BJ)-PBE0/def2-TZVPP//BP86/SV(P) level of theory), followed by $\eta^1(O)$ -binding (+12 and +8 kJ mol^{-1} for indole and skatole respectively), with $\eta^2(\pi)$ -binding being the highest (+18 and +14 kJ mol^{-1} for indole 35 and skatole 36 respectively).

Due to the ability of the gold cation to coordinate to either the carbonyl or the alkyne, further calculations were performed to compare the affinity of the gold in a range of carbonyl-substituted alkynes (Figure 25a). Esters and amides were considered, both with and without a strong electron-donating substituent on the aryl group. ³¹P{¹H} NMR spectra were then recorded with a 2:1 substrate to gold ratio (Figure 25b), and by comparing the chemical shifts observed with two reference species (DMF and an unsymmetrical bis-aryl alkyne, Figure 25c), conclusions were able to be made regarding the assignments of the resonances.

Coordination to the carbonyl was predicted to be favoured with amide 38, and the resonance observed was consistent with the DMF reference (*e.g.* spectra (7) and (3)), at δ_p 29.7. Esters (40 and 41) were predicted to favour alkyne coordination and whilst ester 40 showed no evidence of coordination in NMR spectrum (5), a resonance at δ_p 35.8 was observed with the ester 41, bearing an electron-donating 4-NMe₂-substituent, consistent with coordination to the alkyne (*e.g.* spectra (4) and (2)). 4-NMe₂-substituted amide 39 was predicted to show coordination to both the carbonyl and alkyne, with both resonances indeed observed (spectrum (6)).

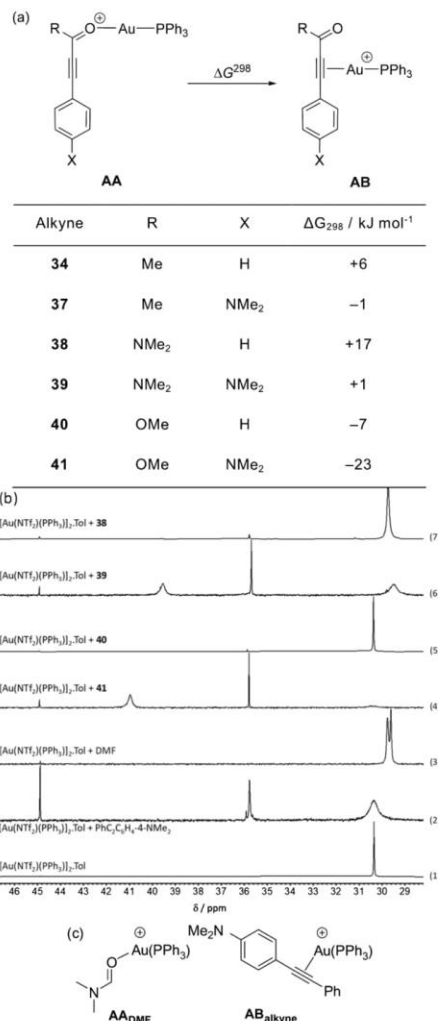


Figure 25. a) Isodesmic reaction used to compare $\eta^1(O)$ -binding and $\eta^2(\pi)$ -binding of substituted alkynes. Energies are Gibbs energies at 298.15 K at the in D3(BJ)-PBE0/def2-TZVPP//BP86/SV(P) level of theory with COSMO solvent correction in CH₂Cl₂. b) ³¹P{¹H} NMR spectra in CD₂Cl₂ showing the interaction between [(PPh₃)AuNTf₂]₂.Tol and different substrates at a 2:1 substrate to gold ratio. c) Proposed $\eta^1(O)$ -binding and $\eta^2(\pi)$ -binding for DMF and PhC₂C₆H₄-4NMe₂ respectively.

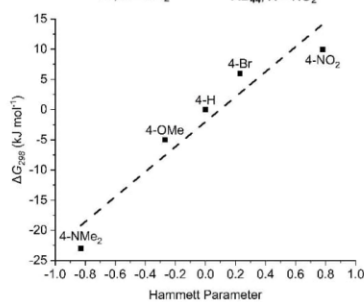
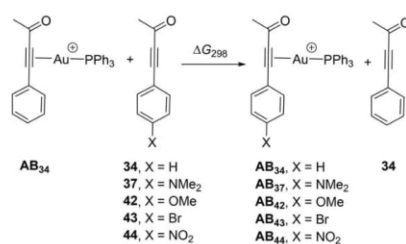


Figure 26. Isodesmic reaction used to calculate gold affinity for substituted alkynes. Energies are Gibbs energies at 298.15 K at the D3(BJ)–PBE0/def2-TZVPP//BP86/SV(P) level of theory with COSMO solvent correction in CH_2Cl_2 (top). Linear free energy relationship between the calculated change in energy and the Hammett parameter, σ_p . Dashed line shows the fit to a least mean squares linear regression ($R^2=0.92$) (bottom).

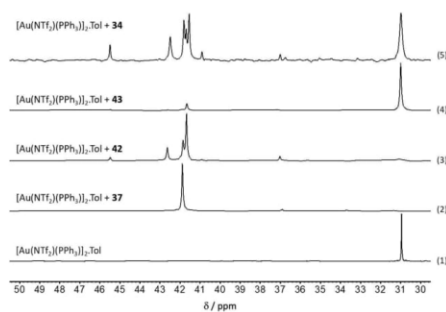


Figure 27. $^{31}P\{^1H\}$ NMR spectra in CD_2Cl_2 showing the interaction between $[(PPh_3)AuNTf_2]_2 \cdot Tol$ and different ynones at a 10:1 substrate to gold ratio.

The effects of substitution on the aryl group were also considered, and the isodesmic reaction between $\eta^2(\pi)$ -coordinated alkyne AB_{34} and uncoordinated alkynes with both electron-donating and withdrawing groups were considered. A

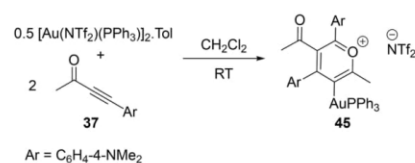


Figure 28. Formation of pyrylium salt **45** from the dimerisation of ynone **37**.

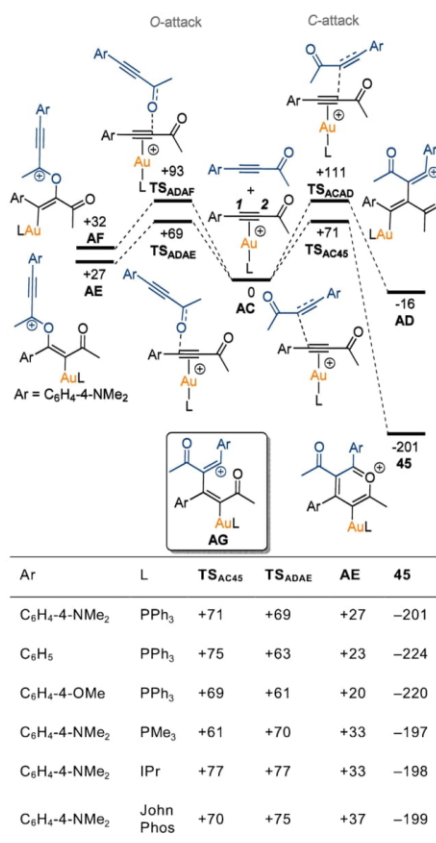
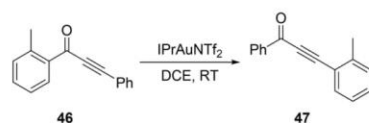


Figure 29. DFT-calculated pathways of gold-mediated ynone dimerisation. Energies are Gibbs energies at 298.15 K in $kJ\ mol^{-1}$ at the D3(BJ)–PBE0/def2-TZVPP//BP86/SV(P) level of theory with solvent correction in CH_2Cl_2 .

Figure 30. Gold-catalysed transposition reaction of ynone **46**.

Hammett plot of the energy difference demonstrated a strong substituent effect on the nature of the equilibrium (Figure 26). $^{31}\text{P}\{^1\text{H}\}$ NMR spectra were recorded with a large excess of substrate (10:1 substrate to gold ratio, Figure 27) which supported the DFT-predicted enhanced gold affinity for electron-rich alkynes. The NMR spectra with 4-Br substituted ynone **43** and unsubstituted ynone **34** showed a large amount of remaining uncoordinated catalyst (e.g. spectra (4), (5) and (1)). Ynone **34** (spectrum (5)) did show a series of new resonances in the region between δ_{p} 40 and 45. The 4-OMe substituted ynone **42** showed full coordination of the gold catalyst but as before a complex set of resonances were again observed (spectrum (3)).

Considering the NMR spectrum of 4-NMe₂-substituted ynone **37** (spectrum (2)), only a single sharp resonance at δ_{p} 41.9 was present, inconsistent with either carbonyl or alkyne coordination. Through further NMR and mass spectroscopy studies, this was assigned as a gold-pyrylium complex (**45**), arising from the dimerisation of the ynone (Figure 28).

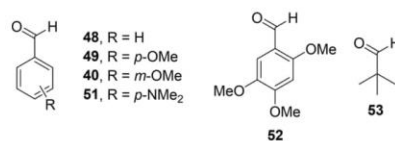


Figure 32. Aldehydes used in the further studies.

DFT was used to examine the dimerisation mechanism in detail (Figure 29). It was proposed that dimerisation occurred via C-attack of the alkyne of one ynone into the $\eta^2(\pi)$ -coordinated alkyne of another ynone (TS_{AC48}). The calculated transition state energy for this was +71 kJ mol⁻¹ from reference state **AC**. This would then be followed by an intramolecular O-cyclisation from intermediate **AG** to afford the gold-pyrylium complex **45**, with an overall energy of -201 kJ mol⁻¹ for the process. A structure for intermediate carbocation **AG** couldn't be located, suggesting that either there is a bifurcated pathway from TS_{AC45} to the pyrylium complex, or that **AG** sits in a shallow minimum.

To further explore the dimerisation process, the transition state for C-attack onto the C2 carbon of the alkyne was found (TS_{AC4d}) which was calculated to be much higher in energy (+111 kJ mol⁻¹). Additionally, two transition states were located for oxo-nucleophilic attack of the carbonyl at +69 (TS_{ADAE}) and +93 kJ mol⁻¹ (TS_{ADAF}). It was proposed that the

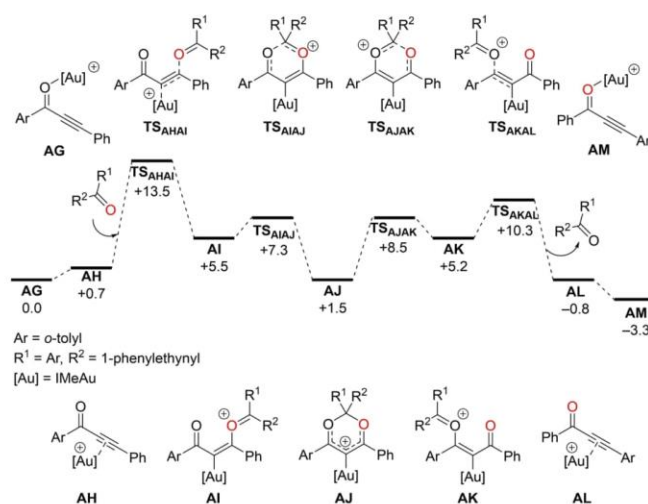


Figure 31. DFT-calculated energies for the gold-catalysed 1,3 transposition of ynone **46**. Energies are Gibbs energies at the TPSS-D3/def2-TZVP//TPSS-D3/def2-SVP level of theory in kcal mol⁻¹ with COSMO solvent correction in CH₂Cl₂. Reproduced with permission from ref [33]. Copyright 2019 American Chemical Society.

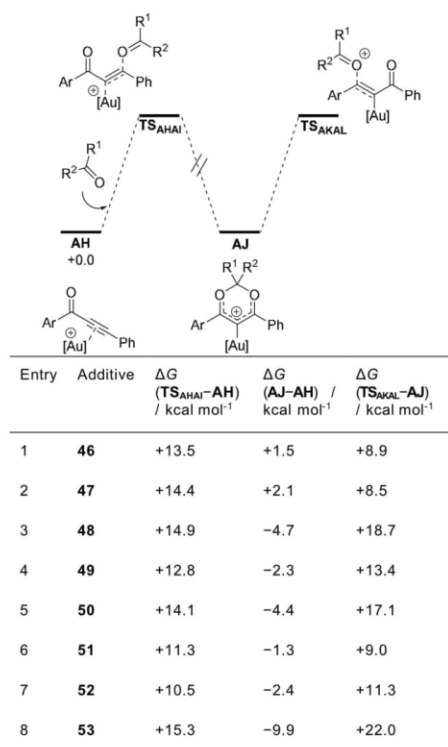


Figure 33. DFT-calculated energies for the key transition states and intermediates of the gold-catalyzed transposition reaction of ynone AH with different additives. Energies are Gibbs energies at the TPSS-D3/def2-TZVP//TPSS-D3/def2-SVP level of theory with COSMO solvent correction in CH₂Cl₂. Reproduced with permission from ref [33]. Copyright 2019 American Chemical Society.

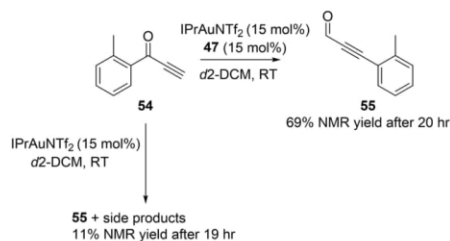


Figure 34. Transposition reaction using challenging substrate **54**.

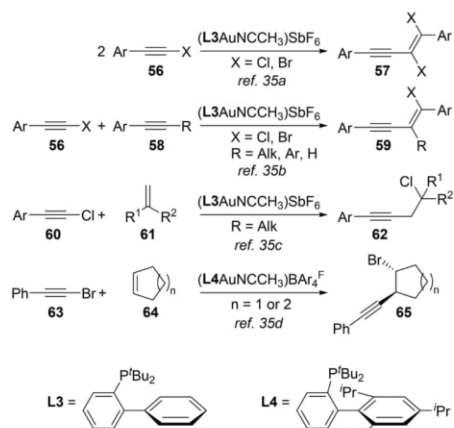


Figure 35. Gold(I)-catalyzed 1,2-haloalkynylation reactions of haloalkynes, alkynes and alkenes.

strong thermodynamic driving force for the formation of the pyrylium complex causes its irreversible formation.

Additional calculations were done to compare the energies of the transition states and intermediates for the lowest energy additions of both *C*- and *O*-attack, for both the unsubstituted (**34**) and 4-OMe-substituted ynone (**42**). In contrast to the 4-NMe₂-substituted ynone, *O*-attack was calculated to be the lowest energy transition state for both substrates, and it was proposed that the lack of selectivity observed in the NMR spectra (Figure 27) discussed originated from side-reactions of **AE**. The effect of the ligand was also explored; however, this was predicted to have little to no effect on the experimental outcomes.

In 2018, Aikonen and co-workers studied the gold-catalyzed 1,3-*O*-transposition of ynone (Figure 30).^[33] Initial kinetic studies highlighted that there was an order in **46** of 1.5 and a small order of 0.15 for **47**, thus two ynone molecules are required in the rate-determining step.

An intermolecular mechanism was therefore proposed, with the energies calculated using DFT (at the TPSS-D3/def2-TZVP//TPSS-D3/def2-SVP level of theory, Figure 31), in which *O*-attack of the carbonyl of one ynone, into the η²(π)-coordinated alkyne of another ynone occurs with a calculated energy of +13.5 kcal mol⁻¹ (TS_{AHAI}), followed by a low energy transition state of +7.3 kcal mol⁻¹ for intramolecular cyclisation (TS_{AIAI}) to form cyclic acetal complex **AJ**. This process then happens in reverse, with the overall reaction yielding an unchanged ynone, and one in which the position of the carbonyl has changed.

It was noted that the carbonyl of the uncoordinated ynone acts as a nucleophile, so studies were performed to see if using an electron-rich aldehyde can increase the rate of reaction. A

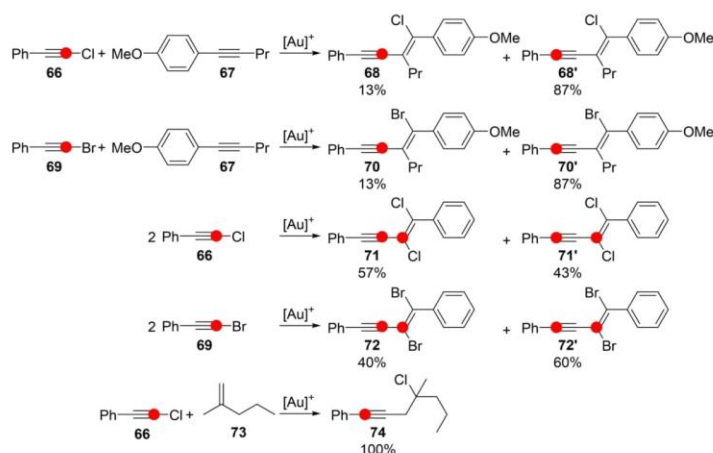


Figure 36. ^{13}C -labelling experiments of 1,2-haloalkynylation reactions. The red circled atoms denote ^{13}C -labelled atoms. $[\text{Au}]^+ = (\text{JohnPhosAuNCMe})^+$.

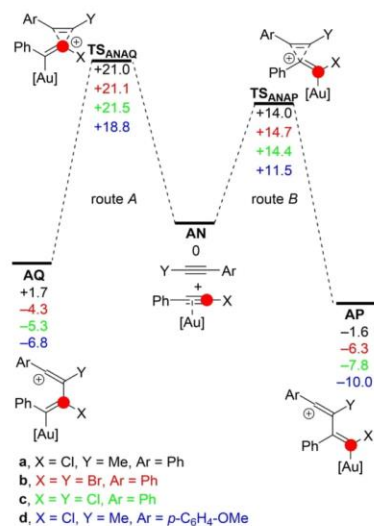


Figure 37. DFT-calculated energies for the initial nucleophilic attack in gold(I)-coordinated alkyne. Energies are Gibbs energies in kcal mol⁻¹ at the B3LYP-D3B//6-311++G(d,p),def2TZVP//B3LYP-D3B//6-31G(d),def2-TZVP level of theory with SMD solvent correction in DCE. $[\text{Au}] = \text{JohnPhosAu}^+$.

range of substituted aldehydes (Figure 32) were tested experimentally, and it was shown that the aldehyde did have a marked effect on the reaction rate, with benzaldehydes bearing electron-donating functionalities in conjugation with the aldehyde showing the greatest increase in reaction rate.

The DFT-calculated energies of the highest transition state barriers (TS_{AHAI} and TS_{AKAL}) were compared to the $\eta^2(\pi)$ -coordinated alkyne **AH** and the cyclic acetal complex **AJ**, for the different additives (Figure 33). This showed a difference in the transition state energies that correlated with the experimental rate differences, with aldehyde **52** showing the largest energy decrease for transition state TS_{AHAI} .

Furthermore, the energy of the transition state for loss of aldehyde (TS_{AKAL}), was calculated to be higher when pivaldehyde **53** was used (+22 kcal mol⁻¹) suggesting a greater kinetic stability for the cyclic acetal intermediate. When the transposition reaction was done with **53** at 15 °C, the characterisation of the cyclic acetal intermediate was possible by recording ¹H and 2D NMR spectra at 15 °C and 0 °C respectively.

Additionally, using this improved methodology allowed for a challenging transposition reaction with terminal alkyne **54** (Figure 34). A marked improvement in the NMR yield of **55** was observed, from 11% to 69%, with fewer side products.

Recent work published by Kreuzahler and Haberhauer,^[34] explored the mechanism of the gold(I)-catalysed 1,2-haloalkynylation reactions of haloalkynes,^[35a] alkynes^[35b] and alkenes^[35c,d] (Figure 35) using DFT and ^{13}C -labelling, to compare previously proposed mechanisms.

^{13}C -labelling experiments (Figure 36) determined that in the 1,2-haloalkynylation of internal alkyne **67**, the ^{13}C -labelled

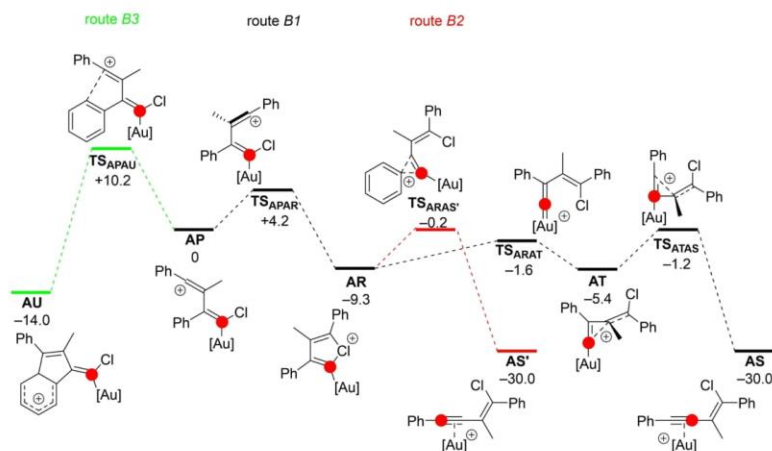


Figure 38. DFT-calculated energies of possible reaction routes from **AP**. Energies are Gibbs energies in kcal mol⁻¹ at the B3LYP-D3BJ//6-311++G(d,p),def2TZVP//B3LYP-D3BJ/6-31G(d),def2-TZVP level of theory with SMD solvent correction in DCE. [Au] = JohnPhosAu⁺.

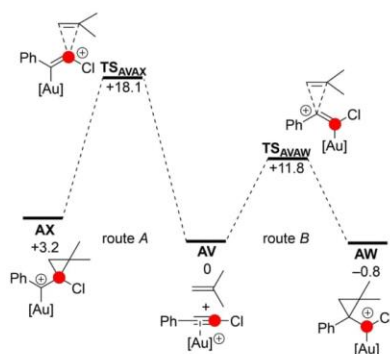


Figure 39. DFT-calculated energies for the initial nucleophilic attack in gold(I)-coordinated alkyne with isobutene. Energies are Gibbs energies in kcal mol⁻¹ at the B3LYP-D3BJ//6-311++G(d,p),def2TZVP//B3LYP-D3BJ/6-31G(d),def2-TZVP level of theory with SMD solvent correction in DCE. [Au] = JohnPhosAu⁺.

atom was heavily biased to be closest to the aryl group in both alkyne products **68** (with chlorophenylacetylene **66**) and **70** (with bromophenylacetylene **69**). Further work which studied the dimerisation reactions of **66** and **69** showed a much less biased distribution of ¹³C-labelled atoms, and the 1,2-haloalkylation reaction with alkene **73** showed a single product (**74**). It was proposed that the selectivity was determined during the initial step and the observed distribution was related to the relative transition state energies.

Initially, the energies of the transition states from both sites of possible nucleophilic attack of an alkyne into the η²(π)-alkyne gold(I) complex were calculated (Figure 37). A range of alkynes were considered and, in each case, route B was significantly lower in energy than route A (7.0–7.4 kcal mol⁻¹), corresponding to preferential attack adjacent to the aryl group of the gold(I)-coordinated alkyne (TS_{ANAP}). Due to the large difference in energies between the two transition states, only a single product isomer of **68**, **70**, **71** and **72** would be expected, if the initial nucleophilic step was key as initially proposed, therefore, the reactivity of carbocation **AP** and **AQ** was considered. Herein only carbocation **AP**, from the lowest energy pathway will be discussed.

Considering vinyl cation **AP** (Figure 38), a transition state for the formation of bicyclic indene complex **AU** was found, however this pathway was predicted to be 8.3 kcal mol⁻¹ in energy higher than the formation of chloronium complex **AR**. This complex can then form enyne **AS*** via direct phenyl migration TS_{ARAS*}, or alternatively, via unusual cyclopropenylmethyl cation **AT** (discussed further in the paper), which facilitates an alkyl-migration via transition state TS_{ATAS} to also yield enyne **AS**, with the ¹³C-labelled carbon in a different position. These two pathways are predicted to differ only by an energy of 1.0 kcal mol⁻¹ and therefore both pathways could be expected to be followed. It should be highlighted here that no direct experimental outcome can be compared as 1-phenyl-1-propyne was used as a model substrate.

A similar series of calculations were performed for the addition of isobutene into chlorophenylacetylene **66**. Again, both possible transition states were considered for the initial

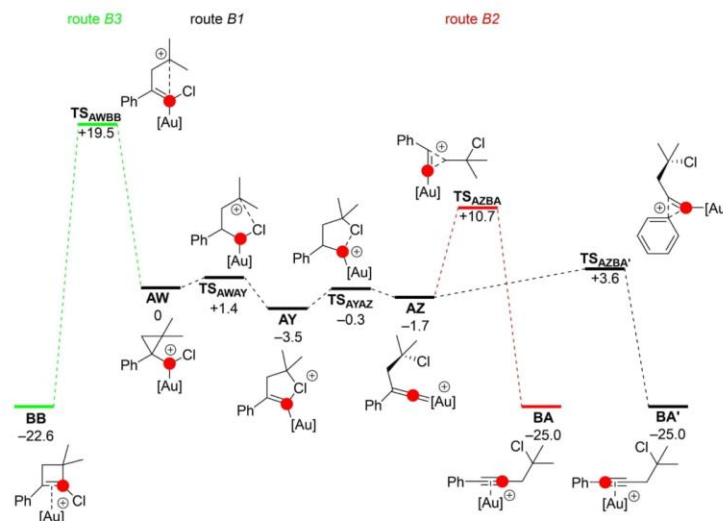


Figure 40. DFT-calculated energies of possible reaction routes from **AW**. Energies are Gibbs energies in kcal mol⁻¹ at the B3LYP-D3BJ//6-311++G(d,p),def2TZVP//B3LYP-D3BJ/6-31C(d),def2-TZVP level of theory with SMD solvent correction in DCE. [Au]=JohnPhosAu⁺.

nucleophilic attack in to the $\eta^2(\pi)$ -alkyne gold(I)-coordinated complex (Figure 39), with addition into the alkyne directly next to the aryl group predicted to be favoured by 6.3 kcal mol⁻¹ via transition state **TS_{AWAW}**. The authors considered the reactivity of carbocation **AW** and **AX**, however, only carbocation **AW**, from the lowest energy pathway will be discussed here.

The fate of carbocation **AW** was considered (Figure 40). A transition state for a cyclisation was found (**TS_{AWBB}**) but this was calculated to be 18.1 kcal mol⁻¹ higher in energy than the transition state for chlorine migration (**TS_{AWAY}**). The resulting chloronium cation (**AY**) can then further migrate to gold(I)-vinylidene complex **AZ** via low-lying transition state **TS_{AYAZ}** (-0.3 kcal mol⁻¹ from carbocation **AY**). From vinylidene complex **AZ**, either an aryl (**TS_{AZBA'}**) or alkyl (**TS_{AZBA}**) migration can take place, but the transition state energy for aryl migration is lower by 7.1 kcal mol⁻¹, so it was proposed that this was the only accessible pathway. This results in alkyne product **BA'** which matches the experimentally observed position of the ¹³C-labelled atom.

With the key transition states that control the position of ¹³C-labelled atom of the haloalkynylation reaction now known, substituent effects were then considered (Figure 41). The transition states **TS_{ARAS-d}** and **TS_{ATAS-d}** were found to only have a 0.6 kcal mol⁻¹ difference in energy when the *p*-methoxy-substituted alkyne (**d** in Figure 41) was investigated. This alkyne was selected as an analogue of **67** to directly compare the experimental outcome (Figure 36) more accurately. The

gold(I)-catalysed dimerisation of chlorophenylacetylene **66** was considered, and a 1.9 kcal mol⁻¹ energy difference between routes B2 and B1, in favour of route B1, was found. This matches the experimentally observed outcome for the ¹³C-labelled position, albeit slightly, with 57% of β -aryl labelled product **72** formed. When the dimerisation of bromophenylacetylene **69** was considered, route B1 was again predicted to be lower in energy by 2.4 kcal mol⁻¹. Whilst it might be expected that experimentally the ratio of β -aryl labelled product **72** should increase, instead a 60% yield of α -aryl labelled product **72'** was achieved, further highlighting that care must be taken when working with calculated relative energy differences which are small, with experimental benchmarking required.

A more significant selectivity effect was observed when comparing the effect of different ligands on the haloalkynylation reaction (Figure 42). Using trimethylphosphine instead of JohnPhos as the gold ligand in the calculations showed a significant change in the predicted selectivity. For the reaction of chlorophenylacetylene **66** and 1-methoxy-4-(prop-1-yn-1-yl)benzene (**d** and **g**), the transition state energy for route B1 using trimethylphosphine (**TS_{ARAT-g}**) was increased to be above that of route B2 (**TS_{ARAS-g}**) by 1.4 kcal mol⁻¹. Experimentally (Figure 43), an increased yield of the α -aryl labelled product **68'** was observed, more closely matching the DFT-predicted outcome.

Furthermore, a similar effect was observed with the dimerisation of chlorophenylacetylene **66**. Instead of an energy

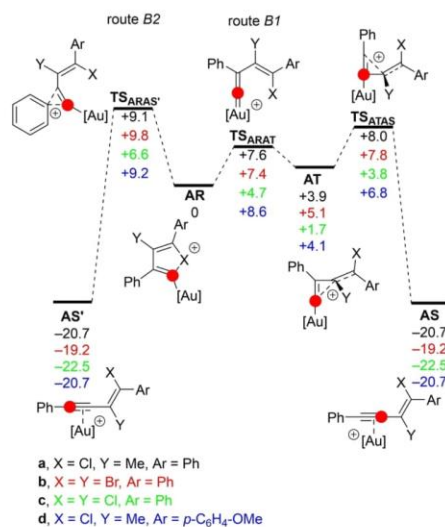


Figure 41. DFT-calculated energies of possible reaction routes from AR, with different reactants. Energies are Gibbs energies in kcal mol⁻¹ at the B3LYP-D3B//6-311 + G(d,p),def2TZVP//B3LYP-D3B//6-31G(d),def2-TZVP level of theory with SMD solvent correction in DCE. [Au] = JohnPhos⁺.

difference of 1.9 kcal mol⁻¹ in favour of route B1 (TS_{ARAT}c) with JohnPhos, the selectivity was reversed and route B2 (TS_{ARAS}f) was favoured by an energy difference of 1.6 kcal mol⁻¹. Experimentally (Figure 43), rather than a 57:43 ratio of products, a 7:93 ratio was observed, with a higher amount of ¹³C-labelling being next to the alkene (71'), matching the DFT-predicted outcome.

4. Summary

Computational chemistry can be an extremely useful tool to better understand reactions when used correctly, with the examples detailed herein demonstrating some such uses in gold(I) catalysis. However, as well as considering the level of theory used, care must also be taken that what is being modelled is an accurate description of the experimental conditions. This includes factors such as using a reasonable conformation of the molecules, factoring solvation into the calculations and whether to include the anion in the reaction.

The question of whether to include the anion from the gold(I) precatalyst in the calculation appears to be best answered on a case-by-case basis. In non-polar solvents, ion separation is not as pronounced, so a consideration of anion effects is particularly important – typically locating this in

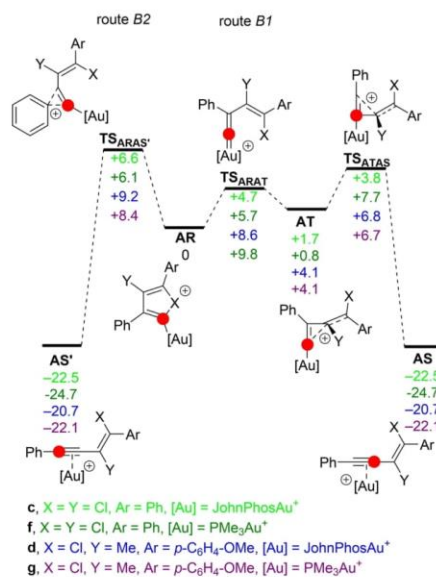


Figure 42. DFT-calculated energies of possible reaction routes from AR, with different ligands. Energies are Gibbs energies in kcal mol⁻¹ at the B3LYP-D3B//6-311 + G(d,p),def2TZVP//B3LYP-D3B//6-31G(d),def2-TZVP level of theory with SMD solvent correction in DCE.

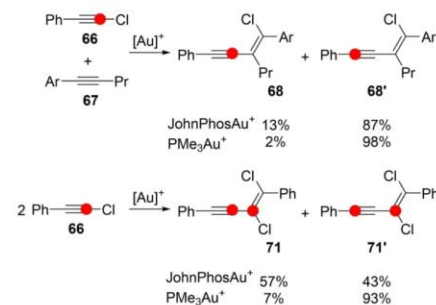


Figure 43. Reactions comparing the ¹³C-labelling of 1,2-haloalkynylation reactions using JohnPhosAu⁺ and PMe₃Au⁺. Ar = C₆H₄-4-OMe.

areas where a positive charge is localised or in positions that hydrogen-bonding can occur. If the reaction modelled directly involves groups where hydrogen-bonding is possible, alcohols or amines for example, then the anion could potentially have a pronounced effect on the observed energies calculated. In

these cases, then it is proposed that the anion should be modelled explicitly, especially if the DFT model does not agree with experiment. In the case of close-contact ion-pairs, then additional evidence may need to be gathered to determine the topology of the ensemble.

Using DFT to explore the selectivity of gold(I)-catalysed reactions is a natural fit due to the often-unsymmetrical nature of the unsaturated C–C bonds which gold chemistry is famed for activating. The regioselectivity can often be accurately predicted by DFT, which can then lead to the development of new substrates or different ligands to see if the selectivity can be improved or altered. Therefore, care must be taken to ensure that over-analysis of small-energy differences does not contradict the experimental outcomes.

Benchmarking the DFT results with comparison to the experiment is key to ensure that the model used is an accurate description. Utilising methods such as NMR spectroscopy and *in situ* IR to monitor reactions in progress could provide the evidence which helps verify the model used. Additionally, exploring the kinetic profile of the reaction and comparing with the calculated transition-state energies is also important.

Acknowledgements

We are grateful to the University of York for PhD studentship to funding to R. G. E. and the EPSRC (EP/H011455/1 and EP/K031589/1) for funding computational equipment used in this study.

References

- [1] For the editorial of a recent *Chemical Reviews* special issue looking at the ‘hot topics’ in gold chemistry, see: A. S. K. Hashmi, *Chem. Rev.* **2021**, *121*, 8309–8310.
- [2] a) L. Ciano, N. Fey, C. J. V. Halliday, J. M. Lynam, L. M. Milner, N. Mistry, N. E. Pridmore, N. S. Townsend, A. C. Whitwood, *Chem. Commun.* **2015**, *51*, 9702–9705; b) N. Hidalgo, J. J. Moreno, M. Pérez-Jiménez, C. Maya, J. López-Serrano, J. Campos, *Organometallics* **2020**, *39*, 2534–2544.
- [3] a) R. L. LaLonde, W. E. Brenzovich Jr., D. Benitez, E. Tkatchouk, K. Kelley, W. A. Goddard III, F. D. Toste, *Chem. Sci.* **2010**, *1*, 226–233; b) Y. Zhu, W. Zhou, E. M. Petryna, B. R. Rogers, C. S. Day, A. C. Jones, *ACS Catal.* **2016**, *6*, 7357–7362.
- [4] a) K. L. Toups, G. T. Liu, R. A. Widenhoefer, *J. Organomet. Chem.* **2009**, *694*, 571–575; b) L. Lempke, T. Fischer, J. Bell, W. Kraus, K. Rurack, N. Krause, *Org. Biomol. Chem.* **2015**, *13*, 3787–3791.
- [5] a) R. Dorel, A. M. Echanvarren, *Chem. Rev.* **2015**, *115*, 9028–9072; b) A. Fürstner, P. W. Davies, *Angew. Chem. Int. Ed.* **2007**, *46*, 3410–3449; *Angew. Chem.* **2007**, *119*, 3478–3519; c) Y. Yamamoto, *J. Org. Chem.* **2007**, *72*, 7817–7831.
- [6] a) D. J. Gorin, B. D. Sherry, F. D. Toste, *Chem. Rev.* **2008**, *108*, 3351–3378; b) Z. Lu, T. Li, S. R. Mudshinge, B. Xu, G. B. Hammond, *Chem. Rev.* **2021**, *121*, 8452–8477.
- [7] For general reviews of DFT use within homogenous transition metal catalysis, see: a) W. M. C. Sameera, F. Maseras, *WIREs Comput. Mol. Sci.* **2012**, *2*, 375–385; b) C. J. Cramer, D. G. Truhlar, *Phys. Chem. Chem. Phys.* **2009**, *11*, 10757–10816; c) P. Sit, L. Zhang, *Heterogeneous Catalysts: Advanced Design, Characterization and Applications, II*, Vol. 1 (Eds: W. Y. Teoh, A. Urakawa, Y. H. Ng, P. Sit), Wiley-VCH, Weinheim **2021**, pp. 405–418.
- [8] a) O. N. Faza, R. A. Rodriguez, C. S. López, *Theor. Chem. Acc.* **2011**, *128*, 647–661; b) P. Nava, D. Hagebaum-Reignier, S. Humbel, *ChemPhysChem* **2012**, *13*, 2090–2096; c) R. Kang, W. Lai, J. Yao, S. Shaik, H. Chen, *J. Chem. Theory Comput.* **2012**, *8*, 3119–3127; d) G. Ciancaleoni, S. Rampino, D. Zuccaccia, F. Tarantelli, P. Belanzoni, L. Belpassi, *J. Chem. Theory Comput.* **2014**, *10*, 1021–1034; e) K. P. Kepp, *J. Phys. Chem. A* **2017**, *121*, 2022–2034.
- [9] a) M. Bandini, A. Bottoni, M. Chiarucci, G. Cera, G. P. Miscione, *J. Am. Chem. Soc.* **2012**, *134*, 20690–20700; b) Y. Li, X. Zhao, *ChemCatChem* **2020**, *12*, 6265–6271; c) Y. Yang, J. Li, R. Zhu, C. Liu, D. Zhang, *ACS Catal.* **2018**, *8*, 9252–9261; d) A. A. Hussein, H. S. Ali, *J. Org. Chem.* **2020**, *85*, 12682–12691; e) L. Zhou, Y. Zhang, R. Fang, L. Yang, *ACS Omega* **2018**, *3*, 9339–9347; f) R. Fang, L. Zhou, P.-C. Tu, A. M. Kirillov, L. Yang, *Organometallics* **2018**, *37*, 1927–1936; g) B. Alcaide, P. Almen-dros, I. Fernández, R. Martín-Montero, F. Martínez-Peña, M. Pilar Ruiz, M. Rosario Torres, *ACS Catal.* **2015**, *5*, 4842–4845; h) Y. Li, J. Zhang, X. Zhao, Y. Wang, *J. Mol. Catal.* **2022**, *519*, 112154.
- [10] a) B. Ranieri, I. Escofet, A. M. Echanvarren, *Org. Biomol. Chem.* **2015**, *13*, 7103–7118; b) Z. Lu, G. B. Hammond, B. Xu, *Acc. Chem. Res.* **2019**, *52*, 1275–1288; c) Z. Lu, J. Han, O. E. Okoromoba, N. Shimizu, H. Amii, C. F. Tormena, G. B. Hammond, B. Xu, *Org. Lett.* **2017**, *19*, 5848–5851.
- [11] a) J. H. Teles, S. Brode, M. Chabanas, *Angew. Chem. Int. Ed.* **1998**, *37*, 1415–1418; *Angew. Chem.* **1998**, *110*, 1475–1478; b) E. Mizushima, T. Hayashi, M. Tanaka, *Org. Lett.* **2003**, *5*, 3349–3352; c) S. Gaillard, J. Bosson, R. S. Ramón, P. Num, A. M. Z. Slawin, S. P. Nolan, *Chem. Eur. J.* **2010**, *16*, 13729–13740.
- [12] Z. Lu, J. Han, G. B. Hammond, B. Xu, *Org. Lett.* **2015**, *17*, 4534–4537.
- [13] D. Wang, R. Cai, S. Sharma, J. Jirak, S. K. Thummanapelli, N. G. Akhmedov, H. Zhang, X. Liu, J. L. Peterson, X. Shi, *J. Am. Chem. Soc.* **2012**, *134*, 9012–9019.
- [14] a) R. S. Paton, F. Maseras, *Org. Lett.* **2009**, *11*, 2237–2240; b) A. S. K. Hashmi, S. Pankajakshan, M. Rudolph, E. Enns, T. Bander, F. Rominger, W. Frey, *Adv. Synth. Catal.* **2009**, *351*, 2855–2875; c) T. Fan, X. Chen, J. Sun, Z. Lin, *Organometallics* **2012**, *31*, 4221–4227; d) J. Jiang, Y. Liu, C. Hou, Y. Li, Z. Luan, C. Zhao, Z. Ke, *Org. Biomol. Chem.* **2016**, *14*, 3558–3563; e) X. Zhang, Z. Geng, *RSC Adv.* **2016**, *6*, 62099–62108; f) B. Herlé, P. M. Holstein, A. M. Echanvarren, *ACS Catal.* **2017**, *7*, 3668–3675; g) C. Wang, Q. Cui, Z. Zhang, Z. Yao, S. Wang, Z. Yu, *Chem. Eur. J.* **2019**, *25*, 9821–9826; h) A. A. Ogunlana, Z. Bao, *Chem. Commun.* **2019**, *55*, 11127–11130.
- [15] a) M. Jia, M. Bandini, *ACS Catal.* **2015**, *5*, 1638–1652; b) J. Schiebl, J. Schulmeister, A. Doppiu, E. Wörner, M. Rudolph, R. Karch, A. S. K. Hashmi, *Adv. Synth. Catal.* **2018**, *360*, 3949–3959; c) A. Zhdanko, M. E. Maier, *ACS Catal.* **2014**, *4*, 2770–2775.
- [16] D. Zuccaccia, L. Belpassi, F. Tarantelli, A. Macchioni, *J. Am. Chem. Soc.* **2009**, *131*, 3170–3171.
- [17] N. Salvi, L. Belpassi, D. Zuccaccia, F. Tarantelli, A. Macchioni, *J. Organomet. Chem.* **2010**, *695*, 2679–2686.
- [18] D. Zuccaccia, L. Belpassi, L. Rocchigiani, F. Tarantelli, A. Macchioni, *Inorg. Chem.* **2010**, *49*, 3080–3082.

- [19] G. Ciancaleoni, L. Biasiolo, G. Bistoni, A. Macchioni, F. Tarantelli, D. Zuccaccia, L. Belpassi, *Organometallics* **2013**, *32*, 4444–4447.
- [20] D. Sorbelli, J. Segato, A. Del Zotto, L. Belpassi, D. Zuccaccia, P. Belanzoni, *Dalton Trans.* **2021**, *50*, 5154–5160.
- [21] a) A. Macchioni, *Chem. Rev.* **2005**, *105*, 2039–2073; b) J. R. Pliego Jr., *Org. Biomol. Chem.* **2021**, *19*, 1900–1914.
- [22] Y. Ma, H. Saqib Ali, A. A. Hussein, *Catal. Sci. Technol.* **2022**, *12*, 674–685.
- [23] a) A. S. K. Hashmi, J. P. Weyrauch, W. Frey, J. W. Bats, *Org. Lett.* **2004**, *6*, 4391–4394; b) A. Cervantes-Reyes, F. Rominger, M. Rudolph, A. S. K. Hashmi, *Chem. Eur. J.* **2019**, *25*, 11745–11757; c) A. Cervantes-Reyes, F. Rominger, M. Rudolph, A. S. K. Hashmi, *Adv. Synth. Catal.* **2020**, *362*, 2523–2533.
- [24] a) C. M. Krauter, A. S. K. Hashmi, M. Pernpointner, *Chem-CatChem* **2010**, *2*, 1226–1230; b) P. M. Stein, M. Rudolph, A. S. K. Hashmi, *Adv. Synth. Catal.* **2021**, *363*, 4264–4271.
- [25] J. C. Timmerman, B. D. Robertson, R. A. Widenhoefer, *Angew. Chem. Int. Ed.* **2015**, *54*, 2251–2254; *Angew. Chem.* **2015**, *127*, 2279–2282.
- [26] A. Couce-Rios, A. Lledós, I. Fernández, G. Ujaque, *ACS Catal.* **2019**, *9*, 848–858.
- [27] N. Fey, J. M. Lynam, *WIREs Comput. Mol. Sci.* **2022**, *12*, e1590.
- [28] Z. Zhang, S. D. Lee, R. A. Widenhoefer, *J. Am. Chem. Soc.* **2009**, *131*, 5372–5373.
- [29] Z. Dong, C.-H. Liu, Y. Wang, M. Lin, Z.-X. Yu, *Angew. Chem. Int. Ed.* **2013**, *52*, 14157–14161; *Angew. Chem.* **2013**, *125*, 14407–14411.
- [30] a) A. D. Patil, A. J. Freyer, L. Killmer, P. Offen, B. Carte, A. J. Jurewicz, R. K. Johnson, *Tetrahedron* **1997**, *53*, 5047–5060; b) F. Marion, D. E. Williams, B. O. Patrick, I. Hollander, R. Mallon, S. C. Kim, D. M. Roll, L. Feldberg, R. Van Soest, R. J. Anderson, *Org. Lett.* **2006**, *8*, 321–324; c) S. Panichanun, I. R. C. Bick, *Tetrahedron* **1984**, *40*, 2685–2689.
- [31] a) S. J. Pastine, S. Won Youn, D. Sames, *Org. Lett.* **2003**, *5*, 1055–1058; b) Y. Yamamoto, S. Kuwabara, Y. Ando, H. Nagata, H. Nishiyama, K. Itoh, *J. Org. Chem.* **2004**, *69*, 6697–6705; c) H. Yamamoto, I. Sasaki, H. Imagawa, M. Nishizawa, *Org. Lett.* **2007**, *9*, 1399–1402; d) R. S. Menon, M. G. Banwell, *Org. Biomol. Chem.* **2010**, *8*, 5483–5485.
- [32] R. G. Epton, W. P. Unsworth, J. M. Lynam, *Organometallics* **2022**, *41*, 497–507.
- [33] S. Aikonen, M. Muuronen, T. Wirtanen, S. Heikkinen, J. Musgreave, J. Burés, J. Helaja, *ACS Catal.* **2018**, *8*, 960–967.
- [34] M. Kreuzahler, G. Haberhauer, *Angew. Chem. Int. Ed.* **2020**, *59*, 17739–17749; *Angew. Chem.* **2020**, *132*, 17892–17902.
- [35] a) M. Kreuzahler, A. Daniels, C. Wölper, G. Haberhauer, *J. Am. Chem. Soc.* **2019**, *141*, 1337–1348; b) M. Kreuzahler, G. Haberhauer, *Angew. Chem. Int. Ed.* **2020**, *59*, 9433–9437; *Angew. Chem.* **2020**, *132*, 9519–9524; c) M. Kreuzahler, G. Haberhauer, *J. Org. Chem.* **2019**, *84*, 8210–8224; d) M. E. de Orbe, M. Zanini, O. Quinero, A. M. Echavarren, *ACS Catal.* **2019**, *9*, 7817–7822.

Manuscript received: May 17, 2022
Revised manuscript received: July 8, 2022
Version of record online: ■■■■■